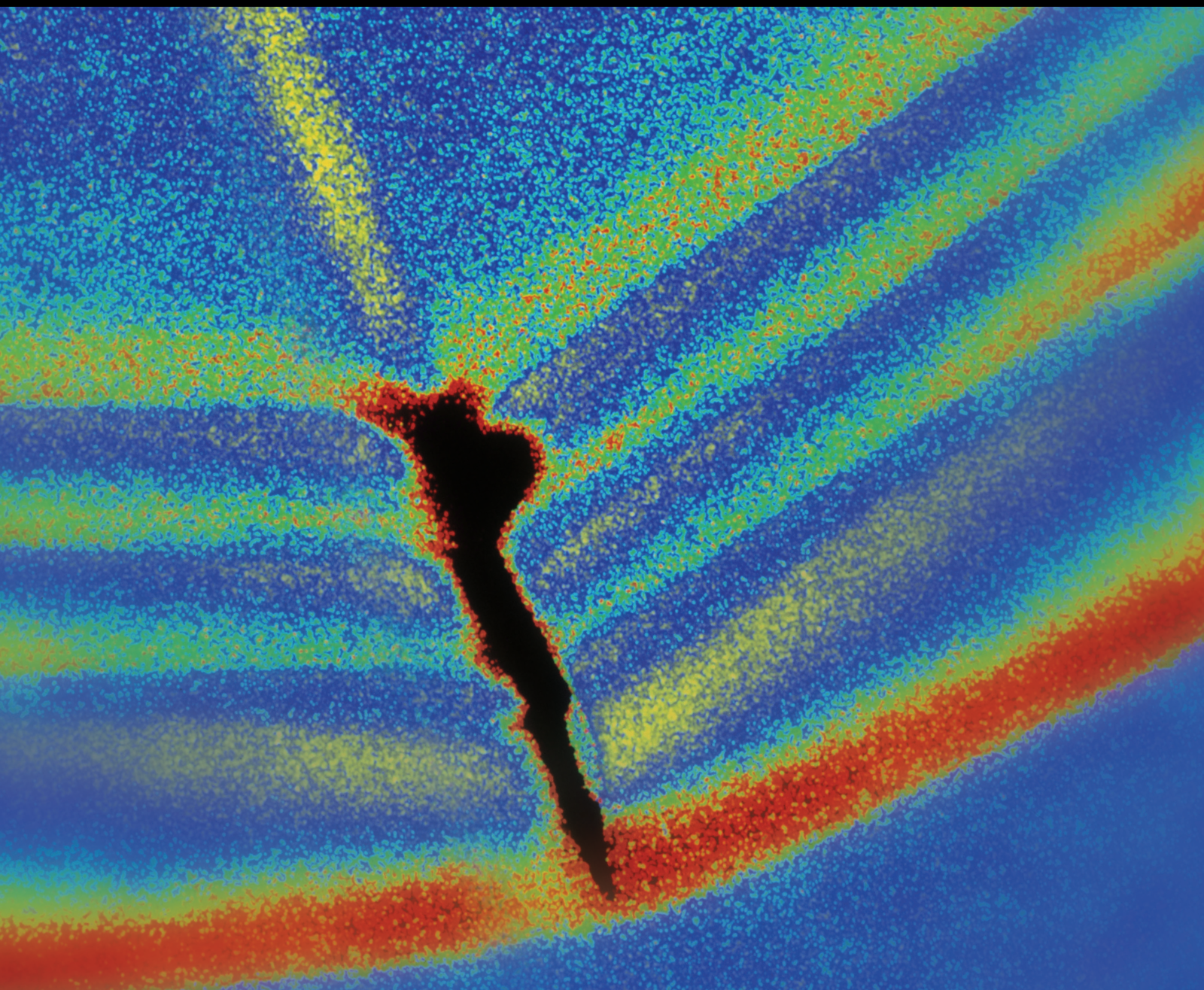


Distributed Sensor Networks for Health Monitoring of Civil Infrastructures

Guest Editors: Ting-Hua Yi, Gangbing Song, Stathis C. Stiros, and Bo Chen





Distributed Sensor Networks for Health Monitoring of Civil Infrastructures

Distributed Sensor Networks for Health Monitoring of Civil Infrastructures

Guest Editors: Ting-Hua Yi, Gangbing Song, Stathis C. Stiros,
and Bo Chen



Copyright © 2015 Hindawi Publishing Corporation. All rights reserved.

This is a special issue published in "Shock and Vibration." All articles are open access articles distributed under the Creative Commons Attribution License, which permits unrestricted use, distribution, and reproduction in any medium, provided the original work is properly cited.

Editor-in-Chief

Mehdi Ahmadian, Virginia Polytechnic Institute and State University, USA

Associate Editors

Brij N. Agrawal, USA
Marco Alfano, Italy
Farbod Alijani, Canada
Sumeet S. Aphale, UK
Hassan Askari, Canada
Matteo Aureli, USA
Ranjan Banerjee, UK
José Villanueva, Spain
Subhamoy Bhattacharya, UK
Ivo Calì, Italy
Antonio Carcaterra, Italy
Dumitru I. Caruntu, USA
Noël Challamel, France
Peng Chen, Japan
Ashwin Chinnayya, France
Giorgio Dalpiaz, Italy
Farhang Daneshmand, Canada
Sergio De Rosa, Italy
Longjun Dong, China
Mohamed El badaoui, France
Mohammad Elahinia, USA
Francesco Franco, Italy
Alessandro Gasparetto, Italy
Anindya Ghoshal, USA

Alicia Gonzalez-Buelga, UK
Hassan Haddadpour, Iran
María I. Herreros, Spain
Hamid Hosseini, Japan
Reza Jazar, Australia
Sakdirat Kaewunruen, UK
Jeong-Hoi Koo, USA
Georges Kouroussis, Belgium
Mickaël Lallart, France
Kenneth J. Loh, USA
Nuno M. Maia, Portugal
Giuseppe C. Marano, Italy
Laurent Mevel, France
Emiliano Mucchi, Italy
Tony Murmu, UK
Sundararajan Natarajan, India
Toshiaki Natsuki, Japan
Miguel Neves, Portugal
Coral Ortiz, Spain
Gyuhae Park, Korea
Evgeny Petrov, UK
Antonina Pirrotta, Italy
Didier Rémond, France
Francesco Ripamonti, Italy

Salvatore Russo, Italy
Edoardo Sabbioni, Italy
Jerzy T. Sawicki, USA
Vadim V. Silberschmidt, UK
Kumar V. Singh, USA
Isabelle Sochet, France
Alba Sofi, Italy
Jussi Sopanen, Finland
Narakorn Srinil, UK
Salvatore Strano, Italy
Chao Tao, China
Mario Terzo, Italy
Tai Thai, Australia
Carlo Trigona, Italy
Federica Tubino, Italy
Nerio Tullini, Italy
Marcello Vanali, Italy
Jörg Wallaschek, Germany
Peijun Xu, USA
Zaili L. Yang, UK
Stana Živanović, UK
Lei Zuo, USA

Contents

Distributed Sensor Networks for Health Monitoring of Civil Infrastructures, Ting-Hua Yi, Gangbing Song, Stathis C. Stiros, and Bo Chen
Volume 2015, Article ID 271912, 3 pages

Early-Warning Method of Train Running Safety of a High-Speed Railway Bridge Based on Transverse Vibration Monitoring, You-Liang Ding, Peng Sun, Gao-Xin Wang, Yong-Sheng Song, Lai-Yi Wu, Qing Yue, and Ai-Qun Li
Volume 2015, Article ID 518689, 9 pages

A Comparative Study of Genetic and Firefly Algorithms for Sensor Placement in Structural Health Monitoring, Guang-Dong Zhou, Ting-Hua Yi, Huan Zhang, and Hong-Nan Li
Volume 2015, Article ID 518692, 10 pages

Study Based on Bridge Health Monitoring System on Multihazard Load Combinations of Earthquake and Truck Loads for Bridge Design in the Southeast Coastal Areas of China, Dezhang Sun, Bin Chen, and Baitao Sun
Volume 2015, Article ID 829380, 12 pages

Estimation of Evolutionary Spectra of Monitored Seismic Ground Motions by Transformation of Correlation Functions, Zhifeng Xu, Li Li, and Liang Hu
Volume 2015, Article ID 846943, 9 pages

Health Status Monitoring of Cuplock Scaffold Joint Connection Based on Wavelet Packet Analysis, Liuyu Zhang, Chenyu Wang, and Gangbing Song
Volume 2015, Article ID 695845, 7 pages

The Long-Term Settlement Deformation Automatic Monitoring System for the Chinese High-Speed Railway, Xu Wang, Liangqin Wu, Yi Zhou, and Yanru Wang
Volume 2015, Article ID 147972, 12 pages

Effect of Temperature Variation on Vibration Monitoring of Prestressed Concrete Girders, Thanh-Canh Huynh, Young-Hwan Park, Jae-Hyung Park, Dong-Soo Hong, and Jeong-Tae Kim
Volume 2015, Article ID 741618, 9 pages

Performance Evaluation on Transmission Tower-Line System with Passive Friction Dampers Subjected to Wind Excitations, Bo Chen, Xiang Xiao, Peng-yun Li, and Wan-li Zhong
Volume 2015, Article ID 310458, 13 pages

Sensor Placement Optimization of Vibration Test on Medium-Speed Mill, Lihua Zhu, Jun Dai, and Guoliang Bai
Volume 2015, Article ID 690196, 9 pages

Research on Impact Process of Lander Footpad against Simulant Lunar Soils, Bo Huang, Zhuji Jiang, Peng Lin, and Daosheng Ling
Volume 2015, Article ID 658386, 24 pages

Evaluation on Impact Interaction between Abutment and Steel Girder Subjected to Nonuniform Seismic Excitation, Yue Zheng, Xiang Xiao, Lunhai Zhi, and Guobo Wang
Volume 2015, Article ID 981804, 14 pages

A Wireless Strain Sensor Network for Structural Health Monitoring, Chengyin Liu, Jun Teng, and Ning Wu
Volume 2015, Article ID 740471, 13 pages

Feasibility Verification of Mountable PZT-Interface for Impedance Monitoring in Tendon-Anchorage, Thanh-Canh Huynh, Young-Hwan Park, Jae-Hyung Park, and Jeong-Tae Kim
Volume 2015, Article ID 262975, 11 pages

Anchor Dragging Analysis of Rock-Berm Using Smoothed Particle Hydrodynamics Method, Jinho Woo, Dongha Kim, and Won-Bae Na
Volume 2015, Article ID 687623, 8 pages

Detection on Structural Sudden Damage Using Continuous Wavelet Transform and Lipschitz Exponent, Bo Chen, Yuan-pin Kang, Peng-yun Li, and Wen-ping Xie
Volume 2015, Article ID 832738, 17 pages

Probability Model of Hangzhou Bay Bridge Vehicle Loads Using Weigh-in-Motion Data, Dezhang Sun, Xu Wang, Bin Chen, and Baitao Sun
Volume 2015, Article ID 576083, 10 pages

Acoustic Emission Signal Recognition of Different Rocks Using Wavelet Transform and Artificial Neural Network, Xiangxin Liu, Zhengzhao Liang, Yanbo Zhang, Xianzhen Wu, and Zhiyi Liao
Volume 2015, Article ID 846308, 14 pages

Life-Cycle Monitoring of Long-Span PSC Box Girder Bridges through Distributed Sensor Network: Strategies, Methods, and Applications, Zheheng Chen, Tong Guo, and Shengyou Yan
Volume 2015, Article ID 497159, 14 pages


Running Safety of Trains under Vessel-Bridge Collision, Yongle Li, Jiangtao Deng, Bin Wang, and Chuanjin Yu
Volume 2015, Article ID 252574, 11 pages

Impact Coefficient Analysis of Long-Span Railway Cable-Stayed Bridge Based on Coupled Vehicle-Bridge Vibration, Yongle Li, Shifu Dong, Yulong Bao, Kejian Chen, and Shizhong Qiang
Volume 2015, Article ID 641731, 9 pages

Seismic Fortification Analysis of the Guoduo Gravity Dam in Tibet, China, Peng Lin, Wenwei Zheng, Bo Huang, and Haichao Zhang
Volume 2015, Article ID 396124, 15 pages

Fatigue Performance Assessment of Composite Arch Bridge Suspenders Based on Actual Vehicle Loads, Bin Chen, Xiaozhang Li, Xu Xie, Zheng Zhong, and Pengzhen Lu
Volume 2015, Article ID 659092, 13 pages

Effects of Concrete on Propagation Characteristics of Guided Wave in Steel Bar Embedded in Concrete, Zhupeng Zheng and Ying Lei
Volume 2014, Article ID 910750, 14 pages



Establishment and Application of the Wind and Structural Health Monitoring System for the Runyang Yangtze River Bridge, Hao Wang, Aiqun Li, Tong Guo, and Tianyou Tao

Volume 2014, Article ID 421038, 15 pages

Free-Interface Modal Synthesis Based Substructural Damage Detection Method, Shanghong Chen, Wei Lin, Jiexin Yu, and Ai Qi

Volume 2014, Article ID 741697, 13 pages

Editorial

Distributed Sensor Networks for Health Monitoring of Civil Infrastructures

Ting-Hua Yi,¹ Gangbing Song,² Stathis C. Stiros,³ and Bo Chen⁴

¹*School of Civil Engineering, Dalian University of Technology, Dalian 116023, China*

²*Department of Mechanical Engineering, University of Houston, Houston, TX 77204-4006, USA*

³*Department of Civil Engineering, Patras University, 26500 Patras, Greece*

⁴*School of Civil Engineering and Architecture, Wuhan University of Technology, Wuhan 430070, China*

Correspondence should be addressed to Ting-Hua Yi; yth@dlut.edu.cn

Received 4 March 2015; Accepted 4 March 2015

Copyright © 2015 Ting-Hua Yi et al. This is an open access article distributed under the Creative Commons Attribution License, which permits unrestricted use, distribution, and reproduction in any medium, provided the original work is properly cited.

Structural Health Monitoring (SHM) implies the integration of nondestructive evaluation methods within a system to enable autonomous state awareness for structural integrity. SHM systems have been optimized to cover wide areas as well as focus on specific “hot-spots” for both metallic and composite structures. They can be configured to monitor adverse “changes” such as fatigue cracks, corrosion, delamination, loose bolts, or impact damage either in real-time or on demand. Immediate benefits of SHM include drastically reducing inspection costs, minimizing preventative maintenance, increasing asset availability, and extending remaining useful life of structures. Future benefits could include using SHM data to improve design-margin efficiency for lighter-weight structures, facilitating structural certification and/or quality assurance, and dynamically controlling operating envelopes. Over the past few years, there has been rapid development of SHM technique; many smart sensors and intelligent algorithms have been developed. Advances in sensing technologies have also enabled the use of large numbers of sensors for health monitoring of civil infrastructures. The sensors utilized in a SHM system are required to monitor not only the structural status including stress, displacement, and acceleration, but also those influential environmental parameters, such as wind speed, temperature, and the quality of its foundation. Since a large-scale sensor network needs to be involved in a SHM system, how to deploy it in a complicated, spatially extended structure and the resulting

best identification of structural characteristics by the data acquired from those locations will be challenging tasks.

Therefore, in the light of the above considerations, this special issue was launched. Numerous investigators worldwide were invited to contribute their original papers and review articles on the theme of this special issue. These papers present the most recent advances, progress, and ideas in the field of distributed sensor networks for SHM and its application includes smart, bioinspired, nanometer, wireless, and remote sensing technology; intelligent algorithms and evaluation criteria in design of sensor networks; uncertainty, sensitivity, reliability, and redundancy in vibration monitoring; vibration data cleaning, compression, mining, and fusing technology; application of large-scale sensor networks for civil infrastructures. In the paper “Fatigue Performance Assessment of Composite Arch Bridge Suspenders Based on Actual Vehicle Loads” by B. Chen et al., the fatigue conditions of bridge suspenders are analyzed according to the Palmgren-Miner linear fatigue cumulative damage criterion. In the paper “Sensor Placement Optimization of Vibration Test on Medium-Speed Mill” by L. Zhu et al., the optimal sensor placement of medium-speed mill is conducted using the effective independence method and QR decomposition algorithm. The results showed that the order of modal shapes had an important influence on the optimization results. The paper “Feasibility Verification of Mountable PZT-Interface for Impedance Monitoring in Tendon-Anchorage” by T.-C. Huynh et al. numerically evaluated the performance

of the mountable PZT-interface for impedance monitoring in tendon-anchorage. In the paper “Effect of Temperature Variation on Vibration Monitoring of Prestressed Concrete Girders” by T.-C. Huynh et al., the effect of temperature variation on vibration monitoring of prestressed concrete girders is experimentally analyzed. The paper “Evaluation on Impact Interaction between Abutment and Steel Girder Subjected to Nonuniform Seismic Excitation” by Y. Zheng et al. investigates the pounding interaction between the abutment and the steel girder underground motions for structural performance assessment. In the paper “The Long-Term Settlement Deformation Automatic Monitoring System for the Chinese High-Speed Railway” by X. Wang et al., using the newly built Shijiazhuang-Jinan passenger railway as an example, the authors developed a set of online monitoring systems, which were automatic, real-time, remote, and visual, and they were suited to the standards of the Beijing-Shanghai high-speed railway. The paper “Impact Coefficient Analysis of Long-Span Railway Cable-Stayed Bridge Based on Coupled Vehicle-Bridge Vibration” by Y. Li et al. discusses the impact effects on main girder, stayed cable, bearings, and bridge tower at various vehicle speeds. The paper “Running Safety of Trains under Vessel-Bridge Collision” investigates the characteristics of a train-bridge system under vessel-bridge collision. The paper “Health Status Monitoring of Cuplock Scaffold Joint Connection Based on Wavelet Packet Analysis” by L. Zhang et al. describes how to use the piezoelectric transducers to monitor cuplock connection for cuplock scaffold based on the wavelet packet analysis. The paper “Study Based on Bridge Health Monitoring System on Multihazard Load Combinations of Earthquake and Truck Loads for Bridge Design in the Southeast Coastal Areas of China” by D. Sun et al. presents a method to combine earthquake load and truck load in the service life of bridges. The paper “Embedded Decentralized Modal Identification of Four-Story Benchmark Structure Using Smart Sensor Network” by A. Y. Fallah et al. proposes a two-step algorithm for system identification of structures using wireless sensing network with decentralized data acquisition strategy. In the paper “Acoustic Emission Signal Recognition of Different Rocks Using Wavelet Transform and Artificial Neural Network” by X. Liu et al., the wavelet transform and artificial neural network is applied to determine rock types from their AE characteristic parameters. The paper “Probability Model of Hangzhou Bay Bridge Vehicle Loads Using Weigh-in-Motion Data” by D. Sun et al. performs a statistical analysis of the vehicle loads on Hangzhou Bay Bridge using more than 3 months of weigh-in-motion data from the site. The paper “Anchor Dragging Analysis of Rock-Berm Using Smoothed Particle Hydrodynamics Method” by J. Woo et al. presents dynamic responses of rock-berm structural system under anchor dragging and accordingly provides the characteristics of the stresses and displacements obtained. The paper “A Wireless Strain Sensor Network for Structural Health Monitoring” by C. Liu et al. presents the design and characterization of a new wireless strain sensor board. The results of the characterization of the fabricated device in combination with IRIS mote show very good performance with respect to the devices’ static, sensitivity, and dynamical

characteristics. The paper “Research on Impact Process of Lander Footpad against Simulant Lunar Soils” by B. Huang et al. investigates the interaction between lunar soil simulants and the lander footpad during the impact process using subscale model tests based on prototype vertical impact test apparatus. The paper “Life-Cycle Monitoring of Long-Span PSC Box Girder Bridges through Distributed Sensor Network: Strategies, Methods, and Applications” by Z. Chen et al. proposes a life-cycle monitoring strategy to well capture the behavior of the bridge during its whole life and to maximize the use of sensors. In the paper “Detection on Structural Sudden Damage Using Continuous Wavelet Transform and Lipschitz Exponent” by B. Chen et al., a detection approach based on the CWT is proposed in terms of the decomposed detailed coefficients of continuous wavelet transform to detect the damage time instant and location. The Lipschitz exponent is mathematically used to estimate the local properties of certain function and is applied to reflect the damage severity. The paper “Estimation of Evolutionary Spectra of Monitored Seismic Ground Motions by Transformation of Correlation Functions” by Z. Xu et al. proposes a method for the estimation of evolutionary power spectral density of a nonstationary process by transforming the correlation functions of its sample time histories. In the paper “Seismic Fortification Analysis of the Guoduo Gravity Dam in Tibet, China” by P. Lin et al., a dam seismic failure risk control method is proposed based on the cracking mechanism induced by the dynamic load to ensure dam safety and stability. The paper “Effects of Concrete on Propagation Characteristics of Guided Wave in Steel Bar Embedded in Concrete” by Z. Zheng and Y. Lei investigates dispersion equations of longitudinal wave propagation in reinforced concrete member for the purpose of monitoring steels embedded in concrete. In the paper “Establishment and Application of the Wind and Structural Health Monitoring System for the Runyang Yangtze River Bridge” by H. Wang et al., the establishment of the Wind and Structural Health Monitoring System (WSHMS) implemented on the Runyang Yangtze River Bridge (RYRB) in China is introduced. The paper “Free-Interface Modal Synthesis Based Substructural Damage Detection Method” by S. Chen et al. proposes a free-interface modal synthesis based substructure sensitivity method for damage detection. The paper “Early-Warning Method of Train Running Safety of a High-Speed Railway Bridge Based on Transverse Vibration Monitoring” by Y.-L. Ding et al. presents an early-warning method of train running safety of the high-speed railway bridge by adopting principal component analysis (PCA) method.

Without a doubt, the papers reflect the state-of-the-art researches and developments of this subject.

Acknowledgments

As the Guest Editors of the special issue, we would like to express our sincere appreciation to all the authors who contributed their work to this exciting special issue. The Guest Editors also thank the reviewers for their valuable and insightful comments that greatly benefited the improvement

of paper quality. This meaningful work was partially supported by the 973 Program (Grant no. 2015CB060000), the National Natural Science Foundation of China (Grant nos. 51421064, 51478081, 51222806, and 51178083), and the Science Fund for Distinguished Young Scholars of Dalian (Grant no. 2014J11JH125).

Ting-Hua Yi
Gangbing Song
Stathis C. Stiros
Bo Chen

Research Article

Early-Warning Method of Train Running Safety of a High-Speed Railway Bridge Based on Transverse Vibration Monitoring

You-Liang Ding,¹ Peng Sun,² Gao-Xin Wang,¹ Yong-Sheng Song,¹ Lai-Yi Wu,³ Qing Yue,³ and Ai-Qun Li¹

¹Key Laboratory of Concrete and Prestressed Concrete Structures of Ministry of Education, Southeast University, Nanjing 210096, China

²Department of Civil and Environmental Engineering, Rice University, Houston, TX 77005, USA

³China Railway Major Bridge (Nanjing) Bridge and Tunnel Inspect & Retrofit Co., Ltd, Nanjing 210032, China

Correspondence should be addressed to You-Liang Ding; civilchina@hotmail.com

Received 13 August 2014; Accepted 10 October 2014

Academic Editor: Bo Chen

Copyright © 2015 You-Liang Ding et al. This is an open access article distributed under the Creative Commons Attribution License, which permits unrestricted use, distribution, and reproduction in any medium, provided the original work is properly cited.

Making use of long-term transverse vibration monitoring data of DaShengGuan Bridge, the early-warning method of train running safety of the high-speed railway bridge is established by adopting principal component analysis (PCA) method. Firstly, the root mean square (RMS) of the transverse acceleration of the main girder is used as the monitoring parameter for the train running safety. The correlation model between the RMS values measured from different positions is further adopted as the evaluating model for the train running safety. Finally, the effects of the environmental changes on the evaluating model are eliminated using the PCA method and the warning index for the train running safety is further constructed. The analysis results show that the correlation between the RMS values of the accelerations from different measuring positions on the main girder can be analyzed by a quadratic polynomial fitting model. The PCA method can effectively remove the environmental effects on the quadratic polynomial fitting model. The proposed warning method provides a good capability for detecting the abnormal changes of the measured transverse accelerations and hence it is suitable for early-warning of the train running safety.

1. Introduction

Nanjing DaShengGuan Bridge, which serves as the shared corridor crossing Yangtze River for both Beijing-Shanghai high-speed railway and Shanghai-Wuhan-Chengdu railway, is the first 6-track high-speed railway bridge with the longest span throughout the world. With its 336 m main span and 6-track railways it ranks itself the largest bridge with heaviest design loading among the high-speed railway bridges by far. Also the design speed of 300 km/h of the bridge is on the advanced level in the world. Due to these remarkable characteristics including long span of the main girder, heavy design loading, and high speed of trains, the considerable transverse vibration of the bridge caused by high-speed trains may threaten the train running safety of DaShengGuan Bridge. Thus the train running safety should be paid

special attention during the bridge operation [1–3]. During the long-time service of the bridge, the environmental actions (wind, temperature, rain, etc.) and the bridge usage (high-speed trains) can continually modify the behavior and local damage of their key positions in the bridge may continually accumulate and cause deterioration of the bridge. In particular the deterioration of the transverse stiffness of the bridge may increase the transverse vibration of the bridge so as to threaten the train running safety. Therefore, research efforts should be focused on the transverse vibration monitoring of the bridge so as to gather reliable information that can be used to guarantee the train running safety.

To realize the transverse vibration monitoring of the bridge, the structural health monitoring system for the DaShengGuan Bridge has been established by the application

of modern techniques in sensing, testing, computing, and network communication. The ideal objective of the bridge health monitoring system is to gather various reliable information that can be used to detect the evolution of the bridge's condition state and perform reliability-based assessment so as to give the engineer or administrant a great variety of options with respect to maintenance intervention [4–6]. However, how to explain the health condition of the bridge structure according to the collected structural responses remains a great challenge in the civil engineering community [7]. It is well known that bridge structures are subject to varying environmental conditions such as loadings and environmental temperature. These environmental effects will cause changes in the measured structural responses that may mask the changes caused by structural damage [8, 9]. Therefore, it is of paramount importance to characterize the normal variability of structural responses due to environmental effects and discriminate such normal variability from abnormal changes in structural responses caused by the deterioration of the bridge. Considerable research efforts have been devoted to investigating the influences of environmental conditions on the measured structural responses of bridges [10–13]. For instance, Ni et al. [10] observed that the normal environmental change of Ting Kau Bridge accounts for relative variation in modal frequencies from 3.22% to 15.07% for the first ten modes. Using the formulated frequency-temperature correlation models, the relative variation of the normalized frequencies after removing the temperature effect was reduced to range from 1.61% to 7.87%. Ni et al. [11] presented a procedure for condition assessment of expansion joints based on long-term monitoring of displacement and temperature. The results revealed that temperature fluctuation mainly accounts for the movement of the expansion joint. However, relevant works focused on the influences of environmental conditions on the measured transverse accelerations of high-speed railway bridges are seldom reported. Hence, it is necessary to present a procedure for early warning of train running safety under changing environmental conditions using the long-term transverse vibration monitoring data of high-speed railway bridges.

Based on the aforementioned motivation, the objective of this paper is to propose an early-warning method of train running safety for high-speed railway bridges. The variability of transverse accelerations of the main girder induced by high-speed trains is quantified and the abnormal changes of the measured transverse accelerations which may threaten the train running safety are detected using the principal component analysis (PCA) method. The paper emphasizes on (i) the choice of monitoring parameter obtained from the transverse accelerations of the main girder; (ii) the establishment of the evaluating model for the train running safety; and (iii) the construction of the warning index using the PCA method. The feasibility of the proposed strategy is demonstrated using 310 days of measured transverse acceleration data on the main girder of Nanjing DaShengGuan Bridge in 2013.

2. Early-Warning Method of Train Running Safety Using Transverse Vibration Monitoring Data

The train running safety is to refer to the safe traveling status of trains without derailment. In particular for high-speed railway bridges, high-speed train derailment incidents may cause heavy casualties and property losses. In the design of high-speed railway bridges, the derailment coefficient and wheel unloading rate are usually used to judge the train running safety. However, Zeng et al. [14] point out that the current limit values of derailment coefficient and wheel unloading rate cannot prevent the happening of derailment. The essential reason of train derailment is that the transverse vibration of the time-variant system of train-railway-bridge becomes unstable. Hence, if the system can maintain a stable transverse vibration condition, the prevention of derailment can be achieved. In the present study, the early-warning method of train running safety of the high-speed railway bridge using transverse vibration monitoring data is established in combination with the theory of energy random analysis of railway derailment proposed by Zeng et al. [14] and structural health monitoring system of railway bridges. The early-warning method of train running safety is to monitor the transverse vibration of the main girder of the bridge. When the high-speed trains pass through the bridge, the various wheel-rail contact states can produce various transverse vibration responses in the main girder of a bridge. Whether the measured transverse vibration of the main girder is stable can indicate the transverse vibration condition of the train-railway-bridge system, which results in the judgment of train running safety. Thus, anomaly alarms for train running safety can be triggered on time if the monitoring transverse vibration data of the main girder disobey the normal pattern due to the deterioration of the bridge.

The early-warning method of train running safety using transverse vibration monitoring data involves three steps:

(1) to extract the monitoring parameter for the train running safety, that is, to extract the monitoring parameter from the transverse acceleration responses of the main girder, which can indicate the train running safety of high-speed railway bridges: this paper will investigate applicability of two monitoring parameters including the peak value and the RMS value of the transverse acceleration;

(2) to construct the evaluation model for the train running safety; due to the strong stochastic features of the transverse acceleration responses of the train-railway-bridge system with high-speed train traveling by, a deterministic evaluation model should be established to represent the stable condition of the transverse vibration for the whole system based on the extracted monitoring parameter;

(3) to establish an early-warning index for the train running safety; the stability of the transverse vibration of the train-railway-bridge system is a basic rule for the judgment of train running safety; hence, a warning index for the train running safety is further constructed from the constructed evaluation model using a statistical pattern recognition

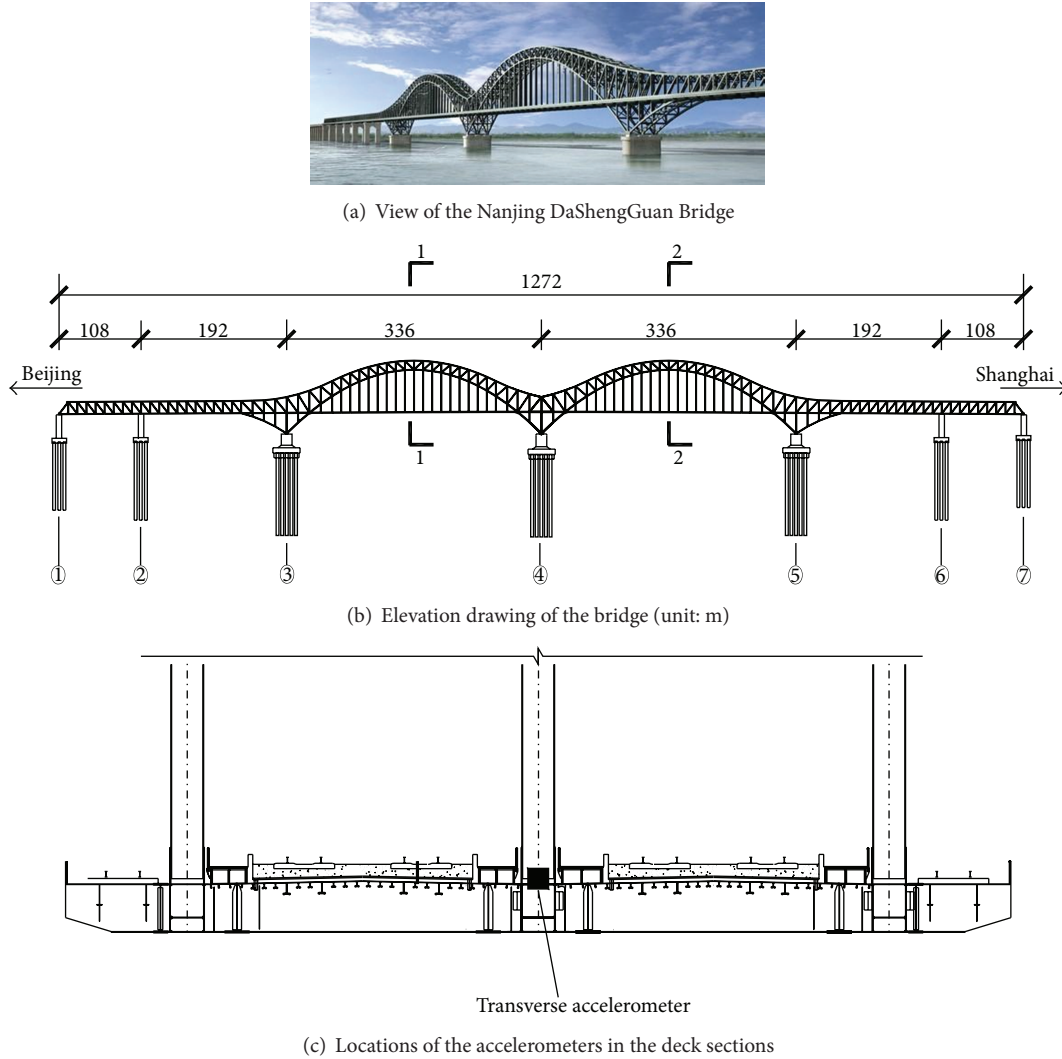


FIGURE 1: View of the Nanjing DaShengGuan Bridge and layout of the transverse vibration monitoring of the main girder.

method; the abnormal condition for the train running safety can be alarmed if the monitoring evaluation model disobeys the normal pattern.

3. Application in Early-Warning of Train Running Safety of DaShengGuan Bridge

3.1. Transverse Vibration Monitoring of the Girder of DaShengGuan Bridge. The subject of this study is Nanjing DaShengGuan Bridge shown in Figure 1(a), which is a steel truss arch bridge with the span arrangement $(108 + 192 + 2 \times 336 + 192 + 108)$ m. The elevation drawing of the bridge is shown in Figure 1(b). The health monitoring system for the DaShengGuan Bridge has been established to real-time monitor the responses of the bridge under the various kinds of environment actions and high-speed trains. In order to monitor the transverse acceleration responses on the two main spans induced by the traveling high-speed trains, one transverse accelerometer has been installed at the 1-1 section

and 2-2 section in the middle of the two main spans, respectively, as shown in Figure 1(c). The two accelerometers are named as JSD-11-04 and JSD-15-06, respectively. The sampling frequency of two accelerometers is 200 Hz. A total of 310 days of transverse acceleration data measured in 2013 are used in this study.

3.2. Analysis of Measured Transverse Vibration Data of the Girder of DaShengGuan Bridge. Figure 2 illustrates the typical transverse acceleration time histories of the main girder measured from two accelerometers. It can be observed that when high-speed train traveled by, there are obvious stochastic vibration features in the transverse accelerations in the middle of the two main spans of the main girder, and the transverse accelerations in the middle of the first span are much smaller than those of the second span. These indicate that although the structural layouts of two main spans of the main girder are the same, there exists significant difference between the transverse vibration characteristics of two main

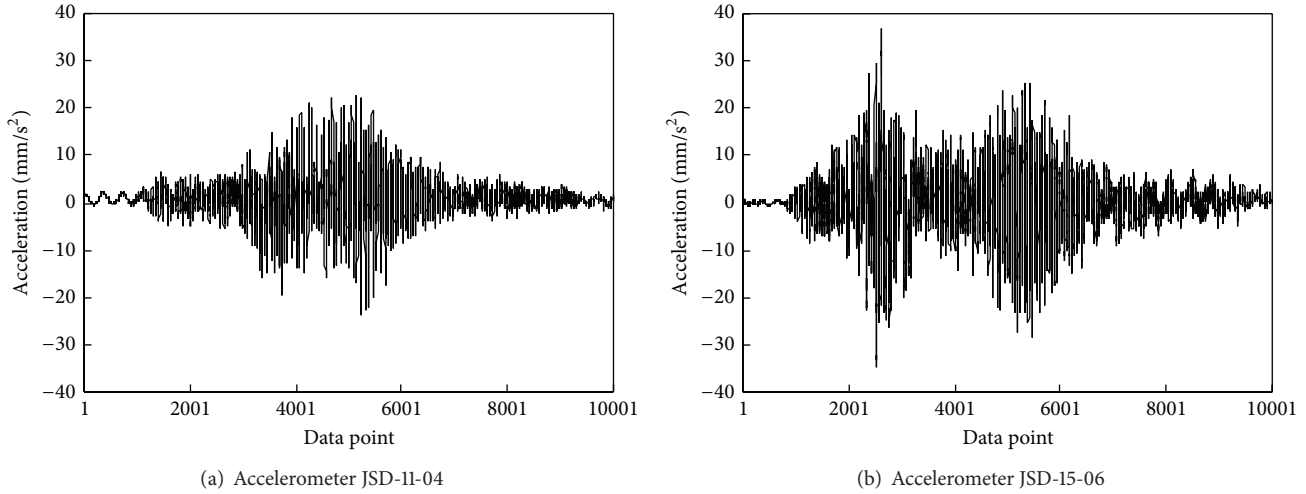


FIGURE 2: Transverse acceleration time histories of the main girder induced by a high-speed train.

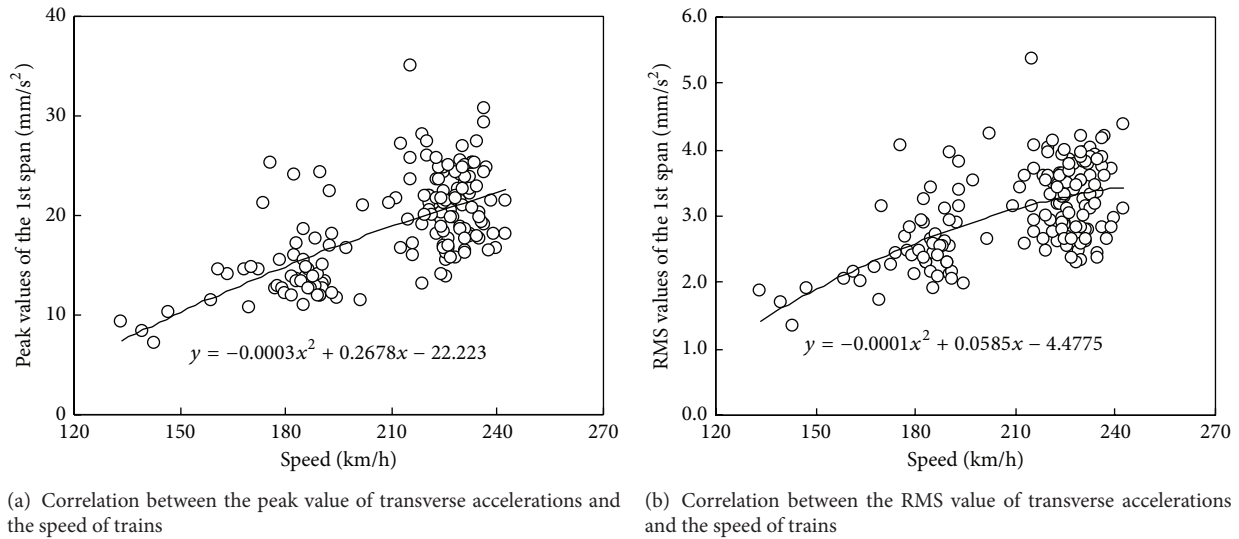


FIGURE 3: Correlations between the amplitude parameters of the transverse accelerations in the middle of the first main span and the speed of the trains.

spans due to the rail irregularity in transverse direction. Thus, there is a need to monitor the transverse accelerations of two main spans in the long term so as to obtain the transverse vibration state of the train-railway-bridge system and realize anomaly alarms for train running safety.

In the present study, the acceleration amplitude parameters are utilized as the monitoring parameters to represent the transverse vibration characteristic of the main girder. The acceleration amplitude usually refers to the maximum or effective value of acceleration responses. For this reason, the applicability of the two acceleration amplitude parameters, the peak value and the RMS value, should be studied in this research. It should be noted that, in the calculation of RMS values of the transverse acceleration of the main girder, the filter bandwidth of the transverse accelerations is set to be 0–20 Hz. Figure 3 shows the scatter plots between the amplitude parameters of the transverse accelerations in

the middle of the first main span and the speed of the trains each time the trains passed by on February 1st, 2013. The train speed is measured using speedometer installed in the middle of the second main span of the main girder. It can be observed that, with the increase of train speed, both the peak value and the RMS value of the transverse accelerations have an upward trend. However, it is obvious that the measurement points in Figure 3 are too dispersed to be an effective description of the correlation between the amplitude parameters and train velocities, especially when the speed of trains exceeds 200 km/h. This implies that the transverse vibration responses of the main girder due to the different trains at the same speed varied much, mainly because of the various wheel-rail contact states of the trains. The analysis results indicate that it is hard to construct an efficient correlation model between the amplitude parameter and the speed of trains so as to represent the transverse vibration state

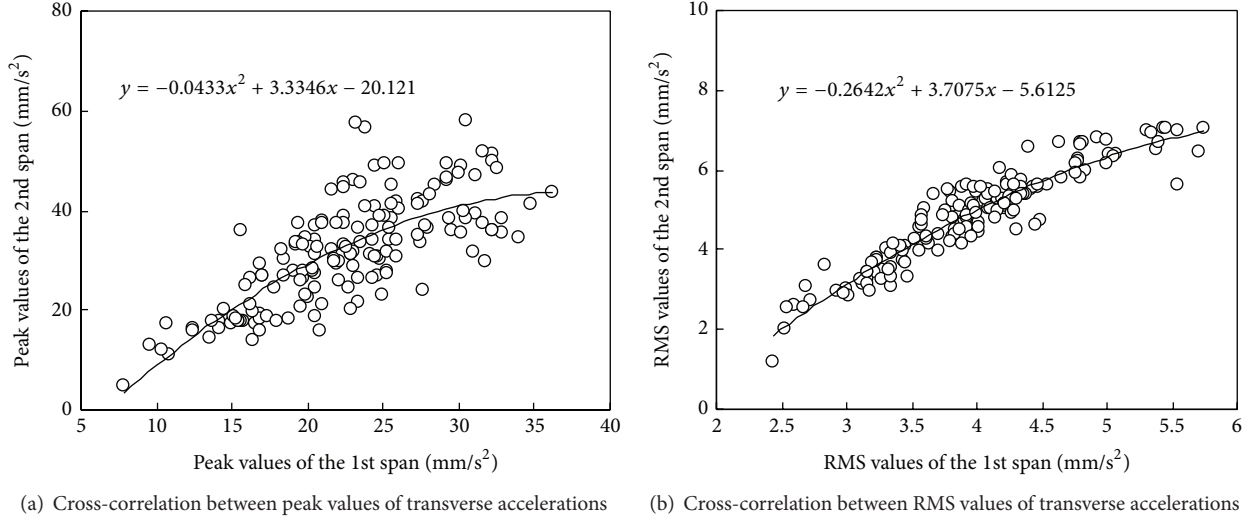


FIGURE 4: Cross-correlations between the amplitude parameters of the transverse accelerations measured in the middle of two main spans.

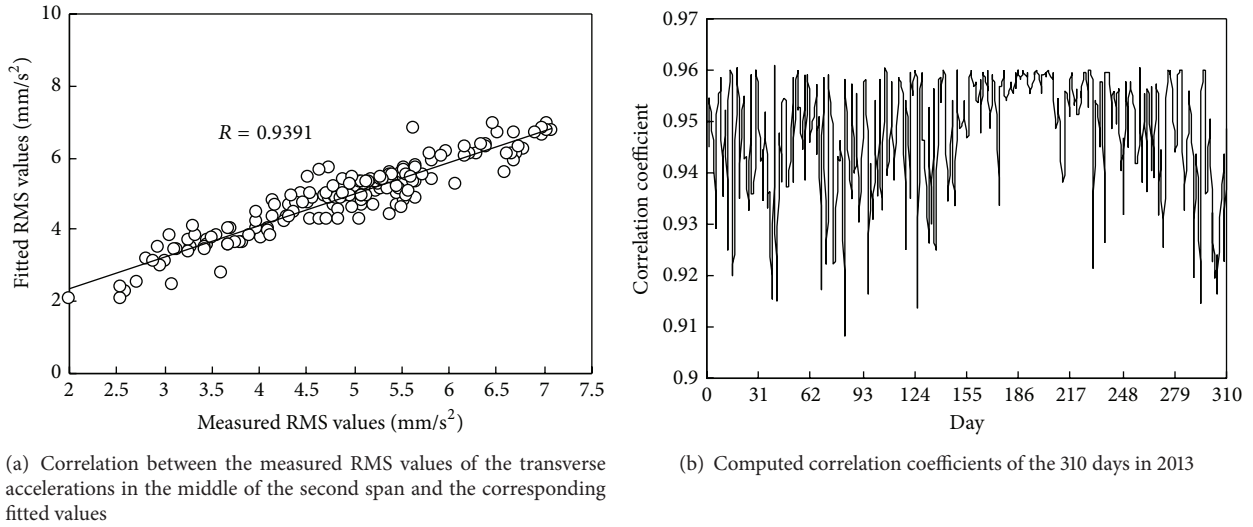


FIGURE 5: Fitting effect of cross-correlation between RMS values of transverse accelerations by using quadratic polynomial.

of the train-railway-bridge system. In addition, it can be also observed from Figure 3 that the fluctuations of the amplitude parameters of the transverse accelerations on the main girder are very high. This is due to the strong stochastic feature of the transverse vibration of the train-railway-bridge system when the high-speed trains pass through the bridge. Hence, it is also hard to construct an efficient evaluation model to represent the transverse vibration state of the train-railway-bridge system simply using transverse accelerations at a single measurement point.

In the next discussion, the cross-correlation between the amplitude parameters of the transverse accelerations in the middle of two main spans is investigated when the high-speed trains pass through the bridge. Figure 4(a) shows the scatter plots between the peak values of the transverse accelerations in the middle of two main spans on February 1st, 2013, and shows the fitted results by using quadratic polynomial as well.

Figure 4(b) shows the scatter plots between the RMS values of the transverse accelerations and shows the fitted results by using quadratic polynomial as well. By comparison, it can be concluded that the cross-correlation by using the RMS values is much better than the cross-correlation by using the peak values. By using the fitting formula constructed in Figure 4(b), scatter plot between the RMS values of the transverse accelerations in the middle of the second span and the corresponding fitted values is drawn as Figure 5(a), where the fitted values were obtained by taking the RMS values of the transverse accelerations in the middle of the first span into the fitting formula of the quadratic polynomial. The correlation coefficient of the measured RMS values and fitted values on February 1st, 2013, is 0.9391, as shown in Figure 5(a). Computed using the same method, all the correlation coefficients of the 310 days in 2013 are more than 0.90, as shown in Figure 5(b).

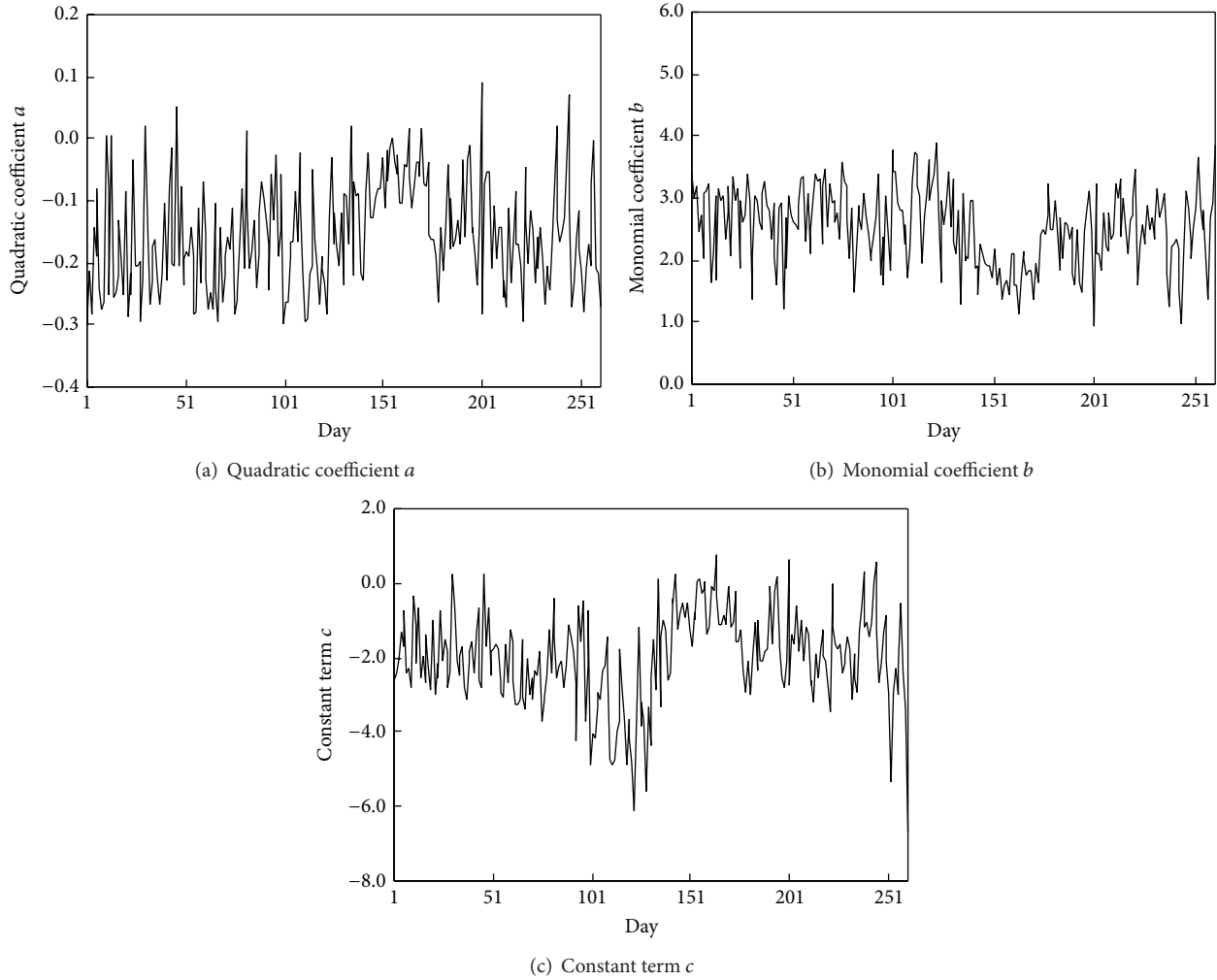


FIGURE 6: Long-term monitoring results of the fitted coefficients of the quadratic polynomial.

The analysis results indicate that good cross-correlation exists between the RMS values of the transverse accelerations on the two main spans. This is because the RMS values of the transverse accelerations represent the vibration energy of the train-railway-bridge system, and the cross-correlation between the RMS values of the accelerations at different measuring positions can represent the spatial distribution of the transverse vibration energy which is inputted into the system by the traveling trains. In this case, the randomness of transverse vibration can be transferred into the deterministic feature of the spatial distribution of the transverse vibration energy. Hence, the cross-correlation model of RMS values of transverse accelerations can represent the transverse vibration state of the system when the high-speed train passes through the bridge. According to the theory of random energy analysis for train derailment [14], a stable transverse-vibration state of the train-railway-bridge system indicates a stable cross-correlation model of RMS values of the transverse accelerations. Hence, a long-term monitoring on the cross-correlation model of RMS values of the transverse accelerations can detect the abnormal changes of

the cross-correlation model and can further realize the early-warning of train running safety.

3.3. Warning Results of Train Running Safety of DaShengGuan Bridge. Based on the results in Section 3.2, the RMS value of the transverse acceleration of the main girder can be a monitoring parameter, and the cross-correlation model of the RMS values of the transverse accelerations from different measuring points can be an evaluation model for the train running safety. This section will discuss the early-warning method of train running safety for high-speed railway bridges.

Firstly, there is a need to study the fitted coefficient of the quadratic polynomial for the cross-correlation model based on the long-term monitoring. Figure 6 provides the fitted coefficients of the quadratic polynomial for the cross-correlation between the RMS values of the transverse accelerations in the middle of two main spans with the quadratic coefficient a , monomial coefficient b , and constant term c , respectively. It can be observed that although the measurements of the transverse accelerations in every single day can

fit a quadratic polynomial model with a good correlation, the coefficients of the quadratic polynomials vary very much from a long-term point of view. This is because of the fact that, with the environmental effects such as temperature and so forth, the transverse vibration characteristics of the train-railway-bridge system will vary in a broad range. These environmental effects will cause changes in three fitted coefficients which may mask the abnormal changes caused by structural deterioration of the bridge. However, due to the diversity of the environmental effects and the complex effects on the transverse vibrations of the bridge, it is hard to accurately measure each environmental effect and to quantitatively remove the influence of each effect. For this reason, this paper investigates the normalization of environmental effects on the three fitted coefficients of the quadratic polynomial models based on PCA method. PCA method theoretically does not need to monitor the variants of environmental effects, so it has a promising prospect of engineering application [15].

Principal component analysis (PCA) method is a statistical procedure that uses an orthogonal transformation to convert a set of observations of possibly correlated variables into a set of values of linearly uncorrelated variables [15]. This method can realize the reduction treatment from a high dimension to a lower one to reveal the key information from the data by maintaining the most information. It is especially suitable for finding the hidden features in multivariate factor analysis.

The basic theory of PCA is that a vector $\mathbf{u} = [u_1 \ u_2 \ \cdots \ u_n]^T$ is operated by the dimension reduction to be a low dimension vector $\mathbf{v} = [v_1 \ v_2 \ \cdots \ v_m]^T$ ($m < n$) as follows:

$$\mathbf{v}_{m \times 1} = \mathbf{A}_{m \times n} \mathbf{u}_{n \times 1}, \quad (1)$$

where \mathbf{A} is the transform matrix. The m components v_1, v_2, \dots, v_m are principal components. The principal component analysis is to find m principal components which can represent more than (80–90)% of the total variance to construct a new vector \mathbf{v} . This vector \mathbf{v} contains the most information of vector \mathbf{u} , so \mathbf{v} realizes the condensation of the original \mathbf{u} . For the purpose of this paper, there is a need to transform the 3-dimensional vector \mathbf{u} constructed by the three fitted coefficients of the quadratic polynomial model to a 1-dimensional vector \mathbf{v} . Results of the computations show that when the samples are enough, the cumulative variance of first principal component can reach 90%.

According to the basic theory of PCA as stated above, the key steps of the warning method of train running safety are listed as follows.

(1) Compute the fitted coefficients of the quadratic polynomial for the RMS values of the transverse accelerations each day under the normal running condition. The three coefficients form the 3-dimensional vector \mathbf{u} .

(2) Reduce the dimension of the 3-dimensional vector \mathbf{u} constructed by using k -day measurement to 1-dimension vector \mathbf{v} , where \mathbf{A} is the transform matrix. The transform

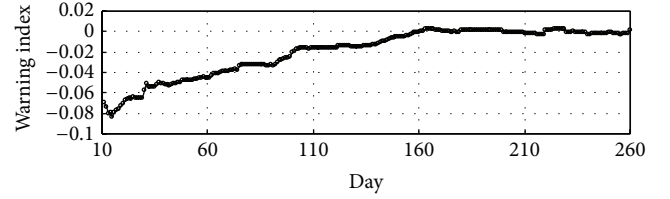


FIGURE 7: Training effect of warning index for train running safety using PCA method.

matrix \mathbf{A} can represent the features of the actual environmental effects so as to effectively remove the environmental effects on the fitted coefficients.

(3) The reconstructed value of the RMS of the transverse accelerations is obtained by referring to the 1-dimensional vector \mathbf{v} , so the warning index D for train running safety can be defined as follows:

$$D(k) = v_m(k) - v_e(k), \quad (2)$$

where $v_m(k)$ is the daily mean value of the RMS values of the transverse accelerations on the k th day; $v_e(k)$ is the daily mean value of the RMS values of the transverse accelerations on the k th day after reconstruction. When the number of monitoring days k is big enough, the warning index tends to be 0.

(4) With the help of PCA, the RMS values of the transverse accelerations in an unknown running condition can be reconstructed by using the transform matrix \mathbf{A} in a normal running condition and the warning index can be computed. Comparing the warning index in a normal running condition and that in an unknown running condition, if the difference of the two is significant, it can give early warning of train running safety because of an abnormal change in the transverse vibration of the main girder.

The analysis of the monitoring data of 310 days in 2013 will be carried out as an example. The first 260-day data of the 310 days will serve as the training samples, the last 50-day data will serve as the test samples. Figure 7 shows the warning index obtained by using PCA method. When the days of training data are fewer, the warning index fluctuates within -0.08 to -0.04 , while with the increase of the number of training days, the warning index gradually approaches to 0; when the number of training days reaches 160, the warning index tends to be stable. The measured data of the last 50 days within the 310 days in 2013 is further processed by using the principal component reconstruction. It should be noted that the transform matrix \mathbf{A} for the PCA reconstruction is obtained by using the measured data of the first 260 days to carry out principal component analysis. Figure 8 shows warning index curve from 160th to 310th days. It can be observed that, regardless of the training samples or the test samples, the warning index varies within -0.002 – 0.002 . This indicates that PCA method is capable of reconstruction and prediction by fully considering the environmental effects.

There is a need to investigate the effectiveness of the proposed method applied to the early-warning of train running safety. The RMS values of the transverse acceleration

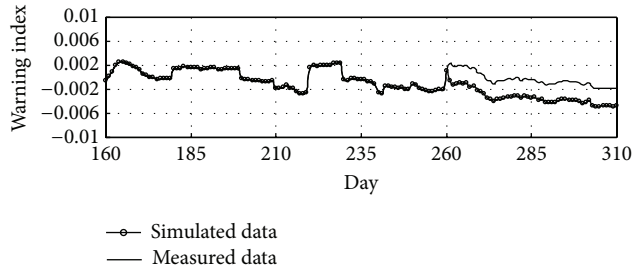


FIGURE 8: Measured waring index curve and simulated warning index curve due to the deterioration of the bridge using PCA method.

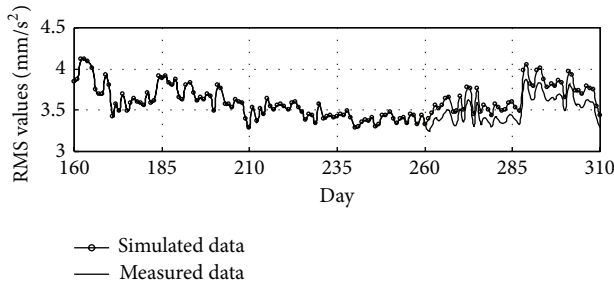


FIGURE 9: Daily mean values of the measured data and the simulated data of the RMS values of the transverse acceleration data in the middle of the second main span.

data (the data of the last 50 days in 2013) in the middle of the second main span are amplified by a factor of 1.05 to simulate the effects of structural deterioration of the bridge on the RMS values of the transverse acceleration. Figure 9 shows the daily mean values of the measured data and the simulated data of the RMS values of the transverse acceleration data in the middle of the second main span. It can be seen from Figure 9 that the RMS values of the transverse accelerations cannot detect the abnormal changes of the transverse accelerations. Figure 8 shows the simulated warning index curve using the simulated transverse acceleration data due to the deterioration of the bridge. The warning index can sensitively detect the abnormal changes of transverse accelerations so as to trigger the alarm for train running safety on time.

4. Conclusions

In this paper by referring to the Nanjing DaShengGuan Bridge, the first 6-track high-speed railway bridge with the longest span throughout the world, the early-warning method of train running safety of the high-speed railway bridge is proposed by adopting principal component analysis (PCA) method based on long-term transverse vibration monitoring data. The following are the findings and conclusions.

(1) When high-speed trains passed by, the transverse vibration of the train-railway-bridge system had a strong stochastic feature. The correlation between transverse accelerations from one measuring position on the main girder and the speed of trains cannot represent the transverse vibration

condition of the whole system and thus cannot be adopted as the evaluating model for the train running safety.

(2) The correlation between the RMS values of the transverse accelerations from different measuring positions on the main girder represents the spatial distribution feature of transverse vibration energy of the whole system and can be effectively analyzed by a quadratic polynomial fitting model. Thus, the corresponding correlation model can be adopted as the evaluating model for the train running safety.

(3) The PCA method can effectively remove the environmental effects on the measured cross-correlation between the RMS values of transverse accelerations. The proposed warning method provides a good capability for detecting the abnormal changes of the measured transverse accelerations and hence it is suitable for early-warning of the train running safety of DaShengGuan Bridge.

Conflict of Interests

The authors declare that there is no conflict of interests regarding the publication of this paper.

Acknowledgments

The authors gratefully acknowledge the National Basic Research Program of China (973 Program) (no. 2015CB060000), the National Science and Technology Support Program of China (no. 2014BAG07B01), the Key Program of National Natural Science Foundation (no. 51438002), the Program of “Six Major Talent Summit” Foundation (no. 1105000268), and the Fundamental Research Funds for the Central Universities and the Innovation Plan Program for Ordinary University Graduates of Jiangsu Province in 2014 (no. KYLX_0156).

References

- [1] N. Zhang, H. Xia, and W. W. Guo, “Vehicle-bridge interaction analysis under high-speed trains,” *Journal of Sound and Vibration*, vol. 309, no. 3–5, pp. 407–425, 2008.
- [2] C. Y. Xia, H. Xia, and G. de Roeck, “Dynamic response of a train-bridge system under collision loads and running safety evaluation of high-speed trains,” *Computers & Structures*, vol. 140, pp. 23–38, 2014.
- [3] S. H. Ju, “Improvement of bridge structures to increase the safety of moving trains during earthquakes,” *Engineering Structures*, vol. 56, pp. 501–508, 2013.
- [4] T. L. Franklin, A. M. Joseph, and S. Emil, “Automated extraction and classification of thunderstorm and non-thunderstorm wind data for extreme-value analysis,” *Journal of Wind Engineering and Industrial Aerodynamics*, vol. 97, no. 3–4, pp. 120–131, 2009.
- [5] T. H. Yi, H. N. Li, and M. Gu, “Optimal sensor placement for structural health monitoring based on multiple optimization strategies,” *Structural Design of Tall and Special Buildings*, vol. 20, no. 7, pp. 881–900, 2011.
- [6] T.-H. Yi, H.-N. Li, and M. Gu, “Recent research and applications of GPS-based monitoring technology for high-rise structures,” *Structural Control and Health Monitoring*, vol. 20, no. 5, pp. 649–670, 2013.

- [7] E. Watanabe, H. Furuta, T. Yamaguchi, and M. Kano, "On longevity and monitoring technologies of bridges: a survey study by the Japanese Society of Steel Construction," *Structure and Infrastructure Engineering*, vol. 10, no. 4, pp. 471–491, 2014.
- [8] Y. L. Ding and A. Q. Li, "Temperature-induced variations of measured modal frequencies of steel box girder for a long-span suspension bridge," *International Journal of Steel Structures*, vol. 11, no. 2, pp. 145–155, 2011.
- [9] A. Deraemaeker, E. Reynders, G. de Roeck, and J. Kullaa, "Vibration-based structural health monitoring using output-only measurements under changing environment," *Mechanical Systems and Signal Processing*, vol. 22, no. 1, pp. 34–56, 2008.
- [10] Y. Q. Ni, J. M. Ko, X. G. Hua, and H. F. Zhou, "Variability of measured modal frequencies of a cable-stayed bridge under different wind conditions," *Smart Structures and Systems*, vol. 3, no. 3, pp. 341–356, 2007.
- [11] Y. Q. Ni, X. G. Hua, K. Y. Wong, and J. M. Ko, "Assessment of bridge expansion joints using long-term displacement and temperature measurement," *Journal of Performance of Constructed Facilities*, vol. 21, no. 2, pp. 143–151, 2007.
- [12] B. Chen, Z. W. Chen, Y. Z. Sun, and S. L. Zhao, "Condition assessment on thermal effects of a suspension bridge based on SHM oriented model and data," *Mathematical Problems in Engineering*, vol. 2013, Article ID 256816, 18 pages, 2013.
- [13] A. D. Orcesi and D. M. Frangopol, "Bridge performance monitoring based on traffic data," *Journal of Engineering Mechanics*, vol. 139, no. 11, pp. 1508–1520, 2013.
- [14] Q. Zeng Y, J. Xiang, P. Lou, and Z. Zhou, "Mechanical mechanism of derailment and theory of derailment prevention," *Journal of Railway Science and Engineering*, vol. 1, no. 1, pp. 19–31, 2004.
- [15] X. G. Hua, Y. Q. Ni, J. M. Ko, and K. Y. Wong, "Modeling of temperature-frequency correlation using combined principal component analysis and support vector regression technique," *Journal of Computing in Civil Engineering*, vol. 21, no. 2, pp. 122–135, 2007.

Research Article

A Comparative Study of Genetic and Firefly Algorithms for Sensor Placement in Structural Health Monitoring

Guang-Dong Zhou,¹ Ting-Hua Yi,² Huan Zhang,¹ and Hong-Nan Li²

¹ College of Civil and Transportation Engineering, Hohai University, Nanjing 210098, China

² School of Civil Engineering, Dalian University of Technology, Dalian 116023, China

Correspondence should be addressed to Guang-Dong Zhou; zhoudg@hhu.edu.cn

Received 11 August 2014; Accepted 1 October 2014

Academic Editor: Bo Chen

Copyright © 2015 Guang-Dong Zhou et al. This is an open access article distributed under the Creative Commons Attribution License, which permits unrestricted use, distribution, and reproduction in any medium, provided the original work is properly cited.

Optimal sensor placement (OSP) is an important task during the implementation of sophisticated structural health monitoring (SHM) systems for large-scale structures. In this paper, a comparative study between the genetic algorithm (GA) and the firefly algorithm (FA) in solving the OSP problem is conducted. To overcome the drawback related to the inapplicability of the FA in optimization problems with discrete variables, some improvements are proposed, including the one-dimensional binary coding system, the Hamming distance between any two fireflies, and the semioriented movement scheme; also, a simple discrete firefly algorithm (SDFA) is developed. The capabilities of the SDFA and the GA in finding the optimal sensor locations are evaluated using two disparate objective functions in a numerical example with a long-span benchmark cable-stayed bridge. The results show that the developed SDFA can find the optimal sensor configuration with high reliability. The comparative study indicates that the SDFA outperforms the GA in terms of algorithm complexity, computational efficiency, and result quality. The optimization mechanism of the FA has the potential to be extended to a wide range of optimization problems.

1. Introduction

The performance deterioration and the total collapse of large-scale civil infrastructures induced by the environment and service loads highlight the importance of structural health monitoring (SHM) as a significant approach for the safe operation and the reasonable maintenance of structures. SHM, which involves an array of sensors to continuously monitor structural behavior, along with the extraction of damage-sensitive features from these measurements and the evaluation of current system health by analysis methods, can be used for rapid condition screening and aims to provide reliable information regarding the integrity of the structure in near real time [1–3]. At present, successful deployment and operation of long-term SHM systems on newly constructed structures and existing structures have been reported throughout the world [4–7]. In an SHM system, the sensor network provides original information indicating structural behavior for further parameter identification; therefore, the efficiency of an SHM system relies

heavily on the reliability of the acquired data measured by the sensor networks on the structure. For the complexity of large-scale structures, such as long-span bridges and high-rise buildings, the degrees of freedom (DOFs) used to characterize structural performance count are on the order of thousands to tens of thousands. It is impossible to distribute sensors on all of the DOFs because of the high costs of data acquisition systems (sensors and their supporting instruments) and technology limitations [8, 9]. Therefore, selecting optimal sensor placement (OSP) is a critical task before a sophisticated SHM system is designed and implemented on a real structure [10].

The problem of determining OSP has been investigated using a large number of interesting approaches and criteria in the past few decades, which can be seen from the abundance of literature. Among them, conventional gradient-based local optimization methods were unable to efficiently handle multiple local optima and may present difficulties in estimating the global minimum. They lack reliability in dealing with the OSP problem, because convergence to the global minimum is

not guaranteed [11, 12]. Thus, the shift of OSP research away from classical deterministic optimization methods toward the use of combinatorial optimization methods based on biological and physical analogues has been motivated by the high computational efficiency and success rate of intelligent optimization methods. Many contributions regarding the adoption of intelligent optimization methods to the OSP problem have been recently made. The genetic algorithm (GA) based on the Darwinian principle of natural selection is a representative example and has proved to be a powerful tool for OSP. Yao et al. [13] demonstrated that the GA can replace the effective independence (Efi) method when using the determinant of the Fisher information matrix (FIM) as the objective function. Subsequently, a number of improvements have been employed to overcome drawbacks of the original GA. To accelerate convergence, the simulated annealing (SA) algorithm was integrated into the GA by Worden and Burrows [14] and Hwang and He [15] to extract the OSP in structural dynamic tests. To keep the sensor number constant during the genetic operation, the coding system was replaced by decimal two-dimensional array coding [16] or dual-structure coding [17]. With the purpose of improving the quality of solutions and convergence speed, two-quarter selection was adopted by Yi et al. [18, 19]. The GA was also extended to the optimal wireless sensor placement, which has many constraints [20–22]. Particle swarm optimization (PSO), which is inspired by the movement of organisms in bird flocking or fish schooling, is another stochastic search technique and was successfully applied to the OSP problem [23, 24]. Furthermore, the monkey algorithm (MA), which imitates the mountain-climbing process of monkeys, is considered to be an effective numerical method in solving complex multiparameter optimization problems. Several changes developed by Yi et al. made the MA excellent in terms of generating optimal solutions, as well as providing fast convergence in dealing with complicated OSP problems [8, 25, 26].

Although the aforementioned methodologies demonstrated a strong capability, to some extent, in finding the acceptable solution for the OSP problem, the complex parameters and searching processes make those methods difficult to operate and susceptible to the application environment. The complexity of the optimal sensor configuration for large-scale structures reveals the necessity for the development of efficient and robust algorithms to accurately explore the optimum solution. Recently, a new metaheuristic search algorithm, which is referred to as the firefly algorithm (FA), has been developed by Yang [27, 28]. The FA algorithm is based on the idealized behavior of the flashing characteristics of fireflies. A firefly tends to be attracted by other fireflies with high flash intensities. Previous studies indicate that the FA is particularly suited for parallel implementation and may outperform existing algorithms, such as PSO, GA, SA, and differential evolution, in terms of efficiency and success rates [28, 29]. At present, the FA has been applied to a large number of optimization problems, including continuous, combinatorial, constrained, multiobjective, and dynamic optimization [30].

However, the coding system and the movement scheme in the FA make it suitable only for global numerical optimization problems with continuous variables. In this paper, some improvements, including the coding system, the suitable distance, and the movement scheme, are introduced, and a simple discrete firefly algorithm (SDFA) is proposed based on the FA such that the outstanding optimization mechanism of the FA can be applicable in the OSP problem with discrete variables. The remaining part of this paper is organized as follows: Section 2 presents a detailed description of the SDFA after an outline of the FA. Section 3 gives a brief introduction to the GA with the aim of facilitating performance comparison between the SDFA and the GA in the next numerical simulations. Section 4 shows the comprehensive evaluation of the SDFA for OSP with different criteria employing a long-span benchmark cable-stayed bridge. Finally, conclusions are drawn in Section 5.

2. Firefly Algorithm

2.1. Outline of Firefly Algorithm. The FA mimics the real firefly's swarm behaviors of communication, its search for food, and its process of finding mates. The optimization process of exploring the optimal solution is modeled in such a way that the firefly with low light intensity is attracted by the firefly with high light intensity and moves toward to it, such that the darker firefly has higher light intensity. Therefore, to establish the mathematical model of this movement, three hypotheses are adopted as follows: (1) the attractive action between two fireflies is only governed by the light intensity; (2) the light intensity of a firefly, which is deduced by the firefly's location, is proportional to the objective function; and (3) the light intensity decreases with increasing distance, such that the brighter firefly can only attract the fireflies within its attractiveness range. Then, the movement of firefly i toward firefly j is formulated as

$$X_i^{t+1} = X_i^t + \beta_0 e^{-\gamma r_{ij}^2} (X_j^t - X_i^t) + \alpha \varepsilon_i^t, \quad (1)$$

where X_i and X_j represent the locations of firefly i and firefly j , respectively, the superscript t denotes time, γ means the light absorption coefficient, r_{ij} is the distance between any two fireflies i and j , and β_0 is the attractiveness at $r = 0$. The third item in (1) is a random vector, where α is a random parameter generated from the interval $[0, 1]$ and ε_i denotes a vector of random numbers drawn from a Gaussian distribution. Thus, the movement of firefly i defined by (1) is not always directed to firefly j . More details can be found in references [25, 29, 31, 32].

The location of a firefly is simply coded using a spatial coordinate, which consists of real vectors and continuous variables. Subsequently, the distance between any two fireflies i and j is generally defined by the Euclidean distance $r_{ij} = \|X_i - X_j\|_2$ or the l_2 -norm. However, it is well known that, from the view of mathematics, the OSP is a specialized knapsack problem where some specified DOFs are selected to be placed by sensors, such that the structural performance can be described effectively. Thus, the parameters that are used for optimizing are states in which those DOFs are

distributed by sensors and are discrete variables. As a result, the coding system and the movement strategies in the FA are inapplicable in the OSP problem with discrete variables. It is essential to do some modifications to the original FA, such that the underlying optimization concept of the FA can be moved to the OSP problem. Here, some improvements are integrated into the FA, and the SDFA is proposed to explore the optimal sensor configuration in structural health monitoring.

2.2. Simple Discrete Firefly Algorithm. Being originated from the FA, the SDFA is integrated by three parts: the coding system, the definition of distance between two fireflies, and the movement scheme. The coding system involves the code of each firefly in feasible space. The distance definition is responsible for describing the distance between two fireflies so that the movement can be realized. And the movement scheme gives the evolution rules of the SDFA. All of the three parts are introduced in next three sections.

2.2.1. Coding System. In the community of applying GA in finding the optimal sensor configuration, a widely used code approach is the one-dimensional binary coding system. Each individual in the population is coded by a one-dimensional binary string. In this code system, all of the candidate DOFs are put in a line. If the sth DOF is placed by a sensor, the value of the sth element in the string is 1. In contrast, if the sth DOF is not placed by a sensor, the value of the sth element in the string is 0. The total number of ones in the string is equal to the number of sensors that needs to be placed. This coding system is intuitive and easy to be initialized and operated. Here, in the SDFA, the one-dimensional binary coding system is employed. Each firefly in the population denotes a feasible sensor configuration, and the location of each firefly is represented by a one-dimensional binary string, as shown in Table 1. In the example of Table 1, it can be found that the 2nd, 3rd, 6th, and 9th DOFs are occupied by sensors. The total numbers of candidate DOFs and sensors are 10 and 4, respectively, because the length of the string is 10 and the total number of ones is 4 in this firefly code. This coding method is very simple and intuitive, which is beneficial for the next optimization operation. When initializing the firefly population, the first n th elements in a string are set to 1, and the left elements are set to 0. Then, the shuffle algorithm is applied five times, such that the fireflies can be distributed in the feasible solution space uniformly as much as possible.

2.2.2. Distance between Two Fireflies. In the FA, the positions of the fireflies are defined in a Cartesian coordinate system, such that the distance between two fireflies can be easily calculated by the l_2 -norm. However, in the SDFA, the positions of the fireflies are represented by binary strings. As a result, the l_2 -norm is no longer suitable for indicating the distance between two fireflies. The Hamming distance [31], which counts the number of positions at which the corresponding symbols are different between two strings of equal length, has many similarities with the problem at hand and is adopted to indicate the distance between any two fireflies. Supposing

TABLE 1: An example of a firefly code.

DOF	1	2	3	4	5	6	7	8	9	10
Code \rightarrow	0	1	1	0	0	1	0	0	1	0

TABLE 2: Codes for firefly i and firefly j .

Firefly $i \rightarrow$	1	0	1	0	0	1	0	1	0	0
Firefly $j \rightarrow$	1	0	1	1	0	0	0	0	0	1

fireflies i and j with binary strings, the Hamming distance is equal to the number of ones in firefly i XOR firefly j , which is

$$r_{ij} = X_i \oplus X_j = (X_i \vee X_j) \wedge \neg (X_i \wedge X_j), \quad (2)$$

where X_i and X_j are vectors, \oplus means XOR, \vee is logical disjunction, \wedge represents logical conjunction, and \neg denotes logical negation.

As a matter of fact, the Hamming distance represents the number of incongruous sensors between two sensor configurations and is equivalent to the number of elements in two strings whose values are different on the corresponding locations. Thus, the Hamming distance between firefly i and firefly j can be rewritten as

$$r_{ij} = X_i \oplus X_j = \sum_{s=1}^d |x_{i,s} - x_{j,s}|. \quad (3)$$

Generally, the number of sensors used for structural monitoring is predetermined, such that the total number of ones in any firefly is the same. If there is an incongruous sensor in firefly i , which is located at the sth DOF, it is not placed by a sensor in firefly j . There must be an incongruous sensor in firefly j , which is located at the p th DOF, which is not placed by a sensor in firefly i . Then, the value of r_{ij} is two. As a result, the distance r_{ij} , which is defined by (3), is always a nonnegative even number and is two times the number of incongruous sensors; this finding is beneficial for establishing the movement scheme. Therefore, the maximum value of r_{ij} is 2ω (where ω is the total number of predetermined sensors), which implies that the sensors of firefly i and the sensors of firefly j are completely deployed on different DOFs in a structure. The minimum value of r_{ij} is zero, which indicates that the sensors of firefly i and the sensors of firefly j occupy the same DOFs. Thus, the distance r_{ij} has the range of $[0, 2\omega]$. Table 2 gives an example of two codes for firefly i and firefly j . The number of ones in firefly i XOR firefly j is four, and the number of incongruous sensors is two. Therefore, the corresponding Hamming distance between firefly i and firefly j is four.

2.2.3. Movement Scheme. The firefly movement in the Cartesian coordinate system is easily performed by changing the coordinate values, as formulated by (1). The distance of the movement is continuous and proportional to the attractiveness. However, the positions of the fireflies in the SDFA are defined by one-dimensional binary strings whose values are 0 and 1. The firefly movement, which indicates that

the values in the string are varied, can only be realized by changing 1 to 0 or 0 to 1. On the other hand, the divergence of two fireflies originates from the incongruous sensors. Thus, replacing some incongruous sensors in a firefly may enhance its light intensity. Therefore, in the SDFA, the movement of firefly i is operated by changing some elements in the string of firefly i from values of 1 to 0 and changing some elements in the string of firefly i from values of 0 to 1, simultaneously. Additionally, to keep the number of ones constant, the time of changing 1 to 0 should be equal to the time of changing 0 to 1. For this reason, the time of changing 1 to 0 or the time of changing 0 to 1 is defined as the movement distance. Under this definition, the nearest and farthest movement distance from firefly i to firefly j is 0 and $0.5r_{ij}$, respectively. By introducing stochastic searching, the movement distance d_{ij} from firefly i to firefly j is selected as

$$d_{ij} = \text{random} (1, 0.5r_{ij}). \quad (4)$$

Generally, the contribution of a sensor located on a DOF to the objective function cannot be predetermined. Therefore, it is difficult to judge which a sensor should be relocated. In the present paper, a semioriented movement scheme is proposed as follows.

Step 1. Calculate the difference between the strings of firefly i and firefly j :

$$\Delta X_{ji} = X_j - X_i. \quad (5)$$

Step 2. Randomly select d_{ij} elements from ΔX_{ji} with a value of 1 and change these elements to -1; again, randomly select d_{ij} elements from ΔX_{ji} with a value of -1 and change these elements to 1. The operated ΔX_{ji} is represented by $[\Delta X_{ji}]$.

Step 3. Replace the string of firefly i by

$$X_i \leftarrow X_i + [\Delta X_{ji}]. \quad (6)$$

In fact, the different light intensity between firefly i and firefly j comes from the ΔX_{ji} term, which is also induced by the incongruous sensors. The operated elements in the ΔX_{ji} term are randomly selected, because it is difficult to predict the influence of each element on the objective function. Therefore, replacing part of the X_i by $[\Delta X_{ji}]$, which implies relocating some incongruous sensors, would enhance the light intensity of firefly i with a high probability. However, the movement cannot guarantee that firefly i moves in a desirable direction. Thus, the movement scheme is described as a semioriented movement scheme. These random factors in the movement scheme are also in accord with the random term in (1).

3. Brief Description of Genetic Algorithm

The GA is briefly described here to facilitate a comparison in next section. The GA, which was first proposed by Holland in 1975 [32], tries to imitate natural evolution by assigning a fitness value to each individual in the problem and by



FIGURE 1: Overview of the cable-stayed bridge.

applying the principle of the survival of the fittest [33]. Each individual has a set of chromosomes that can be mutated and altered. Solutions can be represented by either one-dimensional binary codes, dual-structure codes, or decimal codes. In this paper, the dual-structure coding method is employed to maintain a constant number of sensors. The evolution, which usually starts from a population of randomly generated individuals, is an iterative process and advances towards the next generation by applying genetic operators (crossover and mutation). An individual in the new population is generated by performing the crossover on two selected individuals from the current population and mutation on this generated individual [34]. The two individuals selected for crossover are chosen according to their fitness values. The individual with a good fitness value has a high probability of being chosen. The new generation of individuals is then used in the next iteration of the algorithm. Commonly, the iteration terminates when either a maximum number of generations have been produced or when a satisfactory fitness level has been reached for the population. The GA has a distinct advantage over traditional optimization techniques, which starts from a single point in the solution space. The details about the GA have been presented in references [16, 33, 34].

4. Numerical Example

4.1. Bridge Description. The bridge employed for numerical simulation is a full-scale, cable-stayed bridge benchmark problem organized by the Center of Structural Monitoring and Control at the Harbin Institute of Technology [35], as shown in Figure 1. The bridge was opened to traffic in December 1987 and completely retrofitted in 2007. It comprises a main span of 260 m and two side spans of 25.15 m and 99.85 m each. The total length and width of the bridge are 519 m and 11 m, respectively. The concrete bridge tower consists of two transverse beams with a height of 60.5 m. 74 precast concrete girder segments are employed to integrate the main girder, and a total of 88 pairs of cables containing steel wires that are 5 mm in diameter are adopted to transfer the loads

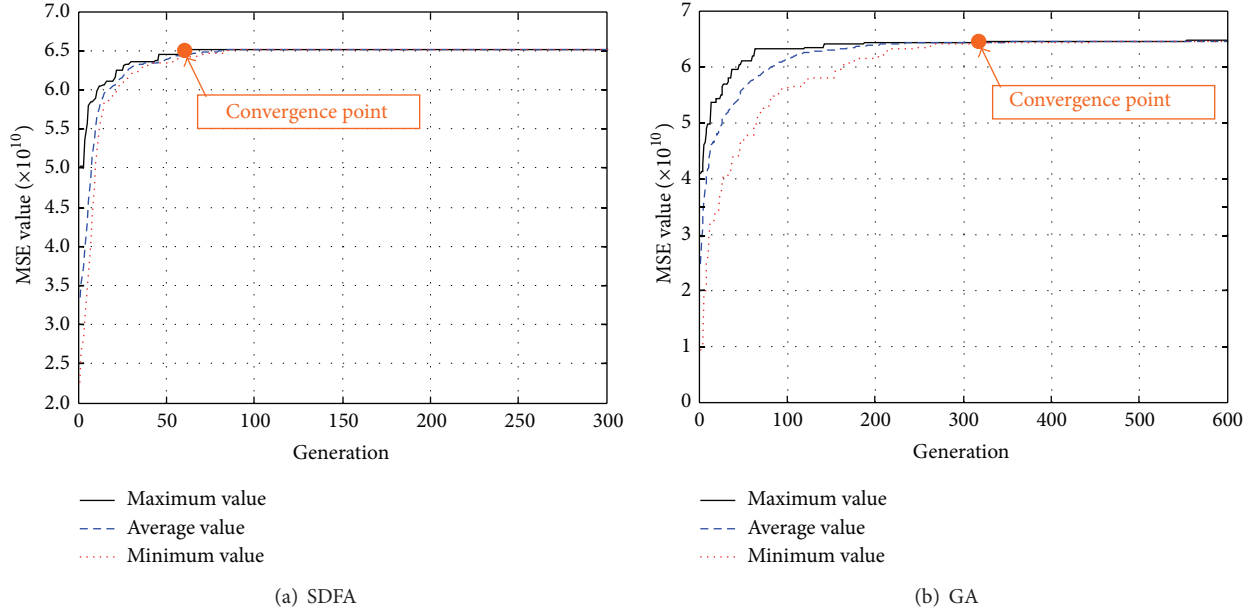


FIGURE 2: Iteration progress of the objective function.

from main girder to the two towers [36]. To understand the behavior of the bridge, an updated three-dimensional finite element model is also provided by the Center of Structural Monitoring and Control at the Harbin Institute of Technology [35]. The towers and the main girder were simulated by three-dimensional beam elements, and the cables were simulated by linear elastic link elements. The concrete transverse beam at every 2.9 m was simplified by a mass element. The main girder was modeled as floating on the main tower, and all of the towers were fixed to the ground. The longitudinal restriction effect of the rubber supports was simulated by linear elastic spring elements. The model consists of 564 beam elements, 88 link elements, 160 mass elements, and 8 spring elements. Modal analysis has been conducted, and the results can be found in [35].

4.2. Results and Discussion. The proposed SDFA is evaluated by two frequently used, but quite different, objective functions. The first objective function is the modal strain energy (MSE). With this objective function, the OSP becomes a maximal optimization problem. The second objective function involves the modal assurance criterion (MAC), which induces the OSP to be a minimal optimization problem. More importantly, a comparative study is conducted between the SDFA and the GA, in terms of computational efficiency and result quality. To achieve this goal, the GA is also applied to find the optimal sensor configuration under the same conditions.

4.2.1. Optimization Based on Modal Strain Energy. Generally, it is desirable that most structural information is obtained through a set of sensors deployed on a structure, such that the structural behaviors can be described well. At present, the structural condition evaluation approaches based on the

structural mode shapes and their derivations have been comprehensively explored. The MSE provides a rough measure of the dynamic contribution of each candidate sensor to the target mode shapes and implies that the DOFs capture most of the relevant dynamic features of the structure. The MSE helps to select those sensor positions with possible large amplitudes, which can increase the signal-to-noise ratio and improve the reliability of the mode identification results [9, 16]. Therefore, the MSE is selected as the first objective function. Supposing that the mode shape matrix of a structure is $\Phi = [\phi_1, \phi_2, \dots, \phi_\omega]$ (ω is the number of mode shape vectors) and the number of measured points is ω , the MSE can be expressed as

$$H = \sum_{m=1}^{\omega} \sum_{n=1}^{\omega} \sum_{u \in \theta} \sum_{v \in \theta} |\phi_{um} k_{uv} \phi_{vn}|, \quad (7)$$

where ϕ_{um} is the u th component in the corresponding m th mode shape, ϕ_{vn} denotes the v th component in the corresponding n th mode shape, k_{uv} represents the stiffness coefficient between the u th DOF and the v th DOF, and $u \in \theta$ and $v \in \theta$ state that u and v are restricted to the locations where the sensors are placed.

Indeed, the improvements applied in the SDFA further simplify the FA algorithm, and only one parameter (i.e., the number of fireflies) needs to be preset. After being explored by a parametric study, the best value for firefly number is selected as 100, which allows the algorithm to achieve the best performance. Being different from the SDFA, the GA has several problematic parameters, such as the population size, the probabilities of selection, the crossover, and the mutation. Parametric studies are also conducted, and the appropriate values are determined. The simplicity and easy implementation of the SDFA is apparent.

TABLE 3: Comparison of optimization results based on the MSE.

Sensor number	20		25		30		35	
Methods	SDFA	GA	SDFA	GA	SDFA	GA	SDFA	GA
Maximum MAC off-diagonal value								
Mean value ($\times 10^{10}$)	6.1416	6.1325	6.5271	6.5102	6.7232	6.7028	6.8195	6.8103
Maximal value ($\times 10^{10}$)	6.2613	6.2537	6.5657	6.5325	6.7382	6.7215	6.8314	6.8217
Standard deviation	0.0291	0.0475	0.0280	0.4652	0.0165	0.3924	0.0121	0.2917

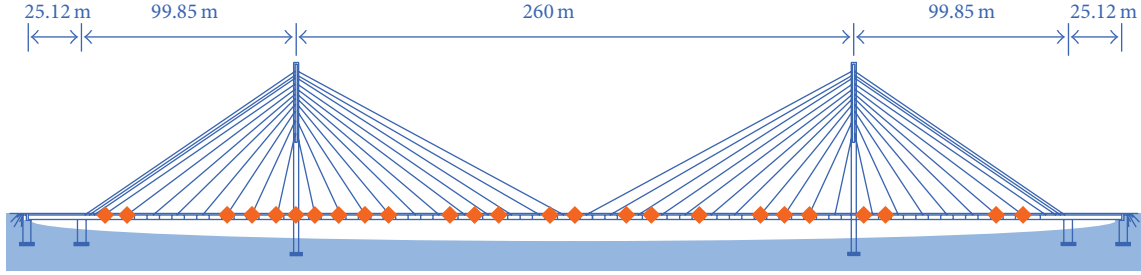


FIGURE 3: The optimal sensor configuration extracted by SDFA with the MSE.

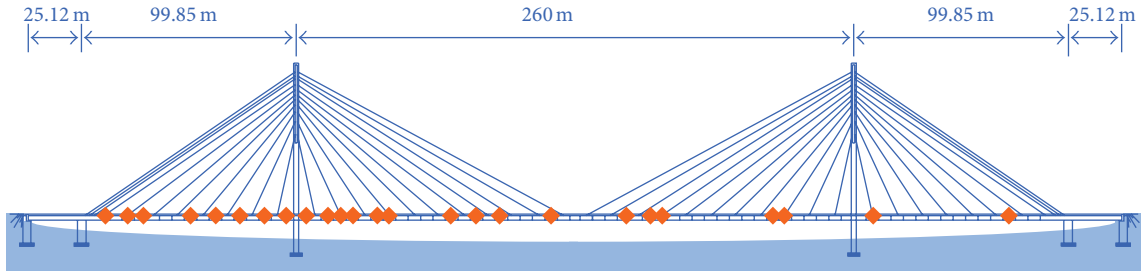


FIGURE 4: The optimal sensor configuration extracted by GA with the MSE.

Four scenarios with 20, 25, 30, and 35 sensors are simulated. In accordance with other heuristic optimization methods, the results extracted by the SDFA and the GA rely heavily on the randomly generated initial population. Therefore, to reduce the influence of the initialized individuals, the SDFA and the GA have been run 10 times with different stochastic initial populations in each occasion. The best iteration progress of the SDFA and the GA with 25 sensors are displayed in Figure 2, and the optimal locations of 25 sensors extracted by the SDFA and the GA with the aim of getting the maximal MSE value are illustrated in Figures 3 and 4, respectively. The statistical results of 10 runs for the four occasions are listed in Table 3. It can be seen from Figure 2 that both the SDFA and the GA can converge at the global optimum. In both Figures 2(a) and 2(b), the values of the objective function in the population increase with an increasing number of generations, and the average and minimum values of the objective function simultaneously approach the maximum value, which indicates good performance regarding optimum exploring. The effectiveness of the improvements adopted in the SDFA is validated. In

the SDFA, the maximum MSE value tends to be a constant after 62 generations with a high speed. However, in the GA, converging to a constant spends 188 generations at an unacceptably low speed. Although increasing the number of individuals may reduce iteration generation, but the time of each generation becomes longer. As a result, the GA spends longer time finding the optimal solution than the SDFA. The high computational efficiency of the SDFA is revealed. Comparing Figures 3 and 4, it can be found that the optimal sensor locations extracted by the SDFA distribute on the span uniformly. However, the sensors in the optimal sensor configuration found by the GA crowd near the left tower, and the vibration and mode shapes of the right part of the bridge cannot be described clearly. Thus, the sensors in the optimal sensor configuration extracted by the SDFA are used with high efficiency and the identified mode shapes are more visual. The statistical results of each ten optimal solutions are listed in Table 3. In the table, the mean value and the maximal value represent the average and the maximal values of the ten optimal solutions, respectively, which indicate the superiority of the optimal solution; the standard deviation denotes

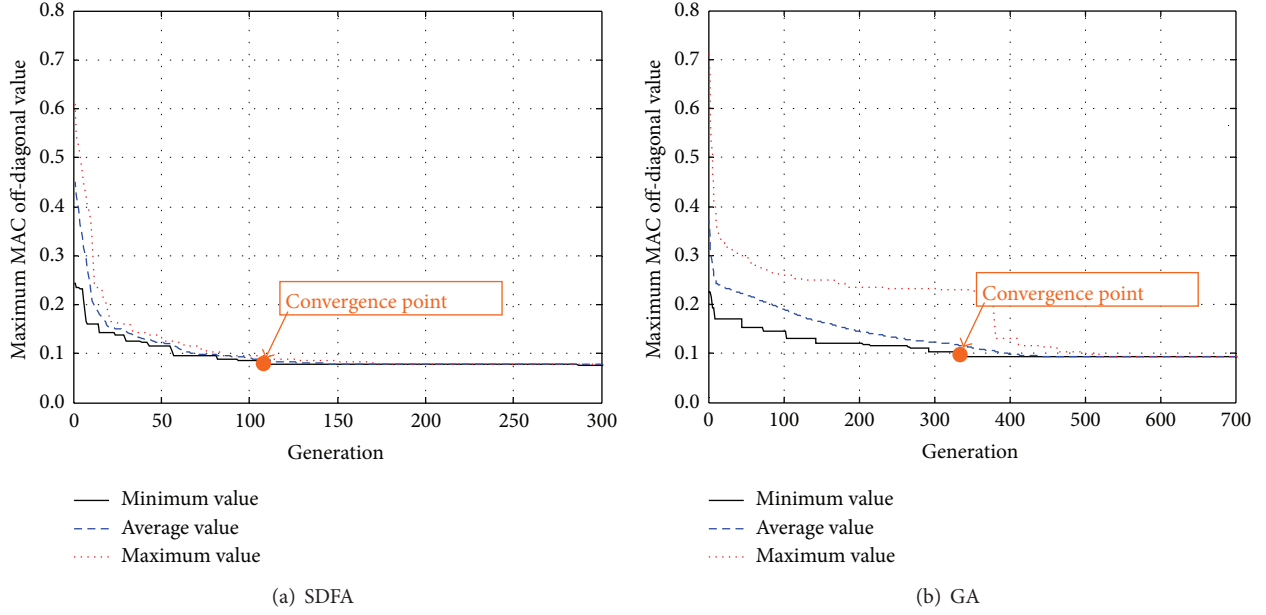


FIGURE 5: Iteration progress of the objective function.

the variability of the ten best solutions, which indicates the robustness of the algorithm. In every occasion, as listed in Table 3, the mean and maximum values of the MSE searched by the SDFA are larger than that explored by the GA. Thus, the solutions found by the SDFA have better quality than those extracted by the GA. Simultaneously, the standard deviation of the 10 results found by the SDFA in all four occasions are smaller than that searched by the GA, which shows that the SDFA can solve the OSP problem with high reliability and strong robustness.

4.2.2. Optimization Based on Modal Assurance Criterion. The vibration-based structural condition assessment methodologies require that the measured mode shapes are discriminable from each other, such that they can be reliably identified. The modal assurance criterion (MAC) proposed by Carne and Dohrmann [16] provides a simple metric to check the linear dependence of the mode shapes. A small maximum off-diagonal term of the MAC matrix implies less correlation between corresponding mode shape vectors and high distinguishability among the identified mode shapes. Thus, the MAC off-diagonal terms are adopted to evaluate the sensor configuration. The MAC is defined as

$$\text{MAC}_{mn} = \frac{\phi_m^T \phi_n}{\sqrt{(\phi_m^T \phi_m)(\phi_n^T \phi_n)}}, \quad (8)$$

where ϕ_m and ϕ_n represent the m th and n th column vectors in matrix Φ , respectively, and the superscript T denotes the transpose of the vector. With this definition, the values of the MAC range from 0 to 1, where 0 indicates that the modal vector is easily distinguishable and 1 indicates that the modal vector is fairly indistinguishable [19].

Consulting the numerical simulation performed in Section 4.2.1, the same parameters of the SDFA and the GA are adopted. The same four occasions are investigated, and each occasion is also calculated 10 times by the two methods. The best convergence process for the two optimization approaches are shown in Figure 5. The MAC values computed by the best sensor configurations obtained by the two methods are illustrated in Figure 6. To clearly show the MAC values of each mode, the maximum MAC off-diagonal values in each of the modes calculated by the SDFA and the GA are compared in Figure 7. The optimal sensor configurations found by the SDFA and the GA are displayed in Figures 8 and 9, respectively. The statistical data of the 10 runs in the four occasions are also listed in Table 4. The mean value, the minimal value, and the standard deviation have the similar meaning as that in Table 3. From the convergence process in Figure 5(a) and the optimal results in Figure 6(a), the strong ability to search for the global optimal solution in the SDFA is again demonstrated from the minimal optimization problem. When comparing the iteration progress in Figure 5(a) with that in Figure 5(b), the higher computational efficiency of the SDFA is further validated. Investigating the optimization results illustrated in Figures 6, 7, 8, and 9, a more desirable sensor configuration can be acquired when using the SDFA. The statistical results listed in Table 4 also indicate that the SDFA has higher reliability and stronger robustness than the GA.

5. Conclusions

Because finding the optimal sensor locations under a certain evaluation criterion is a complicated nonlinear optimization problem, traditional optimization methods often encounter many insurmountable difficulties in solving this problem.

TABLE 4: Comparison of optimization results based on the MAC.

Sensor number	20		25		30		35	
Methods	SDFA	GA	SDFA	GA	SDFA	GA	SDFA	GA
Maximum MAC off-diagonal value								
Mean value	0.0826	0.0937	0.0806	0.0904	0.0793	0.0854	0.0755	0.0796
Minimal value	0.0659	0.0783	0.0614	0.0727	0.0587	0.0657	0.0561	0.0593
Standard deviation	0.0128	0.0203	0.0129	0.0212	0.0116	0.0195	0.0113	0.0221

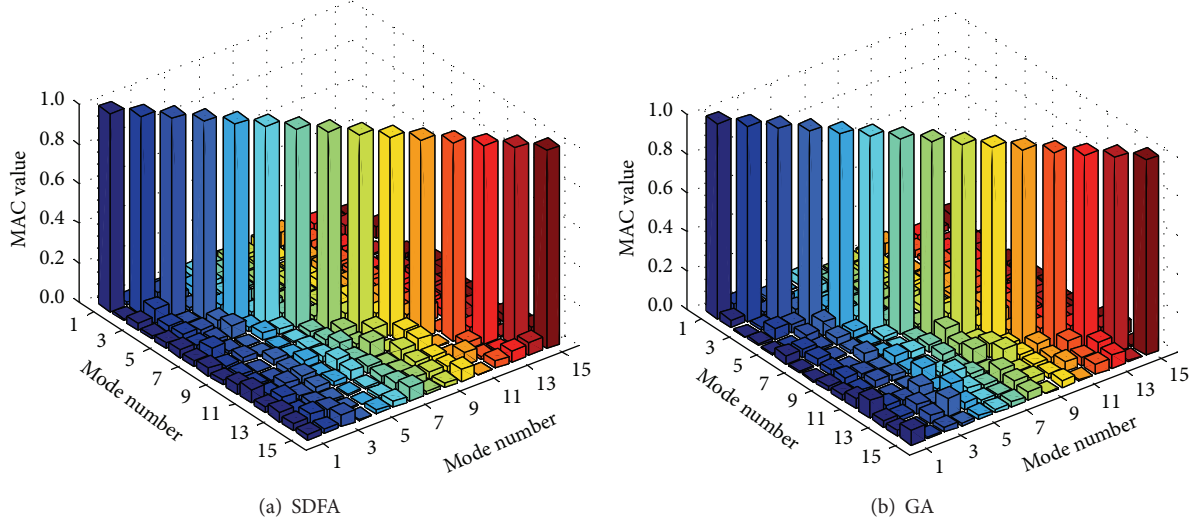


FIGURE 6: MAC values obtained from the optimal sensor configuration.

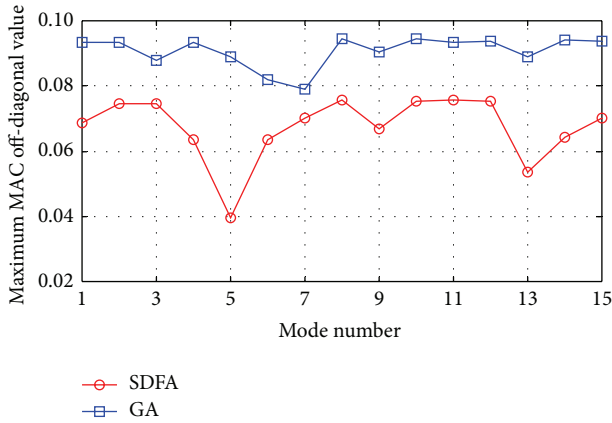


FIGURE 7: Maximum MAC off-diagonal values in each of the modes.

Intelligence optimization algorithms such as the GA and the FA provide powerful approaches to overcome these obstacles. Before implementing a comparative study between the GA and the FA regarding their performance in finding the optimal sensor configuration, some improvement are developed based on the basic FA and the SDFA is proposed. If all candidate DOFs can be accessible in real-word practice, the developed sensor placement method is applicable in any type of tethered sensor. The performance of the SDFA and the GA is compared using a numerical example with a long-span

benchmark cable-stayed bridge. Some conclusions are drawn as follows.

- (1) The one-dimensional binary coding system and the Hamming distance can rationally describe the status of fireflies in the feasible sensor configuration space. The semioriented movement scheme provides an effective tool to move the original movement defined in the Cartesian coordinate system to the one-dimensional binary coding system. These improvements make the underlying optimization mechanism of the FA applicable in discrete optimization problems.
- (2) In the case study, the improved SDFA shows good performance, both in the maximal value problem and the minimal value problem. The simulation results indicate that the SDFA has smooth convergence progress. The effectiveness of the proposed improvements is validated, and the strong capability of FA in finding the global optimization is also revealed.
- (3) Compared with the widely accepted GA, the SDFA, which has only one problematic parameter, can be implemented more easily. Regarding both the MSE and MAC criteria, the SDFA shows superior computational efficiency and robustness versus the GA. The optimal solution extracted by the SDFA is also more desirable than that provided by the GA.

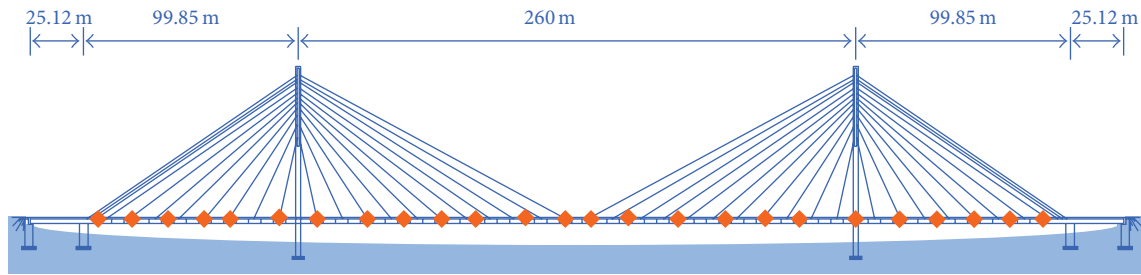


FIGURE 8: The optimal sensor configuration extracted by SDFA with the MAC.

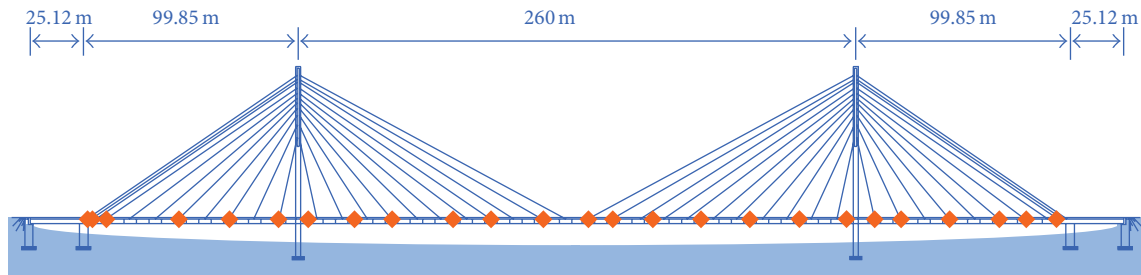


FIGURE 9: The optimal sensor configuration extracted by GA with the MAC.

It should be noted that all the analyses in this paper are conducted based on the assumed theoretical models while the real environment is more complex. The advanced SHM requires a more versatile sensor configuration to comprehensively understand the performance of a structure; therefore, developing algorithms for multiobjective optimization may be a good direction for future work.

Conflict of Interests

The authors declare that there is no conflict of interests regarding the publication of this paper.

Acknowledgments

This research work was jointly supported by the 973 Program (Grant no. 2015CB060000), the National Natural Science Foundation of China (Grants nos. 51421064, 51478081, and 51222806), the Fok Ying Tong Education Foundation (Grant no. 141072), and the Science Fund for Distinguished Young Scholars of Dalian (Grant no. 2014J11JH125).

References

- [1] L. Faravelli, D. Bortoluzzi, T. B. Messervey, and L. Sasek, "Temperature effects on the response of the bridge "ÖBB Brücke Großhaslau", in *Mechanics and Model-Based Control of Advanced Engineering Systems*, pp. 85–94, Springer, Vienna, Austria, 2014.
- [2] Y. Fujino, "Vibration, control and monitoring of long-span bridges—recent research, developments and practice in Japan," *Journal of Constructional Steel Research*, vol. 58, no. 1, pp. 71–97, 2002.
- [3] B. Chen, S. L. Zhao, and P. Y. Li, "Application of Hilbert-Huang transform in structural health monitoring: a state-of-the-art review," *Mathematical Problems in Engineering*, vol. 2014, Article ID 317954, 22 pages, 2014.
- [4] Y. L. Xu, B. Chen, C. L. Ng, K. Y. Wong, and W. Y. Chan, "Monitoring temperature effect on a long suspension bridge," *Structural Control and Health Monitoring*, vol. 17, no. 6, pp. 632–653, 2010.
- [5] G.-D. Zhou and T.-H. Yi, "Recent developments on wireless sensor networks technology for bridge health monitoring," *Mathematical Problems in Engineering*, vol. 2013, Article ID 947867, 33 pages, 2013.
- [6] J. M. Ko and Y. Q. Ni, "Technology developments in structural health monitoring of large-scale bridges," *Engineering Structures*, vol. 27, no. 12, pp. 1715–1725, 2005.
- [7] G.-D. Zhou and T.-H. Yi, "A summary review of correlations between temperatures and vibration properties of long-span bridges," *Mathematical Problems in Engineering*, vol. 2014, Article ID 638209, 19 pages, 2014.
- [8] T.-H. Yi, H.-N. Li, and X.-D. Zhang, "Health monitoring sensor placement optimization for canton tower using immune monkey algorithm," *Structural Control and Health Monitoring*, 2014.
- [9] D. S. Li, G. X. Wang, H. N. Li, L. Ren, and G. B. Song, "On optimal sensor placement for structural health monitoring by subspace approximation," in *Proceedings of the 11th Aerospace Division International Conference on Engineering, Science, Construction, and Operations in Challenging Environments*, 2008.
- [10] M. Meo and G. Zumpano, "On the optimal sensor placement techniques for a bridge structure," *Engineering Structures*, vol. 27, no. 10, pp. 1488–1497, 2005.
- [11] C. Papadimitriou, Y. Haralampidis, and K. Sobczyk, "Optimal experimental design in stochastic structural dynamics," *Probabilistic Engineering Mechanics*, vol. 20, no. 1, pp. 67–78, 2005.
- [12] T.-H. Yi and H.-N. Li, "Methodology developments in sensor placement for health monitoring of civil infrastructures,"

- International Journal of Distributed Sensor Networks*, vol. 2012, Article ID 612726, 11 pages, 2012.
- [13] L. Yao, W. A. Sethares, and D. C. Kammer, "Sensor placement for on-orbit modal identification via a genetic algorithm," *AIAA Journal*, vol. 31, no. 10, pp. 1922–1928, 1993.
 - [14] K. Worden and A. P. Burrows, "Optimal sensor placement for fault detection," *Engineering Structures*, vol. 23, no. 8, pp. 885–901, 2001.
 - [15] S.-F. Hwang and R.-S. He, "A hybrid real-parameter genetic algorithm for function optimization," *Advanced Engineering Informatics*, vol. 20, no. 1, pp. 7–21, 2006.
 - [16] T. G. Carne and C. R. Dohrmann, "A modal test design strategy for modal correlation," in *Proceedings of the 13th International Modal Analysis Conference*, vol. 317, pp. 927–933, Schenectady, NY, USA, February 1995.
 - [17] M. Huang, J. Li, and H. Zhu, "Optimal sensor layout for bridge health monitoring based on dual-structure coding genetic algorithm," in *Proceedings of the International Conference on Computational Intelligence and Software Engineering (CiSE '09)*, pp. 1–4, Wuhan, China, December 2009.
 - [18] T.-H. Yi, H.-N. Li, and M. Gu, "Optimal sensor placement for health monitoring of high-rise structure based on genetic algorithm," *Mathematical Problems in Engineering*, vol. 2011, Article ID 395101, 11 pages, 2011.
 - [19] T.-H. Yi, H.-N. Li, and M. Gu, "Optimal sensor placement for structural health monitoring based on multiple optimization strategies," *Structural Design of Tall and Special Buildings*, vol. 20, no. 7, pp. 881–900, 2011.
 - [20] G.-D. Zhou and T.-H. Yi, "The node arrangement methodology of wireless sensor networks for long-span bridge health monitoring," *International Journal of Distributed Sensor Networks*, vol. 2013, Article ID 865324, 8 pages, 2013.
 - [21] G.-D. Zhou and T.-H. Yi, "The nonuniform node configuration of wireless sensor networks for long-span bridge health monitoring," *International Journal of Distributed Sensor Networks*, vol. 2013, Article ID 797650, 9 pages, 2013.
 - [22] G. D. Zhou, T. H. Yi, and H. N. Li, "Wireless sensor placement for bridge health monitoring using a generalized genetic algorithm," *International Journal of Structural Stability and Dynamics*, vol. 14, no. 5, Article ID 1440011, 21 pages, 2014.
 - [23] P. N. Ngatchou, W. L. J. Fox, and M. A. El-Sharkawi, "Distributed sensor placement with sequential particle swarm optimization," in *Proceedings of the IEEE Swarm Intelligence Symposium (SIS '05)*, pp. 395–398, June 2005.
 - [24] A. R. M. Rao and G. Anandakumar, "Optimal placement of sensors for structural system identification and health monitoring using a hybrid swarm intelligence technique," *Smart Materials and Structures*, vol. 16, no. 6, pp. 2658–2672, 2007.
 - [25] T.-H. Yi, H.-N. Li, and X.-D. Zhang, "A modified monkey algorithm for optimal sensor placement in structural health monitoring," *Smart Materials and Structures*, vol. 21, no. 10, Article ID 105033, 9 pages, 2012.
 - [26] T. H. Yi, H. N. Li, and X. D. Zhang, "Sensor placement on Canton tower for health monitoring using asynchronous-climbing monkey algorithm," *Smart Materials and Structures*, vol. 21, no. 12, Article ID 125023, pp. 1–12, 2012.
 - [27] X. S. Yang, *Nature-Inspired Metaheuristic Algorithm*, Luniver Press, Beckington, UK, 2008.
 - [28] X.-S. Yang, "Firefly algorithms for multimodal optimization," in *Stochastic Algorithms: Foundations and Applications*, vol. 5792 of *Lecture Notes in Computer Science*, pp. 169–178, Springer, Berlin, Germany, 2009.
 - [29] A. H. Gandomi, X.-S. Yang, and A. H. Alavi, "Mixed variable structural optimization using firefly algorithm," *Computers & Structures*, vol. 89, no. 23–24, pp. 2325–2336, 2011.
 - [30] I. Fister, I. Fister Jr., X.-S. Yang, and J. Brest, "A comprehensive review of firefly algorithms," *Swarm and Evolutionary Computation*, vol. 13, pp. 34–46, 2013.
 - [31] R. W. Hamming, "Error detecting and error correcting codes," *The Bell System Technical Journal*, vol. 29, pp. 147–160, 1950.
 - [32] J. H. Holland, *Adaption in Natural and Artificial Systems*, University of Michigan Press, Ann Arbor, Mich, USA, 1975.
 - [33] K. P. Ferentinos and T. A. Tsiligiridis, "Adaptive design optimization of wireless sensor networks using genetic algorithms," *Computer Networks*, vol. 51, no. 4, pp. 1031–1051, 2007.
 - [34] W. Liu, Z. Hou, and M. A. Demetriou, "A computational scheme for the optimal sensor/actuator placement of flexible structures using spatial H_2 measures," *Mechanical Systems and Signal Processing*, vol. 20, no. 4, pp. 881–895, 2006.
 - [35] http://smc.hit.edu.cn/index.php?option=com_content&view=article&id=156&Itemid=81.
 - [36] H. Li, C. M. Lan, Y. Ju, and D. S. Li, "Experimental and numerical study of the fatigue properties of corroded parallel wire cables," *Journal of Bridge Engineering*, vol. 17, no. 2, pp. 211–220, 2012.

Research Article

Study Based on Bridge Health Monitoring System on Multihazard Load Combinations of Earthquake and Truck Loads for Bridge Design in the Southeast Coastal Areas of China

Dezhang Sun,¹ Bin Chen,² and Baitao Sun¹

¹ Institute of Engineering Mechanics, China Earthquake Administration, Harbin 150080, China

² College of Civil Engineering and Architecture, Zhejiang University, Hangzhou 310058, China

Correspondence should be addressed to Bin Chen; jeetchen.123@hotmail.com

Received 8 August 2014; Accepted 1 October 2014

Academic Editor: Bo Chen

Copyright © 2015 Dezhang Sun et al. This is an open access article distributed under the Creative Commons Attribution License, which permits unrestricted use, distribution, and reproduction in any medium, provided the original work is properly cited.

Similar to American *LRFD Bridge Design Specifications*, the current Chinese bridge design code is fully calibrated against gravity load and live load. Earthquake load is generally considered alone and has its own methodology, however, which is not covered in the code in a consistent probability-based fashion. Earthquake load and truck load are the main loads considered in the basis of bridge design in more than 70% of seismic areas in China. They are random processes, and their combination is the main subject of this paper. Seismic characteristics of southeast coastal areas of China are discussed and an earthquake probability curve is calculated through seismic risk analysis. Using measured truck load data from a Bridge Health Monitoring System, the multimodal characteristics of truck load are analyzed and a probability model for a time interval t is obtained by fitting results and reliability theory. Then, a methodology is presented to combine earthquake load and truck load on a probabilistic basis. To illustrate this method, truck load and earthquake load combinations are used. Results conceptually illustrate that truck load and earthquake load are not dominant in southeast coastal areas of China, but the effect of their combination is. This methodology quantitatively demonstrates that the design is controlled by truck load in most ranges; that is, truck load is more important to bridge design in the region.

1. Introduction

In the current bridge design specifications of China [1] a typical bridge is designed for 100 years' service life and the design limit states are only fully calibrated for dead and live loads. Consideration of earthquake load has its own unique approach, principally because data and statistics are rare. Truck load data are old and may not suit the current situation, and they therefore need to be updated. This fact makes it difficult to properly consider both truck load and earthquake load in a consistent fashion. A research project is currently being carried out to establish a methodology to systematically combine truck load and earthquake load. Principle emphasis is given to establishing the proper "demand." In order to pursue the demand side of bridge design specifications, there are numerical challenges that must be overcome in addition to the fact that very limited historical data are available. Truck

load and earthquake load are time-variant random processes. Truck load occurs once in a typical time span of minutes or seconds on a common bridge, while earthquake load occurs once in a typical time span of years or decades. Furthermore, there is no evidence that the occurrence of earthquake loads follows normal distributions. Fortunately, many bridge health monitoring systems (BHMS) have been established, which provide a convenient way to get useful data for this research [2].

To overcome the challenges, many efforts [3–9] have been made in the past decades. However, because numbers of assumptions have to be made in each model, no general conclusions can be drawn about satisfactory approach to deal with load combination of earthquake load and truck load. In more recent papers, a methodology is proposed by Liang and Lee [10, 11]; however, its accuracy is yet to be substantiated.

One objective of this paper is to describe a methodology to handle truck load and earthquake load combinations. Earthquake load is modeled using seismic risk analysis. Truck load is modeled using Stationary Poisson processes based on the BHMS and statistical analysis. Two numerical examples of truck load and earthquake load combinations are used to illustrate the methodology.

2. Earthquake Load

A number of variables describe the effects that earthquakes have on bridges, such as the intensity of acceleration, the rate of earthquake occurrences, the natural period of the bridge, the seismic response coefficient, and the response modification factor. In order to explain the methodology of load combinations, only the intensity of acceleration and the rate of occurrence are chosen as the main variables.

Based on the Poisson process assumption, the probability of exceedance (P_e) in a given exposure time (T_e) is related to the annual probability of exceedance (λ) by [12],

$$P_e = 1 - e^{-\lambda \cdot T_e}. \quad (1)$$

Because the number of earthquakes varies widely from site to site, they are converted to Peak ground acceleration (PGA) and the return period curve ($T_R = 1/\lambda$, T_R is return period). The cumulative probability of an earthquake in time T can be written as

$$P = e^{-T/T_R}. \quad (2)$$

The PGA and frequency of exceedance curve can be obtained from U.S. Geological Survey (USGS) mapping in the United States but cannot be obtained in China. Therefore, seismic risk analysis is used to calculate earthquake probability curve. The procedures are presented just as follows.

For more than one potential seismic source zone, suppose the parameters of the earthquake are random distributions and the probability over 1 year is a stable Poisson process. Based on the total probability theorem, the probability of exceeding a given earthquake intensity S_0 in one site can be expressed by (3), by considering the uncertainties of occurrence and the upper limit magnitude:

$$P_t(S > S_0) = 1 - \prod_{k=1}^K \sum_{i=1}^I W_{r,k}^{(i)} \exp \left[- \sum_{j=1}^J v_{k,j}^{(i)} \cdot P_k^{(j)} W_{u,k}^{(j)} \cdot t \right], \quad (3)$$

where $P_k^{(i)}$ is the probability of the j th upper limit magnitude exceeding a given earthquake intensity S_0 in potential seismic source k , $v_{k,j}^{(i)}$ is the i th year occurrence probability of the j th upper limit magnitude in potential seismic source k , $W_{r,k}^{(i)}$ is the weight of the i th year occurrence probability in potential seismic source k , and $W_{u,k}^{(j)}$ is the weight of the j th upper limit magnitude in potential seismic source k .

The earthquake intensity could be acceleration, velocity, or displacement. For acceleration, $S = \ln a$ (S is earthquake intensity; a is acceleration).

Because of the uncertainties of direction impact of potential seismic source zones, for $t = 1$ year, the probability of exceedance is

$$P_1(S > S_0) = \sum_{k=1}^K \sum_{i=1}^I \sum_{j=1}^J v_k^{(i)} P_k^{(j)} W_{r,k}^{(i)} W_{u,k}^{(j)}, \quad (4)$$

where $P_k^{(j)}$ is the conditional probability of the j th upper limit magnitude.

For disperse potential seismic source areas, the probability of the j th upper limit magnitude can be expressed as

$$P_k^{(j)}(S > S_0 | M_{u,k}) = \frac{\sum_{k=1}^K P_\xi^{(j)}(S > S_0 | R) \Delta A_\xi}{A_k}, \quad (5)$$

where A_k is the area of the potential seismic source k ; ΔA_ξ is the area of zone ξ . If the occurrence probability of 1 year is divided by the weights in each upper limit magnitude of potential seismic source zone, the exceedance probability of the j th upper limit magnitude of potential seismic source k can be given as

$$P_\xi^{(j)} = \frac{\sum_n \xi_n \left\{ K_r [\Phi''_{n+1} - \Phi''_n] + [e^{-\beta M_n^{(j)}} \Phi'_n - e^{-\beta M_{n+1}^{(j)}} \Phi'_{n+1}] \right\}}{\sum_m \xi_m [e^{-\beta M_n^{(j)}} - e^{-\beta M_{n+1}^{(j)}}]} + \Phi_0. \quad (6)$$

According to the seismic belt materials and reports, the southeast coastal area of China has two I degree seismic areas, namely, the South China seismic area and the South China Sea seismic area. The seismic belt of southeast coastal areas of China is located south of the middle Yangtze River seismic belt, bordering on the seismic region of the Tibetan Plateau on the west, and includes Kwangtung province, Hainan province, most of Fujian and Guangxi provinces, and part of Yunnan, Guizhou, and Jiangxi provinces. Crustal thickness ranges between 28 and 40 km, gradually increasing from the southeast coastal area of China to the northwest mountains. An internal secondary elliptical gravity anomaly is relatively developed in the earthquake zones. There are no obvious banded anomalies except the gravity gradient zones of southeast coastal areas and Wuling Mountain. In the zones, magnetic anomalies change gently and there are no larger banded anomalies. Because the southeast coastal areas of China are in the same seismic belt and most of the areas in the zone have a PGA seismic fortification level of 0.1g, Shenzhen city is then used for the basic earthquake probability calculation and comparison in this paper. The South China belt is shown in Figure 1. From Figure 1, it can be seen that there are many higher than Ms 6.0 earthquakes in the southeast coastal areas of China present in the seismic analysis. Earthquake load is still the main load considered for bridge design in these areas.

Based on (3) to (6), the annual exceedance probability of Shenzhen is shown in Figure 2.

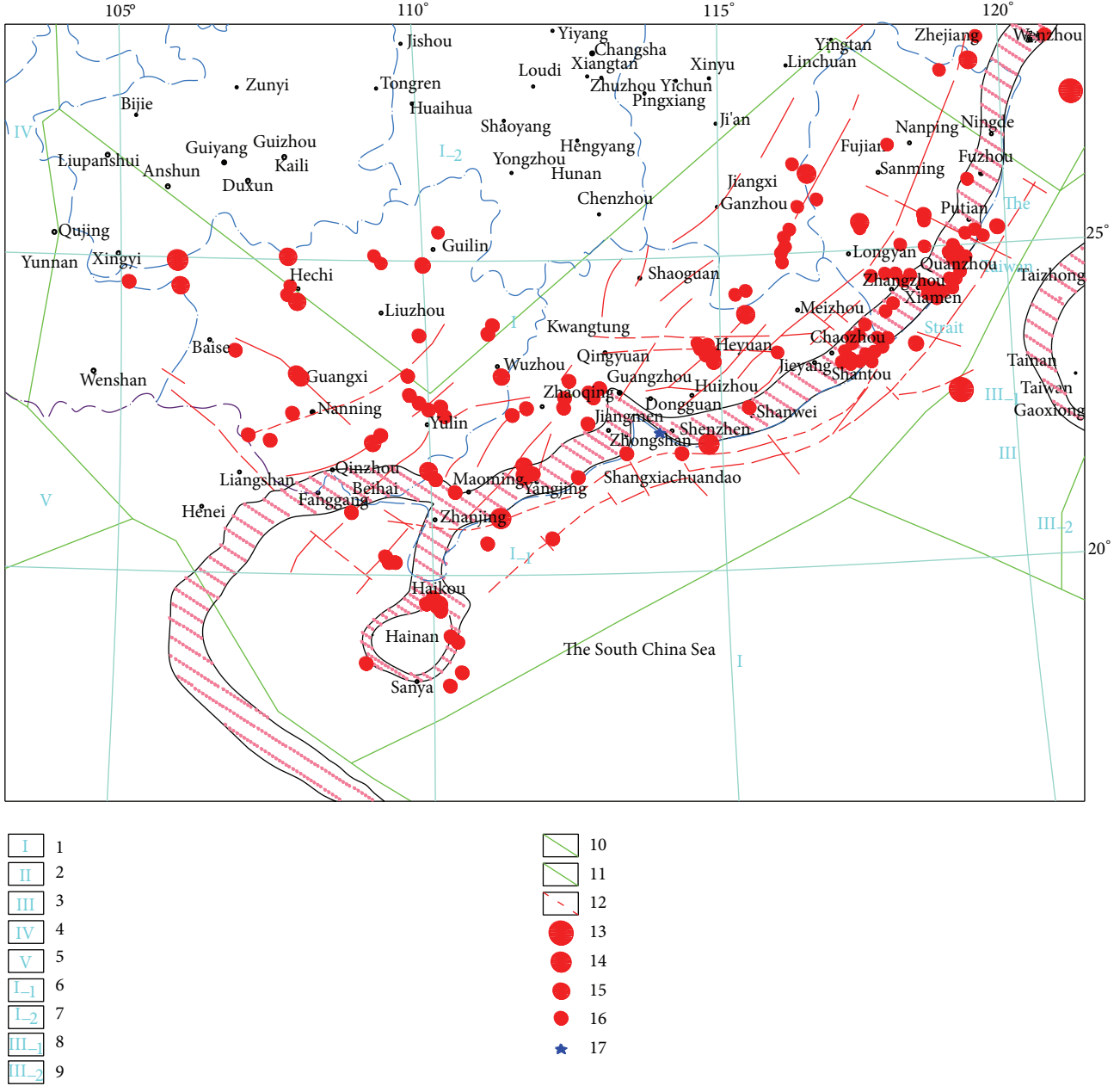


FIGURE 1: The South China belt. (1) The seismic area of South China. (2) The seismic area of South China Sea. (3) The seismic area of Taiwan. (4) The earthquake subregion of middle of Qinghai-Tibet Plateau. (5) The earthquake subregion of south of Qinghai-Tibet Plateau. (6) The southeast coastal seismic belt (South China coastal seismic belt). (7) The seismic zone in the middle reach of Yangtze River. (8) Seismic area of the west of Taiwan. (9) Seismic area of the east of Taiwan. (10) Boundaries of seismic zone. (11) Boundaries of seismic belt. (12) South China coastal seismic rupture. (13) Epicenter of Ms 7 and above. (14) Epicenter of Ms 6.0–6.9. (15) Epicenter of Ms 5.0–5.9. (16) Epicenter of Ms 4.7–4.9. (17) Calculation site.

Assume that the probability density of earthquake load intensity in time T follows a distribution defined as $f_T(y)$, where y is a variable of PGA intensity. Based on the Poisson process assumptions, the cumulative probability function $F_t(y)$ over interval t can be obtained using the following:

$$F_t(y) = [F_T(y)]^{t/T}. \quad (7)$$

The probability density function can then be derived as

$$f_t(y) = \frac{\partial F_t(y)}{\partial y} = \frac{t}{T} \cdot [F_T(y)]^{(t/T)-1} \cdot f_T(y). \quad (8)$$

Note that t and T should have the same dimension.

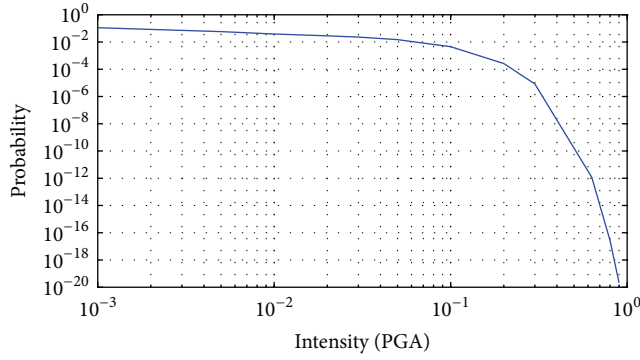


FIGURE 2: Annual exceedance probability of PGA.

3. Truck Load

Studies on truck load have been difficult historically, principally because weighing equipment was lacking and the data are correspondingly rare [13, 14]. Fortunately, the installation of BHMS is required on newly built long-span bridges, including the weighing-in-motion (WIM) system [15–17]. Time, gross weight, axle weight, wheel base, velocity, and so forth are measured and collected. The probability model of truck load can be obtained through statistical analysis.

Nowak [18] indicated that at a specific site heavy trucks may have an average number of 1000, which is also discussed by Ghosn. Moses [19] suggested heavy trucks follow a normal distribution with a mean of 300 kN and a standard deviation of 80 kN (coefficient of variable, COV = 26.5%). Zhao and Tabatabai [20] discussed the local standard vehicle model, using data from about six million vehicles in Washington, which can be used as a reference for a truck load model. In this paper, the truck load model is obtained through data mining from measured WIM data from three bridge sites in Hangzhou, Xiamen, and Shenzhen (Figure 3). Truck load data of 5 axles and more in the three sites are filtered and selected. Through WIM data analysis, truck load probability characteristics of Hangzhou, Xiamen, and Shenzhen are similar, even the shape of truck load probability curves. Considering the three sites have very similar traffic flow, almost equal to 1.0, truck load probability curve of Shenzhen City is used for analysis and validity of subsequent case studies. Truck load probability curve is shown in Figures 4 and 5. The fitted curve is obtained using normal distribution, whose mean value is 294.9 kN, and the coefficient of variance is 37.4%.

For a typical bridge, the truck load will consist of a varying number of trucks on the bridge. The probability function for such a bridge can be obtained using following analysis. Assume A is a set consisting of the elements A_1, A_2, \dots, A_m , which present m events, and the probability of A is $P(A)$, while B is a set consisting of the elements B_1, B_2, \dots, B_n , which present n events, and the probability of B is $P(B)$; so the probability $P(A + B)$ presents the probability of intensity ($A + B$). Then $P(A + B)$ can be calculated by

$$P_{A+B}(k) = \sum_i P_A(i) \cdot P_B(k + 1 - i). \quad (9)$$

Note that the length of $P(A)$ is m and the length of $P(B)$ is n . The sum is over all the values of i which lead to legal subscripts for $A(i)$ and $B(k + 1 - i)$, where k is the k th ($A + B$)(k), $i = \max(1, k + 1 - n) : \min(k, m)$. Equation (9) reflects the probability of combining two sets, and when it comes to a series of sets $\Phi = \Phi_1 + \Phi_2 + \dots + \Phi_N$, (9) can be extended to N dimensions,

$$\begin{aligned} P_\Phi(\phi_1 + \phi_2 + \dots + \phi_N) \\ = \sum (\dots (\sum (\sum P_{\Phi_1}(\phi_1) \cdot P_{\Phi_2}(\phi_2)) \cdot P_{\Phi_3}(\phi_3)) \dots) \\ \cdot P_{\Phi_N}(\phi_N), \end{aligned} \quad (10)$$

where Φ_i in (10) is the i th set of event and $P_{\Phi_i}(\phi_i)$ is the probability of set Φ_i .

Based on total probability theory and Poisson processes, the truck load intensity function for an interval t can be calculated using the following:

$$F_\Phi(\phi)_t = P_{\Phi_0} + \sum_N P_{\Phi_1 + \Phi_2 + \dots + \Phi_N} \cdot p(N), \quad (11)$$

where P_{Φ_0} is the probability with no truck passing on the bridge; $N = 1, 2, \dots$ maximum number of trucks. $P_{\Phi_1 + \Phi_2 + \dots + \Phi_N}$ is the probability of varying number of trucks passing the bridge; $p(N)$ is the probability of occurrence of N trucks on the bridge.

4. Model of Combination

The intensity of dead load is usually defined as a time independent variable, and that of truck load is a time dependent variable, both of whom follow normal distributions [5, 8, 18]. In this paper, a normal distribution is used for dead load, which is considered to maintain more or less the same magnitude, such that it can be treated as a random time independent variable.

As mentioned above, earthquake load and time-variable truck load are assumed to be Poisson processes, each with same distribution and time duration. Based on these assumptions, as mentioned earlier load processes can be converted to a small t interval, in which loads can be combined. The objective of time-variable combination is to find the maximum value of different random variables, namely, the combined value $X = X_1 + X_2 + \dots + X_n$, with an interval t and maximum value $X_{\max, T}$, in a time T . n is the number of loads, X is the intensity of combined load, and X_i is the load intensity of the i th load. The maximum value of X in the lifetime of the bridge can be expressed as

$$X_{\max, T} = \max_T [X_1 + X_2 + \dots + X_n]_t. \quad (12)$$

To simplify the discussion, the number of loads is taken as two, the problem being reduced to the prediction of $X_{1,2} = X_1 + X_2$, where $X_{1,2}$ is the intensity of the union of X_1 and X_2 . Assume that $f_1(x)$ and $f_2(x)$ are the probability density functions of X_1 and X_2 in the interval t and $F_1(x)$ and $F_2(x)$ are the cumulative probability functions of X_1 and X_2 in the



FIGURE 3: Layout of monitoring sites.

interval t . $f_{X_{1,2}}(x)$ and $F_{X_{1,2}}(x)$ are the probability density function and cumulative probability function of $X_{1,2}$. The maximum value of combination in the entire bridge service life is defined as $X_{1,2 \max, T}$, which is defined as

$$X_{1,2 \max, T} = \max_T [X_1 + X_2]_t. \quad (13)$$

The probability density of the combined loads X can be obtained using the convolution integral:

$$f_{X_{1,2}}(x) = f_1 * f_2 = \int_{-\infty}^{+\infty} f_1(\tau) \cdot f_2(x - \tau) d\tau, \quad (14)$$

where “*” is used as convolution symbol.

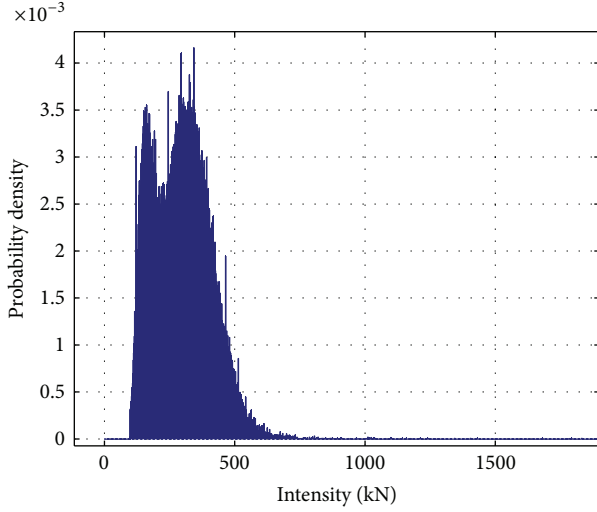


FIGURE 4: Histogram of the monitoring sites.

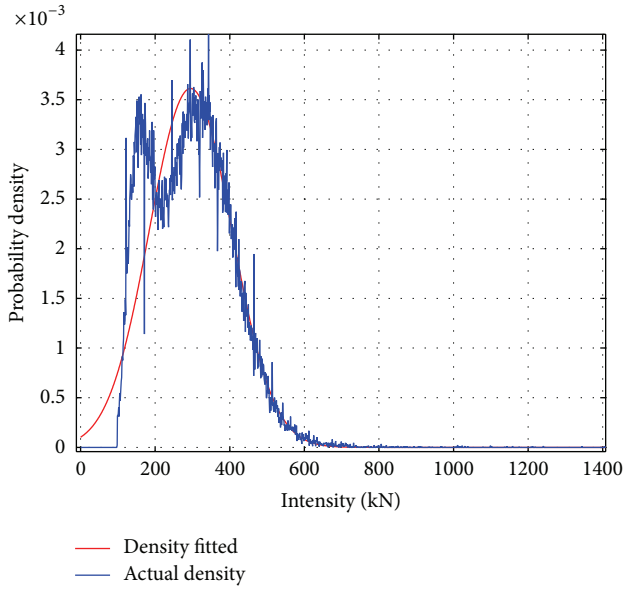


FIGURE 5: Curve fitting of truck load density.

Dirac Delta function is introduced to deal with the characteristics of X and Y in small t interval:

$$\delta(x) = \begin{cases} +\infty, & x = 0, \\ 0, & x \neq 0. \end{cases} \quad (15)$$

Therefore, the probability density can be illustrated as

$$f_i(x) = P_{X_{i,0}} \delta(x) + f'_i(x), \quad i = 1, 2. \quad (16)$$

Note that $P_{X_{i,0}}$ is the probabilities of X_i ($i = 1, 2$) in its “zero points”; namely, the events do not happen (e.g., the maximum trucks on the bridge are 8; $P_{X_{i,0}}$ is the probability of no trucks

on the bridge). $f'_i(x)$ is its probability density functions without “zero points.” Then, the cumulative probability functions of X_1 and X_2 can be calculated through

$$\begin{aligned} F_i(x) &= P_{X_{i,0}} \int_{-\infty}^x \delta(\tau) d\tau + \int_{-\infty}^x f'_i(\tau) d\tau \\ &= P_{X_{i,0}} + \int_{-\infty}^x f'_i(\tau) d\tau, \end{aligned} \quad (17)$$

where $i = 1, 2$.

Based on (16) and (17), the probability density of X then can be grouped as

$$\begin{aligned} f_{X_{1,2}}(x) &= \int_{-\infty}^{+\infty} [P_{X_{1,0}} \delta(\tau) + f'_1(\tau)] \\ &\quad \times [P_{X_{2,0}} \delta(x - \tau) + f'_2(x - \tau)] d\tau \\ &= \int_{-\infty}^{+\infty} \{ [P_{X_{1,0}} P_{X_{2,0}} \delta(\tau) \delta(x - \tau)] \\ &\quad + [P_{X_{1,0}} \delta(x) f'_2(x - \tau)] + [P_{X_{2,0}} \delta(x - \tau) f'_1(\tau)] \\ &\quad + [f'_1(\tau) f'_2(x - \tau)] \} d\tau \\ &= P_{X_{1,0}} P_{X_{2,0}} \delta(x) + P_{X_{1,0}} f'_2(x) + P_{X_{2,0}} f'_1(x) \\ &\quad + \int_{-\infty}^{+\infty} f'_1(\tau) f'_2(x - \tau) d\tau, \end{aligned} \quad (18)$$

where based on the characteristic of Dirac Delta function, which is $\int_{-\infty}^{+\infty} \delta(x) dx = 1$, (18) can be converted to cumulative probability function. Assume the cumulative probability function of $F_{X_{1,2}}(x)$; then

$$\begin{aligned} F_{X_{1,2}}(x) &= \int_{-\infty}^x f_{X_{1,2}}(x) dx \\ &= P_{X_{1,0}} P_{X_{2,0}} + P_{X_{1,0}} F'_2(x) + P_{X_{2,0}} F'_1(x) \\ &\quad + \int_{-\infty}^{+\infty} F'_1(\tau) f'_2(x - \tau) d\tau. \end{aligned} \quad (19)$$

From (19), it is clear that the combined load probability consists of four parts: events X_1 and X_2 are not happening; event X_1 is happening while X_2 is not happening; event X_1 is not happening while X_2 is happening; and X_1, X_2 are both happening.

To further simplify the discussion without losing generality, the probability of two loads occurring simultaneously is neglected. Thus (19) is simplifying to

$$\begin{aligned} F_{X_{1,2}}(x) &= \int_{-\infty}^x f_{X_{1,2}}(x) dx \\ &\approx P_{X_{1,0}} P_{X_{2,0}} + P_{X_{1,0}} F'_2(x) + P_{X_{2,0}} F'_1(x). \end{aligned} \quad (20)$$

Then the cumulative probability function, $F_{X_{1,2,\max,T}}(x)$, of maximum value of load combinations, $X_{1,2,\max,T}(x)$, in time T can be obtained,

$$F_{X_{1,2,\max,T}}(x) = [F_{X_{1,2}}(x)_t]^{T/t}. \quad (21)$$

When the number of loads is more than two and these loads apply to bridge directly while satisfying Poisson process, (14) can be extended to n dimensions. Assume f_1, f_2, \dots, f_n are the probability densities functions of X_1, X_2, \dots, X_n ; F_1, F_2, \dots, F_n are the cumulative probability functions of X_1, X_2, \dots, X_n ; f'_1, f'_2, \dots, f'_n are the probability density functions of X_1, X_2, \dots, X_n without “zero” points; $f_X(x)$ and $F_X(x)$ are the probability density function and cumulative probability function. Then the probability density function is deduced as

$$f_X(x) = f_1(x) * f_2(x) * \dots * f_n(x), \quad (22)$$

where the cumulative probability $F_{X,\max}(x)$, similar to that given by (19), is

$$\begin{aligned} F_X(x) &= \int_{-\infty}^x f_X(x) dx \\ &= \int_{-\infty}^x f_1(x) * f_2(x) * \dots * f_n(x) dx. \end{aligned} \quad (23)$$

Equation (23) can account for load combinations of all loads, which satisfy the first three assumptions. If more than two events occurring simultaneously can be neglected, (23) reduces to

$$\begin{aligned} F_X(x) &= \int_{-\infty}^x f_X(x) dx \\ &\approx P_{X_{1,0}} P_{X_{2,0}} \dots P_{X_{n,0}} + F'_1 P_{X_{2,0}} \dots P_{X_{n,0}} \\ &\quad + \dots + P_{X_{1,0}} P_{X_{2,0}} \dots P_{X_{n-1,0}} F'_n. \end{aligned} \quad (24)$$

Then the maximum value of X in time T can be obtained by

$$F_{X_{\max,T}}(x) = [F_X(x)_t]^{T/t}, \quad (25)$$

where $F_X(x)_t$ is $F_X(x)$ in t interval; $F_{X_{\max,T}}(x)$ is the cumulative probability function of maximum value of X in time T .

Although in our study emphasis is given to formulate the “demand” to establish load combinations, all events must address a capacity issue of the bridge. For example, the earthquake load and truck load combination on a bridge column can either consider the vertical load or the column base shear load. Theoretically, (23) can deal with most load combinations, but as more loads are considered, a more conservative design will be adopted. Based on the methodology and assumptions described above, the maximum load can be combined and the procedures are summarized as follows:

- (1) determine truck load and earthquake load distributions over a particular period;
- (2) using Poisson processes, convert earthquake load and truck load distributions over a particular period to a sufficiently small interval t ;

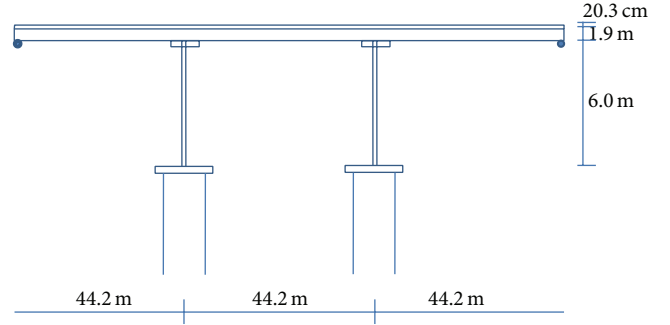


FIGURE 6: Longitudinal profile of the typical bridge.

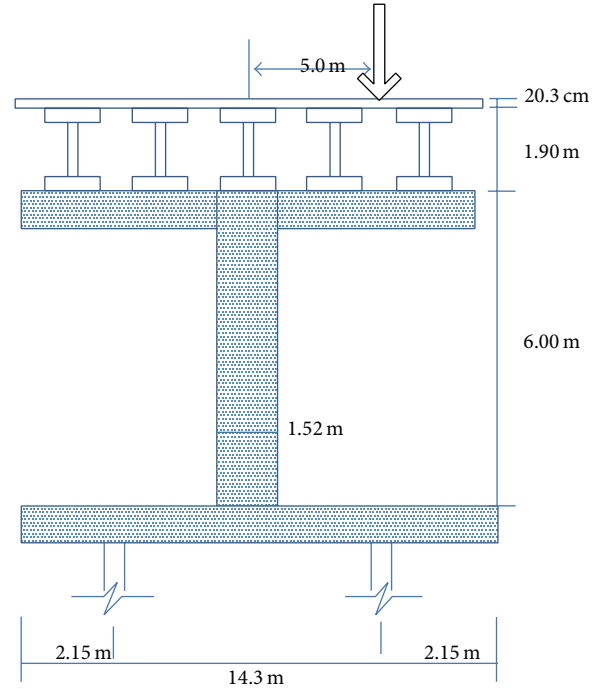


FIGURE 7: Transverse profile of the typical bridge.

- (3) using (23), earthquake and truck load combinations over an interval t can be obtained;
- (4) using (25), the load combinations over an interval t can be converted to the bridge service life interval T .

5. Numerical Examples

Example 1. Using the method of load combination described in the preceding section, a simple example of horizontal load combination is presented here. Profiles of the typical bridge are shown in Figures 6 and 7. The weight of the superstructure at each column is 538 tons, the eccentricity of truck load is 5.0 meters, and the effects of soil and secondary effects of gravity are ignored. Furthermore, it is assumed that the maximum number of trucks on one lane is two. The results are given in Figures 8, 9, 10, 11, 12, 13, and 14. The interval t is 10 seconds, and the average daily truck traffic (ADTT) is about 1947.

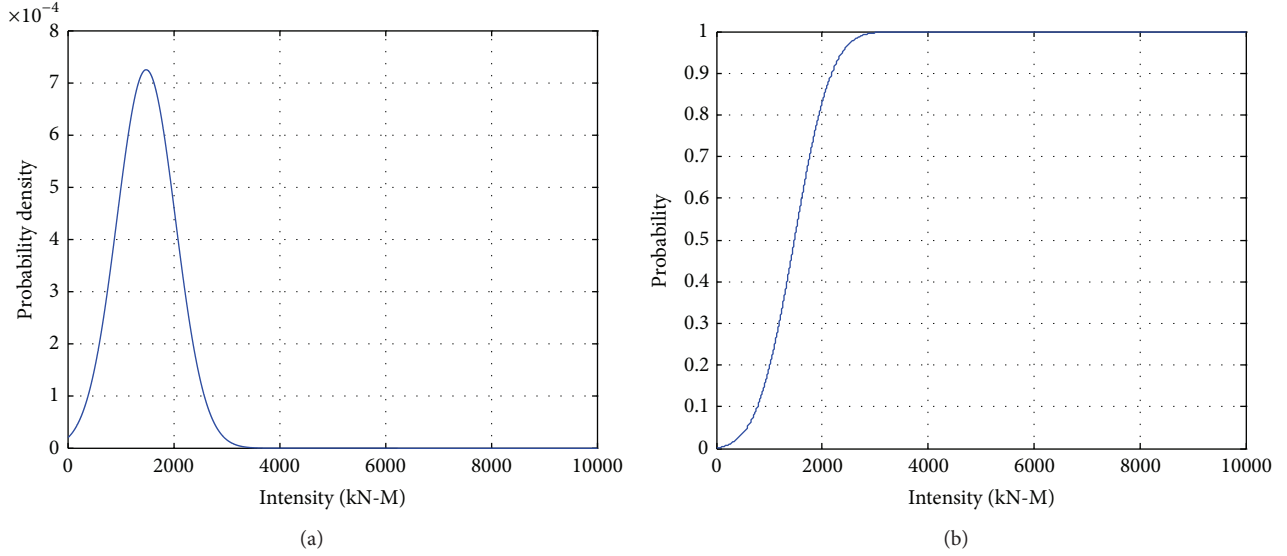


FIGURE 8: Probability curve of each truck load effect.

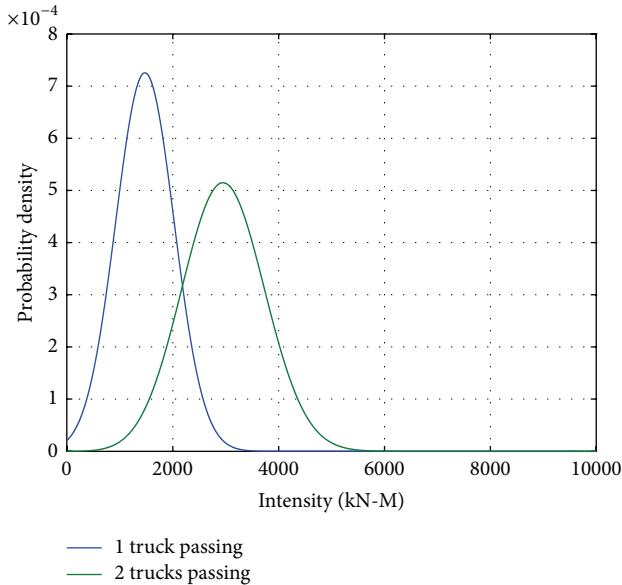
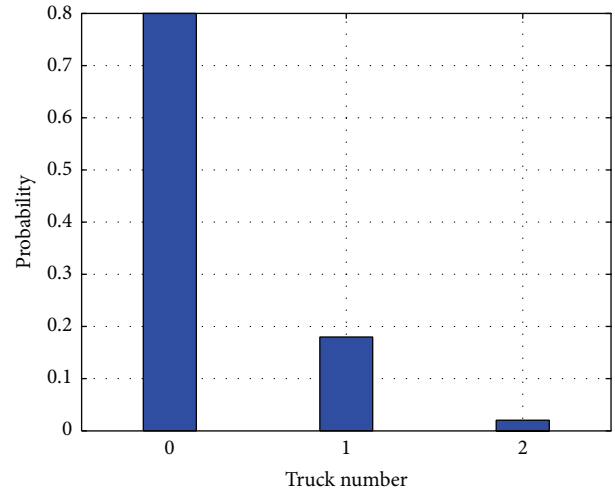


FIGURE 9: Truck load probability density curve for varied number of trucks.

Truck and earthquake load effects are the base moment caused by trucks and earthquakes, respectively. Figure 8 shows the probability curves of each truck load effect, which has a similar shape to truck load. Figure 9 shows the truck load probability density curve for varied numbers of trucks. From Figure 10 we can see that over the interval t the probability of no truck on the bridge is much larger than the other number of trucks passing. Figure 11 shows the combined probability curves for truck load over an earthquake load duration, which indicate that the truck load over an earthquake load duration is larger than each truck load.

FIGURE 10: Probability of passing truck number simultaneously in t interval on the bridge.

From the results shown in Figure 13, it can be seen that curve C and curve A have a similar shape and curve C is displaced to the right. This means that mode and mean value of the truck and earthquake load combination in this example is larger than those of truck load and also illustrates that truck load is more important to bridge design in this area. From Figure 14, we can see more clearly that over most ranges truck load is larger than earthquake load. Because the truck load has a smaller tail, their combination in the tail is close to the earthquake load. Curve D of loads combined directly over 100 years is further away from curve C, which means the combinations of truck load and earthquake load directly over 100 years give a much larger value, and it is not suggested that the bridge design uses the curve D method.

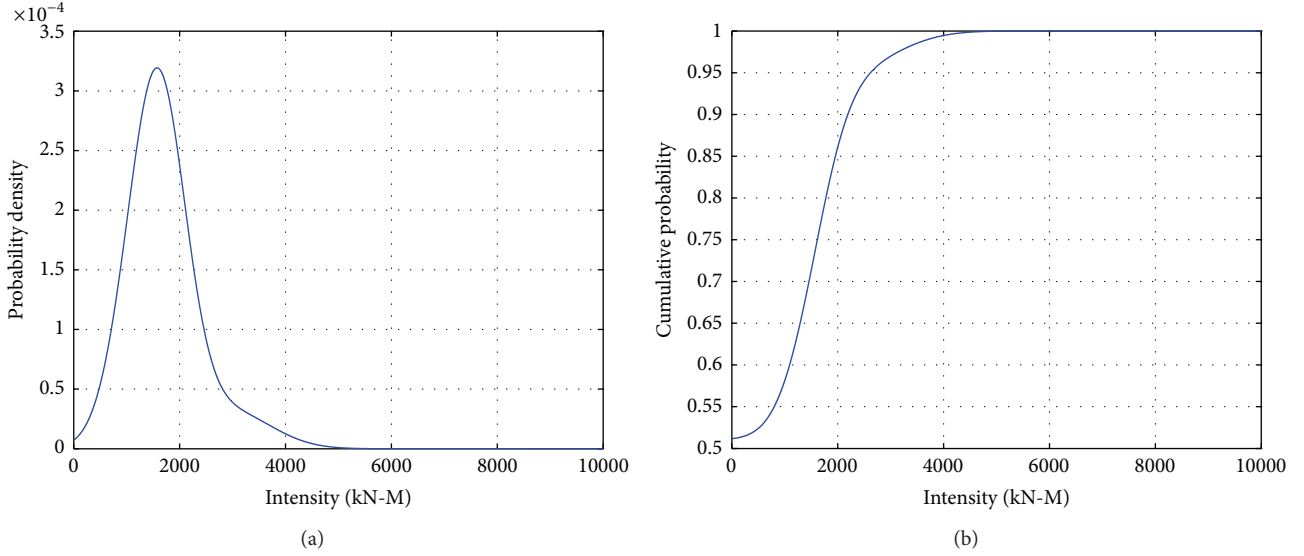


FIGURE 11: Combined probability curves for truck load in earthquake load duration.

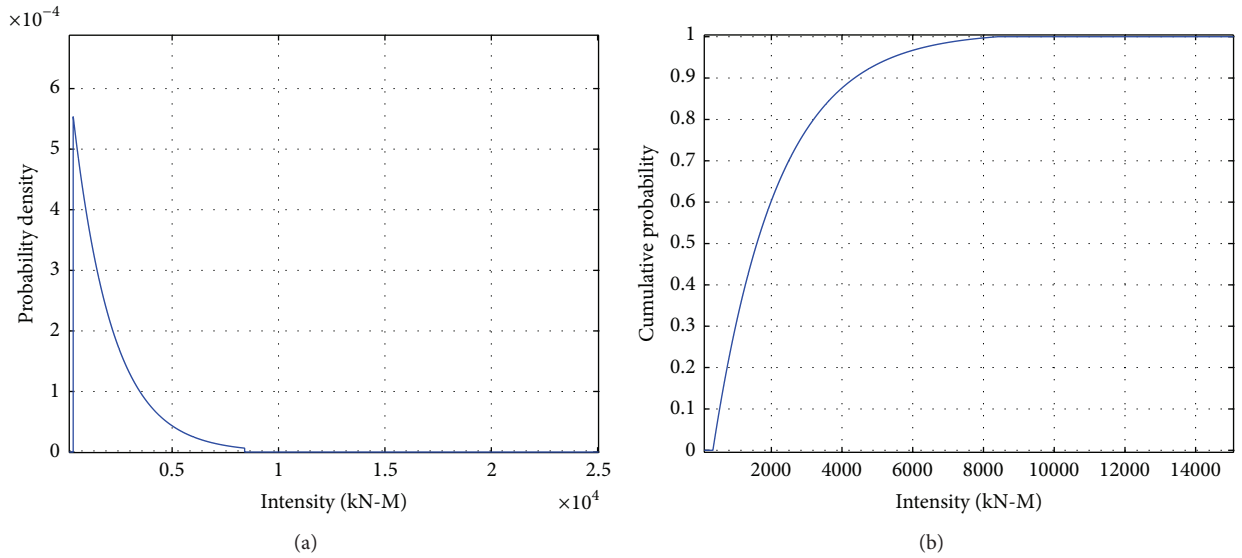


FIGURE 12: Probability curves for earthquake load in 100 years.

Example 2. Example 2 illustrates vertical load combinations. Most of the configurations are the same as used in Example 1. The difference is in the maximum number of trucks; namely, the maximum number of trucks on one lane in this example is four. The results are shown in Figures 15, 16, 17, 18, 19, and 20. Figures 13 and 14 are the results of truck load. Note that in this example the t interval is 10 seconds and T is taken as 100 years.

Figures 15 to 16 show vertical truck load probability curves for varied numbers of trucks and probabilities of passing truck numbers on the bridge, over the interval t . From Figure 16, it can be seen that the probability is very low when the maximum number of trucks on one lane is four. Figures 17 and 18 show similar curve shapes with those

in Figures 13 and 14, which indicate that there is the same rule in load combinations in both the horizontal and vertical directions. Comparing Figures 17 to 20, though the maximum number of trucks is four, because dead load is combined with truck and earthquake load in the gravity direction, the dead load contributes a substantial portion in vertical load combinations.

6. Conclusions

This paper describes a method to combine earthquake load and truck load in the service life of bridges. The following conclusions can be drawn.

- (1) Given the more than 70% seismic areas in China, earthquake load is a main consideration for bridge

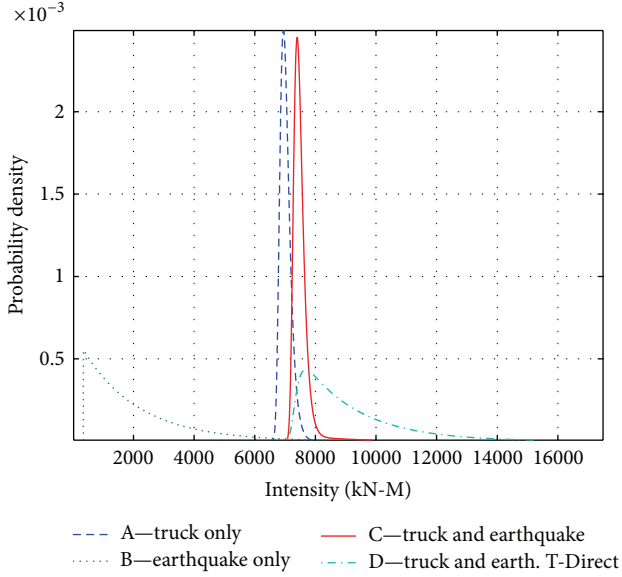


FIGURE 13: Probability density of load combination in 100 years.

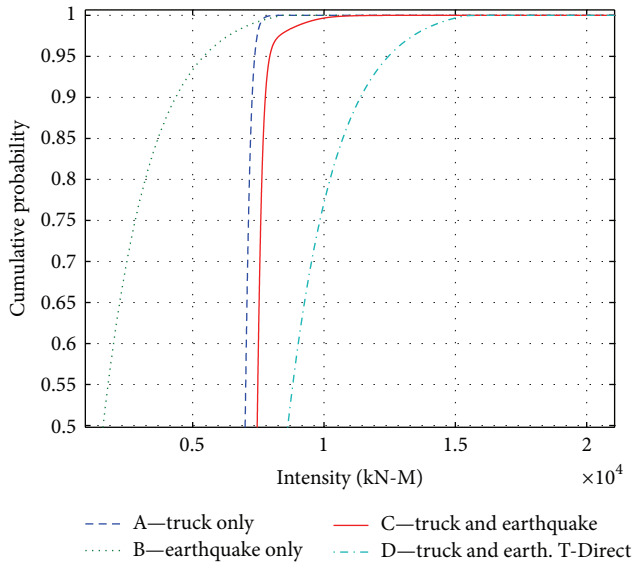


FIGURE 14: Cumulative probability of load combination in 100 years.

design in the southeast coastal areas of China. The earthquake load probability curve is obtained using seismic risk analysis.

- (2) Using measured truck load data from BHMS, multimodal characteristics of truck load are analyzed. The truck load density of each truck is obtained by curve fitting. Considering that truck load may consist of varying numbers of trucks, truck load is calculated through traffic analysis.
- (3) In this method, the maximum value of combined load is defined as $X_{\max,T} = \max_T[X_1 + X_2 + \dots + X_n]_t$, which means $(X_1 + X_2 + \dots + X_n)$ over the interval t is first combined and then the maximum value in the

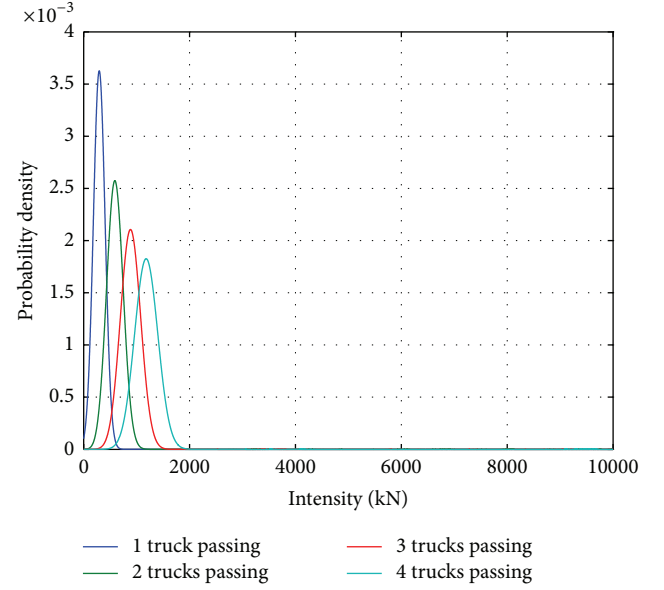
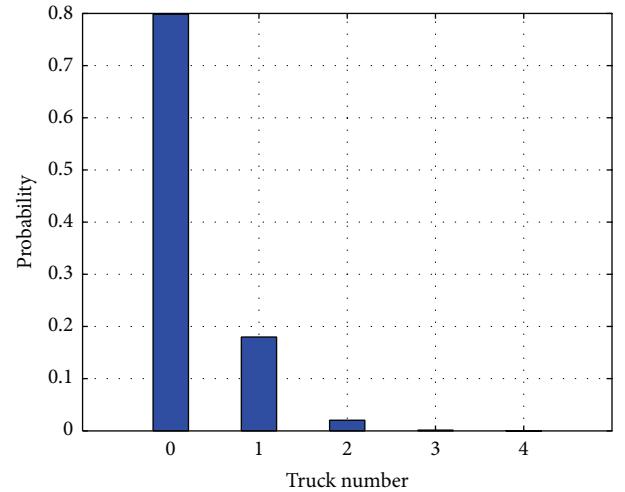


FIGURE 15: Vertical truck load probability density curves for varied number of trucks.

FIGURE 16: Probability of passing truck number simultaneously in t interval on the bridge with maximum number 4.

bridge service life is determined. $X_{\max,T}$ is based on probability, which covers all the probability combinations of the combined situations. In this method, a Dirac Delta function is introduced to deal with X over a small interval t . To demonstrate the methodology intuitively, examples of load combinations in horizontal and vertical directions are provided.

- (4) The shape of the earthquake and truck load combination is similar to that of truck load alone, but the curve is displaced to the right, which means the mode and mean value of truck and earthquake load combination in this example is larger than that of truck load alone. This also illustrates that truck load is

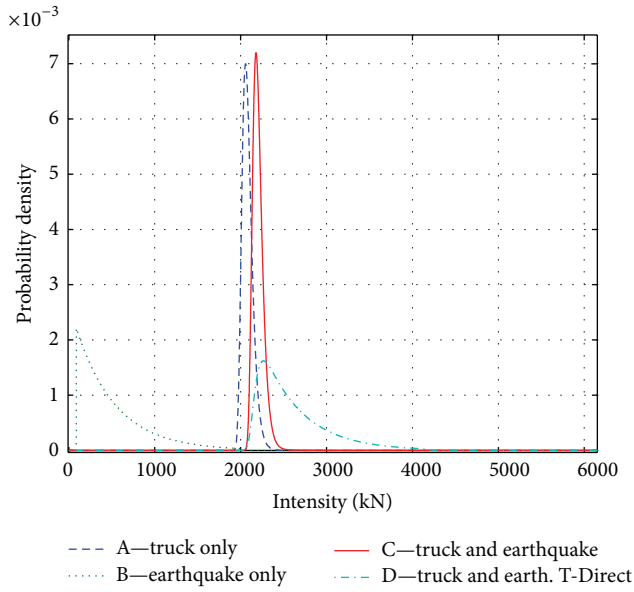


FIGURE 17: Probability density of vertical load combination in 100 years.

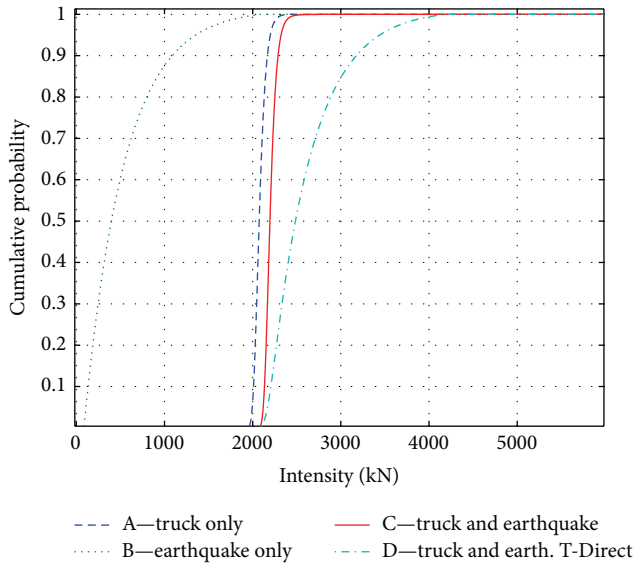


FIGURE 18: Cumulative probability of vertical load combination in 100 years.

more sensitive to bridge design and over most ranges truck load is larger than earthquake load in this area.

- (5) The curve from direct load combined over 100 years is further away from the curve obtained using the method in the paper, with the direct combination of truck load and earthquake load over 100 years giving much larger values. It is not suggested that this method be used in bridge design considerations.
- (6) Because dead load is combined with truck and earthquake load along the direction of gravity, the dead

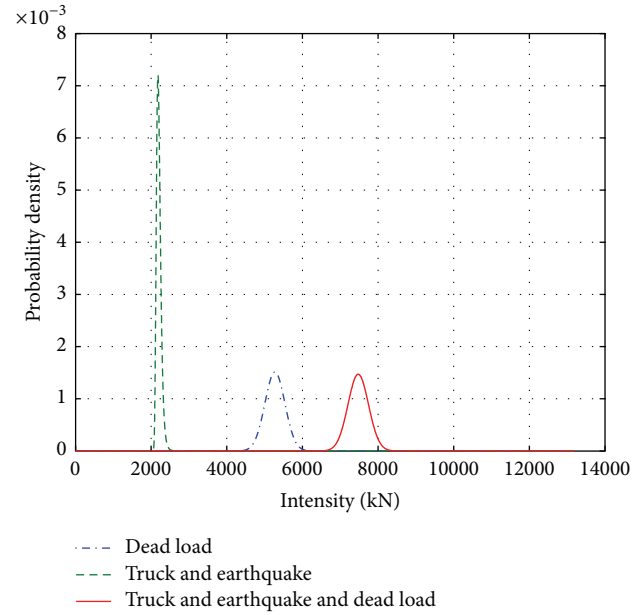


FIGURE 19: Probability density of dead, truck, and earthquake load combination.

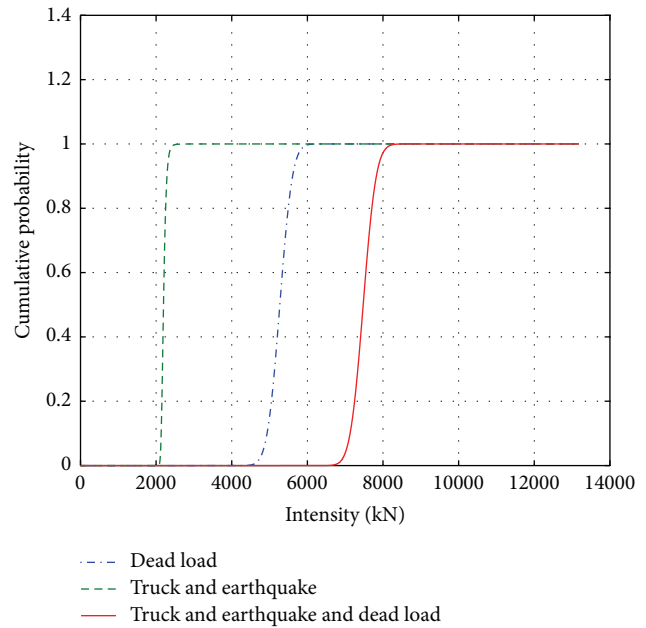


FIGURE 20: Probability curves of dead, truck, and earthquake load combination.

load contributes a substantial portion in vertical load combinations.

Conflict of Interests

The authors declare that there is no conflict of interests regarding the publication of this paper.

Acknowledgments

This study is jointly funded by Basic Institute Scientific Research Fund (Grant no. 2012A02), the National Natural Science Fund of China (NSFC) (Grant no. 51308510), and Open Fund of State Key Laboratory Breeding Base of Mountain Bridge and Tunnel Engineering (Grant no. CQSLBF-Y14-15). The results and conclusions presented in the paper are of the authors and do not necessarily reflect the view of the sponsors.

References

- [1] P. R. China Ministry of Communications, "General code for design of highway bridges and culverts," Tech. Rep. JTG D60-200, China Communications Press, Beijing, China, 2004.
- [2] T.-H. Yi, H.-N. Li, and M. Gu, "Experimental assessment of high-rate GPS receivers for deformation monitoring of bridge," *Measurement: Journal of the International Measurement Confederation*, vol. 46, no. 1, pp. 420–432, 2013.
- [3] C. J. Turkstra and H. O. Madsen, "Load combinations in codified structural design," *Journal of Structural Engineering*, vol. 106, no. 12, pp. 2527–2543, 1980.
- [4] ACI Publication SP-31, *Probabilistic Design of Reinforced Concrete Buildings*, American Concrete Institute, Detroit, Mich, USA, 1971.
- [5] B. Ellingwood, *Development of a Probability Based Load Criterion for American National Standard A58-Building Code Requirements for Minimum Design Loads in Buildings and Other Structures*, U.S. Department of Commerce/National Bureau of Standards, 1980.
- [6] Y. K. Wen, *Development of Reliability-Based Design Criteria for Buildings Under Seismic Load*, National Center for Earthquake Engineering Research, Buffalo, NY, USA, 1994.
- [7] Y.-K. Wen, "Statistical combination of extreme loads," *Journal of Structural Engineering*, vol. 103, no. 5, pp. 1079–1093, 1977.
- [8] M. Ghosn, F. Moses, and J. Wang, "Design of highway bridges for extreme events," NCHRP 489, Transportation Research Board, National Research Council, Washington, D. C., USA, 2003.
- [9] S. E. Hida, "Statistical significance of less common load combinations," *Journal of Bridge Engineering*, vol. 12, no. 3, pp. 389–393, 2007.
- [10] Z. Liang and G. C. Lee, "Towards multiple hazard resilient bridges: a methodology for modeling frequent and infrequent time-varying loads—part I, comprehensive reliability and partial failure probabilities," *Journal of Earthquake Engineering and Engineering Vibration*, vol. 11, no. 3, pp. 293–301, 2012.
- [11] Z. Liang and G. C. Lee, "Towards multiple hazard resilient bridges: a methodology for modeling frequent and infrequent time-varying loads Part II, Examples for live and earthquake load effects," *Journal of Earthquake Engineering and Engineering Vibration*, vol. 11, no. 3, pp. 303–311, 2012.
- [12] E. E. Matheu, D. E. Yule, and R. V. Kala, "Determination of standard response spectra and effective peak ground accelerations for seismic design and evaluation," Tech. Rep. no. ERDC/CHL CHETN-VI-41, 2005.
- [13] H. N. Li, T. H. Yi, M. Gu, and L. Huo, "Evaluation of earthquake-induced structural damages by wavelet transform," *Progress in Natural Science*, vol. 19, no. 4, pp. 461–470, 2009.
- [14] B. Chen, Z. W. Chen, Y. Z. Sun, and S. L. Zhao, "Condition assessment on thermal effects of a suspension bridge based on SHM oriented model and data," *Mathematical Problems in Engineering*, vol. 2013, Article ID 256816, 18 pages, 2013.
- [15] T.-H. Yi, H.-N. Li, and M. Gu, "Wavelet based multi-step filtering method for bridge health monitoring using GPS and accelerometer," *Smart Structures and Systems*, vol. 11, no. 4, pp. 331–348, 2013.
- [16] Y. Xia, B. Chen, X. Q. Zhou, and Y. L. Xu, "Field monitoring and numerical analysis of Tsing Ma suspension bridge temperature behavior," *Structural Control and Health Monitoring*, vol. 20, no. 4, pp. 560–575, 2013.
- [17] G. Fu and J. You, "Extrapolation for future maximum load statistics," *Journal of Bridge Engineering*, vol. 16, no. 4, pp. 527–535, 2011.
- [18] A. S. Nowak, "Calibration of LRFD bridge design code," NCHRP Report, Transportation Research Board of the National Academies, Washington, DC, USA, 1999.
- [19] F. Moses, "Calibration of load factors for LRFD bridge evaluations," NCHRP Report 454, Transportation Research Board of the National Academies, Washington, DC, USA, 2001.
- [20] J. Zhao and H. Tabatabai, "Evaluation of a permit vehicle model using weigh-in-motion truck records," *Journal of Bridge Engineering*, vol. 17, no. 2, pp. 389–392, 2012.

Research Article

Estimation of Evolutionary Spectra of Monitored Seismic Ground Motions by Transformation of Correlation Functions

Zhifeng Xu, Li Li, and Liang Hu

School of Civil Engineering and Mechanics, Huazhong University of Science and Technology, Wuhan 430074, China

Correspondence should be addressed to Liang Hu; lianghu@hust.edu.cn

Received 30 July 2014; Accepted 1 October 2014

Academic Editor: Bo Chen

Copyright © 2015 Zhifeng Xu et al. This is an open access article distributed under the Creative Commons Attribution License, which permits unrestricted use, distribution, and reproduction in any medium, provided the original work is properly cited.

Spatially varying seismic ground motions recorded by distributed structural health monitoring systems (SHMS) can be used to improve the performances of civil engineering structures, necessitating estimation of the evolutionary power spectral density as an indispensable procedure for utilizing records of SHMS. This paper proposes a method for the estimation of evolutionary power spectral density of a nonstationary process by transforming the correlation functions of its sample time histories. First, the background of the theory of evolutionary power spectral density is reviewed in detail. Relationship between the EPSPD and the correlation function of a reference stationary process is then established. Formulas are derived for estimating this correlation function directly from nonstationary sample time histories so that the EPSPD can be obtained. The implementation procedure of the proposed method is also detailed. Finally, a numerical example is presented, which validates the proposed method, demonstrates its application for SHMS, and displays its capabilities by comparison with the traditional method.

1. Introduction

With the emergence of large-scale infrastructures, such as long-span bridges, skyscrapers, and space structures, structural health monitoring system (SHMS), which aims at enhancing the safety and reliability and reducing the operation and maintenance costs, has been an active research regime [1–5]. One necessary application of the SHMS is to record and analyze structural responses under extreme natural effects such as earthquake and wind storms. Estimating the statistical characteristics of these natural effects is therefore an indispensable procedure for exploiting SHMS. Because these natural effects, especially the seismic ground motion records, usually display nonstationary features, methods for accurately estimating some useful statistical characteristics of nonstationary seismic ground motions are of considerable importance for the application of seismic records given by SHMS equipped on long-span civil engineering structures.

For nonstationary stochastic processes such as seismic ground motions or downburst winds, their time-frequency

properties or time-dependent spectra attracted lots of researches in the past fifty years. Some existing approaches for depicting these properties are listed as follows: the evolutionary power spectral density proposed by Priestley [6], which is interpreted as energy distribution over frequency at different time for those can be regarded as quasi-stationary process; the short-time Fourier transform (STFT), obtained by using a sliding window for filtering [7]; the Wigner-Ville distribution (WVD), which is defined as the Fourier transform of an instantaneous correlation function [8]; the wavelet transform (WT) scalogram, which is represented by a group of varied sized wavelets [9]; the Hilbert spectrum acquired by Hilbert Huang transform (HHT), which is represented by Hilbert transform of intrinsic mode function (IMF) components [10]; the Chirplet transform (CT), which can be treated as the extension and combination of STFT and WT [11]. Among them, due to its physical comparability with the power spectral density of stationary processes and its mathematical completeness, the approach of evolutionary power spectral density (EPSPD) is most widely used in earthquake engineering for characterizing seismic ground motions.

Although the concept of EPSP has been developed for a relatively long time period, the methods for estimating EPSP from sample time histories of seismic ground motion still remain only partially resolved. A variety of methods have been proposed for estimation of EPSP. Priestley proposed an original EPSP estimating method through windowed filtering [6]. Conte and Peng introduced multiple-windowed STFT method in the EPSP estimation [12]. Spanos and Failla proposed an innovative approach to estimate the EPSP of univariate nonstationary stochastic process via wavelet transform (WT) [13], which was later extended to multivariate cases by Huang and Chen [14]. Chen estimated the EPSP of downburst wind through time-varying autoregressive mode [15]. Kayhan proposed a data-adaptive method for EPSP estimation [16, 17]. Nevertheless, due to the basic difficulty of estimation of EPSP posed by the limited amount of sample time histories and by the Heisenberg uncertainty principle, none of these methods could perfectly be applicable for most situations. In addition, these methods only take advantage of the time series directly but not of the transformation of correlation function, because of the blurred relationship from nonstationary time-varying correlation function to EPSP.

This paper aims to propose an alternative method for EPSP estimation of a set of multivariate sample time histories, which yields the EPSP by transforming their estimated correlation functions. First, the background information of the theory of EPSP and its traditional estimation method is briefly introduced. On top of that, the relationship between the EPSP and the correlation function of a reference stationary process is established. A method is then derived for estimating this correlation function directly from nonstationary sample time histories, on the basis of which the EPSP can be obtained by transformation. Smoothing procedure necessary for eliminating random fluctuations is also presented. Then the implementation procedure of the proposed method of estimation of EPSP is detailed. Finally, a numerical example is presented in order to demonstrate the validity and the application of the proposed method.

2. Background of Evolutionary Power Spectral Density (EPSP)

Nonstationary seismic ground motions recorded by a SHMS installed on long-span structures usually are modelled as a one-dimensional N -variables (ID- N v) nonstationary stochastic vector process $\mathbf{X}^{(i)}(t)$ consisting of N components $X_1^{(i)}(t), X_2^{(i)}(t), \dots, X_N^{(i)}(t)$, where the superscript (i) denotes the sample of a nonstationary stochastic vector process. For seismic ground motions, the mean values of $\mathbf{X}^{(i)}(t)$ are set equal to zero without loss of generality.

The component process of $\mathbf{X}^{(i)}(t)$ has the following representation [6]:

$$\begin{aligned} X_j^{(i)}(t) &= \int_{-\infty}^{+\infty} A_j(\omega, t) \exp(i\omega t) dZ_j^{(i)}(\omega) \\ &= \int_{-\infty}^{+\infty} \exp(i\omega t) dAZ_j^{(i)}(\omega, t), \end{aligned} \quad (1)$$

where $A_j(\omega, t)$ is the time-frequency modulating function and

$$dAZ_j^{(i)}(\omega, t) = A_j(\omega, t) dZ_j^{(i)}(\omega), \quad (2)$$

where both $dZ_j^{(i)}(\omega)$ and $dAZ_j^{(i)}(\omega, t)$ denote Gaussian stochastic processes with orthogonal increments, which satisfy

$$\begin{aligned} E[dZ_j^{(i)}(\omega) dZ_j^{(i)}(\omega')^*] &= E[dAZ_j^{(i)}(\omega, t) dAZ_j^{(i)}(\omega', t)^*] = 0, \\ E[dZ_j^{(i)}(\omega) dZ_j^{(i)}(\omega)^*] &= S_{jj}^s(\omega), \end{aligned} \quad (3)$$

where $(*)$ denotes complex conjugation and $S_{jj}^s(\omega)$ is the stationary power spectral density of the stationary process to be modulated by (1); and therefore

$$\begin{aligned} S_{jj}^0(\omega, t) d\omega &= |A_j(\omega, t)|^2 E[dZ_j^{(i)}(\omega) dZ_j^{(i)}(\omega)^*] \\ &= E[dAZ_j^{(i)}(\omega, t) dAZ_j^{(i)}(\omega, t)^*], \end{aligned} \quad (4)$$

where $S_{jj}^0(\omega, t)$ is the auto-EPSP of $X_j^{(i)}(t)$. Accordingly, the evolutionary power spectral density (EPSP) matrix of $\mathbf{X}(t)$ is given by

$$\mathbf{S}^0(\omega, t) = \begin{bmatrix} S_{11}^0(\omega, t) & S_{12}^0(\omega, t) & \cdots & S_{1N}^0(\omega, t) \\ S_{21}^0(\omega, t) & S_{22}^0(\omega, t) & & \vdots \\ \vdots & & \ddots & \vdots \\ S_{N1}^0(\omega, t) & \cdots & \cdots & S_{NN}^0(\omega, t) \end{bmatrix}. \quad (5)$$

The elements of the evolutionary power spectral density matrix are defined as

$$S_{jk}^0(\omega, t) = A_j(\omega, t) A_k(\omega, t) S_{jk}^s(\omega), \quad j, k = 1, 2, \dots, N, \quad (6)$$

$$\begin{aligned} S_{jk}^0(\omega, t) d\omega &= A_j(\omega, t) A_k(\omega, t) E[dZ_j^{(i)}(\omega) dZ_k^{(i)}(\omega)^*] \\ &= E[dAZ_j^{(i)}(\omega, t) dAZ_k^{(i)}(\omega, t)^*], \end{aligned} \quad (7)$$

where $A_j(\omega, t)$ is the modulating function and $S_{jk}^s(\omega)$ is the cross stationary power spectral density to be modulated.

The time-varying correlation matrix of $\mathbf{X}(t)$ is given by

$$\begin{aligned} \mathbf{R}^0(t, t + \tau) &= \begin{bmatrix} R_{11}^0(t, t + \tau) & R_{12}^0(t, t + \tau) & \cdots & R_{1N}^0(t, t + \tau) \\ R_{21}^0(t, t + \tau) & R_{22}^0(t, t + \tau) & & \vdots \\ \vdots & & \ddots & \vdots \\ R_{N1}^0(t, t + \tau) & \cdots & \cdots & R_{NN}^0(t, t + \tau) \end{bmatrix}. \end{aligned} \quad (8)$$

The relationship between $\mathbf{S}^0(\omega, t)$ and $\mathbf{R}^0(t, t + \tau)$ is shown by the following transformation:

$$\begin{aligned} R_{jk}^0(t, t + \tau) &= E[X_j^{(i)}(t) X_k^{(i)}(t + \tau)] \\ &= \int_{-\infty}^{+\infty} A_j(\omega, t) A_k(\omega, t + \tau) S_{jk}^s(\omega) \exp(i\omega\tau) d\omega. \end{aligned} \quad (9)$$

The theory of evolutionary processes proposed by Priestley [6] can be applied only for semistationary processes; that is, the nonstationary process can be regarded as “stationary” in a certain period of time Γ . Generally, this time period Γ is defined as follows [6]:

$$\begin{aligned} H(\omega, \theta) &= \frac{1}{2\pi} \int_{-\infty}^{+\infty} A(\omega, t) e^{-it\theta} dt, \\ B_f(\omega) &= \int_{-\infty}^{+\infty} |H(\omega, \theta)| \cdot \theta d\theta, \\ \Gamma &= \sup [B_f(\omega)]. \end{aligned} \quad (10)$$

Apparently, the value of Γ cannot be determined, which is a priori.

2.1. Priestley's Method for Estimation of EPSPD. For estimating the EPSPD from sample time histories, traditionally the method proposed by Priestley [6] is invoked, which is briefly introduced here. This approach is showed by the following transforms:

$$\begin{aligned} U_j^{(i)}(\omega, t) &= \int_0^{+\infty} g(u) X_j^{(i)}(t-u) \exp[-i\omega(t-u)] du \\ SP_{jk}^{(i)}(\omega, t) &= \int_0^{+\infty} W(u) |U_j^{(i)}(\omega, t-u) U_k^{(i)}(\omega, t-u)^*| du, \end{aligned} \quad (11)$$

where $SP(\omega, t)$ is the estimation of EPSPD, $g(u)$ is a window function, and $W(u)$ is a weight function, which are usually selected as

$$\begin{aligned} g(u) &= \begin{cases} \frac{1}{2\sqrt{h\pi}} & (|u| \leq h) \\ 0 & (|u| > h) \end{cases}, \\ W(u) &= \begin{cases} \frac{1}{\Gamma} & (|u| \leq \frac{\Gamma}{2}) \\ 0 & (|u| > \frac{\Gamma}{2}) \end{cases}. \end{aligned} \quad (12)$$

3. EPSPD Estimation via Estimated Correlation Function

To utilize the correlation functions to estimate EPSPD, firstly, a distinct relationship between EPSPD and the correlation function of a reference stationary process of the original nonstationary process is derived, by which the problem is transformed to estimate the correlation function of that specified reference stationary process. Consequently, a set of formulas is derived for a specially designed method to estimate that correlation function from sample time histories and thus enables the estimation of EPSPD. The estimated EPSPD from a limited number of samples may possess large random fluctuations, and a smoothing procedure is presented to address this. For facilitating the application of the proposed method, its implementation procedure is also presented.

3.1. Transforming Correlation Function to EPSPD. With reference to the spectral representation of an evolutionary process

in (1), we can define a family of stochastic processes $TX_j^{(i)}(\kappa)_t$ by fixing the time instant t as follows:

$$TX_j^{(i)}(\kappa)_t = \int_{-\infty}^{+\infty} \exp(i\omega\kappa) dAZ_j^{(i)}(\omega, t); \quad (13)$$

that is, for a specified time instant t , $TX_j^{(i)}(\kappa)_t$ is a stochastic process with respect to the pseudo time κ but not the real time t , and $TX_j^{(i)}(\kappa)_t$ can be regarded as stationary since $dAZ_j^{(i)}(\omega, t)$ does not vary with the pseudo time κ . Consequently, defining $ST_{jk}(\omega)_t$ as the cross power density spectra between the stationary process $TX_j^{(i)}(\kappa)_t$ and the stationary process $TX_k^{(i)}(\kappa)_t$, with $RT_{jk}(\tau)_t$ defined as the correlation function between $TX_j^{(i)}(\kappa)_t$ and $TX_k^{(i)}(\kappa)_t$, the relationship between $ST_{jk}(\omega)_t$ and $RT_{jk}(\tau)_t$ can be depicted as a Fourier transformation pair:

$$ST_{jk}(\omega)_t = \frac{1}{2\pi} \int_{-\infty}^{+\infty} RT_{jk}(\tau)_t \exp(-i\omega\tau) d\tau, \quad (14)$$

$$RT_{jk}(\tau)_t = \int_{-\infty}^{+\infty} ST_{jk}(\omega)_t \exp(i\omega\tau) d\omega. \quad (15)$$

In this context, when the correlation function is calculated by estimating over a period T , for example, by

$$RT_{jk}(\tau)_t = E \left[\frac{1}{T} \int_0^T TX_j^{(i)}(\kappa)_t TX_k^{(i)}(\kappa + \tau)_t d\kappa \right], \quad (16)$$

then $ST_{jk}(\omega)_t$ can be calculated by (14). On the other hand, using (13) $ST_{jk}(\omega)_t$ has the following representation:

$$ST_{jk}(\omega)_t d\omega = E [dAZ_j^{(i)}(\omega, t) dAZ_k^{(i)}(\omega, t)^*]. \quad (17)$$

By comparing (7) with (17), it can be derived that once the pseudo time κ is replaced with real time t , the power spectral density of $TX_j^{(i)}(\kappa)_t$ can be equal to the EPSPD of $X_j^{(i)}(t)$:

$$ST_{jk}(\omega)_t = S_{jk}^0(\omega, t). \quad (18)$$

Jointly invoking (14)–(18), by estimation of the correlation function $RT_{jk}(\tau)_t$ of the reference stationary process $TX_j^{(i)}(\kappa)_t$, the EPSPD of $X_j^{(i)}(t)$ can be readily obtained by Fourier transformation. However, since only the sample time histories of $X_j^{(i)}(t)$ but not of $TX_j^{(i)}(\kappa)_t$ are available, formulas for estimating $TX_j^{(i)}(\kappa)_t$ from $RT_{jk}(\tau)_t$ need to be developed.

3.2. Formulas for Estimating Correlation Function. Recalling that the evolutionary processes are supposed to be semistationary over a time period of Γ such that $t - \Gamma/2 \leq t + \tau \leq t + \Gamma/2$, the following approximate relationship can be presumed for EPSPD:

$$\begin{aligned} dAZ_j^{(i)}(\omega, t) &\approx dAZ_j^{(i)}(\omega, t + \tau), \\ ST_{jk}(\omega)_t &\approx ST_{jk}(\omega)_{t+\tau}. \end{aligned} \quad (19)$$

Utilizing this relationship and taking into consideration the relationship between EPSD and time-varying correlation function of $X_j^{(i)}(t)$ (9), we can derive that

$$\begin{aligned}
 R_{jk}^0(t, t + \tau) &= \int_{-\infty}^{+\infty} A_j(\omega, t) A_k(\omega, t + \tau) S_{jk}^s(\omega) \exp(i\omega\tau) d\omega \\
 &= \int_{-\infty}^{+\infty} \sqrt{S_{jk}^0(\omega, t) S_{jk}^0(\omega, t + \tau)} \exp(i\omega\tau) d\omega \\
 &= \int_{-\infty}^{+\infty} \sqrt{ST_{jk}(\omega)_t ST_{jk}(\omega)_{t+\tau}} \exp(i\omega\tau) d\omega \\
 &\approx \int_{-\infty}^{+\infty} ST_{jk}(\omega)_t \exp(i\omega\tau) d\omega \\
 &\approx RT_{jk}(\tau)_t.
 \end{aligned} \tag{20}$$

Equation (20) indicates that, under the assumption of local stationarity, the correlation function of the reference process $RT_{jk}(\tau)_t$ can be approximated by the nonstationary time-varying correlation functions $R_{jk}^0(t, t + \tau)$ in the time period $-\Gamma/2 \leq \tau \leq \Gamma/2$. Therefore, the correlation function $RT_{jk}(\tau)_t$ can be calculated approximately through the following formula:

$$\begin{aligned}
 \widehat{RT_{jk}(\tau)_t} &= E \left[\frac{1}{\Gamma} \int_{t-\Gamma/2}^{t+\Gamma/2} X_j^{(i)}(t) X_k^{(i)}(t + \tau) dt \right] \\
 &\approx \frac{1}{P} \sum_{i=1}^P \frac{1}{\Gamma} \int_{t-\Gamma/2}^{t+\Gamma/2} X_j^{(i)}(t) X_k^{(i)}(t + \tau) dt.
 \end{aligned} \tag{21}$$

Consequently, $\widehat{S_{jk}(\omega, t)}$ can now be estimated by the Fourier transform of $\widehat{RT_{jk}(\tau)_t}$:

$$\widehat{S_{jk}(\omega, t)} \approx \widehat{ST_{jk}(\omega)_t} = \frac{1}{2\pi} \int_{-\infty}^{+\infty} \widehat{RT_{jk}(\tau)_t} \exp(-i\omega\tau) d\tau. \tag{22}$$

3.3. Smoothing. For estimating EPSD of nonstationary processes from the ground motions recorded by SHMS, an inherent difficulty is that the amount sample of time histories is very limited: usually one set of sample time histories is available. This entails considerable part of the stochastic error in the estimated EPSD $\widehat{S_{jk}(\omega, t)}$, which indicates that $\widehat{S_{jk}(\omega, t)}$ is highly unreliable and thus not applicable in practice. In order to reduce the fluctuations of $\widehat{S_{jk}(\omega, t)}$, two weight functions $GT(v)$ and $GW(u)$ must be included to smooth $\widehat{S_{jk}(\omega, t)}$ in the time domain and in the frequency domain so that

$$\overline{S_{jk}(\omega, t)} = \int_{-\infty}^{+\infty} \int_{-\infty}^{+\infty} GT(v) GW(u) \widehat{S_{jk}(\omega - u, t - v)} du dv, \tag{23}$$

where $\overline{S_{jk}(\omega, t)}$ represents a smoothed result of $\widehat{S_{jk}(\omega, t)}$, which significantly decreases stochastic errors although it may increase the bias of estimated EPSD. In consideration of the constraints due to limited samples, $\widehat{S_{jk}(\omega, t)}$ can be used as an applicable estimation of EPSD.

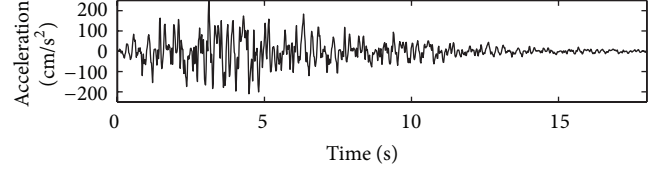


FIGURE 1: Record of the El-Centro seismic ground motion.

3.4. Implementation Procedure. In practice, suppose P sets of sample time histories $X_j^{(i)}(r\Delta t)$ of the seismic ground motion recorded by SHMS are presented. For using the proposed method to estimate the EPSD, the following three steps are included.

- (1) Estimate the correlation function $\widehat{RT_{jk}(\tau)_t}$ of the reference stationary processes from the given sample time histories:

$$\begin{aligned}
 \widehat{RT_{jk}(s\Delta t)_{r\Delta t}} &= \frac{1}{2PK} \sum_{i=1}^P \sum_{\kappa=-K}^{\kappa=K} X_j^{(i)}(r\Delta t + \kappa\Delta t) X_k^{(i)}(r\Delta t + s\Delta t + \kappa\Delta t),
 \end{aligned} \tag{24}$$

where $K = \Gamma/2\Delta t$, Δt is the time step, and P is the total amount of samples.

- (2) Performing the Fourier transform of $\widehat{RT_{jk}(\tau)_t}$, we obtain the unsmooth estimation of EPSD $\widehat{S_{jk}(\omega, t)}$:

$$\widehat{S_{jk}(m\Delta\omega, r\Delta t)} = \frac{\Delta t}{2\pi} \sum_{s=-Ts}^{Ts} \widehat{RT_{jk}(s\Delta t)_{r\Delta t}} \exp(-ims\Delta\omega\Delta t), \tag{25}$$

where $Ts = \Gamma/2\Delta t$ and $\Delta\omega$ is the frequency step.

- (3) Smoothing the unsmoothed estimation of evolutionary spectra $\widehat{S_{jk}(\omega, t)}$ in both the time domain and the frequency domain, we obtain the final result:

$$\begin{aligned}
 \overline{S_{jk}(m\Delta\omega, r\Delta t)} &= \sum_{v=-V}^V \sum_{u=-U}^U GT(v\Delta t) GW(u\Delta\omega) \\
 &\quad \times \widehat{S_{jk}((m-u)\Delta\omega, (r-v)\Delta t)\Delta\omega\Delta t}.
 \end{aligned} \tag{26}$$

4. Numerical Example

In this part, a numerical example is presented to demonstrate the capabilities of the proposed approach in estimating the EPSD of seismic ground motions. Due to the lack of multipoint measurements, the SHMS-recorded ground motions are represented by an ensemble of multivariate nonstationary time histories generated conforming to EPSD of a well-known measured seismic ground motion time history and the coherence function given by statistical results of measurements. Then the method proposed in this paper was adopted to estimate the EPSP of sample time histories.

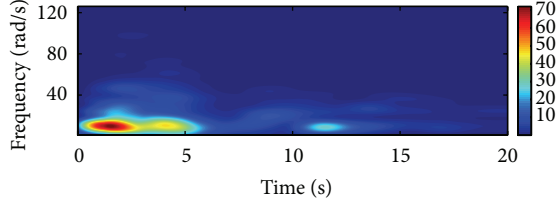


FIGURE 2: EPSPD of the El-Centro seismic ground motion.

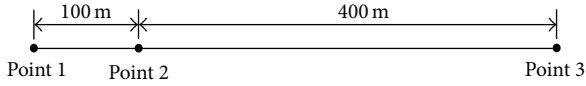


FIGURE 3: Configuration of the three points.

The estimated results are compared with the target EPSPD of the generated samples as well as the corresponding results yielded by traditional estimation method.

4.1. Sample Time Histories of Seismic Ground Motions. In this example, the ground motions were modeled as multivariate nonstationary stochastic vector processes according to the EPSPD of the seismic ground motion record of El-Centro. Figure 1 shows the time history of El-Centro wave. The evolutionary spectrum of the El-Centro wave is denoted by $S^{\text{El}}(\omega, t)$ as showed in Figure 2. The ground motions at three points are treated as trivariate nonstationary stochastic vector processes. The configuration of the three points is displayed in Figure 3. For simplicity, the effect of wave propagation is not considered in this example.

The simulated ground motion at point j is denoted by $X_j^{(i)}(t)$, and the cross-ESPD of $\mathbf{X}^{(i)}(t)$ are given by

$$S_{jk}^0(\omega, t) = \sqrt{S_j(\omega, t) S_k(\omega, t)} \gamma_{jk}(\omega), \quad j, k = 1, 2, 3, \quad (27)$$

where $\gamma_{jk}(\omega)$ is the coherence function between $X_j^{(i)}(t)$ and $X_k^{(i)}(t)$, $S_1(\omega, t) = 1.0S^{\text{El}}(\omega, t)$, $S_2(\omega, t) = 1.2S^{\text{El}}(\omega, t)$, and $S_3(\omega, t) = 0.8S^{\text{El}}(\omega, t)$. The Harichandran-Vanmarcke model [18] is chosen to describe the coherence functions $\gamma_{jk}(\omega)$:

$$\gamma_{jk}(\omega) = A \exp \left[-\frac{2\xi_{jk}}{\alpha\theta(\omega)} (1 - A + \alpha A) \right] + (1 - A) \exp \left[-\frac{2\xi_{jk}}{\theta(\omega)} (1 - A + \alpha A) \right], \quad (28)$$

where ξ_{jk} is the distance between point j and point k and $\theta(\omega)$ is frequency-dependent correlation distance:

$$\theta(\omega) = k \left[1 + \left(\frac{\omega}{\omega_0} \right)^2 \right]^{-1/2}. \quad (29)$$

The spectral representation method (SRM) is employed to generate the sample time histories of $\mathbf{X}^{(i)}(t)$ [19]. Figure 4 shows a set of time histories of simulated ground motions at the three points.

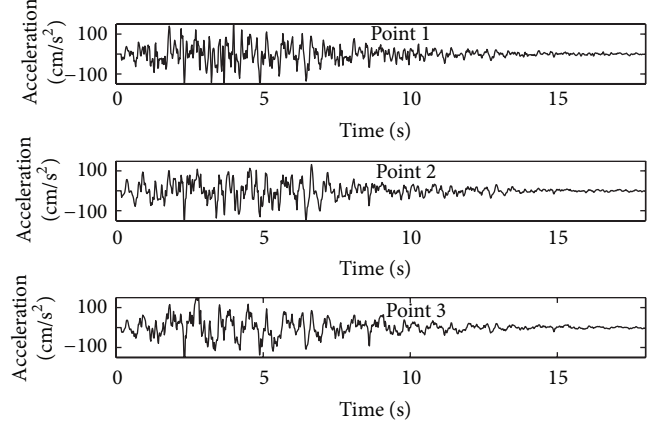


FIGURE 4: A set of sample time histories of seismic ground motions.

4.2. Estimation by the Proposed Method. The proposed method is used to estimate the EPSPD and the correlation functions of the generated sample time histories of seismic ground motions. Parameters used for the estimation are as follows: the time step $\Delta t = 0.02$ s, the length of time period $T = 20$ s, the frequency step $\Delta\omega = 1$ rad/s, and the upper cut-off frequency $\omega_u = 126$ rad/s. The two window functions $GW(u)$ and $GT(v)$ are chosen as the following forms:

$$\begin{aligned} GW(u) &= \frac{1}{\Omega} \quad |u| \leq \frac{\Omega}{2}, \\ GW(u) &= 0 \quad |u| > \frac{\Omega}{2}, \\ GT(v) &= \frac{1}{T'} \quad |v| \leq \frac{T'}{2}, \\ GT(v) &= 0 \quad |v| > \frac{T'}{2}, \end{aligned} \quad (30)$$

where $\Omega = 12$ rad/s and $T' = 1.6$ s.

Figure 5 shows the auto-EPSPD estimated (a) from one sample time history and (b) from the ensemble of ten sample time histories for Point 1. In each subfigure, the estimated EPSPD with and without smoothing are plotted against the smoothed and unsmoothed target EPSPD (i.e., the EPSPD of Point 1 used for generated sample time histories). In Figure 5(a), it can be observed that, for only one sample, the smoothed estimated EPSPD $\widehat{ST}_{jk}(\omega, t)$ is close to the smoothed target EPSPD and is also close to the target EPSPD $S_{jk}^0(\omega, t)$, which indicates that the proposed method can estimate the EPSPD from just one sample time history with satisfying accuracy. If the number of the samples can be increased, for example, a set of 10 samples are available, comparison between Figures 5(b) and 5(a) shows that even the unsmoothed EPSPD $\widehat{ST}_{jk}^r(\omega, t)$ can also be a satisfactory estimation of EPSPD. That is, increasing the number of samples would increase the accuracy of the estimation of EPSPD. Corresponding to Figures 5, 6(a) and 6(b) show the estimated cross EPSPD between Point 1 and Point 2 from one and ten samples respectively, and observations similar to those from

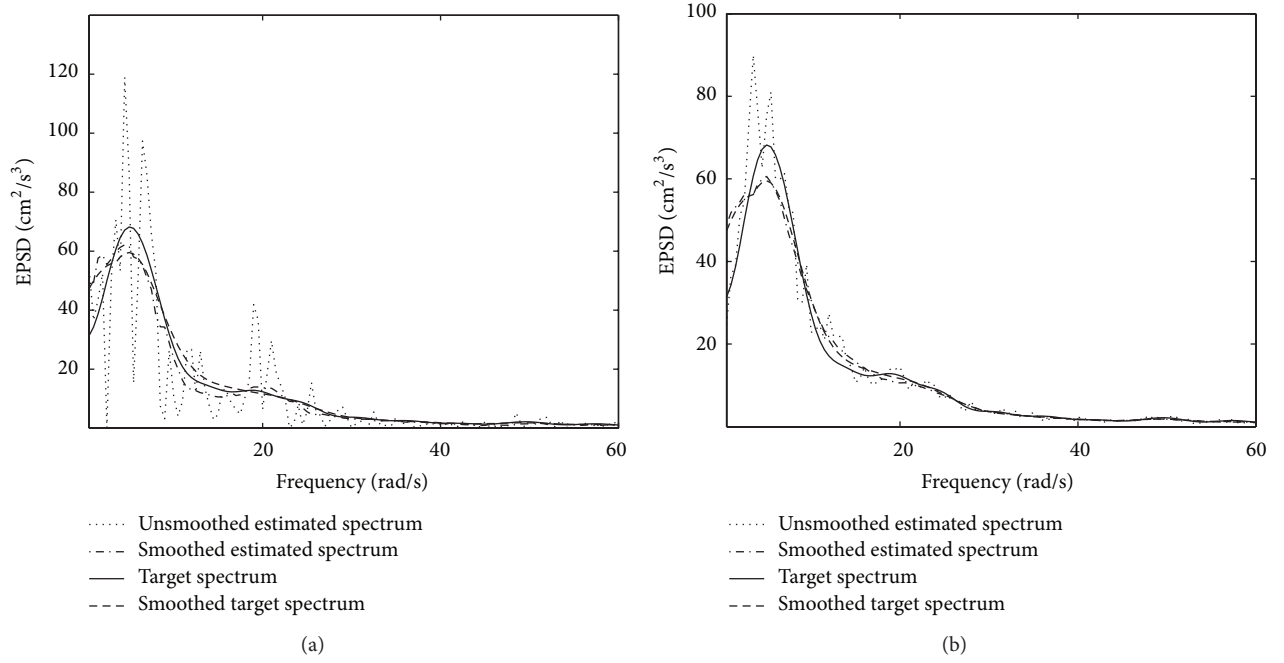


FIGURE 5: Estimated one-sided auto-EPD ($\overline{S_{11}(\omega, t)}$, $\widehat{S_{11}(\omega, t)}$, $\overline{S_{11}^0(\omega, t)}$, and $\widehat{S_{11}^0(\omega, t)}$) at the time instant $t = 2.0$ s: (a) from one set of sample time histories and (b) from ten sets of sample time histories.

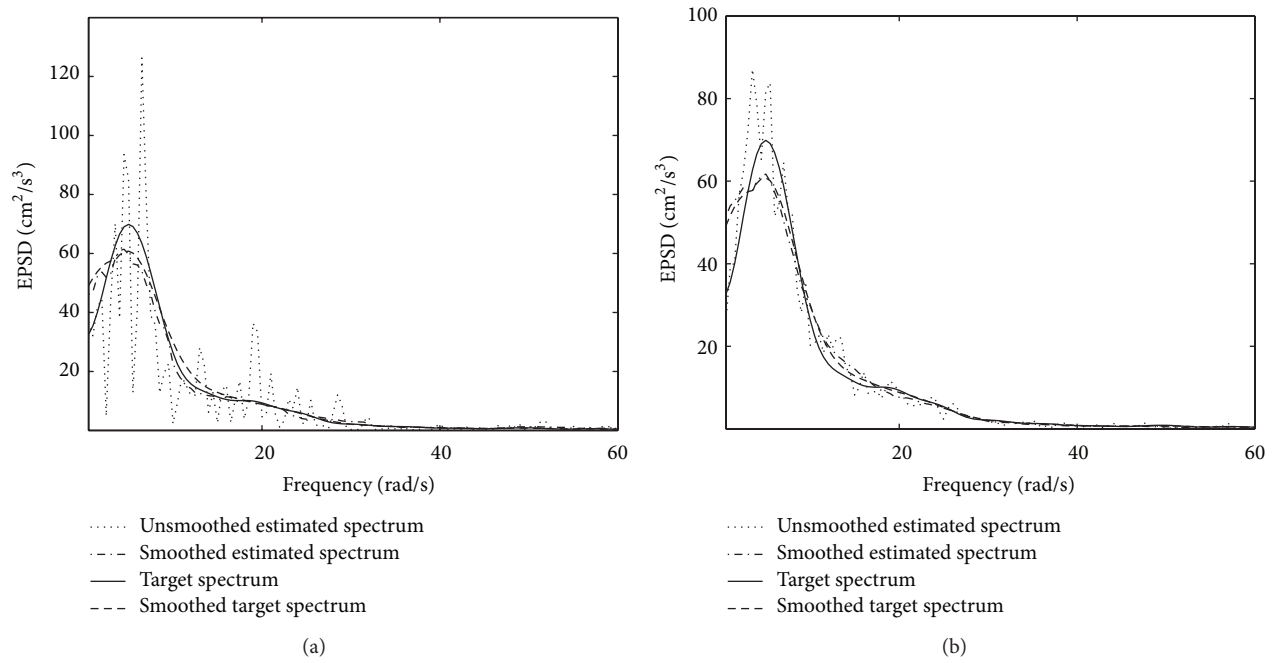


FIGURE 6: Estimated one-sided cross-EPD ($\overline{S_{12}(\omega, t)}$, $\widehat{S_{12}(\omega, t)}$, $\overline{S_{12}^0(\omega, t)}$, and $\widehat{S_{12}^0(\omega, t)}$) at the time instant $t = 2.0$ s: (a) from one set of sample time histories and (b) from ten sets of sample time histories.

Figure 5 can be yielded. Consequently, the proposed method in this paper can accurately estimate the EPD of multivariate nonstationary stochastic seismic ground motions. In addition, increasing the number of the samples can efficiently decrease the stochastic fluctuation of the estimation.

4.3. Comparison with Priestley's Method. To demonstrate the capabilities of the proposed method, both the proposed method and the traditional Priestley method aforementioned are used to estimate the EPD of the same 1000 samples of time histories of seismic ground motions. Figures 7 and 8

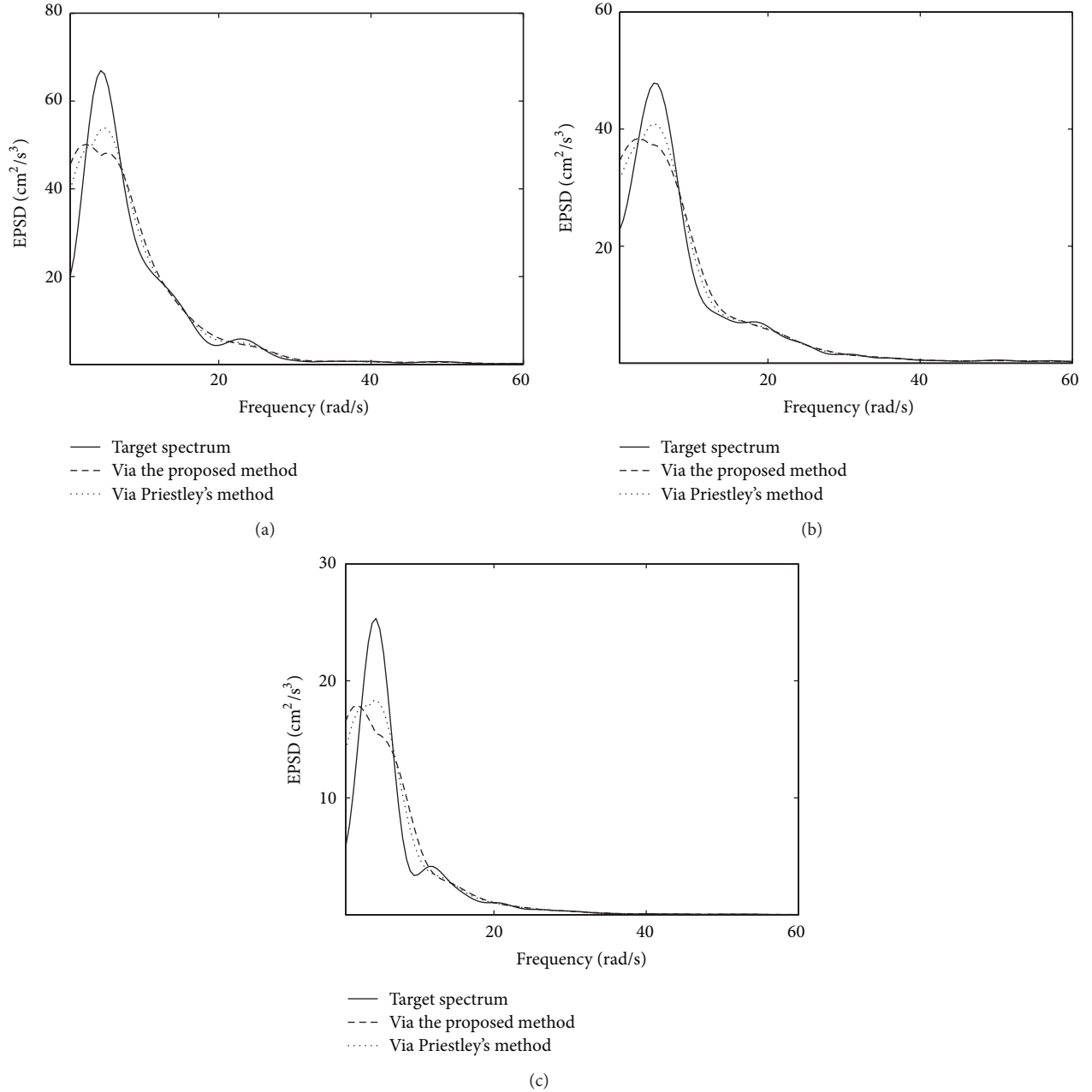


FIGURE 7: Comparison between the bias errors of the proposed method $\overline{S_{12}}(\omega, t)$ and Priestley's method $SP_{12}(\omega, t)$: (a) at time instant $t = 2$ s; (b) at time instant $t = 4$ s; (c) at time instant $t = 12$ s.

compare the mean of the EPSD estimated by the proposed method and the traditional method and the standard deviations of EPSD estimated by the two methods, respectively; each figure contains three subfigures associated with different time instants. From Figure 7 it can be observed that the biases between results of these two methods and the target EPSD are comparable, indicating that the proposed method can lead to accuracy similar to the traditional method. Meanwhile, Figure 8 displays the standard deviation of the EPSD estimated by the proposed method approach which is much lower than those of the traditional Priestley method, which demonstrates that results of the proposed method have

much less fluctuations so that it is more reliable than those of the traditional method.

5. Conclusion

In this paper, a new approach has been proposed to estimate the EPSD of multivariate nonstationary seismic ground motions recorded by SHMS. The method is based on transformation of correlation functions of the reference stationary process, which can be estimated from sample time histories directly by using formulas derived. The smoothing procedure has also been included in the procedure method.

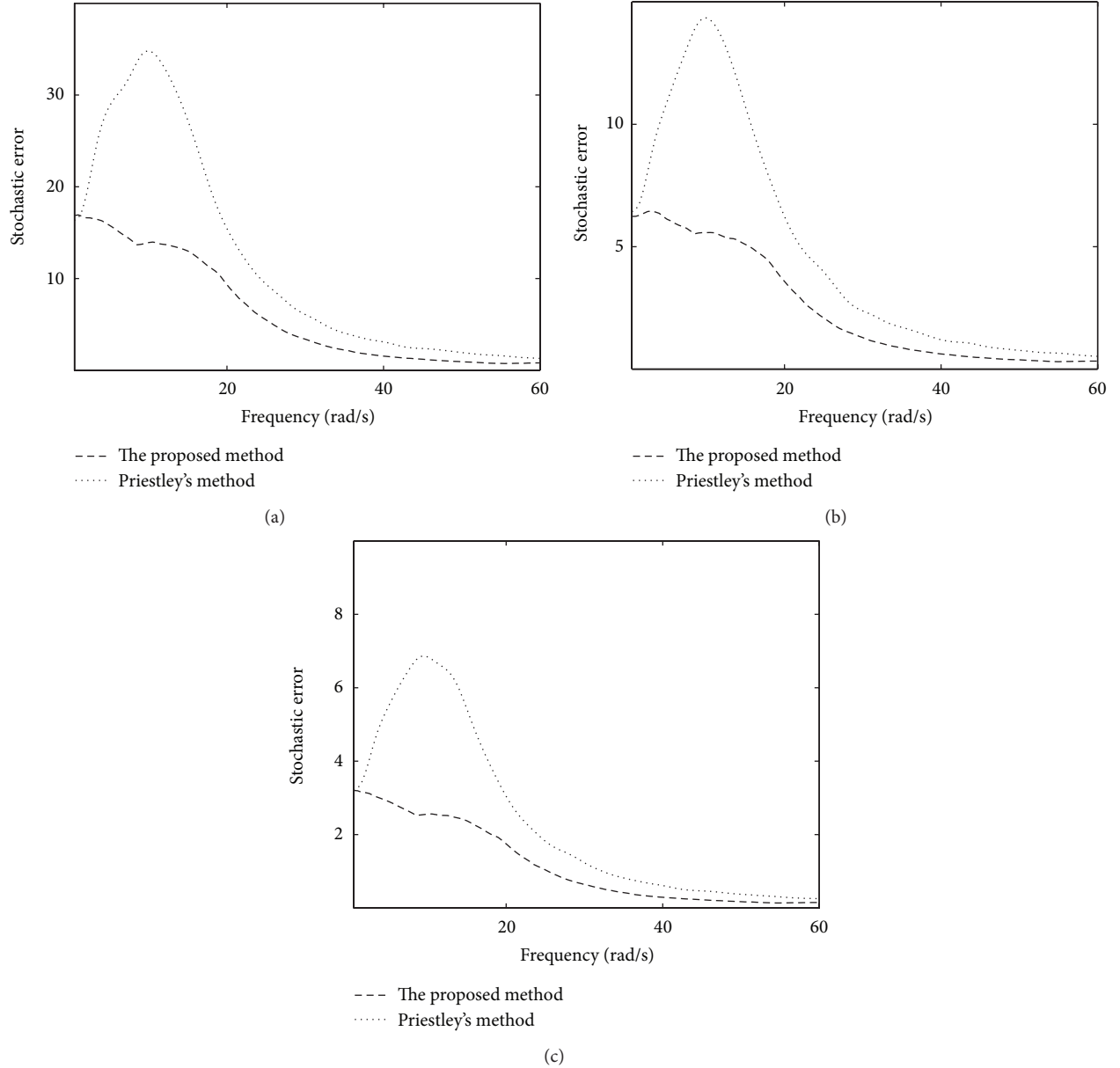


FIGURE 8: Comparison between the stochastic errors of the proposed method $\overline{S_{12}(\omega, t)}$ and Priestley's method $SP_{12}(\omega, t)$: (a) at time instant $t = 2$ s; (b) at time instant $t = 4$ s; (c) at time instant $t = 12$ s.

The whole proposed method can be readily applied by using the implementation steps detailed.

The validity and the accuracy of the proposed method have been demonstrated by a numerical example and the comparison between results yielded by this method and by the traditional Priestley method. This method could approximately estimate the EPSD from only one sample time history, while increasing the number of samples could efficiently increase the accuracy of the estimation dramatically. The biases of the EPSD estimated by these two methods are comparable, while the stochastic fluctuations of the proposed method are much lower than those of Priestley's method. It is worthy to point out that the proposed method is of suitable accuracy and more reliable with less random fluctuation than

the traditional method and thus has potential application for exploiting data recorded by SHMS.

Conflict of Interests

The authors declare that there is no conflict of interests regarding the publication of this paper.

Acknowledgments

This research is jointly supported by the Natural Science Funds of China (no. 51308244), Natural Science Funds of

Hubei Province in China (no. 2012FFB02605), and Niche Area Project of Huazhong University of Science Technology.

References

- [1] T. Yi, H. Li, and M. Gu, "Full-scale measurements of dynamic response of suspension bridge subjected to environmental loads using GPS technology," *Science China Technological Sciences*, vol. 53, no. 2, pp. 469–479, 2010.
- [2] H. Li, T. Yi, L. Ren, D. Li, and L. Huo, "Reviews on innovations and applications in structural health monitoring for infrastructures," *Structural Monitoring and Maintenance*, vol. 1, no. 1, pp. 1–45, 2014.
- [3] B. Chen and Y. Xu, "Integrated vibration control and health monitoring of building structures using semi-active friction dampers: part II-numerical investigation," *Engineering Structures*, vol. 30, no. 3, pp. 573–587, 2008.
- [4] Y. Xu and B. Chen, "Integrated vibration control and health monitoring of building structures using semi-active friction dampers: part I-methodology," *Engineering Structures*, vol. 30, no. 7, pp. 1789–1801, 2008.
- [5] B. Chen, Y. Sun, Y. Li, and S. Zhao, "Control of seismic response of a building frame by using hybrid system with magnetorheological dampers and isolators," *Advances in Structural Engineering*, vol. 17, no. 8, pp. 1199–1216, 2014.
- [6] M. B. Priestley, "Evolutionary spectra and non-stationary processes," *Journal of the Royal Statistical Society. Series B. Methodological*, vol. 27, pp. 204–237, 1965.
- [7] J. B. Allen and L. R. Rabiner, "A unified approach to short-time Fourier analysis and synthesis," *Proceedings of the IEEE*, vol. 65, no. 11, pp. 1558–1564, 1977.
- [8] L. Cohen, *Time-Frequency Analysis: Theory and Applications*, Prentice Hall, New York, NY, USA, 1995.
- [9] K. Gurley and A. Kareem, "Applications of wavelet transforms in earthquake, wind and ocean engineering," *Engineering Structures*, vol. 21, no. 2, pp. 149–167, 1999.
- [10] N. E. Huang, Z. Shen, S. R. Long et al., "The empirical mode decomposition and the Hilbert spectrum for nonlinear and non-stationary time series analysis," *Proceedings of the Royal Society A: Mathematical, Physical and Engineering Sciences*, vol. 454, no. 1971, pp. 903–995, 1998.
- [11] P. D. Spanos, A. Giaralis, and N. P. Politis, "Time-frequency representation of earthquake accelerograms and inelastic structural response records using the adaptive chirplet decomposition and empirical mode decomposition," *Soil Dynamics and Earthquake Engineering*, vol. 27, no. 7, pp. 675–689, 2007.
- [12] J. P. Conte and B. F. Peng, "Fully nonstationary analytical earthquake ground-motion model," *Journal of Engineering Mechanics*, vol. 123, no. 1, pp. 15–24, 1997.
- [13] P. D. Spanos and G. Failla, "Evolutionary spectra estimation using wavelets," *Journal of Engineering Mechanics*, vol. 130, no. 8, pp. 952–960, 2004.
- [14] G. Huang and X. Chen, "Wavelets-based estimation of multivariate evolutionary spectra and its application to nonstationary downburst winds," *Engineering Structures*, vol. 31, no. 4, pp. 976–989, 2009.
- [15] L. Chen, *Vector Time-Varying Autoregressive (TVAR) Models and Their Application to Downburst Wind Speeds*, Texas Tech University, Lubbock, Tex, USA, 2005.
- [16] A. S. Kayhan, A. El-Jaroudi, and L. F. Chaparro, "Evolutionary periodogram for nonstationary signals," *IEEE Transactions on Signal Processing*, vol. 42, no. 6, pp. 1527–1536, 1994.
- [17] A. S. Kayhan, A. El-Jaroudi, and L. F. Chaparro, "Data-adaptive evolutionary spectral estimation," *IEEE Transactions on Signal Processing*, vol. 43, no. 1, pp. 204–213, 1995.
- [18] R. S. Harichandran and E. H. Vanmarcke, "Stochastic variation of earthquake ground motion in space and time," *Journal of Engineering Mechanics*, vol. 112, no. 2, pp. 154–174, 1986.
- [19] G. Deodatis, "Simulation of ergodic multivariate stochastic processes," *Journal of Engineering Mechanics*, vol. 122, no. 8, pp. 778–787, 1996.

Research Article

Health Status Monitoring of Cuplock Scaffold Joint Connection Based on Wavelet Packet Analysis

Liuyu Zhang,^{1,2} Chenyu Wang,² and Gangbing Song²

¹Engineering Research Center for Large Highway Structure Safety of the Ministry of Education, Chang'an University, Xi'an, Shaanxi 710064, China

²Smart Material and Structure Laboratory, Department of Mechanical Engineering, University of Houston, Houston, TX 77004, USA

Correspondence should be addressed to Gangbing Song; gsong@uh.edu

Received 8 August 2014; Accepted 13 October 2014

Academic Editor: Bo Chen

Copyright © 2015 Liuyu Zhang et al. This is an open access article distributed under the Creative Commons Attribution License, which permits unrestricted use, distribution, and reproduction in any medium, provided the original work is properly cited.

The cuplock scaffolds are widely used as a temporary facility in the bridge and other constructions. The looseness of cuplock scaffold connection plays a significant role in the stability of the structure. Contemporary structural health monitoring method is reviewed in this paper at first, and then we proposed wavelet packet analysis based method. In order to detect the looseness of cuplock connection, three stress PZTs and three shear PZTs used as transducers are mounted onto vertical bar and cross bars of cuplock scaffold. Wavelet packet analysis is applied to analyze the transmitted signal energy between two PZTs through cuplock connection. Experimental results show that shear PZT has better performance than stress PZT to be used as actuator and sensor for the wavelet packet analysis based structural health monitoring. Besides, a sensor looseness index matrix (SLIM) is derived to indicate the looseness of the cuplock connection. The experimental results show that looseness index increases as the connection gets loose.

1. Introduction

Scaffolds are widely used in the construction of permanent works such as buildings and bridges. There are two major types of scaffold structures: one is made from prefabricated components and the other is made from steel tubes or bamboo. Cuplock scaffold is one of the scaffold structures which are made from prefabricated components. Cuplock scaffolds are often used in the US and Asia. In China, cuplock scaffolds are promoted promptly in recent years due to their low cost to manufacture, simplicity to assemble and disassemble, and high load capacity. Cuplock scaffold structure is only used as a temporary facility in construction, so the safety issues are overlooked sometimes. Some serious collapse accidents happened in China during the last several years [1–3]. It attracts more and more attention of researchers to the stability and safety issues of cuplock scaffolds.

The scaffold collapses are caused by overload, geometric imperfections, joint connections, and foundation failures [4–7]. Many researchers have carried out a lot of studies on these factors affecting the safety of scaffold structures. The causes of

scaffold collapses were analyzed from eccentric compression of the vertical bar, materials, and management in [8]. The authors obtained the measurements of geometric imperfections and loading eccentricity of cuplock support scaffold systems from various construction sites in Sydney area and presented a study of cuplock scaffold systems joint stiffness [9]. The researchers investigated the effects of uncertainties on the ultimate strength of multistorey steel support scaffold frames through a rational statistical framework and a second-order inelastic finite element analysis [10]. The mode of failure, effects of different random variables on the variability of structural strength, and the reliability of the scaffold structures were investigated in [11]. The authors developed accurate three-dimensional advanced analysis models to capture the behavior of support scaffold systems and proposed methods for modeling spigot joints, semirigid upright-to-beam connections, and base plate eccentricities [12]. The scholars presented an algorithm to model scaffold behavior and follow the full moment-rotation curve including nonlinear loading and unloading behavior and including looseness and obtained that for sway frames looseness makes the frame

unstable but for the braced frame analyzed looseness had little effect on the result in [13]. Nevertheless, no work about the monitoring of the tightness of cuplock connection was done. In the field of construction, the joints will get loose if the workers forget to tighten the top cuplock when the joints are assembled. The joints can also be loose because of the vibration during the construction process. Then a relatively large gap will take place between the vertical bar and the cross bar. So the structural characteristics of scaffold will be essentially changed as well as the parameters of buckling. The author summarized the causes of 120 failures predominantly in the UK with approximately 30% of the failures that happened during construction [14]. Of the known causes of collapse, approximately 40% of the collapses occurred during pouring of concrete [4, 15]. The majority of the scaffold accidents were caused by faulty platforms including platform supports, human error, unsafe working procedures, and faulty access arrangements. In [6], it was presented that the majority of the scaffold failures occurred due to poor site control. Since the instability and failure of structures are very likely to happen, the monitoring of the tightness for cuplock connection is very important.

Structural health monitoring (SHM) is widely used to monitor the real time status of the structure. It is a very effective way to detect the status of pipeline network. The reliability and safety of the pipeline network can be improved by using SHM applications [16]. Piezoelectric lead zirconate titanate (PZT) based approach is always used as transducer in active monitoring of the structure for its great features such as the availability of different shapes, broadband response frequency, low price, and the ability of being employed as actuator or sensor [17]. A new technology called smart aggregate that uses embedded piezoceramic based transducers has been applied to monitor cracks in concrete structures [18–20]. However, SHM with PZT has not been used in detecting the looseness status of cuplock scaffolds by researchers. To monitor the status of a cuplock connection, we propose a SHM system in which PZTs are used as transducers. Two types of PZTs, stress PZT and shear PZT, are commonly used. In our experiment, we use both types of PZT and compare their performance for our scenario. Swept sine wave is used as an excitation, and the signal transmits through the cuplock connection between two PZTs. By using wavelet packet analysis, we can find the relation between the tightness degree and increase of transmitted signal.

Wavelet packet analysis is used as a signal-processing tool to analyze the sensor signal of the embedded PZT patches in the concrete structure and also pipe networks. We use wavelet packet analysis for the reason that it makes the analysis of signal which has narrow frequency bands and short time period available. Various kinds of damage indices have been developed for health monitoring of civil structures in recent years. Root-mean-square deviation (RMSD) is one of the commonly used damage indexes to compare the difference between the signatures of healthy and damaged states. This method can also be used in our analysis. RMSD is used to calculate the looseness index which is for comparing the difference between tightness status and looseness status.

The rest of the paper is organized as follows. In Section 2, the detection principle for cuplock connection looseness status is presented. The experimental setup is introduced in Section 3. In Section 4, the experiments are conducted to validate the relation between the looseness degree and energy of transmitted signal. Concluding remarks are drawn in Section 5.

2. Detection Principle for Cuplock Connection Loosening Based on Wavelet Packet Analysis

2.1. Cuplock Scaffold Structure. The cuplock scaffold is a versatile shoring system used to support formwork. The construct of cuplock scaffold members is shown in Figure 1 [21]. It consists of the vertical bar, cross bar, joints of cross bar, top cuplock, bottom cuplock, and locating dowel pin. The top cuplock can be moved along the vertical bar. By tightening the top cuplock, cross bars can be connected to the vertical bar firmly. The maximum number of cross bars that can be installed at one node is four.

2.2. Active Monitoring Principle Using Piezoelectric Transducers. The cross section of cuplock connection is shown in Figure 2. By tightening the top cuplock, a well-fitted cuplock connection with enough contact can be made. In order to maintain the carrying capacity and stability of cuplock scaffold, there must be enough pressure formed on the contact surface. Moreover, with the increase of cuplock connection tightness, the connection region could be larger and harder pressed.

Two pieces of PZTs are stuck on the cross bar and the vertical bar, respectively, as sensors and an actuator (as shown in Figure 3). PZT 3 (actuator) generates a wave that propagates across the cuplock connection, and then the signal is captured by PZT 1 and PZT 2 (sensor). Between the actuator and the sensor, energy is transmitted through pipes by the propagated waves. Input signal attenuate significantly at cuplock connection for the energy is lost there. There would be less energy of the input signal transmitted through cuplock connection when the connection gets looser and looser. The lost energy is correlated to the tightness of cuplock connection. The PZT can be not only stress PZTs but also shear PZTs.

2.3. Detection Principle for Cuplock Connection Based on Wavelet Packet Analysis. One of the useful methods to analyze the transmitted signal between two PZTs is wavelet packet analysis. A waveform that has an average value of zero in a limited duration can be called a wavelet. In wavelet analysis, a signal can be divided into two parts, low frequency and high frequency, which are approximation and detail, respectively. The approximation itself can be divided into a second level approximation and detail then. The detail can also be split the same way as approximation in wavelet packet analysis. The outstanding feature of wavelet packet analysis is that it makes inspection of relatively narrow frequency bands during a relatively short time window possible.

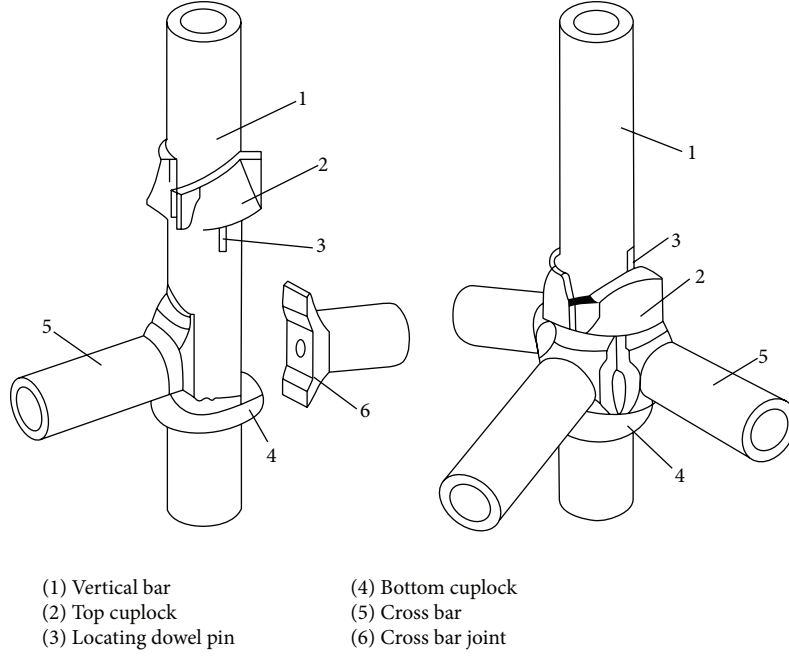


FIGURE 1: The construct of cuplock scaffold members.

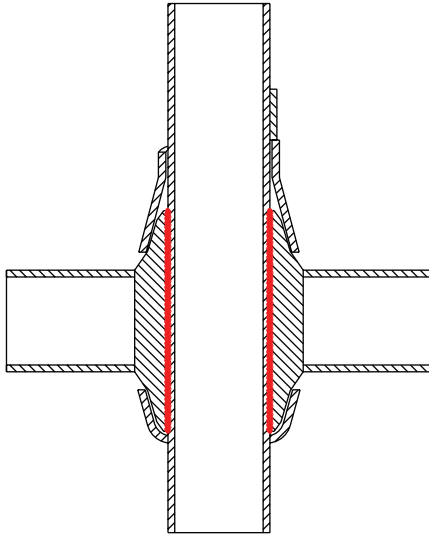


FIGURE 2: Cross section of cuplock connection.

The sensor signal S is decomposed by an n -level wavelet packet decomposition into 2^n signal sets $\{X_1, X_2, \dots, X_{2^n}\}$. $E_{i,j}$ is the energy of the decomposed signal, where i is the tightness index and j is the frequency band ($j = 1, \dots, 2^n$). X_j can be expressed as

$$X_j = [x_{j,1}, x_{j,2}, \dots, x_{j,m}], \quad (1)$$

where m is the amount of sampling data. Energy of the decomposed signal is defined as

$$E_{i,j} = \|X_j\|_2^2 = x_{j,1}^2 + x_{j,2}^2 + \dots + x_{j,m}^2. \quad (2)$$

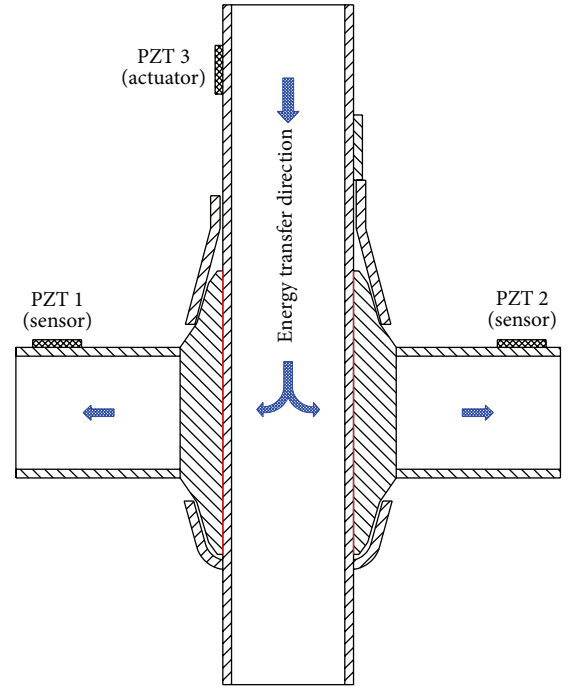


FIGURE 3: Energy transmission at the cuplock scaffold model.

Energy vector at tightness index i is defined as

$$E_i = [E_{i,1}, E_{i,2}, \dots, E_{i,2^n}]. \quad (3)$$

We use root-mean-square deviation (RMSD) as the tightness index to compare the difference between the features of tight and loose states. The tightness index is formed by calculating the RMSD between the energy vectors of the tight

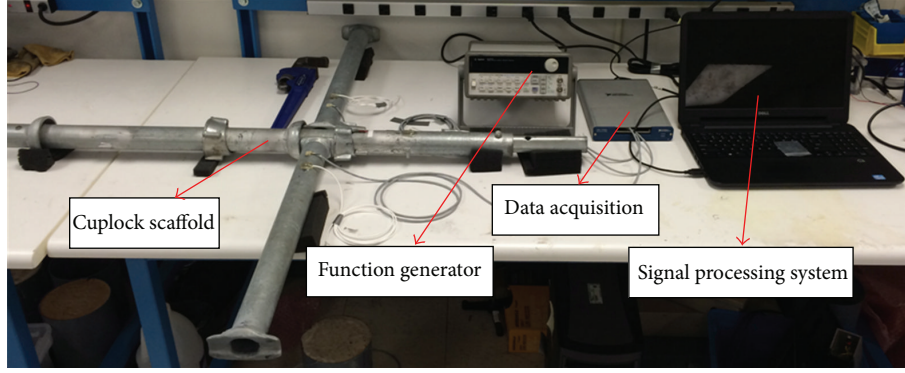


FIGURE 4: Experimental setup.

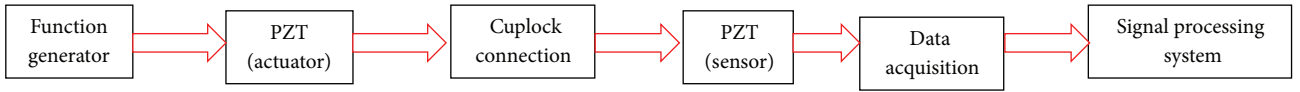


FIGURE 5: Experimental flow.

state and the loose state. The energy vector for tight data is $E_t = [E_{t,1}, E_{t,2}, \dots, E_{t,2^n}]$. The energy vector E_i for the tight state at tightness index i is defined as $E_i = [E_{i,1}, E_{i,2}, \dots, E_{i,2^n}]$. The looseness index at tightness index i is defined as

$$I = \sqrt{\frac{\sum_{j=1}^{2^n} (E_{i,j} - E_{t,j})^2}{\sum_{j=1}^{2^n} E_{t,j}^2}}. \quad (4)$$

The proposed looseness index represents the transmission energy loss portion caused by looseness of cuplock connection. The connection is tight when the looseness index is close to 0. When the looseness index is above a certain threshold, the cuplock connection is not tight anymore. In this case, the instability of the structure increases as the looseness index increases.

To demonstrate the tight status at different tightness levels, one type of looseness index matrix is defined, a tightness-level looseness index matrix.

A sensor looseness index matrix (SLIM) is as follows.

$M_{m \times n}$ is defined as

$$M_{m \times n} = [I_{i,j}] \quad (i = 1, \dots, m, j = 1, \dots, n), \quad (5)$$

where the matrix element at the i th row and j th column, $I_{i,j}$, is the looseness index of the i th PZT at time of j th test, m is the total number of tightness degrees, and n is the total number of PZT sensors. The looseness status at different locations of the scaffold specimen at different tightness degrees can be described by a two-dimensional looseness index matrix. The SLIM is useful in monitoring the looseness evolution process to predict the failure of a structure. For a specific location, you can compare the looseness index with the tightest one to get the looseness of the connection from SLIM.

TABLE 1: Parameters for swept sine wave.

Parameters	Value
Frequency	100 Hz~150 KHz
Amplitude	10 V

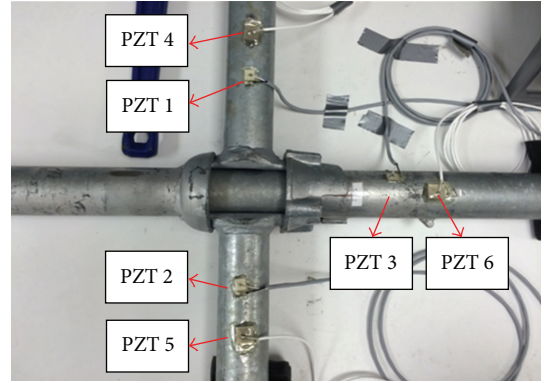


FIGURE 6: Cuplock scaffold structure specimen.

3. Experimental Setup

In Figure 4, it is the experimental setup for active monitoring of a cuplock connection. The experiment flow is shown in Figure 5. The PZT actuator is excited by the swept sine wave (Table 1) which is generated by function generator. Upon excitation, the actuator generates waves that propagate through the cuplock connection. Then the wave will be received by the PZT sensor. We use the data acquisition system to sample the signal sensed by PZT sensor at the rate of 1 MHz and finally use the signal-processing system in the computer to analyze the signal data. The signal received by the sensors can indicate the looseness of the connection. The cuplock scaffold model and six PZTs are shown in Figure 6.

TABLE 2: Cuplock Scaffold model features.

	Diameter (mm)	Wall thickness (mm)	Yield strength (MPa)	Elongation
Vertical bar	48.26	3.175	345	30%
Cross bar	48.26	3.175	345	30%

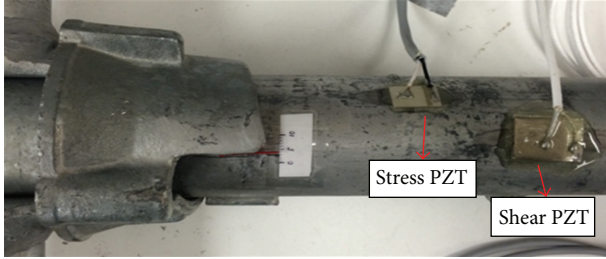


FIGURE 7: Picture of tightness scale and mounted stress PZT and shear PZT.

This cuplock scaffold model is composed of a vertical bar and two cross bars. The features of the cuplock specimen are listed in Table 2. Two cross bars are connected with the vertical bar through the cuplock. The PZTs are mounted on the outside surface of two cross bars and the vertical bar. Figure 7 is the photo of PZT patch transducers on the vertical bar. We use nonconductive epoxy to stick each PZT patch onto the pipe surface. Nonconductive epoxy is also used to protect PZTs from damage by covering their top. We mount a plastic point to the top cuplock and 1 cm ruler on the vertical bar as a scale which shows tightness index i (Figure 7).

There are two types of PZTs used in our experiment, three stress PZTs (PZT 1, 2, and 3) and three shear PZTs (PZT 4, 5, and 6). We have experiment sets 1 and 2 with stress PZTs and shear PZTs, respectively. In experiment 1, the actuator is PZT 3 and the sensors are PZTs 1 and 2. PZT 6 is the actuator for experiment 2, and PZTs 4 and 5 are sensors. The performance of two sets of experiments is compared.

4. Experimental Results and Analysis

Two sets of experiments were done during the cuplock connection monitoring test. In these experiments, we used pipe wrench to screw the connection by 1 mm each time from tightness degree 3 to 6. The tightness degree 3 to 6 are denoted by tightness index 1 to 4. The lowest tightness degree 3 is chosen for the reason that it is the degree that can be tightened by hand. The highest tightness degree 6 is the degree that can be tightened by the pipe wrench. These two degrees are chosen based on the practical field operation conventions. When the workers build the cuplock structure in field, the first step for them is to tighten the cuplock connection by hand and then use hammer to tighten it.

The PZTs are utilized for the structure monitoring of the cuplock scaffold specimen. In the structural health monitoring algorithm, wavelet packet analysis is used as a signal-processing tool to analyze the sensor signal. The sensor signal is decomposed by a 5-level wavelet packet decomposition

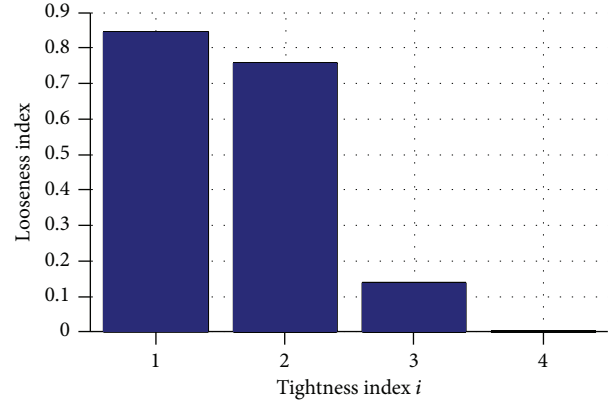


FIGURE 8: Looseness index (PZT 3 as actuator and PZT 1 as sensor).

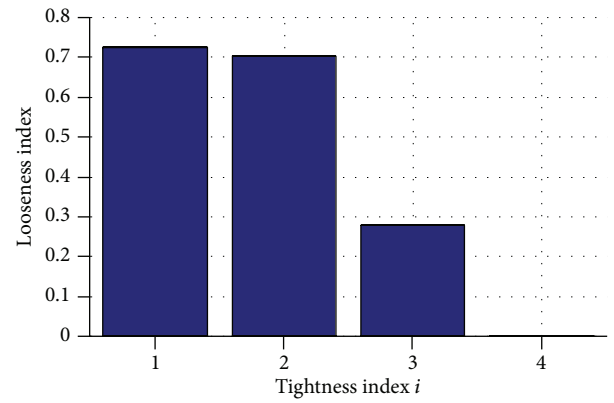


FIGURE 9: Looseness index (PZT 3 as actuator and PZT 2 as sensor).

into 32 signal sets. 32 signal sets are enough for the analysis. The wavelet packet based looseness index matrix proposed previously has been utilized for the cuplock scaffold structure looseness monitoring.

4.1. Experiment Set 1 with Stress Wave PZTs. Figures 8 and 9 are the looseness index graphs in which the data is sensed by PZTs 1 and 2, respectively, for stress PZTs. In the experiment, tests were done in the same condition. So we compare the results of Figures 8 and 9 at first. The difference of the looseness for tightness indexes 1 and 2 is little. It is because the contact surface of the cuplock scaffold specimen is not smooth, so when the cuplock was tightened the transmitted signal energy did not change much. It also may be caused by the characteristic of stress wave; when the contact area is not enough, the transmitted signal energy does not change much. When the cuplock got tightened from tightness 2 to tightness 3, the difference is very significant.

4.2. Experiment Set 2 with Shear Wave PZTs. Figures 10 and 11 are the looseness index graphs in which the data is sensed by PZTs 4 and 5, respectively, for shear PZTs. In the experiment, tests were done in the same condition. Comparing the results of Figures 10 and 11, we found the loose index changes gradually from tightness degree 1 to 4. The possible reason is

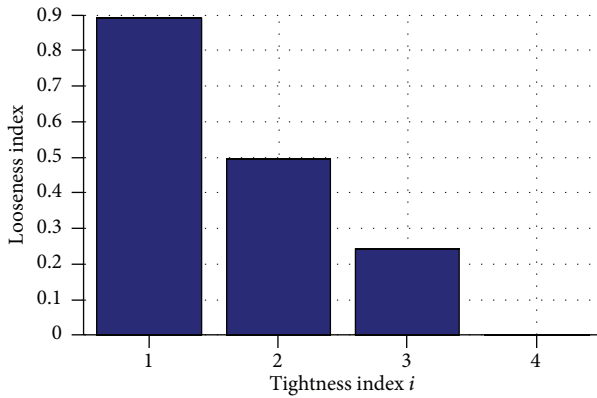


FIGURE 10: Looseness index (PZT 6 as actuator and PZT 4 as sensor).

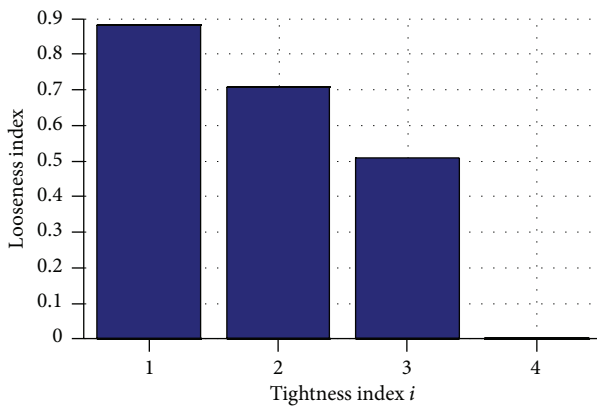


FIGURE 11: Looseness index (PZT 6 as actuator and PZT 5 as sensor).

that those shear waves transmit through the specimen well. The transmitted signal energy increased continuously with the incensement of the tightness index.

For both experiments, we can find that both stress and shear PZTs can be used to monitor the looseness of the cuplock connection. Comparing the results of experiments 1 and 2, we find that the shear PZTs work better than stress PZTs in our experiments. It is better to use shear PZTs to monitor the health status of cuplock connections in the construction field.

5. Conclusions

In this paper, we used piezoelectric transducers to monitor cuplock connection for cuplock scaffold based on the wavelet packet analysis. According to the experimental results, the looseness index decreased with the cuplock connection tightened. In summary, the looseness of cuplock connection can be monitored by the proposed method. The proposed active sensing method with piezoelectric transducers has the potential to be implemented in the health monitoring of structures with similar connections in construction.

Conflict of Interests

The authors declare that there is no conflict of interests regarding the publication of this paper.

References

- [1] Y. Zhao and K. Liu, "Safety accident of formwork engineering and its prevention in china," *Architecture Technology*, vol. 39, no. 7, pp. 492–496, 2008 (Chinese).
- [2] L. Ming and L. Kaiming, "Statistics and analysis of collapse accident of high scaffolding in china," *Annual meeting of National Building formwork And Scaffolding Committee*, vol. 36, pp. 80–84, 2009 (Chinese).
- [3] J. Mi, "Cause and solution of scaffold collapse accident," *Architecture Technology*, vol. 32, no. 4, pp. 260–264, 2001 (Chinese).
- [4] F. Hadipriono and H. K. Wang, "Causes of falsework collapses during construction," *Structural Safety*, vol. 4, no. 3, pp. 179–195, 1987.
- [5] J. Peng, A. Pan, D. Rosowsky, W. Chen, T. Yen, and S. Chan, "High clearance scaffold systems during construction—I. Structural modelling and modes of failure," *Engineering Structures*, vol. 18, no. 3, pp. 247–257, 1996.
- [6] R. G. Beale, "Scaffold research—a review," *Journal of Constructional Steel Research*, vol. 98, pp. 188–200, 2014.
- [7] J. Xie and J. Wang, "Analysis and prevention technology measure of the collapse accidents of falsework system," *Construction Technology*, vol. 33, no. 2, pp. 35–37, 2004 (Chinese).
- [8] W. K. Yu, K. F. Chung, and S. L. Chan, "Structural instability of multi-storey door-type modular steel scaffolds," *Engineering Structures*, vol. 26, no. 7, pp. 867–881, 2004 (Chinese).
- [9] T. Chandransu and K. J. Rasmussen, "Investigation of geometric imperfections and joint stiffness of support scaffold systems," *Journal of Constructional Steel Research*, vol. 67, no. 4, pp. 576–584, 2011.
- [10] H. Zhang, T. Chandransu, and K. J. R. Rasmussen, "Probabilistic study of the strength of steel scaffold systems," *Structural Safety*, vol. 32, no. 6, pp. 393–401, 2010.
- [11] H. Zhang, K. J. R. Rasmussen, and B. R. Ellingwood, "Reliability assessment of steel scaffold shoring structures for concrete formwork," *Engineering Structures*, vol. 36, pp. 81–89, 2012.
- [12] T. Chandransu, K. Rasmussen, and K. J. Rasmussen, "Structural modelling of support scaffold systems," *Journal of Constructional Steel Research*, vol. 67, no. 5, pp. 866–875, 2011.
- [13] U. Prabhakaran, R. Beale, and M. Godley, "Analysis of scaffolds with connections containing looseness," *Computers & Structures*, vol. 89, no. 212, pp. 1944–1955, 2011.
- [14] A. Walker, *Study and Analysis of the First 120 Failure Cases, Structural Failures in Buildings*, The Institution of Structural Engineers, 1981.
- [15] F. C. Hadipriono and H.-K. Wang, "Analysis of causes of falsework failures in concrete structures," *Journal of Construction Engineering and Management*, vol. 112, no. 1, pp. 112–121, 1986.
- [16] F. Bouchoucha, M. Akrou, T. Fakhfakh, M. Ichchou, and M. Haddar, "Damage detection in cylindrical pipe through diffusion matrix in wave finite element method," *Advances in Structural Engineering*, vol. 15, no. 3, pp. 435–446, 2012.
- [17] Z. Shi and T. Zhang, "Bending analysis of a piezoelectric curved actuator with a generally graded property for the piezoelectric parameter," *Smart Materials and Structures*, vol. 17, no. 4, Article ID 045018, 2008.

- [18] G. Song, Y. L. Mo, K. Otero, and H. Gu, "Health monitoring and rehabilitation of a concrete structure using intelligent materials," *Smart Materials and Structures*, vol. 15, no. 2, p. 309, 2006.
- [19] G. Song, H. Gu, Y. L. Mo, T. T. C. Hsu, and H. Dhonde, "Concrete structural health monitoring using embedded piezo-ceramic transducers," *Smart Materials and Structures*, vol. 16, no. 4, pp. 959–968, 2007.
- [20] G. Song, H. Gu, and Y.-L. Mo, "Smart aggregates: multi-functional sensors for concrete structures—a tutorial and a review," *Smart Materials and Structures*, vol. 17, no. 3, Article ID 033001, 2008.
- [21] Y. Chen, L. Liu, and Y. Duan, "Study on the mechanical characteristic and safety measures of bowl-scaffold," *Procedia—Social and Behavioral Sciences*, vol. 96, pp. 304–309, 2013.

Research Article

The Long-Term Settlement Deformation Automatic Monitoring System for the Chinese High-Speed Railway

Xu Wang,^{1,2} Liangqin Wu,³ Yi Zhou,¹ and Yanru Wang⁴

¹ State Key Laboratory Breeding Base of Mountain Bridge and Tunnel Engineering, Chongqing Jiaotong University, Chongqing 400074, China

² Key Laboratory of Structure and Wind Tunnel of Guangdong Higher Education Institutes, Shantou 515063, China

³ Department of Civil Engineering and Architecture, East China Jiaotong University, Nanchang 330013, China

⁴ Oujian College, Wenzhou University, Wenzhou 325035, China

Correspondence should be addressed to Yanru Wang; yanrupiaoyang@163.com

Received 20 August 2014; Accepted 31 October 2014

Academic Editor: Bo Chen

Copyright © 2015 Xu Wang et al. This is an open access article distributed under the Creative Commons Attribution License, which permits unrestricted use, distribution, and reproduction in any medium, provided the original work is properly cited.

The Beijing-Shanghai high-speed railway is one of the milestones of China's high-speed railway development and its security plays a significant role in China's economic and social development. However, the evaluation methods used for large-scale security operations and important infrastructure systems, such as the high-speed railways, are discrete and nonlinear; thus they cannot issue emergency warnings in a timely manner. The emergence of optical fiber sensing technology can solve this problem. This technology has progressed rapidly in its application to the monitoring of railway security and it has attracted much attention within the industry. This study considers the newly built passenger railway line between Shijiazhuang and Jinan as an example. The web-based, all-in-one fiber Bragg grating static level is described as well as a set of online monitoring systems, which is automated, real-time, remote, visual, and adaptable to the standards of the Beijing-Shanghai high-speed railway. According to our theoretical analysis, the planned automated monitoring of settlement deformation for the Beijing-Shanghai high-speed railway and the real-time analysis and calculation of monitoring data can ensure the operational security of this section of China's high-speed railway system.

1. Introduction

The Beijing-Shanghai high-speed railway is one of the milestones in China's high-speed railway development and its security plays a significant role in national economic and national development. However, during the long-term service of the high-speed railway bridge and subgrade, or the construction process of adjacent structures, many of its structures will experience natural aging and damage accumulation due to the long-term impacts of external environmental factors and man-made negative conditions related to its engineering. The settlement and deformation of high-speed railway bridges and subgrades can also result in disastrous accidents. Therefore, monitoring the health of the bridge integrity can effectively prevent disasters and timely controls can limit defects, reduce costs, avoid casualties, and ensure the operational security of the Beijing-Shanghai high-speed railway.

At present, the operational state of large-scale infrastructures, such as the high-speed railway, is evaluated mostly by combining traditional field measurements with industrial analysis evaluations in China. However, this method is discrete and nonlinear; thus problems with the infrastructure will not be found in a timely manner and accidents will not be easy to prevent. The Beijing-Shanghai high-speed railway is mostly in a closed state, so traditional manual measurements will be difficult to obtain and monitor continuously. The regional settlement deformation detection technology that is used widely both domestically and abroad mainly comprises total station instrument measurements, global positioning system (GPS) measurements, static level measurements, synthetic aperture (difference) radar interferometry measurement (InSAR, D-InSAR) [1–7], precise leveling measurements, and inertia measurements [8]. The cost of equipment is high, including GPS measurement technology,

inertia measurement technology, and D-InSAR technology, and their precision only reaches the centimeter level, which cannot meet the monitoring requirements for the settlement deformation of a high-speed railway bridge. At present, precise leveling measurement technology is adopted universally to obtain settlement deformation state measurements for high-speed railway bridge pile foundations. However, the influence of severe environmental factors means that the datum points for pile foundations and for deposition observation points are difficult to set. The requirements for observations are strict and complex climatic conditions are difficult to overcome; thus the precision might fail to meet the monitoring requirements for settlement deformation after the construction of pile foundations.

With the development of various optical fiber sensing techniques, various sensing methods based on optical fiber technology have appeared in recent years, especially for optical fiber sensor technologies based on sensitive telescopic materials and optical fiber sensors based on fiber Bragg grating (FBG), which have good application prospects [9–11]. Optical fiber sensing technology has already been applied to railway security measurements and it has attracted much attention in the industry. In 2007, Tarn et al. [12] placed an FBG sensing network on a steel rail line with a length of 26 km to measure the wheel-rail force, which allowed the counting of axles passing through the monitoring region. The practical status of track vibrations and the wheel-track affinity have also been studied using these types of measurement data. Willsch worked with the railway department, where an FBG strain sensor was buried in the track beside a high-speed railway to measure changes in the track state [13]. The feasibility of wheel tread detection based on wheel-track affinity was addressed by Li using a monitoring region built from an FBG sensor array [14]. Ho et al. analyzed the strain placed on a rail by the train wheels. The strain was measured using FBG sensors and the feasibility of rail damage detection based on the monitoring results was discussed [15]. To obtain measurements from the HK Tsing Ma Bridge, Chan et al. installed 40 FBG sensors on cable, bearing, and truss beams and compared the real-time data with the original data to analyze the health of the system. Based on long-term monitoring and comparison, the accuracy and reliability of the monitoring results obtained using the FBG sensors were demonstrated [16]. Yi et al. proposed an optimal sensor placement (OSP) strategy based on multiple optimization methods and an OSP selection scheme was applied to the Guangzhou New TV Tower based on the developed toolbox [17]. As stated above, the application of optical fiber sensing technology to monitor the status of rail systems has become a hot research topic. Due to the advantages of FBG sensors, they have been applied in many engineering domains for monitoring vehicle states, orbit temperatures, strain states, orbit and track slab structures, bridge tunnels, the side slopes of railway lines, and other similar structures. The continuous development and improvements in FBG sensor technology mean that it will play an increasingly important role in the monitoring of railway track systems.

To consider various comprehensive factors, the construction process for the Beijing-Shanghai high-speed railway

focused on using optical grating technology to monitor the settlement deformation of the bridge and track during the railway construction, and data were retrieved that reliably reflected the influences on the construction. During the construction, because of the complex effects of the geological conditions, loading conditions, material properties, construction techniques, and other external factors, the practical situation was often different from theory. Thus, in addition to strictly controlled construction measurements, remote, real-time, online, and automatic monitoring had to be performed to guarantee the structural security, thereby ensuring the operational security of the Beijing-Shanghai high-speed railway. Therefore, this approach has fundamental significance for engineering and value in the development of automatic settlement deformation monitoring systems for the Beijing-Shanghai high-speed railway. These systems can be built using a set of online monitoring techniques, which are automatic, real-time, remote, visual, and suited specifically to the standards of the Beijing-Shanghai high-speed railway.

2. Engineering Condition

2.1. The Condition of the Shijiazhuang-Jinan Passenger Railway Line. The starting point of the newly built Shijiazhuang-Jinan passenger railway line is Shijiazhuang station and its terminal point is Wulitang station, where the length is 323.096 km (Figure 1). The main track is a double line, its design speed is 250 km/h, the radius of the minimum curve is 4000 m, the maximum gradient is 20‰, and the line spacing is 5.0 m. The connecting track at the southern end of Dezhou is a double line, its design speed is 160 km/h, the radius of the minimum curve is 1300 m, the maximum gradient is 20‰, and the line spacing is 4.2 m. The connecting track at the east of Jinan is a double line, its design speed is 250 km/h, the radius of the minimum curve is 4000 m, the maximum gradient is 20‰, and the line spacing is 4.6 m. The beam of the newly built Shijiazhuang-Jinan passenger railway is a track strain beam and the pier has double lines with round ends at the bottom.

The emphasis during the project construction process was to automatically monitor the settlement with a line spacing of less than 25 m and specific structure sections between 25 m and 50 m for railway bridges. The data acquired reliably reflected the external influences acting on the Shijiazhuang-Jinan passenger railway line.

2.2. Engineering Geological Characteristics. The unfavorable geological conditions along the line mainly comprised issues with ground settlement, ground fissures, and earthquake-induced liquefaction. The distribution of the weak soil foundation was widespread along the line. The new loess, cohesive soil, silt, and sandy soil of the quaternary Holocene surface were characterized by their low bearing capacity, high moisture capacity, and middle-high compressibility, which readily generated compressive deformation.

The causes of ground settlement along the line were related to two main factors: the groundwater was exploited excessively, and thus the water level was largely in decline; and the water head had reduced, which caused an effective strain on the interior strata. This made the soil body produce

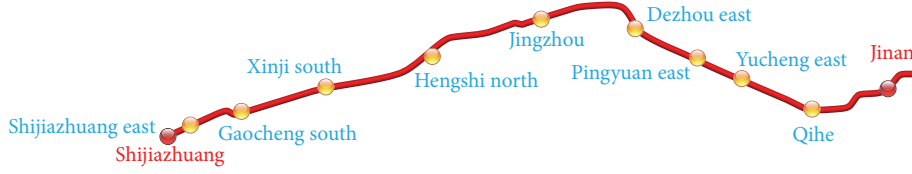


FIGURE 1: The newly built Shijiazhuang-Jinan passenger railway line.

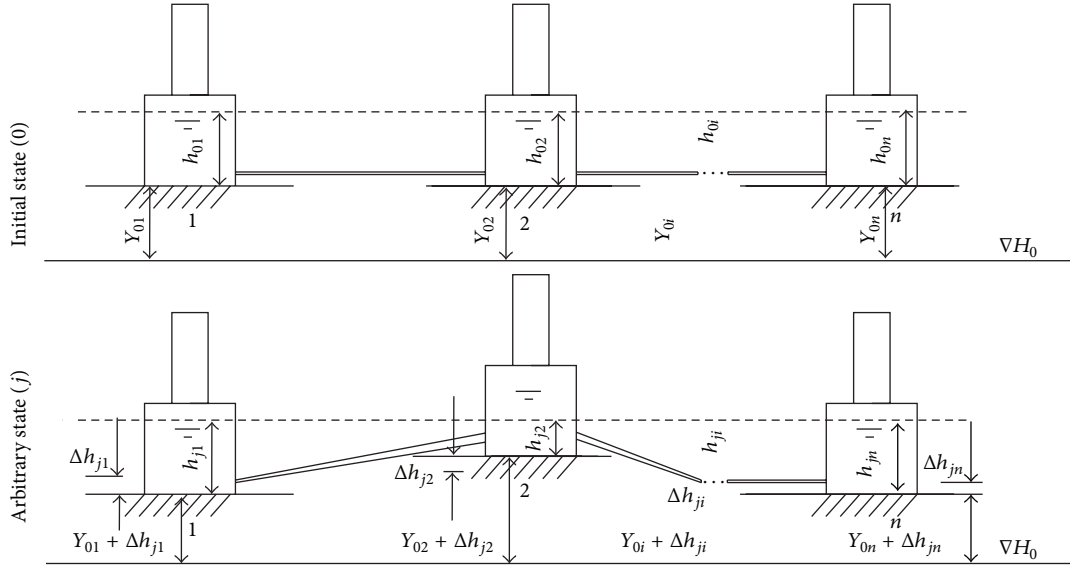


FIGURE 2: Schematic diagram of an FBG.

compression deformation and ground settlement formed, in addition to the natural consolidation and compaction of the soil layer and geotectonic movement. The exploitation of underground water was the main reason for the nonsettlement of the soil.

3. Automatic Settlement Monitoring

3.1. Principle of Settlement Measurement. The automatic settlement monitoring process used a communication tube to measure relative changes in the liquid level of each measuring point vessel and the relative subsidence was compared with the base point, which was obtained by calculation. As shown in Figure 2, it is assumed that there are n points and the first is the relative datum point. In the initial state, the distances between various measurement setting elevations and reference elevation planes ∇H_0 are $Y_{01}, Y_{02} \dots Y_{0i} \dots Y_{0n}$ (i is the measurement point number, where $i = 0, 1 \dots n$). The distances between various measurement setting elevations and liquid levels are $h_{01}, h_{02}, h_{0i} \dots h_{0n}$; that is,

$$Y_{01} + h_{01} = Y_{02} + h_{02} = \dots Y_{0i} + h_{0i} = \dots Y_{0n} + h_{0n}. \quad (1)$$

When differential settlement occurs, it is assumed that the variation between the measurements of the setting elevations and benchmark reference elevation planes is ∇H_0 , that is, $\Delta h_{j1}, \Delta h_{j2} \dots \Delta h_{ji} \dots \Delta h_{jn}$ (j is measuring point number, where $j = 0, 1 \dots n$). The distances between

various measurement setting elevations and liquid levels are $h_{j1}, h_{j2}, \dots, h_{ji}, \dots, h_{jn}$, where the following formula can be obtained based on Figure 2:

$$(Y_{01} + \Delta h_{j1}) + h_{j1} = (Y_{02} + \Delta h_{j2}) + h_{j2}. \quad (2)$$

The relative settlement between the j th measurement i point and datum point 1 is as follows:

$$H_{i1} = \Delta h_{ji} - \Delta h_{j1}. \quad (3)$$

The following formula can be obtained from formula (2):

$$\Delta h_{j1} - \Delta h_{ji} = (Y_{0i} - Y_{01}) + (h_{ji} - h_{j1}). \quad (4)$$

The following formula can be obtained from formula (1):

$$(Y_{0i} - Y_{01}) = -(h_{0i} + h_{01}). \quad (5)$$

The following formula can be obtained by substituting formula (5) into formula (4):

$$H_{i1} = (h_{ji} - h_{j1}) - (h_{0i} - h_{01}). \quad (6)$$

Only the distances h_{ji} (including h_{j1} and first h_{0i}) between the liquid levels within various measuring point vessels at various times and the setting elevations of the point can be measured using FBG sensor technology. Thus, the relative elevation differences can be obtained between

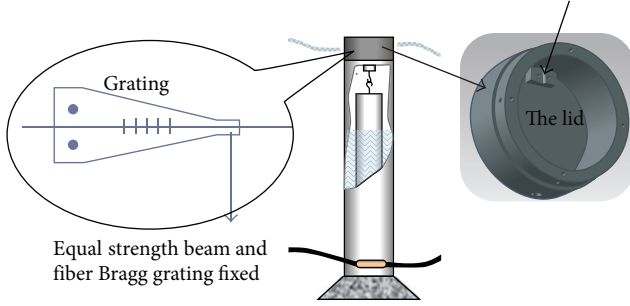


FIGURE 3: Schematic diagram of an FBG.

various points at a specific moment and datum point 1. If any point j ($1, 2, \dots, i, n$) is considered to be the relative datum point and the measurement time f is considered to be the reference time, the relative elevation differences H_{ij} between various measurement points and measurement point g (measurement time f is considered to be the datum value) can be obtained according to formula (6):

$$H_{ij} = (h_{ij} - h_{ig}) - (h_{fj} - h_{fg}). \quad (7)$$

As shown in Figure 3, given a downward force with equal strength, the optical grating pasted on the beam with equal strength is slightly stretched under the force, where the relationship between the stretching value and tension is linear. Because the relationship between the stretching value and the wavelength is linear and the relationship between the tension and liquid level is linear, the height of the liquid level can be measured based on the variation in the wavelength of the optical fiber. To achieve temperature compensation, two optical gratings can be created on the same optical fiber and pasted at the front and back with equal strength. The variation in the two wavelengths is subtracted, which can increase the sensitivity and facilitate compensation temperature. The FBG static level comprises the main vessel, communicating tube, FBG sensors, and so forth (Figure 7). The relative settlement of the measurement point can be calculated by the measurement instruments based on the variations in the FBG wave.

3.2. Principle of the Acquisition of Settlement Data. Using the light sensitivity of the optical fiber material, the FBG writes coherent field patterns for incident light into the fiber core via UV light exposure. The periodical change in the refractive index produced in the fiber core along the fiber core axis has allowed the development of a perpetually spatial phase grating, which essentially acts as a narrow-band (transmission or reflect) filter or reflector in the fiber core. When wide spectrum light passes through the FBG, a wave that satisfies the FBG's condition will produce a reflection and other wavelengths will transmit continuously through the FBG (Figure 4). The relationship between the reflected wavelength and the optical grating is as follows:

$$\lambda = 2n\Lambda, \quad (8)$$

where n is the refractive index of the optical fiber cores and Λ is the period of the optical grating.

TABLE 1: Performance indexes for the FBG interrogator.

Project name	Performance index
Channel number	16/8/4
Maximum measuring points of each channel	12
Wavelength range	1525–1565 nm
Repeatability of wavelength measurements	2 pm
Resolution	1 pm
Dynamic range	>50 dB
Scanning frequency	1–5 Hz (low speed)
Scanning mode	Parallel scanning of all channels
Spectrum	Full spectrum
Optics interface	FC/APC
Measurement distance	20 km
Communication interface	100 M Ethernet, GPRS communication module
Power source	Interflow 20 V/50 Hz
Power consumption	<10 W
Work environment	Temperature: -10 to 50°C ; humidity: 0–80%; no condensation
Storage environment	Temperature: -20 to 60°C ; humidity: 0–95%; no condensation
Weight	3 kg
External size	(L) $482 \times$ (W) $300 \times$ (H) 89 mm

This method is suitable for general engineering applications. FBG sensors are formed using epoxy resin adhesive with a protective encapsulation for protection.

The FBG only reflects certain wavelengths; thus the variation in reflection is measured using an FBG interrogator. In general, many FBG sensors are used to measure wavelength division multiplexing, which is determined in tandem with many FBGs based on the central wavelengths of each FBG. As well as ensuring that a dynamic range of measurements is obtained, there is no overlapping among the wavelengths of various FBGs. The measurements of the reflective wavelengths for different FBG sensors are obtained using the FBG interrogator (Table 1) and they are then transformed into pressure or strain data (Figure 5).

3.3. Automatic Measurement Instrument and Technical Index

3.3.1. Optical Fiber Interrogator. The Copal Network AIO machine, produced by Hangzhou Copal Internet of Things Science and Technology Company, was used to obtain automatic measurements, as shown in Figure 6.

This equipment can work in demanding conditions and it has a built-in security feature. Thus, in the event of system accidents or malfunctions, it can recover on its own. Built-in GPRS communication and an Ethernet module can allow

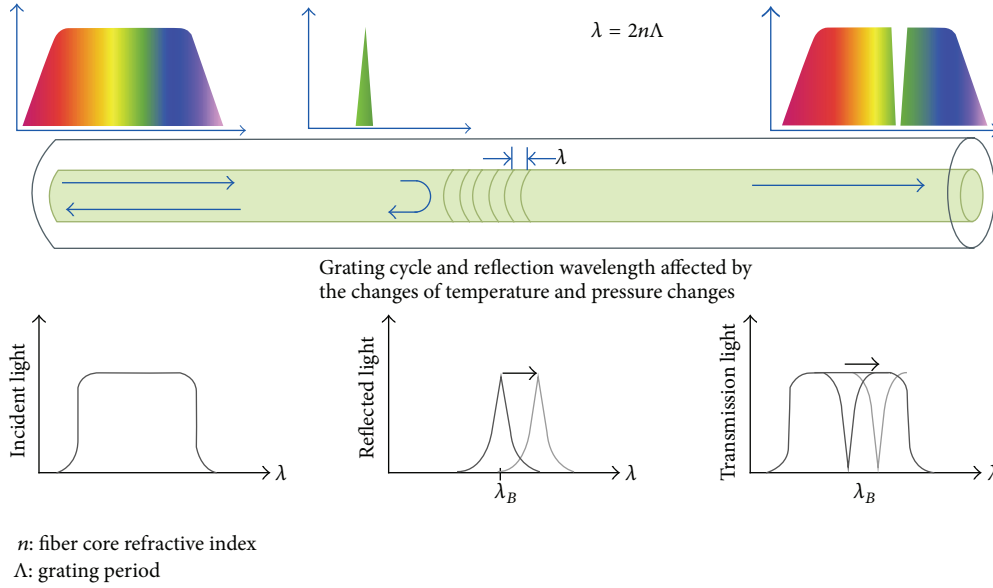


FIGURE 4: Schematic diagram of an FBG sensor.

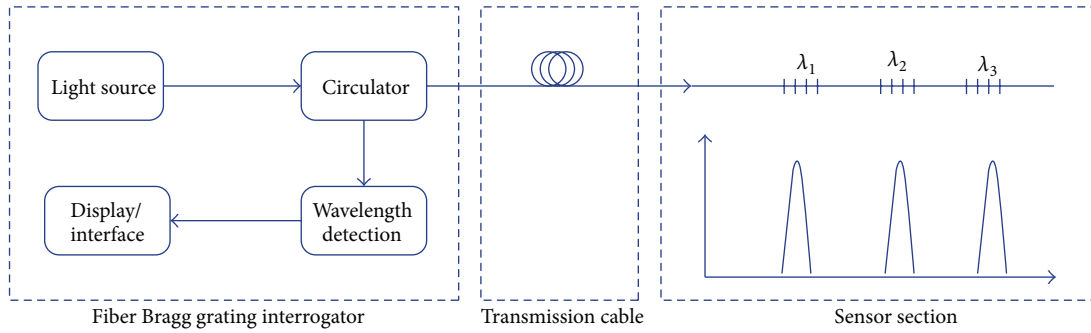


FIGURE 5: Structure of a typical FBG sensor system.



FIGURE 6: FBG interrogator.

remote data acquisition. Its unique network technique can remotely set parameters and it does not have to be modified while in use.

3.3.2. FBG Static Level. The FBG static level produced by Hangzhou Copal Internet of Things Science and Technology

TABLE 2: Technical indexes for the FBG static level.

Project	Technical index
Standard mileage	100 mm
Measurement accuracy	0.1‰ F.S. (0.1 mm)
Resolution	0.02‰ F.S. (0.02 mm)
Wavelength range	1525–1565 nm
Size	Φ100 × 290 mm
Connection mode	FC/PC or welding
External package	Stainless steel cover
Installation mode	Punching or weld installation
Temperature compensation form	Self-compensating
Usage temperature	−30°C to 85°C

Company was used to obtain automatic measurements, as shown in Figure 6. Its technical indexes are shown in Table 2.

3.4. Monitoring Scheme Design

3.4.1. Monitoring Section Layout. Based on the specific conditions used to collect material and for working in the field, the range of all line spacings was less than 25 m and special



FIGURE 7: FBG static level.

structural sections could have line spacings between 25 m and 50 m. The total detection range was 48.518 km, including seven special sections where the line spacing was less than 25 m and four special structural sections where the line spacing was between 25 m and 50 m.

Because the length of the parallel sections of the railway line could be longer and to obtain the best measurement points for the FBG interrogator, the overall monitoring range was divided into 27 monitoring sections (section numbers A–Z and AA). The monitoring range comprised sets with 1549 monitoring sections, 97 turning point sections, 15 base point sections, 1507 monitoring piers, and roadbeds that measured 739.09 m in length.

3.4.2. Measurement Point Layout

(1) *Monitoring Point Layout for the Monitoring Sections of the Simply Supported Beams.* Every section had two automatic monitoring points on a lateral and longitudinal bearing on the beam, as shown in Figure 8.

(2) *Monitoring Point Layout for the Monitoring Section on a Continuous Beam.* Every section had two automatic settlement monitoring points, which were laid out on the side-span, mid-span, and inside of the diaphragm plate, as shown in Figure 9.

(3) *Monitoring Point Layout for Additional Sections of the Large-Span Side Pier.* A pair of monitoring points was added to the support beam of the large-span side pier, which corresponded to the section monitoring points of the large-span side pier, as shown in Figure 10.

(4) *Monitoring Point Layout for Turning Point Sections.* Every turning point section had two automatic settlement monitoring points, which are called turning points (Figure 11). Two monitoring points could be set on the monitoring section, which then collected data during the overall process.

The overall monitoring system comprised 1549 monitoring sections that corresponded to 3098 monitoring points, 97 turning point sections that corresponded to 194 turning points, and 15 base point sections that corresponded to 30 monitoring base points. In total, there were 3322 automatic

static levels. A physical map of the automatic monitoring system is shown in Figure 12.

3.5. *Bracket Mounting.* The automatic level installation used a general column style bracket. The fixed position of the column style bracket was located at the bottom of the instrument. The height of the instrument was adjusted using a basic steel drum and bolt. The base steel plate of the instrument and the base board of the box girder were connected using epoxy resin glue stick steel. Figure 13 shows the column style installation used on the Beijing-Tianjin and Tianjin-Qinhuangdao high-speed railways.

3.6. *Pipe Laying.* The pipeline was laid in a box girder along the base plate. The laying position was adjustable via a diaphragm and the teeth block of the beam, but the elevation of the liquid-containing tube needed to be maintained below the bottom of the instrument. In the section of the bridge that reached the road, the pipeline was laid out on the two sides of the railway along the shoulder. The part of the pipeline that was subject to wear (e.g., the beam joint, or the up and down position of the bridge) contained a wiring duct that measured 5×5 cm to protect the liquid-containing tube, air hose, and optical fiber. Figure 14 shows the layout of the wiring duct used in the Beijing-Tianjin and Tianjin-Qinhuangdao high-speed passenger railways.

4. Automatic Monitoring Systems

4.1. *System Construction.* By combining the different engineering characteristics, the developed monitoring system mainly comprised six subsystems, which were ranked as follows from low to high importance.

- (1) *Sensor Subsystem.* Mainly the hardware sensors, including the static level.
- (2) *Video Monitoring Subsystem.* Mainly the monitoring probe.
- (3) *Data Acquisition and Transmission Subsystem.* The core of the overall monitoring system, including the FBG interrogator, automatic data acquisition unit hardware, hard disk video, and data acquisition and transmission software.
- (4) *Data Processing and Control Subsystem.* For data processing and storage.
- (5) *Database Subsystem.* Mainly the SQL database used to store massive volumes of monitoring data.
- (6) *Monitoring and Management Subsystem.* Software running on a personal computer. The software provided a visual interface so the user could monitor the project, submit data queries, and perform project management. The software provided automatic warnings and produced monitoring reports.

4.2. *Monitoring and Management Analysis Subsystem.* The monitoring and management analysis subsystem software adopted the Client-Server mode and it ran on a personal computer. The system was divided into seven modules, as

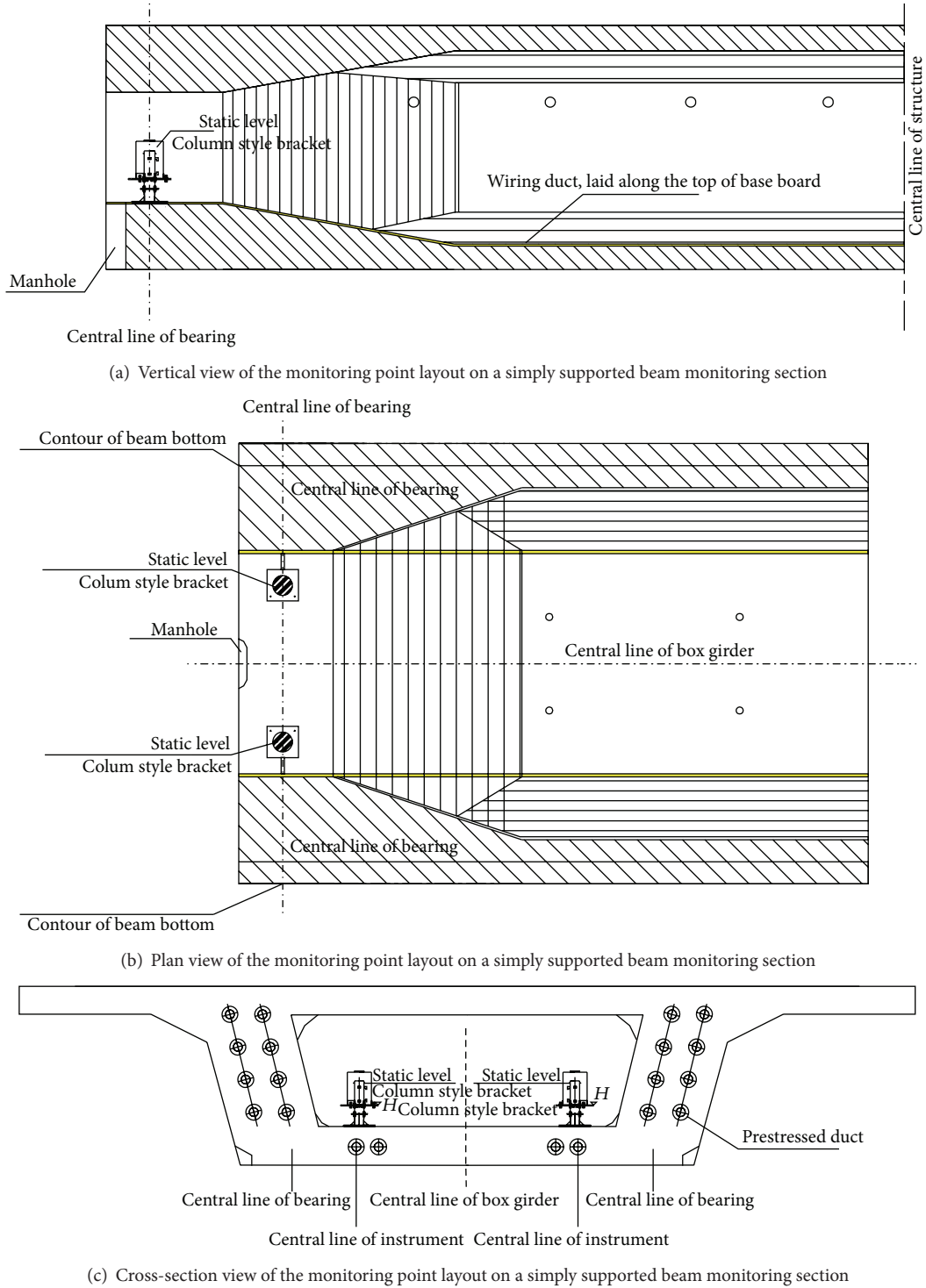


FIGURE 8: Monitoring point layout on a simply supported beam.

shown in Figure 17. The first five modules orient all of the users and they facilitate the submission of data queries and the management of monitoring projects. The “integrated management” module orients the system administrator in how to use the system for the management of existing

projects, as well as person and functions. Figure 15 displays the interface of the automatic monitoring analysis system used by the high-speed railway. Figures 16 and 17 show the pictures of real-time display of monitoring data and interface for data queries, respectively.

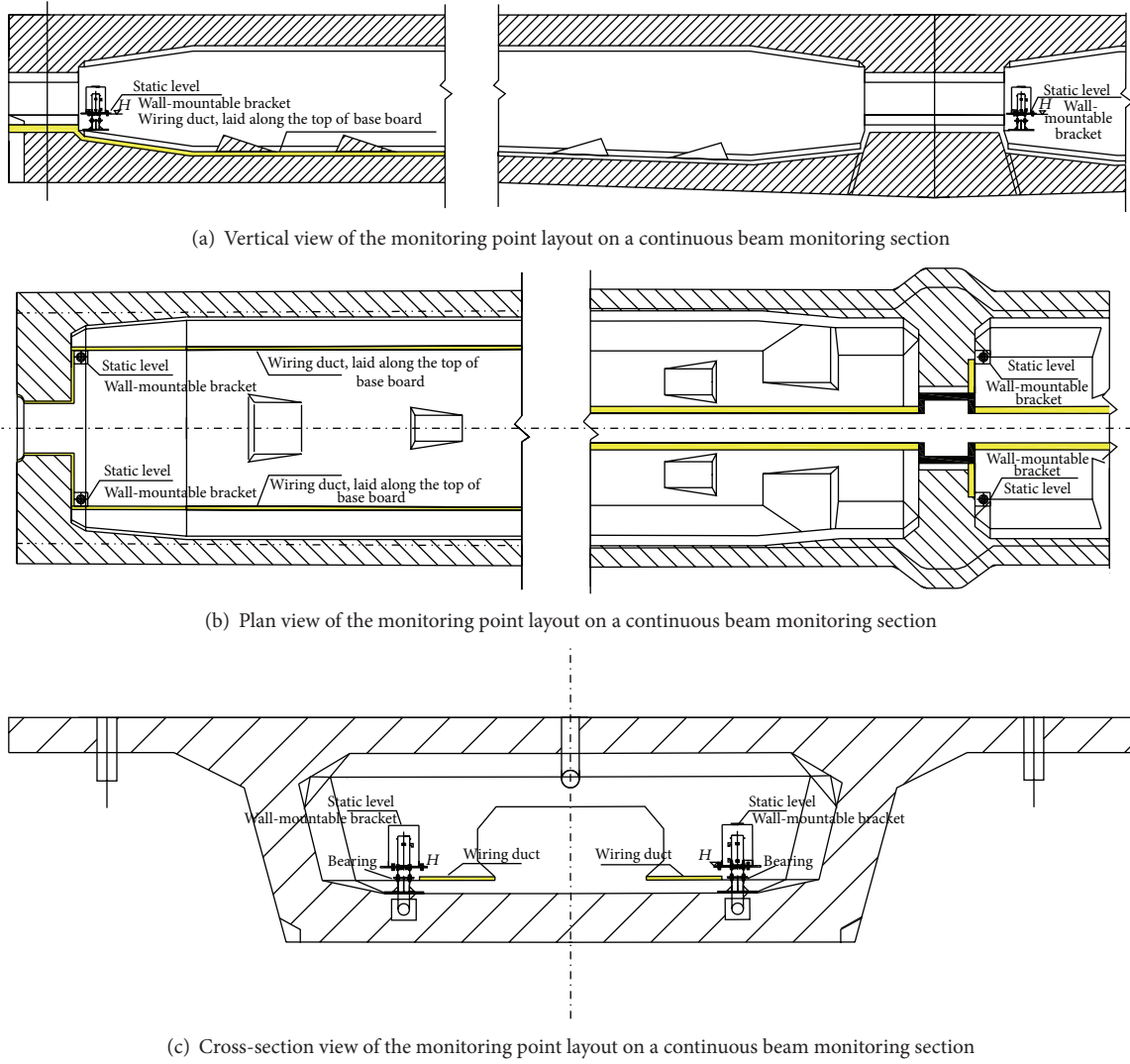


FIGURE 9: Monitoring point layout on a continuous beam.

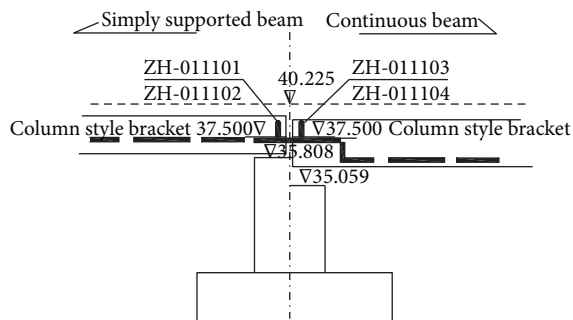


FIGURE 10: Monitoring point layout for an additional section of a continuous beam side pier.

5. Monitoring Frequency and Warning Index

5.1. Monitoring Frequency. The automatic monitoring analysis system for high-speed railway settlement and deformation

TABLE 3: Postconstruction settlement limiting values for statically determined structures on an abutment basis.

Subsidence type	Track type on the bridge	Limiting value
Pier uniform settlement	Ballast track	30 mm
	Ballastless track	20 mm
Differential settlement of adjacent pier	Ballast track	15 mm
	Ballastless track	5 mm

had a very high acquisition capability, where the highest frequency was 5 seconds per interval. Before construction, the trial of the automatic system collected 10 sets of effective data for use in the initial automatic monitoring. During one of the most critical periods of construction (from the start of construction until the completion of track-laying), the monitoring frequency was five times per minute. After construction, that is, three months after the track-laying was completed, the monitoring frequency was once per hour.

TABLE 4: Refinements and assessments of the effects of the Shijiazhuang-Jinan passenger railway on the settlement of the existing Beijing-Shanghai high-speed railway.

Serial number	Worksite name	Line spacing	Assessment value Additional settlement (mm)
1	Ordinary pier height of supported beam (pier with a height of 7 m)	25 m	−1.47
2	High pier of supported beam (pier with a height of 12 m)	25 m	−1.46
3	Large-span continuous beam to large-span continuous beam (across 353 provincial roads)	30 m	−1.85
4	Shijiazhuang-Jinan passenger railway across Beijing-Shanghai high-speed railway	42 m	−0.72
5	Frame structure to frame structure (gateway medium bridge)	50 m	−0.73
6	Shijiazhuang-Jinan passenger railway parallel to Beijing-Shanghai roadbed section	36 m	−1.23
7	Large-span continuous beam to a simply supported beam (Tuhaihe river)	25 m	−1.76
8	Four-line parallel, large-span continuous beam to large-span continuous beam (104 national roads)	40 m	−2.46

TABLE 5: The warning value for differential settlement deformation in a Beijing-Shanghai high-speed railway pier.

Section	Δ_{initial} (mm)	$\Delta_{\text{assessment}}$ (mm)	$\Delta_{\text{reservation}}$ (mm)	Δ_{standard} (mm)
Bridge section	0.5	Obtain assessment values at various work sites	1	4
Roadbed section	0.5		1	4

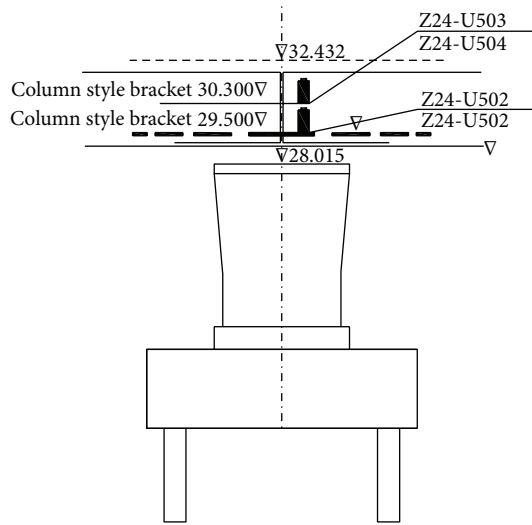


FIGURE 11: Monitoring point layout of a turning point section.

The monitoring system provided warnings according to a three-level warning scale. The monitoring results were controlled with a yellow, orange, and red warning system. Based on certain standards, the monitoring warning value was confirmed based on settlement after construction, differential settlement, the limiting value of a track profile irregularity, and detailed safety assessment results.

5.2. Standard Limiting Value. The “High-speed railway design specifications (trial) (TB10621-2009)” provide explicit definitions of settlement after construction, the roadbed, and the limiting value requirements for settlement and differential settlement after construction of the bridge, as shown in Table 3.

5.3. Assessment Values for Pier Settlement Deformation. According to the different line spacing of parallel sections when refining the safety assessment, the effects of building the Shijiazhuang-Jinan passenger railway on the settlement of the Beijing-Shanghai high-speed railway are shown in Table 4.

5.4. Warning Value Determination. The principles used to determine the warning values for the differential settlement of the Beijing-Shanghai high-speed railway piers (Table 5) were as follows:

- (1) yellow limiting value = $\Delta_{\text{initial}} + \Delta_{\text{assessment}}$;
- (2) orange limiting value = $(\Delta_{\text{standard}} - \Delta_{\text{initial}} - \Delta_{\text{assessment}} - \Delta_{\text{forewarning}}) \times 65\% + \Delta_{\text{yellow}}$;
- (3) red limiting value = $(\Delta_{\text{standard}} - \Delta_{\text{initial}} - \Delta_{\text{assessment}} - \Delta_{\text{forewarning}}) \times 85\% + \Delta_{\text{yellow}}$,

where Δ_{initial} is the mean differential settlement value based on the monitoring measurements until the end of the initial value measurement cycle, which was 0.5 mm according to our experience; $\Delta_{\text{assessment}}$ is the differential settlement determined by security assessment reports during the construction



FIGURE 12: Images of the automated monitoring project.



FIGURE 13: Column style installation used in the Beijing-Tianjin and Tianjin-Qinhuangdao high-speed railways.

graph phase; $\Delta_{\text{forewarning}}$ is the safety reserve value of the existing track irregularity, which was temporarily set at 1 mm; and Δ_{standard} is the admissible value for differential settlement given in the “High-speed railway design specifications (trial),” which was 5 mm.

The warning value for pier horizontal deformation is $\Delta_{\text{initial}} + \Delta_{\text{assessment}} - \Delta_{\text{initial}}$, which is the mean value of the differential settlement from the start of the monitoring measurements until the completion of the initial value measurement cycle, which was 0.5 mm according to our experience. $\Delta_{\text{assessment}}$ is the horizontal deformation of the pier according to the report assessments.

6. Conclusions

Given the discretionary and nonlinear nature of most methods used for safety evaluations in large-scale infrastructure

projects, such as high-speed railways, it can be assumed that there is no timely warning system for emergency situations. Thus, using the newly built Shijiazhuang-Jinan passenger railway as an example, we developed a set of online monitoring systems, which were automatic, real-time, remote, and visual, and they were suited to the standards of the Beijing-Shanghai high-speed railway. The aims and significance of this monitoring system can be summarized as follows.

- (1) Based on monitoring the settlement of the Beijing-Shanghai high-speed railway, real-time analysis processes, and calculations of the monitoring data, predictions and feedback can be assessed to monitor the effects of construction on the bridge and roadbed of the Beijing-Shanghai high-speed railway, thereby ensuring the safety of the high-speed railway.
- (2) Accurate and real-time feedback is provided to facilitate engineering construction. The rationality of construction technology and processes are guided and assessed. The construction scheme is adjusted in a timely manner based on warnings and the elimination of construction risks. The construction safety is also ensured and informative construction data are produced.
- (3) Many practical field data were used to ensure the accuracy of the design theory and modifications of the construction process, which made the design process of high quality, safe, economical, and fast.
- (4) The monitoring mode adopted in this project was automatic. Based on the refinement of safety assessment results and existing settlement monitoring material for the Beijing-Shanghai high-speed railway,



FIGURE 14: Wiring duct layout used in the Beijing-Tianjin and Tianjin-Qinhuangdao high-speed railways.

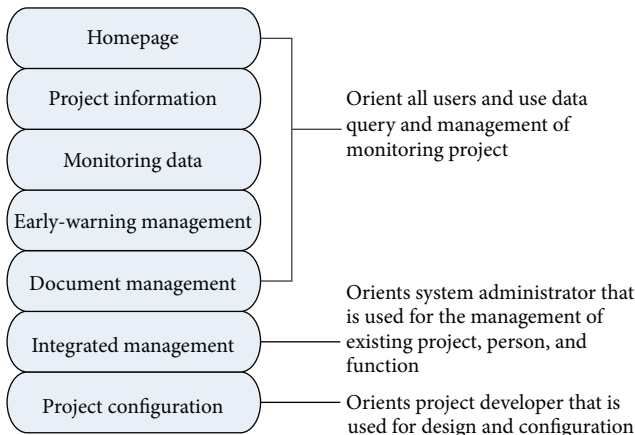


FIGURE 15: Modules of the monitoring and management analysis subsystem.

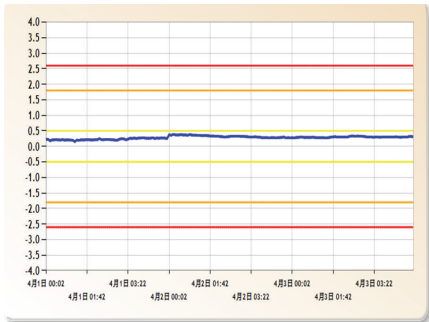


FIGURE 17: Interface for data queries.

Conflict of Interests

The authors declare that there is no conflict of interests regarding the publication of this paper.

Acknowledgments

This project is supported by the open fund of the State Key Laboratory Breeding Base of Mountain Bridge and Tunnel Engineering (CQSLBF-Y14-15), the National Program on Key Basic Research Project (973 Program) Grant no. 2012CB723305, the Chinese National Natural Science Foundation (51308510), and Zhejiang Provincial Natural Science Foundation (Q12E080026) which are gratefully acknowledged.

References

[1] S. Stramondo, F. Bozzano, F. Marra et al., “Subsidence induced by urbanisation in the city of Rome detected by advanced InSAR technique and geotechnical investigations,” *Remote Sensing of Environment*, vol. 112, no. 6, pp. 3160–3172, 2008.

[2] Y. Xia, B. Chen, X.-Q. Zhou, and Y.-L. Xu, “Field monitoring and numerical analysis of Tsing Ma suspension bridge temperature behavior,” *Structural Control and Health Monitoring*, vol. 20, no. 4, pp. 560–575, 2013.



FIGURE 16: Real-time display of monitoring data.

a practical, effective, safe, and reliable monitoring system was developed to ensure that the layout of the monitoring network was reasonable, while the monitoring content was comprehensive, the degree of automation was high, and the monitoring data were reliable.

- [3] T.-H. Yi, H.-N. Li, and M. Gu, "Recent research and applications of GPS-based monitoring technology for high-rise structures," *Structural Control and Health Monitoring*, vol. 20, no. 5, pp. 649–670, 2013.
- [4] A. K. Gabriel, R. M. Goldstein, and H. A. Zebker, "Mapping small elevation changes over large areas: differential radar interferometry," *Journal of Geophysical Research*, vol. 94, no. 7, pp. 9183–9191, 1989.
- [5] B. Chen, Y.-Z. Sun, G.-J. Wang, and L.-Y. Duan, "Assessment on time-varying thermal loading of engineering structures based on a new solar radiation model," *Mathematical Problems in Engineering*, vol. 2014, Article ID 639867, 15 pages, 2014.
- [6] A. Ferretti, C. Prati, and F. Rocca, "Nonlinear subsidence rate estimation using permanent scatterers in differential SAR interferometry," *IEEE Transactions on Geoscience and Remote Sensing*, vol. 38, no. 5, pp. 2202–2212, 2001.
- [7] T. H. Yi, H. N. Li, and M. Gu, "Experimental assessment of highrate GPS receivers for deformation monitoring of bridge," *Measurement*, vol. 46, no. 1, pp. 420–432, 2013.
- [8] B. Chen, Z. W. Chen, Y. Z. Sun, and S. L. Zhao, "Condition assessment on thermal effects of a suspension bridge based on SHM oriented model and data," *Mathematical Problems in Engineering*, vol. 2013, Article ID 256816, 18 pages, 2013.
- [9] A. Ferretti, C. Prati, and F. Rocca, "Permanent scatterers in SAR interferometry," *IEEE Transactions on Geoscience and Remote Sensing*, vol. 38, pp. 2202–2212, 2000.
- [10] D. M. Tralli, R. G. Blom, E. J. Fielding, A. Donnellan, and D. L. Evans, "Conceptual case for assimilating interferometric synthetic aperture radar data into the HAZUS-MH earthquake module," *IEEE Transactions on Geoscience and Remote Sensing*, vol. 45, no. 6, pp. 1595–1604, 2007.
- [11] J. Xu, M. Zhang, and C. He, "Summary of several typical sensors for kinematical measurement," *Journal of Geomatics*, vol. 30, no. 2, pp. 44–46, 2005.
- [12] H. Y. Tarn, T. Lee, S. L. Ho et al., *Utilization of Fiber Optic Bragg Grating Sensing Systems for Health Monitoring in Railway Applications*, Photonics Research Centre, The Hong Kong Polytechnic University, Hong Kong, 2007.
- [13] R. Willsch, "Optical fiber sensor systems based on nanostructures and examples of their applications," in *Proceedings of the OIDA Photonic Sensor Workshop*, Ottawa, Canada, 2007.
- [14] J. J. Pan, W. L. Li, and Y. F. Zhang, "Track strain field analysis for positing FBG sensor in fiber optic axle detecting," in *Photonics and Optoelectronics Meetings (POEM): Fiber Optic Communication and Sensors*, 7514IF, vol. 7514 of *Proceedings of SPIE*, Wuhan, China, August 2009.
- [15] T. K. Ho, S. Y. Liu, Y. T. Ho et al., "Signature analysis on Wheel-rail interaction for rail defect detection," in *Proceedings of the 4th IET International Conference on Railway Condition Monitoring (RCM '08)*, vol. 1, pp. 1–6, June 2008.
- [16] T. H. T. Chan, L. Yu, H. Y. Tam et al., "Fiber Bragg grating sensors for structural health monitoring of Tsing Ma bridge: background and experimental observation," *Engineering Structures*, vol. 28, no. 5, pp. 648–659, 2006.
- [17] T.-H. Yi, H.-N. Li, and M. Gu, "Optimal sensor placement for structural health monitoring based on multiple optimization strategies," *The Structural Design of Tall and Special Buildings*, vol. 20, no. 7, pp. 881–900, 2011.

Research Article

Effect of Temperature Variation on Vibration Monitoring of Prestressed Concrete Girders

**Thanh-Canh Huynh,¹ Young-Hwan Park,² Jae-Hyung Park,³
Dong-Soo Hong,⁴ and Jeong-Tae Kim¹**

¹Department of Ocean Engineering, Pukyong National University, 599-1 Daeyeon-3-dong, Nam-gu, Busan 608-737, Republic of Korea

²Structural Engineering Division, Korea Institute of Construction Technology, Gyeonggi-do 411-472, Republic of Korea

³Department of Ocean Engineering, Pukyong National University, Busan 608-737, Republic of Korea

⁴BT Consultant Co., Gyeonggi-do 411-472, Republic of Korea

Correspondence should be addressed to Jeong-Tae Kim; j0k9180@gmail.com

Received 5 September 2014; Accepted 10 November 2014

Academic Editor: Ting-Hua Yi

Copyright © 2015 Thanh-Canh Huynh et al. This is an open access article distributed under the Creative Commons Attribution License, which permits unrestricted use, distribution, and reproduction in any medium, provided the original work is properly cited.

The effect of temperature variation on vibration monitoring of prestressed concrete (PSC) girders is experimentally analyzed. Firstly, vibration features such as autoregressive (AR) coefficient, correlation coefficient of power spectral density (CC of PSD), natural frequency, and mode shape are selected to estimate the effect of temperature variation on vibration characteristics of PSC girders. Secondly, vibration experiments on a lab-scale PSC girder are performed under the condition of temperature variation. Finally, the vibration features with respect to the temperature variation are analyzed to estimate the effect of temperature in vibration characteristics of the PSC girder.

1. Introduction

For the past decades, the interest in structural health monitoring of prestressed concrete (PSC) structures has been increased. In a variety of civil engineering structures, PSC girders are main components to resist against external loadings [1]. For a PSC girder bridge, flexural stiffness in girder and prestress force in tendon are two essential parameters that should be secured for its serviceability and safety against external loadings. Unless the PSC girder bridges are instrumented at the time of construction, the occurrence of damage cannot be directly monitored and other alternative methods should be sought.

Since as early as 1970s, many researchers have focused on the possibility of using vibration characteristics of a structure as an indication of its structural damage [2–6]. The most appealing feature associated with using vibration properties is that they are relatively simple to measure and to utilize for a prompt diagnosis. Recently, research efforts have been made to monitor the change in modal properties of the PSC structures in relation to the change in prestress forces [7], to investigate the dynamic behaviors of prestressed composite

girder bridges [8], and to identify the change in prestress forces by measuring dynamic responses of prestressed beams [9–11].

However, the practicality of the so-called “bridge diagnosis via vibration monitoring” is limited for real PSC girder bridges since even significant damage sources may not be revealed as remarkable changes in vibration features due to temperature-induced uncertainty [12–17]. In a real-life situation of a PSC girder bridge, it is reasonable to say that temperature differences are about 10~20°C during day and night and about 20~50°C during a year. To account for the significant condition, therefore, temperature-induced changes in vibration properties should be accounted for the PSC girder bridge.

This study presents the effect of temperature on vibration responses of the prestressed concrete girder and also estimates the relative sensitivities of the selected vibration features. The following approaches are implemented to achieve the objective. Firstly, vibration features such as autoregressive coefficient, power spectral density, natural frequency, and mode shape are selected for estimating the effect of temperature variation on PSC girders. Secondly, experiments

on a lab-scale PSC girder are described. The experiments are performed under the condition of temperature variation. Finally, vibration characteristics of the PSC girder are analyzed with respect to the temperature variation. Temperature-induced effects on vibration monitoring of the PSC girder are estimated for the selected vibration features.

2. Vibration Features for Estimation of Temperature Effect

Vibration features selected to estimate the effect of temperature variation on the PSC girder include autoregressive model (AR model), correlation coefficient of power spectral density (CC of PSD), natural frequency, and mode shape. Once acceleration responses are measured at distributed location, the vibration features are extracted for the structure. For each type of vibration features, the effect of temperature is estimated by regression analysis.

2.1. Autoregressive Model. AR model is one of the time series analysis methods. It forecasts future responses from past time history responses. In this study, the AR model is defined in terms of acceleration responses as follows [18]:

$$\ddot{v}(t) = \sum_{j=1}^a \varphi_j \ddot{v}(t-j) + e(t), \quad (1)$$

where $\ddot{v}(t)$ is the time history of acceleration at time step t , φ_j is the j th AR coefficient, a is the order of AR model, and $e(t)$ is the residual error. The change in AR coefficients represents the change in structural parameters.

Mahalanobis squared distance (MSD) is utilized to calculate the change of AR coefficients due to structural change. Consider

$$D_{\zeta} = (\varphi_{\zeta} - \bar{\varphi})^T S^{-1} (\varphi_{\zeta} - \bar{\varphi}), \quad (2)$$

where D_{ζ} is the MSD value, φ_{ζ} is the AR coefficient vector (outlier), $\bar{\varphi}$ is the mean vector of n sets of AR coefficient, and S is the covariance matrix of n sets of AR coefficient. The variation of MSD indicates the variation of AR coefficients due to structural change. The number of set, n , is determined by partial autocorrelation function of the first acceleration sample in intact state. It is noted that the number of set should be larger than the order of AR model.

2.2. Correlation Coefficient of Power Spectral Density. Assume there are two acceleration signals, $x(t)$ and $y(t)$, measured before and after structural change, respectively. The corresponding power spectral densities, S_{xx} and S_{yy} , are calculated from Welch's procedure as [18]

$$S_{xx}(f) = \frac{1}{n_d T} \sum_{i=1}^{n_d} |X_i(f, T)|^2, \quad (3)$$

$$S_{yy}(f) = \frac{1}{n_d T} \sum_{i=1}^{n_d} |Y_i(f, T)|^2, \quad (4)$$

where X and Y are the frequency response transformed from correspondent acceleration signal; n_d is the number

of divided segments; and T is the data length of divided segment.

The correlation coefficient (CC) of PSDs represents the linear identity between the two PSDs obtained before and after structural change, as follows:

$$\rho_{XY} = \frac{E[S_{xx}S_{yy}] - \mu_{S_{xx}}\mu_{S_{yy}}}{\sigma_{S_{xx}}\sigma_{S_{yy}}}, \quad (5)$$

where $E[\cdot]$ is the expectation operator and $\sigma_{S_{xx}}$ and $\sigma_{S_{yy}}$ are the standard deviations of PSDs of acceleration signals measured before and after structural change, respectively. If any structural change occurs in target structure, its acceleration responses would be affected and, consequently, the decrement of CC can be a warning sign for the presence of the special cause in the structure.

For estimating CC of PSDs due to temperature variation, the excitation force should be consistently maintained during experiments. In the lab-scale experiment, the impact testing can be easily maintained to be consistent. However, the excitation magnitude can be different for each testing in the full-scale civil engineering structures. For such cases, the vibration responses should be normalized according to the excitation magnitude. In addition, the ambient vibration data seems to be difficult to apply as the input excitation varies over time, which results in different CC of PSDs although the temperature remains the same.

2.3. Modal Parameters. Frequency domain decomposition (FDD) method [19, 20] is used to extract modal parameters such as natural frequency and mode shape. The singular values of the PSD function matrix $\mathbf{S}(\omega)$ are used to estimate the natural frequencies instead of the PSD functions themselves as follows [20]:

$$\mathbf{S}(\omega) = \mathbf{U}(\omega)^T \mathbf{\Sigma}(\omega) \mathbf{V}(\omega), \quad (6)$$

where $\mathbf{\Sigma}$ is the diagonal matrix consisting of the singular values, σ_i 's ($i = 1, \dots, N$), and \mathbf{U} and \mathbf{V} are unitary matrices. Since $\mathbf{S}(\omega)$ is symmetric, \mathbf{U} becomes equal to \mathbf{V} . In this FDD method, the natural frequencies can be determined from the peak frequencies of the singular value and the mode shape from any one of the column vectors of $\mathbf{U}(\omega)$ at the corresponding peak frequencies. In this study, the first singular value $\sigma_1(\omega)$ is used to estimate the modal parameters.

Mode shapes measured before and after structural change are examined by modal assurance criterion (MAC). The MAC provides a measure of the least squares deviation or scatter of the points from the linear correlation

$$\text{MAC}(\phi_i, \phi_i^*) = \frac{[\phi_i^T \phi_i^*]^2}{[\phi_i^T \phi_i][\phi_i^{*T} \phi_i^*]}, \quad (7)$$

where ϕ_i and ϕ_i^* are the modal vectors which are extracted from acceleration signals measured before and after structural change, respectively. The MAC value provides quantifying of the comparison between the two sets of mode shape data. In practice, a value of MAC close to the unity is expected

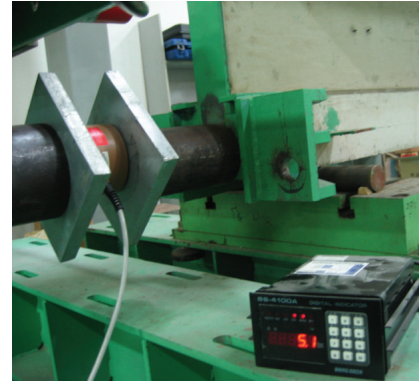
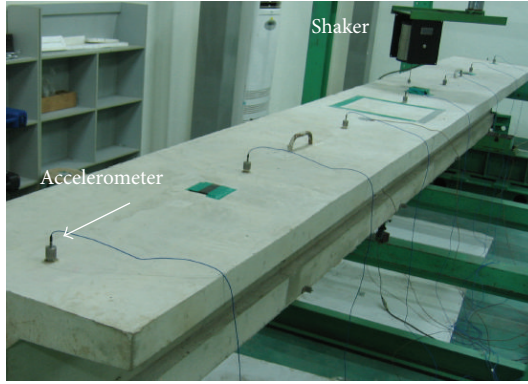
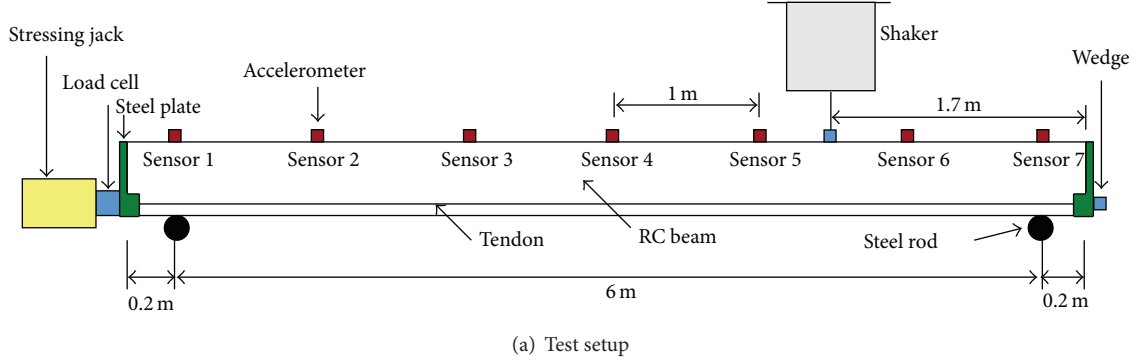


FIGURE 1: Vibration tests on PSC girder.

if the two sets of mode shapes have no differences caused by structural change; otherwise, the MAC value would decrease. This method can be utilized to obtain the information on what vibration modes are more sensitive to the structural change.

2.4. Regression Analysis. Regression analysis gives the information on the relationship between a response variable and one or more independent variables. From regression analysis, the response variable is expressed as a function of the predictor variables. The relationship obtained from regression analysis can be used to predict values of the response variable and identify variables that most affect the response. The value of each predictor variable can be accessed through statistical tests on the estimated coefficients of the predictor variables.

An example of a regression model is the simple linear regression model which is a linear relationship between response variable (RV) and the predictor variable (T) of the form

$$RV = a + bT \quad (8)$$

in which a and b are regression coefficients which are unknown modal parameters. In this study, the response variables are MSD of AR coefficient (2), CC of PSDs (3), and natural frequency and mode shape calculated by (6). Also, the predictor variable T is temperature measured from the experiment. The error term has to be equal to zero on

average. In statistics, simple linear regression is the least squares estimator of a linear regression model with a single predictor variable. Simple linear regression fits a straight line through the set of n points in such a way that makes the sum of squared residuals of the model (i.e., vertical distances between the points of the data set and the fitted line) as small as possible.

3. Experiments on PSC Girder

As illustrated in Figure 1, dynamic tests were performed on a lab-scaled PSC girder. While room temperatures were handled to vary in the range of about $5\sim 23^\circ\text{C}$, a set of prestress cases were simulated to the PSC girder from which vibration responses were measured to determine vibration features and modal parameters. In this study, vibration features of interest include autoregressive coefficient and power spectral density. Also, modal parameters of interest are natural frequencies and mode shape. Note that damping properties of the PSC girder are not dealt with due to the difficulties in measurement and interpretation.

The PSC girder was simply supported and installed on a rigid testing frame. Two simple supports were modeled by steel rods between the girder and the rigid frame. As detailed in existing publications [21], the PSC girder model has the T-section reinforced in both longitudinal and transverse direction with 10 mm diameter reinforcing bars. As the prestressing tendon, a seven-wire monostrand with 15.2 mm

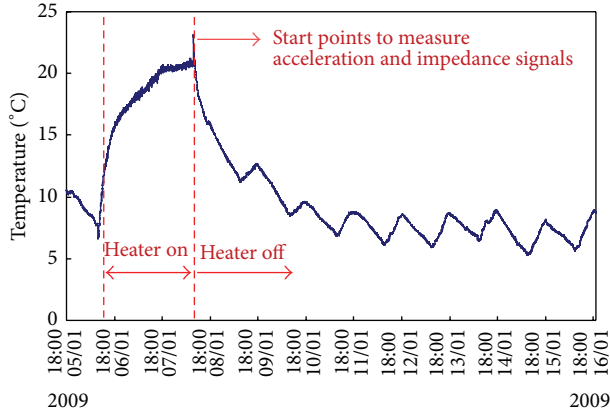


FIGURE 2: Time history of temperature during experiments.

diameter was embedded in a 25 mm diameter duct. During the tests, the prestress force was fixed as 98.0 kN.

Seven accelerometers noted as Sensors 1–7 in Figure 1(a) were placed in the girder with a constant 1 m interval. The impact excitation was applied in vertical direction by an electromagnetic shaker VTS100 at a location 1.7 m distanced from the right edge. The impact magnitude of the impact testing was consistently maintained during the experimental tests. Each accelerometer (PCB 393B04) has nominal sensitivity of 1 V/g and specified frequency range ($\pm 5\%$) of 0.06–450 Hz. The sampling frequency of 500 Hz was used to measure dynamic responses. The data acquisition system consists of a 16-channel PXI-4472 DAQ, a NI controller with LabVIEW, and MATLAB software. Temperature data were measured by using K-type thermocouple wires and KYOWA (EDX-100A) Dynamic Logger.

A series of tests were performed for 9 consecutive days. Figure 2 shows time history of room temperature during the test period. During the tests on the PSC girder, temperatures varied between 5°C and 23°C. Humidity in the laboratory was kept close to 40–45% in order to minimize the effect of humidity variation on the vibration characteristics. Temperature was controlled as designed for the tests by air conditioners and heaters (e.g., heater on and off). Vibration tests started at 18:00 hour of January 8 as the laboratory temperature reached up to 23°C. Then the room temperature was controlled to be decreased gradually for the remaining days. It is noted that the room temperature changed day and night.

4. Temperature Effect on Vibration Features of PSC Girder

4.1. AR Model. As the first vibration feature, AR model is used to estimate temperature effects on vibration characteristics of the PSC girder. The overall steps are as follows: firstly, a set of vibration responses are measured for various temperatures from the reference PSC girder; secondly, vibration features are extracted for the temperature variation by computing AR coefficient (1) and MSD (2); thirdly, time histories of temperature and MSD values are analyzed; finally, regression

analysis is performed by fitting (8) to estimate the linear relationship between temperature variation and the extracted AR features.

As the first step, acceleration responses were measured from the PSC girder. Figure 3(a) shows the acceleration signals measured from Sensor 5. For temperature 22.5°C, 2048 acceleration data were sampled for 4 seconds by a single impulse excitation. As the second step, AR features were extracted from the measured acceleration signals. Figure 3(b) shows partial autocorrelation data for the acceleration signals of Sensor 5, from which the order of AR model was decided as 50. Using the decided order 50, AR coefficients for all acceleration signals measured from Sensor 5 were estimated for temperatures 5.4°C~22.5°C, as shown in Figure 3(c).

As the final step, the linear regression between temperature variation and AR coefficients was analyzed by the use of MSDs of AR coefficients. Figure 4(a) shows the time history for MSDs of AR coefficients calculated for temperatures 5.4°C~22.5°C. Figure 4(b) shows the linear relationship between the temperatures and the MSDs of AR coefficients. The empirical equation of the MSD as a function of temperature (T) is as follows:

$$\text{MSD} = -3283T + 74569 \quad (9)$$

in which the MSD value changes as 3283 when temperature (T) changes by 1°C. It is noted that the correlation level was low. It is also noted that the AR model provided less consistent but rather poor estimation of the temperature effect on the vibration characteristics of the PSC girder. It is also noted that the quality of the AR model was dependent upon the amount of sampled data and the type of excitation sources.

4.2. CC of PSD. As the second feature, CC of PSDs was selected to estimate temperature effect on vibration characteristics of the PSC girder. The overall steps are as follows: firstly, acceleration data and temperature data are measured from selected distributed locations; secondly, CC of PSDs (3) and LCL (5) are computed for feature extraction; thirdly, time histories of temperature and CC of PSDs values are analyzed; and finally, a linear regression is estimated by fitting (8) for the relationship between temperature variation and the CC of PSDs.

For temperatures 5.4°C~22.5°C, as shown in Figure 5(a), PSDs were extracted from the acceleration signals of Sensor 5, at which 2048 acceleration data were sampled for 4 seconds by a single impulse excitation. As shown in Figure 5(b), CC of PSDs were computed for temperatures 5.4°C~22.5°C by using PSDs at the maximum 22.5°C as the reference. It is observed that CC of PSDs varies along with the variation of room temperature. Figure 5(c) shows the linear regression between the temperatures and the CC of PSDs. The empirical equation of the CC of PSDs as a function of temperature (T) is as follows:

$$\text{CC} = 0.019T + 0.676 \quad (10)$$

in which the CC of PSDs changes as 0.019 when temperature (T) changes by 1°C. It is noted that the correlation level was relatively moderate according to Dancey and Reidy's

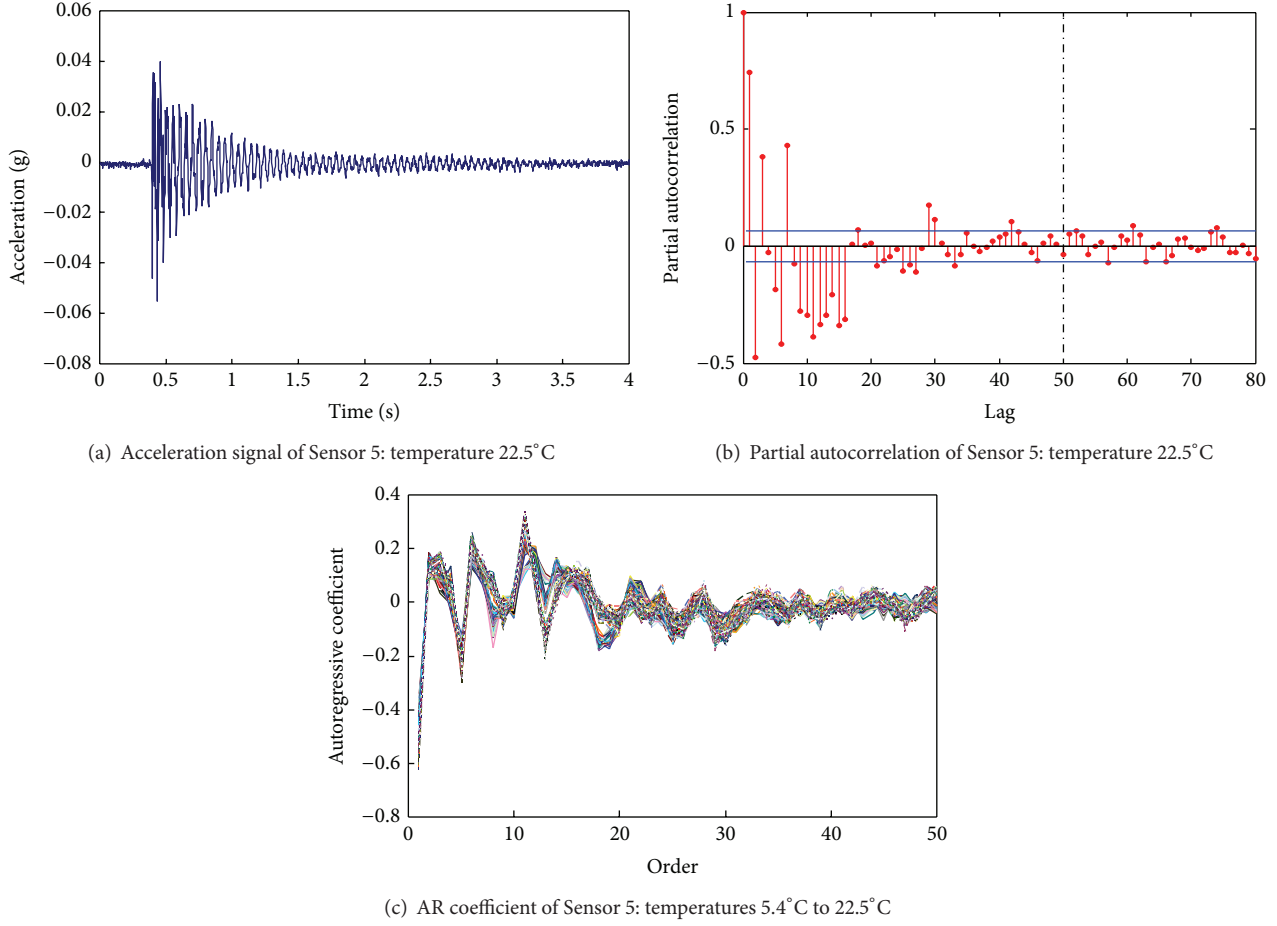


FIGURE 3: Acceleration signals and AR coefficients for estimation of AR model.

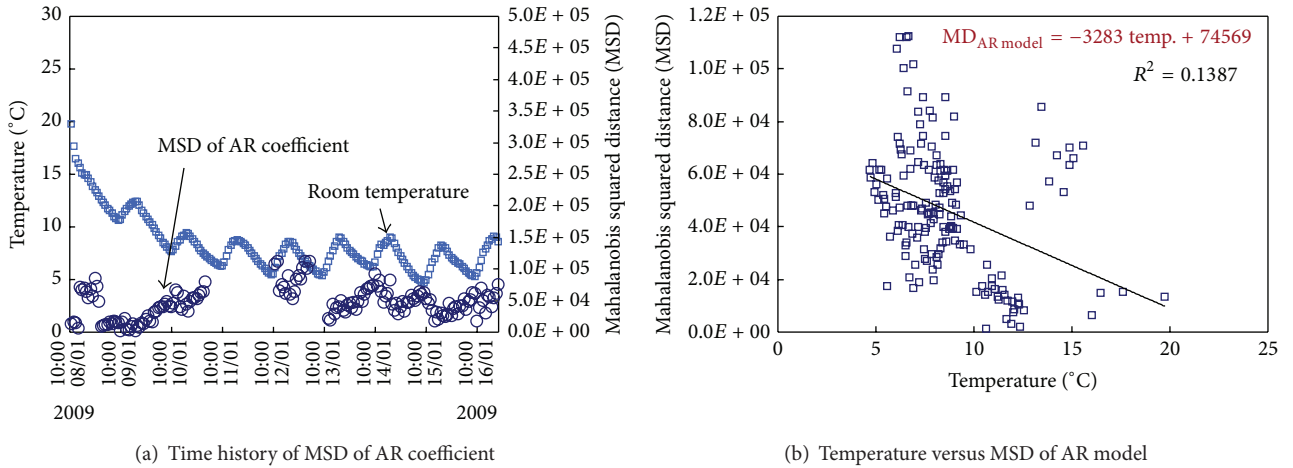


FIGURE 4: Linear regression analysis result for acceleration-based AR model.

categorization [22]. However, the CC of PSDs gave relatively consistent estimation of the temperature effect on the vibration characteristics of the PSC girder.

4.3. Natural Frequency. Next, temperature effect on vibration feature is estimated by natural frequency of the PSC girder.

The overall steps are as follows: first, acceleration data and temperature data are measured from selected distributed locations; secondly, from the FDD method defined as (6), natural frequencies were estimated by the singular values of the PSD function matrix $S(\omega)$; thirdly, time histories of temperature and natural frequencies are analyzed; and finally,

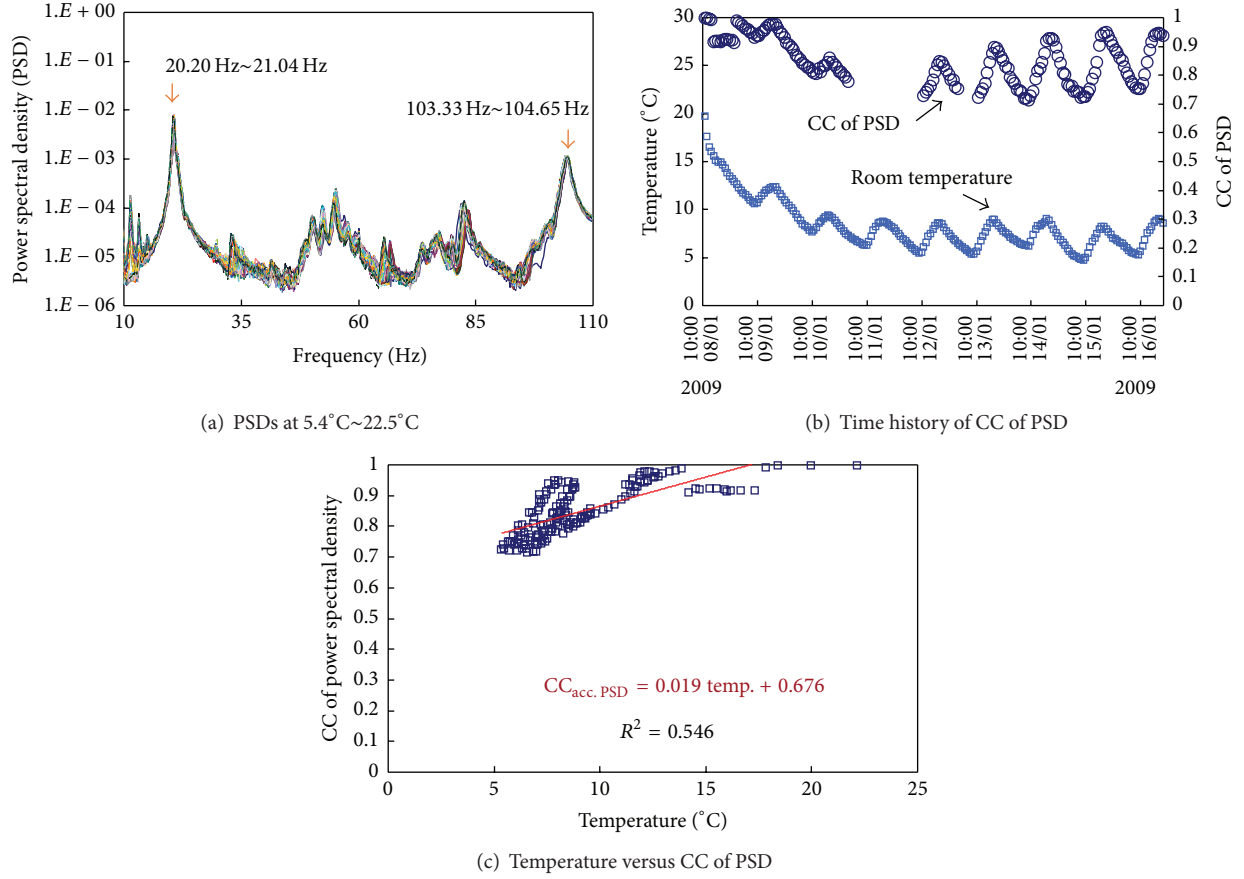


FIGURE 5: Linear regression analysis for correlation coefficient of power spectral density.

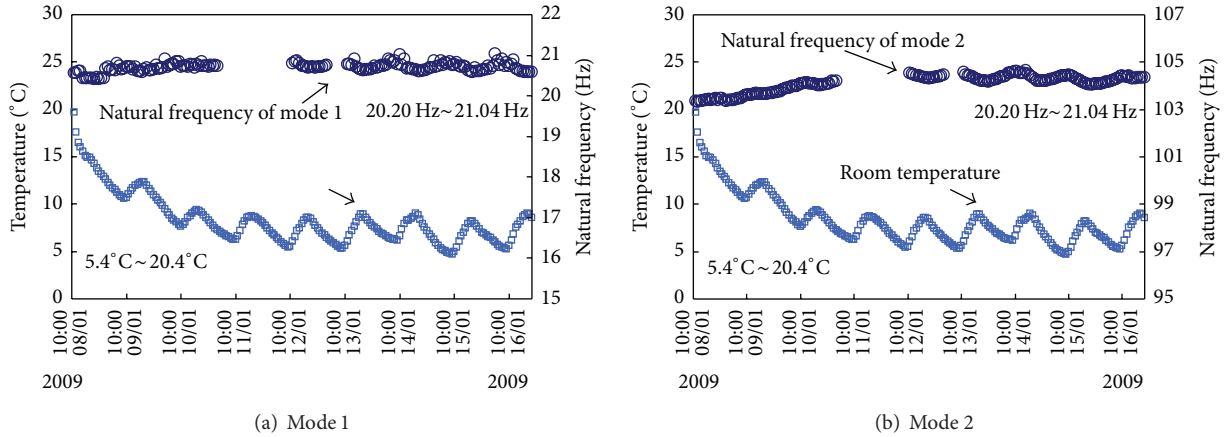


FIGURE 6: Time history of temperature for natural frequencies.

a linear regression is estimated for the relationship between temperature variation and the extracted natural frequencies.

Acceleration signals of Sensors 1–7 were utilized for the modal extraction. From each sensor, 2048 acceleration data were sampled for 4 seconds by a single impulse excitation. Figure 6 shows time histories of temperatures and natural frequencies of the first two modes of the PSC girder. Natural frequencies of the two modes were extracted as temperatures

varied between 5.4°C and 20.4°C. In mode 1, changes in natural frequencies were very small as temperatures varied up to 15°C, as shown in Figure 6(a). In mode 2, however, changes in natural frequencies were relatively high due to the temperature variation, as shown in Figure 6(b).

From regression analysis, linear relationships between the two modes' natural frequencies and temperatures were estimated as shown in Figure 7. For the two modes, the empirical

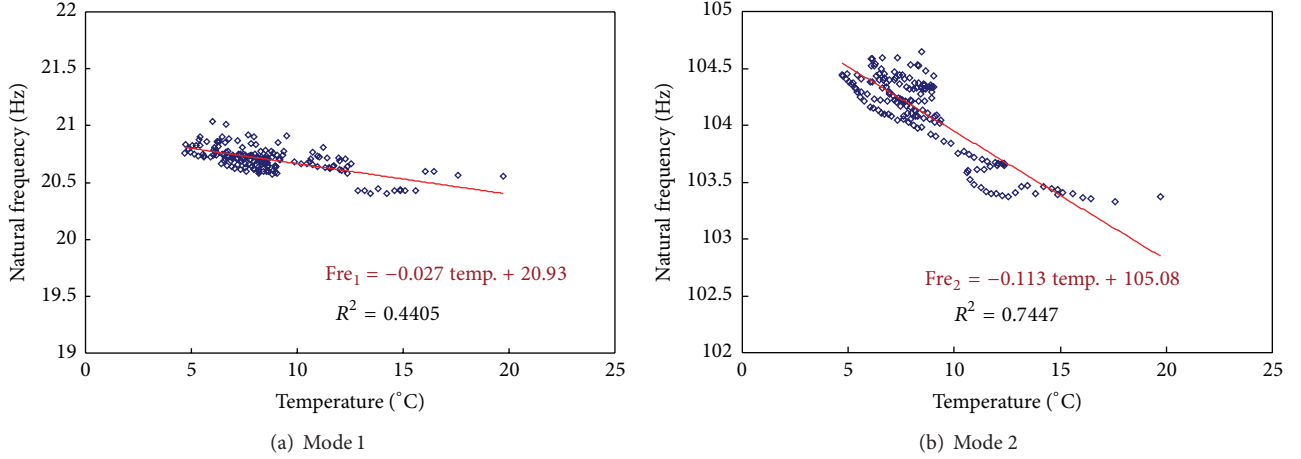


FIGURE 7: Linear relationship between temperature and natural frequencies.

equations of the natural frequencies as a function of temperature (T) are, respectively, as follows:

$$\text{Freq}_1 = -0.027T + 20.93, \quad (11a)$$

$$\text{Freq}_2 = -0.113T + 105.08 \quad (11b)$$

in which the first mode's natural frequencies (Freq_1) decrease as 0.027 as temperature (T) increases by 1°C ; and the second mode's natural frequencies (Freq_2) decrease as 0.113 as temperature (T) increases by 1°C . It is noted that the correlation levels were relatively moderate for mode 1 but relatively strong for mode 2 [22]. It is also noted that natural frequencies gave relatively consistent estimation of the temperature effect on the vibration characteristics of the PSC girder.

4.4. Mode Shape. Next, temperature effect on vibration feature is estimated by mode shapes of the PSC girder. The overall steps are as follows: first, acceleration data and temperature data are measured from selected distributed locations; secondly, mode shapes were estimated by the singular values of the PSD function matrix $S(\omega)$ from the FDD method (6); thirdly, MAC values are calculated by (7); fourthly, time histories of temperature and MAC values are analyzed; and finally, a linear regression is estimated for the relationship between temperature variation and the MAC values.

The same sets of acceleration signals and temperature signals as used for the analysis of natural frequencies were utilized for the analysis of mode shapes. Figure 8 shows mode shapes of the PSC girder measured by Sensors 1–7 as temperatures varies between 5.4°C and 22.5°C . It is observed that overall changes in mode shapes due to temperature variation look small in both mode 1 and mode 2. Figure 9 shows time histories of temperatures and mode shapes of the first two modes. In mode 1, the change in mode shape was very small as temperatures varied up to 15° . In mode 2, however, the change in mode shape was relatively high due to the temperature variation.

From regression analysis, linear relationships between the two mode shapes and temperatures were estimated as shown

in Figure 10. For the two modes, the empirical equations of the mode shapes as a function of temperature (T) are, respectively, as follows:

$$\text{MAC}_1 = -0.00002T + 0.9999, \quad (12a)$$

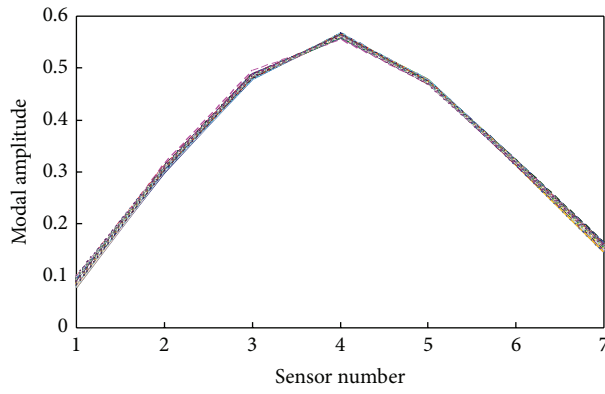
$$\text{MAC}_2 = -0.0002T + 0.9976 \quad (12b)$$

in which the first mode's modal assurance criterion (MAC_1) almost does not change as temperature (T) changes; but the second mode's modal assurance criterion (MAC_2) changes as 0.0002 as temperature (T) increases by 1°C . It is noted that the correlation levels were relatively weak in mode 1 but relatively moderate in mode 2 [22]. It is also noted that modal assurance criteria of the two modes (MAC_1 and MAC_2) gave relatively consistent estimation of the temperature effect on the vibration characteristics of the PSC girder.

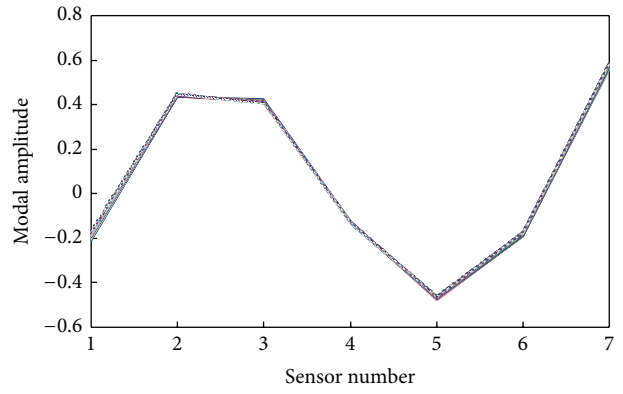
5. Summary and Conclusion

In this paper, the effect of temperature variation on vibration monitoring of prestressed concrete (PSC) girders was experimentally analyzed. Firstly, vibration features such as autoregressive (AR) coefficient, correlation coefficient of power spectral density (CC of PSD), natural frequency, and mode shape were selected to estimate the effect of temperature variation on PSC girders. Secondly, vibration experiments on a lab-scale PSC girder were performed under the condition of temperature variation. Finally, the selected vibration features were analyzed to estimate temperature-induced effects on vibration monitoring of the PSC girder.

Major results from the analysis on the four vibration features with respect to temperature variation are summarized as follows. Firstly, the AR model produced rather poor estimation of the temperature effect on the vibration characteristics of the PSC girder. Secondly, the CC of PSD gave relatively consistent estimation of the temperature effect on the vibration characteristics of the PSC girder. However, its correlation level of the linear regression analysis was relatively moderate. Thirdly, the natural frequencies produced

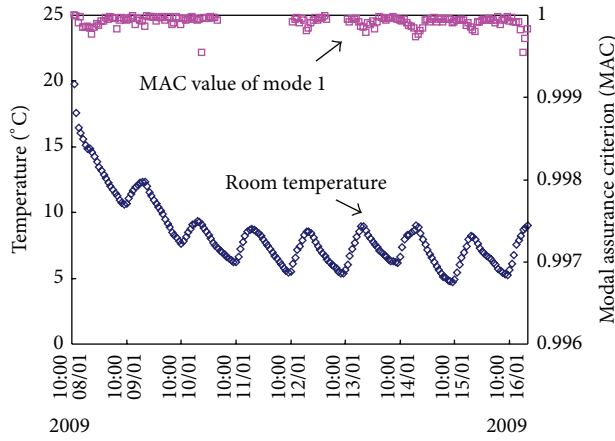


(a) Mode 1: 20.20 Hz–21.04 Hz

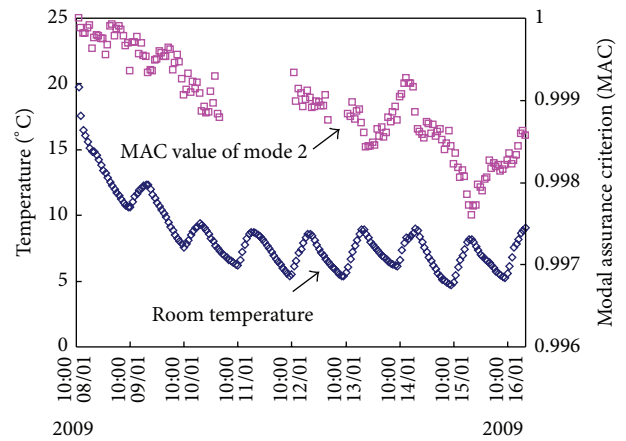


(b) Mode 2: 103.33 Hz–104.65 Hz

FIGURE 8: Natural frequency and mode shape on temperature conditions for PSC girder: prestress force 98 kN, temperatures 5.4°C–22.5°C.

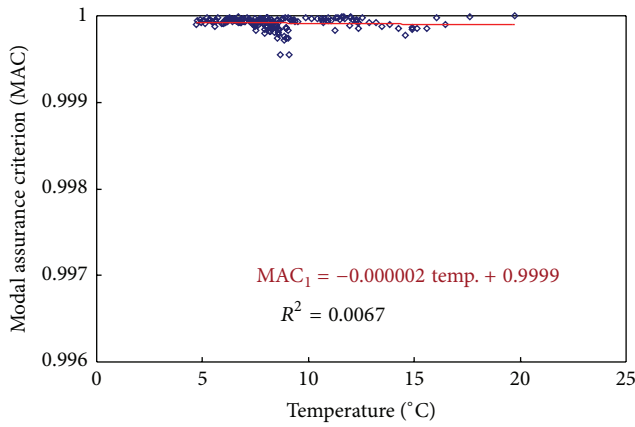


(a) Mode 1

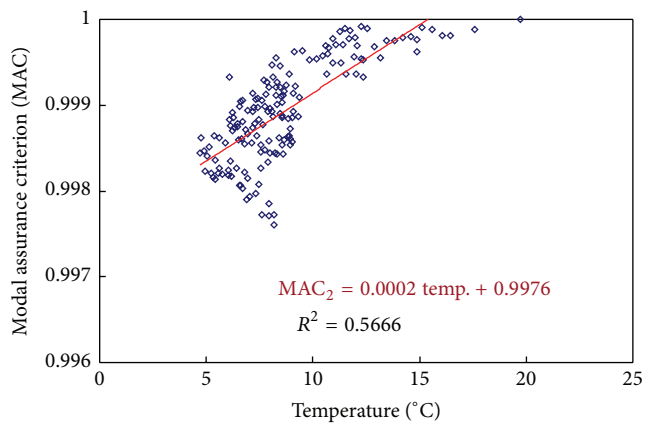


(b) Mode 2

FIGURE 9: Time history of temperature for mode shapes of PSC girder.



(a) Mode 1



(b) Mode 2

FIGURE 10: Linear relationship between temperature and mode shapes.

relatively consistent estimation of the temperature effect on the vibration characteristics of the PSC girder. For the natural frequencies, the correlation levels of the linear regression analysis were relatively moderate in mode 1 but relatively strong in mode 2. Finally, modal assurance criteria of the first two modes gave relatively consistent estimation of the temperature effect on the vibration characteristics of the PSC girder. For the mode shapes, the correlation levels of the linear regression analysis were relatively weak in mode 1 but relatively moderate in mode 2. From the comparative analyses, it can be said that the natural frequency is highly correlated with temperature.

Conflict of Interests

The authors declare that there is no conflict of interests regarding the publication of this paper.

Acknowledgments

This research was supported by a grant from a strategic research project (Development of Smart Prestressing and Monitoring Technologies for Prestressed Concrete Bridges) funded by the Korea Institute of Construction Technology. Graduate students involved in this research were also partially supported by the Brain Korea 21 Plus program of Korean Government.

References

- [1] E. G. Nawy, *Prestressed Concrete—A Fundamental Approach*, Prentice Hall, New York, NY, USA, 1996.
- [2] R. D. Adams, P. Cawley, C. J. Pye, and B. J. Stone, “A vibration technique for non-destructively assessing the integrity of structures,” *Journal of Mechanical Engineering Science*, vol. 20, no. 2, pp. 93–100, 1978.
- [3] N. Stubbs and R. Osegueda, “Global non-destructive damage evaluation in solids,” *The International Journal of Analytical and Experimental Modal Analysis*, vol. 5, no. 2, pp. 67–79, 1990.
- [4] J. T. Kim and N. Stubbs, “Model-uncertainty impact and damage-detection accuracy in plate girder,” *Journal of Structural Engineering*, vol. 121, no. 10, pp. 1409–1417, 1995.
- [5] S. W. Doebling, C. R. Farrar, and M. B. Prime, “A summary review of vibration-based damage identification methods,” *Shock and Vibration Digest*, vol. 30, no. 2, pp. 91–105, 1998.
- [6] J.-T. Kim, Y.-S. Ryu, H.-M. Cho, and N. Stubbs, “Damage identification in beam-type structures: frequency-based method vs mode-shape-based method,” *Engineering Structures*, vol. 25, no. 1, pp. 57–67, 2003.
- [7] M. Saiidi, B. Douglas, and S. Feng, “Prestress force effect on vibration frequency of concrete bridges,” *Journal of Structure Engineering*, vol. 120, no. 7, pp. 2233–2241, 1994.
- [8] A. Miyamoto, K. Tei, H. Nakamura, and J. W. Bull, “Behavior of prestressed beam strengthened with external tendons,” *Journal of Structural Engineering*, vol. 126, no. 9, pp. 1033–1044, 2000.
- [9] J.-T. Kim, C.-B. Yun, Y.-S. Ryu, and H.-M. Cho, “Identification of prestress-loss in PSC beams using modal information,” *Structural Engineering and Mechanics*, vol. 17, no. 3-4, pp. 467–482, 2004.
- [10] S. S. Law and Z. R. Lu, “Time domain responses of a prestressed beam and prestress identification,” *Journal of Sound and Vibration*, vol. 288, no. 4-5, pp. 1011–1025, 2005.
- [11] O. Huth, G. Feltrin, J. Maeck, N. Kilic, and M. Motavalli, “Damage identification using modal data: experiences on a prestressed concrete bridge,” *Journal of Structural Engineering*, vol. 131, no. 12, pp. 1898–1910, 2005.
- [12] M. A. Wahab and G. de Roeck, “Effect of temperature on dynamic system parameters of a highway bridge,” *Structural Engineering International*, vol. 7, no. 4, pp. 266–270, 1997.
- [13] H. Sohn, M. Dzwonczyk, E. G. Straser, A. S. Kiremidjian, K. Law, and T. Meng, “An experimental study of temperature effect on modal parameters of the Alamosa Canyon Bridge,” *Earthquake Engineering and Structural Dynamics*, vol. 28, no. 7-8, pp. 879–897, 1999.
- [14] C. R. Farrar, P. J. Cornwell, S. W. Doebling et al., “Structural health monitoring studies of the Alamosa Canyon and I-40 bridges,” Los Alamos National Laboratory Report LA-13635-MS, 2000.
- [15] J. T. Kim, C. B. Yun, and J. H. Yi, “Temperature effects on frequency-based damage detection in plate-girder bridges,” *KSCE*, vol. 7, no. 6, pp. 725–733, 2003.
- [16] Y. Q. Ni, X. G. Hua, K. Q. Fan, and J. M. Ko, “Correlating modal properties with temperature using long-term monitoring data and support vector machine technique,” *Engineering Structures*, vol. 27, no. 12, pp. 1762–1773, 2005.
- [17] D.-S. Hong, K.-D. Nguyen, I.-C. Lee, and J.-T. Kim, “Temperature-compensated damage monitoring by using wireless acceleration-impedance sensor nodes in steel girder connection,” *International Journal of Distributed Sensor Networks*, vol. 2012, Article ID 167120, 12 pages, 2012.
- [18] J. S. Bendat and A. G. Piersol, *Engineering Applications of Correlation and Spectral Analysis*, Wiley-Interscience, New York, NY, USA, 2003.
- [19] D. Otte, P. V. de Poonseele, and J. Leuridan, “Operational shapes estimation as a function of dynamic loads,” in *Proceedings of the 8th International Modal Analysis Conference*, Florida, Fla, USA, January 1990.
- [20] J.-H. Yi and C.-B. Yun, “Comparative study on modal identification methods using output-only information,” *Structural Engineering and Mechanics*, vol. 17, no. 3-4, pp. 445–466, 2004.
- [21] D.-D. Ho, J.-T. Kim, N. Stubbs, and W.-S. Park, “Prestress-force estimation in PSC girder using modal parameters and system identification,” *Advances in Structural Engineering*, vol. 15, no. 6, pp. 997–1012, 2012.
- [22] C. P. Dancey and J. Reidy, *Statistics without Maths for Psychology*, Prentice Hall, 2004.

Research Article

Performance Evaluation on Transmission Tower-Line System with Passive Friction Dampers Subjected to Wind Excitations

Bo Chen,¹ Xiang Xiao,² Peng-yun Li,³ and Wan-li Zhong³

¹ Key Laboratory of Roadway Bridge and Structural Engineering, Wuhan University of Technology, Mail Box No. 219, No. 122, Luoshi Road, Wuhan 430070, China

² School of Transportation, Wuhan University of Technology, Wuhan 430070, China

³ Guangdong Power Grid Corporation Co. Ltd., Guangzhou 510080, China

Correspondence should be addressed to Bo Chen; cbsteven@163.com

Received 30 August 2014; Accepted 21 October 2014

Academic Editor: Ting-Hua Yi

Copyright © 2015 Bo Chen et al. This is an open access article distributed under the Creative Commons Attribution License, which permits unrestricted use, distribution, and reproduction in any medium, provided the original work is properly cited.

The vibration control and performance evaluation on a transmission-tower line system by using friction dampers subjected to wind excitations are carried out in this study. The three-dimensional finite element (FE) model of a transmission tower is firstly constructed. A two-dimensional lumped mass model of a transmission tower is developed for dynamic analysis. The analytical model of transmission tower-line system is proposed by taking the dynamic interaction between the tower and the transmission lines into consideration. The mechanical model of passive friction damper is presented by involving the effects of damper axial stiffness. The equation of motion of the transmission tower-line system incorporated with the friction dampers disturbed by wind excitations is established. A real transmission tower-line system is taken as an example to examine the feasibility and reliability of the proposed control approach. An extensive parameter study is carried out to find the optimal parameters of friction damper and to assess the effects of slipping force axial stiffness and hysteresis loop on control performance. The work on an example structure indicates that the application of friction dampers with optimal parameters could significantly reduce wind-induced responses of the transmission tower-line system.

1. Introduction

Overhead transmission tower-line system is a typical kind of electrical power infrastructures widely used throughout the world for energy supplying. To be a high-rise structure, the transmission tower-line system is prone to strong wind excitations due to its small damping [1–3]. The excessive vibration of a transmission tower-line system due to strong wind loadings may induce the structural damage or failure associated with the events such as member fracture, member buckling, and tower collapse. The failure of the towers under wind loading has been frequently reported across the world [4–6]. To mitigate the dynamic responses of the transmission tower-line system, many theoretical, experimental, and field measurement investigations have been carried out during the past two decades [7–9]. The current approaches and techniques used for performance evaluation and control can be classified into two major categories. The first one

is the conventional approach developed by increasing the structural stiffness while accepting an intensive level of wind excitations. The other one is an alternative approach to prevent structural failure by installing vibration control devices.

Current studies on the vibration control of transmission tower-line systems focus on the application of dynamic absorbers and energy-dissipating dampers [10]. A typical device commonly utilized for vibration mitigation of the high-rise structures is the tuned mass damper (TMD). The application of the TMD can reduce the structural dynamic responses to some extent while several additional masses should be installed on top of a transmission tower which requires the occupancy of the structural space. In addition, due to the passive nature of TMD, it can only suppress the vibration of tuned mode shapes instead of the global dynamic responses. Therefore, the control performance of the TMD on transmission tower-line system is limited. To

overcome the shortcoming of the dynamic absorbers, many energy-dissipating dampers have been developed recently as an alternative approach for dynamic mitigation of transmission tower-line system. Up to now, the vibration control of transmission tower-line system subjected to dynamic excitations has been investigated rarely [11, 12]. Chen et al. proposed a new method for the wind-resistant design of the transmission tower-line system by using viscoelastic dampers [13]. Chen et al. also proposed a novel approach for the wind-induced semiactive vibration control of transmission tower-line system by using magnetorheological (MR) dampers. However, it is widely reported that the performance of the viscoelastic dampers can be substantially weakened under the harsh environment, which cannot be avoided for the transmission tower-line system in the open air [10, 14]. The configuration and fabrication of the semiactive control devices, such as MR damper, are quite complicated and the requirement in the additional energy supply during the vibration control process is unrealistic while accepting strong excitations. Therefore, the passive friction dampers with a simple configuration and excellent environmental adaptability can be adopted to suppress the wind-induced responses of the transmission tower-line system. The friction damper is a typical energy-dissipating device utilized in the structural response control application and it can be manufactured as an axial member to replace common structural members of a tower without requiring the additional space occupancy.

To this end, the vibration control and performance evaluation on a transmission tower-line system with passive friction dampers subjected to wind loading is actively carried out in this study. The three-dimensional finite element model of a transmission tower is firstly constructed and then a two-dimensional lumped mass model is also developed. The analytical model of transmission tower-line system is proposed by taking the dynamic interaction between the tower and the transmission lines into consideration. The mechanical model of the friction damper is presented by considering the effects of damper axial stiffness. The equation of motion of the transmission tower-line system incorporated with the friction dampers disturbed by wind excitations is established for both the in-plane and out-of-plane vibration, respectively. A real transmission tower-line system constructed in southern China is taken as an example to examine the feasibility and reliability of the proposed control approach. In addition, a parametric study is conducted in detail in order to examine the effects of the slipping force, the axial stiffness, and the hysteresis loop on the control performance. The made observations indicate that the passive friction dampers can be utilized to suppress the wind-induced vibration control of the transmission tower-line system due to its satisfactory energy-dissipating capacity if the damper parameters are optimally determined.

2. Model of Transmission Tower-Line System

2.1. Model of Transmission Tower. To be a typical truss tower constructed by using steel members, a transmission tower can

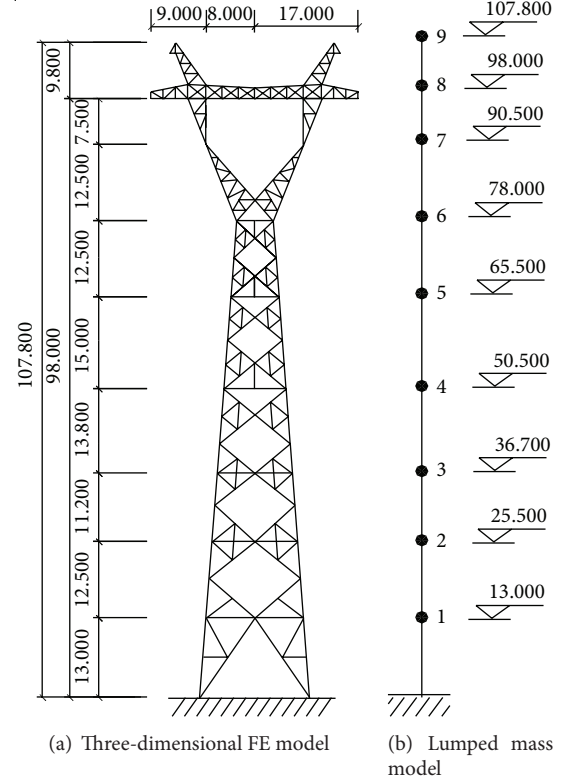


FIGURE 1: Analytical model of a transmission tower.

be commonly modelled by using the beam elements based on the finite element (FE) method [15, 16]. The mass matrix of a single member of the tower can be expressed as

$$\mathbf{M}^{(i)} = \mathbf{T}_e^{(i)T} \mathbf{M}_e^{(i)} \mathbf{T}_e^{(i)} \quad (1)$$

in which $\mathbf{M}^{(i)}$ and $\mathbf{M}_e^{(i)}$ denote the element mass matrix of the i th element in the global coordinate system (GCS) and the local coordinate system (LCS), respectively; $\mathbf{T}_e^{(i)}$ denotes the coordinate transformation matrix of the i th element.

Similarly, the element stiffness matrix of the i th element in the GCS $\mathbf{K}^{(i)}$ can be expressed as the multiple of the element stiffness matrix $\mathbf{K}_e^{(i)}$ in the LCS with the coordinate transformation matrix $\mathbf{T}_e^{(i)}$

$$\mathbf{K}^{(i)} = \mathbf{T}_e^{(i)T} \mathbf{K}_e^{(i)} \mathbf{T}_e^{(i)}. \quad (2)$$

The global mass matrix \mathbf{M}_t and the stiffness matrix \mathbf{K}_t of a transmission tower can be expressed as follows:

$$\begin{aligned} \mathbf{M}_t &= \sum_{i=1}^{ne} \mathbf{T}^{(i)T} \mathbf{M}^{(i)} \mathbf{T}^{(i)} \\ \mathbf{K}_t &= \sum_{i=1}^{ne} \mathbf{T}^{(i)T} \mathbf{K}^{(i)} \mathbf{T}^{(i)}, \end{aligned} \quad (3)$$

where ne is the number of elements of the tower model; $\mathbf{T}^{(i)}$ is the freedom transform matrix from the LCS to the GCS.

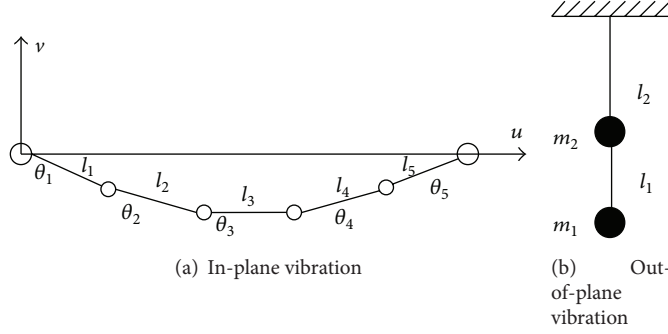


FIGURE 2: MDOF elastic model of a transmission line.

The three-dimensional (3D) FE model of a transmission tower is displayed in Figure 1(a). If the configuration of a transmission tower is quite complicated due to a great number of structural members and components, a remarkable number of the degree of freedoms (DOFs) of the tower can be expected. Therefore, it is impractical for the dynamic response computation and the investigation on the control performance because the numerical step-by-step integration in the time domain will be very time-consuming. In addition, the dynamic excitation on the tower such as wind loads can commonly be modeled as a stationary or nonstationary stochastic process in time and nonhomogeneous in space. The simulation of dynamic loading of a complicate three-dimensional FE model of a transmission tower requires enormous computation efforts. From the practical viewpoint, a simple analytical model of the transmission tower with limited DOFs is more reasonable for the investigation on structural dynamic responses and the parametric study. In this regard, a two-dimensional (2D) lumped mass model is commonly used in practice to examine the dynamic responses of a complicated transmission tower.

When a 3D FE dynamic model of a transmission tower is reduced to a 2D lumped mass model, some assumptions are commonly adopted. As far as the 2D lumped model is concerned, the masses of the transmission tower, including the masses of all structural components and all nonstructural components, are first concentrated at several floors only. The average of the displacements of all nodes at a certain floor is defined as the nominal displacement of that floor in that direction. Then, the number of dynamic degrees of freedom of the 2D lumped mass model is the number of the selected floors. The mass matrix \mathbf{M} of the 2D lumped mass model is a diagonal matrix which can be expressed as

$$\mathbf{M} = \begin{bmatrix} m_1 & & & & \\ & m_2 & & & \\ & & \ddots & & \\ & & & m_j & \\ & & & & \ddots \\ & & & & & m_{nm} \end{bmatrix} \quad (j = 1, 2, \dots, nm) \quad (4)$$

in which m_j denotes the mass of the j th floor; nm is the floor number of the transmission tower. The stiffness matrix \mathbf{K} of the 2D lumped mass model can be obtained based on the 3D

FE model of the transmission tower by taking the following steps.

- (1) Apply the same horizontal force at each node at the i th floor of the 3D model such that the sum of all forces equals 1.
- (2) Determine the horizontal displacement of each node at the j th floor. Define the nominal displacement of the j th floor to have the flexibility coefficient δ_{ji} ($i, j = 1, 2, \dots, nm$).
- (3) Form the flexibility matrix Ψ and inverse the flexibility matrix to obtain the 2D stiffness matrix \mathbf{K} of the transmission tower.

2.2. Model of Transmission Tower-Line System. The transmission line can be modeled as several lumped masses connected with many elastic elements [17, 18]. The analytical models of a transmission line for in-plane/out-of-plane vibration with six lumped masses and five elastic elements are displayed in Figure 2. Regarding the in-plane vibration of the transmission line, the kinetic energy and the potential energy of a transmission line can be computed by using the generalized velocity and generalized displacement, respectively. The application of the Hamilton's variational principle can lead to the equation of motion of a transmission line [19]. The kinetic energy of the transmission line can be expressed based on the Lagrange formulation

$$T_{\text{line}} = \sum_{i=1}^4 \frac{1}{2} m_i (\dot{u}_i^2 + \dot{v}_i^2) \quad (5)$$

$$= T_{\text{line}} (\dot{\xi}_2, \dot{\xi}_3, \dot{\xi}_4, \delta \dot{l}_1, \delta \dot{l}_2, \delta \dot{l}_3, \delta \dot{l}_4, \delta \dot{l}_5),$$

where ξ and δ are the generalized coordinates of a transmission line related to the difference of the angle θ and length l , respectively; u_i and v_i are the displacement of the i th lumped mass in the horizontal and vertical direction, respectively.

Similarly, the potential energy of the transmission line is given by

$$U_{\text{line}} = \sum_{i=1}^4 m_i g v_i + \sum_{j=1}^5 \frac{EA}{2} \left(\frac{(l_{js} + \delta l_j)^2}{l_{j0}} - \frac{l_{js}^2}{l_{j0}} \right), \quad (6)$$

where E and A are Young's modulus and the cross section area of a transmission line; l_{j0} is the length of the j th element; l_{js} is the length of the j th element after deformation. The mass matrix \mathbf{M}_l^{in} can be determined by computing the partial differential of the kinetic energy to the generalized velocity. Similarly, the stiffness matrix \mathbf{K}_l^{in} can be determined by computing the partial differential of the potential energy to the generalized displacement.

Figure 2(b) displays the analytical model of transmission line for the out-of-plane vibration. The transmission line can be taken as a hanging line with several lumped masses. The mass matrix $\mathbf{M}_l^{\text{out}}$ and stiffness matrix $\mathbf{K}_l^{\text{out}}$ of the transmission line can be expressed as

$$\mathbf{M}_l^{\text{out}} = \begin{bmatrix} m_1 & \\ & m_2 \end{bmatrix}$$

$$\mathbf{K}_l^{\text{out}} = \begin{bmatrix} \frac{m_1 g}{l_1} & -\frac{m_1 g}{l_1} \\ -\frac{m_1 g}{l_1} & \frac{m_1 g}{l_1} + \frac{(m_1 + m_2) g}{l_2} \end{bmatrix}. \quad (7)$$

The kinetic energy of the tower-line system for the in-plane vibration is given by

$$T = \sum_{i=1}^{nl} T_{\text{line}}^i + \sum_{j=1}^{nt} T_{\text{tower}}^j \quad (8)$$

in which nl and nt are the number of the transmission lines and towers of the transmission tower-line system, respectively. Similarly, the potential energy of the tower-line system is given by

$$U = \sum_{i=1}^{nl} U_{\text{line}}^i + \sum_{j=1}^{nt} U_{\text{tower}}^j. \quad (9)$$

By substituting (8) and (9) into the Lagrange equation, the mass matrix \mathbf{M}^{in} and stiffness matrix \mathbf{K}^{in} of a transmission tower-line system for the in-plane vibration can be determined by computing the partial differential of the kinetic energy T and potential energy U to generalize coordinates and its first time derivatives. Similarly, the mass matrix \mathbf{M}^{out} and stiffness matrix \mathbf{K}^{out} of the transmission tower-line system for the out-of-plane vibration can be determined by consideration of the coupled effects induced by transmission lines [1].

3. Model of Friction Damper

Passive friction dampers are the devices utilizing the mechanism of the solid friction to achieve the energy dissipation. In reality, this concept has been successfully used by mechanical engineers to control the motion of machinery and automobiles. The passive friction damper can be designed with a specific optimum slip force under a particular external excitation (Figure 6). The development of friction damping devices was pioneered in the early 1980s, thereafter, a considerable progress in developing a number of energy-dissipating devices in the structural vibration control [20–23]. The configuration of a typical passive friction damper

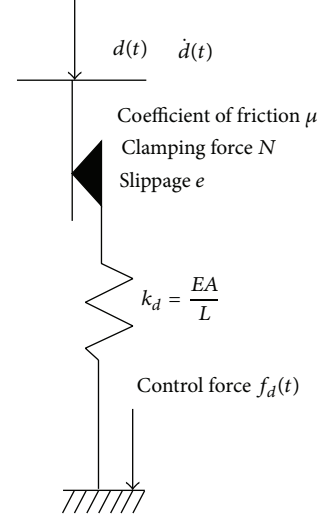


FIGURE 3: Configuration of passive friction damper.

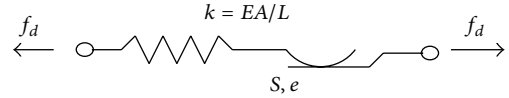


FIGURE 4: Mechanical model of friction damper.

is displayed in Figure 3. In the early stage, the control force of the friction damper is expressed as the product of the clamping force N and the coefficient of friction μ without considering the effects of the damper axial stiffness k_d . However, it is found that the performance of the friction damper is tightly related to the axial stiffness of the damper and many mechanical models with the elastic axial member are developed based on the experimental observations.

Commonly, the control force of a friction damper is transferred to the structure through an elastic axial member. Thus, the model of a friction damper should include the stiffness of the elastic member as shown in Figure 4. In Figure 4, S denotes the slip force of the i th friction damper which equals the product of the clamping force N and the friction coefficient μ ; e denotes the slip deformation of the i th friction damper and it is equal to zero initially; E denotes Young's modulus of the damper; A is the cross section area of the i th elastic member; and L is the length of the i th member. The control force of the i th friction damper can be expressed as

$$u_i = u(k, e, S), \quad (10)$$

where k denotes the axial stiffness of a passive friction damper.

The clamping force of a passive friction damper is set in advance and its friction force is constant during the slipping process. The condition and control force of the i th passive friction damper can be determined using the following rules.

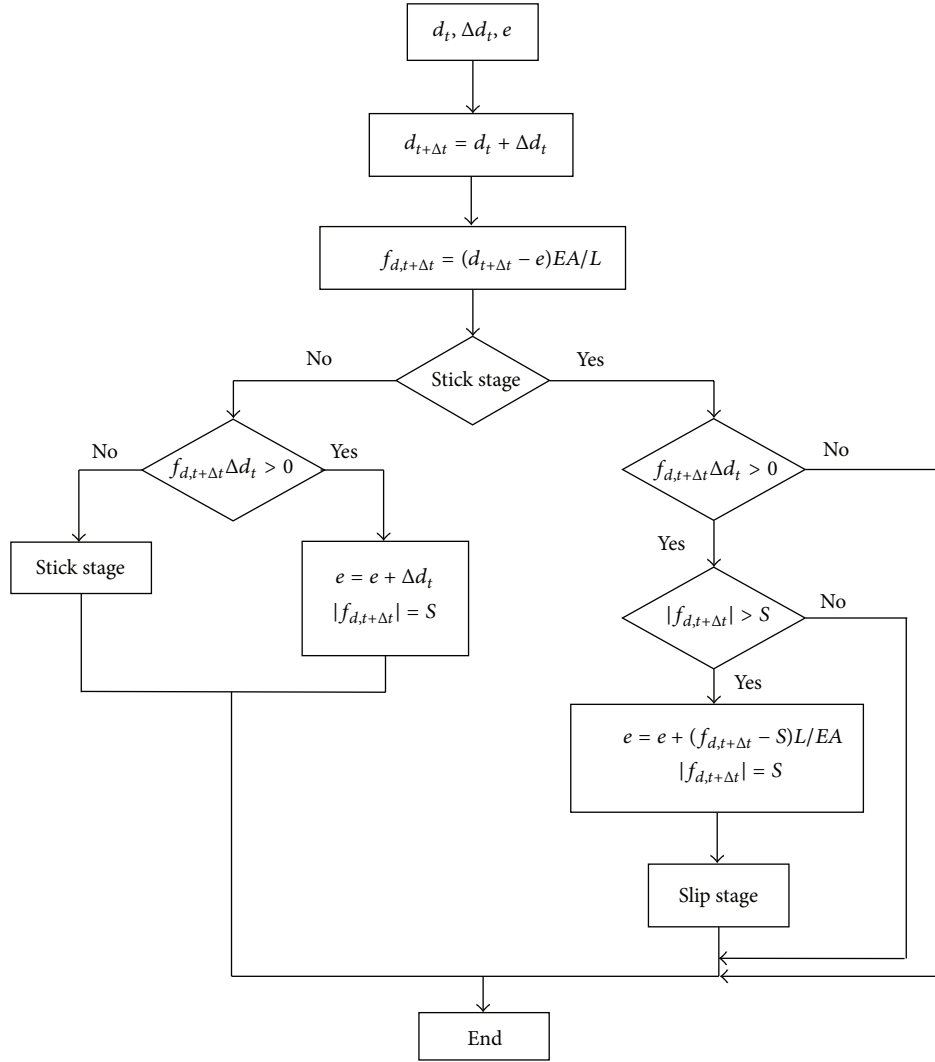


FIGURE 5: Force flow chart of passive damper.

(1) If the friction damper has no slippage, then

$$f_d^i = (d_i - e_i) \frac{EA_i}{L_i} \quad (11)$$

$$\dot{e}_i = 0.$$

(2) If the friction damper has a slippage

$$|f_d^i| = S_i = f_d^i N_i \operatorname{sgn}(\dot{d}_i) \quad (12)$$

$$\dot{e}_i = \dot{d}_i,$$

where d_i and \dot{d}_i are relative displacement and velocity between the two ends of the i th friction damper, respectively. Furthermore, if the relative displacement increment of the two ends of the i th friction element Δd_i is larger than zero, the control force is tensile. Otherwise, the control force is compressive.

(3) If the control force u_i is of different sign with the relative displacement increment Δd_i , the friction damper is in the stick stage. Under this circumstance, the resistant force and slippage of friction damper should be determined following (11).

The flow chart for judging the slipping condition and the control force of a friction damper is indicated in Figure 5.

4. Equation of Motion of Transmission Tower-Line System

The wind loading acting on a transmission tower-line system can be simulated with the aids of the spectral representation approach by assuming the wind excitations to be a stationary stochastic process. The stochastic wind fields

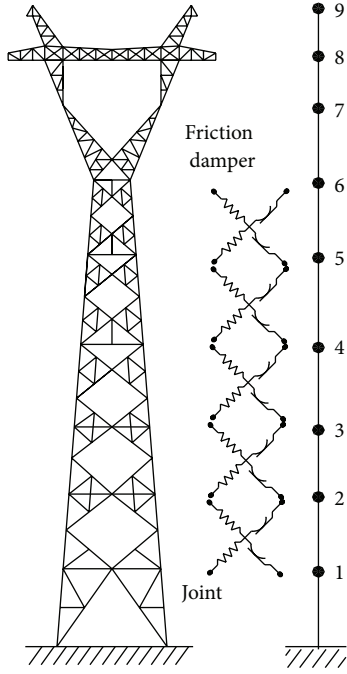


FIGURE 6: Installation scheme of friction damper.

$p_j^0(t)$, $j = 1, 2, \dots, nm$, can be simulated by using the following series [24]:

$$p_j(t) = 2\sqrt{\Delta\omega} \sum_{m=1}^j \sum_{l=1}^N |H_{jm}(\omega_{ml})| \cos(\omega_{ml}t - \theta_{jm}(\omega_{ml}) + \phi_{ml})$$

$$\Delta\omega = \frac{\omega_{up}}{N}, \quad (13)$$

where N is a sufficiently large number; $\Delta\omega$ is the frequency increment; ω_{up} is the upper cutoff frequency with the condition that when $\omega > \omega_{up}$, the value of the cross spectral density matrix $\mathbf{S}^0(\omega)$ is trivial; ϕ_{ml} represents a sequence of independent random phase angles, uniformly distributed over the interval $[0, 2\pi]$; $H_{jm}(\omega)$ is a typical element of matrix $\mathbf{H}(\omega)$, which is defined with the Cholesky decomposition of the $\mathbf{S}^0(\omega)$; $\theta_{jm}(\omega)$ is the complex angle of $H_{jm}(\omega)$.

The equation of motion of the transmission tower-line system for in-plane vibration subjected to wind loading is given by

$$\mathbf{M}^{\text{in}} \ddot{\mathbf{x}}^{\text{in}}(t) + \mathbf{C}^{\text{in}} \dot{\mathbf{x}}^{\text{in}}(t) + \mathbf{K}^{\text{in}} \mathbf{x}^{\text{in}}(t) = \mathbf{P}^{\text{in}}(t), \quad (14)$$

where $\mathbf{x}^{\text{in}}(t)$, $\dot{\mathbf{x}}^{\text{in}}(t)$, and $\ddot{\mathbf{x}}^{\text{in}}(t)$ are the displacement, velocity, and acceleration responses for the in-plane vibration, respectively; \mathbf{M}^{in} , \mathbf{C}^{in} , and \mathbf{K}^{in} are mass and damping and stiffness matrices of the tower-line system for the in-plane vibration, respectively; $\mathbf{P}^{\text{in}}(t)$ is the wind loading vector for the in-plane

TABLE 1: Parameters of friction damper.

Young's modulus (N/m)	Cross section area (m ²)	Maximum slippage (m)
2.06×10^{11}	7.5×10^{-4}	0.08

vibration. Similarly, the equation of motion for the out-of-plane vibration can be expressed as

$$\mathbf{M}^{\text{out}} \ddot{\mathbf{x}}^{\text{out}}(t) + \mathbf{C}^{\text{out}} \dot{\mathbf{x}}^{\text{out}}(t) + \mathbf{K}^{\text{out}} \mathbf{x}^{\text{out}}(t) = \mathbf{P}^{\text{out}}(t). \quad (15)$$

The meanings of the symbols in (15) are similar to those in (14).

The equations of motion of the transmission tower-line system with friction dampers for both the in-plane and out-of-plane vibration can be expressed as follows:

$$\begin{aligned} \mathbf{M}^{\text{in}} \ddot{\mathbf{x}}^{\text{in}}(t) + \mathbf{C}^{\text{in}} \dot{\mathbf{x}}^{\text{in}}(t) + \mathbf{K} \mathbf{x}^{\text{in}}(t) &= \mathbf{P}^{\text{in}}(t) + \mathbf{H}^{\text{in}} \mathbf{f}_d^{\text{in}}(t) \\ \mathbf{M}^{\text{out}} \ddot{\mathbf{x}}^{\text{out}}(t) + \mathbf{C}^{\text{out}} \dot{\mathbf{x}}^{\text{out}}(t) + \mathbf{K} \mathbf{x}^{\text{out}}(t) &= \mathbf{P}^{\text{out}}(t) + \mathbf{H}^{\text{out}} \mathbf{f}_d^{\text{out}}(t), \end{aligned} \quad (16)$$

where $\mathbf{f}_d^{\text{in}}(t)$ and $\mathbf{f}_d^{\text{out}}(t)$ are the control forces of friction dampers for in-plane vibration and out-of-plane vibration, respectively; \mathbf{H}^{in} and \mathbf{H}^{out} are the influence matrix for the control forces for the in-plane vibration and out-of-plane vibration, respectively.

5. Case Study

To examine the feasibility of the proposed control approach based on friction dampers, a real transmission tower-line system constructed in China is taken as the example structure to investigate the control performance. The tower has a height of 107.8 m and the span of the transmission line is 400 m as shown in Figure 1. The axial rigidity EA of the transmission line is 4.8×10^7 N and the weight per meter of the transmission line is 1.394 kN/m. A 3D model is constructed based on the FE method and a two-dimensional lumped mass model is also developed. The wind excitations are numerically simulated by using the spectral representation method. The Rayleigh damping assumption is adopted to construct the structural damping matrix. The damping ratios in the first two modes of vibration of the tower are assumed to be 0.02. Twenty passive friction dampers are evenly distributed along the main body of the tower with ten dampers placed in the in-plane direction and the other ten dampers placed in the out-of plane direction. Table 1 lists the physical parameters of the passive friction damper adopted in this study for the wind-induced vibration mitigation.

The comparison between the maximum responses with-out/with friction dampers is carried out for both the in-plane and out-of-plane vibration, respectively. Four scenarios of slipping forces of the friction dampers are selected for the assessment on the control performance, namely, 20 kN, 40 kN, 60 kN, and 80 kN. Displayed in Figure 7 are the maximum displacement, velocity, and acceleration responses of the transmission tower under different slipping forces of

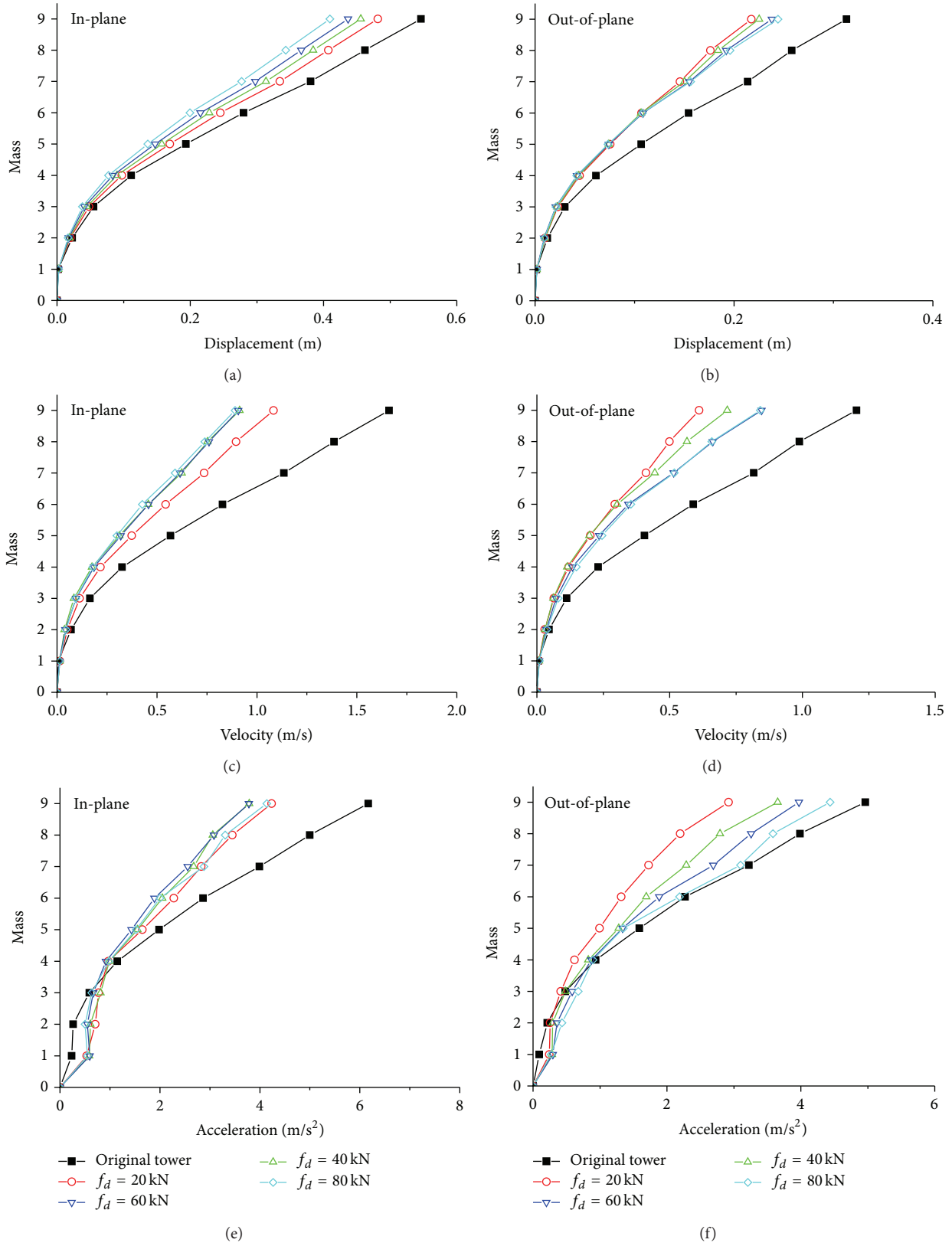
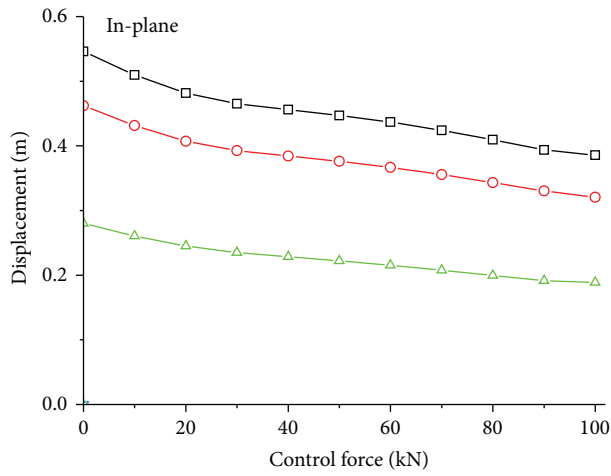
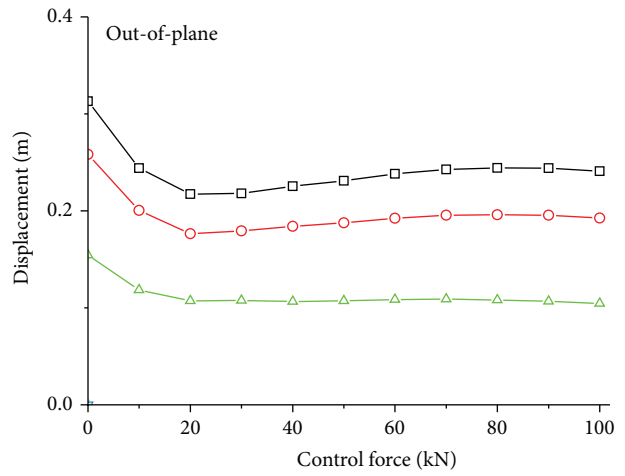


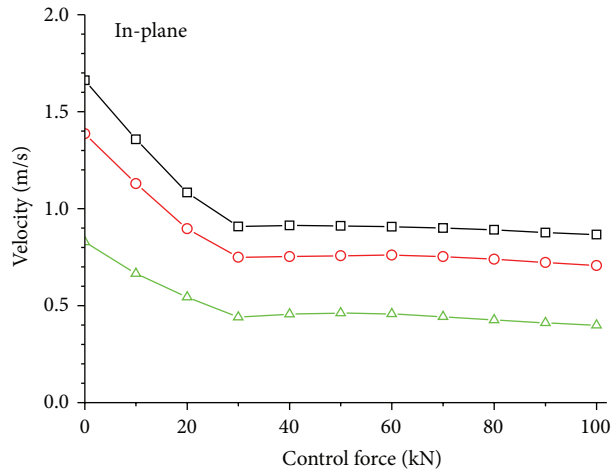
FIGURE 7: Maximum responses under different damper force.



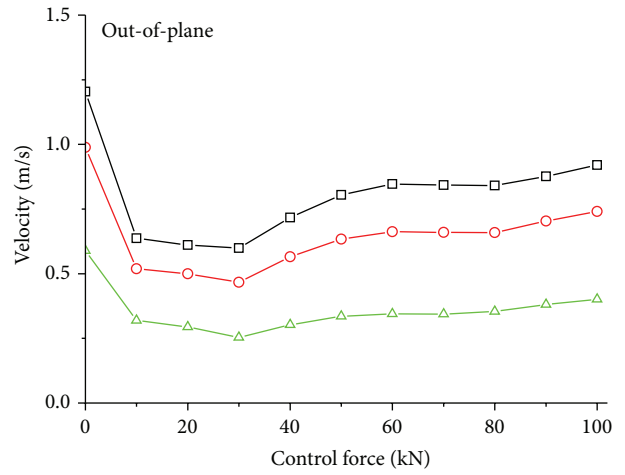
(a)



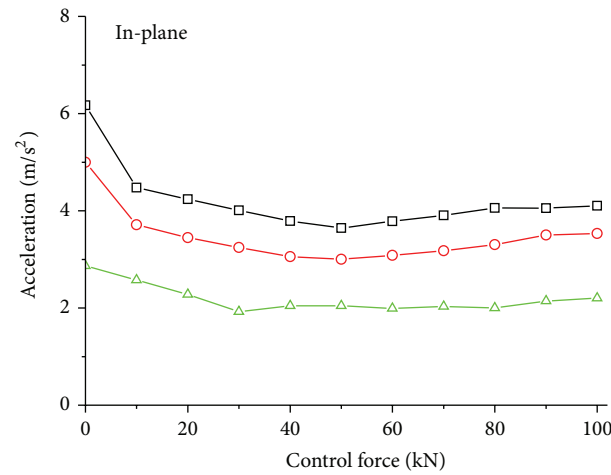
(b)



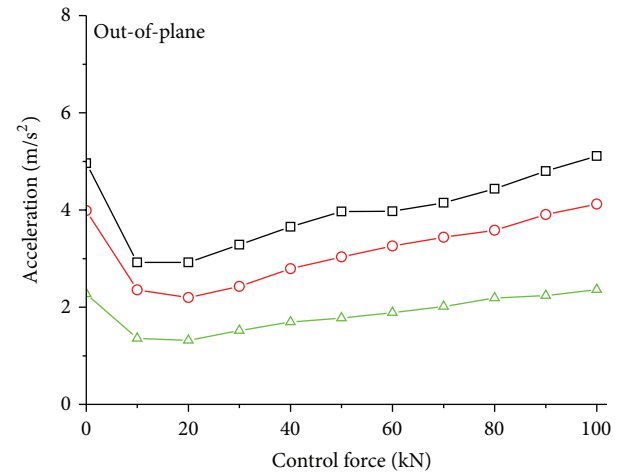
(c)



(d)



(e)



(f)

—□— Mass number 9 (top)
 —○— Mass number 8 (crossarm)
 —△— Mass number 6

—□— Mass number 9 (top)
 —○— Mass number 8 (crossarm)
 —△— Mass number 6

FIGURE 8: Variation of maximum responses with damper force.

friction dampers in comparison with those without control. It is seen that the peak dynamic responses of the transmission tower can be remarkably reduced by incorporating the friction dampers. As far as the in-plane vibration is concerned, the peak displacement is gradually reduced with the increasing damper slipping force. The control scenario with 80 kN presents the best control performance on the peak displacement responses despite the peak velocity and acceleration responses. Similar observations can be made from the results of the out-of-plane vibration. Therefore, the installation of the friction dampers can substantially suppress the wind-induced vibration of the transmission tower-line system for both the in-plane and out-of-plane vibration, respectively.

6. Parametric Investigation

6.1. Effects of Damper Force. The variations of peak responses of tower with respect to the slipping forces of the friction dampers are examined and displayed in Figure 8. Three typical positions are selected, namely, the tower top (mass number 9), the crossarm (mass number 8), and the top of the tower body (mass number 6). It is seen from Figure 8(a) that the peak displacement at the tower top, crossarm, and top of tower body gradually decreases when increasing the slipping forces of the friction dampers. Similar variation trends can be found for the out-of-plane vibration while the peak displacement slightly increases when the slipping force is larger than 20 kN. The variations of peak velocity displayed in Figures 8(b) and 8(c) present different characteristics compared to the peak displacement. The peak velocity and acceleration responses dramatically reduce at the beginning when the damper control forces are small. Then, the increment in the control forces of the friction damper has almost no efficacy on the peak velocity and acceleration responses for the in-plane vibration. For the out-of-plane vibration, the continuous increment in the control force may induce the slight increase of the peak velocity and acceleration responses. The same observations can be made from the dynamic responses of the other lumped masses such as the crossarm and the top of the tower body (mass number 6).

It is seen that no matter which tower mass is selected, there is an optimal value of control forces by which the best performance of the friction damper can be achieved. To compare the control performance of the three types of the dynamic responses of different places, one can find that there exists a small difference for the displacement, velocity, and acceleration responses. The optimal slipping forces of the friction dampers are about 40 kN and 20 kN for the in-plane vibration and out-of-plane vibration, respectively. If the damper control force is increased after reaching the optimal value, the damper performance will deteriorate gradually. A possible explanation of such a phenomenon is that the unlimited increment in control forces may induce the stick of friction dampers when subjected to strong wind excitations. Under these circumstances, the friction dampers have no slippage and behave the same as a brace. The displacement responses may be reduced due to the stiffness increment of the tower while the velocity and acceleration responses

cannot be improved because the damper has no slippage and energy dissipation. Similar results can be observed for other lumped masses. Therefore, the optimal slipping forces of the friction dampers are set as 40 kN and 20 kN for the in-plane vibration and out-of-plane vibration, respectively, in the parametric investigation.

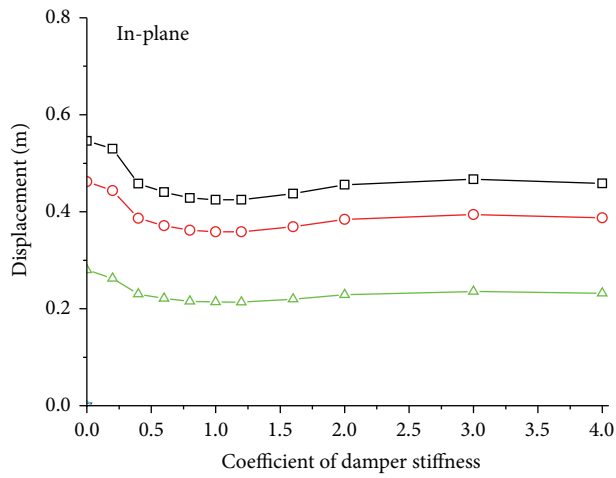
6.2. Effects of Damper Stiffness. Figure 9 displays the variations of the peak displacement, velocity, and acceleration responses of the tower with respect to the brace stiffness of friction dampers. The stiffness coefficient of the damper is defined as

$$SC = \frac{k^d}{k_0^d}, \quad (17)$$

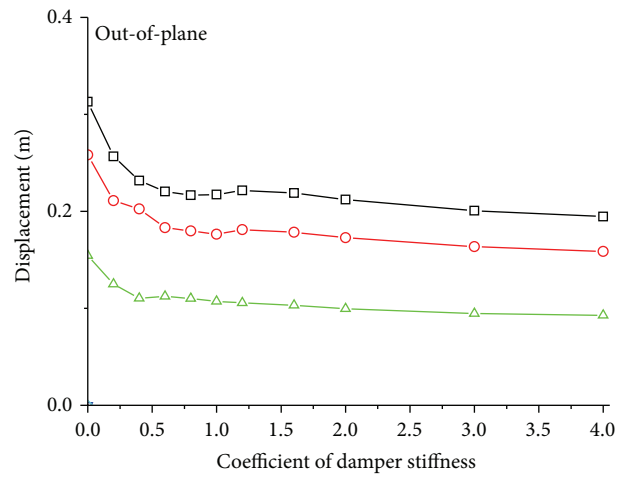
where k^d denotes the damper stiffness used in the analysis, and k_0^d denotes the stiffness parameter of a friction damper.

It is seen that the all the three types of dynamic responses for both the in-plane and out-of-plane vibration reduce rapidly when the stiffness coefficient of dampers increases from 0.0 to about 1.0. Afterwards, the peak responses vary slightly with increasing stiffness coefficient of dampers. When the stiffness coefficient exceeds 2.0, the damper stiffness has almost no effects on the structural peak responses. Similar results can be observed for other lumped masses as shown in Figure 9. As a result, the optimum stiffness coefficient of the friction dampers for the wind-induced response control of the example transmission tower is about 1.0. Further increase in the damper stiffness cannot substantially improve the control performance and leads to unnecessary cost increases.

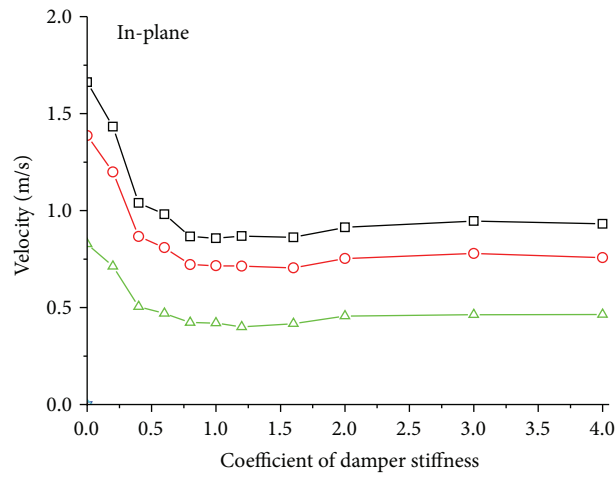
6.3. Comparison on Hysteresis Loops. It is noted that the enclosed area of a hysteresis loop reflects the energy dissipated by the friction damper when subjected to dynamic excitations. Thus, the hysteresis loop with large enclosed area indicates the satisfactory control performance of the friction dampers. To this end, the present section contains the comparison on the force-displacement responses of the friction dampers with different stiffness coefficients. Figure 10 displays the hysteresis loops of a friction damper for the in-plane vibration. The slipping forces of all the friction dampers for the in-plane vibration are set as 40 kN. In reality, the axial stiffness of the friction damper can be reflected by the slope of the hysteresis loop. It is seen from Figure 10(a) that if the axial stiffness is small, there will be a distinct axial deformation of the damper, which means that the damper slippage is small and the energy-dissipating of the damper is limited. To increase the damper axial stiffness, the friction damper is easy to slide and dissipate the vibrant energy. If the axial stiffness of a friction damper is large enough under the unchanged slipping force, its effects on the hysteresis loops keep constant and thus the improvement on control performance is minor. Displayed in Figure 11 is the comparison on hysteresis loops of friction dampers with different slipping forces and the same axial stiffness for the in-plane vibration. It is seen that the slope of the hysteresis loops of the damper decreases with the increasing



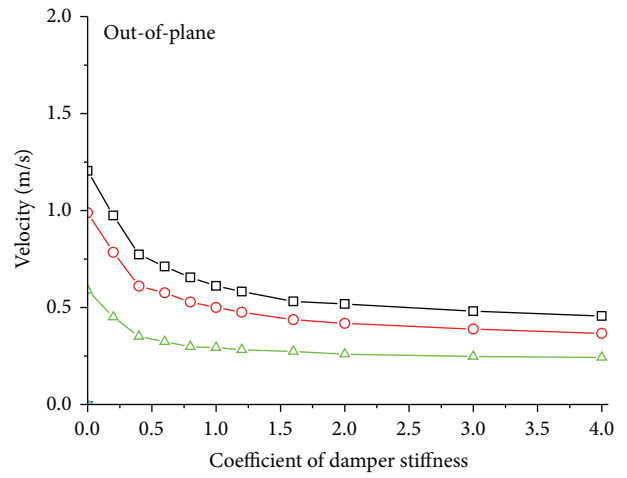
(a)



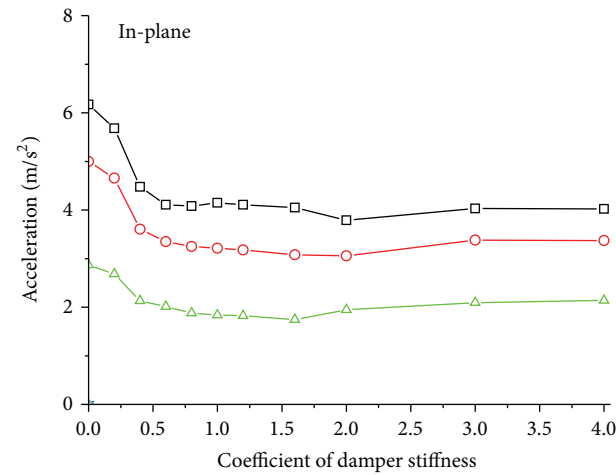
(b)



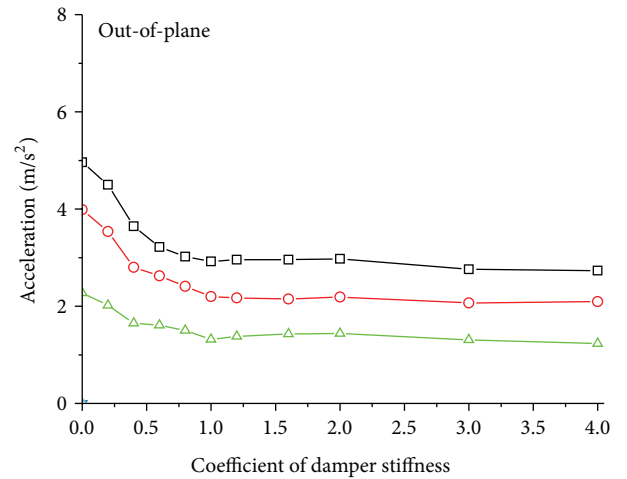
(c)



(d)



(e)



(f)

—□— Mass number 9 (top)
 —○— Mass number 8 (crossarm)
 —△— Mass number 6

—□— Mass number 9 (top)
 —○— Mass number 8 (crossarm)
 —△— Mass number 6

FIGURE 9: Variation of maximum responses with damper stiffness.

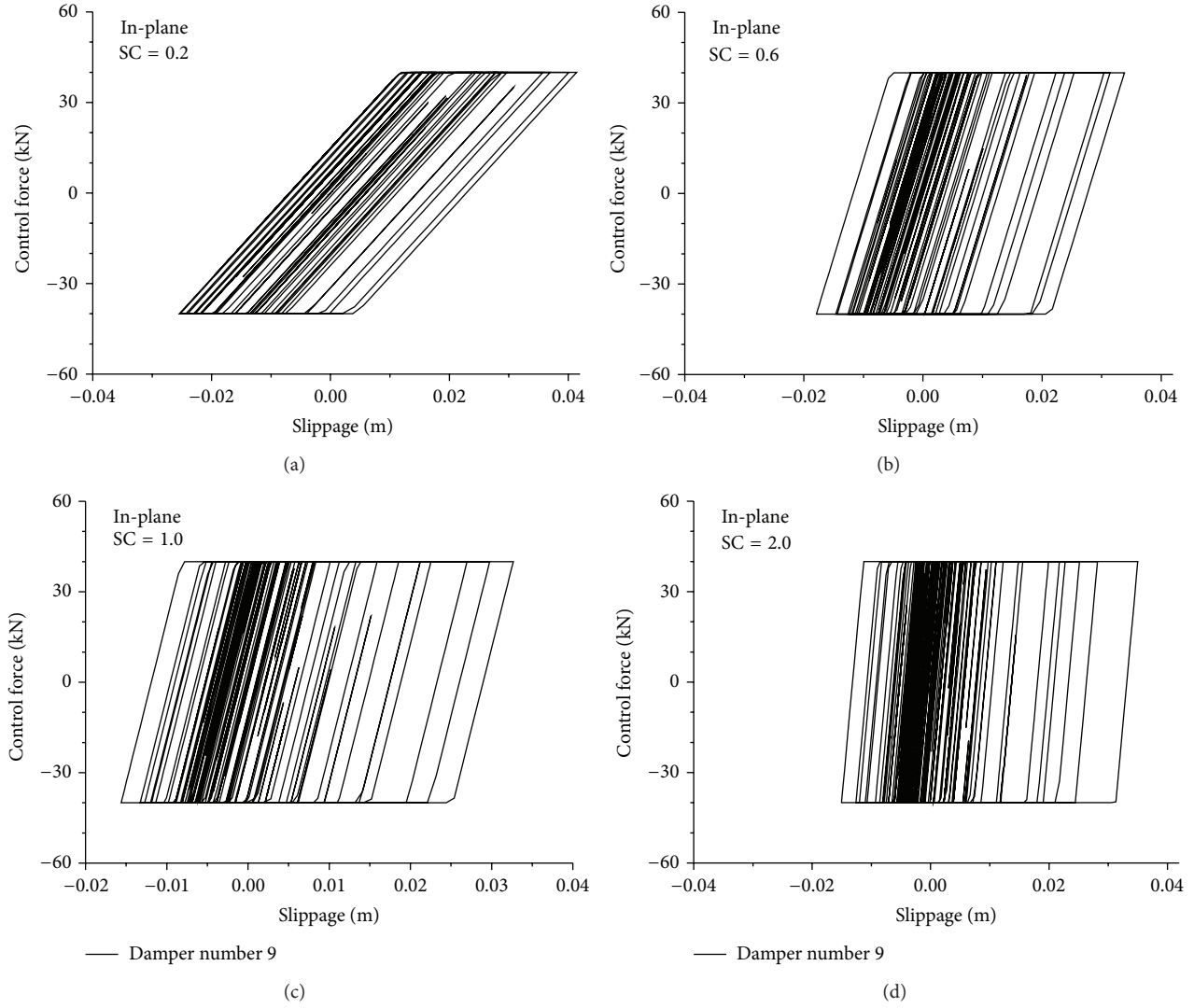


FIGURE 10: Hysteresis loops of friction damper for the in-plane vibration.

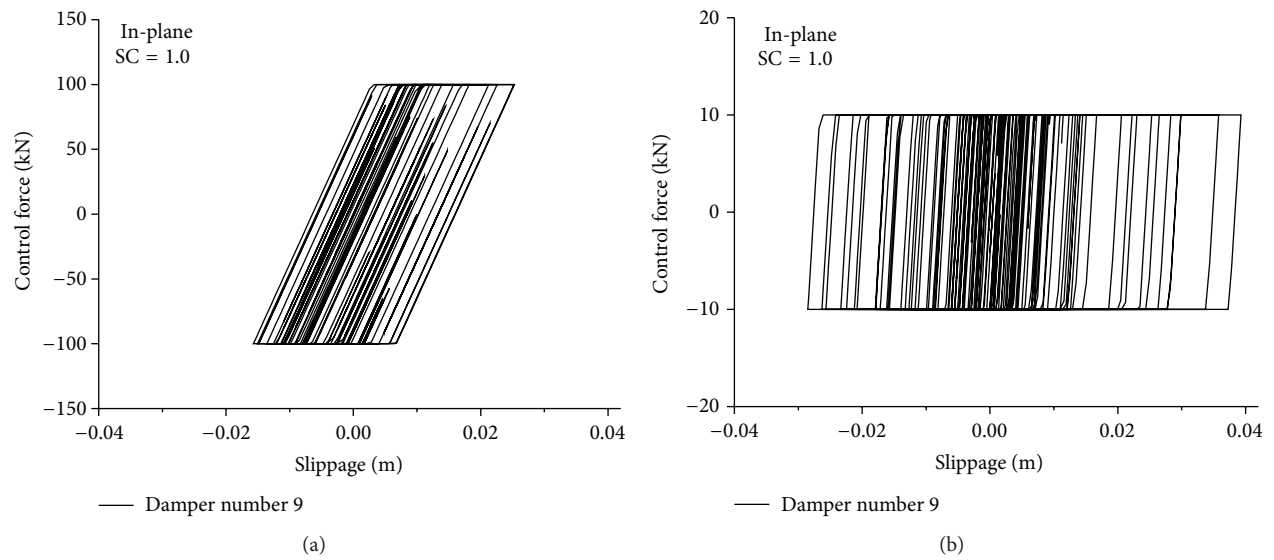


FIGURE 11: Comparison on hysteresis loops of friction damper for the in-plane vibration.

slipping forces. Therefore, the control performance cannot be substantially improved by merely increasing the slipping forces of the damper. The axial stiffness of the friction damper should be increased accordingly with the increasing damper slipping force. Similar observations can be made from the control evaluation for the out-of-plane vibration which is not displayed due to page limitation. It can be concluded that the optimal axial stiffness of the friction damper is tightly related to the damper slipping force. A large value of the optimal axial stiffness is expected if the slipping force of the damper is large.

7. Concluding Remarks

The feasibility of using passive friction dampers to suppress the dynamic responses of a transmission tower-line system under wind excitations is performed in this study. A 2D lumped mass model of a transmission tower is developed for the dynamic analysis by simplifying the 3D FE model. The analytical model for the transmission tower-line system is developed by simulating the transmission line as several lumped masses connected with elastic elements. The mechanical model of the passive friction damper is presented by involving the effects of the damper axial stiffness. A real transmission tower-line system is taken as the example to investigate the efficacy of the proposed control approach through the detailed parametric study.

The made observations demonstrate that the installation of the friction dampers can substantially suppress the wind-induced vibration of the transmission tower-line system for both the in-plane and out-of-plane vibration, respectively, because of its satisfactory energy-dissipating capacity. It is seen that no matter which tower mass is selected, there is an optimal value of control forces by which the best performance of the friction damper can be achieved. If the damper control force is increased after reaching the optimal value, the damper performance will deteriorate gradually. The dynamic responses for both the in-plane and out-of-plane vibration can be reduced rapidly when the stiffness coefficient of dampers increases from zero to the optimal axial stiffness value. Further increase in damper stiffness cannot substantially improve the control performance and leads to unnecessary cost increases. The optimal axial stiffness of the friction damper is tightly related to the damper slipping force.

Conflict of Interests

The authors declare that there is no conflict of interests regarding the publication of this paper.

Acknowledgments

The authors are grateful for the financial support from the National Natural Science Foundation of China (51178366), the technological project of the Chinese Southern Power Grid Co. Ltd. (K-GD2013-0783), the Fok Ying-Tong Education Foundation (131072), and the Natural Science Foundation of Hubei Province (2014CFA026).

References

- [1] B. Chen, J. Zheng, and W. Qu, "Control of wind-induced response of transmission tower-line system by using magnetorheological dampers," *International Journal of Structural Stability and Dynamics*, vol. 9, no. 4, pp. 661–685, 2009.
- [2] H.-F. Bai, T.-H. Yi, H.-N. Li, and L. Ren, "Multisensors on-site monitoring and characteristic analysis of UHV transmission tower," *International Journal of Distributed Sensor Networks*, vol. 2012, Article ID 545148, 10 pages, 2012.
- [3] E. Simiu and R. Scanlan, *Wind Effects on Structures*, John Wiley and Sons, New York, NY, USA, 3rd edition, 1996.
- [4] Q. Xie and L. Sun, "Failure mechanism and retrofitting strategy of transmission tower structures under ice load," *Journal of Constructional Steel Research*, vol. 74, pp. 26–36, 2012.
- [5] E. Savory, G. A. R. Parke, M. Zeinoddini, N. Toy, and P. Disney, "Modelling of tornado and microburst-induced wind loading and failure of a lattice transmission tower," *Engineering Structures*, vol. 23, no. 4, pp. 365–375, 2001.
- [6] R. C. Battista, R. S. Rodrigues, and M. S. Pfeil, "Dynamic behavior and stability of transmission line towers under wind forces," *Journal of Wind Engineering and Industrial Aerodynamics*, vol. 91, no. 8, pp. 1051–1067, 2003.
- [7] H.-N. Li, S.-Y. Tang, and T.-H. Yi, "Wind-rain-induced vibration test and analytical method of high-voltage transmission tower," *Structural Engineering and Mechanics*, vol. 48, no. 4, pp. 435–453, 2013.
- [8] P. S. Lee and G. McClure, "Elastoplastic large deformation analysis of a lattice steel tower structure and comparison with full-scale tests," *Journal of Constructional Steel Research*, vol. 63, no. 5, pp. 709–717, 2007.
- [9] T. Okamura, T. Ohkuma, E. Hongo, and H. Okada, "Wind response analysis of a transmission tower in a mountainous area," *Journal of Wind Engineering and Industrial Aerodynamics*, vol. 91, no. 1-2, pp. 53–63, 2003.
- [10] G. W. Housner, L. A. Bergman, T. K. Caughey et al., "Structural control: past, present, and future," *Journal of Engineering Mechanics*, vol. 123, no. 9, pp. 897–971, 1997.
- [11] S. Ozono and J. Maeda, "In-plane dynamic interaction between a tower and conductors at lower frequencies," *Engineering Structures*, vol. 14, no. 4, pp. 210–216, 1992.
- [12] H. Verma and P. Hagedorn, "Wind induced vibrations of long electrical overhead transmission line spans: a modified approach," *Wind and Structures*, vol. 8, no. 2, pp. 89–106, 2005.
- [13] B. Chen, J. Zheng, and W. L. Qu, "Practical method for wind-resistant design of transmission tower-line system by using viscoelastic dampers," in *Proceedings of the 2nd International Conference on Structural Condition Assessment, Monitoring and Improvement*, pp. 1028–1034, Changsha, China, 2007.
- [14] B. Chen, Y. L. Xu, and W. L. Qu, "Evaluation of atmospheric corrosion damage to steel space structures in coastal areas," *International Journal of Solids and Structures*, vol. 42, no. 16-17, pp. 4673–4694, 2005.
- [15] M. Kleiber and T. D. Hien, *The Stochastic Finite Element Method: Basic Perturbation Technique and Computer Implementation*, John Wiley & Sons, New York, NY, USA, 1992.
- [16] K. J. Bathe, *Finite Element Procedures*, Prentice-Hall, New Jersey, NJ, USA, 1996.
- [17] H. M. Irvine, *Cable Structure*, The MIT Press, New York, NY, USA, 1981.

- [18] L. Kempner Jr. and S. Smith, "Cross-rope transmission tower-line dynamic analysis," *Journal of Structural Engineering ASCE*, vol. 110, no. 6, pp. 1321–1335, 1984.
- [19] B. Chen, W. H. Guo, P. Y. Li, and W. P. Xie, "Dynamic responses and vibration control of the transmission tower-line system: a state-of-the-art review," *The Scientific World Journal*, vol. 2014, Article ID 538457, 20 pages, 2014.
- [20] A. S. Pall and C. Marsh, "Response of friction damped braced frames," *Journal of the Structural Division*, vol. 108, no. 6, pp. 1313–1323, 1982.
- [21] D. K. Nims, P. J. Richter, and R. E. Bachman, "The use of the energy dissipating restraint for seismic hazard mitigation," *Earthquake Spectra*, vol. 9, no. 3, pp. 467–489, 1993.
- [22] Y. L. Xu and B. Chen, "Integrated vibration control and health monitoring of building structures using semi-active friction dampers. Part I-methodology," *Engineering Structures*, vol. 30, no. 7, pp. 1789–1801, 2008.
- [23] B. Chen and Y. L. Xu, "Integrated vibration control and health monitoring of building structures using semi-active friction dampers. Part II. Numerical investigation," *Engineering Structures*, vol. 30, no. 3, pp. 573–587, 2008.
- [24] M. Shinozuka and G. Deodatis, "Simulation of stochastic processes by spectral representation," *Applied Mechanics Reviews*, vol. 44, no. 4, pp. 191–204, 1991.

Research Article

Sensor Placement Optimization of Vibration Test on Medium-Speed Mill

Lihua Zhu,^{1,2} Jun Dai,¹ and Guoliang Bai¹

¹*School of Civil Engineering, Xi'an University of Architecture and Technology, Xi'an 710055, China*

²*Department of Civil, Structural and Environmental Engineering, University at Buffalo, State University of New York, Buffalo, NY 14260, USA*

Correspondence should be addressed to Lihua Zhu; zhulihuaxa@163.com

Received 8 September 2014; Revised 22 December 2014; Accepted 24 December 2014

Academic Editor: Stathis C. Stiros

Copyright © 2015 Lihua Zhu et al. This is an open access article distributed under the Creative Commons Attribution License, which permits unrestricted use, distribution, and reproduction in any medium, provided the original work is properly cited.

Condition assessment and decision making are important tasks of vibration test on dynamic machines, and the accuracy of dynamic response can be achieved by the sensors placed on the structure reasonably. The common methods and evaluation criteria of optimal sensor placement (OSP) were summarized. In order to test the vibration characteristic of medium-speed mill in the thermal power plants, the optimal placement of 12 candidate measuring points in X, Y, and Z directions on the mill was discussed for different targeted modal shapes, respectively. The OSP of medium-speed mill was conducted using the effective independence method (EfI) and QR decomposition algorithm. The results showed that the order of modal shapes had an important influence on the optimization results. The difference of these two methods on the sensor placement optimization became smaller with the decrease of the number of target modes. The final scheme of OSP was determined based on the optimal results and the actual test requirements. The field test results were basically consistent with the finite element analysis results, which indicated the sensor placement optimization for vibration test on the medium-speed mill was feasible.

1. Introduction

The model updating, condition identification, condition assessment, and decision making of the concerned structure require enough efficient data to reflect structural properties. It is a common way to achieve the related data by sensors. However, restricted by testing technology and cost, a practical problem is how to select a set with a minimum number of sensor locations from all possibilities [1]. Optimal sensor placement (OSP) has been one of the more important tasks in dynamic test, especially for those high-rise buildings and complicated structures.

The basic principle of sensor placement optimization is that limited measuring points can get enough efficient data which can reflect the structural properties. Recently, most methods aim to achieve the best identification of structural characteristics, including the frequencies and mode shapes. Among these methods, effective independence (EfI) method is the most widely used method, which was proposed by Kammer [2]. For modal kinetic method (MKE), the target of

OSP is to ensure the maximization of the measured kinetic mode energy that improves signal-to-noise ratio [3]. Besides, EfI is an iterated version of the MKE with reorthonormalized mode shapes [4]. The modal assurance criterion (MAC) method is based on QR decomposition with column pivoting, and these measuring points are chosen to minimize off-diagonal element of MAC matrix [5].

So far, a multitude of researches have been conducted on sensor placement optimization for large-span bridges and high-rise buildings in civil engineering. Yi et al. conducted sensor placement optimization for Dalian International Trade Mansion [1]. Chow et al. presented optimal sensor configuration of a typical transmission tower for the purpose of structural model updating [6]. Wang et al. established the wind and structural health monitoring system implemented on the Runyang Yangtze River Bridge [7]. However, there are few researches on the sensor placement optimization for those structures which are not very high or large, while the vibration modes are very complicated. The medium-speed mill is one of the most commonly used auxiliary power items

of equipment in thermal power plants. It generates significant disturbing force when it is running, so it is very important to monitor its vibration condition. The study of Zhu et al. shows that vibration modes of medium-speed mill are very complicated [8].

In order to obtain the reliable dynamic response, reasonable condition assessment, and decision making of medium-speed mill, the measuring points should be placed on the locations that reflect abundant structural information of medium-speed mill. So the OSP for vibration test on medium-speed mill is extremely necessary. In this paper, a reliable finite element model (FEM) of medium-speed mill supported by spring vibration-isolated foundation is built, and two OSP methods are applied to the vibration test of medium-speed mill. Finally, considering the actual situation of vibration test, an OSP scheme is proposed in the vibration test on medium-speed mill.

2. The Algorithm and Evaluation Criteria of OSP

2.1. Effective Independence Method. The aim of the Efi method is to select measurement positions that make the mode shapes of interest as linearly independent as possible while containing sufficient information about the target modal responses in the measurements.

The measured structural response can be expressed as

$$\mathbf{u} = \Phi \mathbf{q} + \mathbf{w} = \sum_{i=1}^N q_i \phi_i + \mathbf{w}, \quad (1)$$

where Φ is the matrix of FEM target mode shapes, \mathbf{q} is the coefficient response vector and also is modal coordinate, and \mathbf{w} is a sensor noise vector, assumed stationary random process with a mean value zero. There must be a deviation for corresponding real generalized coordinate $\hat{\mathbf{q}}$. Assuming that this process is an effective unbiased estimation, the covariance matrix \mathbf{J} is obtained as

$$\mathbf{J} = E[(\mathbf{q} - \hat{\mathbf{q}})(\mathbf{q} - \hat{\mathbf{q}})^T] = [\sigma^{-2} \Phi^T \Phi]^{-1} = \mathbf{Q}^{-1}, \quad (2)$$

where \mathbf{Q} is the Fisher information matrix (FIM) by assuming the measured noise is independent and has the same statistical properties. The matrix \mathbf{Q} can be written as

$$\mathbf{Q} = \sigma^{-2} \Phi^T \Phi = \sigma^{-2} \mathbf{A}. \quad (3)$$

Then, the maximization of \mathbf{Q} is equivalent to the maximization of \mathbf{A} , and thus \mathbf{A} can be used to simplify FIM. Constructing matrix \mathbf{E}_D ,

$$\mathbf{E}_D = \Phi [\Phi^T \Phi]^{-1} \Phi^T, \quad (4)$$

where \mathbf{E}_D is the effective independence allocation matrix. The diagonal elements of the \mathbf{E}_D represent the contribution of the candidate points to the modal matrix linearly independent.

2.2. The Algorithm for OSP Based on QR Decomposition. QR decomposition is derived from the maximization of the

FIM. The linearly independent row vectors are extracted from modal matrix by QR decomposition that ensures a larger norm of matrix. These degrees of freedom (DOFs) corresponding with linearly independent row vectors can be used as an ideal placement for sensors. The decomposition can be expressed as

$$\mathbf{A} = \Phi^T \mathbf{E} = \mathbf{Q} \mathbf{R}, \quad (5)$$

where \mathbf{E} is the unit conversion matrix, descending order according to the value of the diagonal elements of \mathbf{R} . We choose the modal DOFs in accordance with the sequence of the elements in \mathbf{E} .

2.3. The Evaluation Criteria of OSP

2.3.1. Fisher Information Matrix Determinant. According to the principle of Efi method, the greater the trace or the value of FIM determinant is, the smaller the covariance \mathbf{J} is and the more effective the modal coordinate is. Meanwhile, FIM also measures the abundance modal information from the response of structures, and the greater the determinant value is, the more abundant modal information it contains [5].

2.3.2. Modal Assurance Criterion. The quantity of measured DOFs is far less than the whole DOFs of structural model and the responses are affected by measurement accuracy and noise; thus, the modal vector measured cannot retain the original space property. MAC is a good method to evaluate the space angle of modal vectors [9]. The formula is expressed as

$$\text{MAC}_{ij} = \frac{(\phi_i^T \phi_j)^2}{(\phi_i^T \phi_i)(\phi_j^T \phi_j)}, \quad (6)$$

where ϕ_i and ϕ_j are the i th and j th modal vectors, respectively. The off-diagonal elements of MAC matrix should be minimized for OSP, and thus the modal matrix measured can keep better orthogonality.

3. OSP for Vibration Test on Medium-Speed Mill

3.1. Description of the Medium-Speed Mill. Medium-speed mill is an important auxiliary dynamic machine in the thermal power plants. To mitigate the vibration, the spring vibration-isolated foundation is normally used to support the mill. A spring vibration-isolated foundation for medium-speed mill is typically comprised of upper and lower bedplates and spring isolators. An elevation view of a vibration-isolated foundation for medium-speed mill is shown in Figure 1. As shown, there are two buttresses over the lower bedplate, and the distance between the upper bedplate and buttresses is 330 mm. Spring isolators are placed between the two buttresses and the upper bedplate. Twelve sets of spring isolators are placed on each buttress; thus, a total of 24 sets of isolators are placed.

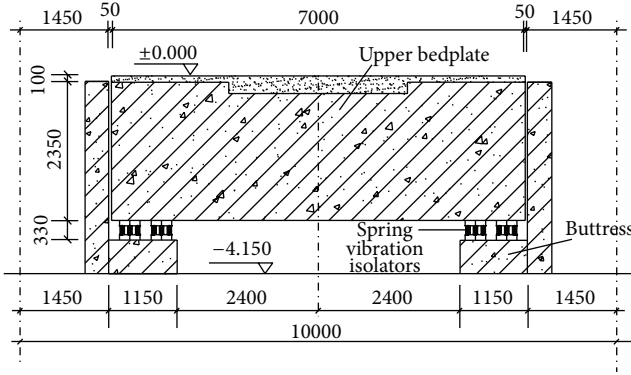


FIGURE 1: Spring vibration-isolated foundation of medium-speed mill.

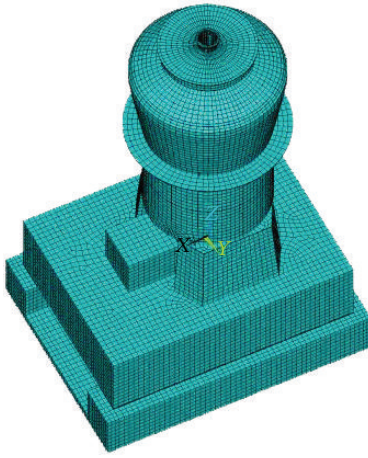


FIGURE 2: Finite element model.

3.2. Finite Element Analysis

3.2.1. Modeling. A medium-speed mill in the Yuzhou power plant (Henan Province, China) was used as the prototype for the developed finite element model. In order to provide the input data for the optimization analysis, a three-dimensional finite element coupled model of a medium-speed mill and its foundation was built using ANSYS (version 12.0) [10]. SOLID185 elements were used to simulate the foundation, the mill, and the motor; SHELL181 elements were used for the frame and chassis; BEAM188 elements were used for the pressure frame; COMBINE14 elements were used for the isolators; and MASS21 elements were used for the load.

The frame, motor, and mill were rigidly connected with the upper bedplate of the foundation. The boundary condition of the lower bedplate of the foundation was simulated using spring elements, which represented the constraint effect of the soil on the foundation. For the coordinate system of the model, X represented the transverse direction of the foundation of medium-speed mill and Y represented the longitudinal direction. The mesh size of the finite element model was between 100 and 200 mm. The finite element model was shown in Figure 2, and the primary parameters of the mill and vibration isolator were listed in Table 1.

3.2.2. Modal Analysis. After building a FE model of the medium-speed mill with spring vibration-isolated foundation, a modal analysis was done using the block Lanczos method. The vibration modal shapes and corresponding frequencies were shown in Figure 3 and Table 2.

3.3. Selection of Candidate Measuring Points. The medium-speed mill is an axial symmetric structure. According to ANSYS analysis, the primary vibration mode shapes of medium-speed mill include horizontal longitudinal vibration, horizontal transverse vibration, and vertical vibration. And also considering the cost and technical factors, measuring points were placed along one side of the medium-speed mill. 12 measuring points were set as candidate points. Each point had DOFs of X , Y , and Z direction; thus, there were a total of 36 DOFs. Efl and QR methods were employed to optimize the sensors placement of medium-speed mill and the first 3, 4, 5, and 6 were taken as the monitoring modal shapes, respectively. The placement of candidate measuring points was shown in Figure 4.

36 DOFs were analyzed preliminarily using Efl method with MATLAB software. According to E_D , the contribution of 12 DOFs in Z direction to modal matrix linear independence was far less. There is no sufficient reason to believe that the FE model can simulate the actual structure accurately, so removing the DOFs in Z direction just based on the optimization results of 36 DOFs, the vibration characteristic of medium-speed mill may not be understood comprehensively. Motivated by the above consideration, it is determined to optimize the placement of 12 DOFs in X , Y , and Z direction, respectively.

3.4. Results of OSP. The OSP of 12 candidate measuring points was conducted using Efl method and QR decomposition algorithm for different target mode shapes in X , Y , and Z direction, respectively, and the results of OSP were presented in Table 3. It was noted that those measuring points in brackets were suboptimal ones. The suboptimal measuring points were not included in the optimization results in this paper, while the referred optimization results meant that the number of measuring points was consistent with the number of target mode shapes.

In Table 3, it was found that two optimization results did not agree with each other exactly. The optimization results of the first 3 and 4 mode shapes in X direction were consistent exactly, but they were different for one and two measuring points in the first 5 and 6 mode shapes, respectively. The optimization results in X direction had the trend that the fewer the number of target mode shapes was, the smaller the difference in two results was. Although the same trend did not appear in Y and Z directions, the optimization results were still consistent basically. Therefore, Efl and QR decomposition algorithms in OSP for medium-speed mill were feasible.

FIM determinant behavior was recorded in terms of percentage of its initial value against the decrease in candidate measuring points [11], and the results were shown in Figure 5. It was noted that the FIM determinant in lower orders of target mode shapes had larger value in case of the

TABLE 1: Parameters of the mill and vibration isolator.

Medium-speed mill ZGM113G	Total weight of the mill/t	157.40
	Total weight of the foundation/t	398.74
	Total weight of the mill and foundation/t	556.14
	Mass ratio of the foundation to the mill	2.53
Vibration isolator SPV2076.12.12	Vertical stiffness of the vibration isolator/kN/mm	12.10
	Horizontal stiffness of the vibration isolator/kN/mm	9.50
	Vertical damping factor/kNs/m	240
	Horizontal damping factor/kNs/m	160
	Damping ratio of the structure	0.02
	Disturbing force/kN	X direction = 10 Y direction = 10 Z direction = 40

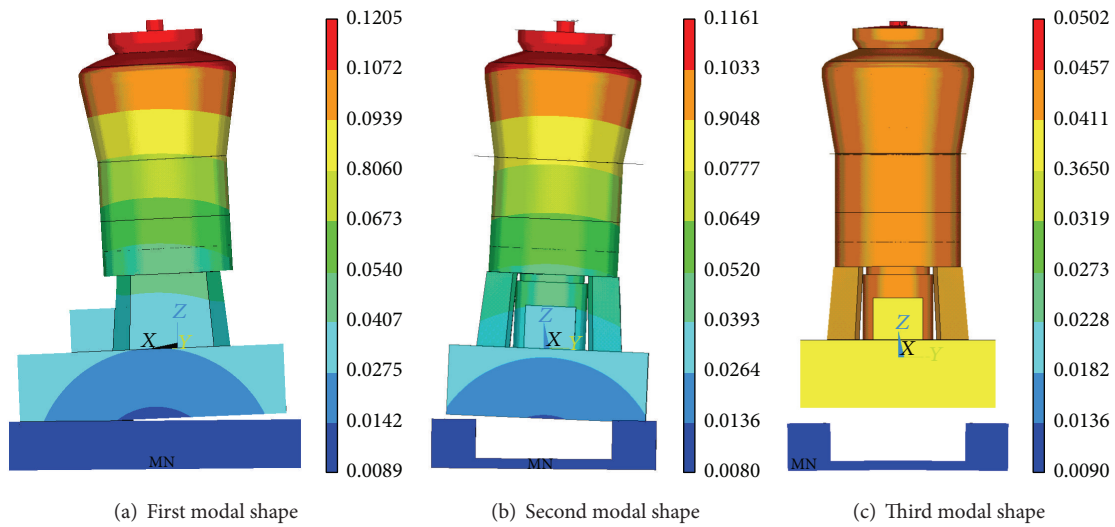


FIGURE 3: First three modes.

TABLE 2: Vibration frequencies.

Order	Frequency f/Hz	Vibration modal shape
1	1.828	X direction horizontal vibration
2	2.003	Y direction horizontal vibration
3	3.578	Vertical vibration
4	4.078	Rotation around horizontal axis of the mill
5	4.235	Torsion around the vertical axis
6	4.422	Horizontal oblique translational vibration

same number of measuring points, which meant that these measuring points were more efficient in getting concerned information of the medium-speed mill. On the other hand, the value of FIM determinant increased more significantly when adding a measuring point in case of the same number of measuring points, which meant that the optimization results in larger orders were more sensitive to the number of measuring points. So the target modal played a significant role in the final scheme of the OSP.

The average values of off-diagonal elements of MAC matrix were shown in Figure 6. The average values of off-diagonal elements of MAC matrix were greater even if when 12 candidate measuring points were all placed. It was explained that the vibration modes of medium-speed mill were very complicated and even 12 measuring points cannot capture its dynamic characteristics expectedly. But the average value of off-diagonal elements of MAC increased a little in Y direction using these two optimal methods to decrease the number of measuring points, while the average values in X and Z directions decreased, in particular in Z direction. In other words, the expected optimal results could be achieved. Meanwhile, it could be confirmed that Efi method was much better due to smaller average values of MAC.

It was easy to find that the selection of suboptimal measuring points using two methods was significantly different. The values of FIM determinant after adding the suboptimal points to the optimization results and the final results were shown in Table 4. The value of FIM using Efi method was greater than that of QR decomposition method. The

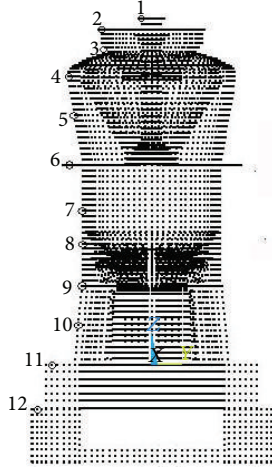


FIGURE 4: Placement of candidate measuring points.

TABLE 3: Optimization results of measuring points.

Order	Direction					
	X (Efl)	X (QR)	Y (Efl)	Y (QR)	Z (Efl)	Z (QR)
6	1	1	3	1	1	1
	4	4	4	4	2	2
	7	8	5	5	4	6
	8	9	9	9	5	7
	9	10	10	10	10	10
	11	11	11	11	11	11
5	1	1	3	1	1	1
	4	4	4	4	2	2
	8	9	5	5	6	6
	9	10	10	10	10	10
	11	11	11	11	11	11
	(7)	(2)	(7)	(2)	(4)	(8)
4	1	1	3	1	1	1
	4	4	4	4	4	6
	10	10	7	7	10	10
	11	11	10	10	11	11
	(9)	(8)	(1)	(8)	(6)	(8)
	(6)	(2)	(5)	(2)	(9)	(2)
3	1	1	3	1	1	1
	6	6	4	4	10	6
	11	11	10	10	11	10
	(5)	(7)	(1)	(7)	(6)	(7)
	(3)	(8)	(2)	(8)	(9)	(8)
	(4)	(2)	(5)	(2)	(4)	(2)

effect of optimization using Efl method was better, and the corresponding measuring points had a stronger ability to get the information of the medium-speed mill.

4. The Experimental Results of OSP

4.1. Final Scheme of OSP. Based on the analysis of Section 3.2.2, the *X*-translational vibration was the primary

vibration mode of medium-speed mill, so the optimal results of *X* direction in the first 3 mode shapes using Efl method were employed. Considering the stability of data and security of sensors, the measuring point 1 was changed to point 2, and they had the same testing condition. In addition, the data collected by the measuring point 2 was an important indicator to decide the working state of medium-speed mill. In order to reduce the effects of environmental and operational variability and noise contamination, the measuring points 2 and 6 with more modal kinetic energy were selected to improve the signal-to-noise ratio [3, 12–14]. The analysis of OSP showed that the contribution of the actual measuring point 12 in *X*, *Y*, and *Z* directions is minimal, and it should be removed in theory. Considering that one of the aims of vibration test is to understand the isolation effect of the spring vibration-isolated foundation, the measuring point 12 was retained. From Table 3, the contribution of the measuring point 11 on the vibration of medium-speed mill in three directions was great, and the vertical vibration of medium-speed mill also should be tested. Therefore, the measuring points 2, 6, 11, and 12 were chosen as the final scheme of OSP.

In order to place the sensors in site easily, the measuring points were renumbered, which were shown in Figure 7. Among these test points, the HTP1 sensor was used to measure the horizontal vibration of the lower bedplate of the foundation or ground; the HTP2 sensor was attached to the upper bedplate; the HTP3 sensor was attached to the middle of the mill; and the HTP4 sensor was attached to the top of the mill. The VTP1 sensor was used to measure the vertical vibration of the lower bedplate of the foundation or ground; and the VTP2 sensor was attached to the upper bedplate of the foundation.

4.2. Field Tests. In order to verify the feasibility of OSP results, the medium-speed mill in the Yuzhou thermal power plant was tested in site. In the field test, 891-II type vibration measurement instruments including six sensors, amplifiers with a frequency response ranging from 0.5 Hz to 100 Hz, an INV306 intelligent signal acquisition and processing analysis system, and a DASP data processing program were used. The sensors were placed according to the final scheme of OSP. The sensors used in the experiment were manufactured by the Institute of Engineering Mechanics, China Earthquake Administration. The sensors have four gears, which are used to test the large displacement, small displacement, velocity, and acceleration. Actually, they are displacement sensors. In this test, the gear of small displacement was used. The elevation view of the tested medium-speed mill was shown in Figure 8, and the sensor in close-up was shown in Figure 9.

The vibration test on the medium-speed mill was conducted in the plant, so the variability of physical property with thermal effect can be ignored [13]. The primary noise contamination was sourced from other nearby dynamic machines. The vibration data was recorded when the medium-speed mill did not run, which was used in the next filtering [12].

Field tests were conducted during the working steady stage of the medium-speed mill, and the vibration displacements were tested by the described sensors. The collection time was 60 seconds per sample. In this condition,

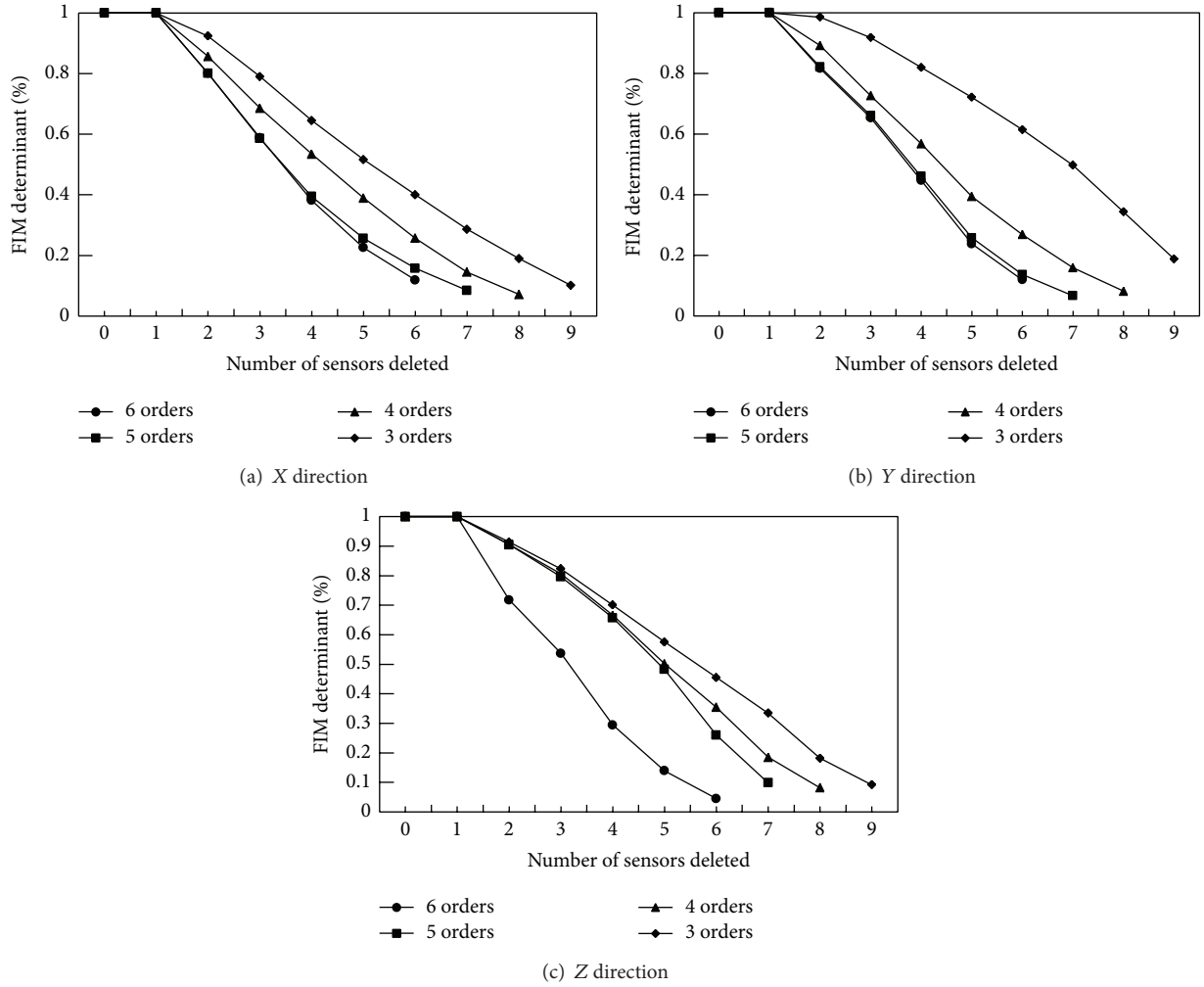


FIGURE 5: Fisher information matrix determinant.

TABLE 4: Results of Fisher information matrix determinant.

Direction	Order					
	X (Efl)	X (QR)	Y (Efl)	Y (QR)	Z (Efl)	Z (QR)
5	3.53×10^{-17}	1.03×10^{-17}	7.17×10^{-23}	5.71×10^{-23}	2.61×10^{-20}	1.24×10^{-19}
4	2.49×10^{-11}	1.19×10^{-11}	4.28×10^{-20}	3.14×10^{-20}	8.60×10^{-15}	5.50×10^{-15}
3	1.27×10^{-8}	1.17×10^{-8}	1.51×10^{-13}	1.09×10^{-13}	3.41×10^{-9}	1.35×10^{-9}

the vibrations of the foundation and mill body were assumed to be the ergodic and stationary random processes; the collected samples can thus describe the vibration characteristics of the mill. The noise was eliminated using filter techniques with DASP software and the typical vibration curves for the mill obtained from the test were shown in Figure 10. It should be noted that only vibration displacement ranging from 0 to 10 second were shown in Figure 10.

4.3. Comparison of Vibration Displacement. Harmonic response analysis at the service load was performed by ANSYS. The analytical results of the vibration amplitude of each measuring point were compared with the test results, which was presented in Table 5. The test results in Table 5 were

the maximum vibration displacements of these measuring points. The calculation results generally agreed with the field test results in X direction, which indicated that the FE model could simulate the dynamic characteristics of the medium-speed mill. It was also noted that the simulation in Z and Y directions was less effective than that in X direction. From the location of measuring points, the test point 4 was more satisfactory, and the test points 2 and 3 were followed. Abundant dynamic characteristics of medium-speed mill were achieved based on the final sensors placement scheme, and the finite element analysis results were basically consistent with the field test results, which indicated the sensor placement optimization for vibration test on the medium-speed mill was effective and economical.

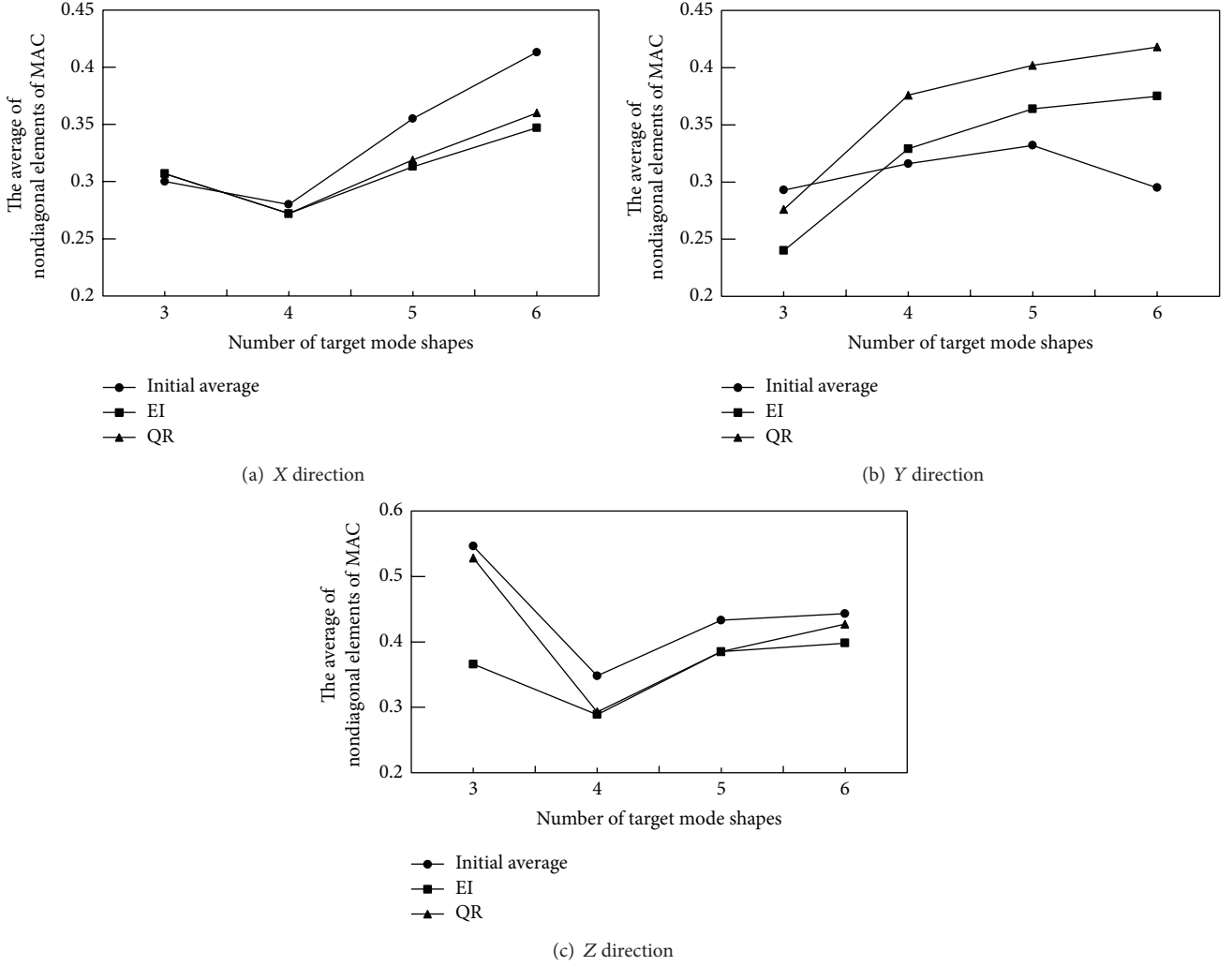


FIGURE 6: Average values of MAC matrix off-diagonal elements.

TABLE 5: Comparison of vibration displacement between the finite element analysis results and the field test results.

Measuring points	2(X)/mm	3(X)/mm	4(X)/mm	2(Y)/mm	3(Y)/mm	4(Y)/mm	2(Z)/mm
Test results	0.062	0.132	0.421	0.103	0.226	0.246	0.106
Calculation results	0.051	0.101	0.385	0.080	0.169	0.202	0.082
Error (%)	17.5	23.5	8.6	22.4	25.1	18.3	22.6

5. Conclusion

In this paper, the common methods and evaluation criteria for OSP had been summarized. The OSP of vibration test on medium-speed mill supported by spring vibration-isolated foundation was conducted using Efl and QR decomposition methods. It was found that these two methods for vibration test on medium-speed mill were all feasible, although this was different for some measuring points in different directions, and the difference became smaller with the decrease of the number of target mode shapes. For the evaluation criteria of FIM determinant, the effect was better in the case of small number of target mode shapes when the measuring points were certain; on the other hand, the effects in more target

mode shapes were much more sensitive to the number of measuring points. For MAC, Efl method was more efficient than QR decomposition method. In addition, the OSP based on Efl method can achieve more efficient suboptimal measuring points.

The final scheme of OSP was based on the result that the first three mode shapes in X direction were set as the targeted modal shapes. Six sensors were placed to achieve the dynamic response of the medium-speed mill, and the effect of the environmental and operational variability and noise contamination was reduced by filtering technique. The field test results were basically consistent with the calculation results by ANSYS, and the FEM of the medium-speed mill with spring vibration-isolated foundation could simulate

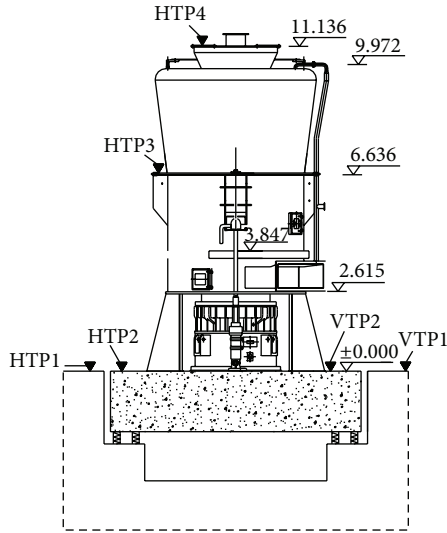


FIGURE 7: Placement of sensors (HTP: horizontal test point, VTP: vertical test point).



FIGURE 8: The elevation view of the tested medium-speed mill.



FIGURE 9: The sensor shown in close-up.

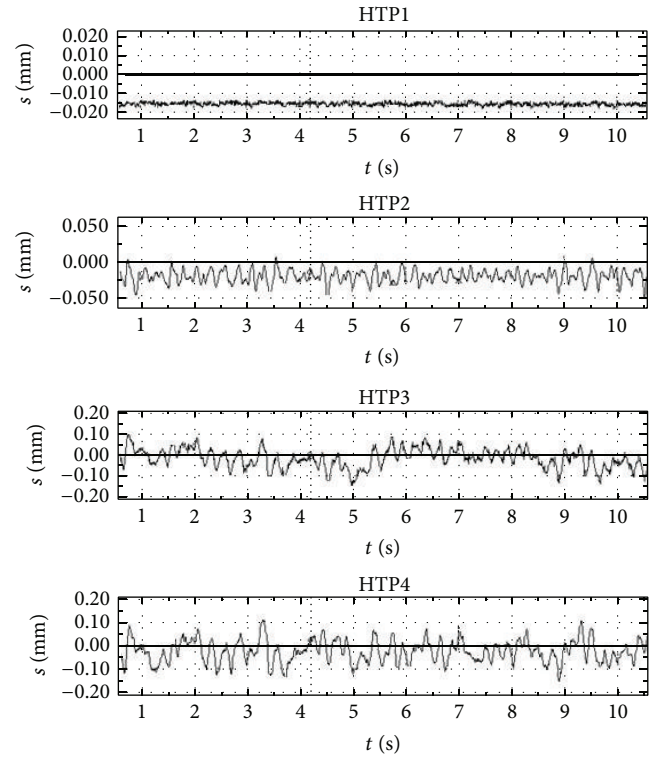


FIGURE 10: Horizontal vibration displacement in X direction.

the vibration characteristic well. The sensor placement optimization for vibration test on the medium-speed mill was effective and economical.

Conflict of Interests

The authors declare that there is no conflict of interests regarding the publication of this paper.

Acknowledgments

The presented work was supported by the project of Shaanxi Province Excellent Young Scholars (2013KJXX-53), China Scholarship for Study Abroad, Program for Changjiang Scholars and Innovative Research Team in University, and Innovation Team of Xi'an University of Architecture and Technology.

References

- [1] T. H. Yi, H. N. Li, and M. Gu, "Sensor placement optimisation for Dalian international trade mansion focusing on application demands," *International Journal of Sensor Networks*, vol. 15, no. 3, pp. 157–162, 2012.
- [2] D. C. Kammer, "Sensor placement for on-orbit modal identification and correlation of large space structures," *Journal of Guidance, Control, and Dynamics*, vol. 14, no. 2, pp. 251–259, 1991.
- [3] M. Papadopoulos and E. Garcia, "Sensor placement methodologies for dynamic testing," *AIAA Journal*, vol. 36, no. 2, pp. 256–263, 1998.

- [4] D. S. Li, H. N. Li, and C. P. Fritzen, "The connection between effective independence and modal kinetic energy methods for sensor placement," *Journal of Sound and Vibration*, vol. 305, no. 4-5, pp. 945-955, 2007.
- [5] F. Cui, W. C. Yuan, and J. J. Shi, "Optimal sensor placement algorithms in bridge health monitoring," *Journal of Tongji University*, vol. 27, no. 2, pp. 165-169, 1999 (Chinese).
- [6] H. M. Chow, H. F. Lam, T. Yin, and S. K. Au, "Optimal sensor configuration of a typical transmission tower for the purpose of structural model updating," *Structural Control and Health Monitoring*, vol. 18, no. 3, pp. 305-320, 2011.
- [7] H. Wang, A. Li, T. Guo, and T. Tao, "Establishment and application of the wind and structural health monitoring system for the Runyang Yangtze River Bridge," *Shock and Vibration*, vol. 2014, Article ID 421038, 15 pages, 2014.
- [8] L. H. Zhu, G. L. Bai, Y. L. Peng, F. J. Zhang, and X. L. Sun, "Vibration test and shock absorption research on medium-speed mill in thermal power plants," *Journal of Building Structures*, vol. 34, no. 5, pp. 43-51, 2013 (Chinese).
- [9] T. G. Carne and C. R. Dohrmann, "A modal test design strategy for model correlation," in *Proceedings of the 13th International Modal Analysis Conference*, pp. 927-933, Nashville, Tenn, USA, February 1995.
- [10] ANSYS Academic Research, Release 12.0.
- [11] D. C. Kammer, "Sensor set expansion for modal vibration testing," *Mechanical Systems and Signal Processing*, vol. 19, no. 4, pp. 700-713, 2005.
- [12] F. Moschas and S. C. Stiros, "Three-dimensional dynamic deflections and natural frequencies of a stiff footbridge based on measurements of collocated sensors," *Structural Control and Health Monitoring*, vol. 21, no. 1, pp. 23-42, 2014.
- [13] P. Cornwell, C. R. Farrar, S. W. Doebling, and H. Sohn, "Environmental variability of modal properties," *Experimental Techniques*, vol. 23, no. 6, pp. 45-48, 1999.
- [14] R. Castro-Triguero, S. Murugan, R. Gallego, and M. I. Friswell, "Robustness of optimal sensor placement under parametric uncertainty," *Mechanical Systems and Signal Processing*, vol. 41, no. 1-2, pp. 268-287, 2013.

Research Article

Research on Impact Process of Lander Footpad against Simulant Lunar Soils

Bo Huang,¹ Zhujin Jiang,² Peng Lin,³ and Daosheng Ling¹

¹MOE Key Laboratory of Soft Soils and Geoenvironmental Engineering, Department of Civil Engineering, Zhejiang University, Hangzhou 310058, China

²Urban Traffic and Underground Space Design Institute, Shanghai Municipal Engineering Design Institute (Group) Co., Ltd. (SMEDI), Shanghai 200092, China

³State Key Laboratory of Hydrosience and Engineering, Tsinghua University, Beijing 100084, China

Correspondence should be addressed to Daosheng Ling; dsling@zju.edu.cn

Received 5 August 2014; Revised 10 November 2014; Accepted 31 January 2015

Academic Editor: Stathis C. Stiros

Copyright © 2015 Bo Huang et al. This is an open access article distributed under the Creative Commons Attribution License, which permits unrestricted use, distribution, and reproduction in any medium, provided the original work is properly cited.

The safe landing of a Moon lander and the performance of the precise instruments it carries may be affected by too heavy impact on touchdown. Accordingly, landing characteristics have become an important research focus. Described in this paper are model tests carried out using simulated lunar soils of different relative densities (called “simulant” lunar soils below), with a scale reduction factor of 1/6 to consider the relative gravities of the Earth and Moon. In the model tests, the lander was simplified as an impact column with a saucer-shaped footpad with various impact landing masses and velocities. Based on the test results, the relationships between the footpad peak feature responses and impact kinetic energy have been analyzed. Numerical simulation analyses were also conducted to simulate the vertical impact process. A 3D dynamic finite element model was built for which the material parameters were obtained from laboratory test data. When compared with the model tests, the numerical model proved able to effectively simulate the dynamic characteristics of the axial forces, accelerations, and penetration depths of the impact column during landing. This numerical model can be further used as required for simulating oblique landing impacts.

1. Introduction

Landing on the Moon has long been a dream of mankind. In the 1960s, dozens of lunar exploration activities were carried out by the USA and the Soviet Union, which opened a new era of human exploration of the Moon. Moon landings have led to many lunar surface activities, such as lunar surface travelling, drilling, excavating, establishing shallow foundations, and the extraction of resources.

During the landing process, the response to impact of the footpad is very important. The footpad is the part of the lunar lander directly touching and impacting the lunar soil. Ever since the 1970s, scientists, mainly in the USA, have carried out much research on the impact process during landing [1, 2], in order to verify the stability and reliability of the lander, as it actually lands. These studies have investigated the influence of the following: types of simulant lunar soils, impact velocities, and model scales, on impact response.

Since it is hard to measure the real impact procedure of Moon lander, just as Stiros and Psimoulis [3] did on the moving train during its passage over a railway bridge, the landing-impact model tests and numerical simulation [4–7] have the same importance. In China, since completion of the first stage of the lunar exploration mission, Moon landing preparation work has been an ongoing task. A major task in the design and optimization of the lunar lander is to determine the loads, the footpad bears, and the landing penetration depth [8].

In this paper, studies of the interaction between the footpad and simulant lunar soils are described in detail. The studies combined model tests and numerical simulation analyses similar to other experimental and numerical studies in civil structural engineering [9–11]. Based on a prototype vertical impact model test apparatus, 1/6 subscale model experiments were carried out, focusing on vertical impact landing. The time-history characteristics and peak characteristics of the footpad during impact were studied as

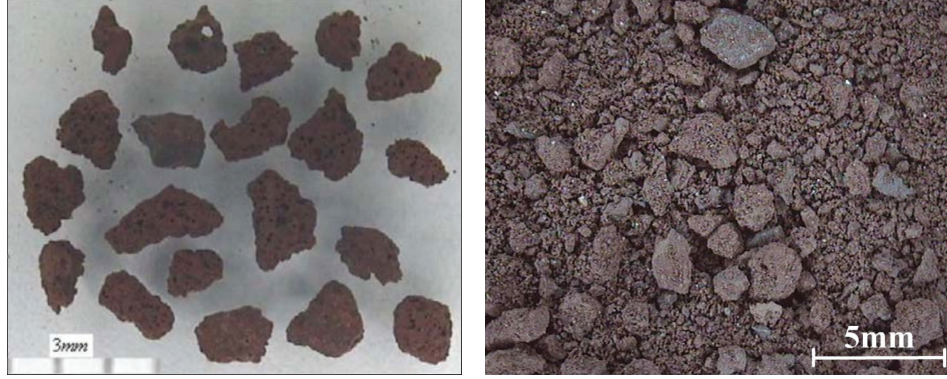


FIGURE 1: SEM image of TJ-1 particles.

well as the variations in axial forces and footpath penetration depths for different relative densities of simulant lunar soil, different impact masses, and impact velocities. Described in this paper is also a dynamic simulation approach for analyzing the footpad impact process using a 3D dynamic finite element method. The commercial software Abaqus [12] was selected for the study for its friendly application development environment and powerful dynamics analysis capabilities. The footpad is modeled as a rigid block with specified mass and velocity, while the lunar soil is represented by the Mohr-Coulomb model which conforms to the nonassociative flow rule and can take into account strain-softening properties. The soil-footpad interaction is assumed to conform to the ideal elastoplastic relationship. The material parameters used in the numerical model were obtained from the monotonic and cyclic tests on a simulant lunar soil named TJ-1. A comparison with model test results proved the numerical model to be valid.

2. Vertical Impact Model Test

2.1. Properties of Simulant Lunar Soil (Named TJ-1) Used in the Model Test. Tens of individual lunar explorations have brought back a total mass of about 382.0 kg of lunar regolith [13], and following testing of these lunar soils, Vinogradov [14], Costes et al. [15], Mitchell et al. [16], Carrier et al. [17, 18], and McKay et al. [4] have reported the properties of lunar soil in detail. Several lunar soil simulants have since been developed and used widely in experiments, including MLS-1, ALS, JSC-1, FJS-1, MKS-1, LSS, and GRC-1 [19–25]. Chinese scientists have also developed several lunar soil simulants, including NAO-1 [26], CAS-1 [27], and TJ-1 [28]. TJ-1, developed from volcanic ash, has a low production cost and possesses good similarity to lunar soil. Thus, TJ-1 was adopted for this study.

As shown in Figure 1, the particles of TJ-1 are multiangular, with holes existing in large particles. The physical and mechanical properties of TJ-1 are given in Table 1, where the property parameters of real lunar soil are also given for comparison. The internal friction angle of lunar soil = $25^{\circ}\sim 50^{\circ}$, the cohesion = $0.1\sim 15$ kPa, and the compression index at medium compactness = $0.1\sim 0.11$ corresponding to a

normal pressure range of $12.5\sim 100$ kPa. Bulk density is $1.30\sim 2.29$ g/cm³, and the void ratio is $= 0.67\sim 2.37$. Relevant values for TJ-1 are all within those ranges.

Figure 2 shows the stress-strain curves for TJ-1 obtained from triaxial tests under confining pressures below 60 kPa. As gravity on the Moon is only 1/6 of that on the Earth, the overburden stresses in soil layers lying within the impact influence range are not large. The relative densities of TJ-1 samples are 40%, 60%, and 80%, representing medium, dense, and very dense states, respectively. Within the tested stress range, TJ-1 soil samples exhibited strong strain-softening behaviour with increase of confining pressure and relative density. The residual strengths were almost 60%~90% of peak strengths. Furthermore, influenced by the engagement of soil particles that are subangular to angular in shape, the lunar soil simulant shows large apparent cohesion properties and internal friction angle.

2.2. Test Model and Device. When the footpad touches the lunar soil, the lander has to withstand a huge impact. The entire interaction process can be divided into the 3 stages shown in Figure 3: impacting vertically, sliding horizontally, and achieving hydrostatic equilibrium. The first two stages happen almost simultaneously. The impacting process is the most dangerous stage, and this aspect is the focus of this paper.

Figure 4(a) shows a schematic diagram of the vertical impact test. The shock tube with a mass m , consisting of footpad and counterweights, impacts against TJ-1 soil site at a velocity v , forming a crater of a certain depth on the site surface. Despite the differences between the simplified model and real landing conditions, characteristics of the dynamic interaction between the footpad and simulant lunar soil can be obtained. Such characteristics are suitable for use in the design of the lander.

Since it is difficult to simulate the full-lunar surface environment which no doubt affected the landing interactions, the key factors which influence impact responses should be considered. The lunar gravity is quite different from that of the Earth, by about one sixth, so a scale factor of 6 was selected for the model tests. Scales of other regular physical quantities are given in Table 2. Zhang et al. [29] compared

TABLE 1: Comparison of properties between lunar soil and TJ-1.

Soil type	Lunar soil	TJ-1
Specific gravity	2.9~3.5 (McKay et al. [4]) 3.1 (Willman and Boles [35]) 3.1 (Kanamori et al. [21])	2.72 (Jiang and Sun [28]) 2.7 (tested by ourselves)
Bulk density (g/cm ³)	1.35~2.15 (Mitchell et al. [16]) 1.45~1.9 (Carrier et al. [17, 18]) 1.53~1.63 (Kanamori et al. [21])	1.36 (Jiang and Sun [28]) 1.02~1.639 (tested by ourselves)
Friction angle (deg)	37°~47° (Mitchell et al. [16]) 25°~50° (Carrier et al. [36])	47.6° (Jiang and Sun [28]) Max.: 40.0°~50.9° (tested by ourselves) Res.: 38.5°~43.6° (tested by ourselves)
Apparent cohesion (kPa)	0.15~15 (Jaffe [37]) 1.0 (McKay et al. [4]) 0.1~1 (Kanamori et al. [21])	0.86 (Jiang and Sun [28]) Max.: 0~38.7 (tested by ourselves) Res.: 0~9.3 (tested by ourselves)
Compression index (MPa ⁻¹)	0.01~0.11 (Gromov [38])	0.086 (Jiang and Sun [28]) 0.025~0.1 (tested by ourselves)

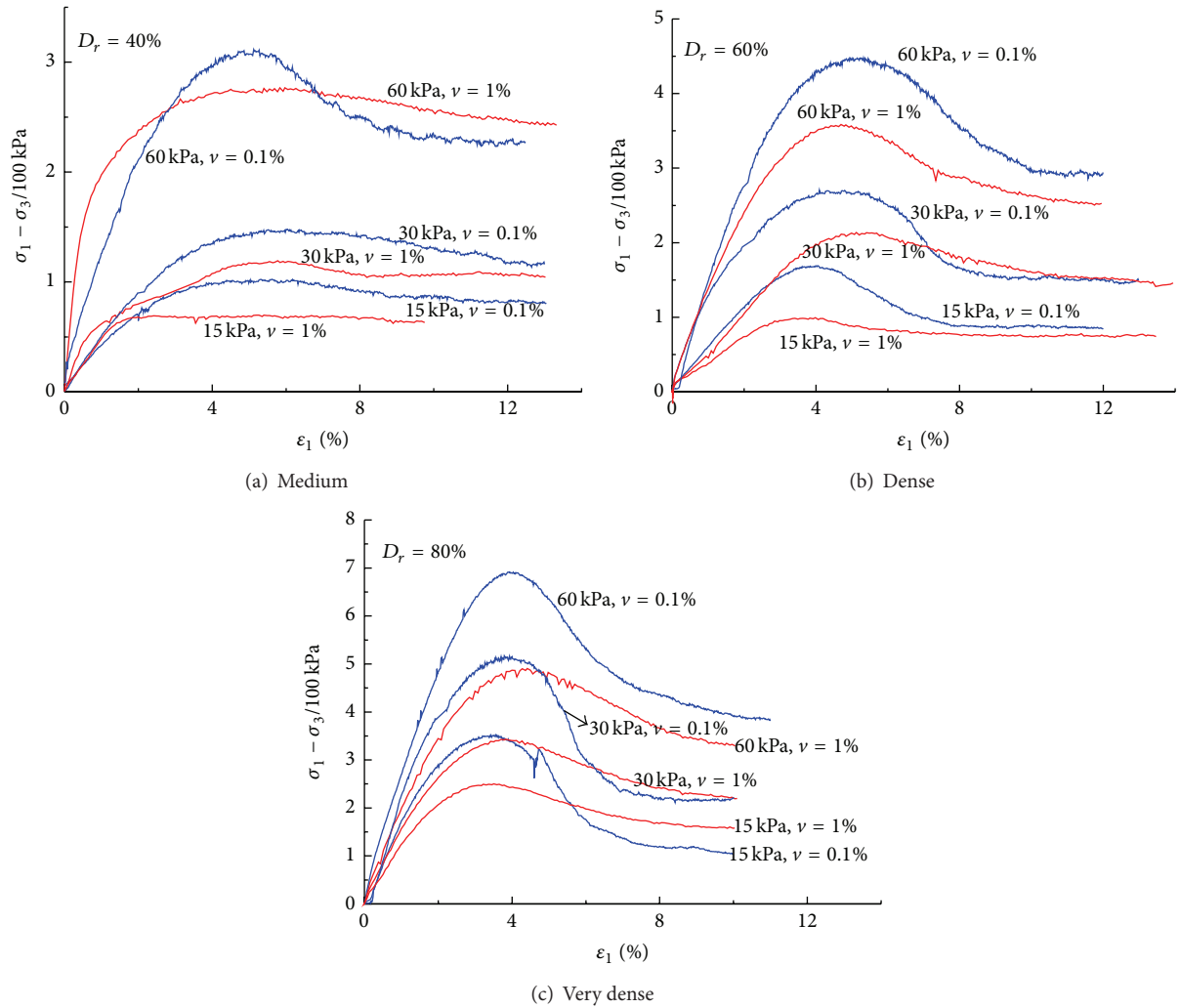


FIGURE 2: Stress-strain curves of TJ-1.

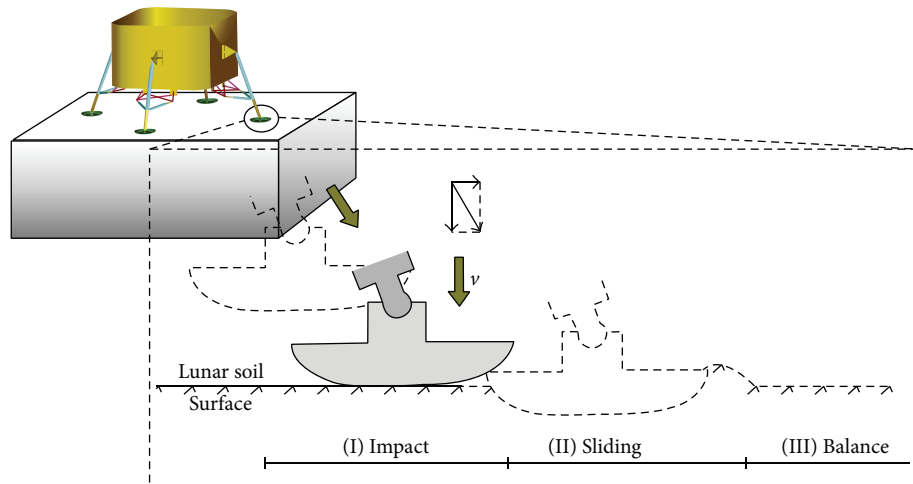
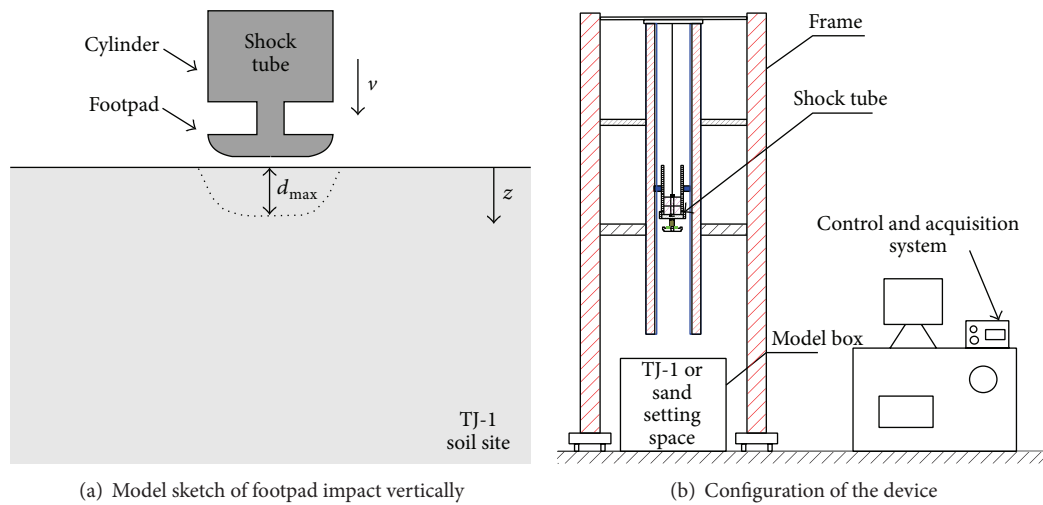
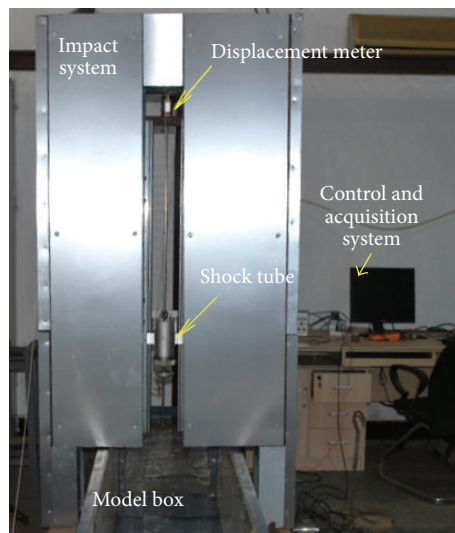


FIGURE 3: Landing process of footpad.



(a) Model sketch of footpad impact vertically

(b) Configuration of the device



(c) Photo of the self-made apparatus

FIGURE 4: Impact model and test apparatus.

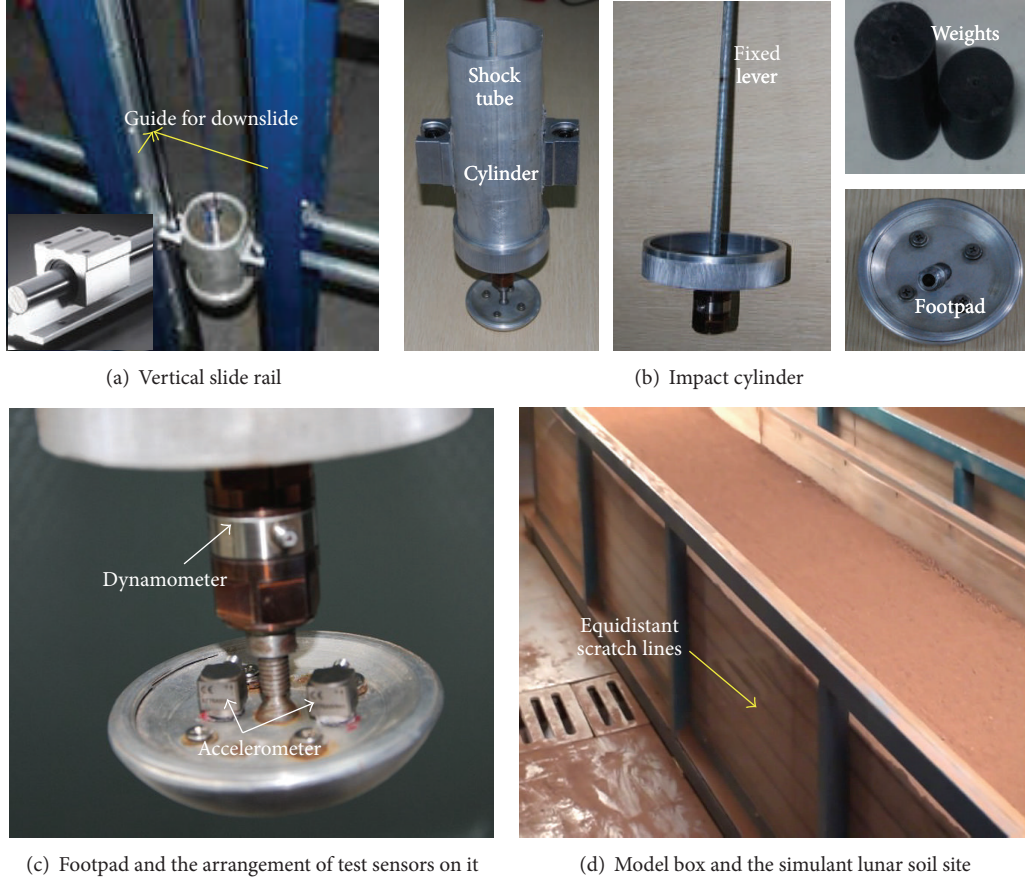


FIGURE 5: Detail of the apparatus component.

TABLE 2: Similar scale between Earth and Moon.

Quantities	Acceleration	Length	Velocity	Force	Stress	Mass
Scale factor	n	$1/n$	1	$1/n^2$	1	$1/n^3$
Test scale	6	$1/6$	1	$1/36$	1	$1/216$

the results of $1/6$ scale tests when under an Earth gravity field and the full-scale tests under a simulated lunar gravity field showed a remarkable degree of similarity. Other scholars also have done researches in this area [30–32]. Because of space restrictions, this paper does not detail the feasibility of the scale selected.

A prototype landing test device, which is used to research response law of footpad in various masses and velocities, includes impact, control and acquisition systems, and a model box, as shown in Figures 4(b) and 4(c). The impact system consists of an overall frame, vertical slide rail, and shock tube. The shock tube has a certain mass and can fall freely along the vertical slide rail at a certain velocity to impact the soil site in the model box, as shown in Figure 5(a). The specified impact velocity is obtained by adjusting the drop height.

The shock tube is composed of a cylinder, fixed lever, weights, and footpad, as shown in Figure 5(b). The footpad, made of hard aluminum, is fixed on a fixed lever and the

weights are fastened by the fixed lever and bolts in the cylinder to avoid collision, one with the other. The impact mass is controlled by changing the numbers of weights.

As shown in Figure 6, there are three kinds of high precision transducers in the impact test. Figure 6(a) shows the magnetostrictive displacement/speed sensor produced by the MTS Systems Corporation, type RHM1200MR021V0. It can be used to measure the changes of velocity and displacement of the footpad simultaneously. Its displacement measurement range is $0\sim 5000$ mm, with a precision of 0.001% FSO (i.e., $\pm 5\ \mu\text{m}$). The velocity measurement range is $0\sim 10$ m/s, with a precision of 0.5% FSO; its resolution is ± 0.1 mm/s, and frequency response time is up to 0.2 ms. Figure 6(b) shows the piezoelectric dynamometer produced by Jiangsu Lianneng Electronic Technology Co., Ltd. in China, type CL-YD-320, with a measurement range of $0\sim 5$ kN and an error range of $\pm 1\%$ FSO. Figure 6(c) shows the uniaxial piezoelectric accelerometer produced by Kistler Group in Switzerland, type 8776A50. Its range is $0\sim 50$ g, frequency range $0.5\sim 10000$ Hz, and amplitude nonlinearity $\pm 1\%$ FSO. The accelerometer and dynamometer are arranged, as in Figure 5(c), to measure acceleration and impact force. Two accelerometers are set along the radial direction for mutual checking.

In the mixed-measurement system, studies have shown that there is a phase delay between the records of different

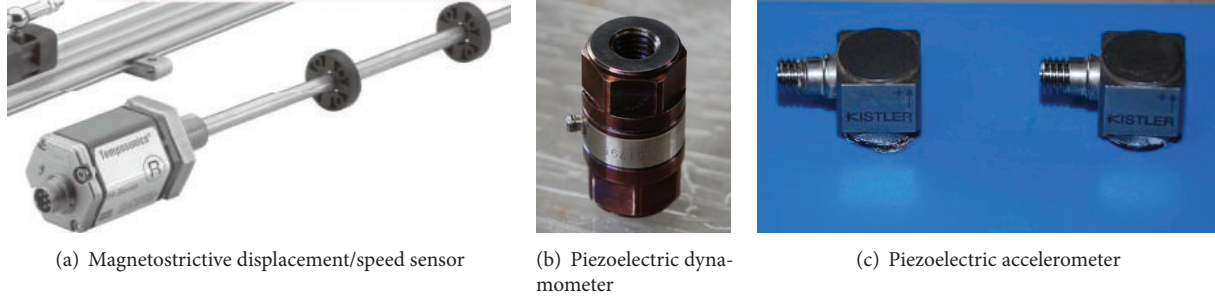


FIGURE 6: Transducers used in the impact test.



FIGURE 7: Data acquisition system of NI.

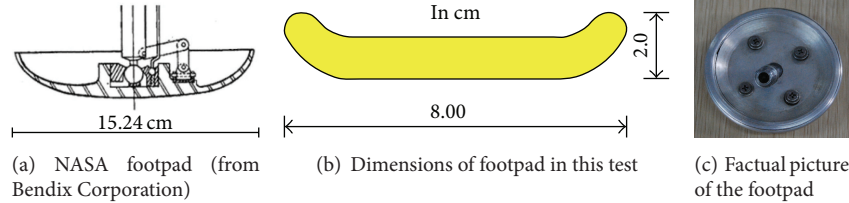


FIGURE 8: Experimental footpad.

sensors [33]. The sensors' synchronization is important especially when the impact of the landing lasts only a few milliseconds. The Compact DAQ-based data acquisition system produced by National Instruments is used in the experiment. The system controls the state of motion and collects the real-time dynamic response data relating to the footpad. The hardware contains a four-slot chassis cDAQ-9174 and 32-channel acquisition module NI-9205, as shown in Figure 7. This system features 16-bit resolution and a maximum sample rate of 250 kS/s. It has four 32-bit timers that are built in to share clocks for the mixed-measurement systems. In the experiment, digital analog converter will record the sampling time, up to 0.1 ms. Settling time for multichannel measurements is ± 120 ppm of full-scale step (± 8 LSB) with $4 \mu\text{s}$ convert interval.

The footpad used in the experiment is modeled after some simplification on the NASA footpad mentioned by Bendix Corporation [2], as shown in Figure 8.

The model box, of size $399 \text{ cm} \times 49 \text{ cm} \times 50 \text{ cm}$, consists of steel frames and plexiglass installed as side walls to ensure overall stiffness and visibility. Equidistant scratch lines, every

5 cm, are scribed into the surface of the plexiglass as shown in Figure 5(d).

2.3. Experimental Procedures

2.3.1. Calibration. Before the experiment, each sensor was calibrated and showed good linearity. Because of space limitations the relevant curves are not given in this paper.

The relationship between the drop height and impact velocity was also confirmed by carrying out drop tests. The results are shown in Figure 9 and illustrate good repeatability. The drop height and impact velocity relationship fits a quadratic relationship.

2.3.2. Site Preparation. Owing to the uneven distribution of lunar soil simulant particle sizes, the dry pluviation sample preparation method causes coarse and fine particles to segregate, leading to various and undesirable relative densities [34]. To ensure overall uniformity, the tamping method (layering, filling, compaction, and leveling) was used to prepare soil sites with 6 layers in total, 5 cm per layer.

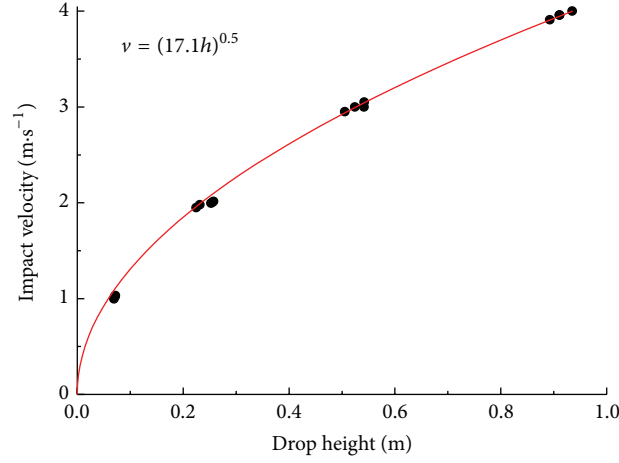


FIGURE 9: Relation between drop height and impact velocity.

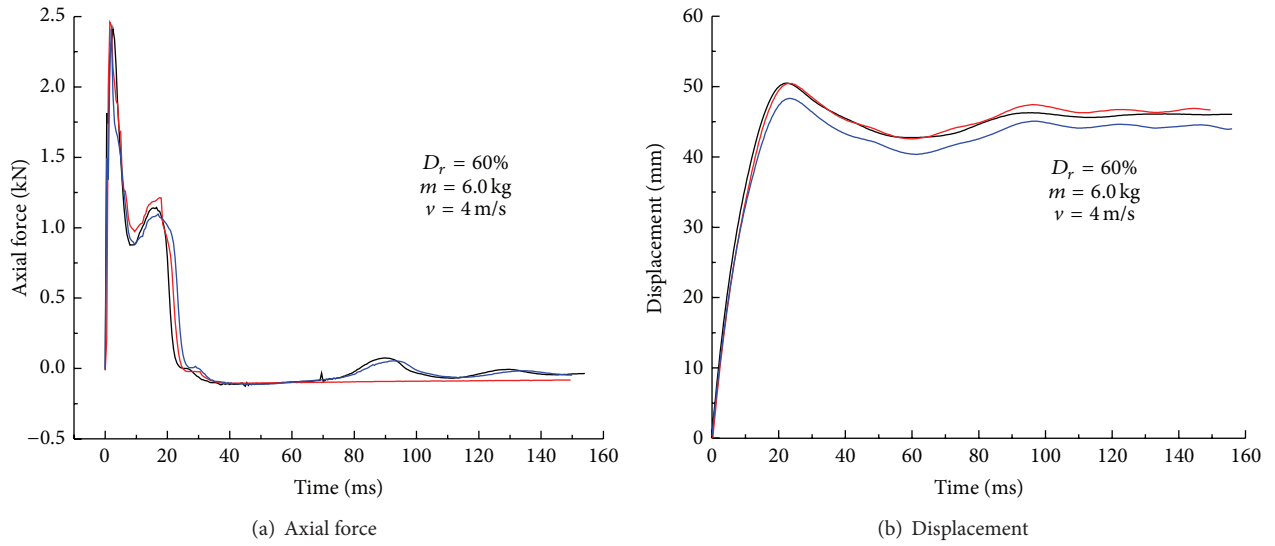


FIGURE 10: Time-history curves of impact response.

TABLE 3: Comparison of impact velocity.

Cases	NASA test [2]	Apollo [39]	Luna 16 [40]
velocity/m·s ⁻¹	0.3~4.57	0.3~0.9	<2.4

For each relative density, soil with a specified mass was uniformly placed into each layer and aligned with the scratch lines as shown in Figure 5(d). The relative densities selected in the model tests were 40%, 60%, and 80%, respectively, corresponding to the density of the simulant lunar soil samples in triaxial tests.

2.3.3. Test Scheme and Procedures. According to the mass of the lunar lander being simulated, the shock tube mass was variously set at 1.5 kg, 3.0 kg, and 6.0 kg. Table 3 presents the impact velocities in the impact model tests, values that can be reached in the real landing process.

TABLE 4: Scheme of the model tests.

Variables	$D_r/\%$	$v/\text{m}\cdot\text{s}^{-1}$	m/kg	Test number
Value	40, 60, 80	1.0, 2.0, 4.0	1.5, 3.0, 6.0	27

The scheme of the impact model tests is detailed in Table 4, which mainly includes the influencing factors of relative density, impact velocity, and impact mass.

The steps taken in each test are as follows.

- (1) Prepare the soil sites with a specific relative density.
- (2) Lift the shock tube with a particular mass, and fasten it at the height calibrated by the displacement meter.
- (3) Turn on the acquisition system.
- (4) Release the shock tube to impact soil site, and monitor and save the test data.

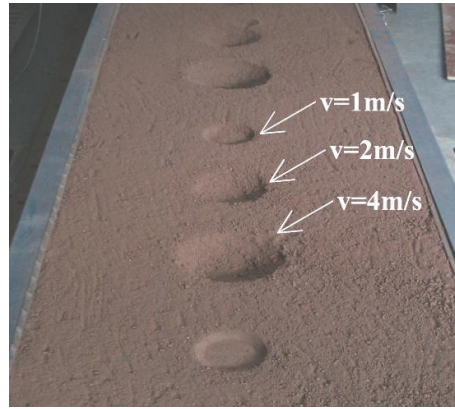
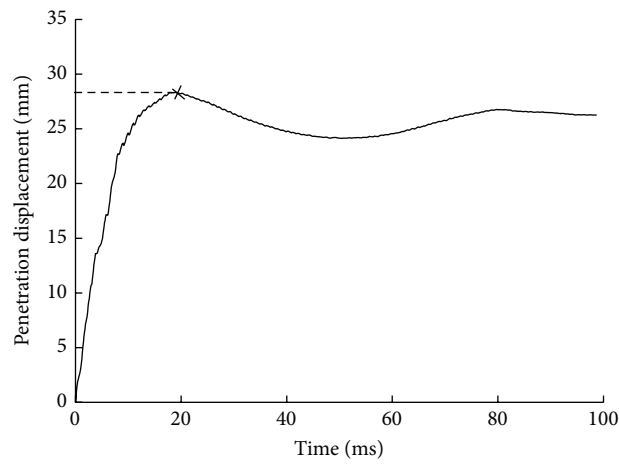
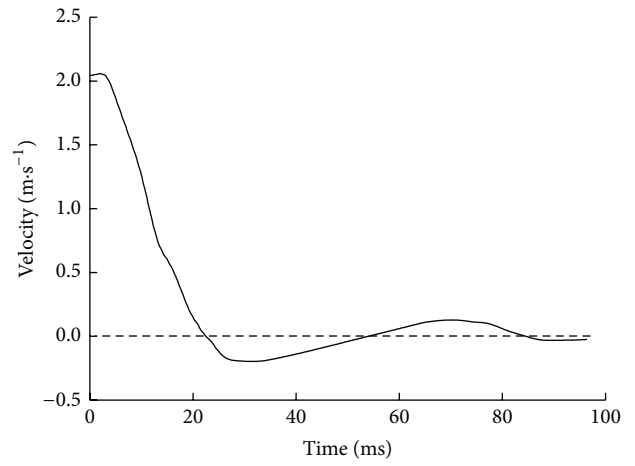


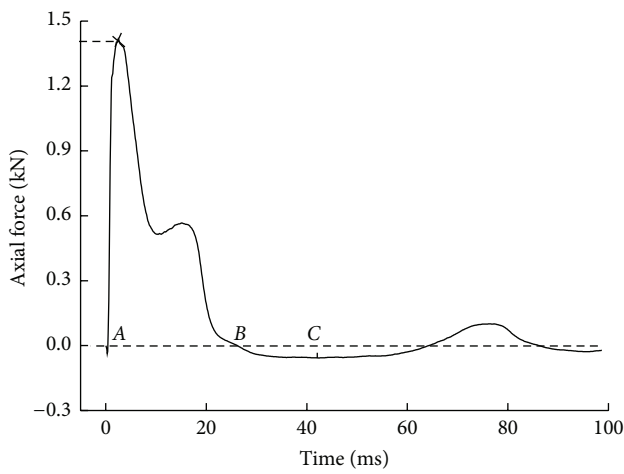
FIGURE 11: Impact craters on TJ-1 soil site ($D_r = 60\%$).



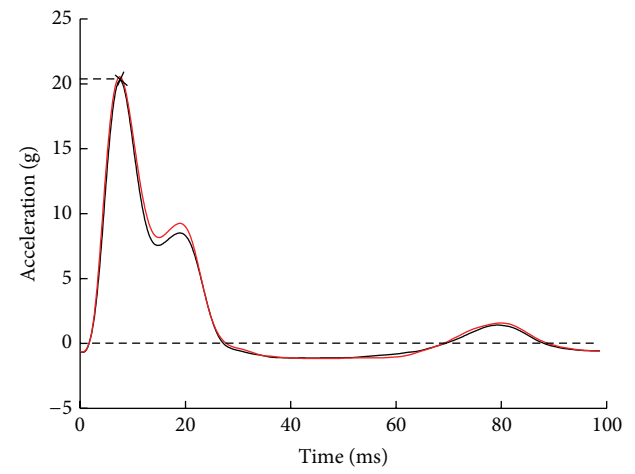
(a) Curves of displacement



(b) Curves of velocity



(c) Curves of axial force



(d) Curves of acceleration

FIGURE 12: Time-history curves of contact-dynamic characteristics with $D_r = 60\%$, $v = 2 \text{ m/s}$, and $m = 6 \text{ kg}$.

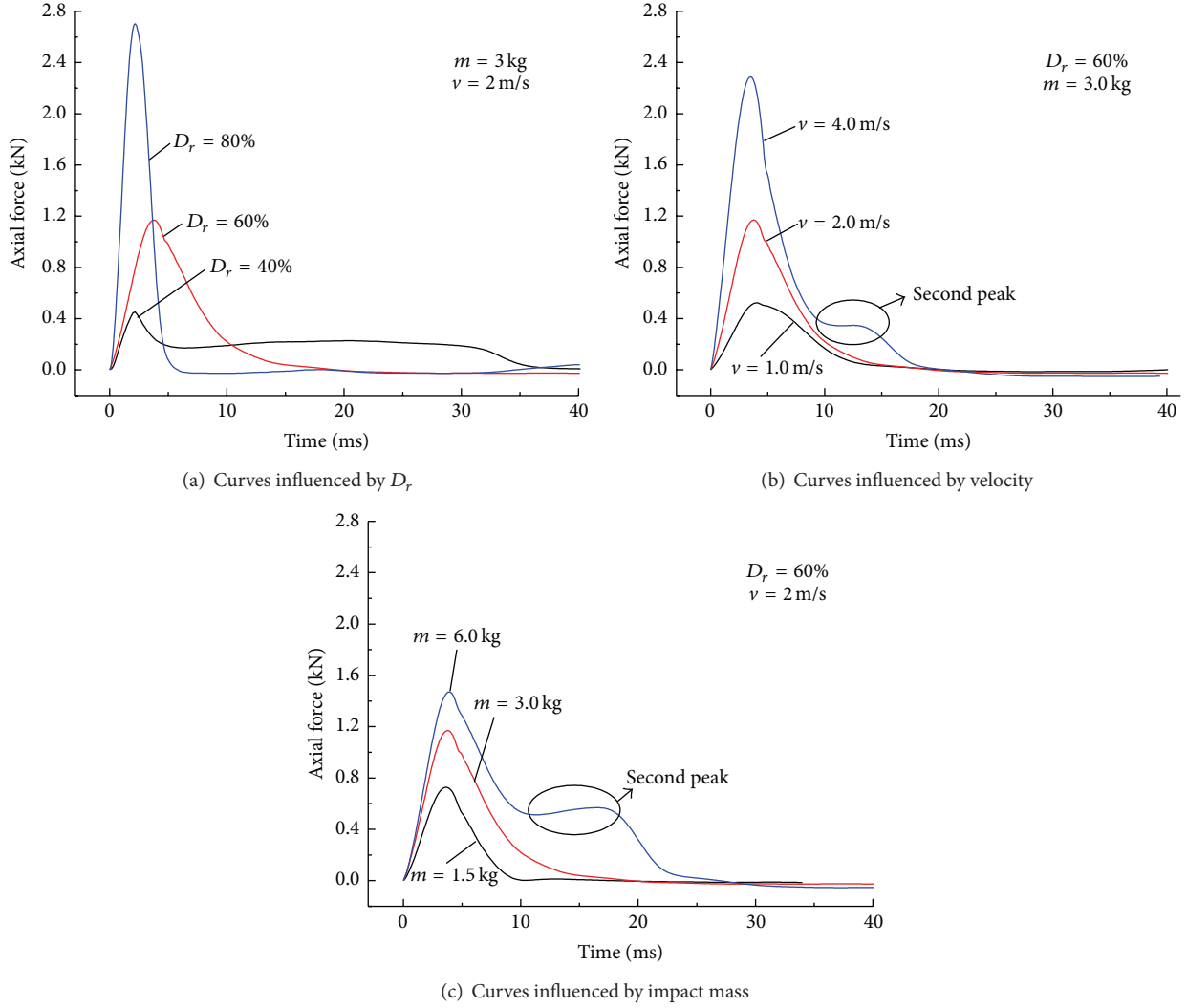


FIGURE 13: Time-history curves of axial force under different testing condition.

3. Results of the Vertical Impact Tests

Repeated tests were conducted under the same conditions to verify the reliability of the test results. Figure 10 shows the time-history curves of axial force and penetration displacement, which show good repeatability, proving that the test results are reliable.

3.1. Site Deformation. The results of 27 groups of tests indicate that the shapes of impact craters are similar and resemble a basin. The sizes and depths of the craters, however, are different due to changes in test conditions. Larger impact velocities generate dramatically larger and deeper craters. Figure 11 shows the craters formed by the shock tube impacting with different velocities on the TJ-1 simulant soil site when $D_r = 60\%$.

3.2. Time-Related Characteristics of Response. The shapes of the dynamic response curves are similar even for different testing conditions. Figure 12 gives the typical time-history

dynamic response curves for the footpad, including displacement, velocity, axial force, and acceleration curves at the instant of contact, when $D_r = 60\%$, $v = 2$ m/s, and $m = 6$ kg. It can be seen in Figure 12(a) that the footpad reaches the maximum penetration depth at 25 milliseconds. With the time increasing, the penetration depth initially decreases, increases later, and eventually reaches stability. This indicates that the footpad rebounds after it reaches the maximum depth, then again impacts the simulant lunar soil site, and after further small vibrations tends to finally become stable.

The velocity time-history curve shown in Figure 12(b) indicates that the initial high velocity is at 1 ms~3 ms, since at that stage gravity far overcomes the resistance of the lunar soil stimulant, before decreasing rapidly. It then fluctuates weakly on the horizontal axis and trends to zero.

Figure 12(c) indicates that the axial force in the footpad reaches its maximum value in the initial 5 milliseconds before reducing and creating a second peak. The resultant impulse is found to be 13.02 N·s, the integral given by the area enclosed by curve *ab* in Figure 12(c), which approximately equals

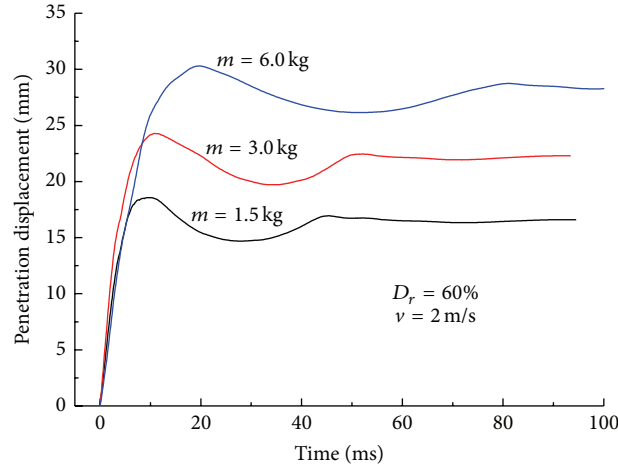


FIGURE 14: Time-history curves of penetration displacement with $D_r = 60\%$, $v = 2$ m/s.

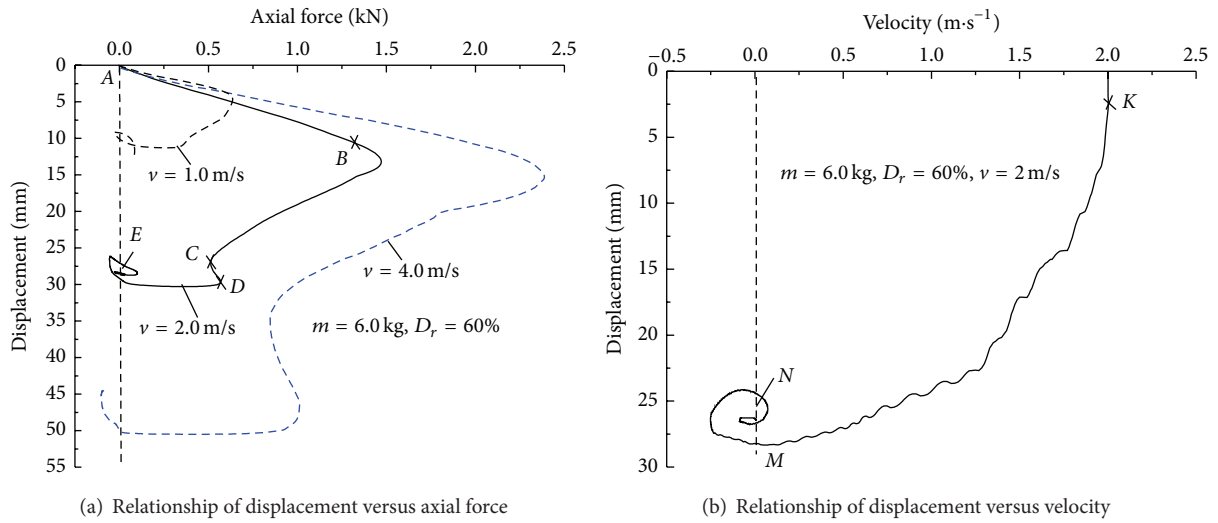


FIGURE 15: Test result of $D_r = 60\%$, $m = 6$ kg.

the change in momentum, of 13.09 kg·m/s (based on the reduction in initial velocity 2 m/s downwards to the velocity 0.182 m/s upwards). A comparison of Figures 12(c) and 12(a) indicates that the displacement response lags behind that of the axial force.

As shown in Figure 12(d), the two acceleration time-history curves recorded by the two accelerometers set on the footpad as shown in Figure 5(c) are in good agreement. A comparison of Figures 12(d) and 12(c) shows that acceleration and axial force responses are in phase.

The force the footpad bears during the impact process is critical for a safe landing. Figure 13 shows the time-history curves of axial force for various relative densities, impact velocities, and impact masses. These curves indicate that the various modes of axial force are similar; in the initial instant contact force grows quickly to its peak value in only a few milliseconds. It then declines to a lower level and tends to be finally equal to the weight of the shock tube.

Figure 13(a) shows the axial force response to the impact for soils of 3 different densities, which indicate that the

denser the site, the larger the peak axial force and the shorter the impact duration time. Figure 13(b) illustrates that the axial force increases approximately linearly with increasing impact velocity but the impact duration time increases little. Figure 13(c) demonstrates that the bigger the impact mass, the larger the peak axial force and the longer the impact duration time.

It is noteworthy that the axial forces remain almost unchanged in some cases in Figure 13 between the two peaks over quite long periods with respect to the whole process. A similar phenomenon was found in the footpad impact study made by NASA [2]. This phenomenon gives proof that the simulant lunar soil site reached a state of “flow failure” under impact. As in soil mechanics, “flow failures are characterized by a sudden loss of strength followed by a rapid development of large deformations [41].” The term “flow failure” is adopted here to describe the phenomenon that the deformation increases sharply when the axial force has a sharp decrease. From the present experiment, the occurrence of this phenomenon is conditioned. When the relative density

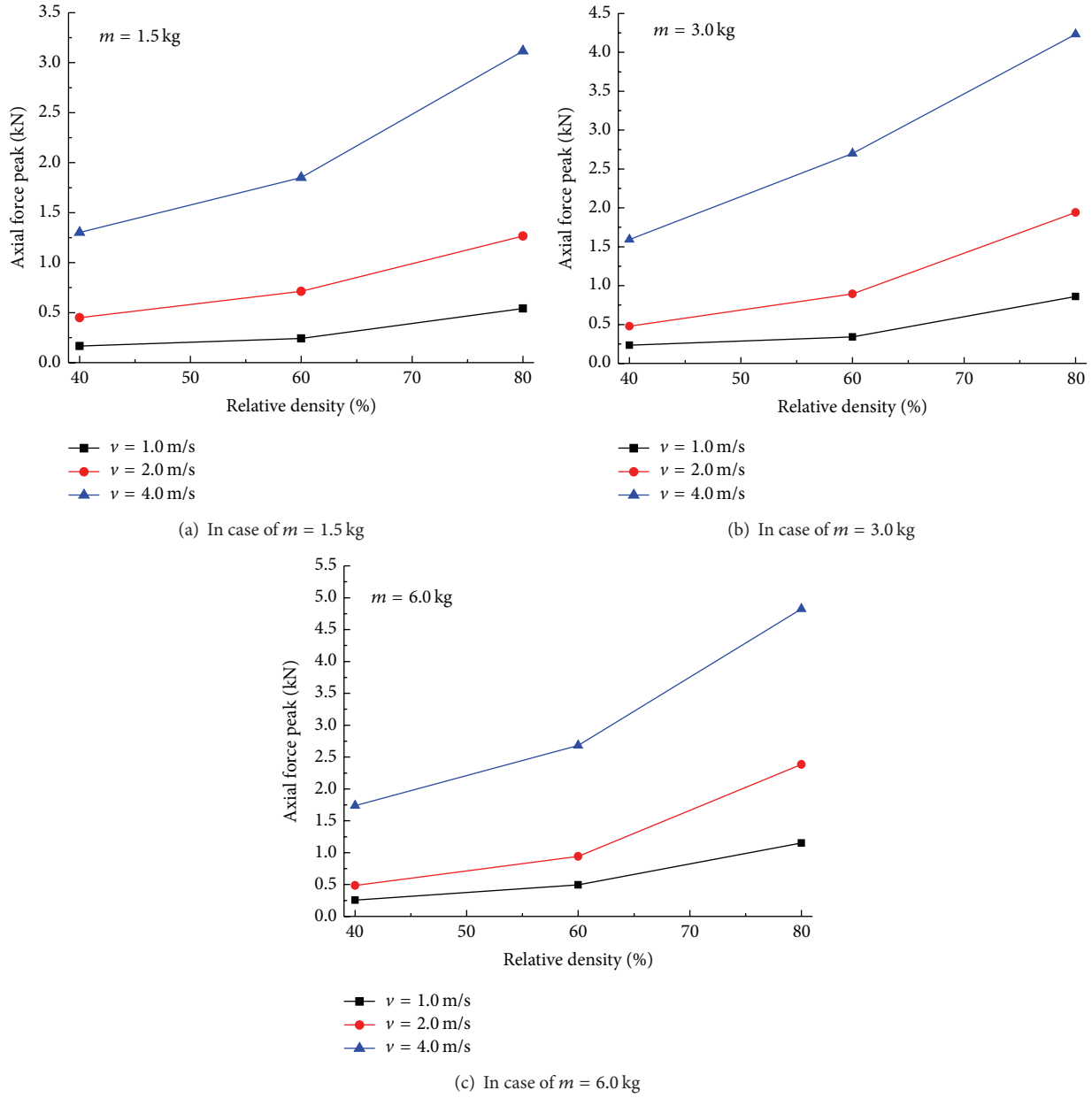


FIGURE 16: Effect of relative density on peak axial force.

of the simulant lunar soil site is low, the flow failure is more pronounced. For a specified relative density, the larger the impact velocity and the impact mass are, the easier it is for flow failure to occur. It can be deduced that there exists a critical impact momentum or kinetic energy value for a simulant lunar soil site of a specified density. When less than that critical value, the impact will not cause flow failure of the simulant lunar soil site. The explanation is that, with the footpad penetration depth increasing, if the underlying soil of the ground is not able to bear the impact, the soil will exhibit plastic flow failure; otherwise, if the underlying soil has a relatively great strength which is enough to carry the impact force, flow failure will not occur.

Penetration displacement is another major factor affecting landing safety. Figure 14 shows the time-history curves

of penetration displacement for $D_r = 60\%$ and $v = 2$ m/s and different impact masses. The time of the first impact all begins from the 0 point. The variations in penetration displacement patterns are similar, that is, a quick increase once the lander touches the site, a rebound after reaching the peak value, followed by a slight further impact before reaching an ultimate stability. The larger the impact mass, the larger the peak value and the ultimate stable penetration depth and the longer the rebound duration time.

3.3. Correlation of Axial Force and Penetration Displacement. Figure 15(a) shows the relationship between penetration displacement and axial force for $D_r = 60\%$, $m = 6$ kg, and different impact velocities. The curves shapes are similar.

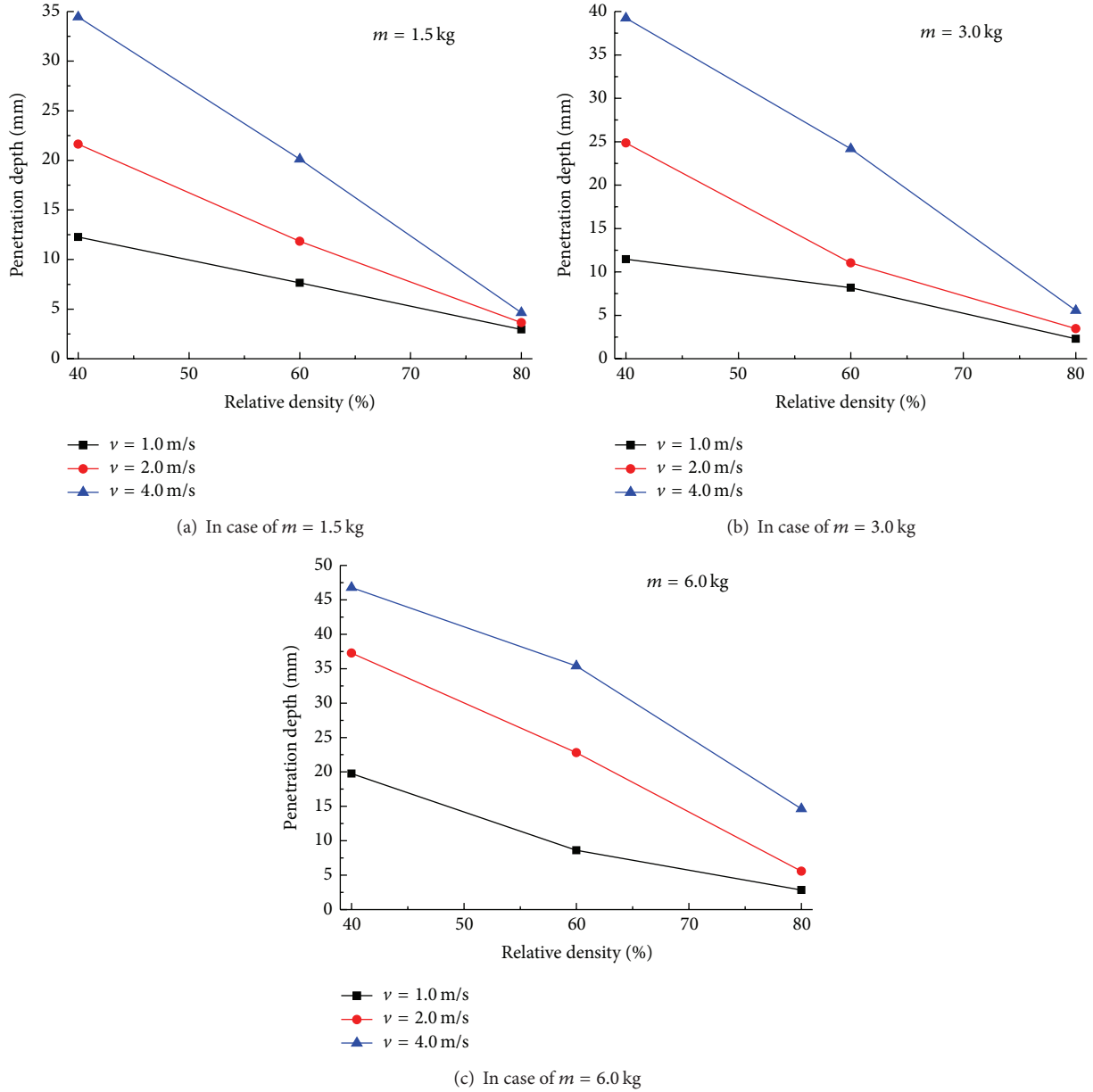


FIGURE 17: Effect of relative density on penetration depth.

The whole curve can be divided into 4 stages, denoted by the characters A, B, C, D, E as shown in Figure 15(a).

The curve in stage AB is approximately linear. The axial force on the footpad is generated by the dynamic interaction between shock tube and the compressed soil. The penetration displacement mainly is one of elastic compression deformation of the soil during this stage. In the shearing stage BC, part of the soil element under the footpad reaches failure, and the soil resistance decreases allowing shear deformation to occur. That is why the slope of the curve becomes negative. In the flow failure stage CD, due to the expansion of the affect zone surrounding the footpad, the resistance of the soil remains stable or increases a little, but large vertical deformation occurs and the footpad is deeply pierced. Note

that when the impact momentum or energy is smaller, there is no flow failure stage CD, as in the case of $v = 1.0$ m/s, as shown in Figure 15(a). In stage DE, because of the weak elastic properties of the lunar soil simulant, the footpad rebounds even off the surface, and the axial force decreases sharply and even turns negative. After fluctuating weakly, the displacement of the footpad tends to reach the ultimate point E and the axial force tends to be equal to the shock tube's gravity induced weight.

The velocity variation of the footpad on the vertical motion track is shown in Figure 15(b). In the instant of contact, the velocity increases to peak point K within a 2~3 mm penetration displacement due to the shock tube inertia. The velocity then decreases gradually until reaching

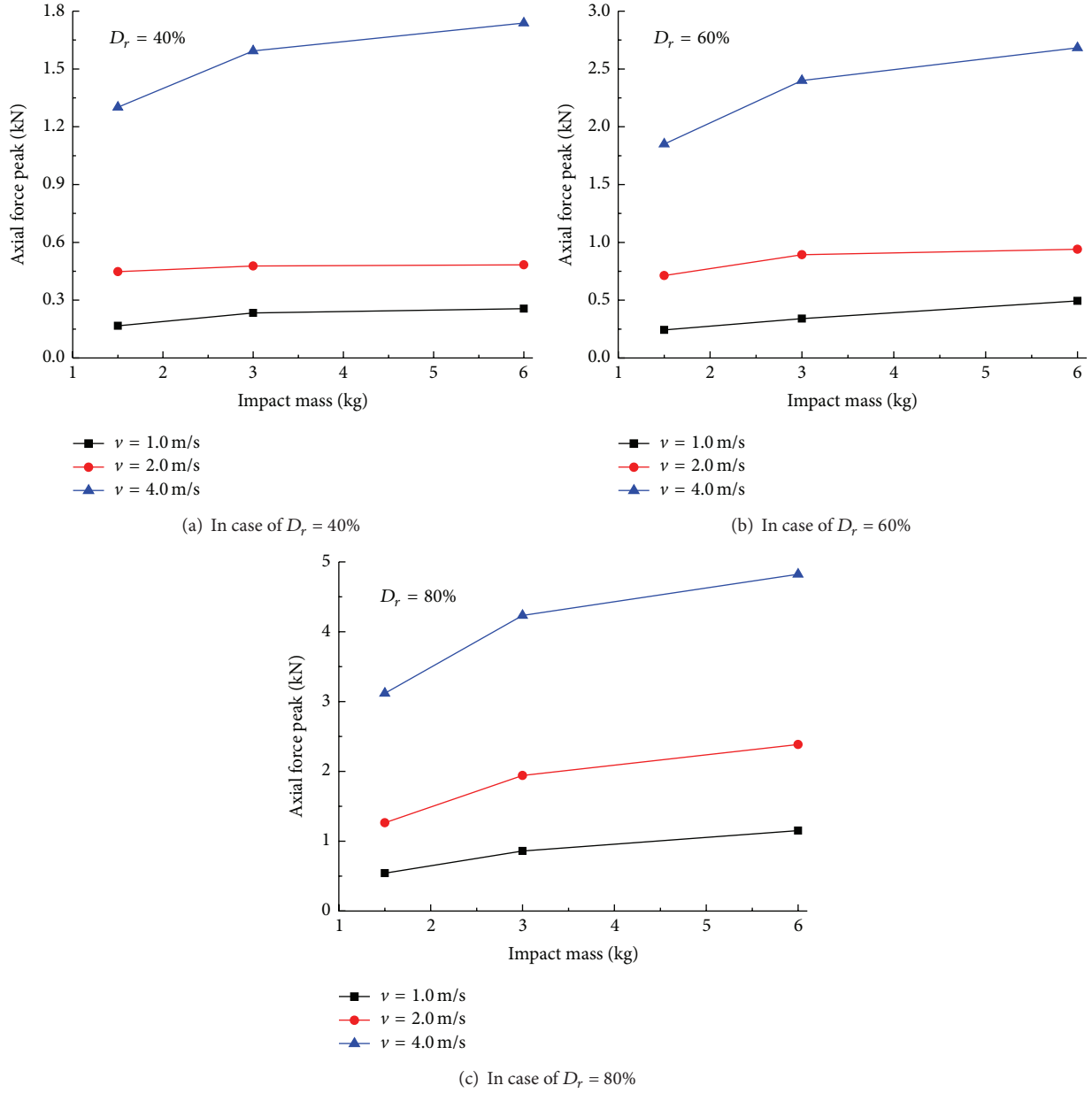


FIGURE 18: Effect of impact mass on peak axial force.

the maximum penetration displacement point M when the velocity equals zero. After fluctuating several times, it finally reaches the ultimate penetration point N .

3.4. Peak Feature of Dynamic Response. Other than the time-history characteristics of the footpad dynamic response in the instant of contact, the peak values themselves are essential for the design of the lander buffering system, especially the extent of penetration which is the stable penetration displacement. Peak values of axial force and acceleration are also essential.

Figures 16 and 17 show the effect of relative density on peak axial force and penetration depth, which indicates that peak axial force increases significantly as relative density increases in all test conditions, while penetration depth is reduced.

Figure 18 demonstrates that peak axial force is little affected by impact mass. When the impact mass is four times greater, peak axial force is only increased by 13%. In contrast to the influence of relative density, penetration depth increases almost linearly as impact mass increases, as shown in Figure 19, with an increase to 215% of the initial lowest impact mass.

Figure 20 shows the peak axial force is evidently affected by impact velocity; the increase ranges around 318%~693% as impact velocity increases four times. Figure 21 shows that the penetration depth also increases significantly as impact velocity increases in all test conditions.

In general, the peak axial force is influenced more significantly by relative density and impact velocity than by impact mass.

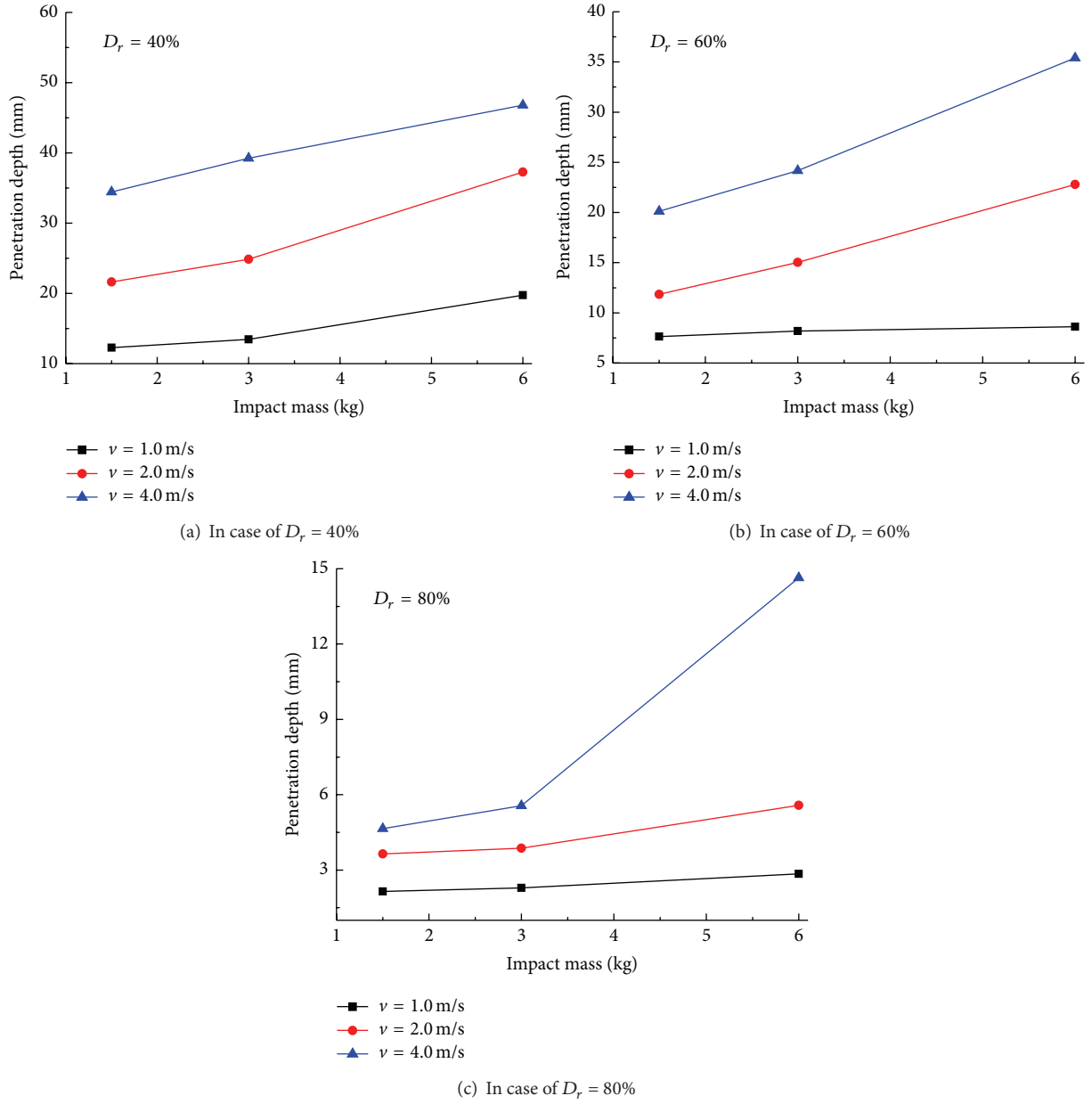


FIGURE 19: Effect of impact mass on penetration depth.

In order to comprehensively consider the influence of all control variables, the impact kinetic energy was set as an independent variable and the relationships between peak value dynamic responses of the footpad and kinetic energy are drawn as dots in Figure 22.

It can be concluded that, for different relative densities, the larger relative density leads to greater axial force and acceleration but smaller penetration depth; for the same relative density, the responsive peaks (axial force, penetration, and $m \cdot a_{\max}$) increase steadily as impact kinetic energy grows. The relationship can be expressed in the following exponential form:

$$C_j = a_j \cdot \left[\frac{(m \cdot v^2)}{2} \right]^{b_j}; \quad (j = 1, 2, 3), \quad (1)$$

where C_j ($j = 1, 2, 3$) are F_{\max} , d_{\max} , and $m \cdot a_{\max}$, respectively, and a_j , b_j ($j = 1, 2, 3$) are material parameters related to the relative density of lunar soil, as listed in Table 5. For a given impact kinetic energy and site relative density, the dynamic responsive peak can be calculated using (1). From the test results, the constants are given below. The curves employing the following constants are shown highlighted in the solid lines in Figure 22.

4. Numerical Study of the Impact Process

Since impact experiments are costly and the environmental conditions on the Moon are difficult to fully simulate, numerical analysis is commonly adopted to help understand the impact process consequences and make further predictions

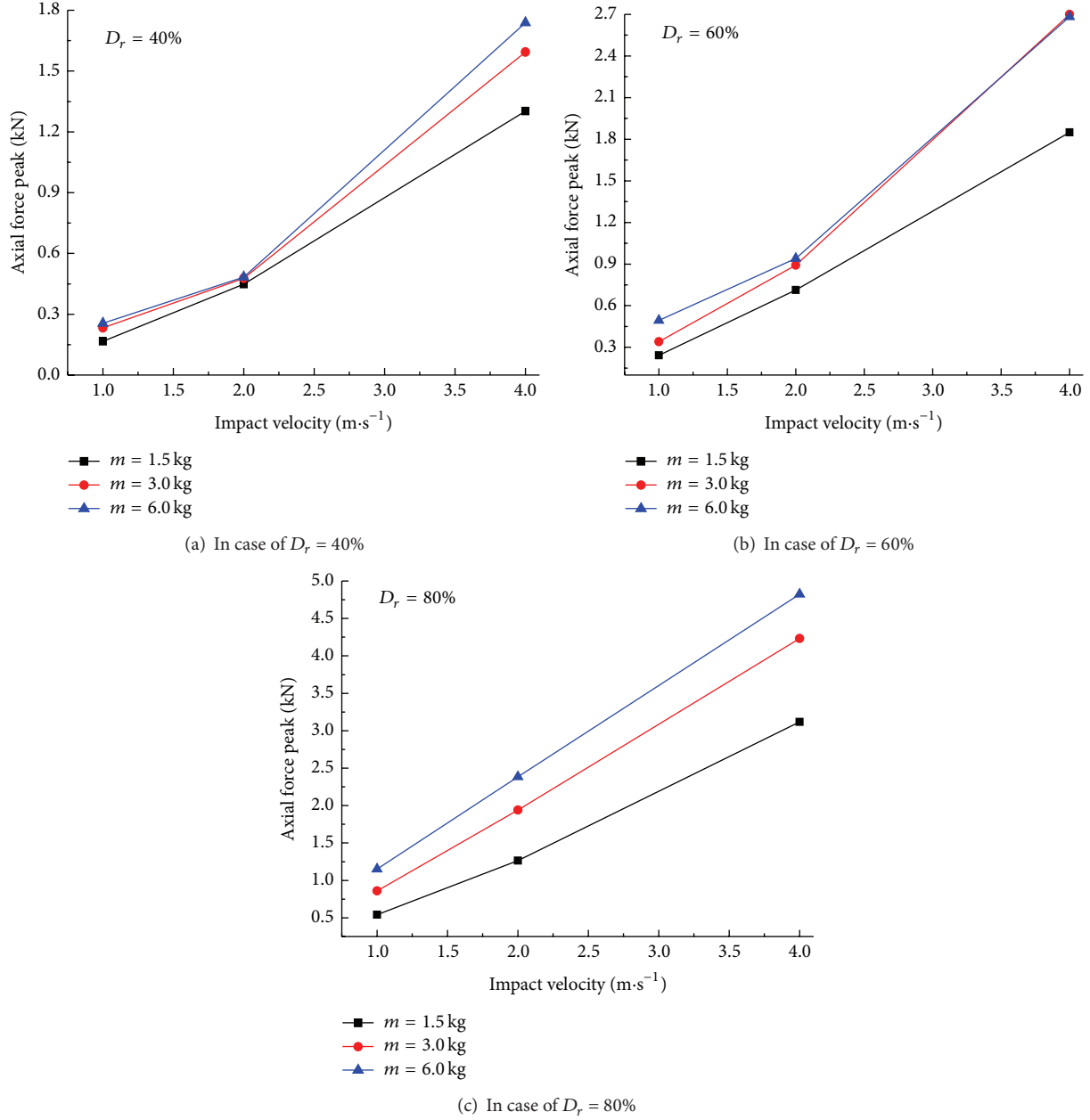


FIGURE 20: Effect of impact velocity on peak axial force.

TABLE 5: Values of a_j, b_j .

D_r	Peak axial force		Penetration depth		$m \cdot a_{\max}$	
	a_1	b_1	a_2	b_2	a_3	b_3
40%	257.03	0.52	18.87	0.42	11.84	0.49
60%	434.13	0.50	9.51	0.41	32.33	0.43
85%	822.51	0.47	4.80	0.32	57.33	0.43

[42]. Considering the special granularity and interparticle attraction of lunar soil, it is of great interest to simulate lunar soil by discrete element method (DEM) [43]. However, the finite element method (FEM) is still used in this

paper for the relatively mature commercial software and more understanding of the parameters required for analysis. In this paper, the numerical simulation is carried out on the commercial software Abaqus, for its good capabilities in analyzing nonlinear, transient dynamics problems. The numerical simulation is carried out on the EXPLICIT module, in a 3D visualization dynamic format, with geometric large deformation nonlinear analysis. The impact experiment model is taken as the prototype of the numerical FEM analysis. Then the results of the numerical analysis were compared with those of experiment, so as to verify the validity of the numerical model. The brief description of the numerical modeling and the simulation is given below; some details can also be seen in [44].

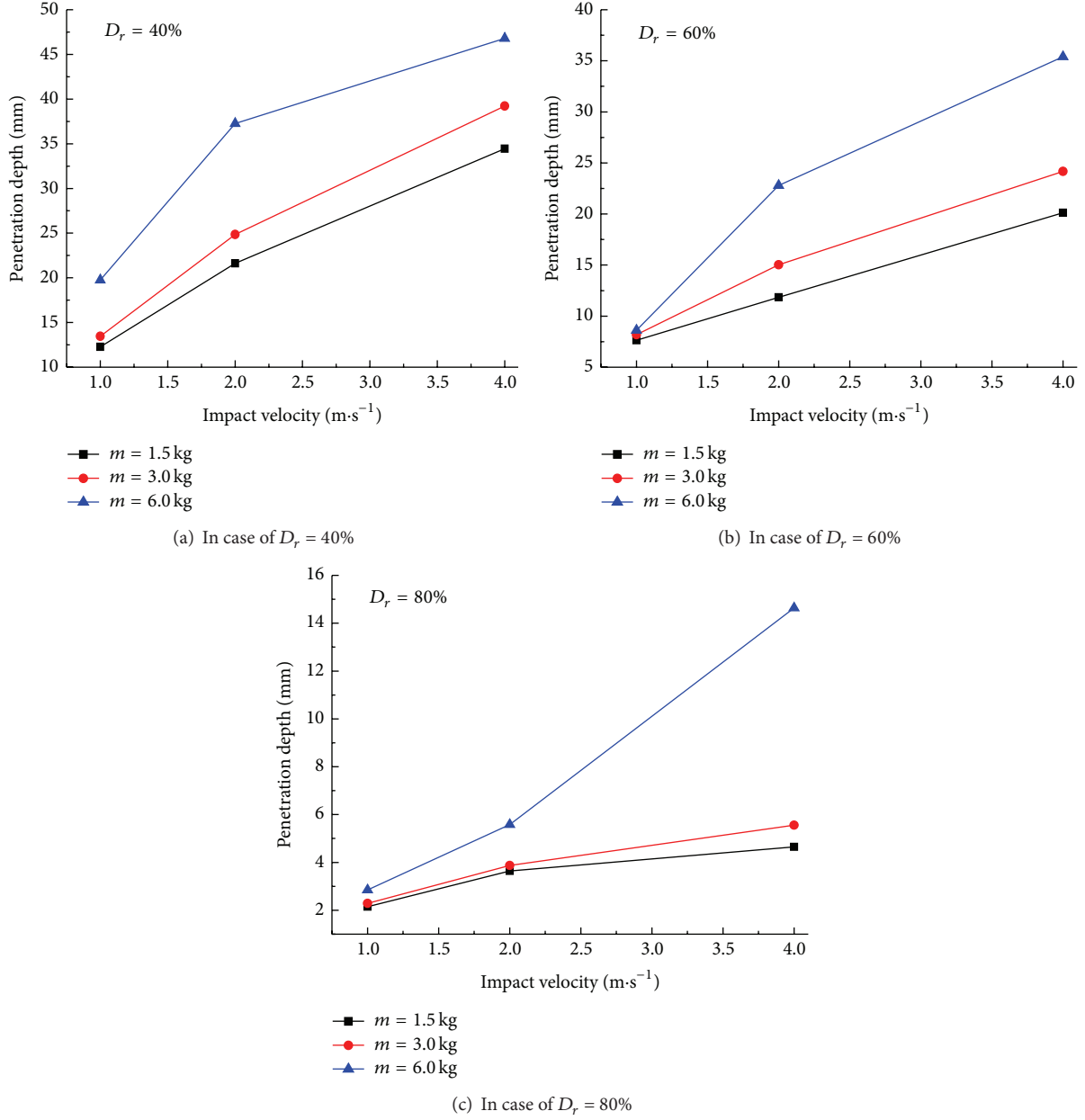


FIGURE 21: Effect of impact velocity on penetration depth.

4.1. FEM Model

4.1.1. Model of Shock Tube and Site. The appearance of the footpad model is shown in Figure 23(a). Due to the irregular shape, the shock tube is represented as thousands of four-node, 3D tetrahedron elements. The mass of the shock tube is controlled by adjusting the height of the cylinder.

Using the artificial truncation boundary, a cube with side length L was taken as the finite element analysis area, discretized into 8-node hexahedron elements. L is the characteristic width of the simulant soil site in the numerical simulation model, which is determined by trial computations until the boundary effect is eliminated. The site area was divided into two meshing zones as shown in Figure 23(b). Zone 1, where stress is concentrated and large plastic deformation

occurs under impact load, is meshed into even smaller and denser grids than those of Zone 2. In our study, L was set as 500 mm, and the side length of Zone 1 with cell size 2.5 mm was 250 mm, while the cell size in Zone 2 was 5 mm.

4.1.2. Model of Soil-Footpad Interface. The shock tube and simulant lunar soil interact at the soil-footpad interface. As shown in Figure 24, the contact face transfers interaction forces in both tangential and normal directions. The contact stresses are applied to the following restrictions.

When the footpad and the simulant lunar soil are not in contact,

$$\sigma_n = 0, \quad \tau_s = 0. \quad (2)$$

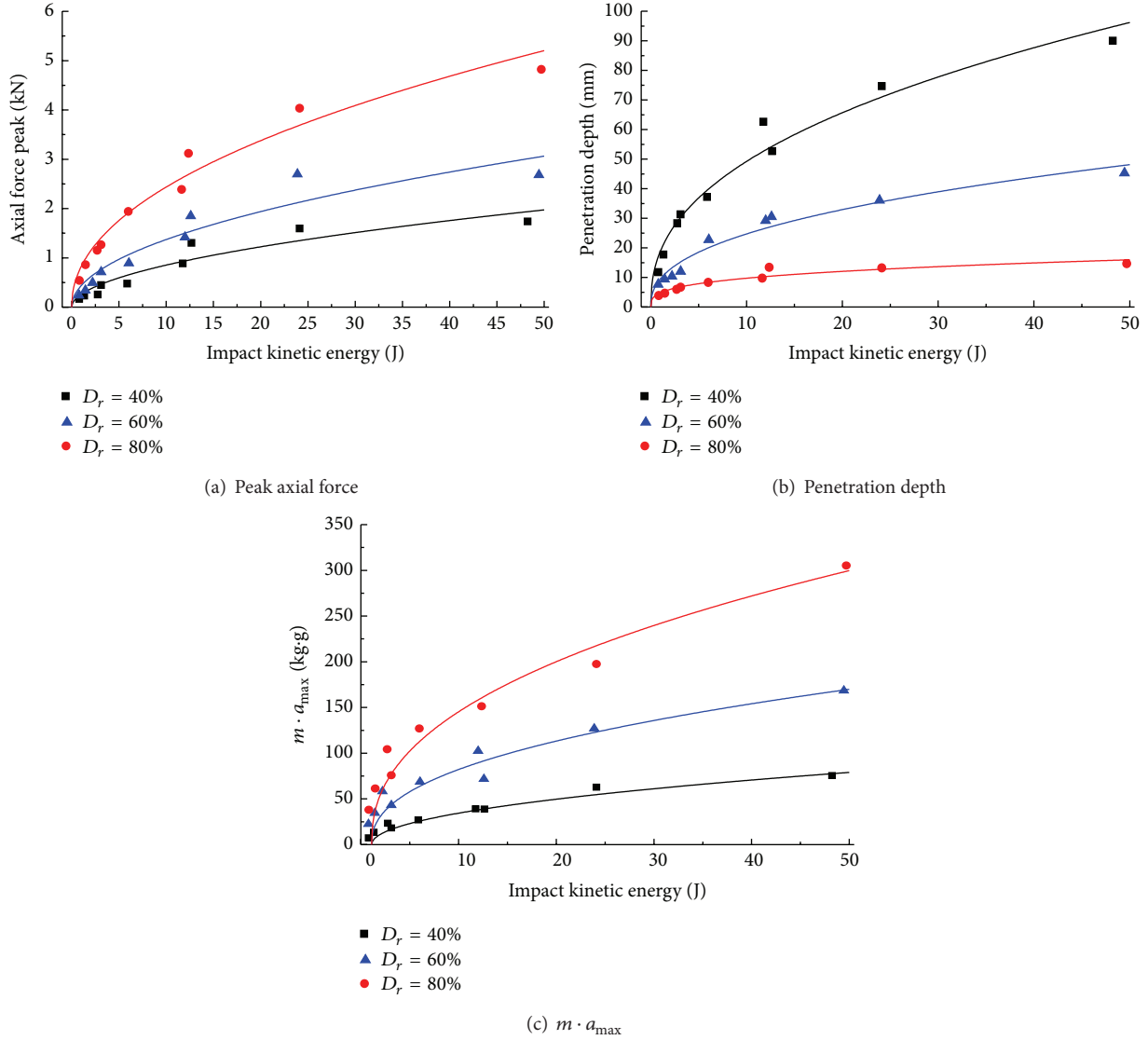


FIGURE 22: Relationship of peak features with impact kinetic energy.

Normal stress is generated as the two sides make contact. The stresses on the nodes of the contact surface satisfy the following relationships:

$$\begin{aligned} \sigma_n(\text{footpad}) &= \sigma_n(\text{soil}), \\ \tau_s(\text{footpad}) &= \tau_s(\text{soil}) \leq \tau_{\text{crit}}. \end{aligned} \quad (3)$$

σ_n is not allowed tensile stress; when tensile stress appears it is considered the separation which appeared. For τ_s , when the shear stress in the interface is less than the limiting value, the two sides bond, and when the limiting shear stress is reached, the two sides begin to slip. The critical value is given by

$$\tau_{\text{crit}} = \mu \cdot \sigma_n, \quad (4)$$

where μ is the friction coefficient, determined from interface shearing tests of the footpad made aluminum alloy and the TJ-1.

In the Abaqus software, the master-slave interface model was adopted to simulate the interaction. The bottom surface of the footpad was set as the master surface and the top surface of the simulant lunar soil sites as the slave surface, shown in Figure 24. Through face-face mesh generation method and setting the friction coefficient, the aforementioned contact model is established.

Figure 25 shows the interface friction characteristics between the lunar soil simulant and the hard aluminum (the same material as the footpad) gained from direct shear tests. The interface shear behavior can be regarded as ideal elastoplastic. The range of friction coefficient at the contact surface is 0.58~0.64 by fitting test data, which is little affected by relative density. In this study, the friction coefficient has been taken as 0.62.

4.1.3. Constitutive Model of Lunar Soil Simulant TJ-1. Taking the two characteristics of TJ-1 into account, that is, the

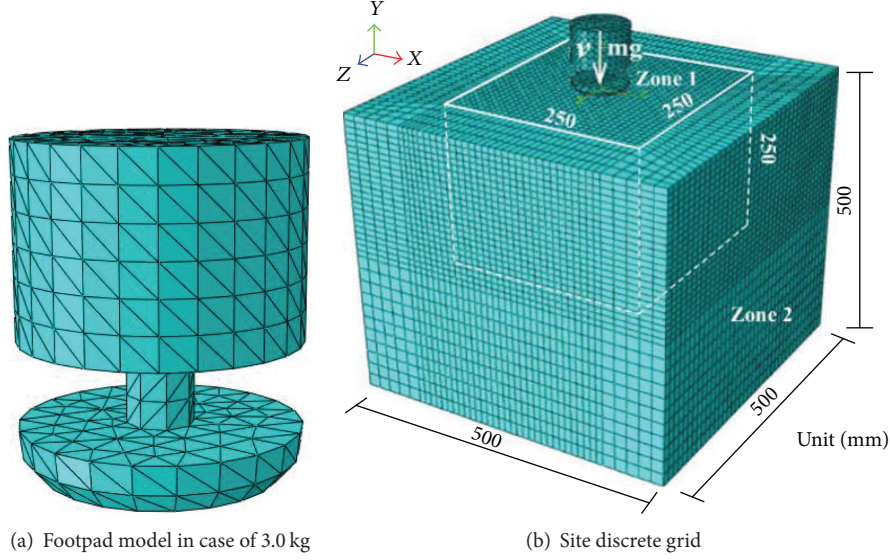


FIGURE 23: Grid of calculated model.

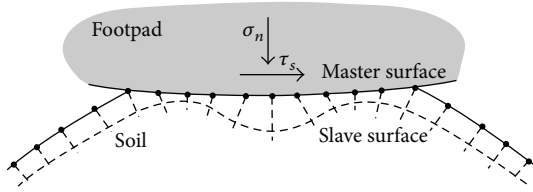


FIGURE 24: Footpad and soil in contact.

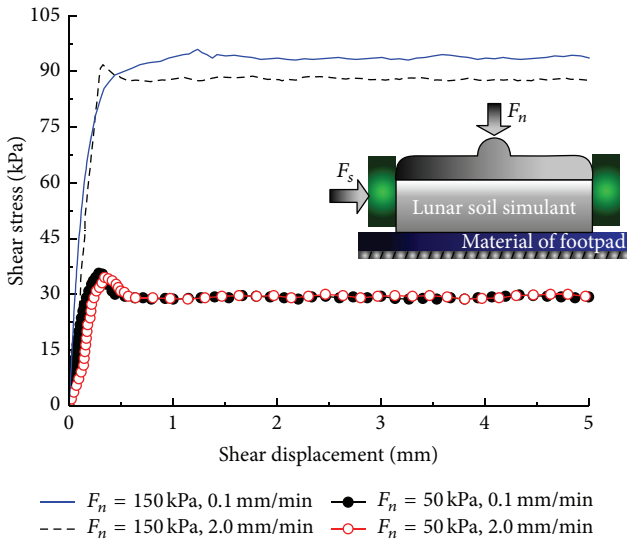


FIGURE 25: Shear test curves of soil-structure interface.

large internal friction angle ($38.5^\circ \sim 50.9^\circ$) and the strong strain-softening behavior, as shown in Figure 2, the elastoplastic Mohr-Coulomb constitutive model which satisfies

the nonassociative flow rule was selected for the study. The function of the yield surface in p - q space (Figure 26) is

$$F = R_{mc}q - p \tan \varphi - c, \quad (5)$$

where

$$p = \frac{1}{3} (\sigma_1 + \sigma_2 + \sigma_3),$$

$$q = (\sigma_1 - \sigma_3),$$

$$R_{mc} = \frac{\sin(\Theta + \pi/3)}{(\sqrt{3} \cos \varphi)} + \frac{\cos(\Theta + \pi/3) \tan \varphi}{3}, \quad (6)$$

$$\cos 3\Theta = \frac{J_3}{q^3}$$

and J_3 is the third invariant of the stress tensor, φ the internal friction angle, and c cohesion of the simulant lunar soil. The cohesion c was set as the hardening parameter to describe the strain-softening properties, which vary with equivalent plastic strain $\bar{\epsilon}^p$, as shown in Figure 26(b), where c_p and c_r are the peak and residual cohesion values, respectively.

In the elastic stage, the stress-strain relationship obeys Hooke's law, and the relevant parameters are Young's modulus and Poisson's ratio. Since the affected area is near the surface, Young's modulus is fitted from the laboratory results under small confining pressures. The empirical formula proposed by Janbu [45] is utilized in this paper, as shown in

$$E = K \cdot p_a \cdot \left(\frac{\sigma_3}{p_a} \right)^n, \quad (7)$$

where p_a is atmospheric pressure, σ_3 is confining pressure, and K and n are material constants. The parameters used are listed in Table 6.

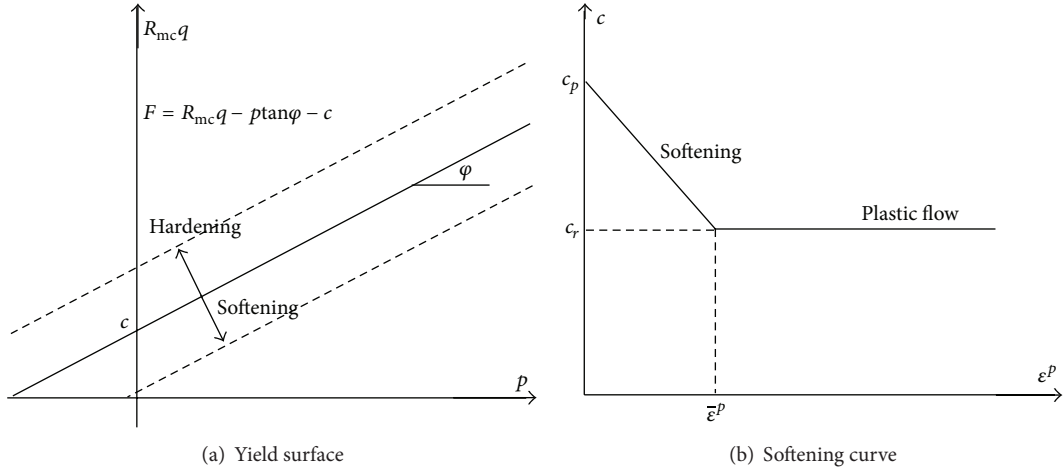
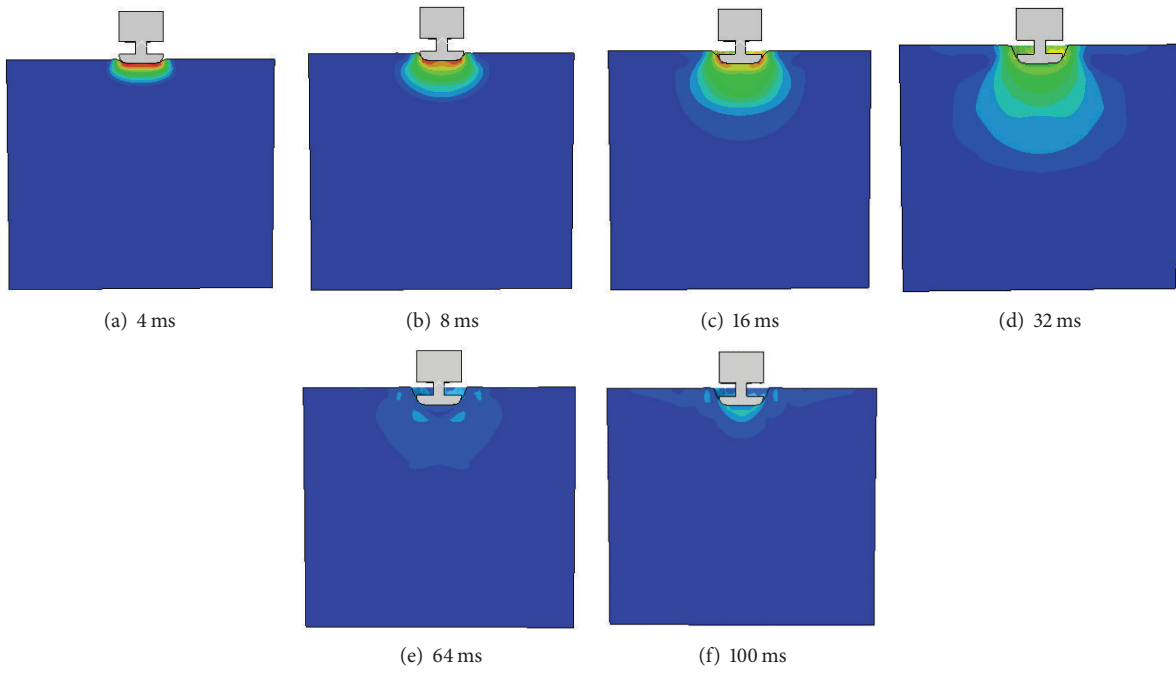


FIGURE 26: Constitutive model of lunar soil simulant TJ-1.

FIGURE 27: Mises stress distribution when $D_r = 60\%$, $v = 4$ m/s, and $m = 3$ kg.

Poisson's ratio of lunar soil simulant under different confining pressures and relative densities is expressed by the following formula:

$$\mu = \frac{(v_p^2 - 2v_s^2)}{2(v_p^2 - v_s^2)}, \quad (8)$$

where v_p is compression wave velocity and v_s shear wave velocity. Test results indicate that the range of Poisson's ratio is 0.31~0.34, is little affected by confining pressure and relative density, and is taken as 0.32 in this study.

The triaxial tests demonstrate that the internal friction angle of the lunar soil simulant increases as relative density increases, which is mainly distributed around 45° . Peak and

residual cohesion values of the lunar soil simulant for three different relative densities are listed in Table 1 after considering the influence of shear rates. Figure 1 also indicates that when plastic flow occurs, the equivalent plastic strain is about 8.2%~15.3%, which, in this study, has been taken as 12%.

Table 6 lists interface and lunar soil simulant parameters based on laboratory tests, including value ranges and the specific values chosen for this study.

4.1.4. Initial Conditions and Boundary Conditions. In order to make comparisons with the model test results, the gravitational weights of both shock tube and soil are allowed in the FEM model, and the penetration displacement and velocity are set as zero at the initial time. The dynamic response at

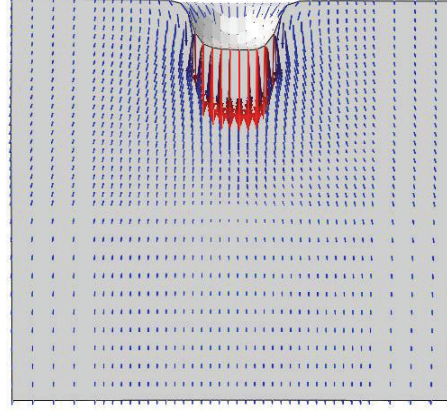


FIGURE 28: Penetration deformation calculated when $D_r = 60\%$, $v = 4$ m/s, and $m = 6$ kg.

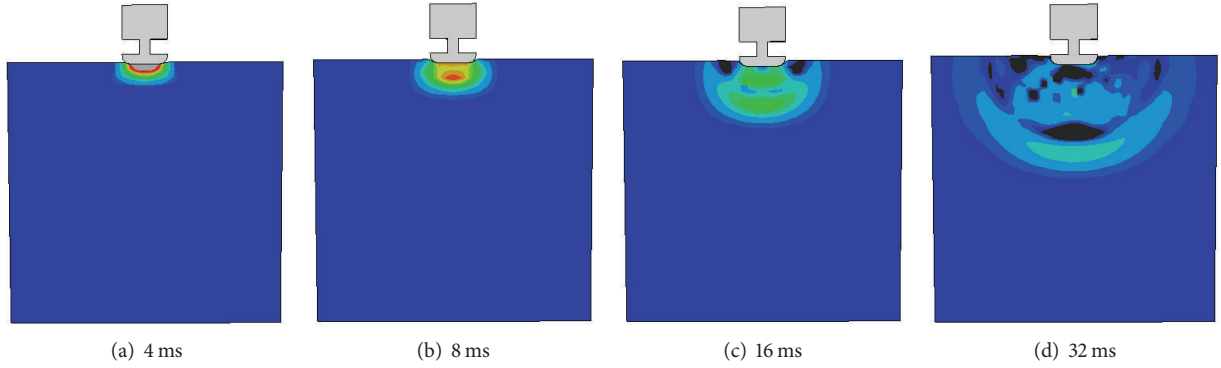


FIGURE 29: Propagation of compression wave when $D_r = 60\%$, $v = 4$ m/s, and $m = 3$ kg.

TABLE 6: Parameters of interface and lunar soil simulant selected in numerical simulation.

Materials	Parameter/unit	D_r	Value range	Value used
Lunar soil simulant	E/MPa	0.4	0.1~1.5	0.75
		0.6	1.2~4.1	1.30
		0.8	1.8~5.0	2.15
	μ		0.31~0.34	0.32
		0.4		1.8
	c_p/kPa	0.6	0.8~27.0	4.5
		0.8		15.0
		0.4		0.4
	c_r/kPa	0.6	0.1~15.2	1.2
		0.8		10
Interface	$\bar{\epsilon}^p$		8.2~15.3	12.0
	$\varphi/^\circ$		39~51	45.0
	$\bar{\eta}$		0.16~0.33	0.2
	μ_f		0.58~0.64	0.62

the interface, the peak axial force, and penetration depth are the three items of most interest during the impact process. In order to improve computational efficiency, the normal

displacement at the truncating boundary is constrained instead of utilizing the transmitting boundary.

4.2. Numerical Results and Discussions. After establishing the numerical model as above, 27 groups of studies were taken under the same conditions shown in Table 4.

4.2.1. Response of Overall Site. Results show the overall site response in different cases is similar. Figure 27 illustrates the Misses stress distribution at different times when $D_r = 60\%$, $v = 4$ m/s, and $m = 3$ kg, which is within the range 0.0 kPa~28.2 kPa. At the initial time, seen in Figure 27(a), there exists a flat area beneath the footpad with very high stress levels due to the inertia force and lateral restraint. As the stress wave propagates outward, the stress amplitude then decreases while the regional influence expands gradually. The maximum influenced depth reaches about 25 cm, three times the diameter of the footpad. Finally, the stress dissipates and the influenced region reduces and disappears ultimately. The plastic zone is ellipsoidal in shape, varying from flat with its long axis in the horizontal direction to taper with its long axis in the vertical direction during the impact process. This differs from the cone shape plastic zone put forward by NASA scholars [2].

Figure 28 demonstrates penetration displacement vector distribution at 16 ms when $D_r = 60\%$, $v = 4$ m/s,

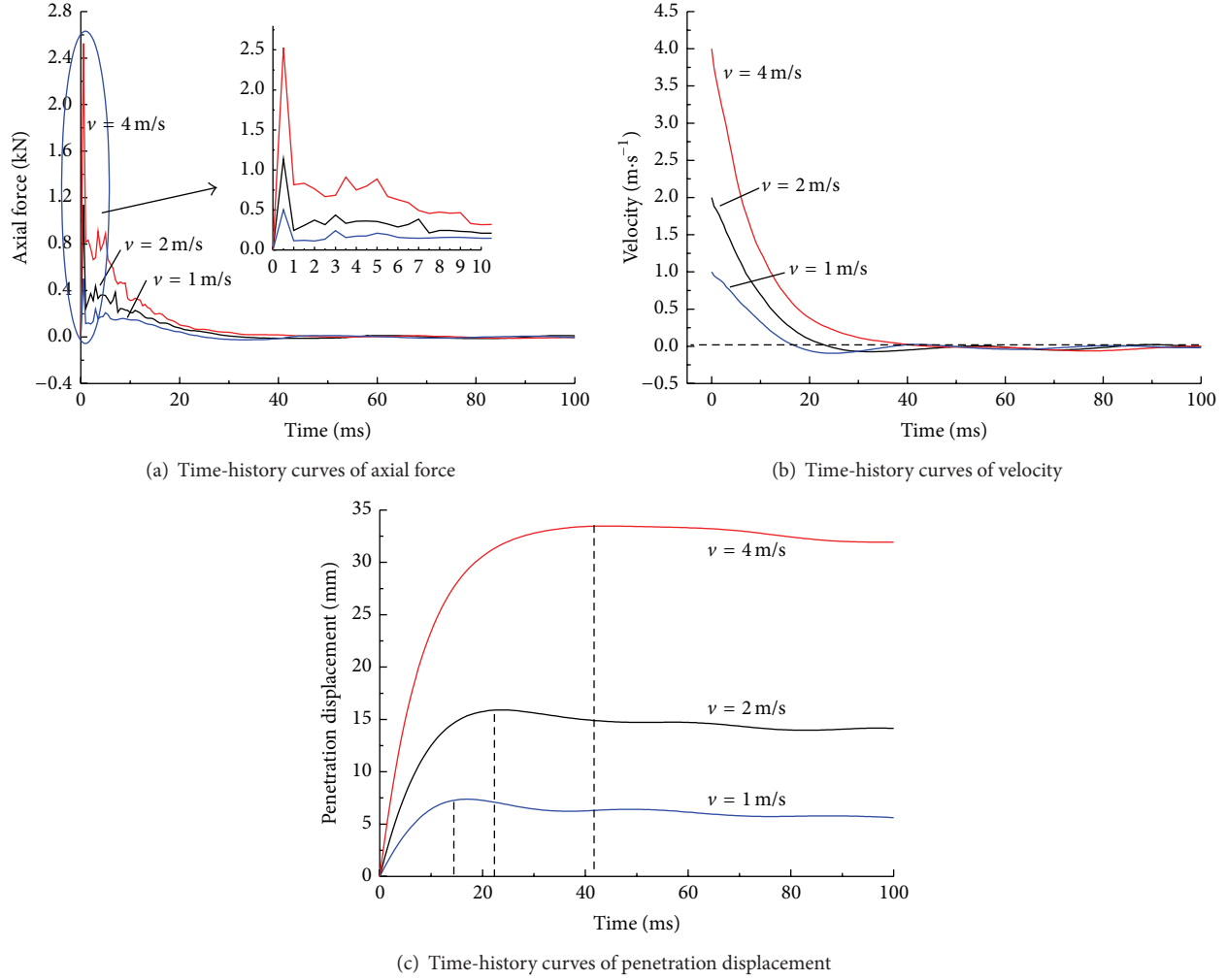


FIGURE 30: Curves of dynamic response when $D_r = 60\%$ and $m = 3$ kg at different impact velocities.

and $m = 6$ kg. The figure indicates that the simulant lunar soil beneath the footpad moves downward and extrudes towards the periphery, resulting in a basin-shaped crater. The displacement mainly occurs over a region 2~3 times the diameter of the footpad. Figure 11 shows the impact crater formed in the test under different impact velocities. Comparing Figure 28 with Figure 11 shows that the deformation calculated by the FEM model is consistent with that of the test.

Figure 29 represents compression wave at different times when $D_r = 60\%$, $v = 4$ m/s, and $m = 3$ kg. The results demonstrate that the compression wave propagates outward taking an axisymmetric spherical shape.

4.2.2. Response of Footpad. Figure 30 shows the time-history response curves of the footpad (axial force, velocity, and penetration displacement) under different impact velocities when $D_r = 60\%$ and $m = 3$ kg. It implies in Figure 30(a) that the axial force in the footpad reaches its peak in a very short time followed by a second impact. The axial force then decays gradually until it equals the weight of the shock tube. Figure 30(b) shows that the decay of velocity of the

shock tube lags behind the axial force, and after a rapid attenuation from its initial value, the velocity changes slightly along the horizontal axis ($v = 0$) and tends finally to $v = 0$. Figure 30(c) indicates that the penetration displacement curves are the most hysteretic. After achieving the maximum depth, the shock tube rebounds slightly and then tends towards the reach ultimate penetration depth. Comparison of these displacement curves indicates that the greater the impact velocity, the deeper the reach of the shock tube and the longer the duration time when the shock tube to achieve is stable.

Numerical analysis also demonstrates that the shock tube response amplitudes are different under different impact masses, impact velocities, and relative soil densities, but their response variations are similar. Figure 31 manifests that the peak axial force and penetration depth both increase exponentially with increasing impact kinetic energy. The denser the soil, the smaller the penetration depth and the larger the axial force. Figure 31 also gives the comparison between numerical and measured results, where the solid points are the measured values obtained from model tests, and the hollow points are the numerical results.

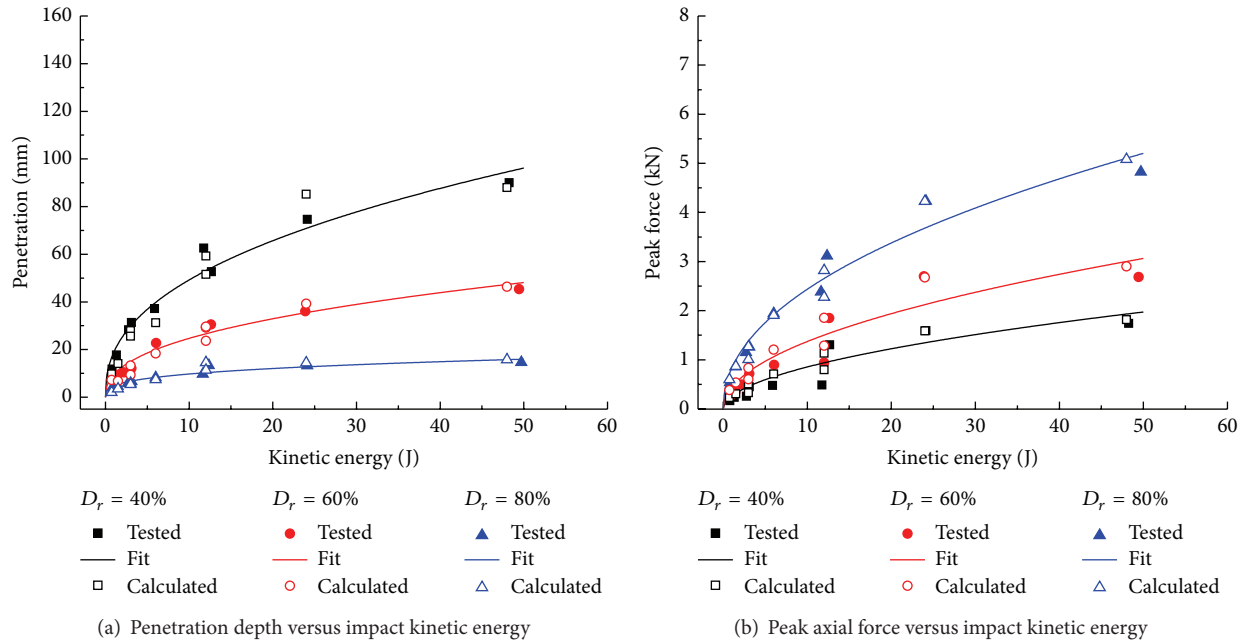


FIGURE 31: Comparison between calculated and tested results.

5. Conclusions

An investigation into the interaction between lunar soil simulants and the lander footpad during the impact process using subscale model tests based on prototype vertical impact test apparatus has been described in this paper. In addition a 3D dynamic finite element model was established to simulate the impact process. The main conclusions are as follows.

The impact duration time is short in the tests, with magnitudes in tens of milliseconds. The relative density of the lunar soil simulant site has the most significant influence on the dynamic response during impact, followed by the impact velocity; the impact mass has the least influence. For a given shape and dimensions of the footpad, the peak axial force and penetration depth increase in an exponential form as impact kinematic energy increases. There exists a critical value of impact momentum or energy for a given relative density of simulant lunar soil site. When the value is less than the critical value, the simulant soil site does not reach flow failure under impact of the footpad. The flow failure phenomenon under impact is more likely to occur for lower relative simulant lunar soil site densities. There exists a secondary rebound of the footpad after impacting the simulant lunar soil site, and a basin-shaped crater is formed.

Numerical simulation demonstrated that the displacement caused by the footpad impact affects a region of mainly 2~3 times the diameter of the footpad. The shape of the plastic deformation zone in the simulant lunar soil site is an approximate ellipsoid, which is different from the cone shape assumed by former scholars. Numerical simulation provided the dynamic responses of the simulant lunar soil in the cases of axial force, velocity, and displacement of the footpad. The numerical model was proved to give valid information based on comparison with model test results.

The work described in this paper provides a basis for further research into landing simulations, the modeling of the simulant lunar soil site, the dynamic responses to oblique landing impact on the simulant lunar soil, and also the design of the lander buffering system of the lander among other design aspects.

Conflict of Interests

The authors declare that there is no conflict of interests regarding the publication of this paper.

Acknowledgments

This research work was supported by the National Natural Science Foundation (nos. 51178427, 51278451) and the National Basic Research Program (no. 2014CB047005) of China.

References

- [1] F. B. Sperling, "The surveyor shock absorber," in *Proceedings of the Aerospace Mechanisms Series*, pp. 211–217, AIAA, 1970.
- [2] Bendix Corporation, *Lunar Module (LM) Soil Mechanics Study: Final Report*, Energy Controls Division, Analytical Mechanics Engineering Department, Bendix Corporation, 1968.
- [3] S. C. Stiros and P. A. Psimoulis, "Response of a historical short-span railway bridge to passing trains: 3-D deflections and dominant frequencies derived from Robotic Total Station (RTS) measurements," *Engineering Structures*, vol. 45, pp. 362–371, 2012.
- [4] D. S. McKay, G. H. Heiken, A. Basu et al., "The lunar regolith," in *Lunar Source Book*, pp. 285–356, Cambridge University Press, Cambridge, Mass, USA, 1991.

- [5] S. W. Johnson and K. M. Chua, "Properties and mechanics of the lunar regolith," *Applied Mechanics Reviews*, vol. 46, no. 6, pp. 285–300, 1993.
- [6] E. Robens, A. Bischoff, A. Schreiber, A. Dabrowski, and K. K. Unger, "Investigation of surface properties of lunar regolith: part I," *Applied Surface Science*, vol. 253, no. 13, pp. 5709–5714, 2007.
- [7] S. W. Perkins and C. R. Madson, "Scale effects of shallow foundations on lunar regolith," in *Proceedings of the 5th International Conference of Space*, pp. 963–972, ASCE, New York, NY, USA, 1996.
- [8] D. Wang, X. Huang, and Y. Guan, "GNC system scheme for lunar soft landing spacecraft," *Advances in Space Research*, vol. 42, no. 2, pp. 379–385, 2008.
- [9] P. Lin, T. H. Ma, Z. Z. Liang, C. A. Tang, and R. Wang, "Failure and overall stability analysis on high arch dam based on DFPA code," *Engineering Failure Analysis*, vol. 45, pp. 164–184, 2014.
- [10] P. Lin, B. Huang, Q. Li, and R. Wang, "Hazard and seismic reinforcement analysis for typical large dams following the Wenchuan earthquake," *Engineering Geology*, 2014.
- [11] P. Lin, W. Y. Zhou, and H. Y. Liu, "Experimental study on cracking, reinforcement, and overall stability of the Xiaowan super-high arch dam," *Rock Mechanics and Rock Engineering*, 2014.
- [12] *Abaqus User's Manual Version 6.11*, Dassault Systemes, 2011.
- [13] Z. Y. Ouyang, *Introduction of Lunar Sciences*, China Aerospace Publishing House, Beijing, China, 2005 (Chinese).
- [14] A. P. Vinogradov, "Preliminary data on lunar ground brought to Earth by automatic probe," in *Proceedings of the Lunar and Planetary Science Conference*, vol. 2, pp. 1–16, 1971.
- [15] N. C. Costes, G. T. Cohron, and D. C. Moss, "Cone penetration resistance test—an approach to evaluating in-place strength and packing characteristics of lunar soils," in *Proceedings of the Lunar and Planetary Science Conference*, vol. 2, pp. 1973–1987, 1971.
- [16] J. K. Mitchell, W. N. Houston, R. F. Scott, N. C. Costes, W. D. Carrier III, and L. G. Bromwell, "Mechanical properties of lunar soil: density, porosity, cohesion and angle of internal friction," in *Proceedings of the Lunar and Planetary Science Conference*, vol. 3, pp. 3235–3253, 1972.
- [17] W. D. Carrier III, G. R. Olhoeft, and W. Mendell, "Physical properties of the lunar surface," in *Lunar Source Book*, pp. 475–594, Cambridge University Press, Cambridge, UK, 1991.
- [18] D. W. Carrier III, "Particle size distribution of lunar soil," *Journal of Geotechnical and Geoenvironmental Engineering*, vol. 129, no. 10, pp. 956–959, 2003.
- [19] S. W. Perkins and C. R. Madson, "Mechanical and load-settlement characteristics of two lunar soil simulants," *Journal of Aerospace Engineering*, vol. 9, no. 1, pp. 1–9, 1996.
- [20] S. Sture, "A review of geotechnical properties of lunar regolith simulants," in *Earth & Space 2006*, pp. 1–6, ASCE, Houston, Tex, USA, 2006.
- [21] H. Kanamori, S. Udagawa, T. Yoshida et al., "Properties of lunar soil simulant manufactured in Japan," in *Proceedings of the 6th International Conference and Exposition on Engineering, Construction, and Operations in Space (Space '98)*, pp. 462–468, April 1998.
- [22] H. A. Oravec, X. Zeng, and V. M. Asnani, "Design and characterization of GRC-I: a soil for lunar terramechanics testing in Earth-ambient conditions," *Journal of Terramechanics*, vol. 47, no. 6, pp. 361–377, 2010.
- [23] J. L. Klosky, S. Sture, H.-Y. Ko, and F. Barnes, "Geotechnical behavior of JSC-1 lunar soil simulant," *Journal of Aerospace Engineering*, vol. 13, no. 4, pp. 133–138, 2000.
- [24] H. Arslan, S. Batiste, and S. Sture, "Engineering properties of lunar soil simulant JSC-1A," *Journal of Aerospace Engineering*, vol. 23, no. 1, pp. 70–83, 2010.
- [25] D. S. McKay, J. L. Carter, W. W. Boles et al., "JSC-1: a new lunar soil simulant," in *Engineering, Construction, and Operations in Space IV*, vol. 2, pp. 857–866, 1994.
- [26] Y. Li, J. Liu, and Z. Yue, "NAO-1: lunar highland soil simulant developed in China," *Journal of Aerospace Engineering*, vol. 22, no. 1, pp. 53–57, 2009.
- [27] Y. Zheng, S. Wang, Z. Ouyang et al., "CAS-1 lunar soil simulant," *Advances in Space Research*, vol. 43, no. 3, pp. 448–454, 2009.
- [28] M. J. Jiang and Y. G. Sun, "A new lunar soil simulant in China," *Earth & Space*, pp. 3617–3623, 2010.
- [29] Z.-M. Zhang, H. Nie, J.-B. Chen, and L.-C. Li, "Investigation on the landing-impact tests of the lunar lander and the key technologies," *Journal of Astronautics*, vol. 32, no. 2, pp. 267–276, 2011.
- [30] H. H. Bui, T. Kobayashi, R. Fukagawa, and J. C. Wells, "Numerical and experimental studies of gravity effect on the mechanism of lunar excavations," *Journal of Terramechanics*, vol. 46, no. 3, pp. 115–124, 2009.
- [31] W. Zhu and J.-Z. Yang, "Modeling and simulation of landing leg for the lunar landing gear system," *Journal of Astronautics*, vol. 29, no. 6, pp. 1723–1728, 2008 (Chinese).
- [32] J.-Q. Li, M. Zou, Y. Jia, B. Chen, and W.-Z. Ma, "Lunar soil simulant for vehicle-terramechanics research in lab," *Rock and Soil Mechanics*, vol. 29, no. 6, pp. 1557–1561, 2008 (Chinese).
- [33] F. Moschas and S. Stiros, "Phase effect in time-stamped accelerometer measurements—an experimental approach," *EDP Sciences*, vol. 3, pp. 161–167, 2012.
- [34] T. P. Gouache, C. Brunskill, G. P. Scott, Y. Gao, P. Coste, and Y. Gourinat, "Regolith simulant preparation methods for hardware testing," *Planetary and Space Science*, vol. 58, no. 14–15, pp. 1977–1984, 2010.
- [35] B. M. Willman and W. W. Boles, "Soil-tool interaction theories as they apply to lunar soil simulant," *Journal of Aerospace Engineering*, vol. 8, no. 2, pp. 88–99, 1995.
- [36] W. D. Carrier III, L. G. Bromwell, and R. T. Martin, "Strength and compressibility of returned lunar soil," in *Proceedings of the 3rd Lunar and Planetary Science Conference*, vol. 3, pp. 3223–3234, The MIT Press, 1972.
- [37] L. D. Jaffe, "Surface structure and mechanical properties of the lunar maria," *Journal of Geophysical Research*, vol. 72, no. 6, pp. 1727–1731, 1967.
- [38] V. Gromov, "Physical and mechanical properties of lunar and planetary soils," in *Laboratory Astrophysics and Space Research*, vol. 236 of *Astrophysics and Space Science Library*, pp. 121–142, Springer, Dordrecht, The Netherlands, 1999.
- [39] Z. Shen, "The survey of Apollo LM during the descent to the lunar surface," *Spacecraft Recovery & Remote Sensing*, vol. 29, no. 1, pp. 11–14, 2008 (Chinese).
- [40] National Space Science Data Center, "Luna 16," NSSDC ID: 1970-072A, <http://nssdc.gsfc.nasa.gov/nmc/spacecraftDisplay.do?id=1970-072A>.
- [41] D. Wanatowski and J. Chu, "Static liquefaction of sand in plane strain," *Canadian Geotechnical Journal*, vol. 44, no. 3, pp. 299–313, 2008.

- [42] Z. W. Yin, X. L. Ding, and Y. S. Zheng, "Finite element modeling and simulative analysis for lunar regolith based on ABAQUS," *Universal Technologies & Products*, vol. 11, pp. 46–48, 2008 (Chinese).
- [43] C. Modenese, S. Utili, and G. T. Houlsby, "DEM modelling of elastic adhesive particles with application to lunar soil," *Earth and Space*, vol. 1, pp. 45–54, 2012.
- [44] D.-S. Ling, Z.-J. Jiang, S.-Y. Zhong, and J.-Z. Yang, "Numerical study on impact of lunar lander footpad against simulant lunar soil," *Journal of Zhejiang University (Engineering Science)*, vol. 47, no. 7, pp. 1171–1177, 2013 (Chinese).
- [45] N. Janbu, "Soil compressibility as determined by oedometer and triaxial tests," in *Proceedings of the European Conference on Soil Mechanics and Foundation Engineering*, vol. 1, pp. 19–25, 1963.

Research Article

Evaluation on Impact Interaction between Abutment and Steel Girder Subjected to Nonuniform Seismic Excitation

Yue Zheng,¹ Xiang Xiao,² Lunhai Zhi,³ and Guobo Wang³

¹ Department of Civil and Environmental Engineering, Hong Kong Polytechnic University, Kowloon, Hong Kong

² School of Transportation, Wuhan University of Technology, Wuhan 430070, China

³ School of Civil Engineering and Architecture, Wuhan University of Technology, Wuhan 430070, China

Correspondence should be addressed to Xiang Xiao; cexiaox@163.com

Received 1 September 2014; Accepted 27 September 2014

Academic Editor: Bo Chen

Copyright © 2015 Yue Zheng et al. This is an open access article distributed under the Creative Commons Attribution License, which permits unrestricted use, distribution, and reproduction in any medium, provided the original work is properly cited.

This paper aims to evaluate the impact interaction between the abutment and the girder subjected to nonuniform seismic excitation. An impact model based on tests is presented by taking material properties of the backfill of the abutment into consideration. The conditional simulation is performed to investigate the spatial variation of earthquake ground motions. A two-span continuous steel box girder bridge is taken as the example to analyze and assess the pounding interaction between the abutment and the girder. The detailed nonlinear finite element (FE) model is established and the steel girder and the reinforced concrete piers are modeled by nonlinear fiber elements. The pounding element of the abutment is simulated by using a trilinear compression gap element. The elastic-perfectly plastic element is used to model the nonlinear rubber bearings. The comparisons of the pounding forces, the shear forces of the nonlinear bearings, the moments of reinforced concrete piers, and the axial pounding stresses of the steel girder are studied. The made observations indicate that the nonuniform excitation for multisupport bridge is imperative in the analysis and evaluation of the pounding effects of the bridges.

1. Introduction

Long span bridges are subjected to environmental loadings and dynamic excitations due to the interaction between the bridges and the surrounding environment [1–3]. External excitations acting on bridges, such as earthquakes, may induce the structural deformation and stresses due to the indeterminacy, which may cause the damage events of the structural components [4, 5]. The out-of-phase oscillation in adjacent structures due to the difference in dynamic characteristics and the spatial variations of earthquake ground motion may result in the collision if their structural separation is not enough to accommodate the relative displacement. Reconnaissance shows that the pounding scenario is one of the most critical factors resulting in damages and failures of highway bridges [6]. The collision between bridge decks and abutments commonly results in the extensive damages to the highway bridges with seat abutment in many earthquakes, such as the 1971 San Fernando earthquake. Desroches and Fenves [7] reported that the frame stiffness ratios, earthquake

loading, hinge gap, frame yield strength, and restrainer stiffness are the major factors in quantizing the pounding effects in multiple-frame bridges. Maragakis et al. [8] investigated the effects of energy losses when the bridge deck collides with the abutment. Various damper elements were placed on the abutment to account for the energy dissipation during the pounding action. Many parameters, such as coefficient of restitution, abutment and deck stiffness, gap, and deck to abutment mass ratio, have been studied to prove that the pounding effect plays an important disadvantageous role in the seismic action on bridges with flexural abutments. Guo et al. [9] presented an experimental and analytical study on the pounding reduction of highway bridges subjected to seismic excitations by using magnetorheological dampers. However, the aforementioned references do not consider the effects of spatial variation of the earthquake ground motions on the impact between the girder and the abutment. Bi et al. [10] found that the minimum gap should be provided to avoid the pounding at the abutments and between the girders. Nevertheless, if the expansion joint between

the abutment and the girder is too large, it may disturb the comfortable experience of drivers and passengers. Therefore, the pounding interaction between the abutment and the girder subjected to the uniform and nonuniform excitations should be systematically investigated.

Prior to conducting the impact analysis, a rational impact model is essential to reflect the physical collision scenario. There exist many pounding models which have been presented to account for the impact effect between adjacent structures in the past several decades. Muthukumar and DesRoches [11] gave the cogency of various impact models in capturing the impact response of neighboring structures. Four impact models, namely, the contact force-based linear spring model, the Kelvin model, the Hertz model, and the restitution-based stereomechanical model, have been widely utilized in the pounding analysis. However, the four impact models do not well model the performance response of the collision between the girder and the abutment when the bridge is subjected to intensive earthquakes. It is worth noting that the axial stiffness between the girder and the abutment, which is a critical parameter in the impact model, is associated with the material properties of the backfill. An approximate stiffness is proposed based on many large-scale abutment tests [12, 13].

The spatial variations include three aspects [14, 15]: (1) local site effects caused from the variation by filtering effects of overlying soil columns; (2) wave passage, where the nonvertical waves arrive at different points of the ground surface at different times; (3) geometric incoherence results in the scattering in the heterogeneous ground. The numerical simulation of spatial variations is imperative because the asynchronous ground motions can significantly affect the pounding responses of the abutment. The nonstationary conditional simulation approach presented by Vanmarcke et al. [16] is widely used by many researchers due to its simplicity. Therefore, this approach is utilized in this study to generate the earthquake ground motions at each support of the continuous bridge.

The primary objective of this study is to investigate the pounding interaction between the abutment and the steel girder subjected to the uniform and nonuniform excitations with different wave propagation speeds. An elastic-perfectly plastic element is used to simulate the nonlinear rubber bearings. A trilinear impact model based on experimental data is adopted to simulate the pounding effects between the abutment and the girder. The FE model is established in the package Open System for Earthquake Engineering Simulation (OpenSees). The steel girder and the reinforced concrete piers are modeled by nonlinear displacement-based fiber elements. The nonstationary conditional simulation is performed to generate the asynchronous ground motions. A real two-span continuous steel box girder bridge is taken as the example to analyze and assess the pounding interaction between the abutment and the girder. The comparisons of the pounding forces, the shear forces of nonlinear bearings, the moments of reinforced concrete piers, and axial pounding stresses of the steel girder are studied. The made observations indicate that the nonuniform excitation for multisupport bridge is imperative in the analysis and evaluation of

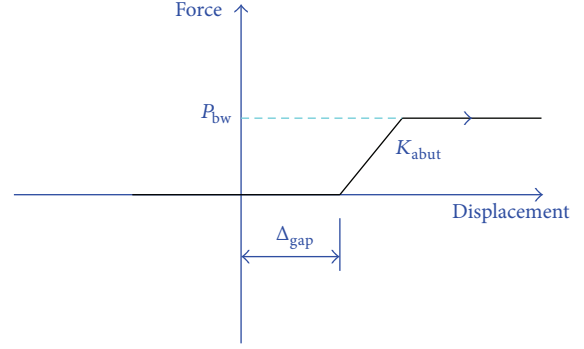


FIGURE 1: Force-deflection relationship of the abutments.

the pounding effects of the highway bridges for it always results in disadvantageous load case.

2. Impact Interactions between Abutment and Steel Girder

2.1. Impact Model. Several impact models have been presented by many researchers [17]. However, the impact mechanism between the abutment and the girder is not similar to collision between two rigid or elastic bodies completely. Therefore, Clatrans [18] recommended a trilinear approximation of the force-deformation relationship to simulate the longitudinal response of seat abutment; see Figure 1. The trilinear model consists of three segments: (i) a zero stiffness segment, which accounts for the expansion gap; (ii) a realistic stiffness segment of the embankment fill response; and (iii) a yielding stage segment with ultimate longitudinal force capacity P_{bw} . The stiffness of the abutment K_{abut} (kN/m) can be given by

$$K_{abut} = K_i \times w_{bw} \times \left(\frac{h_{bw}}{1.7} \right), \quad K_i \approx 28.7. \quad (1)$$

The passive pressure force resisting the moment at the abutment is expressed as

$$P_{bw} = A_e \times 239 \times \left(\frac{h_{bw}}{1.7} \right), \quad (2)$$

where w_{bw} and h_{bw} are projected width and height of the back wall for seat abutment, respectively. The area of a seat abutment is

$$A_e = h_{bw} \times w_{bw}. \quad (3)$$

It is noted that the initial stiffness K_i for embankment fill material should meet the requirements of the Caltrans Standard Specifications. For clarity, the contact force based on the bilinear model can be formulated as

$$\begin{aligned} F_c &= 0 & u_i - u_j - g_p &\leq 0, \\ F_c &= K_{abut} \times (u_i - u_j - g_p) & 0 < u_i - u_j - g_p &\leq \frac{P_{bw}}{K_{abut}}, \\ F_c &= P_{bw} & u_i - u_j - g_p &> \frac{P_{bw}}{K_{abut}}, \end{aligned} \quad (4)$$

where F_c is contact force; u_i and u_j are displacements of pounding nodes i and j , respectively; g_p is the distance of the gap.

2.2. Simulation on Ground Motion. The out-of-phase effect on the pounding of adjacent girder and the abutment is mainly investigated in this paper. Therefore, as one of the primary factors resulting in the inhomogeneous phenomenon at different supports of the bridge, the spatial variation of seismic waves is an imperative issue required to be solved. Three factors may affect the spatial variations of seismic ground motion, the wave passage effect, the incoherence effect, and the local site effect [19]. Many researchers have presented several solutions for this critical issue [16, 20, 21]. Among these approaches, the conditional simulation of a nonuniform seismic ground motion field based on nonstationary theory developed by Vanmarcke et al. [16] is adopted in this study due to its simplicity. This critical principle of the method is concisely introduced in the following paragraph.

Let us consider a segment of the ground motion at a point x_i and assume it can be represented by a nonergodic, zero-mean, homogeneous, mean-square continuous space time process $Z_i(t)$. The process $Z_i(t)$ can be expressed as a sum of independent frequency-specific spatial processes in consecutive constant-size frequency intervals as follows:

$$Z_i(t) = \sum_{k=1}^K [A_{ik} \cos(\omega_k t) + B_{ik} \sin(\omega_k t)],$$

$$\omega_k = (k-1) \Delta\omega \quad (k = 1, 2, \dots, K),$$

$$\Delta\omega = \frac{2\pi}{t_f + \Delta t},$$

where the coefficients A_{ik} and B_{ik} are zero-mean random variables; t_f is the length of the process. For a discrete-time process, defined at times

$$t_j = (j-1) \Delta t \quad (k = 1, 2, \dots, K),$$

$$\Delta t = \frac{t_f}{K-1},$$

the coefficients A_{ik} and B_{ik} are related to $Z_i(t_j)$ through the discrete Fourier Transform,

$$A_{ik} = \frac{1}{K} \sum_{j=1}^K Z_i(t_j) \cos\left(\frac{2\pi(k-1)(j-1)}{K}\right),$$

$$B_{ik} = \frac{1}{K} \sum_{j=1}^K Z_i(t_j) \sin\left(\frac{2\pi(k-1)(j-1)}{K}\right).$$

The following symmetry conditions about the Nyquist frequency, $\omega_{1+K/2} = \pi/\Delta t$, apply to the Fourier coefficients A_{ik} and B_{ik} when the process $Z_i(t)$ is real:

$$A_{ik} = A_{i(K-k+2)},$$

$$B_{ik} = -B_{i(K-k+2)},$$

$$k = 2, 3, \dots, 1 + \frac{K}{2}.$$

It is shown that the covariance between coefficients at points x_i and x_j , $C_{ij}(\omega_k)$, can be written as [22]

$$C_{ij}(\omega_k) = E(A_{ik} A_{jk}) = \begin{cases} \frac{1}{2} \rho_{\omega_k}(\gamma_{ij}) G(\omega_k) \Delta\omega, & \text{for } k = 1, \\ \frac{1}{4} \{ \rho_{\omega_k}(\gamma_{ij}) G(\omega_k) + \rho_{\omega_{K-k+2}}(\gamma_{ij}) G(\omega_{K-k+2}) \} \Delta\omega, & \text{for } k = 2, \dots, \frac{K}{2}, \\ \rho_{\omega_k}(\gamma_{ij}) G(\omega_k) \Delta\omega, & \text{for } k = \frac{K}{2} + 1, \end{cases}$$

$$\gamma_{ij} = x_i - x_j, \quad (9)$$

where γ_{ij} is the relative position vector, $G(\omega)$ is the one-sided "point" spectral density function, and $\rho_{\omega_k}(\gamma_{ij})$ is the frequency-dependent spatial correlation function. Note that

$$E(A_{ik} A_{jk}) = E(B_{ik} B_{jk}) = C_{ij}(\omega_k) \quad \text{for } k = 2, \dots, \frac{K}{2}. \quad (10)$$

The spatially correlated ground motions can then be obtained by the following steps: (i) generate sets of Fourier coefficients A_{ik} and B_{ik} , for each frequency ω_k ($k = 1, 2, \dots, 1 + K/2$); (ii) obtain the remainder using the symmetry conditions in (3); and (iii) use the Fast Fourier Transform algorithm to perform the inverse discrete transform.

Consider the simulation of seismic ground motions at a set of m target points x_β , given that some motions have been recorded at a set of $n = N - m$ measurement points, where N is the total number of points. The covariance matrix, $C_k = [C_{ij}(\omega_k)]$ ($i, j = 1, 2, \dots, n + m$), for each Fourier frequency ω_k ($k = 1, 2, \dots, 1 + K/2$) can be assembled and expressed as

$$C_k = \begin{bmatrix} C_{\alpha\alpha} & C_{\alpha\beta} \\ C_{\alpha\beta}^T & C_{\beta\beta} \end{bmatrix}. \quad (11)$$

Assume a set of simulated Fourier coefficients

$$A_s = \{A_{s\alpha}, A_{s\beta}\}, \quad (12)$$

where $A_{s\alpha}$ and $A_{s\beta}$ denote the coefficients at recording and target points, respectively. A set of simulated Fourier coefficients B_s can be defined in the same way. To simulate A_s and B_s , the covariance matrix C_k is evaluated for frequencies up to $\omega_{1+K/2} = \pi/\Delta t$. For admissible spatial correlation and spectral density functions, C_k is positive definite and can be expressed as the product of a nonsingular lower triangular matrix, L_k , and its transpose by means of the Cholesky decomposition

$$C_k = L_k L_k^T. \quad (13)$$

In case the limited-duration segment of the ground motion can be modelled as a Gaussian process, two sets of independent standard normal random variables can be simulated for each frequency:

$$\begin{aligned} U_k &= \{U_{1k}, U_{2k}, \dots, U_{Nk}\}, \\ V_k &= \{V_{1k}, V_{2k}, \dots, V_{Nk}\}. \end{aligned} \quad (14)$$

Sets A_s and B_s are then generated by

$$\begin{aligned} A_s &= L_k U_k, \\ B_s &= L_k V_k. \end{aligned} \quad (15)$$

It is easy to see that A_s and B_s have the proper covariance structure. Based on the subsets of simulation values at the recording points, $A_{s\alpha}$ and $B_{s\alpha}$, the linear prediction estimators at the target points are given by

$$\begin{aligned} A_{s\beta}^* &= C_{\alpha\beta}^T C_{\alpha\alpha}^{-1} A_{s\alpha}, \\ B_{s\beta}^* &= C_{\alpha\beta}^T C_{\alpha\alpha}^{-1} B_{s\alpha}. \end{aligned} \quad (16)$$

The conditional simulation now involves generating for each frequency ω_k sets of Fourier coefficients $A_{sc,k}$ and $B_{sc,k}$ at target points x_β , according to the conditional simulation algorithm

$$\begin{aligned} A_{sc,k} &= \{A_\beta^* + A_{s\beta} - A_{s\beta}^*\}_{(k)}, \\ B_{sc,k} &= \{B_\beta^* + B_{s\beta} - B_{s\beta}^*\}_{(k)}, \end{aligned} \quad (17)$$

where A_β^* and B_β^* are the linear prediction estimators based on the observed Fourier coefficients at the recording points A_α and B_α :

$$\begin{aligned} A_\beta^* &= C_{\alpha\beta}^T C_{\alpha\alpha}^{-1} A_\alpha, \\ B_\beta^* &= C_{\alpha\beta}^T C_{\alpha\alpha}^{-1} B_\alpha. \end{aligned} \quad (18)$$

The remaining Fourier coefficients at frequency ω_k ($k = 2 + K/2, \dots, K$) are then obtained using the symmetry conditions. Once coefficients have been generated for the entire frequency range, an inverse FFT can be applied to yield a set of ground motion time histories at the target points. The conditional simulation of seismic ground motions is displayed in Figure 2.

2.3. Equation of Motion for Pounding Action. For a lumped mass system, the dynamic equilibrium equation in terms of the nonuniform excitation can be written as

$$\begin{aligned} \begin{bmatrix} \mathbf{M}_{ss} & \mathbf{0} \\ \mathbf{0} & \mathbf{M}_{bb} \end{bmatrix} \begin{Bmatrix} \ddot{\mathbf{u}}_s^t \\ \ddot{\mathbf{u}}_b^t \end{Bmatrix} + \begin{bmatrix} \mathbf{C}_{ss} & \mathbf{C}_{sb} \\ \mathbf{C}_{bs} & \mathbf{C}_{bb} \end{bmatrix} \begin{Bmatrix} \dot{\mathbf{u}}_s^t \\ \dot{\mathbf{u}}_b^t \end{Bmatrix} \\ + \begin{bmatrix} \mathbf{K}_{ss} & \mathbf{K}_{sb} \\ \mathbf{K}_{bs} & \mathbf{K}_{bb} \end{bmatrix} \begin{Bmatrix} \mathbf{u}_s^t \\ \mathbf{u}_b^t \end{Bmatrix} + \begin{bmatrix} \mathbf{K}_{ss}^p & \mathbf{K}_{sb}^p \\ \mathbf{K}_{bs}^p & \mathbf{K}_{bb}^p \end{bmatrix} \begin{Bmatrix} \mathbf{d}_s^p \\ \mathbf{d}_b^p \end{Bmatrix} = \begin{Bmatrix} \mathbf{0} \\ \mathbf{0} \end{Bmatrix}, \end{aligned} \quad (19)$$

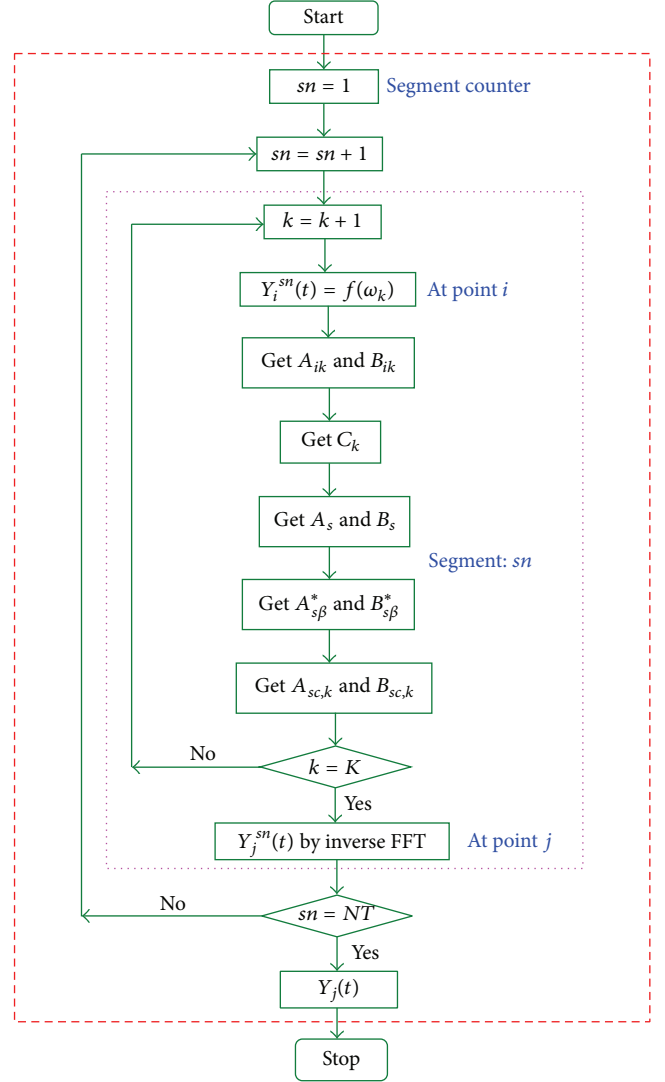
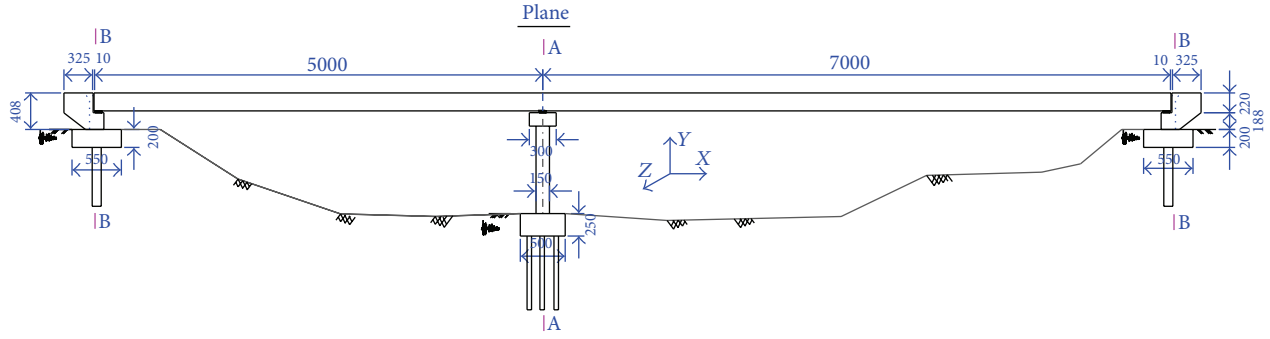
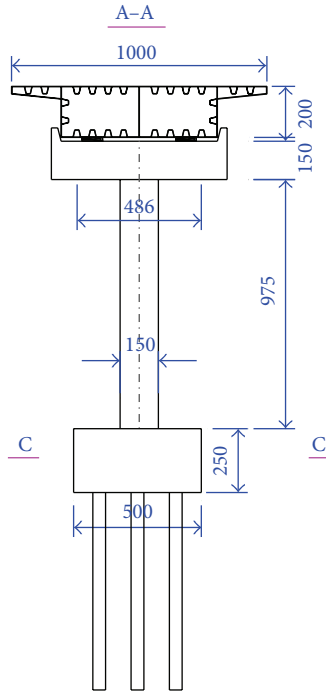


FIGURE 2: Flowchart of conditional simulation.

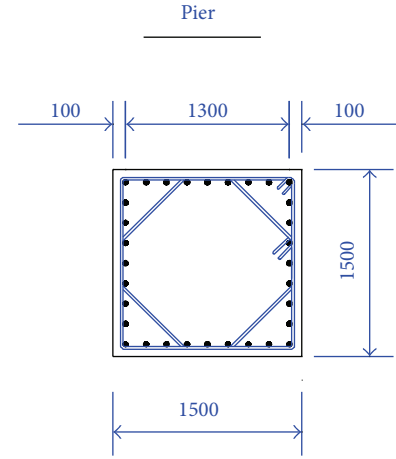
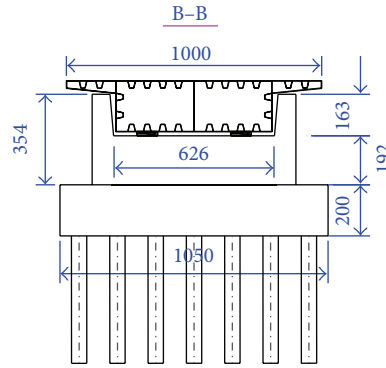
where the subscript s and b denote the superstructure and base foundation, respectively; \mathbf{M}_{ss} and \mathbf{M}_{bb} are the lumped mass matrices of the superstructure and foundation, respectively; \mathbf{C}_{ss} , \mathbf{C}_{sb} , \mathbf{C}_{bs} , and \mathbf{C}_{bb} are damping matrices, respectively, in terms of damping of superstructure and foundation; similarly, \mathbf{K}_{ss} , \mathbf{K}_{sb} , \mathbf{K}_{bs} , and \mathbf{K}_{bb} are the matrices with respect to stiffness of the superstructure and the foundation, respectively; \mathbf{I} is the earthquake influence coefficient vector; $\ddot{\mathbf{u}}_s^t$ and $\ddot{\mathbf{u}}_b^t$ are the absolute acceleration vector of the superstructure and the foundation, respectively; $\dot{\mathbf{u}}_s^t$ and $\dot{\mathbf{u}}_b^t$ are the absolute velocity vectors of the superstructure and the foundation, respectively; \mathbf{u}_s^t and \mathbf{u}_b^t are the absolute displacement matrices of the superstructure and the foundation, respectively; \mathbf{K}_{ss}^p are the stiffness matrix of the partial superstructure where the impact occurs; \mathbf{K}_{sb}^p and \mathbf{K}_{bs}^p are the stiffness matrices of the coupled part of the superstructure and the foundation where the pounding occurs; \mathbf{K}_{bb}^p are the stiffness matrix of foundation at which the impact occurs; \mathbf{d}_s^p and \mathbf{d}_b^p are the relative displacement matrices between



(a) Profile of a two-span steel continuous girder bridge (unit: cm)



(b) Detailed cross section of the pier and abutment (unit: cm)



(c) Detailed cross section of a pier (unit: mm)

FIGURE 3: Profile of a steel continuous girder bridge.

adjacent components located in the superstructure and the foundation, respectively.

It is noted that the pounding scenario which generates high magnitude and short duration acceleration pulse during an earthquake will make the numerical convergence difficult. Therefore, a variable time stepping procedure is utilized to determine the impact time and solve the equation of motion.

3. Pounding Effect of the Bridge

3.1. Structural Description. To assess the pounding interaction between the girder and the abutment subjected to the nonuniform seismic excitations, a real two-span continuous steel girder bridge constructed in China is selected as an example. The bridge is supported on reinforced concrete piers and the two spans are 50 m and 70 m, respectively, as shown in Figure 3(a). The detailed profile of the pier and the abutment

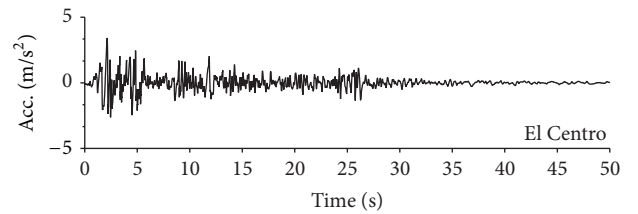


FIGURE 4: Original time histories of El Centro (NS).

is displayed in Figure 3(b) and the reinforcement details of a pier section are shown in Figure 3(c). The longitudinal, transversal, and vertical directions are denoted by X, Y, and Z, respectively. The bridge pier consists of single square column and the cross-sectional area is 2.25 m^2 . The clear height of the column is 9.75 m. The rubber bearings are placed

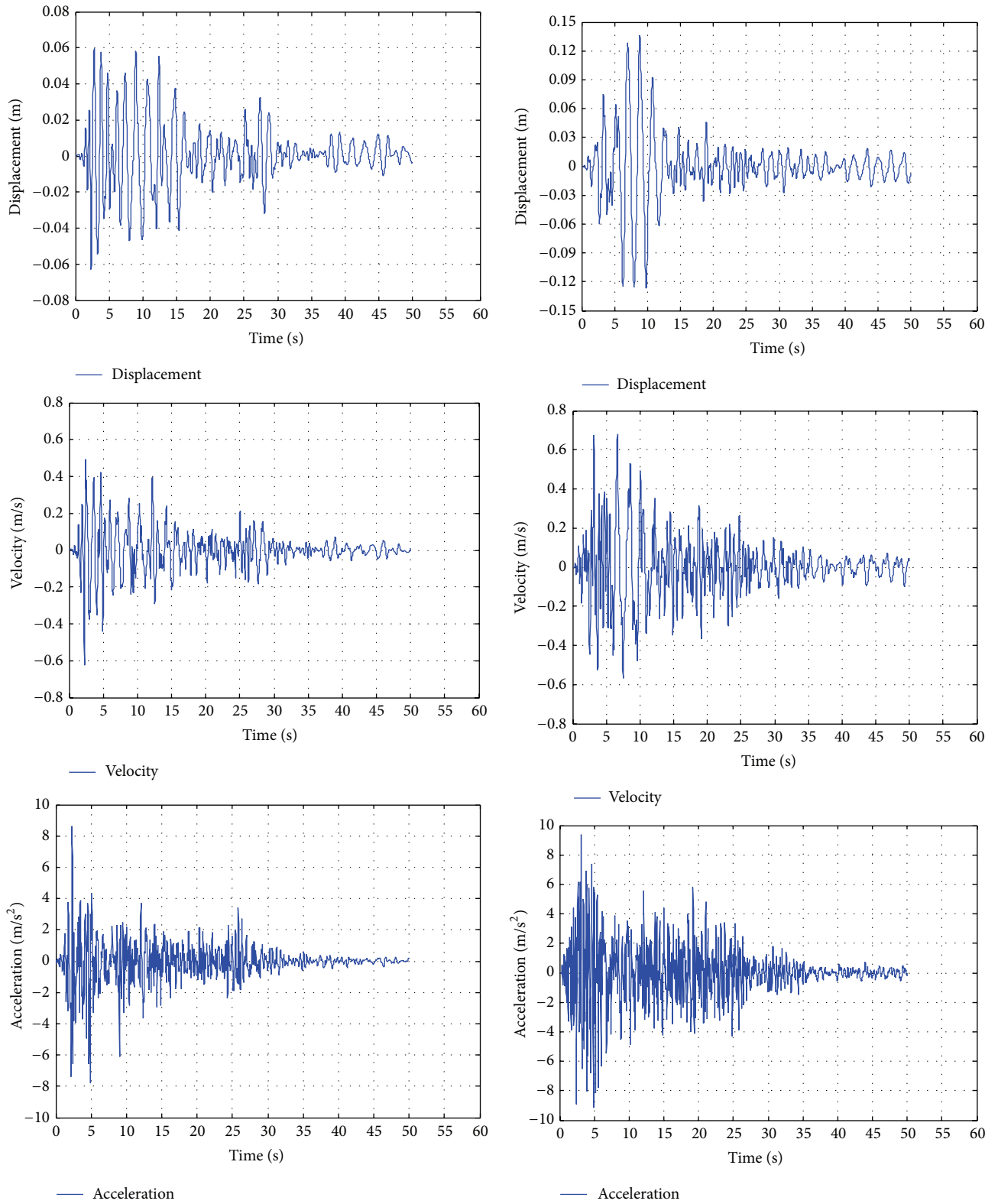


FIGURE 5: Dynamic responses of abutments ($V_w = 400$ m/s).

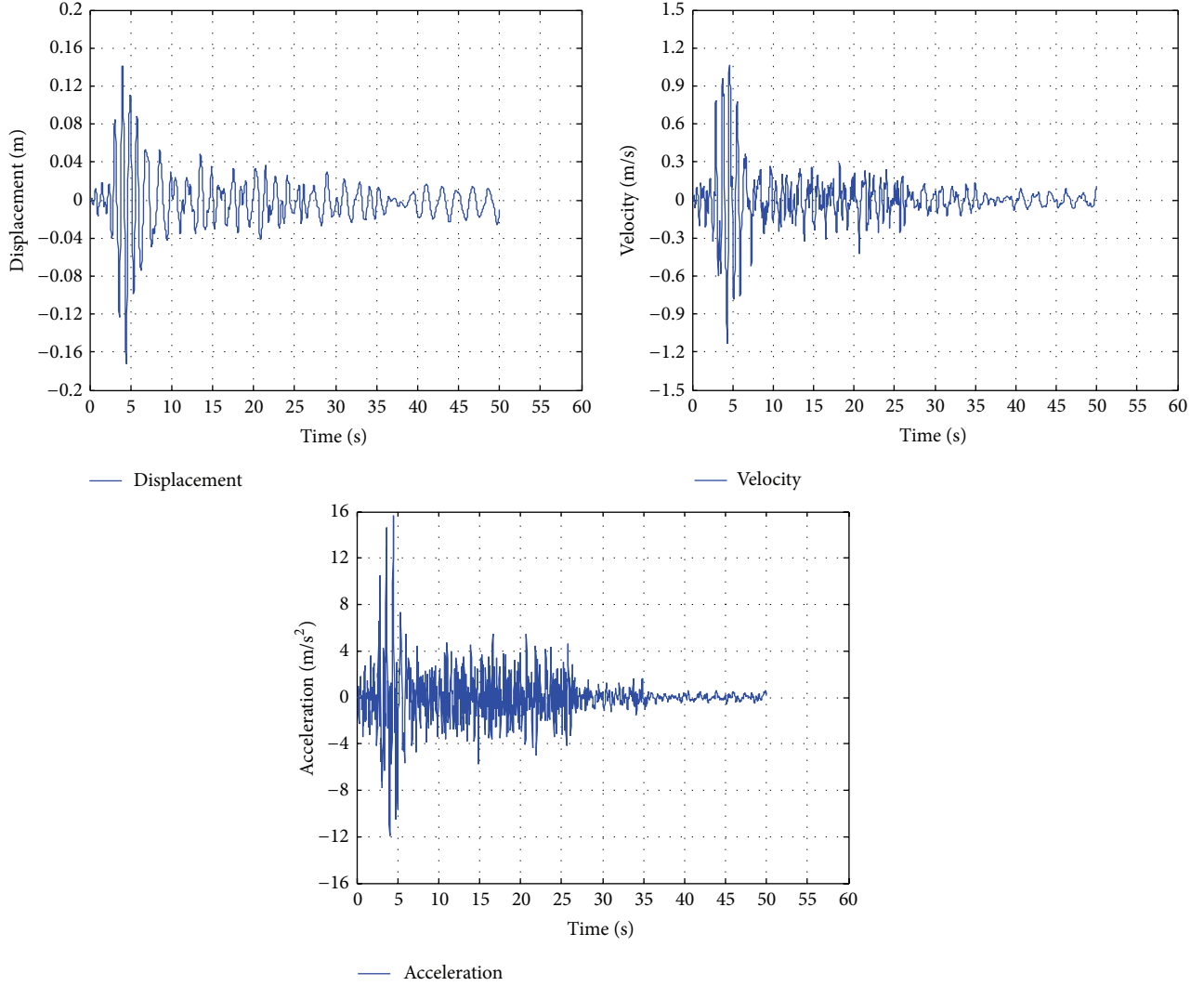


FIGURE 6: Dynamic responses of the middle foundation ($V_w = 400$ m/s).

on the bent cap and the abutments. The space between two rectangular octagonal hoops is 0.4 m. The densities of the steel and the reinforced concrete are 7850 and 2500 kg/m³, respectively. The diameters of longitudinal and transversal reinforcing bars are 32 mm and 16 mm, respectively. The yield strength f_y of the reinforcing steel is 280 MPa. Young's modulus of the steel E_s and the concrete E_c are 2.0×10^5 MPa and 3.0×10^4 MPa, respectively. The parameters about the rubber bearing are tabulated in Table 1. The shear modulus and the height of all the bearings are 1.0 GPa and 0.15 m, respectively. The bearings at left and right abutments have the same size of which the area of cross section and the shear stiffness (K_h) are 0.03 m² and 209.0 kN/m, respectively. The counterparts of the bearing at middle bent cap are 0.126 m² and 838.0 kN/m, respectively. The yielding strengths of two types of bearing are 20.9 kN and 83.8 kN, respectively.

The FE model of this bridge is established with the aids of the package OpenSees. The steel box girder and the reinforced concrete pier are modeled by using nonlinear fiber elements. The rubber bearings are modeled by using an elastic-perfectly

plastic zero-length element. A trilinear zero-length element is used to simulate the impact effects between the abutment and the girder. The dynamic equilibrium equation involved multisupport excitation which can be solved using the Newmark-beta method with a self-adaptive integration time step from 1.0×10^{-4} s to 2.0×10^{-2} s to ensure the numerical convergence at the end of each step. The Rayleigh damping assumption is adopted to construct the structural damping matrix, and the damping ratio of the bridge is set as 0.03 [22–25].

3.2. Conditional Simulation of Ground Motion at Three Support Points. To evaluate the pounding interaction between the girder and the abutment of the continuous steel girder bridge, the El Centro NS (1940) ground motion is selected as inputs to the example bridge structure. The time history of the seismic record is shown in Figure 4. The original peak ground acceleration (PGA) of the seismic record is 3.417 m/s². The original time history of the seismic record is scaled to 8.6 m/s² to perform the pounding analysis. Three scenarios are taken into consideration to investigate the pounding effects under

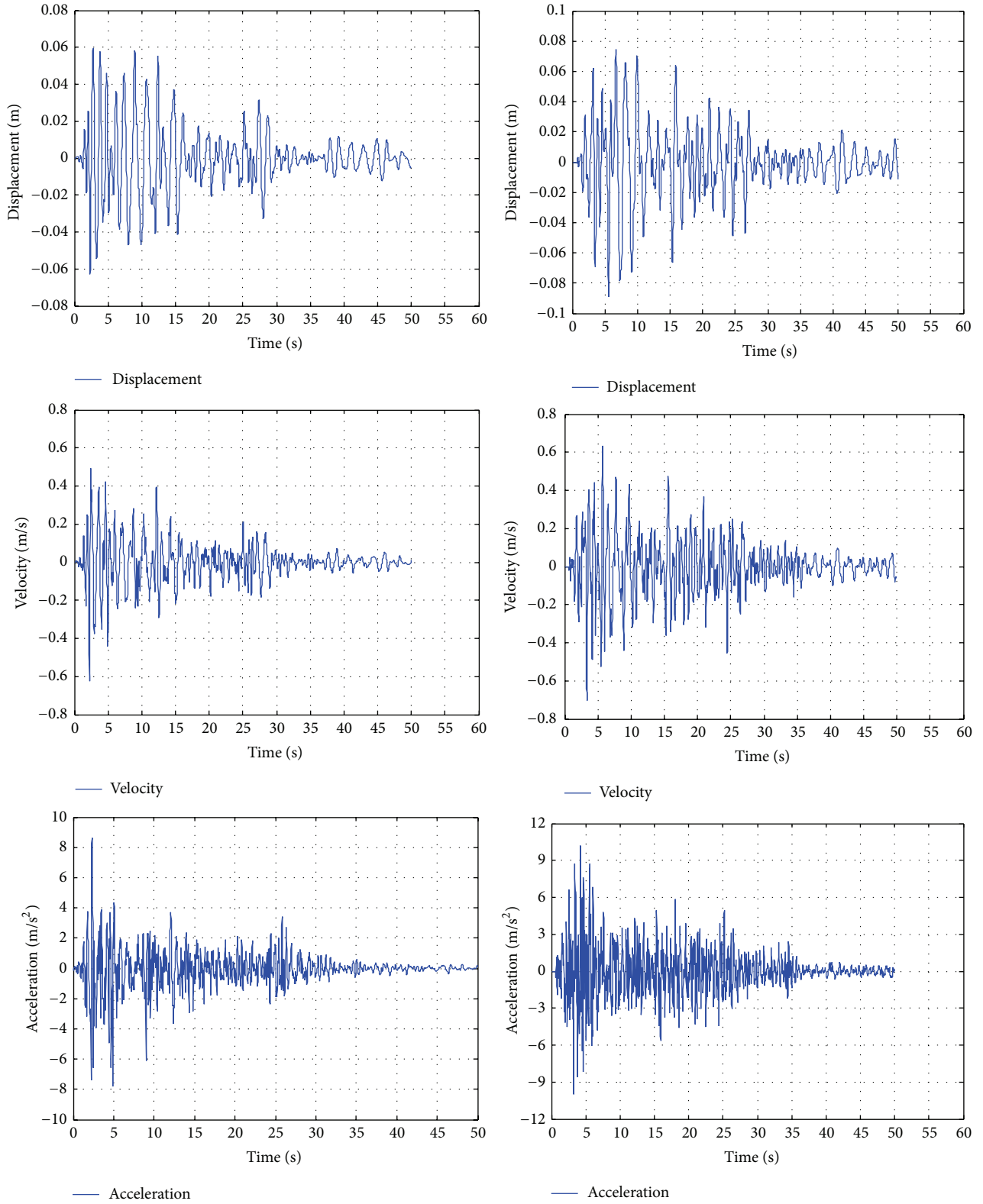


FIGURE 7: Dynamic responses of abutments ($V_w = 200$ m/s).

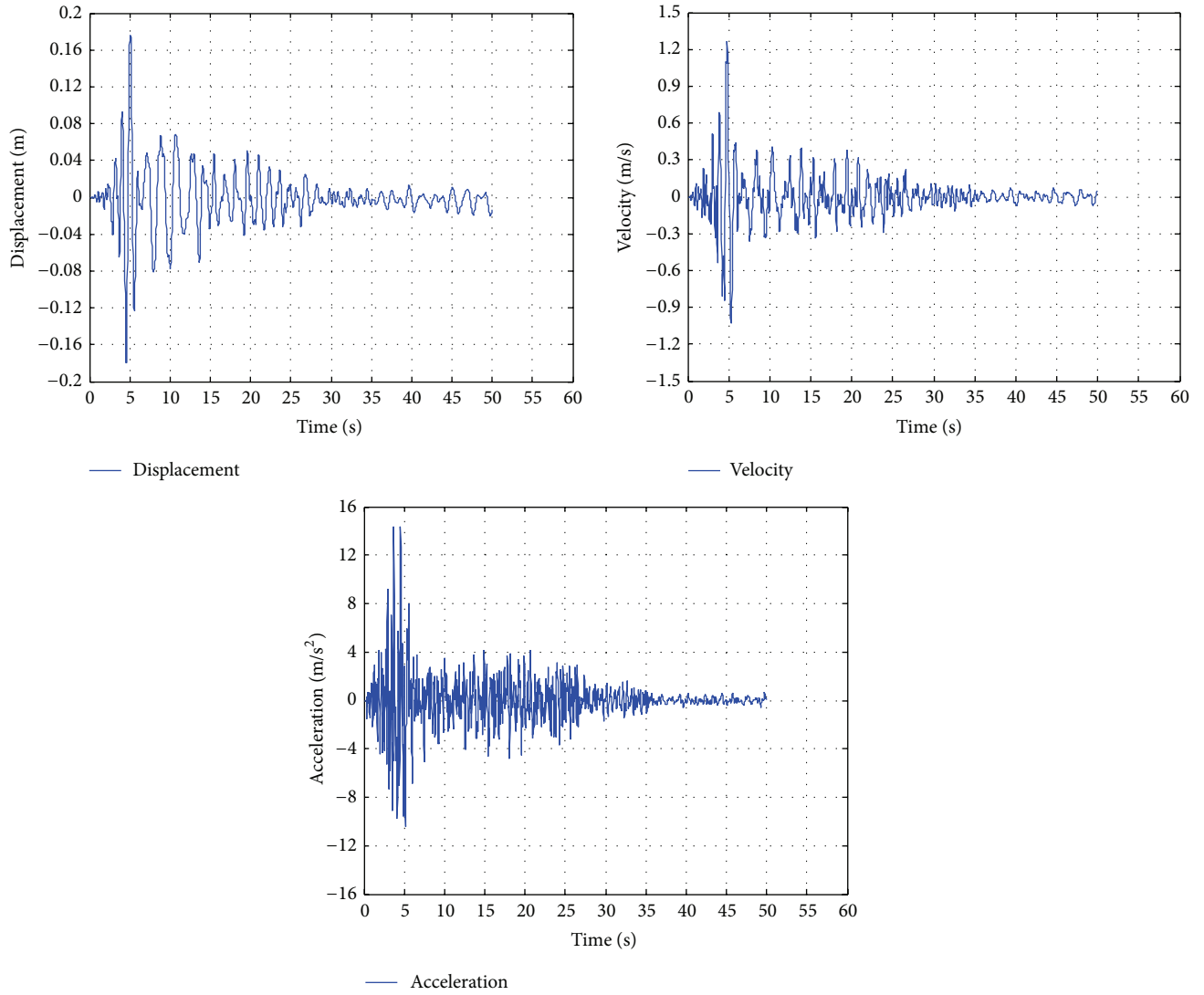
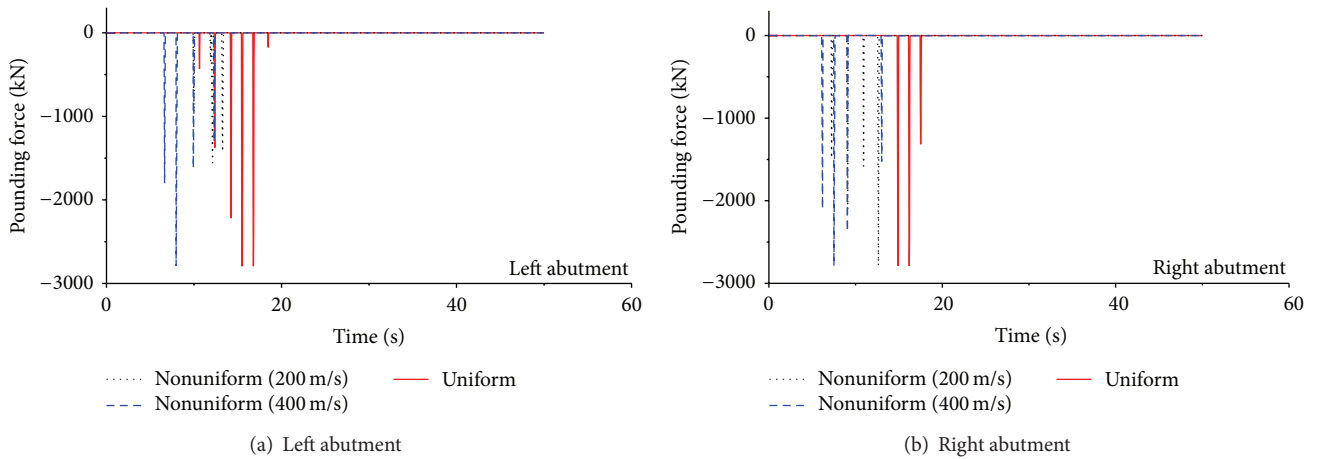
FIGURE 8: Dynamic responses of the middle foundation ($V_w = 200$ m/s).

FIGURE 9: Time history of pounding force at abutments.

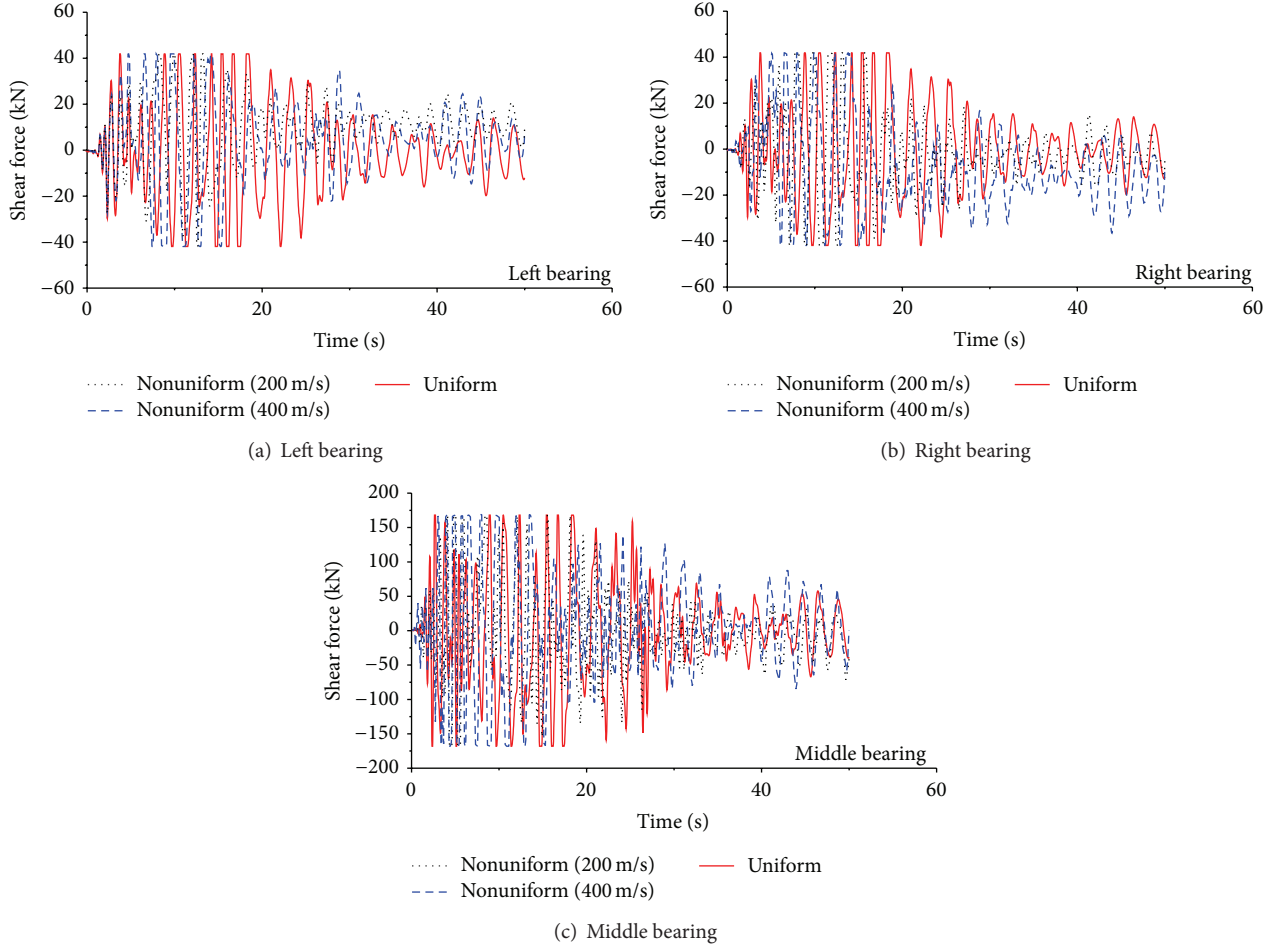


FIGURE 10: Time history of shear force of bearings.

TABLE 1: Bearing properties.

Location of bearings	G (kPa)	A (m ²)	h (m)	$K_h = GA/h$ (kN/m)	Yielding strength (kN)
Left abutment	1.0×10^3	0.03	0.15	209.0	20.9
Middle pier cap	1.0×10^3	0.126	0.15	838.0	83.8
Right abutment	1.0×10^3	0.03	0.15	209.0	20.9

both uniform and nonuniform excitations with two wave propagation velocities V_w , namely, 200 m/s and 400 m/s. The simulated acceleration time histories at three supports of the bridge are indicated in Figures 5, 6, 7, and 8, respectively, for the two wave propagation velocities. In the simulation of the ground motion, the frequency-dependent spatial correlation function of phase-aligned ground acceleration presented by Harichandran and Vanmarcke [26] is adopted:

$$\rho_{\omega_k}(\gamma_{ij}) = 0.736e^{-0.536(|\gamma_{ij}|/\theta_\omega)} + 0.264e^{-0.744(|\gamma_{ij}|/\theta_\omega)}, \quad (20)$$

$$\theta_\omega = 5210 \left\{ 1 + \left(\frac{\omega}{2.17\pi} \right)^{2.78} \right\}^{-1/2},$$

where θ_ω is the frequency-dependent scale of the fluctuation. In addition, it is noted that the ground motion used in the computation is divided into five segments with the time

duration of 1.48 s, 4.32 s, 20.8 s, 8.4 s, and 15 s, respectively. Each of the five segments is assumed as a stationary process. Then the five segments are assembled together through the linear interpolation and the wave propagation phase delays are postprocessed. Finally, the velocity and displacement time histories at each support can be calculated by integrating the acceleration time histories with respect to time, respectively.

4. Seismic Response Analyses

4.1. Response of Abutment. As discussed above, three scenarios are considered to evaluate the dynamic responses of pounding interaction between the abutment and the steel girder. Figure 9 shows the time histories of pounding forces at the abutment and the peak responses of the pounding force are listed in Table 2. It is seen from Figure 9 and Table 2

TABLE 2: Peak response of pounding force.

Location	Uniform		Nonuniform (400 m/s)		Nonuniform (200 m/s)	
	Time (s)	Force (kN)	Time (s)	Force (kN)	Time (s)	Force (kN)
Left abutment	15.46	2.79×10^3	7.96	2.79×10^3	12.12	1.57×10^3
Right abutment	14.88	2.79×10^3	7.52	2.79×10^3	12.62	2.79×10^3

TABLE 3: Peak responses of shear forces.

Location	Uniform		Nonuniform (400 m/s)		Nonuniform (200 m/s)	
	Time (s)	Force (kN)	Time (s)	Force (kN)	Time (s)	Force (kN)
Left bearing	3.74	41.9	4.7	41.9	8.2	41.9
Middle bearing	2.34	168.0	3.02	168.0	4.02	168.0
Right bearing	3.74	41.9	5.08	41.9	7.10	41.9

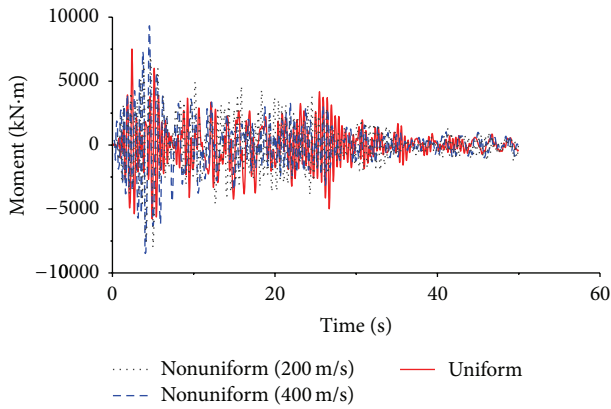


FIGURE 11: Time histories of moment force at the bottom of RC pier.

that the right abutment experienced yielding state under both uniform and nonuniform excitations. The nonuniform excitation with the wave propagation speed of 400 m/s is the most critical loading case for the right abutment. The right abutment is the latest one to trigger yielding state when subjected to uniform excitation. However, the left abutment does not reach yielding state in the case of nonuniform excitation with the propagation speed of 200 m/s. In this case, the peak pounding force is 1.57×10^3 kN which is much less than that of the right abutment. The comparison between two abutments indicates that the spatial variations of the ground motion should be taken into consideration in the assessment on the pounding effects because it provides the disadvantageous loading excitations.

4.2. Response of Rubber Bearing. Figure 10 displays the time histories of the shear forces of the bearings at the left abutment, the middle bent cap, and the right abutment for the concerned three scenarios. Listed in Table 3 are the peak responses and the time occurrence of shear forces of bearing at three locations. It can be observed that the bearings at the three locations experience the yielding stages for all the three loading cases. As far as one rubber bearing among them is concerned, it yields at first when subjected to the uniform excitation in comparison with the case under the nonuniform

TABLE 4: Peak response of moment force and curvature.

Case	Curvature (1/m)	Moment (kN·m)
Uniform	0.0026	7.51×10^3
Nonuniform (400 m/s)	0.0051	9.28×10^3
Nonuniform (200 m/s)	0.0032	8.06×10^3

excitation. The three bearings reach the yielding state latest when they are subjected to nonuniform excitation with the wave propagation speed of 200 m/s.

4.3. Response of Reinforced Concrete Pier. Figure 11 displays the time histories of moment of the pier and Figure 12 indicates the moment versus the curvature relationship of the pier. The peak moment is listed in Table 4. The curvature and the moment responses at the bottom of the pier are variable with the types of the excitation, of which the nonuniform excitation with wave propagation speed of 400 m/s is the most critical case. The most critical peak curvature and moment are 0.0051 1/m and 9.28×10^3 kN·m, respectively. The moment versus the curvature hysteretic loop under nonuniform excitation with wave propagation speed of 400 m/s is plumper than the other two cases, which indicates that the pier dissipates much energy of the earthquake input. The case of uniform excitation is the one that experienced the smallest damage.

4.4. Response of Steel Box Girder. To be the primary component of the bridge, the steel girder bears the moments induced by various loadings, such as dead load, live load, and temperature load. If the pounding interaction between the girder and the abutment occurs during an earthquake, the axial stress in the girder may increase sharply to induce damage events of the steel girder. The time histories of axial stress at both ends of the girder are computed and displayed in Figure 13. The peak axial stresses are tabulated in Table 5.

The axial stress responses of the steel girder indicate that the most dangerous loading case for both ends of the steel girder is the nonuniform excitation with the wave propagation speed of 400 m/s. However, the nonuniform excitation

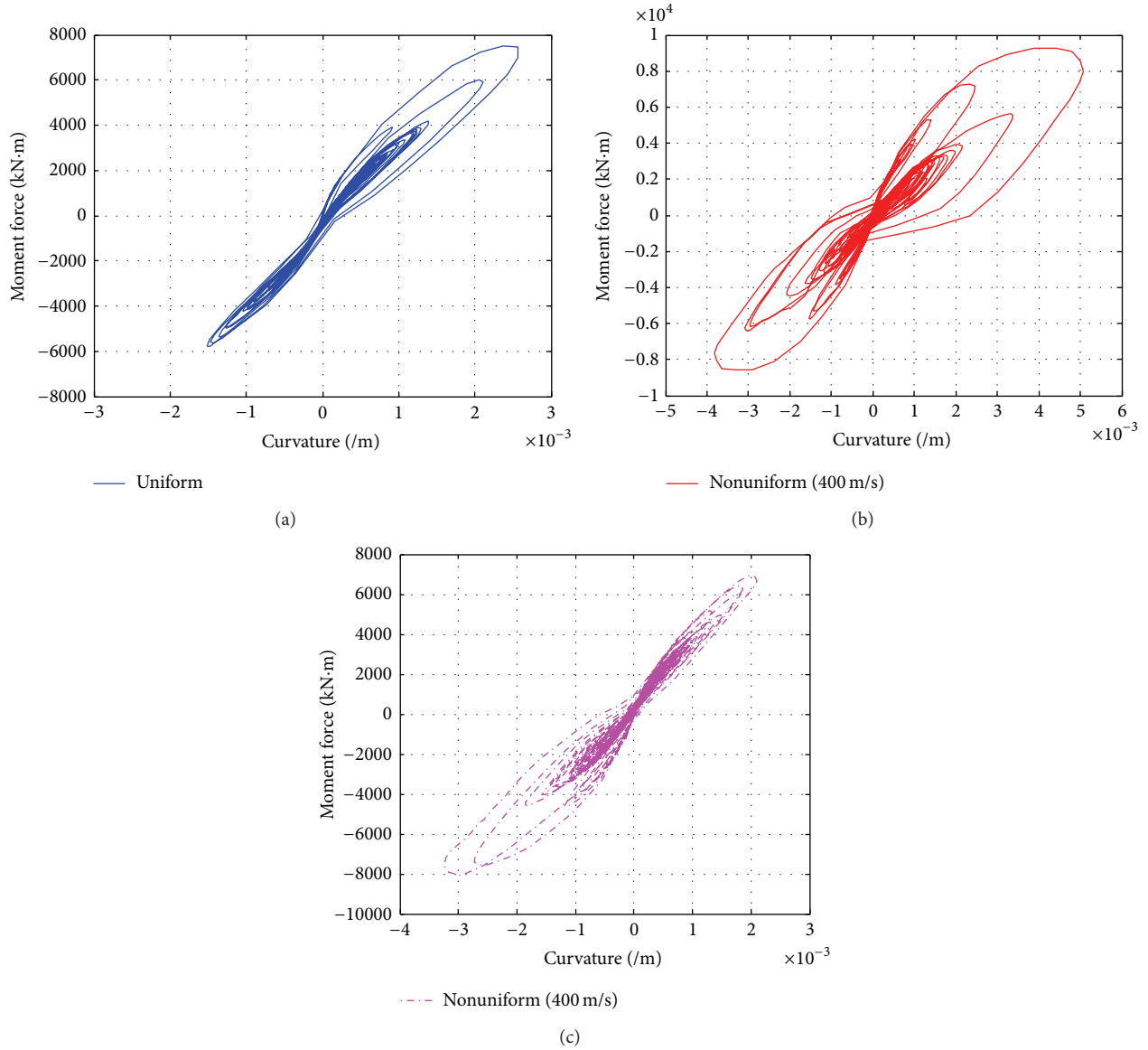


FIGURE 12: Moment versus curvature relationship of piers.

TABLE 5: Peak response of axial stress of steel girder.

Location	Uniform		Nonuniform (400 m/s)		Nonuniform (200 m/s)	
	Time (s)	Stress (kPa)	Time (s)	Stress (kPa)	Time (s)	Stress (kPa)
Left end	15.28	8.26×10^3	7.78	8.39×10^3	11.92	4.44×10^3
Right end	16.0	8.05×10^3	7.34	8.96×10^3	12.44	7.97×10^3

with the wave propagation speed of 200 m/s presents the smallest seismic responses.

5. Concluding Remarks

The paper investigates the pounding effects between the abutment and the steel girder by considering the uniform

and nonuniform excitation with different wave propagation speeds. A detailed nonlinear FE model is established and two types of zero-length nonlinear elements are used to model the pounding interaction between the girder and the abutment and the rubber bearings, respectively. In addition, two types of nonlinear fiber displacement-based elements are used to model the steel box girder and the reinforced concrete pier, respectively. The dynamic analyses on impact effects are

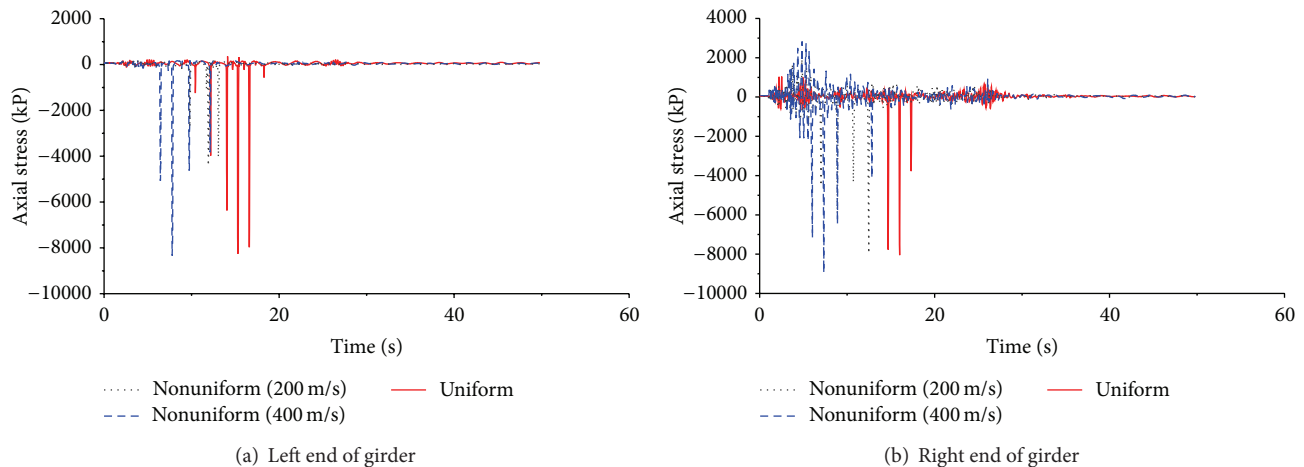


FIGURE 13: Time history response of axial stress in steel girder.

carried out under the uniform and nonuniform excitations with two wave propagation speeds. The comparison of the seismic responses, such as the pounding force between the abutment and the girder, the shear forces of the rubber bearings, the moments of reinforced concrete pier, and the axial pounding stresses in the steel girder is performed.

The consequence of the comparison indicates that the nonuniform excitation always results in the disadvantageous responses in the seismic analysis of the bridge under impact action.

Conflict of Interests

The authors declare that there is no conflict of interests regarding the publication of this paper.

Acknowledgments

The authors are grateful for the financial support from the National Natural Science Foundation of China (51178366), the Technological Project of the Chinese Southern Power Grid Co. Ltd. (K-GD2013-0222), the Fok Ying-Tong Education Foundation (131072), and the Natural Science Foundation of Hubei Province (2014CFA026).

References

- [1] Y. L. Xu, B. Chen, C. L. Ng, K. Y. Wong, and W. Y. Chan, "Monitoring temperature effect on a long suspension bridge," *Structural Control and Health Monitoring*, vol. 17, no. 6, pp. 632–653, 2010.
- [2] B. Chen, Z. W. Chen, Y. Z. Sun, and S. L. Zhao, "Condition assessment on thermal effects of a suspension bridge based on SHM oriented model and data," *Mathematical Problems in Engineering*, vol. 2013, Article ID 256816, 18 pages, 2013.
- [3] Y. Xia, B. Chen, X.-Q. Zhou, and Y.-L. Xu, "Field monitoring and numerical analysis of Tsing Ma suspension bridge temperature behavior," *Structural Control and Health Monitoring*, vol. 20, no. 4, pp. 560–575, 2013.
- [4] H. Ostuka, S. Unjoh, T. Terayama, J. Hoshikuma, and K. Kosa, "Damage to highway bridges by the 1995 Hyogoken Nambu earthquake and the retrofit of highway bridges in Japan," in *Proceedings of the 3rd U. S. Japan Workshop on Seismic Retrofit of Bridge*, Osaka, Japan, December 1996.
- [5] B. Chen, Y. Z. Sun, Y. L. Li, and S. L. Zhao, "Control of seismic response of a building frame by using hybrid system with magnetorheological dampers and isolators," *Advances in Structural Engineering*, vol. 17, no. 8, pp. 1199–1215, 2014.
- [6] Earthquake Engineering Research Institute. Northridge Earthquake Reconnaissance Report, vol. 1, Supplement C to vol. 11, April 1995.
- [7] R. Desroches and G. L. Fenves, "New design and analysis procedures for intermediate hinges in multiple-frame bridges," Tech. Rep. no. UCB/EERC-97/12, Earthquake Engineering Research Center, University of California, Berkeley, Calif, USA, 1997.
- [8] E. Maragakis, B. Douglas, and S. Vrontinos, "Classical formulation of the impact between bridge deck and abutments during strong earthquakes," in *Proceedings of the 6th Canadian Conference on Earthquake Engineering*, Toronto, Canada, 1991.
- [9] A. Guo, Z. Li, H. Li, and J. Ou, "Experimental and analytical study on pounding reduction of base-isolated highway bridges using MR dampers," *Earthquake Engineering and Structural Dynamics*, vol. 38, no. 11, pp. 1307–1333, 2009.
- [10] K. Bi, H. Hao, and N. Chouh, "Required separation distance between decks and at abutments of a bridge crossing a canyon site to avoid seismic pounding," *Earthquake Engineering and Structural Dynamics*, vol. 39, no. 3, pp. 303–323, 2010.
- [11] S. Muthukumar and R. DesRoches, "A Hertz contact model with non-linear damping for pounding simulation," *Earthquake Engineering & Structural Dynamics*, vol. 35, no. 7, pp. 811–828, 2006.
- [12] B. H. Maroney, *Large scale abutment tests to determine stiffness and ultimate strength under seismic loading [Ph.D. dissertation]*, University of California, Davis, Calif, USA, 1995.
- [13] A. Shamsabadi, K. M. Rollins, and M. Kapuskar, "Non-linear soil-abutment-bridge structure interaction for seismic performance-based design," *Journal of Geotechnical and Geoenvironmental Engineering*, vol. 133, no. 6, pp. 707–720, 2007.
- [14] N. A. Abrahamson, J. F. Schneider, and J. C. Stepp, "Empirical spatial coherency function for application to soil structure

- interaction analysis," *Earthquake Spectra*, vol. 7, no. 1, pp. 1–27, 1991.
- [15] C.-C. Tsai and Y. M. A. Hashash, "Evaluation of two approaches to simulate spatially variable ground motions," *Journal of Earthquake Engineering*, vol. 14, no. 2, pp. 293–308, 2010.
 - [16] E. H. Vanmarcke, E. Heredia-Zavoni, and G. A. Fenton, "Conditional simulation of spatially correlated earthquake ground motion," *Journal of Engineering Mechanics*, vol. 119, no. 11, pp. 2332–2352, 1993.
 - [17] W. Goldsmith, *Impact: The Theory and Physical Behavior of Colliding Solids*, Edward Arnold, London, UK, 1960.
 - [18] California Department of Transportation (CLATTRANS), *Seismic Design Criteria, Version 1.6*, California Department of Transportation (CLATTRANS), Sacramento, Calif, USA, 2010.
 - [19] A. Zerva, "Spatial variability of seismic motions recorded over extended ground surface areas," in *Wave Motion in Earthquake Engineering*, E. Kausel and G. Manolis, Eds., The MIT Press, Cambridge, Mass, USA, 1999.
 - [20] G. Deodatis, "Non-stationary stochastic vector processes: seismic ground motion applications," *Probabilistic Engineering Mechanics*, vol. 11, no. 3, pp. 149–167, 1996.
 - [21] E. Heredia-Zavoni, *On the response of multi-support MDOF systems to spatially varying earthquake ground motion [Ph.D. dissertation]*, Department of Civil Engineering and Operations Research, Princeton University, 1993.
 - [22] B. Chen, J. Zheng, and W. Qu, "Control of wind-induced response of transmission tower-line system by using magnetorheological dampers," *International Journal of Structural Stability and Dynamics*, vol. 9, no. 4, pp. 661–685, 2009.
 - [23] B. Chen, Y. L. Xu, and X. Zhao, "Integrated vibration control and health monitoring of building structures: a time-domain approach," *Smart Structures and Systems*, vol. 6, no. 7, pp. 811–833, 2010.
 - [24] H. N. Li, T. H. Yi, M. Gu, and L. Huo, "Evaluation of earthquake-induced structural damages by wavelet transform," *Progress in Natural Science*, vol. 19, no. 4, pp. 461–470, 2009.
 - [25] T.-H. Yi, H.-N. Li, and M. Gu, "Wavelet based multi-step filtering method for bridge health monitoring using GPS and accelerometer," *Smart Structures and Systems*, vol. 11, no. 4, pp. 331–348, 2013.
 - [26] R. S. Harichandran and E. H. Vanmarcke, "Stochastic variation of earthquake ground motion in space and time," *Journal of Engineering Mechanics*, vol. 112, no. 2, pp. 154–174, 1986.

Research Article

A Wireless Strain Sensor Network for Structural Health Monitoring

Chengyin Liu,^{1,2} Jun Teng,² and Ning Wu²

¹Key Laboratory of C&PC Structures, Southeast University, Nanjing 211189, China

²Department of Civil and Environmental Engineering, Harbin Institute of Technology, Shenzhen Graduate School, Shenzhen 518055, China

Correspondence should be addressed to Chengyin Liu; chengyin.liu08@gmail.com

Received 7 August 2014; Accepted 15 January 2015

Academic Editor: Gangbing Song

Copyright © 2015 Chengyin Liu et al. This is an open access article distributed under the Creative Commons Attribution License, which permits unrestricted use, distribution, and reproduction in any medium, provided the original work is properly cited.

Structural strain under external environmental loads is one of the main monitoring parameters in structural health monitoring or dynamic tests. This paper presents a wireless strain sensor network (WSSN) design for monitoring structural dynamic strain field. A precision strain sensor board is developed and integrated with the IRIS mote hardware/software platform for multichannel strain gauge signal conditioning and wireless monitoring. Measurement results confirm the sensor's functionality regarding its static and dynamic characterization. Furthermore, in order to verify the functionality of the designed wireless strain sensor for dynamic strain monitoring, a cluster-star network evaluation system is developed for strain modal testing on an experimental steel truss structure. Test results show very good agreement with the finite element (FE) simulations. This paper demonstrates the feasibility of the proposed WSSN for large structural dynamic strain monitoring.

1. Introduction

In order to improve the safety level of engineering structures, structural health monitoring (SHM) has become a popular research topic to determine the condition of the monitored structure and identify potential problems at an early stage [1]. The SHM system often offers an opportunity to reduce the cost for maintenance, repair, and retrofit throughout the lifetime of structure. Estimates of the health of structure can be realized through monitoring the physical behavior and environmental condition, for example, acceleration, strain, and temperature. Traditional SHM approaches collect measured responses from a centralized data acquisition and analysis system, but they suffer from problems like expensive sensor installation/wiring, signal degradation along lengthy cables, and data flooding.

With the rapid advancement in smart sensing technology and wireless communication technology, wireless sensor network (WSN) offers an alternative solution to SHM [2]. Compared to the traditional methods, the use of wireless technologies offers distinctive advantages in the field. For

example, low-cost WSN instrumentation promises dense deployment of wireless sensors, which can increase the accuracy of the collected SHM data. Also, it promises fast and dense deployment and easier maintenance. Dense arrays of low-cost smart wireless sensor networks (WSNs) have the potential to improve the quality of the SHM dramatically using their on-board computational and wireless communication capabilities.

The Berkeley Mote smart sensor developed by Hill et al. [3] has emerged as an important new open hardware/software platform for SHM. The mote platform has a microprocessor and radio communication system. Users can easily customize both the hardware and software. Kurata et al. [4] have reported their experiences using the Mica mote wireless sensing platform for structural monitoring. Based on the Mica and Imote platforms [5], related work on using WSNs for structural monitoring includes notable experiments like Wisden, Tenet [6], and the Golden Gate Bridge deployment [7]. These WSNs provide rich information which SHM algorithms can utilize to detect, locate, and assess the structural damage caused by severe loading events and progressive

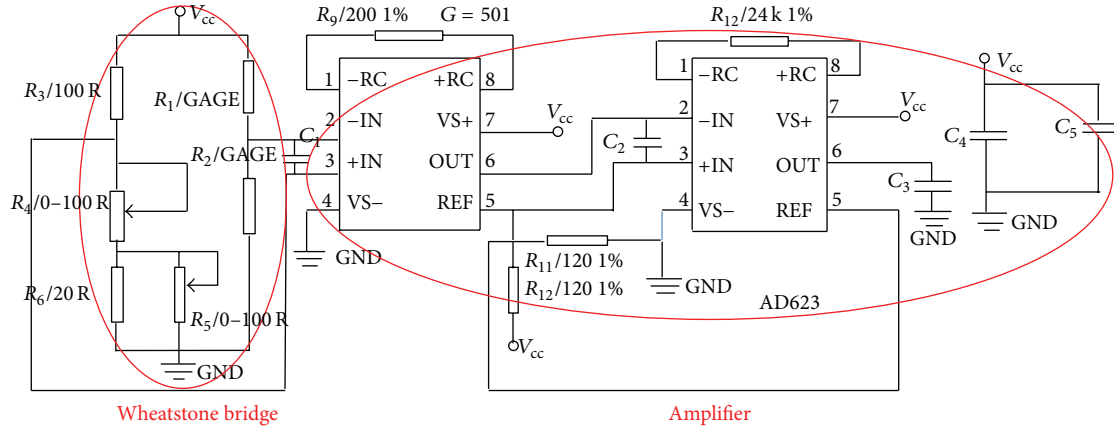


FIGURE 1: Wireless strain sensor board circuit schematic.

environmental deterioration as well as economical realization of the SHM system [8].

In recent years, several other WSN systems have been proposed for SHM. Lynch et al. [9] deployed 14 wireless sensors to monitor the forced acceleration responses of Geundang Bridge in Korea. However, their system is also of single-hop network type. Bocca et al. [10–12] introduced a time-synchronized WSN and a WSN with embedded Goertzel algorithm to process the acceleration data locally and in real time. In this work, the network is based on ISMO-2 nodes and organized into a star topology to enable accelerometer measurement on a wooden model bridge.

In addition to acceleration, strain is one of the most important physical quantities to judge the health of a structure [13]. As an effective sensing unit, the strain gauge has been applied to local monitoring for a long time [14]. For traditional strain collection and transmission systems, the strain collection device is big in volume, the circuit performance and collection precision is affected by the wire length, and the installation and maintenance cost can be very high. All these factors have limited the application of local sensing units. To find a good solution to extricate strain monitoring from this dilemma, in the past decade, magnetically soft sensors, self-diagnosis materials, and fiber optics sensing technology have been mostly deployed [15–17]. In particular, the fiber Bragg grating sensors have been demonstrated to be capable obtaining precise amounts of strain of structures [18, 19]. The utility of FBG sensors has been demonstrated in field applications, as well as in numerous laboratory tests. Meanwhile, research on structural local monitoring using wireless sensing technology is increasing. Whelan et al. [20] recently addressed the strain-based low-power monitoring problem with a WSN, and a customized data acquisition platform (called WSS) based on Tmote Sky Mote was proposed, which conducts strain-based monitoring through a switch. Gangone et al. [21] discussed the load testing and the rating of a simply supported bridge, in which WSS from strain measurements was deployed. This approach can provide complete information for SHM. However, large-scale communication issue in SHM could not

be addressed because this system relies on single-hop, star topology wireless communication between sensors and base stations. Currently, most of the available sensor boards paired to the Berkeley Mote are not specially designed for strain field monitoring on large structures.

This paper aims to present a WSN-based strain monitoring system, and a customized wireless strain sensor board for multichannel strain gauge signal conditioning and monitoring is developed based on a commercially available IRIS mote platform. This system was developed with the objective of integration, miniaturization, high-reliability, and low cost. The WSSN is suitable for monitoring static and dynamic structural strain responses under random loads and is thus capable of continuous monitoring. A multihop, cluster-star network is developed and its performance is experimentally validated on a steel truss structure. The test results along with the FE simulations will be shown to prove the feasibility of the WSSN for large structural dynamic strain monitoring.

2. Wireless Sensor for Dynamic Strain Monitoring

A wireless strain sensor is composed of strain sensor board, IRIS mote, and strain gauges with the resistance of 120 ohm. Due to IRIS mote's scalable design, user can customize the hardware and software according to the application needs. In this paper, a new strain sensor board is developed, and the hardware and software integration with the IRIS mote will be addressed in the following paragraphs.

2.1. Strain Sensor Board Design. As shown in Figure 1, the strain board circuit is designed for the sensor input unit. The circuit is composed of three parts, the bridge circuit, the amplifier, and the output circuit. A quarter Wheatstone bridge circuit and two variable gain amplifiers are implemented to achieve a wide measurement range due to the IRIS's 10 bit ADC restriction.

A quarter Wheatstone bridge is designed with one working resistance strain gauge and another temperature



FIGURE 2: (a) Strain sensor board and (b) IRIS mote.

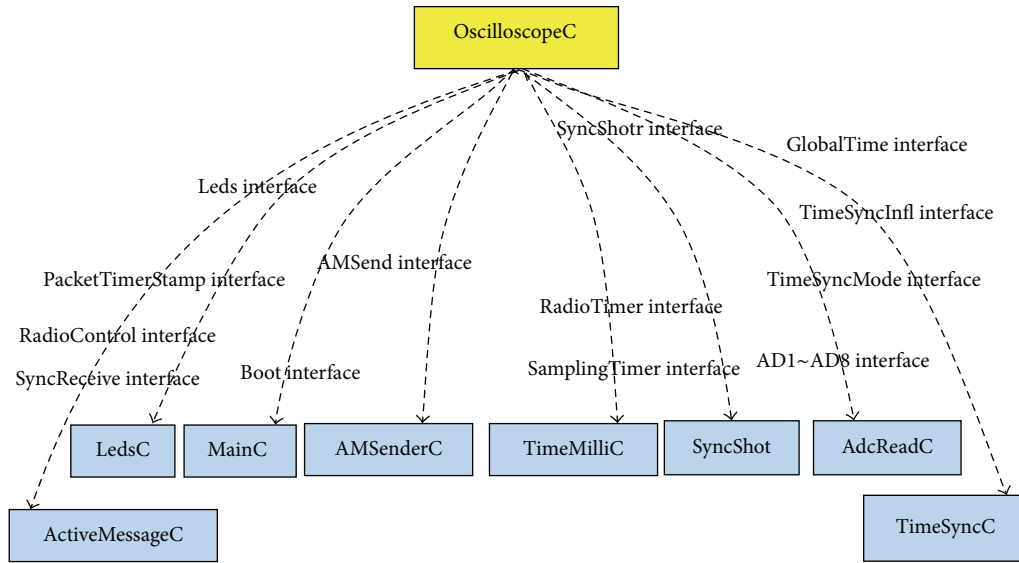


FIGURE 3: The application components for wireless strain sensor.

compensation resistance strain gauge. As the signal being amplified two times, the Wheatstone bridge should be absolute equilibrium otherwise the unbalanced errors can be amplified too. Therefore, a leveling circuit is designed in the Wheatstone bridge including coarse tuning and fine tuning. The coarse tuning is achieved by the adjustable resistance R4. The fine tuning is achieved by the resistance R6 and adjustable resistance R5 in parallel.

Two instrumentation amplifiers AD623 are adopted to magnify the bridge circuit output. As a low-power instrumentation amplifier, the AD623 can offer excellent accuracy for the sensor input unit of the wireless sensor nodes. A low-pass filter is designed to eliminate the high frequency noise. This filter also reduced the problem of aliasing. Note that the dynamic signal may be below 0; the strain sensor board is accordingly designed to make certain that the input signals are always above 0 to satisfy the sensor input voltage range requirement.

2.2. IRIS Mote Platform. The developed strain sensor board shown in Figure 2(a) is connected to IRIS mote platform through a 51-pin expansion connector. The IRIS mote as shown in Figure 2(b) and has an Intel Xscale processor and RAM of 256 KB. The radio components are capable of transmitting data at transmission rate of 250 Kbps. The 51-pin expansion connector supports 8 channel analog inputs which can be used to acquire the analog signals. The hardware is appropriate for strain monitoring application. IRIS motes run on TinyOS [2] operating system platform that handles task scheduling, radio communication, time synchronization, and I/O processing, and so forth.

2.3. Software Design for Wireless Strain Sensor. To support the wireless strain sensor node hardware integration, an open source operating system, TinyOS, is utilized to program the IRIS. The application components used for wireless strain sensor integration are presented in Figure 3. Component

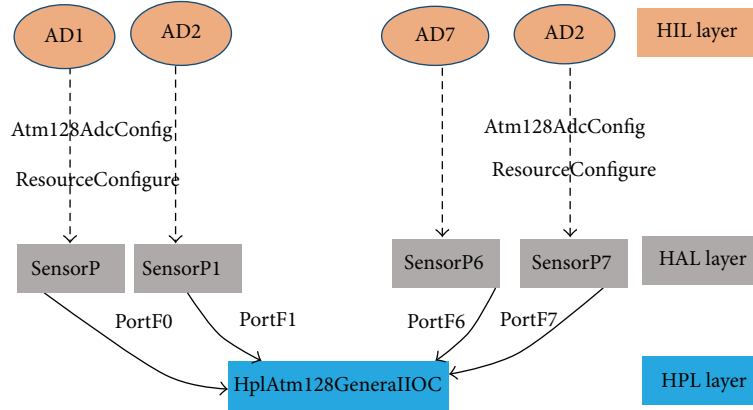


FIGURE 4: Pins driver program.



FIGURE 5: Static experiment setup.

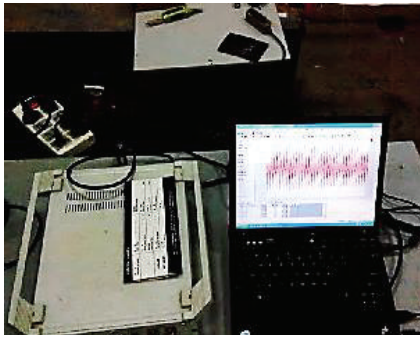


FIGURE 6: Data acquisition system.

AdcReadC is a driver module used to drive the AD channels. The 51-pin expansion connector of IRIS mote supports 8 channel analog inputs for collecting strain signals. Hence, only 8 channel analog pins need to be driven. Figure 4 shows the process of the developed driver module driving the IRIS mote from the hardware interface layer (HIL) to the hardware presentation layer (HPL) step by step. With the pins driver program we can control the AD channels for strain signals. Note that a triggering timer component is specially developed for periodic sampling of dynamic strain signals.

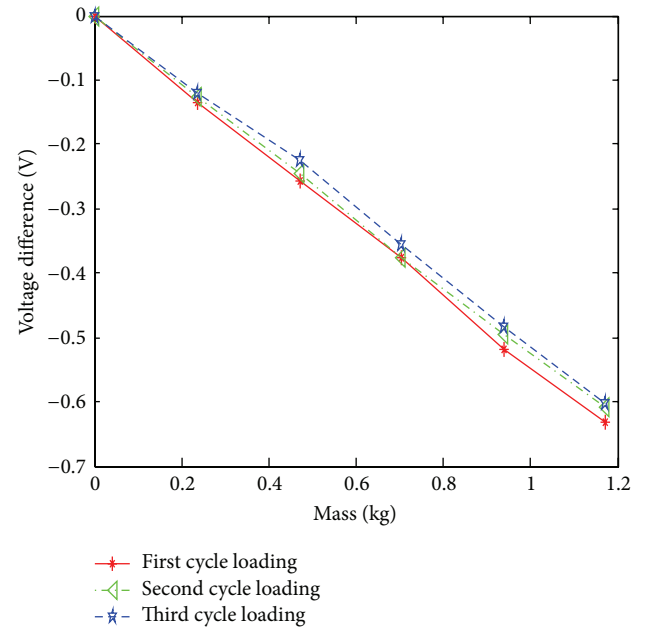


FIGURE 7: Three cycles loading.

3. Wireless Strain Sensor Characterization

After the fabrication of the sensor node, node characterization is performed in a laboratory environment. In this paper, the characterization for the sensor node is to investigate its static and dynamic performance of strain signal acquisition and sensitivity coefficient calibration.

3.1. Static Characterization. The first test is to investigate the linearity error and repeatability error of the strain sensor signal acquisition. Figure 5 shows the picture of the setup for the static characterization. 4 strain gauges are attached to the upper and lower surface of an equal intensity beam. DH5922 data acquisition system, as shown in Figure 6, is used to form measuring bridge. Table 1 lists the experimental data of the sensor input unit through repetitive loading to the equal intensity beam. The results are used to calculate

TABLE 1: Loading and unloading of three cycles.

Load (kg)	Output (V)					
Mass	First cycle		Second cycle		Third cycle	
Δm	Loading	Unloading	Loading	Unloading	Loading	Unloading
0	2.1284	2.1143	2.1143	2.1267	2.1267	2.1274
0.236	1.9946	1.9996	1.9874	1.9855	2.0074	2.0164
0.472	1.8724	1.8784	1.8684	1.8806	1.9018	1.9108
0.704	1.7535	1.7680	1.7385	1.7565	1.7723	1.7629
0.938	1.6088	1.6361	1.6183	1.6264	1.6421	1.6418
1.170	1.4970	1.4970	1.5065	1.5065	1.5247	1.5247

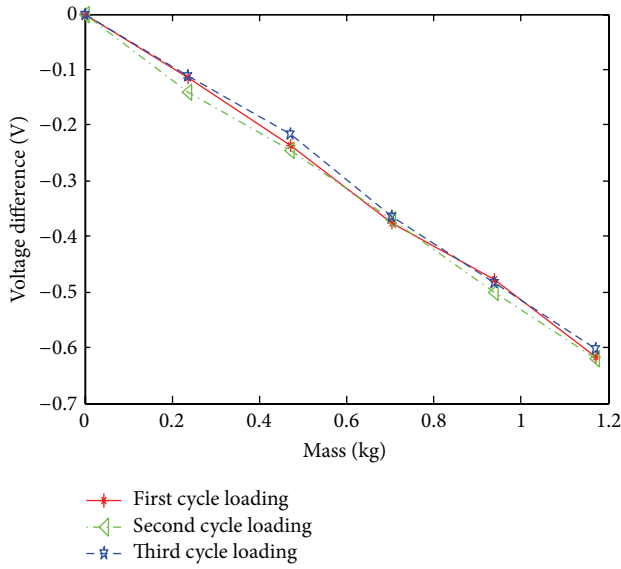


FIGURE 8: Three cycles unloading.

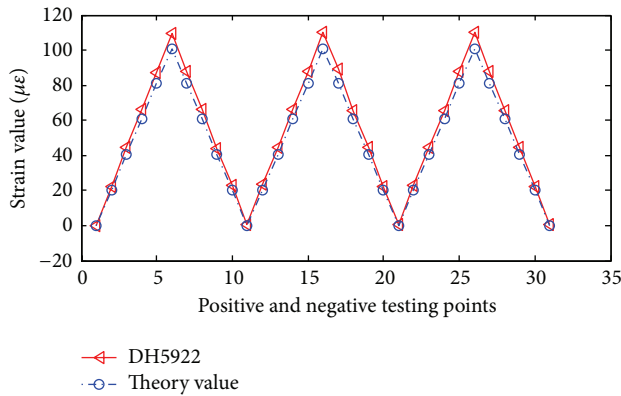


FIGURE 9: Strain data measured by DH5922 versus theoretic value.

the linearity error and repeatability error which are critical to the sensitivity coefficient calibration.

The values of mass Δm and output voltage variation ΔU are summarized in Table 2. In Figures 7 and 8, the changes of output voltage variation ΔU are plotted versus mass variation Δm for loading and unloading cases, respectively.



FIGURE 10: Vibration exciter.



FIGURE 11: Signal Generator.

A linear approximation can be observed from Figure 7. In consequence, a linear fit equation is obtained in the following form:

$$\Delta U = -0.5114 \times \Delta m - 0.0124. \quad (1)$$

Table 3 lists the largest deviation ΔL_{\max} for output voltage variation ΔU obtained in testing. In Table 3, the largest deviation is found to be $\Delta L_{\max} = -0.0275$. Define the linearity error as

$$\gamma_L = \pm \frac{\Delta L_{\max}}{y_{FS}} \times 100\%, \quad (2)$$

where y_{FS} is the full scale output. For the static characterization, the largest linearity error $\gamma_L = 4.356\%$ is acceptable for engineering application.

TABLE 2: Relation of variation Δm and variation ΔU .

Load (kg)	Voltage difference (V)					
Mass	First cycle		Second cycle		Third cycle	
Δm	Loading	Unloading	Loading	Unloading	Loading	Unloading
0	0	0	0	0	0	0
0.236	-0.1338	-0.1147	-0.1269	-0.1412	-0.1193	-0.1110
0.472	-0.256	-0.2359	-0.2459	-0.2461	-0.2249	-0.2166
0.704	-0.3749	-0.375	-0.3758	-0.3702	-0.3544	-0.3645
0.938	-0.5196	-0.4782	-0.496	-0.4997	-0.4846	-0.4822
1.170	-0.6314	-0.6173	-0.6078	-0.6206	-0.602	-0.6027

TABLE 3: The value of ΔL_{\max} .

Load (kg)	Voltage difference (V)						Equation (1)	ΔL
Mass	First cycle		Second cycle		Third cycle		ΔU	ΔL_{\max}
Δm	Loading	Unloading	Loading	Unloading	Loading	Unloading		
0	0	0	0	0	0	0	-0.0124	-0.0124
0.236	-0.1338	-0.1147	-0.1269	-0.1412	-0.1193	-0.1110	-0.1331	-0.0221
0.472	-0.2560	-0.2359	-0.2459	-0.2461	-0.2249	-0.2166	-0.2438	-0.0272
0.704	-0.3749	-0.3750	-0.3758	-0.3702	-0.3544	-0.3645	-0.3724	-0.018
0.938	-0.5196	-0.4782	-0.4960	-0.4997	-0.4846	-0.4822	-0.4921	-0.0275
1.170	-0.6314	-0.6173	-0.6078	-0.6206	-0.6020	-0.6027	-0.6107	-0.0207

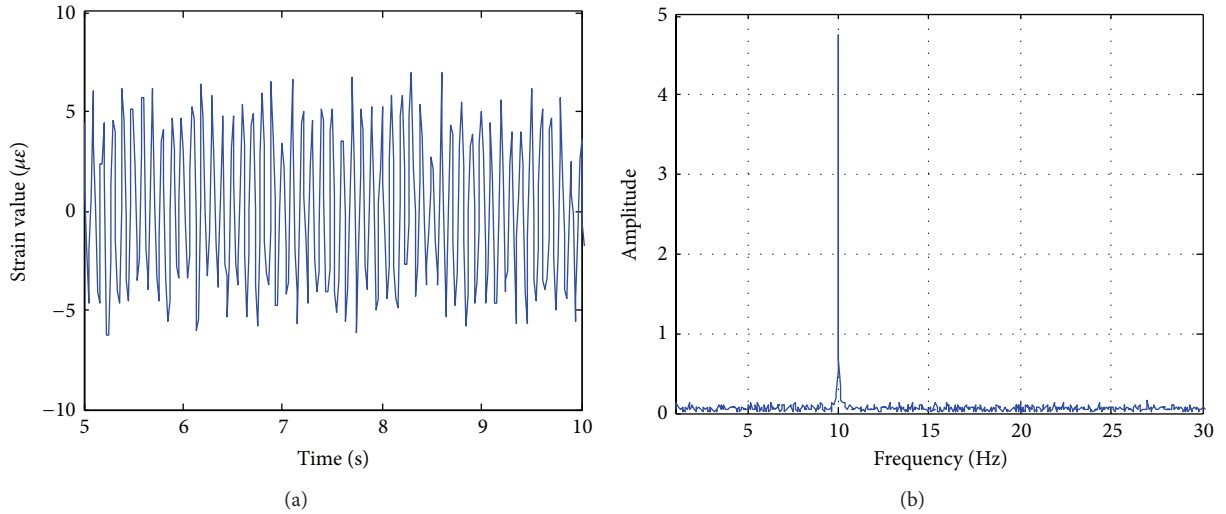


FIGURE 12: 10 Hz input wave: (a) strain signal and (b) frequency spectrum of the signal.

The linearity error is considered as a residual error in random distribution. Its standard deviation can be calculated as

$$\delta = \sqrt{\frac{1}{n-1} \sum_{i=1}^n (\Delta L)^2} \quad (3)$$

in which n is the number of testing points and ΔL is the residual error. The repeatability error for the wireless strain sensor can be represented by γ_R given by

$$\gamma_R = \pm \left(\frac{3\delta}{\gamma_{FS}} \right) \times 100\%. \quad (4)$$

Substituting the test data in Table 3 into formula (3) and formula (4), the standard deviation and repeatability error can be calculated as $\delta = 0.01273$ and $\gamma_R = 6.049\%$. Experimental results show that the developed wireless strain sensor has a good static performance.

3.2. Sensitivity Coefficient Calibration. From Figure 9, we can see that the data measured by DH5922 is perfect compared to the theoretical value. The sensitivity coefficient of the DH5922 is set to 2 and the measuring bridge is the same with the wireless experiment when taking the experiments. Same as static performance tests, the relationship of mass variation

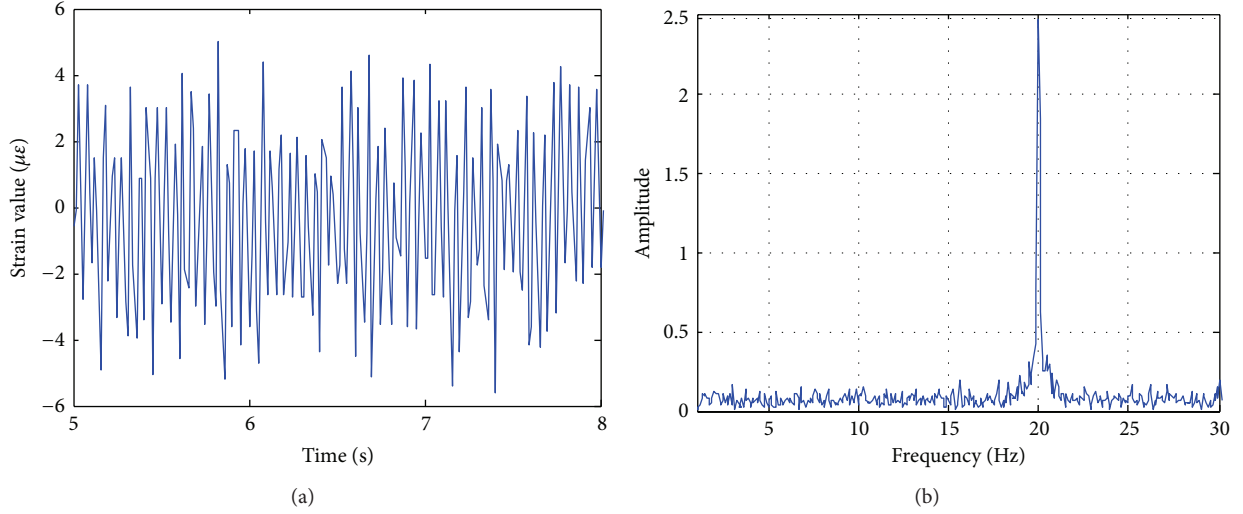


FIGURE 13: 20 Hz input wave: (a) strain signal and (b) frequency spectrum of the signal.

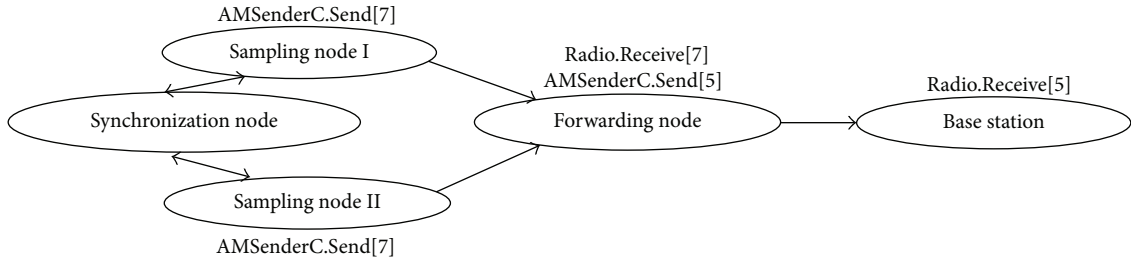


FIGURE 14: Workflow of data communication.

Δm and strain variation $\Delta \epsilon$ can be obtained with a linear fit, as shown in formula

$$\Delta \epsilon = 93.7003 \times \Delta m + 0.3233. \quad (5)$$

For a quarter Wheatstone-Bridge, we have

$$\Delta \epsilon = \frac{4\Delta U}{U_O \times K_s}, \quad (6)$$

where U_O is the value of power supply voltage and K_s is the sensitivity coefficient which needs to be calculated.

Substituting (1) into (5) to eliminate the parameter Δm , we can get

$$\Delta \epsilon = -183.223\Delta U + 1.949. \quad (7)$$

Considering the amplification factors $Gain1$ and $Gain2$, thus (6) can be reformed as

$$\frac{4}{U_O \times K_s \times Gain1 \times Gain2} = -183.223 \times 10^{-6}, \quad (8)$$

where the predefined amplification factors $Gain1$ and $Gain2$ are 501 and 5.16667, respectively.

From (8), we can obtain the sensitivity coefficient for the wireless strain sensor $K_s = 2.2195$.

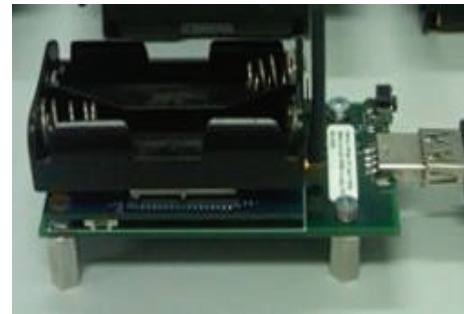


FIGURE 15: IRIS mote and MIB520.



FIGURE 16: Interface of the serial software.

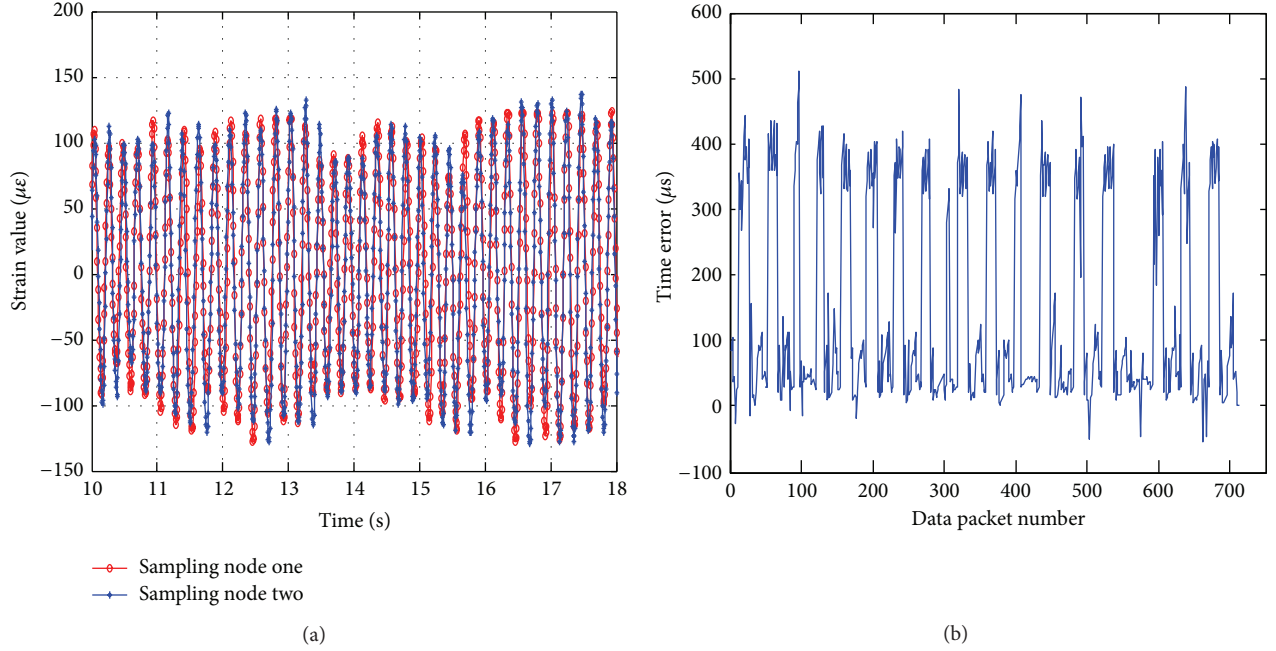


FIGURE 17: Time synchronization error of 128 Hz: (a) time history signal and (b) time error.

3.3. Dynamic Characterization. The response of the developed device to dynamic strain input is essential for determining the sensor's potential for monitoring the strains occurring during dynamic physical exercises such as walking or running. The objective is to find out to what extent the measurement channel's fill level is able to follow the periodic dynamic strain input without suffering from the loss of sensitivity.

For testing, a signal generator and a vibration exciter are added to the previous measurement setup as shown in Figures 10 and 11. The signal generator sends wave commands to the vibration exciter, and, therefore, the cantilever beam is moved up and down by the vibration exciter with a specific frequency (signal generator controlled). Two input wave frequencies, 10 Hz and 20 Hz, are chosen in this study for the characterization of the sensor devices, respectively.

The measurement results of the dynamic characterization of the strain sensor and frequency spectrum after Fourier transformation are shown in Figures 12 and 13. It can be observed that the target and actual frequencies are consistent at 10 Hz and 20 Hz, respectively. Therefore, the potential for dynamic applications of the wireless strain sensor device can be expected.

4. Wireless Strain Sensor Network Design

In order to show the monitoring capability of the wireless sensor network, a two-tier wireless network is adopted to overcome time synchronization problems as well as the challenges in data transmission rates and power efficiency. The cluster head nodes communicating with the corresponding local leaf nodes form the bottom tier, and the base station communicating with the cluster head nodes forms the top

tier. Accordingly, the middleware services developed on TinyOS for this application are thus including the signal acquisition module, the forwarding module, the base station module, and the time synchronization program embedded module. Figure 14 shows the workflow of data communication in the WSSN. By defining the components module active message (AM) type through TinyOS, the network route can be achieved. For example, the forwarding node can only receive signal from the node whose AMSenderC AM type is 7 and can only send signal to the node whose Radio.Receive AM type is 5.

4.1. Sampling Module. In the signal acquisition module, known as leaf node, the AdcReadC component is developed to drive the analog ports. The component TimeMilliC is applied to control the sampling frequency of the sensor. TimesynC is used to synchronize sampling nodes and make sure that signals of the two nodes are synchronized. AMSenderC component is very important for WSSN data communication. It controls the receiving and transmitting signals between the determined nodes through predefining the node's active message (AM) type.

The forwarding module, also called the cluster head, is used to send the received signal from the sampling node to the computer through the base station. Similarly, this point to point data transmission is realized by predefining the AM type of the AMSenderC component.

Base station module functions as a bridge connecting WSSN and the computer. It sends instructions from computer to WSSN and transmits signals from WSSN to computer. The base station is composed of a programming board MIB520 and an IRIS node, as shown in Figure 15. It transmits data through a USB cable to the computer. Figure 16 shows

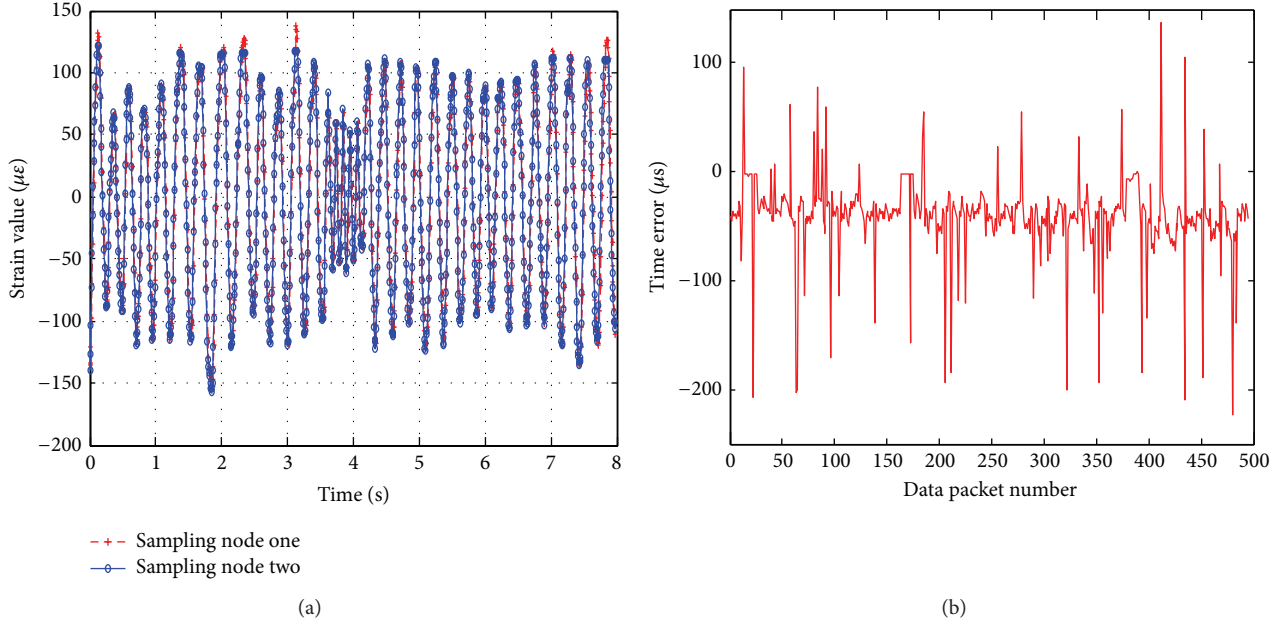


FIGURE 18: Time synchronization error of 64 Hz: (a) time history signal and (b) time error.



FIGURE 19: Test truss structure.

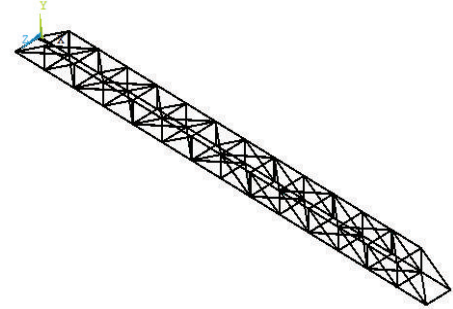


FIGURE 20: FE model.

a sample of original data package collected from the computer interface. The original data is in hexadecimal format which needs to be converted to decimal notation before processing.

4.2. Time Synchronization Module. Time synchronization in a wireless sensor network is important for routing and power conservation. Time synchronization error in a smart sensor network can cause inaccuracy in SHM applications. Global time synchronization allows the nodes to cooperate and transmit data in a scheduled manner. Time synchronization is a middleware service common to smart sensor applications and has been widely investigated [22–24]. In this study, the TinyOS is utilized to program the time synchronization implementation.

Time synchronization is operated between the two sensor nodes. Each sensor node has its own local clock, which is not synchronized initially. By communicating with the

surrounding nodes, smart sensors can assess the relative difference among their local clocks. Two tests have been carried out in this experiment, one is for 128 Hz sampling frequency and the other is for 64 Hz sampling frequency. The time synchronization results are presented in Figures 17 and 18. It can be found that the synchronization error between the two sensing units is measured to be within 100 μs which is ignorable in practice. However, it should be noted that the sampling frequency of sensor has major effect on the time synchronization error. The time synchronization error for 128 Hz sampling frequency is almost 5 times that of sampling frequency of 64 Hz.

5. Evaluation on a Real Truss Structure

In order to validate the capability of the designed wireless sensor network for structural dynamic strain monitoring, a multipoint strain monitoring system is developed on a 3D truss structure.

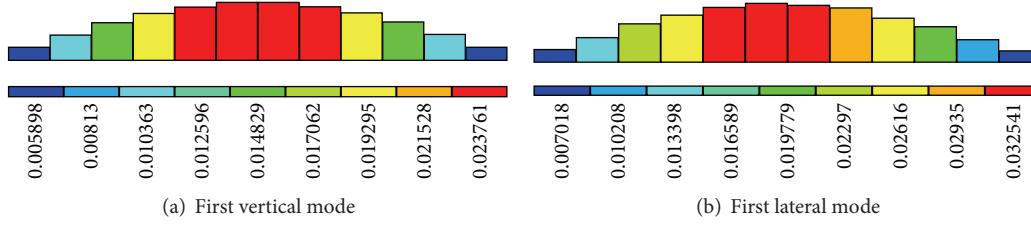


FIGURE 21: Strain modes identified by FE simulation.

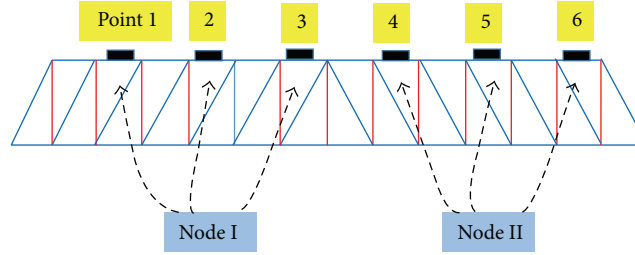


FIGURE 22: The arrangement of the measure points.

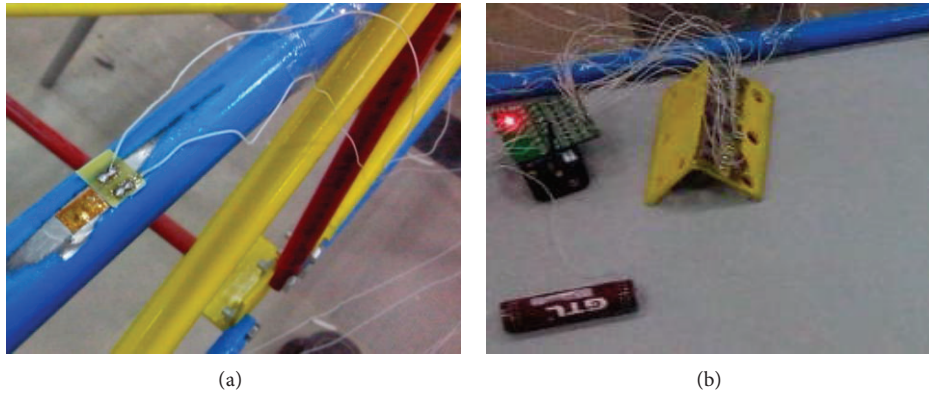


FIGURE 23: Experiment: (a) resistance strain gauge and (b) compensated strain gauge.

5.1. Experimental Truss Structure. The test structure is a steel truss with 14 bays, as shown in Figure 19. Each bay is 585 mm long, 490 mm wide, and 350 mm high. Totally, the steel truss has 52 longitudinal chords, 50 crosswise chords, and 54 diagonal chords. Each chord is forged with steel pipe. The chord section is hollow circular with an outer diameter of 18 mm and inner diameter of 12 mm. The rods are bolted on the gusset plates which are equilateral angle steel. The structure is simply supported with movement in the longitudinal direction only.

5.2. Finite Element Analysis. Finite element (FE) simulation is performed for the test structure in order to export modal parameters and give a comparison to the following experiment results. Link element has been used to simulate all members. The mass of the gusset is distributed on all the members. The established FE model is shown in Figure 20. The FE analysis results of natural frequencies of the test structure are listed in Table 4. From the table, we can see that the test structure has relatively high natural frequencies and

many coupled vibration modes due to its large stiffness in both vertical and lateral direction. The first two strain mode shapes are shown in Figure 21. They are pure bending modes in vertical and lateral direction.

5.3. Dynamic Strain Monitoring Based on Developed WSSN. The developed wireless strain sensor nodes are attached to the truss model at 6 points of the upper chords, as shown in Figure 22. The left three measure points (1, 2, and 3) are located at even across and the right three measure points (4, 5, and 6) are located at odd across. Leaf node I is used to acquire dynamical strain signals for the left three points and leaf node II for the right three points. Figure 23(a) shows the strain gauge attached to the chord surface. Figure 23(b) shows a leaf sensor node and the temperature compensating elements implemented on a steel angle.

5.4. Experimental Data Analysis. Figure 24 shows the time history curve and frequency spectrum of dynamical strain signals for measuring points 4, 5, and 6, which are collected

TABLE 4: Result of modal analysis.

Mode	First vertical	First lateral	Lateral and torsion	Torsion and vertical	Second vertical
Natural frequency (Hz)	8.785	11.293	19.833	28.934	32.265

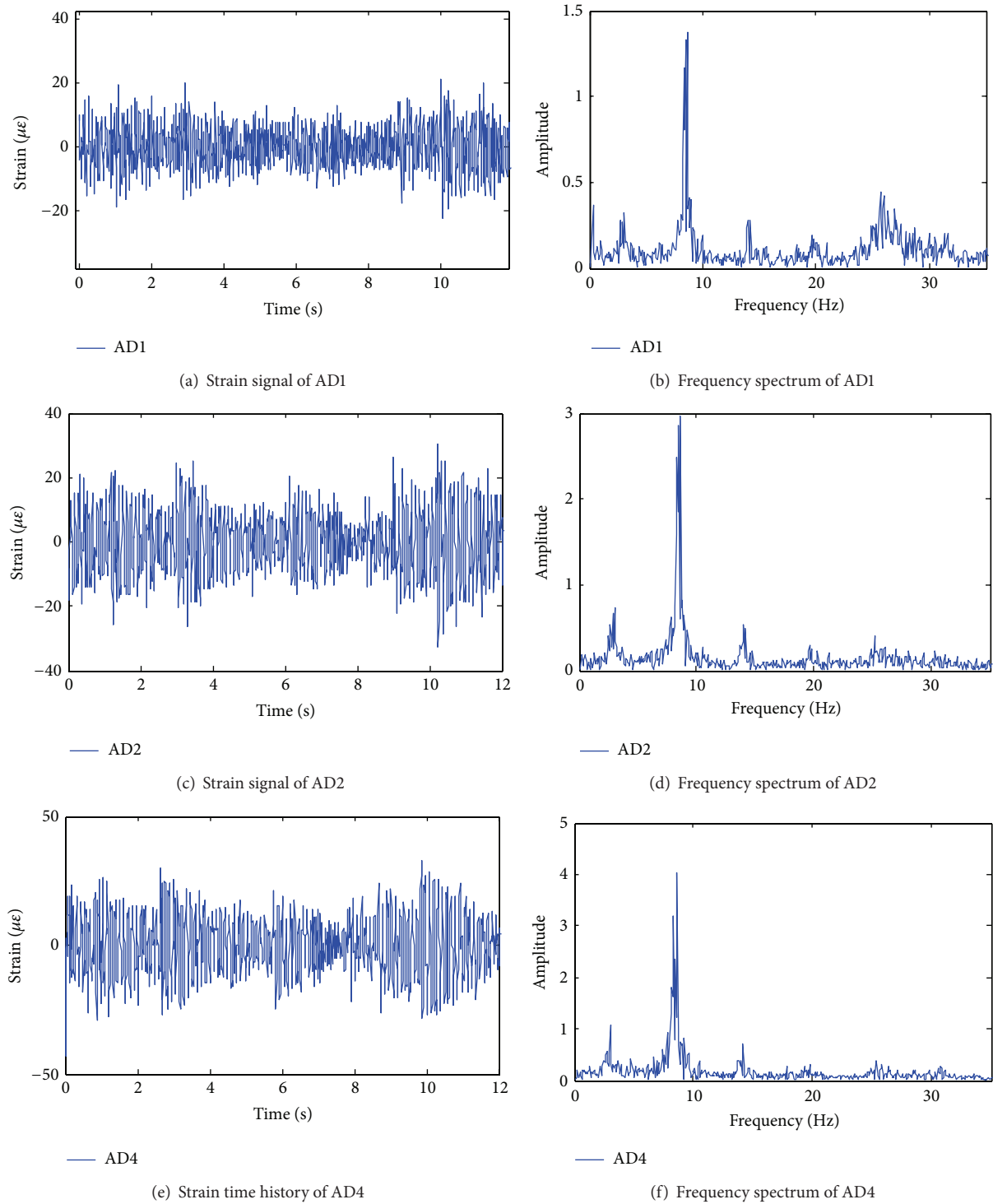


FIGURE 24: Strain signals and frequency spectrums of node II.

TABLE 5: FDD frequency identification compared to FE modal analysis.

Method	1st vertical	1st lateral	Lateral and torsional	Vertical and torsional	2nd vertical
WSSN	8.518	14.080	19.643	26.770	30.420
FE	8.785	11.239	19.833	28.934	32.365

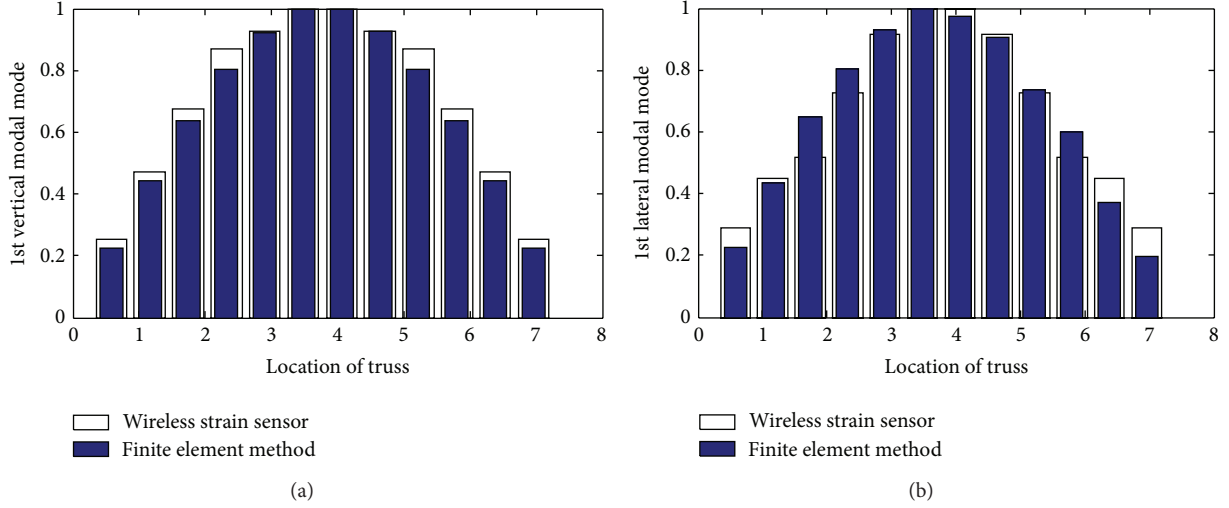


FIGURE 25: Modes identified by the WSSN: (a) 1st vertical mode and (b) 1st lateral mode.

by the AD4, AD2, and AD1 channels of node II, respectively. Node I has similar results.

Point 6 close to the end of span has the minimum vertical strain value. It contains other components such as lateral signal or reverse signal which is the properties of end bay. Point 4 locates at the middle span and it has the maximum strain value and the maximum amplitude of spectrum. From the frequency spectrum, we can see that the amplitude of the first vertical vibration mode is the highest, and, therefore, it satisfies the sensitivity of the strain property in low order vibration mode.

Considering the symmetrical characteristic of the test structure, the measuring data are analyzed using frequency domain decomposition (FDD) method to extract strain modal parameters (vibration modes and natural frequencies). Table 5 lists the natural frequencies of the test structure obtained by WSSN and FE simulation. It can be found that the identified natural frequencies are in good agreement. The fundamental natural frequency of test structure is 8.518 Hz, which is higher than that of many real civil infrastructures.

Figures 25(a) and 25(b) show the first vertical and first lateral modal shapes of the test structure obtained from experiment, respectively. They are almost identical to the modal shapes obtained in FE simulation in Section 5.3. The experiment results demonstrate that the WSSN can accurately identify low order vibration modes, while other identified higher order vibration modes are irregular, due to the large stiffness of the test structure. This difficulty mainly comes from synchronization. When the larger sampling frequency is used, time synchronization error between two sampling nodes becomes higher, leading to a larger phase

error between two measuring points. For most real civil infrastructures, their fundamental frequencies are lower than those of the test structure in this study, which indicates that the proposed WSSN could satisfy the SHM application requirements.

6. Conclusions

This work presents the design and characterization of a new wireless strain sensor board. The results of the characterization of the fabricated device in combination with IRIS mote show very good performance with respect to the devices' static, sensitivity, and dynamical characteristics. The experimental verification of the WSSN on a truss structure combined with FE simulation demonstrates that the developed WSSN is able to verify the natural frequencies and lower order strain mode shapes. However, difficulties are found in the identification of higher order strain modal shapes due to phase errors in time synchronization. The requirements on the time synchronization for modal analysis need to be assessed mainly from the viewpoint of mode shape phases. Despite the inaccuracy of modal identification in higher order vibration modes, the developed WSSN offers the potential of dynamic strain field monitoring of civil infrastructures, which is very important with respect to the acceptance of this new system. For future work, hardware capabilities of the wireless strain sensor node need further improvement in order to satisfy the transmission rate and bandwidth requirements for large volume deployment in real applications.

Conflict of Interests

The authors declare that there is no conflict of interests regarding the publication of this paper.

Acknowledgments

This work is supported by National Key Technology R&D Program (Grant no. 2014BAL05B06), Natural Science Foundation of China (Grant no. 51108129), Guangdong Major Science and Technology Plan (Grant no. 2012A080104014), Shenzhen Overseas Talents Project (Grant no. KQCX20120802140634893), and the Ministry of Education Key Laboratory of C&PC Structures.

References

- [1] V. Giurgiutiu, J. M. Redmond, D. P. Roach, and K. Rackow, "Active sensors for health monitoring of aging aerospace structures," in *7th Annual International Symposium on Smart Structures and Materials*, vol. 3985 of *Proceedings of SPIE*, pp. 294–305, The International Society for Optical Engineering, June 2000.
- [2] B. F. Spencer, "Opportunities and challenges for smart sensing technology," in *Proceedings of the 1st International Conference on Structural Health Monitoring and Intelligent Infrastructure*, pp. 65–72, Tokyo, Japan, 2003.
- [3] J. Hill, R. Szweczyk, A. Woo, S. Hollar, D. Culler, and K. Pister, "System architecture directions for networked sensors," in *Proceedings of the 9th International Conference on Architectural Support for Programming Languages and Operating Systems*, pp. 93–104, Cambridge, Mass, USA, 2000.
- [4] N. Kurata, B. F. Spencer, M. Ruiz-Sandoval, Y. Miyamoto, and Y. Sako, "A study on building risk monitoring using wireless sensor network MICA-Mote," in *Proceedings of the 1st International Conference on Structural Health Monitoring and Intelligent Infrastructure*, pp. 353–363, Tokyo, Japan, 2003.
- [5] Crossbow Technology Incorporated, <http://www.xbow.com.cn/>.
- [6] J. Paek and R. Govindan, "RCRT: rate-controlled reliable transport protocol for wireless sensor networks," *ACM Transactions on Sensor Networks*, vol. 7, no. 3, article 20, 2010.
- [7] S. Kim, S. Pakzad, D. Culler et al., "Health monitoring of civil infrastructures using wireless sensor networks," in *Proceedings of the 6th International Conference on Information Processing in Sensor Networks*, pp. 254–263, Cambridge, Mass, USA, 2007.
- [8] B. A. Sundaram, K. Ravisankar, R. Senthil, and S. Parivallal, "Wireless sensors for structural health monitoring and damage detection techniques," *Current Science*, vol. 104, no. 11, pp. 1496–1505, 2013.
- [9] J. P. Lynch, Y. Wang, K. H. Law, J. H. Yi, C. G. Lee, and C. B. Yun, "Validation of a large-scale wireless structure monitoring system on the Geumdang bridge," in *Proceedings of the 4th International Conference on Safety and Structural Reliability (ICOSSAR '05)*, Rome, Italy, 2005.
- [10] M. Bocca, E. I. Cosar, J. Salminen, and L. M. Eriksson, "A reconfigurable wireless sensor network for structural health monitoring," in *Proceedings of the 4th International Conference on Structural Health Monitoring on Intelligent Infrastructure (SHMII '09)*, pp. 22–24, Zurich, Switzerland, 2009.
- [11] M. Bocca, L. M. Eriksson, A. Mahmood, R. Jäntti, and J. Kullaa, "A synchronized wireless sensor network for experimental modal analysis in structural health monitoring," *Computer-Aided Civil and Infrastructure Engineering*, vol. 26, no. 7, pp. 483–499, 2011.
- [12] M. Bocca, J. Toivola, L. M. Eriksson, J. Hollmén, and H. Koivo, "Structural health monitoring in wireless sensornetworks by the embedded Goertzel algorithm," in *Proceedings of the IEEE/ACM International Conference on Cyber-Physical Systems (ICCPs '11)*, pp. 206–214, IEEE, Chicago, Ill, USA, April 2011.
- [13] J. S. Leng, D. Winter, R. A. Barnes, G. C. Mays, and G. F. Fernando, "Structural health monitoring of concrete cylinders using protected fibre optic sensors," *Smart Materials and Structures*, vol. 15, no. 2, pp. 302–308, 2006.
- [14] H. de Backer, W. de Corte, and P. van Bogaert, "A case study on strain gauge measurements on large post-tensioned concrete beams of a railway support structure," *Insight: Non-Destructive Testing and Condition Monitoring*, vol. 45, no. 12, pp. 822–830, 2003.
- [15] K. G. Ong and C. A. Grimes, "Tracking the harmonic response of magnetically-soft sensors for wireless temperature, stress, and corrosive monitoring," *Sensors and Actuators A: Physical*, vol. 101, no. 1-2, pp. 49–61, 2002.
- [16] M. Shiraishi, H. Kumagai, H. Inada, Y. Okuhara, and H. Matsubara, "The SHM system using self-diagnosis material and wireless data measurement device," in *Smart Structures and Materials 2005: Sensors and Smart Structures Technologies for Civil, Mechanical, and Aerospace Systems*, vol. 5765 of *Proceedings of SPIE*, pp. 187–194, 2005.
- [17] R. C. Tennyson, T. Coroy, G. Duck et al., "Fibre optic sensors in civil engineering structures," *Canadian Journal of Civil Engineering*, vol. 27, no. 5, pp. 880–889, 2000.
- [18] J. T. DeWolf, R. G. Lauzon, and M. P. Culmo, "Monitoring bridge performance," *Structural Health Monitoring*, vol. 1, no. 2, pp. 129–138, 2002.
- [19] E. Shehata and S. Rizkall, "Intelligent sensing for innovative bridges," *Journal of Intelligent Material Systems and Structures*, vol. 10, no. 4, pp. 304–313, 1999.
- [20] M. J. Whelan, M. V. Gangone, and K. D. Janoyan, "Highway bridge assessment using an adaptive real-time wireless sensor network," *IEEE Sensors Journal*, vol. 9, no. 11, pp. 1405–1413, 2009.
- [21] M. V. Gangone, M. J. Whelan, and K. D. Janoyan, "Wireless monitoring of a multispan bridge superstructure for diagnostic load testing and system identification," *Computer-Aided Civil and Infrastructure Engineering*, vol. 26, no. 7, pp. 560–579, 2011.
- [22] S. W. Doebling, C. R. Farrar, M. B. Prime, and D. W. Shevitz, "Damage identification and health monitoring of structural and mechanical systems from changes in their vibration characteristics: a literature review," Tech. Rep. LA-13070-MS, Los Alamos National Laboratory, 1996.
- [23] Y. Lei, A. S. Kiremidjian, K. K. Nair, J. P. Lynch, and K. H. Law, "Algorithms for time synchronization of wireless structural monitoring sensors," *Earthquake Engineering & Structural Dynamics*, vol. 34, no. 6, pp. 555–573, 2005.
- [24] Y. Wang, J. P. Lynch, and K. H. Law, "A wireless structural health monitoring system with multithreaded sensing devices: Design and validation," *Structure and Infrastructure Engineering*, vol. 3, no. 2, pp. 103–120, 2007.

Research Article

Feasibility Verification of Mountable PZT-Interface for Impedance Monitoring in Tendon-Anchorage

Thanh-Canh Huynh,¹ Young-Hwan Park,² Jae-Hyung Park,¹ and Jeong-Tae Kim¹

¹*Department of Ocean Engineering, Pukyong National University, 599-1 Daeyeon 3-dong, Nam-gu, Busan 608-737, Republic of Korea*

²*Structural Engineering Division, Korea Institute of Construction Technology, Gyeonggi-do 411-472, Republic of Korea*

Correspondence should be addressed to Jeong-Tae Kim; j0k9180@gmail.com

Received 5 September 2014; Accepted 27 November 2014

Academic Editor: Ting-Hua Yi

Copyright © 2015 Thanh-Canh Huynh et al. This is an open access article distributed under the Creative Commons Attribution License, which permits unrestricted use, distribution, and reproduction in any medium, provided the original work is properly cited.

This study has been motivated to numerically evaluate the performance of the mountable PZT-interface for impedance monitoring in tendon-anchorage. Firstly, electromechanical impedance monitoring and feature classification methods are outlined. Secondly, a structural model of tendon-anchorage subsystem with mountable PZT-interface is designed for impedance monitoring. Finally, the feasibility of the mountable PZT-interface is numerically examined. A finite element (FE) model is designed for the lab-scaled tendon-anchorage. The FE model of the PZT-interface is tuned as its impedance signatures meet the experimental test results at the same frequency ranges and also with identical patterns. Equivalent model properties of the FE model corresponding to prestress forces inflicted on the lab-tested structure are identified from the fine-tuning practice.

1. Introduction

The fundamental of the impedance-based method is to utilize the electromechanical (EM) impedance of a coupled PZT-structure system to detect the change in structural characteristics at local critical region. This monitoring technique was first proposed by Liang et al. [1]. Since then, many researchers have improved the method and applied it into various damage detection problems [2–7]. Kim et al. [8, 9] applied the impedance-based method for prestress-loss monitoring in tendon-anchorage connection by detecting the change in the pattern of the impedance responses at the anchorage.

Although the method has shown the excellent performance in detecting prestress-loss in tendon-anchorage, it still has several limitations for practical applications. Firstly, the effective frequency band which is sensitive to the variation of prestress force could be very significant, even above 800 kHz [9]. In this case, a high performance impedance analyzer is needed to get signals from such a high frequency range. Therefore, it is almost impossible to adopt a wireless impedance device which has a measurable frequency range of 10 kHz~100 kHz [10, 11]. Secondly, the impedance frequency

bands which are sensitive to prestress-loss should be predetermined before employing the impedance-based method for the damage detection job. Generally, the effective frequency range is varied dependent on target structures and usually determined by trial and error. This causes difficulty when dealing with real structures.

To overcome the abovementioned limitations, Nguyen and Kim [12] designed a fixed-type PZT-interface for monitoring prestress-loss in tendon-anchorage subsystems. The implementation of the PZT-interface was successful as sensitively indicating various prestress-losses in the tendon-anchorage. Also, the sensitive frequency range to prestress-loss was reduced to below 100 kHz. However, this design of PZT-interface must be installed during the construction of the tendon-anchorage connection. So it is impossible to apply it into existing cable-supported structures. Also, the presence of the aluminum PZT-interface between anchor and bearing plate may cause the loss of the bearing capacity of the connection.

To deal with these drawbacks of the fixed-type PZT-interface, a mountable PZT-interface was proposed by Huynh and Kim [13], as shown in Figure 1, for impedance monitoring of

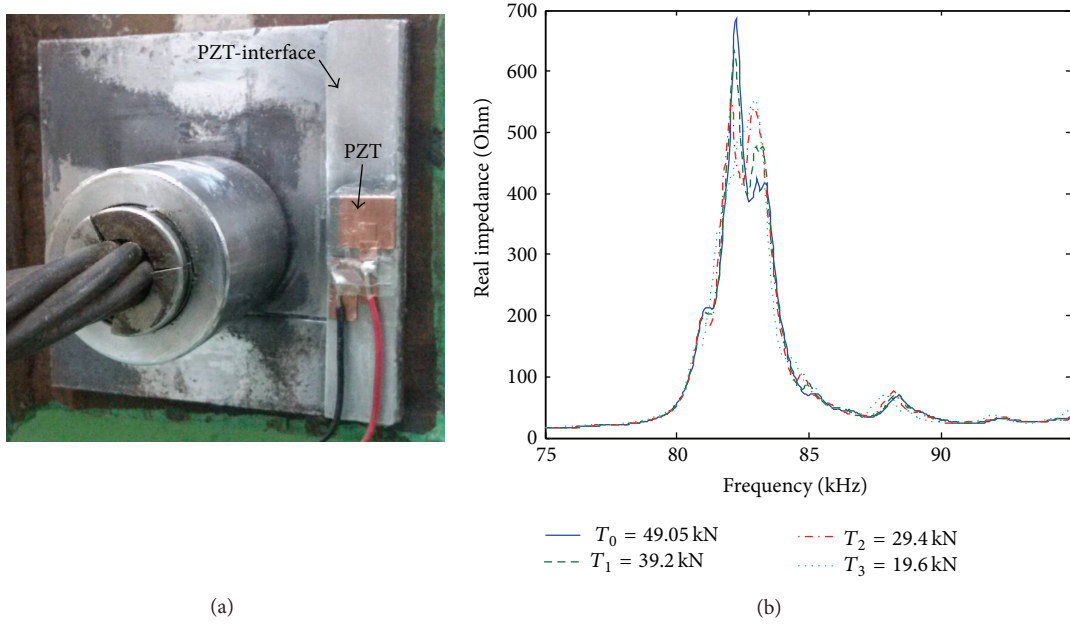


FIGURE 1: Prestress-loss monitoring using PZT-interface [13]: (a) mountable PZT-interface and (b) impedance signatures for prestress forces.

tension forces from existing tendon-anchorage. This interface can be easily bonded on and also detached from the anchorage surface as it is a clamped-clamped beam embedded with a PZT patch. Although the new PZT-interface was successfully tested for tension-loss monitoring from a lab-scaled tendon-anchorage, its feasibility should be verified by numerical simulation. Since the PZT-interface's geometry should be fitted dependent on host structures, the numerical simulation (as well as verification) is the key to the design of appropriate PZT-interfaces corresponding to the target's specifications.

In the numerical simulation of the electromechanical impedance, the coupling interaction between the PZT sensor and the host structure is an important issue. Several simplified impedance models have been proposed for describing the PZT sensor-structure interaction. Liang et al. [1] developed a 1-dof spring-mass-damper system via combining the electromechanical analysis of a PZT sensor and the structural dynamic analysis of the host structure. To consider the multidirectional effects caused by the PZT sensor's vibration, Zhou et al. [14] and Bhalla and Soh [15] introduced two-dimensional impedance models from which the planar coupled vibration was taken into account. By adopting the effective impedance concept, Zuo et al. [16] have developed a three-dimensional PZT-structure model considering the coupled vibration along the radial direction and along the thickness direction of the PZT sensor. The performance evaluation of the theoretical impedance models has been validated by experimental tests conducted on beam-like structures [1, 17] and thin plates [14, 15] with bonded PZT actuators. However, the direct application of the so-called "impedance model" is limited when dealing with host structures with complex characteristics (i.e., geometry, material

properties, and boundary conditions). In such cases, appropriate modeling techniques are needed to fully capture the coupled vibration of the PZT sensor and the host structure.

This study has been motivated to numerically evaluate the performance of the mountable PZT-interface for impedance monitoring in tendon-anchorage. Firstly, electromechanical impedance monitoring and feature classification methods are outlined. Secondly, a structural model of the anchorage's components is designed from the force equilibrium state. In the model, the tension force is represented by interfacial structural parameters of the tendon-anchorage connection. A mountable PZT-interface is designed for tension-loss monitoring from postinstallation into existing anchorages. Finally, the feasibility of the mountable PZT-interface is numerically examined. A finite element (FE) model is designed for the lab-scaled tendon-anchorage. The FE model of the PZT-interface is tuned as its impedance signatures meet the experimental test results (presented by [13]) at the same frequency ranges and also with identical patterns. Equivalent model properties of the FE model corresponding to prestress forces inflicted on the lab-tested structure are identified from the fine-tuning practice.

2. Theory of Impedance Monitoring

2.1. Electromechanical Impedance. To monitor structural change, a piezoelectric material (e.g., PZT) is surface-bonded to structure at the examined region. As shown in Figure 2, the interaction between the PZT and the structure is simply explained by the 1D free-body diagram of PZT-structure system. Due to the inverse piezoelectric effect, an input harmonic voltage $V(\omega)$ induces a deformation of PZT. Because

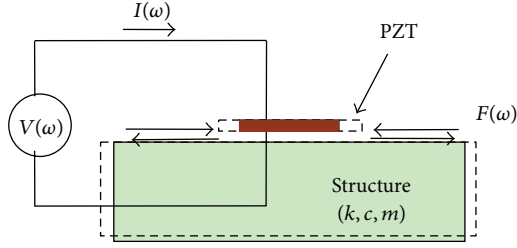


FIGURE 2: Model of coupling interaction between PZT transducer and structure.

the PZT is bonded to the structure, a force $F(\omega)$ against that deformation is induced into the structure and the PZT as well.

For 1-dof system, structural mechanical impedance of the host structure is obtained by the ratio of force $F(\omega)$ to velocity $\dot{u}(\omega)$ as follows [1]:

$$Z_s(\omega) = \frac{F(\omega)}{\dot{u}(\omega)} = c + m \frac{\omega^2 - \omega_n^2}{\omega}, \quad (1)$$

where c and m are the damping coefficient and the mass of the structure, respectively; ω_n is the angular natural frequency of the structure; and ω is the angular frequency of the excitation voltage. As shown in (1), structural mechanical impedance is a function of mass, damping, and stiffness (i.e., stiffness is introduced from natural frequency, $k = m\omega_n^2$). Thus, the change in structural parameters can be represented by the change in structural mechanical impedance.

In practice, the electric current $I(\omega)$ is measured and then it is utilized to calculate electromechanical impedance as follows [1]:

$$Z(\omega) = \frac{V}{I} = \left\{ i\omega \frac{w_a l_a}{t_a} \left[\epsilon_{33}^T - \frac{1}{Z_a(\omega)/Z_s(\omega) + 1} d_{3x}^2 \hat{Y}_{xx}^E \right] \right\}^{-1}, \quad (2)$$

where $\hat{Y}_{xx}^E = (1 + i\eta)Y_{xx}^E$ is the complex Young's modulus of the PZT patch at zero electric field; $\hat{\epsilon}_{xx}^T = (1 - i\delta)\epsilon_{xx}^T$ is the complex dielectric constant at zero stress; d_{3x} is the piezoelectric coupling constant in x -direction at zero stress; $k = \omega \sqrt{\rho/\hat{Y}_{xx}^E}$ is the wave number where ρ is the mass density of the PZT patch; and w_a , l_a , and t_a are the width, length, and thickness of the piezoelectric transducer, respectively. The parameters η and δ are structural damping loss factor and dielectric loss factor of piezoelectric material, respectively.

As shown in (2), the electromechanical impedance, $Z(\omega)$, is a combining function of the mechanical impedance of the host structure, $Z_s(\omega)$, and that of the piezoelectric patch, $Z_a(\omega)$. Therefore, the change in structural parameters (k , m , and c) can be represented by the change in electromechanical impedance.

An important issue for impedance monitoring is to decide the target frequency range. The frequency range should be selected appropriately in order to realize structural change in electromechanical impedance. Generally, if the excitation

frequency is not identical to the natural frequency of the host structure (i.e., $\omega \neq \omega_n$), the impedance of the structure is very large compared with the mechanical impedance of the PZT sensor (i.e., $Z_s(\omega) \gg Z_a(\omega)$). As a result, the term $Z_a(\omega)/Z_s(\omega)$ is neglected in (2). On the other hand, if the PZT sensor is excited by a frequency matching with the natural frequency of the structure (i.e., $\omega = \omega_n$), structural mechanical impedance takes only the term of damping coefficient (i.e., $Z_s(\omega) = c$). Consequently, the structural impedance for that frequency is comparable with the mechanical impedance of the PZT, and electromechanical impedance is expressed as follows:

$$Z(\omega) = \left\{ i\omega \frac{w_a l_a}{t_a} \left[\epsilon_{33}^T - \frac{1}{Z_a/c + 1} d_{3x}^2 \hat{Y}_{xx}^E \right] \right\}^{-1}. \quad (3)$$

In (3), the contribution of structural mechanical impedance to electromechanical impedance is the damping coefficient c , which causes resonant responses in electromechanical impedance signature. It means that electromechanical impedance at resonance represents not only modal damping, but also the natural frequency of the structure. Therefore, the structural change could be identified sensitively by the change in electromechanical impedance at the resonant frequency.

2.2. Quantification of Electromechanical Impedance. To quantify the change in electromechanical impedance, the root mean square deviation (RMSD) index is utilized. RMSD index is calculated as [18]

$$\text{RMSD}(Z, Z^*) = \sqrt{\frac{\sum_{i=1}^N [Z^*(\omega_i) - Z(\omega_i)]^2}{\sum_{i=1}^N [Z(\omega_i)]^2}}, \quad (4)$$

where $Z(\omega_i)$ and $Z^*(\omega_i)$ are the impedances measured at two events for the i th frequency, respectively, and N denotes the number of frequency points in the sweep. Ideally, the RMSD is equal to 0 if the two events are identical (e.g., there is no structural change). Otherwise, the RMSD is larger than 0.

The correlation coefficient deviation (CCD) index can also be used to quantify the change of the whole impedance signatures [3]. The CCD index is calculated as follows:

CCD

$$= 1 - \frac{1}{\sigma_Z \sigma_Z^*} E \left\{ [\text{Re}(Z_i) - \text{Re}(\bar{Z})] [\text{Re}(Z_i^*) - \text{Re}(\bar{Z}^*)] \right\}, \quad (5)$$

in which $E[\cdot]$ is the expectation operation; $\text{Re}(Z_i)$ signifies the real parts of the electromechanical impedances of the i th frequency; $\text{Re}(\bar{Z})$ signifies the mean values of impedance signatures (real part); and σ_Z signifies the standard deviation values of impedance signatures. Note that the asterisk (*) denotes the structural change. The CCD index is equal to 0 if there is no structural change. Otherwise, the CCD is larger than 0.

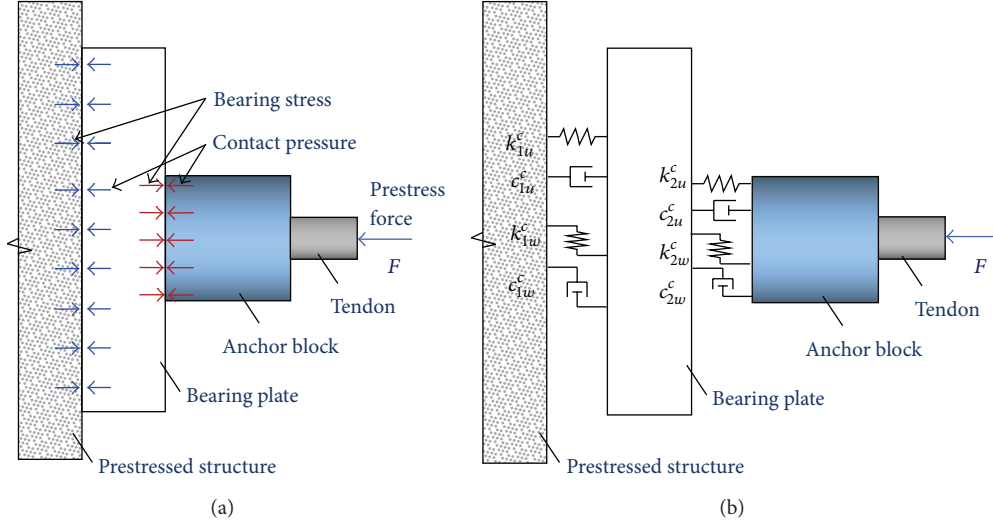


FIGURE 3: Structural model of tendon-anchorage: (a) force equilibrium and (b) analytical model.

3. Mountable PZT-Interface for Tendon-Anchorage Connection

3.1. Structural Model of Tendon-Anchorage. A tendon-anchorage subsystem can be modeled by a series of components such as bearing plate, anchor block, and tendon and contact forces in equilibrium condition, as shown in Figure 3(a). The prestress force is modeled by tendon force acting on the anchor block and transformed to contact pressure and bearing stress in the interface of anchor block and bearing plate. According to the contact mechanism [19], the interaction in the contact interface can be simplified by damping coefficients and spring stiffness parameters, as shown in Figure 3(b). On the other hand, the variation of interfacial stiffness and damping parameters are associated with the variation of contact pressures [20]. Hence, the variation of tendon force can be treated as the variation of those structural parameters at the contact interface.

3.2. Structural Model of Tendon-Anchorage with Mountable PZT-Interface. A fixed-type PZT-interface was proposed to overcome the difficulties in monitoring the high frequency response corresponding to the change in the tendon-anchorage system [12]. The interface is a thin plate equipped with a PZT patch. It reduces the frequency range enough to deal within 10–100 kHz measurement. However, the fixed-type design of this interface has drawbacks since it interferes with the bearing capacity of the tendon-anchorage and also it needs to be installed during the construction.

As an alternative measuring technique, a mountable PZT-interface has been newly modeled in order to overcome the limitations of the fixed-type interface in practice, as shown in Figure 4(a). The mountable interface is a clamped-clamped beam with a PZT patch bonded on its middle. As tightly bonded to the surface of the bearing plate, the clamped interfacing makes the stress fields of the PZT-interface almost equivalent to those of the bearing plate on its surface, while

the top and bottom midsurfaces are freely deformed along with the deformation in the bearing plate. Therefore, any change in structural parameters due to cable force-loss would lead to the change in the EM impedance response of PZT-interface (Figure 4(b)).

On the basis of the coupling interaction between the PZT sensor and the host structure [1, 17], a 1-dof structural model using a series of mass-spring-dampness is proposed as shown in Figure 4(c). The clamped-clamped PZT-interface is modeled as 1-dof system with its mass (m^i), stiffness (k^i), and damping parameters (c^i), as shown in Figure 4(c). Also, the tendon-anchorage is modeled as bearing plate's mass (m^b), bearing plate's stiffness (k^b) and damping (c^b), contact stiffness (k_1^c, k_2^c), and contact damping (c_1^c, c_2^c). The series model is selected for the simplification since the bearing plate is target structure and the contact parameters are considered as boundary conditions. The equivalent structural stiffness of the PZT-interface on the bearing plate ($k_e^{\text{interface}}$) is simplified as follows:

$$k_e^{\text{interface}} = \frac{\gamma k^c k^i}{\gamma k^c + k^i}, \quad (6)$$

where k^c is the total contact stiffness ($k^c = k_1^c + k_2^c$) and γ is a factor representing the ratio of the bearing plate's stiffness to the total contact stiffness as

$$\gamma = \frac{\alpha}{1 + \alpha}, \quad \alpha = \frac{k^b}{k^c}. \quad (7)$$

Suppose $\beta = k^i/(\gamma k^c)$ is the ratio of the PZT-interface's stiffness to the equivalent contact stiffness; the equivalent structural stiffness of the PZT-interface can be rewritten as

$$k_e^{\text{interface}} = \left(\frac{\beta}{1 + \beta} \right) \gamma k^c. \quad (8)$$

For the simplified model of the tendon-anchorage without the mountable PZT-interface ($k^i = \beta = 0$), the bearing plate is

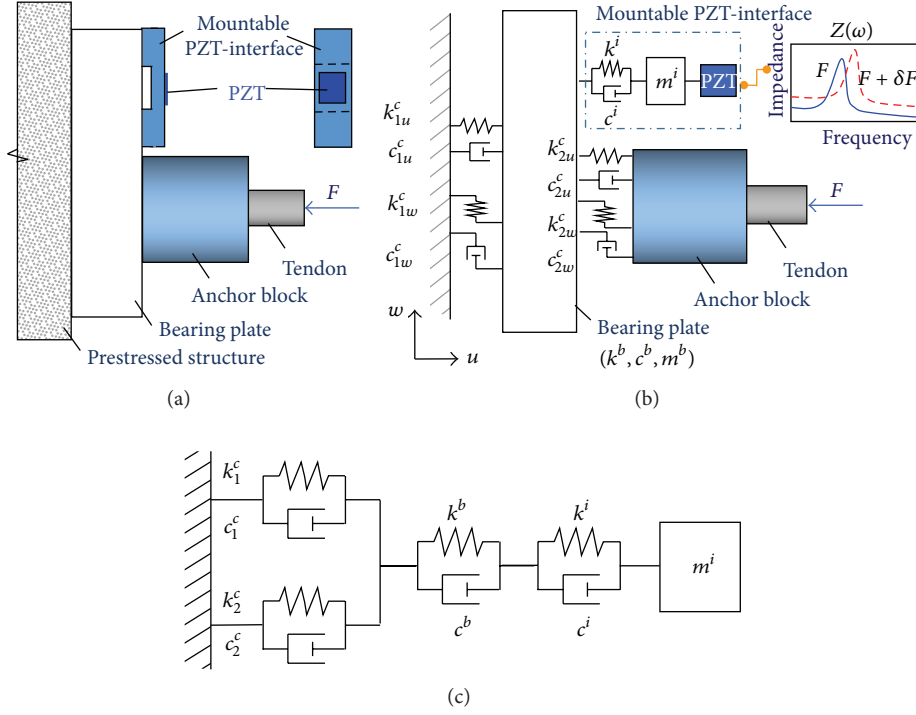


FIGURE 4: Structural model of tendon-anchorage with a mountable PZT-interface: (a) tendon-anchorage with PZT-interface; (b) analytical model; and (c) 1-dof model.

the target structure and its equivalent structural stiffness k_e^{bearing} is derived on the basis of (8) as follows:

$$k_e^{\text{bearing}} = \gamma k^c. \quad (9)$$

Since the bearing plate is clamped between two surfaces, its equivalent stiffness would be very large due to the contact pressure and the stress field acting at the interface. Substituting (9) into (8) leads the ratio of the equivalent stiffness with the PZT-interface ($k_e^{\text{interface}}$) to that of the bearing plate (k_e^{bearing}) as follows:

$$\frac{k_e^{\text{interface}}}{k_e^{\text{bearing}}} = \frac{\beta}{1 + \beta}. \quad (10)$$

As the stiffness of the PZT-interface is much smaller than the contact stiffness (i.e., $\beta \ll 1$), (10) is simplified as $k_e^{\text{interface}}/k_e^{\text{bearing}} \approx \beta$ and it leads $k_e^{\text{interface}} \ll k_e^{\text{bearing}}$. Assume the mass of the PZT-interface is comparable with that of the bearing plate, natural frequencies of the PZT-interface subsystem would be quite reduced as compared to those of the tendon-anchorage model.

For simplified structural models, structural parameters are needed to be determined to obtain the consistent experimental results. The structural parameters could be identified from the fine-tuning process by matching the calculated resonant response of the simplified model and the measured resonant response of the experimental model [20, 21]. In the present study, the 1-dof structural model of the PZT-interface was proposed firstly to explain how to represent the

loss of cable force from the change in the electromechanical impedance (Figure 4(c)) and secondly to prove that the sensitive frequency band could be reduced when the PZT-interface device is implemented into tendon-anchorage (see (10)).

4. Numerical Verification of Mountable PZT-Interface for Cable Force Monitoring

4.1. FE Modeling for Numerical Simulation of Tendon-Anchorage. In order to numerically evaluate the applicability of the PZT-interface device for cable force monitoring using impedance-based technique, FE model of tendon-anchorage connection was established by the commercially available FE package, COMSOL Multiphysics [22]. Figure 5 shows the geometry of the FE model that was in accordance with the lab-scale model test presented by Huynh and Kim [13]. It should be noted that the bonding layers between the PZT sensor and PZT-interface with the mother structure were not simulated in the present work. In FE modeling, the bearing plate, anchor head, and the PZT-interface were discretized by the elastic solid elements in 3D, as shown in Figure 6(a). The properties of the steel anchorage and the aluminum interface specified in the FE model are listed in Table 1. The PZT patch is added by the piezoelectric material, PZT-5A type as shown in Table 2, which could deal with both mechanical and electrical fields. To acquire the electromechanical impedance, a harmonic excitation voltage with an amplitude of 1 V was simulated to the top surface of the PZT patch, and the bottom one was set as the ground electrode.

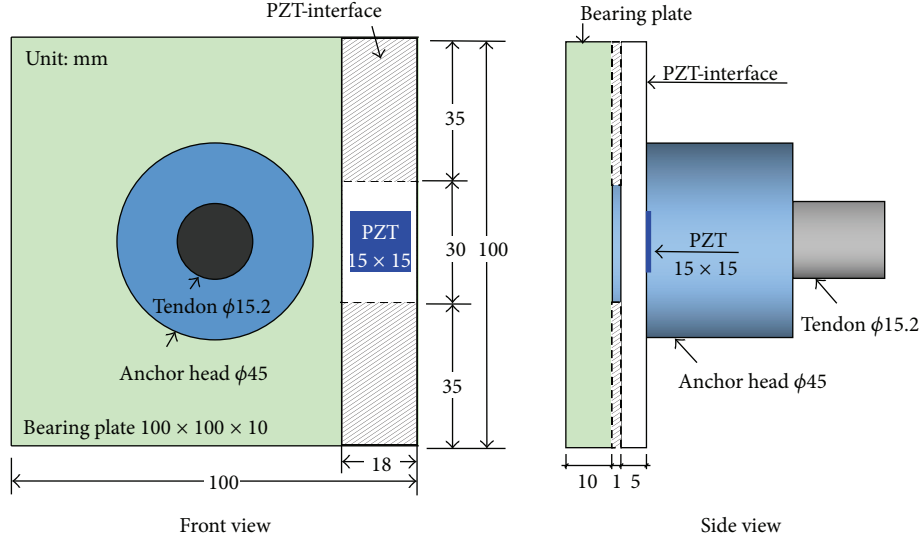


FIGURE 5: Geometry of lab-scaled tendon-anchorage equipped with PZT-interface [13].

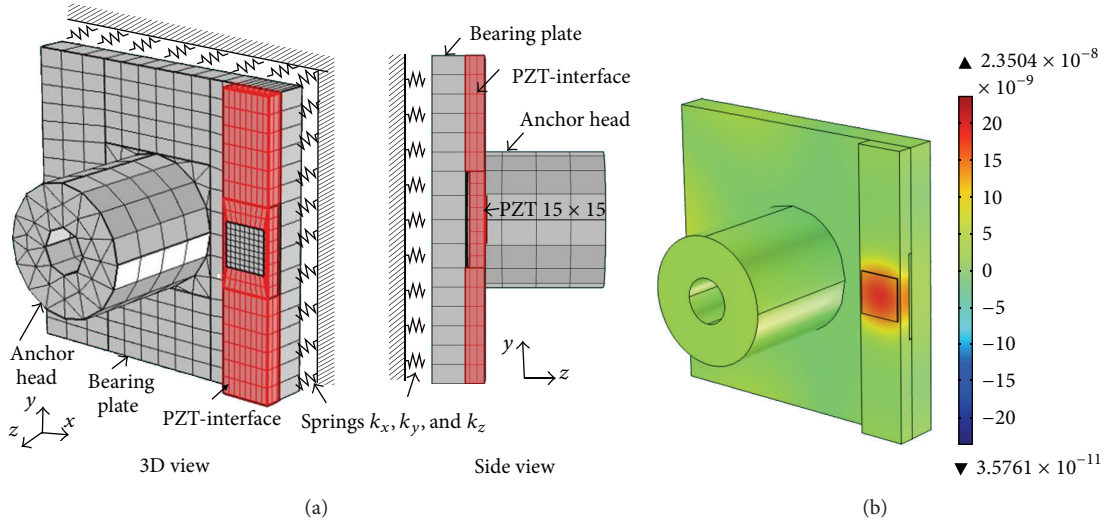


FIGURE 6: FE model of tendon-anchorage subsystem: (a) meshing and boundary condition and (b) deformation excited by PZT sensor at 19.52 kHz.

TABLE 1: Material properties of cable-anchorage connection.

Parameters	PZT-interface	Bearing plate and anchor head
Young's modulus, E (GPa)	70	200
Poisson's ratio, ν	0.33	0.3
Mass density, ρ (kg/m ³)	2700	7850
Damping loss factor, η	0.001	0.02

According to the foregoing analytical model of tendon-anchorage connection, the variation of tendon force can be treated as the variation of structural parameters at the contact interface. Therefore, the cable force can be monitored via

the interfacial structural stiffness (so-called contact stiffness). As shown in Figure 6(a), spring elements in the x -, y -, and z -axes were added to the contact surface of the bearing plate to represent the contact stiffness caused by cable force. It is assumed that the structural parameters are uniformly distributed on the contact boundary surface. As given in Table 3, four cases of spring stiffness (i.e., C0, C1, C2, and C3) were considered to investigate the change in the piezoelectric impedance response of PZT-interface. By assuming that the variation of cable force mainly causes the variation of spring constant in the direction normal to the contacting surface, only the variation of k_z is simulated in the FE analysis.

As shown in Figure 7, the real part of the electromechanical impedance computed by the numerical simulation (case C0 in Table 3) is compared to the corresponding experimental

TABLE 2: Properties of PZT-5A patch [23].

Parameters	Value
Elastic compliance, s_{ijkl}^E (m^2/N)	$\begin{pmatrix} 16.4 & -5.74 & -7.22 & 0 & 0 & 0 \\ -5.74 & 16.4 & -7.22 & 0 & 0 & 0 \\ -7.22 & -7.22 & 18.8 & 0 & 0 & 0 \\ 0 & 0 & 0 & 47.5 & 0 & 0 \\ 0 & 0 & 0 & 0 & 47.5 & 0 \\ 0 & 0 & 0 & 0 & 0 & 44.3 \end{pmatrix} \times 10^{-12}$
Dielectric coupling constant, d_{kij} (C/N)	$\begin{pmatrix} 0 & 0 & -171 \\ 0 & 0 & -171 \\ 0 & 0 & 374 \\ 0 & 584 & 0 \\ 584 & 0 & 0 \\ 0 & 0 & 0 \end{pmatrix} \times 10^{-12}$
Permittivity, ϵ_{jk}^T (farad/m)	$\begin{pmatrix} 1730 & 0 & 0 \\ 0 & 1730 & 0 \\ 0 & 0 & 1700 \end{pmatrix} \times (8.854 \times 10^{-12})$
Mass density, ρ (kg/m^3)	7750
Damping loss factor, η	0.005
Dielectric loss factor, δ	0.015

TABLE 3: Interfacial stiffness versus resonant frequency.

Scenarios	Interfacial stiffness (N/m^2)			Resonant frequency (kHz)			
	$k_x = k_y$	k_z	Δk_z (%)	f_1	Δf_1 (%)	f_1	Δf_1 (%)
C0	15×10^{11}	40×10^{11}	0	19.68	0	82.68	0
C1	15×10^{11}	35×10^{11}	-12.5	19.64	-0.20	82.60	-0.10
C2	15×10^{11}	30×10^{11}	-25	19.56	-0.61	82.56	-0.14
C3	15×10^{11}	25×10^{11}	-37.5	19.52	-0.81	82.52	-0.19

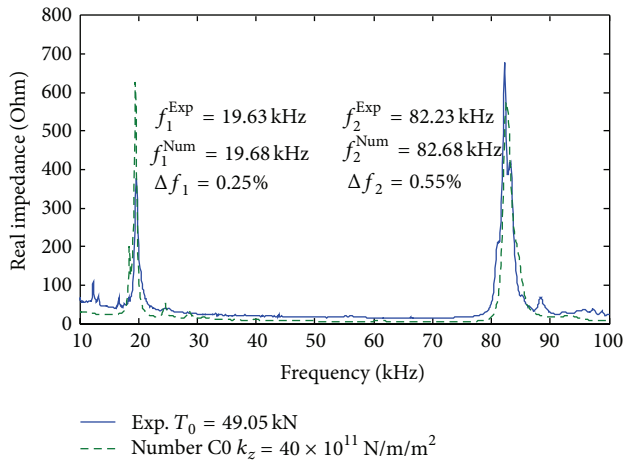


FIGURE 7: Numerical versus experimental impedance signatures.

result (for tension force 49.05 kN). It is worth noting that the spring constants specified in the C0 scenario were obtained by using trial-and-error method, and the identification of the contact stiffness is beyond the scope of this paper. As observed in Figure 7, the resonance occurred within

10 kHz~100 kHz, and both resonant and nonresonant regions of the numerical impedance signatures show good agreement with those of the experimental result [13].

The difference in the resonant frequencies between the FE modeling and the lab-scaled testing is very small, about 0.25% and 0.55% for the first and the second resonant vibrations, respectively. It indicates that the FE simulation can provide reasonable impedance responses for cable force monitoring via interfacial stiffness monitoring. As shown in Figure 6(b), the deformation contour of the anchorage excited by PZT patch was generated at the resonant frequency of 19.52 kHz. It is also observed that the maximum displacement of the PZT-interface is about 2.35×10^{-8} m due to the resonance event.

4.2. Contact Stiffness versus Impedance Response. Figure 8 shows real impedance signatures of the PZT-interface obtained by the FE modeling in the wide frequency range 10 kHz~100 kHz and two sensitive frequency ranges of 15–25 kHz and 75–95 kHz for four contact stiffness scenarios (as listed in Table 3). Similar to the experiment, the impedance signatures were recorded with 901 interval points for the frequency band of 10–100 kHz and 501 points for both frequency bands of 15–25 kHz and 75–95 kHz. As observed in Figures 8(b) and 8(c), the impedance signatures in

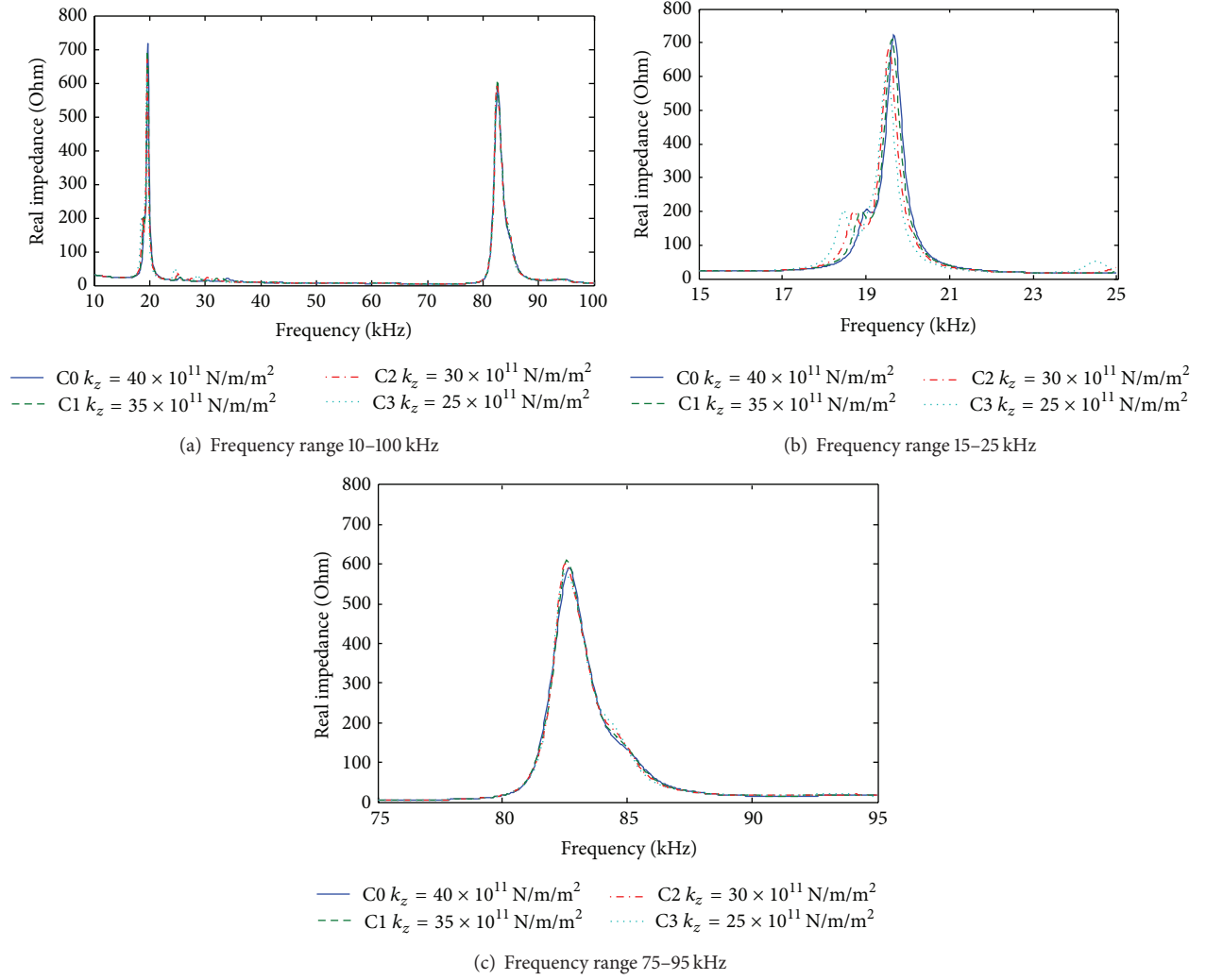


FIGURE 8: Impedance signatures of PZT-interface under various contact stiffness.

the resonant bands of 15–25 kHz and 75–95 kHz are varied when decreasing the contact stiffness k_z . The frequency range of 15–25 kHz is more sensitive than that of 75–95 kHz. The resonant frequencies tend to decrease when decreasing the spring stiffness k_z . The change in the resonant frequency due to the contact stiffness-loss is summarized in Table 3. The frequency-shift is very small, 0.81% and 0.19% for the first and the second resonant frequencies, respectively. Obviously, the pattern of the numerical impedance variation due to the change in contact stiffness is well-matched with the experimental observations [13]. Furthermore, the impedance response via the PZT-interface was sensitive to the change in contact stiffness even when the examined frequency range was 10 kHz~100 kHz.

For contact stiffness monitoring, both RMSD values (see (4)) and CCD indices (see (5)) are examined. Figures 9 and 10, respectively, show the change in RMSD and CCD indices associated with the decrement of contact stiffness for the wide frequency band (i.e., 10–100 kHz) and the narrow ones (i.e., 15–25 kHz and 75–95 kHz). As observed in the

figures, RMSD and CCD indices increase linearly with the loss of interfacial stiffness. It is also observed that RMSD and CCD indices of the wide frequency range 10–100 kHz show a good indication of the contact stiffness-loss as the sensitive frequency range 15–25 kHz. In comparison, of RMSD and CCD approaches, RMSD indices are varied much higher than the CCD indices due to the contact stiffness variation for all considered frequency ranges (i.e., 10–100 kHz, 15–25 kHz, and 75–95 kHz). These numerical results are consistent with the experimental results obtained from the lab-scaled test structure described previously. From the feature analysis of the impedance signatures, the RMSD is found to be the sensitive indication of the contact stiffness-loss as the prestress force was reduced.

5. Summary and Conclusions

In this study, the feasibility of the mountable PZT-interface was numerically analyzed for impedance monitoring in the tendon-anchorage connection. Firstly, electromechanical

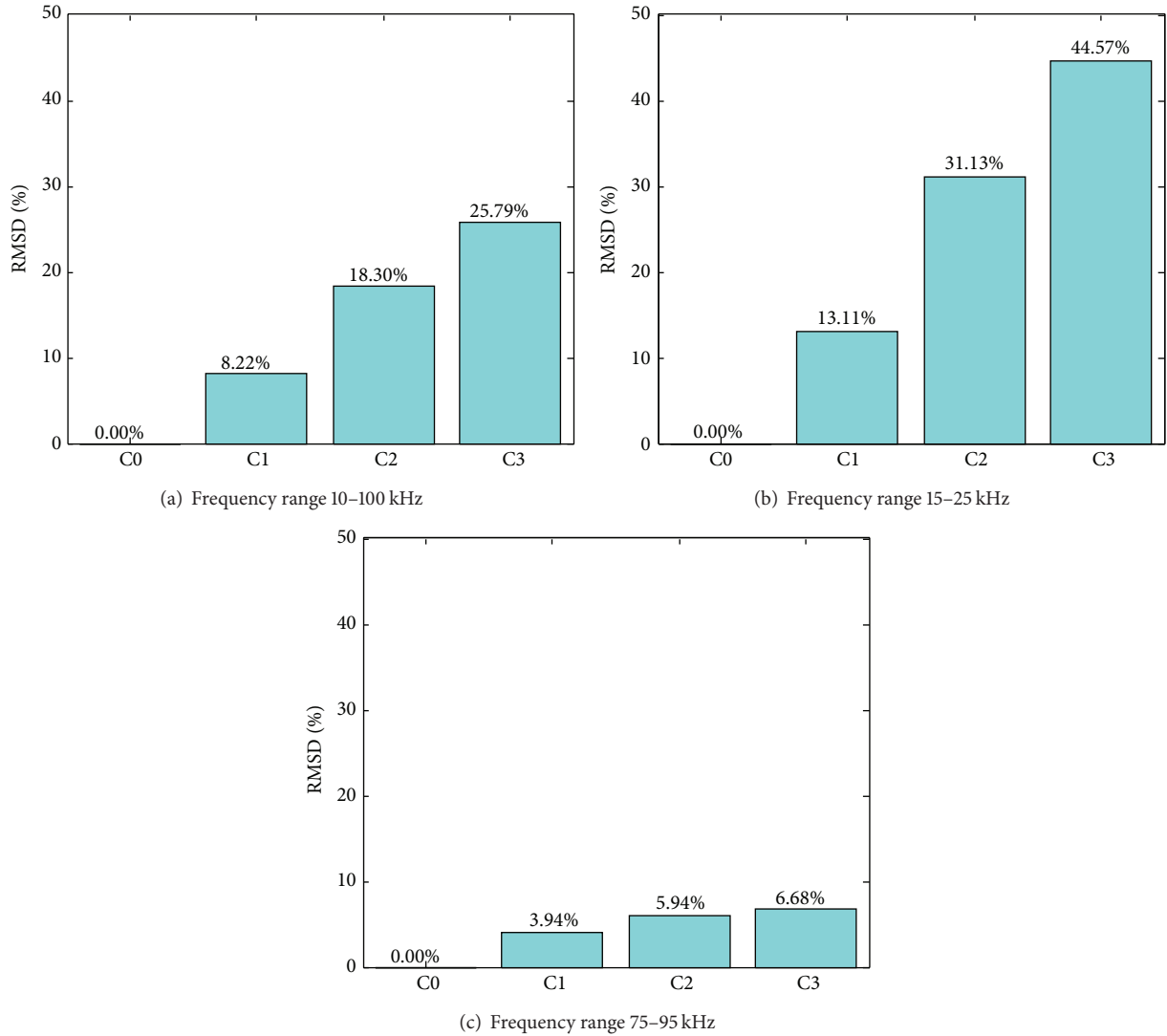


FIGURE 9: Contact stiffness monitoring by RMSD index.

impedance monitoring and feature classification methods were outlined. Secondly, a structural model of tendon-anchorage subsystem with mountable PZT-interface was designed for impedance monitoring. Finally, the feasibility of the mountable PZT-interface was numerically examined. A finite element (FE) model was designed for the lab-scaled tendon-anchorage. The FE model of the PZT-interface was tuned as its impedance signatures met the experimental test results presented by Huynh and Kim [13]. Equivalent model properties of the FE model corresponding to prestress forces inflicted on the lab-tested structure were identified from the fine-tuning practice.

The interfacial stiffness which represents the prestress force in the tendon-anchorage subsystem was successfully monitored by the electromechanical impedance response of the PZT-interface. The feature analysis of the impedance signatures shows that the RMSD changed to make the sensitive indication of the contact stiffness-loss as the prestress

force was reduced. The impedance response via the PZT-interface was sensitive to the change in contact stiffness even when the examined frequency range was 10 kHz~100 kHz. It is noted that two resonance frequencies occurred near 20 kHz and 82 kHz by implementing the mountable interface device. Since the PZT-interface is mobile and adaptable to be applied in any existing cable-anchorage connections, this numerical evaluation is promising for designing appropriate devices for practical applications. As for the future work, the bonding layer should be considered in the numerical simulation to examine its effect on the electromechanical impedance of the PZT-interface.

Conflict of Interests

The authors declare that there is no conflict of interests regarding the publication of this paper.

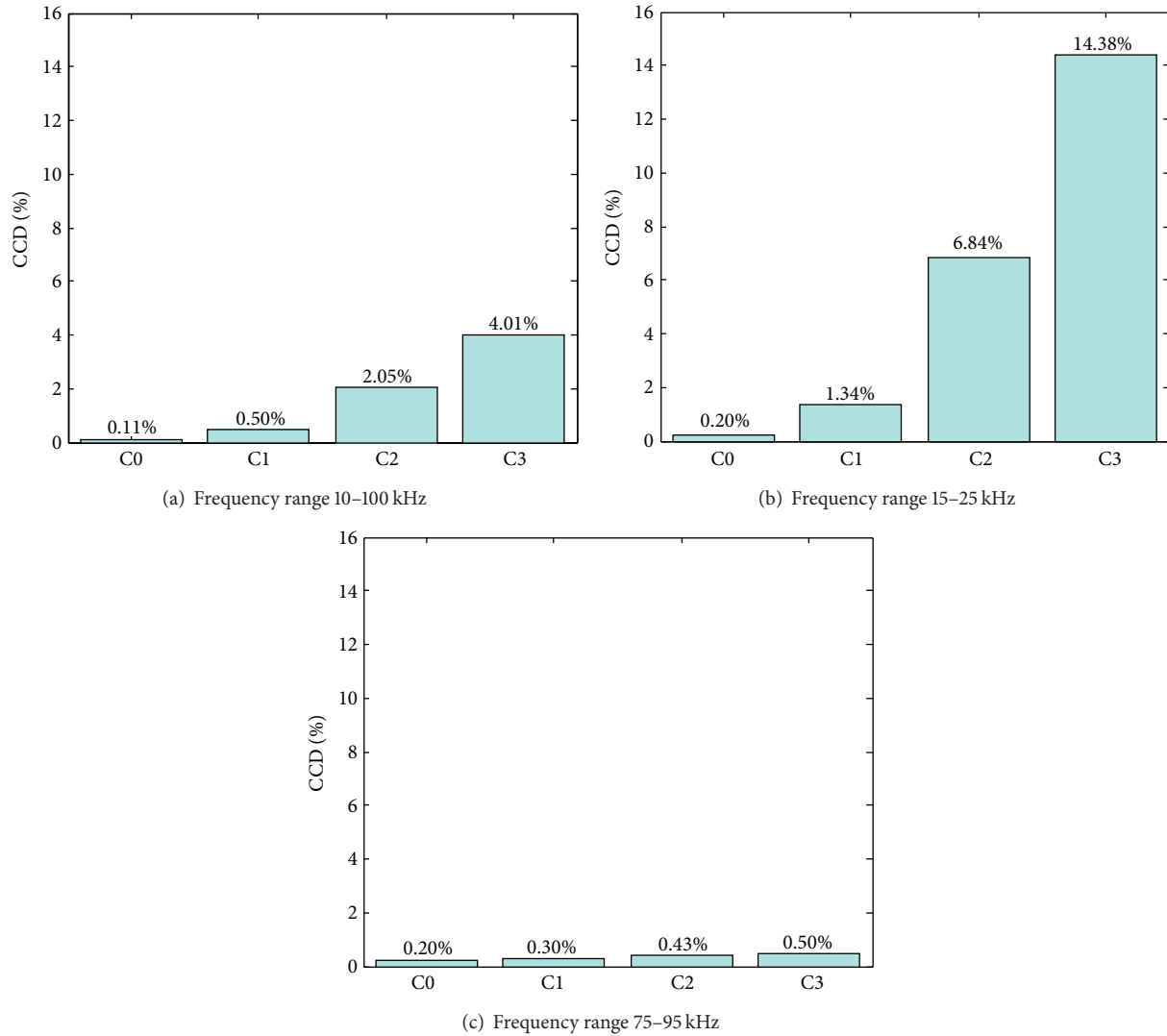


FIGURE 10: Contact stiffness monitoring by CCD index.

Acknowledgments

This research was supported by a grant from a Strategic Research Project (Development of Smart Prestressing and Monitoring Technologies for Prestressed Concrete Bridges) funded by the Korea Institute of Construction Technology. The graduate student, Mr. Thanh-Canh Huynh, involved in this research was also partially supported by the Brain Korea 21 Plus (BK21 Plus) Program of Korean Government.

References

- [1] C. Liang, F. P. Sun, and C. A. Rogers, "Coupled electro-mechanical analysis of adaptive material systems—determination of the actuator power consumption and system energy transfer," *Journal of Intelligent Material Systems and Structures*, vol. 5, no. 1, pp. 12–20, 1994.
- [2] G. Park, H. H. Cudney, and D. J. Inman, "Feasibility of using impedance-based damage assessment for pipeline structures," *Earthquake Engineering and Structural Dynamics*, vol. 30, no. 10, pp. 1463–1474, 2001.
- [3] A. N. Zagari and V. Giurgiutiu, "Electro-mechanical impedance method for crack detection in thin plates," *Journal of Intelligent Material Systems and Structures*, vol. 12, no. 10, pp. 709–718, 2001.
- [4] S. Bhalla and C. K. Soh, "Structural impedance based damage diagnosis by piezo-transducers," *Earthquake Engineering & Structural Dynamics*, vol. 32, no. 12, pp. 1897–1916, 2003.
- [5] Y. Yang, Y. Hu, and Y. Lu, "Sensitivity of PZT impedance sensors for damage detection of concrete structures," *Sensors*, vol. 8, no. 1, pp. 327–346, 2008.
- [6] J.-T. Kim, W.-B. Na, J.-H. Park, and D.-S. Hong, "Hybrid health monitoring of structural joints using modal parameters and EMI signatures," in *Smart Structures and Materials 2006—Sensors and Smart Structures Technologies for Civil, Mechanical, and Aerospace Systems*, vol. 6174 of *Proceedings of the SPIE*, San Diego, Calif, USA, March 2006.

- [7] D. L. Mascarenas, *Development of an impedance-based wireless sensor node for monitoring of bolted joint preload [M.S. thesis]*, Department of Structural Engineering, University of California, San Diego, Calif, USA, 2006.
- [8] J. T. Kim, J. H. Park, D. S. Hong, H. M. Cho, W. B. Na, and J. H. Yi, "Vibration and impedance monitoring for prestress-loss prediction in PSC girder bridges," *Smart Structures and Systems*, vol. 5, no. 1, pp. 81–94, 2009.
- [9] J.-T. Kim, J.-H. Park, D.-S. Hong, and W.-S. Park, "Hybrid health monitoring of prestressed concrete girder bridges by sequential vibration-impedance approaches," *Engineering Structures*, vol. 32, no. 1, pp. 115–128, 2010.
- [10] D. L. Mascarenas, M. D. Todd, G. Park, and C. R. Farrar, "Development of an impedance-based wireless sensor node for structural health monitoring," *Smart Materials and Structures*, vol. 16, no. 6, pp. 2137–2145, 2007.
- [11] J.-H. Park, J.-T. Kim, D.-S. Hong, D. Mascarenas, and J. Peter Lynch, "Autonomous smart sensor nodes for global and local damage detection of prestressed concrete bridges based on accelerations and impedance measurements," *Smart Structures and Systems*, vol. 6, no. 5-6, pp. 711–730, 2010.
- [12] K.-D. Nguyen and J.-T. Kim, "Smart PZT-interface for wireless impedance-based prestress-loss monitoring in tendon-anchorage connection," *Smart Structures and Systems*, vol. 9, no. 6, pp. 489–504, 2012.
- [13] T.-C. Huynh and J.-T. Kim, "Impedance-based cable force monitoring in tendon-anchorage using portable PZT-interface technique," *Mathematical Problems in Engineering*, vol. 2014, Article ID 784731, 11 pages, 2014.
- [14] S.-W. Zhou, C. Liang, and C. A. Rogers, "An impedance-based system modeling approach for induced strain actuator-driven structures," *Journal of Vibration and Acoustics*, vol. 118, no. 3, pp. 323–331, 1996.
- [15] S. Bhalla and C. K. Soh, "Structural health monitoring by piezo-impedance transducers. I: modeling," *Journal of Aerospace Engineering*, vol. 17, no. 4, pp. 154–165, 2004.
- [16] C. Zuo, X. Feng, and J. Zhou, "A three-dimensional model of the effective electromechanical impedance for an embedded PZT transducer," *Mathematical Problems in Engineering*, vol. 2013, Article ID 218026, 10 pages, 2013.
- [17] V. Giurgiutiu and A. N. Zagari, "Embedded self-sensing piezoelectric active sensors for on-line structural identification," *Journal of Vibration and Acoustics*, vol. 124, no. 1, pp. 116–125, 2002.
- [18] F. P. Sun, Z. Chaudhry, C. Liang, and C. A. Rogers, "Truss structure integrity identification using PZT sensor-actuator," *Journal of Intelligent Material Systems and Structures*, vol. 6, no. 1, pp. 134–139, 1995.
- [19] K. L. Johnson, *Contact Mechanics*, Cambridge University Press, Cambridge, UK, 1985.
- [20] S. Ritdumrongkul, M. Abe, Y. Fujino, and T. Miyashita, "Quantitative health monitoring of bolted joints using a piezoceramic actuator-sensor," *Smart Materials and Structures*, vol. 13, no. 1, pp. 20–29, 2004.
- [21] V. Giurgiutiu and C. A. Rogers, "Modal expansion modeling of the electro-mechanical (E/M) impedance response of 1-D structures," in *Proceedings of the European COST F3 Conference on System Identification & Structural Health Monitoring*, Universidad Politecnica de Madrid, Madrid, Spain, June 2000.
- [22] COMSOL, Inc., 2013, <http://www.comsol.com>.
- [23] Efunda Inc., 2010, <http://www.efunda.com>.

Research Article

Anchor Dragging Analysis of Rock-Berm Using Smoothed Particle Hydrodynamics Method

Jinho Woo, Dongha Kim, and Won-Bae Na

Department of Ocean Engineering, Pukyong National University, Busan 608-737, Republic of Korea

Correspondence should be addressed to Won-Bae Na; arizcat@gmail.com

Received 7 August 2014; Accepted 19 October 2014

Academic Editor: Ting-Hua Yi

Copyright © 2015 Jinho Woo et al. This is an open access article distributed under the Creative Commons Attribution License, which permits unrestricted use, distribution, and reproduction in any medium, provided the original work is properly cited.

This study presents dynamic responses of rock-berm structural system under anchor dragging and accordingly provides the characteristics of the stresses and displacements obtained. For the purpose, first, a rock-berm was modeled by the SPH (smoothed particle hydrodynamics) method and piecewise Drucker-Prager material model by facilitating the associated software package—ANSYS-AUTODYN. Second, 2-ton stockless anchor was modeled as a rigid body and eventually dragging external force was obtained. Then, the dragging velocity (1 and 2 m/s) was considered as a parameter to investigate the effect of its variation on the responses. Finally, the dragging tensile forces of the anchor cable were obtained and compared according to the dragging velocities. It is shown that the four-layer rock-berm gives the safety margin to the submarine power cable according to the unaffected gauge points near the cable. This safety is accomplished by the four layers (related to rock-berm height) and the number of rock particles at each layer (related to rock-berm widths).

1. Introduction

Submarine power cables have been used to connect dots and accordingly transmit electric power from the main land to an island. Recent developments in ocean renewable energies make the conventional energy flows in another direction such as offshore wind farms to the main land. This innovation requires the frequent use of submarine power cables; hence, their safety assurance methods have been developed.

Among the methods, rock-berms have been used in relatively deep waters because of their easy installation and inexpensive cost. A recent study showed that rock-berm height and rock size are important parameters against an accidental load—anchor collision [1]. Along with anchor collision, anchor dragging is also important for the protecting structures [2]. Yoon and Na [2] investigated the dynamic responses of a flexible concrete mattress through field experiments. However, no one has investigated the behaviors of rock-berms under anchor dragging so far.

This fact extends to numerical studies because the conventional Lagrange method is not applicable in the modeling of rocks [3] but applicable in tunnel-type protective structures [4, 5]. Accordingly, it is demanded to develop a numerical

procedure, to evaluate the dynamic behaviors of a rock-berm under anchor dragging, and to acquire the safety assessment of submarine power cables, which are installed under rock-berms.

This study presents dynamic responses of rock-berm behaviors under anchor dragging and accordingly provides the characteristics of the stresses and displacements obtained. For the purpose, first, a rock-berm was modeled by the SPH (smoothed particle hydrodynamics) method and piecewise Drucker-Prager material model by facilitating the associated software package—ANSYS-AUTODYN [6]. Second, 2-ton stockless anchor was modeled as a rigid body and eventually dragging external force was obtained. Then, the dragging velocity (1 and 2 m/s) was considered as a parameter to investigate the effect of its variation on the responses. Finally, the dragging tensile forces of the anchor cable were obtained and compared according to the dragging velocities.

It should be noted here that this study is limited to investigating the dynamic responses of the target structure under anchor dragging. Other issues such as monitoring of the transient responses [7], multistage structural damage diagnosis [8], and more detailed signal process [9] should be considered in further research activities.

2. Materials and Methods

The SPH method was initially developed by Gingold and Monaghan [10] and Lucy [11] for astrophysical problems. It has been used in many research fields such as astrophysics, ballistics, volcanology, and oceanography because it is a mesh-free Lagrange method and resolution can easily be adjusted according to variables such as the density. Most initial problems are fluid-related by dividing the fluid into a set of discrete elements (particles). Libersky and Petschek [12] extended the SPH to solid mechanics. The main advantage of SPH in solids is the possibility of dealing with the larger local distortion than grid-based methods; hence, it has been exploited in many applications in solid mechanics such as metal forming, collision, crack growth, fracture, and fragmentation. The detailed description of the SPH method and associated references can be found in the literature [13]. Here, we introduce the brief concept of the SPH method.

The SPH method uses kernel approximation, which is based on randomly distributed interpolation points with no assumptions about which points are neighbors, to calculate spatial derivatives and particle density using Kernel estimation [14]. The particle density can be expressed using kernel approximation as follows:

$$\rho^I = \sum_{j=1}^N m^j W^{IJ} (x^I - x^j, h), \quad (1)$$

where ρ^I is the density of I th particle, m^j is the mass of J th particle, and $W^{IJ}(x^I - x^j, h)$ is the weight function according to particle size h . x^I and x^j are x -coordinates of I th and J th particle. In the SPH method, the particle density can be obtained as mass of neighbor particle multiplied by weight function. Figure 1 shows a schematic of the weight function in SPH method. In the study, the Kernel B-spline is used as the weight function. The basic form of weight function is as follows:

$$w(u) = \begin{cases} 1 - 6u^2 + 6u^3, & 0 \leq u \leq \frac{1}{2}, \\ 2(1 - u)^3, & \frac{1}{2} < u \leq 1, \\ 0, & u > 1, \end{cases} \quad (2)$$

where u is a parametric variable defined by $u = |x^I - x^j|/(2h)$.

Two contact conditions were considered, as shown in Figure 2. First, the interface between rock and other materials (basement and anchor) is based on the contact algorithms used in Lagrange-oriented finite element codes. Second, the interface between the stones (particle to particle contact) is based on the meshless approach [15]. If other material intersects the circle of a particle, then contact is assumed to be occurred. When contact occurs, the restoring force is applied along the normal to the surface. In the particle to particle contact, restoring forces are applied between particles.

Rock-berm is a typical example on which the SPH method is applicable because rock-berm is a structure constructed by stacking rocks to protect lifelines (e.g., submarine power cables and pipelines) and to build breakwaters.

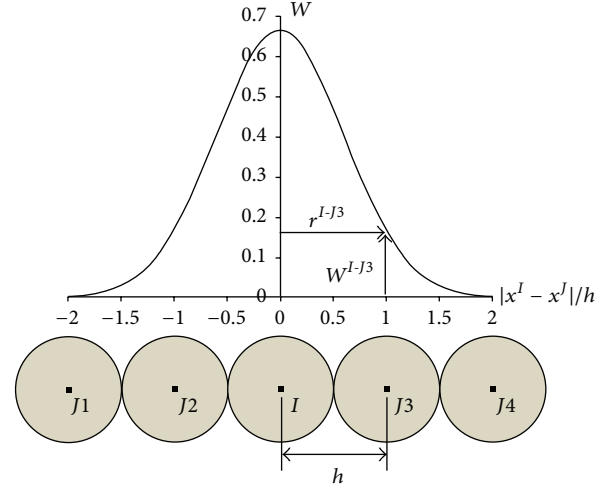


FIGURE 1: The schematic of the weight function.

TABLE 1: Material properties of seabed (sand).

	Density (kg/m ³)	Young's modulus (MPa)	Poisson ratio
Elastic sand	2200	81	0.3

Figure 3 shows a rock-berm consisting of rock particles (the upper layers) modeled by the SPH method and lower seabed layers modeled by 8-node solid elements. The linear elastic material properties were used for modeling of the seabed layers, as shown in Table 1. The piecewise Drucker-Prager material model was used for modeling of the rock layers because the material model is frequently used for the discrete materials such as concrete, rocks, and soils [16, 17]. In the rock material model, we used the material properties of Table 2, which is proposed by Chen et al. [18] and the associated pressure-yield stress curve, shown in Figure 4.

The rock-berm size was determined according to C-berm, which was proposed by the Korean Electric Power Corporation [19]. The bottom width is 7 m, the top width is 2 m, the height is 1.2 m, and the slope angle is 25.64° as shown in Figure 3. The diameters of the rocks typically range from 100 to 300 mm in the practice; hence, the upper bound 300 mm was used in the study. In reality, the rock-berm extends to the z and $-z$ directions for the continuous layout; hence, two symmetry planes (the boundary planes A and B in Figure 3) were assumed and constrained in the horizontal (z and $-z$) directions. In addition, the seabed bottom plane was constrained in the vertical direction.

The target anchor (2-ton stockless) is one of anchors frequently used in commercial and other vessels in the Korean waters. It was modeled according to the Korea Standard [20] and modeled by 4-node shell elements for the dragging analysis, as shown in Figure 5. Moreover, the anchor is assumed to be a rigid body because the density (7200 kg/m³) and Young's modulus (170 GPa) are much larger than those of the rocks and seabed. Table 3 shows the anchor considered and its representative dimensions [20]. As shown in Figure 3,

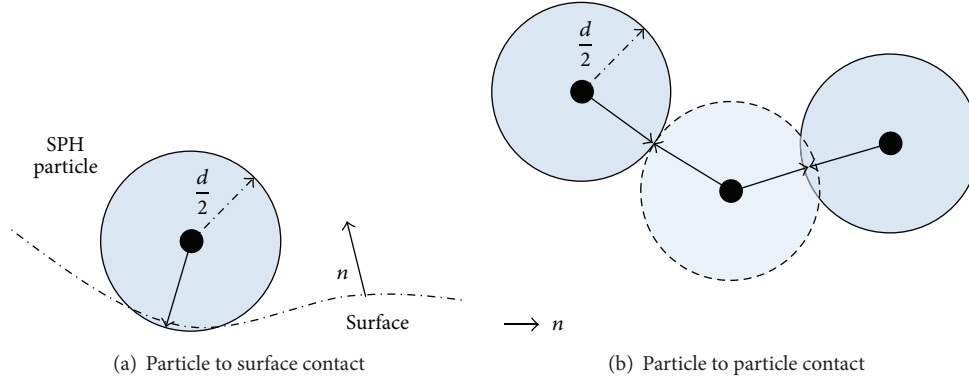


FIGURE 2: Contact conditions: (a) particles to surface contact and (b) particle to particle contact.

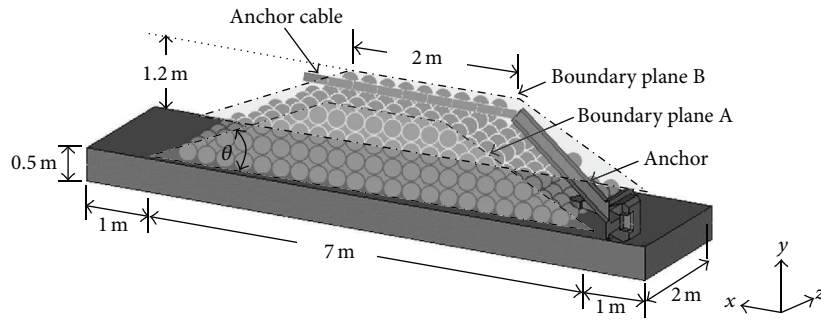


FIGURE 3: Dimension of rock-berm and its boundary planes (A and B).

TABLE 2: Material properties of rock for Drucker-Prager model.

Parameter	Value
Density (kg/m^3)	2750
Bulk modulus (GPa)	35.7
Pressure 1 (MPa)	-30
Pressure 2 (MPa)	-26.7
Pressure 3 (MPa)	200
Pressure 4 (MPa)	1000
Pressure 5 (MPa)	2500
Shear modulus (GPa)	17.44
Hydro tensile limit (MPa)	30
Yield stress 1 (MPa)	0
Yield stress 2 (MPa)	40
Yield stress 3 (MPa)	450
Yield stress 4 (MPa)	1430
Yield stress 5 (MPa)	2530

TABLE 3: Specifications of target anchors.

Anchor type	Width of anchor (mm)	Height of shank (mm)	Height of anchor (mm)
2-ton stockless	1040	2404	1340

the 2-ton stockless anchor was guided (attached) by the anchor cable, which is modeled by line (link) elements

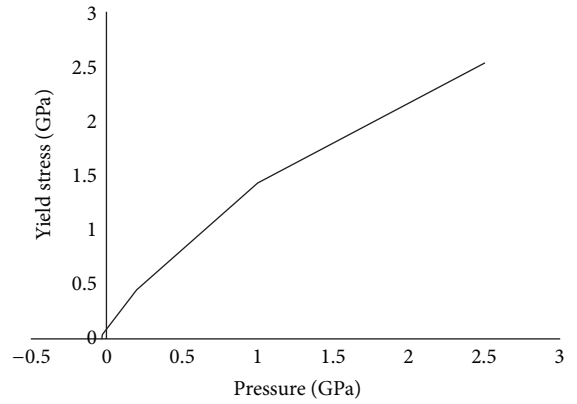


FIGURE 4: Pressure-yield stress curve for piecewise Drucker-Prager model.

(density: 7850 kg/m^3 and Young's modulus: 210 GPa). The cable is always under tension; hence, the conventional cable element which can resist the tension only is not necessary. Besides, the geometrical nonlinearity of the anchor cable was not considered because of the external force is tension-only. The dragging location was assumed to be the bottom of the 2nd layer (Layer B) at the boundary plane A, as shown in Figure 6. Two dragging scenarios were made by considering two dragging velocities (1 and 2 m/s).

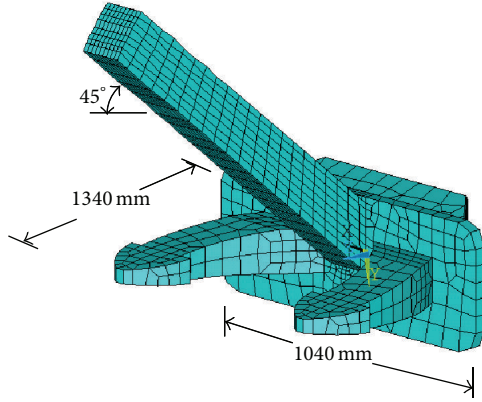


FIGURE 5: 2-ton stockless anchor model.

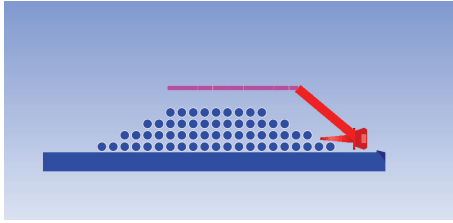


FIGURE 6: Cross-section at the symmetric boundary plane A.

To get the dynamic responses, 11 gauge points are specified as shown in Figure 7. In the figure, each layer has its own name, for example, Layer A, Layer B, Layer C, and Layer D; hence, the gauge points are named to indicate the layers. For example, A1 denotes the first gauge point locating at Layer A. The coordinates of the gauge points are given in Table 4. It should be noted here that the location of submarine power cables is just below A1 because the position of the number “1” is the center of the rock-berm (y -axis).

3. Results and Discussions

The von-Mises stress (equivalent stress) is often used in determining whether a material will yield when subjected to a complex loading condition. Figure 8 shows the von-Mises stresses at the gauge points (A1–D2) when dragging velocity is 1 m/s (first scenario). Initially, the stresses at A3 and B3 are distinct because the anchor dragging starts at the right side between Layer A and Layer B. The stresses at B3 are bigger than those at A3 due to the dragging direction (left or $+x$ direction) and the bottom boundary condition. After approximately 1.5 sec, the stresses at C2 and D2 exceed the stresses at A3, which indicates that the anchor is moving up. Then, the stresses at C1 and D1 exceed the stresses at A3 after around 2.0 sec, which denotes that the anchor reaches at the top layer (Layer D). It should be emphasized that the stresses at A1 are almost zero; hence, the submarine power does not tends to experience stresses. Over the period, the maximum von-Mises stress is approximately 4.3 kPa, which occurs at C2 and D2, as shown in Table 5.

Figure 9 shows the horizontal displacements (UX). Initially, the front particles (A3, A4, and B3) move to the left

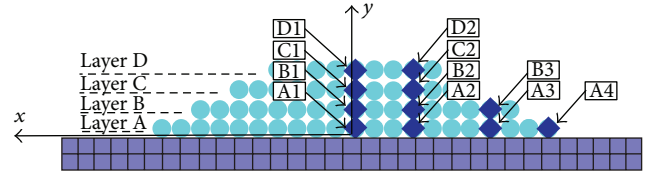


FIGURE 7: Gauge points of rock-berm.

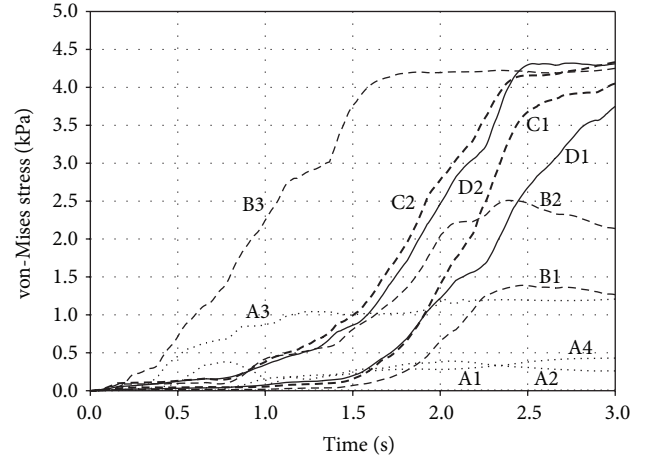


FIGURE 8: von-Mises stresses at gauge points when dragging velocity is 1 m/s.

TABLE 4: Coordinates of gauge points.

Gauge points	x -coordinate (m)	y -coordinate (m)	z -coordinate (m)
A1	−0.05	0.15	0.15
A2	−0.95	0.15	0.15
A3	−2.15	0.15	0.15
A4	−3.05	0.15	0.15
B1	−0.05	0.45	0.15
B2	−0.95	0.45	0.15
B3	−2.15	0.45	0.15
C1	−0.05	0.75	0.15
C2	−0.95	0.75	0.15
D1	−0.05	1.05	0.15
D2	−0.95	1.05	0.15

($+x$ direction) according to the anchor dragging and then followed by C2 and D2 and accordingly D1. The horizontal displacements at the gauge points A1, A2, and B1 are almost zero, which indicate that the particles do not receive main effect from the dragging movement. The maximum UX are about 855 mm at D1. Figure 10 shows the vertical displacements (UY). Initially, the front particles (A3 and B3) move upward ($+y$ direction) and then followed by C1 and D1. An interesting factor is that the D2 experiences the downward movement ($-y$ direction) after around 2.0 sec. This means the corresponding particle is disintegrated. It is also shown that the vertical displacements at A1, A2, A4, and B1 are almost

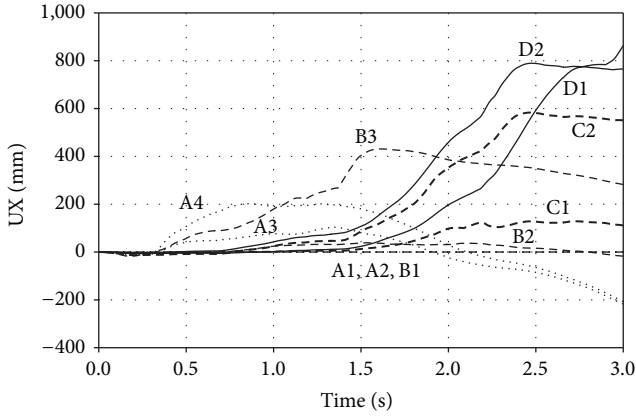


FIGURE 9: Horizontal displacements (UX) at gauge points when dragging velocity is 1 m/s.

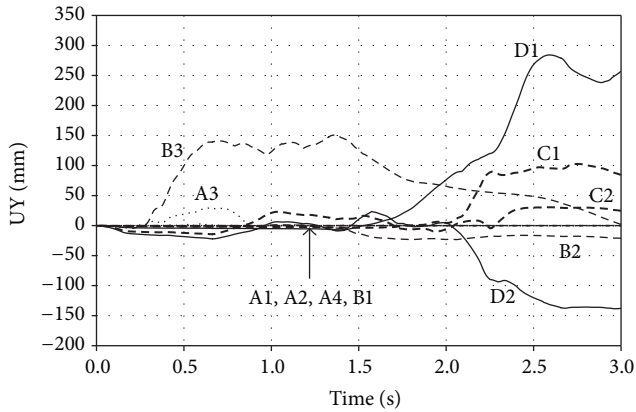


FIGURE 10: Vertical displacements (UY) at gauge points when dragging velocity is 1 m/s.

TABLE 5: Maximum von-Mises stresses at gauge points when dragging velocity is 1 m/s.

Gauge point	Max. von-Mises stress (kPa)
A1	0.0003
A2	0.3930
A3	1.2220
A4	0.4300
B1	1.3890
B2	2.5090
B3	4.2500
C1	4.0480
C2	4.3310
D1	3.7490
D2	4.3190

zero over the time interval, standing for less effective zone of the anchor dragging. The maximum UY is approximately 283 mm at D1.

To pinpoint the particle movement, Figure 11 shows the movement sequence according to time. From the figure,

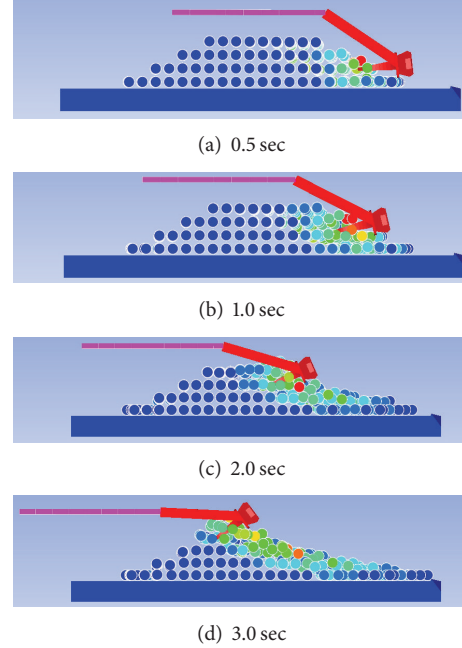


FIGURE 11: von-Mises stress according to time when dragging velocity is 1 m/s.

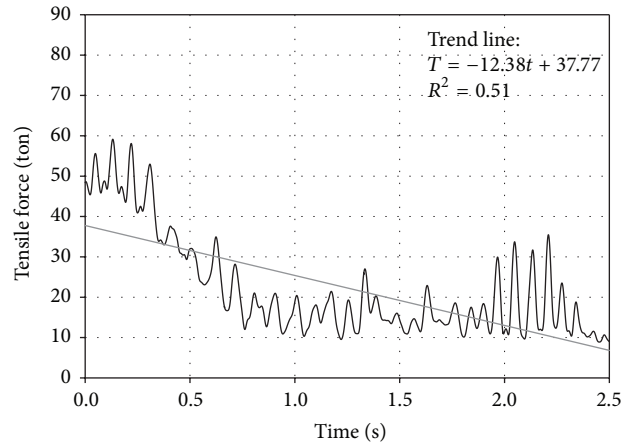


FIGURE 12: Tensile force of cable when dragging velocity is 1 m/s.

it is clearly observed that the stockless anchor penetrated, dragged, and disintegrated the rocks as time goes. However, it does not cause a significant response at A1, which locates at the top of the submarine power cable. Thus, the dragging scenario does not threaten the safety of the power cable. Figure 12 shows the tensile force of the anchor cable. The initial tensile force is 50 ton, then the force tends to decrease to 10 to 25 ton when the anchor penetrated the rocks (between 0.7 and 2.0 sec), and then the force increases to 10 to 35 ton when the anchor gives a deeper penetration into the rocks (after 2 sec). This late increase of the tensile force is caused by the upper layer rocks, which do not roll down from the rock-berm as shown in Figure 11.

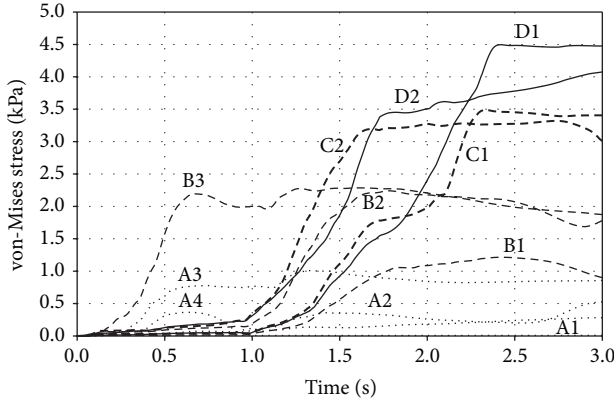


FIGURE 13: von-Mises stresses at gauge points when dragging velocity is 2 m/s.

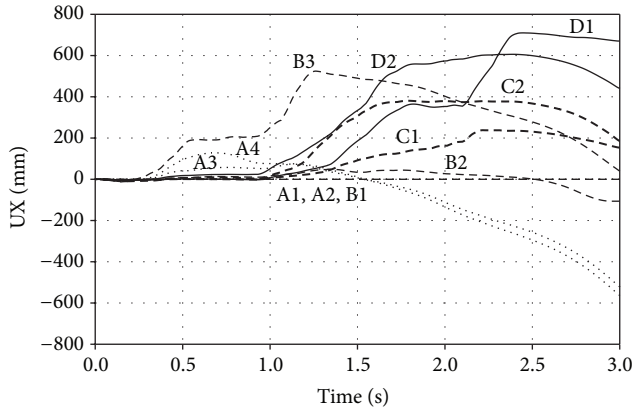


FIGURE 14: Horizontal displacements (UX) at gauge points when dragging velocity is 2 m/s.

Figure 13 shows the von-Mises stresses at the gauge points (A1–D2) when dragging velocity is 2 m/s. Initially, the stresses at A3, A4, and B3 are distinct because the anchor dragging starts at the right side between Layer A and Layer B. The stresses at B3 are bigger than those at A3 and A4 due to the dragging direction (+ x direction) and the bottom boundary condition. After approximately 1.3 sec, the stresses at C2 and D2 exceed the stresses at A3, which indicates that the anchor is moving up. Then, the stresses at C1 and D1 exceed the stresses at A3 after around 1.5 sec, which denotes that the anchor reaches at the top layer (Layer D). It should be emphasized that the stresses at A1 are almost zero; hence, the submarine power does not tend to experience stresses. Over the period, the maximum von-Mises stress is approximately 4.5 kPa, which occurs at D1, as shown in Table 6. In comparison with the first scenario, the second scenario shows the similar characteristics but little earlier occurrence than those of 1 m/s because of the faster dragging velocity (2 m/s).

Figure 14 shows the horizontal displacements (UX) in the case of 2 m/s of dragging velocity. Initially, the front particles (A3, A4, and B3) move to the left (+ x direction) according to the anchor dragging and then followed by C2

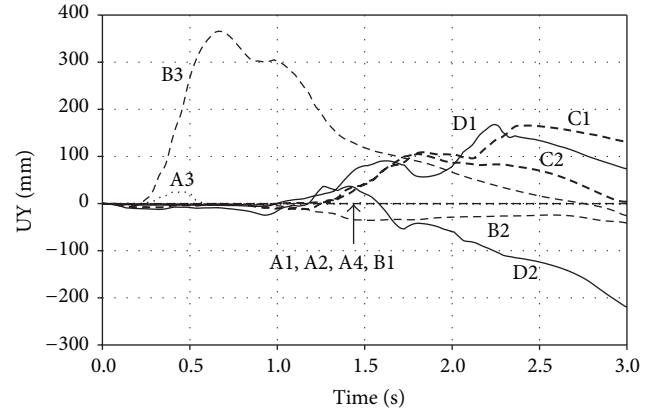


FIGURE 15: Vertical displacements (UY) at gauge points when dragging velocity is 2 m/s.

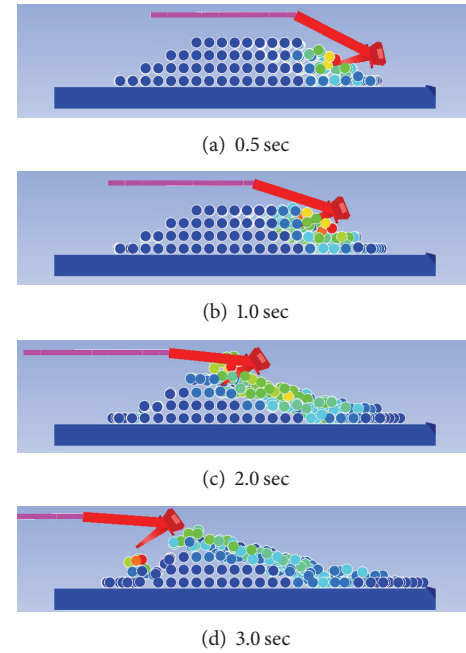


FIGURE 16: von-Mises stress according to time when dragging velocity is 2 m/s.

and D2 and accordingly D1. The horizontal displacements at the gauge points A1, A2, and B1 are almost zero, which indicate that the particles do not receive main effect from the dragging movement. The maximum UX are about 710 mm at D1. Figure 15 shows the vertical displacements (UY) in the second scenario. Initially, the front particles (A3 and B3) move upward (+ y direction) and then followed by C1 and D1. An interesting factor is that the D2 experiences the downward movement (– y direction) after around 1.7 sec. This means the corresponding particle is totally disintegrated. It is also shown that the vertical displacements at A1, A2, A4, and B1 are almost zero over the time interval, standing for less effective zone of the anchor dragging. The maximum UY is approximately 365 mm at B3, unlike the first scenario

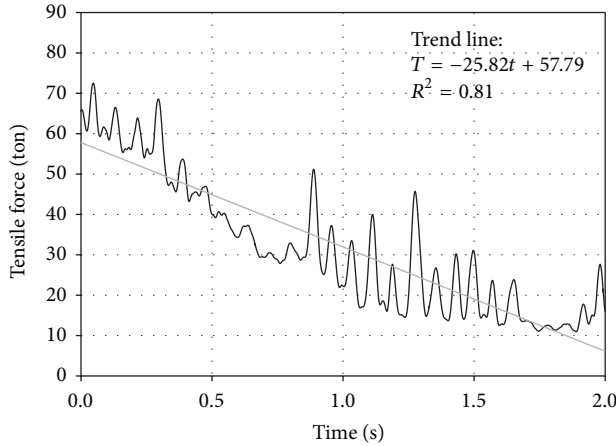


FIGURE 17: Tensile force of cable when dragging velocity is 2 m/s.

TABLE 6: Maximum von-Mises stresses at gauge points when dragging velocity is 2 m/s.

Gauge point	Max. von-Mises stress (kPa)
A1	0.0028
A2	0.5250
A3	1.0080
A4	0.3650
B1	1.2140
B2	2.2410
B3	2.2850
C1	3.4890
C2	3.3200
D1	4.4960
D2	4.0750

showing that the maximum UY occurs at D1. This indicates that higher dragging velocity causes larger vertical movement at the initial period. In comparison with the first scenario, the second scenario shows the similar characteristics but little earlier movement than those of 1 m/s because of the faster dragging velocity (2 m/s).

To pinpoint the particle movement, Figure 16 shows the movement sequence according to time. From the figure, it is clearly observed that the stockless anchor penetrated, dragged, and disintegrated the rocks as time goes. However, it does not cause a significant response at A1, which locates at the top of the submarine power cable. Thus, the dragging scenario does not threaten the safety of the power cable. In comparison with the first scenario, as shown in Figures 8 and 13, the higher dragging velocity causes much faster anchor movement, and accordingly the stockless anchor is already separated from the rock-berm at 3.0 sec. Thus, more disintegration or disturbance of the rocks happens in the second scenario. Figure 17 shows the tensile force of the anchor cable. The initial tensile force is 65 ton, and then the force tends to decrease as time goes. The tensile force of the second scenario has a more distinct decreasing pattern than that of the first scenario (see the trend lines and

their characters of Figures 12 and 17). This can be explained by the early escape of the anchor from the rock-berm in the second scenario.

4. Conclusion

By facilitating the SPH method, it is shown that the global behavior of the rock-berm is not much sensitive to the dragging velocity. This indicates that the gauge points give similar responses although the responding moments are little different according to the velocity variation. However, the faster dragging force (2 m/s) gives more rapid disintegration of the rock-berm, and accordingly the late responses are relatively distinguishable. Moreover, considering the tensile force of the anchor cable, the higher velocity (2 m/s) gives a more distinct decreasing pattern of the tensile force than that of the lower velocity (1 m/s) as time goes because of the early escape of the anchor from the rock-berm. The four-layer rock-berm gives the safety margin to the submarine power cable according to the unaffected gauge points near the cable. This safety is accomplished by the four layers (rock-berm height) and the number of rock particles at each layer (related to rock-berm widths and slope angle). Therefore, the dimensions (height = 1.2 m, lower width = 7 m, upper width 2 m, and slope angle = 25.64°) provide the safety of submarine power cables under the anchor dragging scenarios.

Conflict of Interests

The authors declare that there is no conflict of interests regarding the publication of this paper.

Acknowledgment

This research was a part of the project titled “Development on the Guidelines of Safety Assessment for Submarine Cable Protection Facilities in Shallow Water” funded by the Ministry of Land, Transport and Maritime Affairs, Korea (KIMT-2012-20120018).

References

- [1] J. Woo and W. B. Na, “Safety assessment of rock-berms under anchor collision for protecting submarine power cables,” *Ocean Engineering*. In press.
- [2] H.-S. Yoon and W.-B. Na, “Safety assessment of submarine power cable protectors by anchor dragging field tests,” *Ocean Engineering*, vol. 65, pp. 1–9, 2013.
- [3] J. Woo, D. Kim, H.-S. Yoon, and W.-B. Na, “Characterizing Korean general artificial reefs by drag coefficients,” *Ocean Engineering*, vol. 82, pp. 105–114, 2014.
- [4] J. Woo and W. B. Na, “Analyses of the maximum response of cylinders-connected protectors under anchor colliding and dragging,” *Journal of Ocean Engineering and Technology*, vol. 24, pp. 81–87, 2010 (Korean).
- [5] J. Woo, W. B. Na, and H. T. Kim, “Numerical simulation of arch-type submarine cable protector under anchor collision,” *Journal of Ocean Engineering and Technology*, vol. 23, pp. 96–103, 2009 (Korean).

- [6] ANSYS, *AUTODYN User Manual Version 12.0*, ANSYS, Canonsburg, Pa, USA, 2009.
- [7] T. H. Yi, H. N. Li, and M. Gu, "A new method for optimal selection of sensor location on a high-rise building using simplified finite element model," *Structural Engineering and Mechanics*, vol. 37, no. 6, pp. 671–684, 2011.
- [8] T.-H. Yi, H.-N. Li, and H.-M. Sun, "Multi-stage structural damage diagnosis method based on "energy-damage" theory," *Smart Structures and Systems*, vol. 12, no. 3-4, pp. 345–361, 2013.
- [9] H. Li, T. Yi, M. Gu, and L. Huo, "Evaluation of earthquake-induced structural damages by wavelet transform," *Progress in Natural Science*, vol. 19, no. 4, pp. 461–470, 2009.
- [10] R. A. Gingold and J. J. Monaghan, "Smoothed particle hydrodynamics: theory and application to non-spherical stars," *Monthly Notices of the Royal Astronomical Society*, vol. 181, pp. 375–389, 1977.
- [11] L. B. Lucy, "A numerical approach to the testing of the fission hypothesis," *The Astronomical Journal*, vol. 82, pp. 1013–1024, 1977.
- [12] L. D. Libersky and A. G. Petschek, "Smooth particle hydrodynamics with strength of materials," in *Advances in the Free-Lagrange Method Including Contributions on Adaptive Gridding and the Smooth Particle Hydrodynamics Method*, vol. 395 of *Lecture Notes in Physics*, pp. 248–257, Springer, Berlin, Germany, 1991.
- [13] J. Lin, H. Naceur, D. Coutellier, and A. Laksimi, "Efficient meshless SPH method for the numerical modeling of thick shell structures undergoing large deformations," *International Journal of Non-Linear Mechanics*, vol. 65, pp. 1–13, 2014.
- [14] C. J. Hayhurst, R. A. Clegg, I. H. Livingstone, and N. J. Francis, "The application of SPH techniques in AUTODYN-2D to ballistic impact problems," in *Proceeding of the 16th International Symposium on Ballistics*, San Francisco, Calif, USA, 1996.
- [15] S. Seo and O. Min, "Axisymmetric SPH simulation of elastoplastic contact in the low velocity impact," *Computer Physics Communications*, vol. 175, no. 9, pp. 583–603, 2006.
- [16] W. K. Liu, S. Jun, S. Li, J. Adee, and T. Belytschko, "Reproducing kernel particle methods for structural dynamics," *International Journal for Numerical Methods in Engineering*, vol. 38, no. 10, pp. 1655–1679, 1995.
- [17] X. H. Zhu and Y. J. Jia, "3D mechanical modeling of soil orthogonal cutting under a single reamer cutter based on Drucker-Prager criterion," *Tunnelling and Underground Space Technology*, vol. 41, no. 1, pp. 255–262, 2014.
- [18] S. G. Chen, J. Zhao, A. Makurati, and C. Madshus, "Discrete element modeling of an explosion test in granite," in *Proceedings of GeoEng2000: An International Conference on Geotechnical & Geological Engineering, 19–24 November 2000, Melbourne Exhibition and Convention Centre, Melbourne, Australia*, pp. 1474–1481, 2000.
- [19] KEPSCO, *Field Test Report for Installation of Rock Berm in the Shallow Water of Jindo-Jeju Island HVDC Interconnection Project*, Korea Electric Power Corporation, 2010 (Korean).
- [20] KS V 3311, Anchors, Korean Standards Association, 2012.

Research Article

Detection on Structural Sudden Damage Using Continuous Wavelet Transform and Lipschitz Exponent

Bo Chen,¹ Yuan-pin Kang,¹ Peng-yun Li,² and Wen-ping Xie²

¹Key Laboratory of Roadway Bridge and Structural Engineering, Wuhan University of Technology, Mail Box No. 219, No. 122 Luoshi Road, Wuhan 430070, China

²Guangdong Power Grid Corporation Co. Ltd., Guangzhou 510080, China

Correspondence should be addressed to Bo Chen; cbsteven@163.com

Received 3 August 2014; Accepted 12 October 2014

Academic Editor: Ting-Hua Yi

Copyright © 2015 Bo Chen et al. This is an open access article distributed under the Creative Commons Attribution License, which permits unrestricted use, distribution, and reproduction in any medium, provided the original work is properly cited.

The degradation of civil engineering structures may lead to a sudden stiffness reduction in a structure and such a sudden damage will cause a discontinuity in the dynamic responses. The detection on structural sudden damage has been actively carried out in this study. The signal singularity of the acceleration responses with sudden stiffness reduction is characterized by the coefficients of continuous wavelet transform with fine scales. A detection approach based on the CWT is proposed in terms of the decomposed detail coefficients of continuous wavelet transform to detect the damage time instant and location. The Lipschitz exponent is mathematically used to estimate the local properties of certain function and is applied to reflect the damage severity. Numerical simulation using a five-story shear building under different types of excitation is carried out to assess the validity of the proposed detection approach for the building at different damage levels. The sensitivity of the damage index to the intensity and frequency range of measurement noise is also investigated. The effects of both measurement noise intensity and frequency range on the damage detection are numerically investigated.

1. Introduction

The wavelet transform is an extension of the traditional Fourier transform with adjustable window location and size. Wavelet analysis combines both time and frequency analysis, which allows it to zoom in on time without any loss of scale resolution. The wavelet transform has recently emerged as a promising tool for structural health monitoring and it is an ideal tool in addressing the issue of time locality of structural damages [1–4]. The earliest work of applying wavelet analysis in structural health monitoring dated back to the work of Masuda and his group in 1995 [5, 6]. Faults in gear systems were detected using wavelet approaches and some results were verified by an inspection [7]. Hong et al. [8] studied the effectiveness of the wavelet transform in detecting structural cracks. In their analysis, the magnitude of the Lipschitz exponent is used as a useful indicator of the damage extent. The detection results from both numerical simulation and experiment prove the efficiency of wavelet based damage detection approaches.

The degradation of civil engineering structures may lead to a sudden stiffness reduction in a structure associated with the events such as weld fracture, column buckling, and brace breakage [9]. Such a sudden damage of stiffness in a structure will cause a discontinuity in acceleration responses and can be detected by using signal based detection approaches such as wavelet transform, empirical mode decomposition, time series, and time-frequency analysis. Hou et al. [10, 11] proposed a wavelet-based approach to identify the damage time instant and damage location of a simple structural model with breakage springs. Sohn et al. [12] used wavelet transform and the Holder exponent to detect the time varying nature of discontinuities. Their experimental results demonstrated that the Holder exponent could be an effective tool for identifying certain types of events that introduce discontinuities in the measured dynamic response data. The same idea for detecting sudden damage was adopted by Vincent et al. [13] and Yang et al. [9, 14] but using empirical mode decomposition to decompose the vibration signal to capture the signal discontinuity. In addition to the above-mentioned numerical

studies, Xu and Chen [15] carried out experimental studies on the applicability of empirical mode decomposition for detecting structural damage caused by a sudden change of structural stiffness. Chen and Xu [16] proposed two online detection approaches for the sudden damage detection.

The sudden stiffness loss of structural components may induce the signal discontinuity in the acceleration responses close to the damage location at the damage time instant. It is reported that the time instant and location of the sudden stiffness loss can be detected by using the discrete WT. However, the severity of different sudden damage events cannot be estimated directly by the WT. In this regard, the investigation of detection on sudden damage event of building structures has been actively carried out in this study. The signal feature of the structural acceleration responses of an example building is examined. Three types of dynamic loading, sinusoidal, seismic, and impulse excitations are taken as the inputting excitations. The signal singularity of the acceleration responses with sudden stiffness reduction is characterized by the coefficients of continuous wavelet transform with fine scales. A detection approach based on the CWT is proposed in terms of the decomposed detail coefficients of continuous wavelet transform to detect the damage time instant and location. The Lipschitz exponent is mathematically used to estimate the local properties of certain function and is applied to reflect the damage severity. Numerical simulation using a five-story shear building under different types of excitation is carried out to assess the validity of the proposed detection approach for the building at different damage levels. The sensitivity of the damage index to the intensity and frequency range of measurement noise is also investigated. The effects of both measurement noise intensity and frequency range on the damage detection are numerically investigated. The made observations demonstrate that the proposed approach can accurately identify the damage events and the damage severity can be estimated by the Lipschitz exponent.

2. Wavelet Transform

Morlet and Grossmann initially proposed wavelet theory and Meyer developed the mathematical foundations of wavelets. The two America-based researchers Daubechies [17] and Mallat [18, 19] changed this by defining the connection between wavelets and digital signal processing. Wavelets have been applied to a number of areas, including data compression, image processing, and time-frequency spectral estimation. A mother wavelet $\psi(t)$ is a waveform that has limited duration and an average value of zero. Based on this mother wavelet, the wavelet kernel can be expressed by

$$\psi_{a,b}(t) = \frac{1}{\sqrt{a}} \psi\left(\frac{t-b}{a}\right), \quad (1)$$

where a and b are dilation and translation parameters, respectively. Both are real numbers and a must be positive. Similar to the Short Time Fourier Transform, one can analyze square-integrable function $f(t)$ with wavelet transform,

which decomposes a signal in the time domain into a two-dimensional function in the time-scale plane (a, b)

$$\begin{aligned} Wf(a, b) &= \int_{-\infty}^{+\infty} f(t) \psi_{a,b}^*(t) dt \\ &= \frac{1}{\sqrt{a}} \int_{-\infty}^{+\infty} f(t) \psi_{a,b}^*\left(\frac{t-b}{a}\right) dt, \end{aligned} \quad (2)$$

where $*$ denotes complex conjugation. The term frequency instead of scale has been used in order to aid in understanding, since a wavelet with large-scale parameter is related to low-frequency content component and vice versa. The mother wavelet $\psi(t)$ should satisfy the following admissibility condition to ensure existence of the inverse wavelet transform such as

$$C_\psi = \int_{-\infty}^{+\infty} \frac{|\hat{\psi}(\omega)|^2}{|\omega|} d\omega < +\infty, \quad (3)$$

where $\hat{\psi}(\omega)$ is the Fourier transform of $\psi(t)$. The existence of the integral in (3) requires that

$$\hat{\psi}(0) = 0, \quad \text{i.e.,} \quad \int_{-\infty}^{+\infty} \psi(x) dx = 0. \quad (4)$$

The signal $f(t)$ can be reconstructed by an inverse wavelet transform of $Wf(a, b)$ as defined by

$$f(t) = \frac{1}{C_\psi} \iint_{-\infty}^{+\infty} Wf(a, b) \psi_{a,b}\left(\frac{t-b}{a}\right) \frac{1}{a^2} da db. \quad (5)$$

The calculating wavelet coefficients at every possible scale will generate a lot of redundant data. In some practical signal processing cases, the discrete version of the wavelet is often utilized by discretizing the dilation parameter a and the translation parameter b . The procedure becomes much more efficient if dyadic values of a and b are used; that is,

$$a = 2^j; \quad b = 2^j k \quad j, k \in Z, \quad (6)$$

where Z is the set of positive integers. For some special choices of $\psi(t)$, the corresponding discrete wavelets can be written to constitute an orthonormal basis

$$\psi_{j,k}(t) = 2^{j/2} \psi(2^j t - k), \quad j, k \in Z. \quad (7)$$

Using the orthonormal basis, the wavelet expansion of a function $f(t)$ and the coefficients of the wavelet expansion are defined as

$$\begin{aligned} f(t) &= \sum_j \sum_k \alpha_{j,k} \psi_{j,k}(t), \\ \alpha_{j,k} &= \int_{-\infty}^{+\infty} f(t) \psi_{j,k}^*(t) dt. \end{aligned} \quad (8)$$

3. Signal Feature due to Sudden Damage

The signal feature due to a sudden stiffness reduction is firstly investigated by taking a five-story shear building as

an example structure (Figure 1). The elevation of the shear building is displayed in Figure 2. The building is subject to different types of external excitations and a sudden stiffness loss occurs in the first story. The mass and horizontal stiffness of the undamaged building are uniform for all stories and the floor mass and stiffness are 1.3×10^6 kg and 4.0×10^9 N/m, respectively. The Rayleigh damping assumption is adopted to construct the structural damping matrix with the damping ratios in the first two vibration modes being set as 0.05. The original building is supposed to suffer a sudden 20% stiffness reduction in the first story while the horizontal stiffness in other stories remains unchanged. The frequency reduction due to 20% stiffness reduction in the first story is small with a maximum reduction no more than 5% in the first natural frequency. The sinusoidal excitation, seismic excitation, and impulse excitation are utilized, respectively, to calculate the acceleration responses of the example building to examine the signal features due to the sudden stiffness reduction. The seismic excitation used is the first 10 second portion of the El-Centro 1940 earthquake ground acceleration (S-N component) with a peak amplitude 1.0 m/s^2 . A sinusoidal excitation expressed by (9) with 10 second duration is assumed to act on each floor of the building

$$f(t) = 1300 \cdot \sin(4\pi t) \quad (0 \leq t \leq 10 \text{ s}) \text{ (kN)}. \quad (9)$$

An impulse excitation represented by 0.1 m/s initial velocity is supposed to occur on the first floor of the building. The damage time instant of the building is set as 6.0 s for seismic excitation and sinusoidal excitation and 0.2 s for impulse excitation. The dynamic responses under each type of external excitation are computed by using the Newmark- β method with a time interval of 0.002 s . The two factors in the Newmark- β method are selected as $\alpha = 1/2$ and $\beta = 1/4$.

The acceleration time histories of the first floor under seismic, sinusoidal, and impulse excitations are computed and displayed in Figure 2, respectively. To direct visual inspection of the original acceleration responses, one cannot easily find the signal feature due to the sudden damage event. Therefore, the 0.2 second portions of the acceleration responses under three external excitations are expanded to permit a detailed examination at the signal feature due to sudden stiffness loss. It is seen from Figure 2(a) that there exists a sudden jump in the original acceleration time histories at the damage time instant. The same observations made from the acceleration responses under sinusoidal and impulse excitations. It is clear that the sudden reduction of horizontal stiffness of the first floor causes a clear signal discontinuity in the acceleration response time history at the damage time instant. Since the signal discontinuity is of very high frequency, the WT can be applied to decompose the original acceleration responses and extract the signal induced by sudden damage events.

4. Detection on Sudden Damage Event

4.1. Description on Signal Singularity Using Lipschitz Exponent. An important property of the WT is the ability to characterize the local regularity of a certain function. To characterize singularity due to sudden stiffness loss, it is

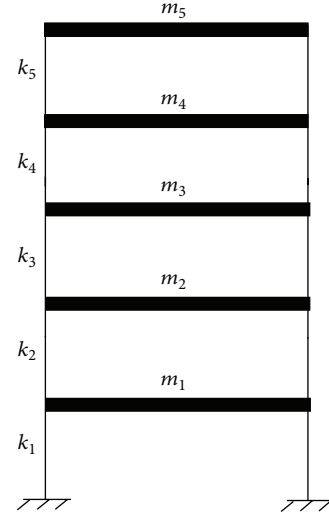


FIGURE 1: Elevation of a five-story building model.

necessary to precisely estimate the local singularity of an acceleration signal $f(t)$. Lipschitz exponents provide uniform singularity measurements over time intervals, but also at any point v . If the acceleration response $f(t)$ has a singularity at v , which means that it is not differentiable at v , then the Lipschitz exponent at v characterizes this signal singular behaviour. An acceleration signal function $f(t)$ is said to be pointwise Lipschitz $\alpha \geq 0$ at v if there exists $K > 0$ and a polynomial p_v of degree m (m is the largest integer satisfying $m \leq \alpha$) such that

$$\begin{aligned} f(t) &= p_v(t) + \varepsilon_v(t) \\ |\varepsilon_v(t)| &= |f(t) - p_v(t)| \leq K |t - v|^\alpha. \end{aligned} \quad (10)$$

For instance, a signal function is not differentiable at $f = v$ if $0 < \alpha < 1$. Therefore, the Lipschitz exponent α characterizes the nature of singularity at $f = v$. The traditional approach for regularity of the acceleration signal function $f(t)$ is related to the asymptotic decay of its Fourier transform. An acceleration signal function $f(t)$ is bounded and uniformly Lipschitz α over \mathbb{R} if

$$\int_{-\infty}^{+\infty} |\hat{f}(\omega)| (1 + |\omega|^\alpha) d\omega < +\infty. \quad (11)$$

Equation (14) can be applied to estimate the minimum global regularity of acceleration time histories with sudden damage events. However, it is not possible to analyze the singularity of $f(t)$ at a particular point v from the decay of $|\hat{f}(\omega)|$ at high frequencies ω . In contrast, since wavelets are well localized in time, the wavelet transform gives Lipschitz singularity over intervals and at points.

When the building structure suffers a sudden stiffness loss during the vibration, the extent of the signal discontinuity in acceleration time histories at the vicinity of the damage varies with different damage severities. Small damage is difficult to be identified using traditional vibration based approaches, but it still introduces some sorts of singularities

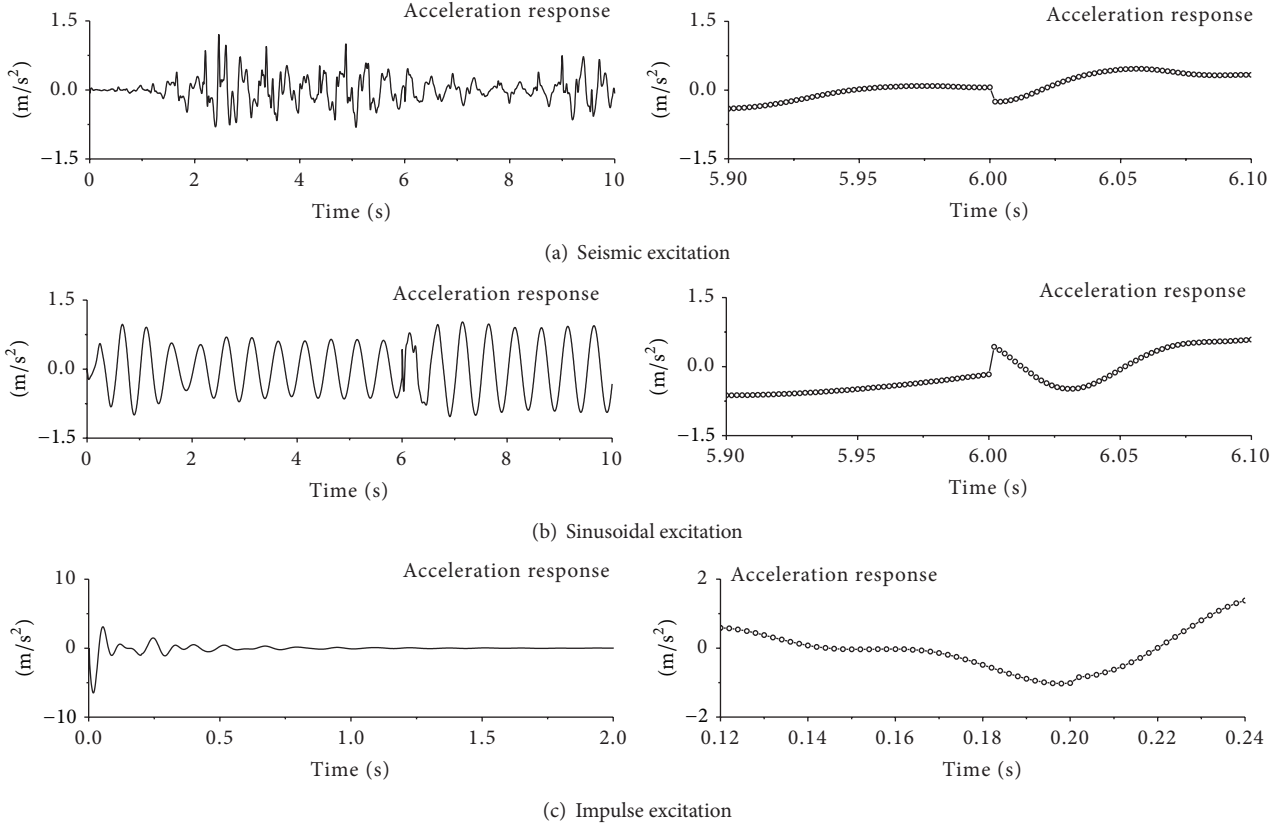


FIGURE 2: Signal discontinuity due to sudden damage.

to the acceleration responses. These singularities may be characterized by using the Lipschitz exponent with the aiding of the wavelet transform. To measure the local regularity of the acceleration signal by utilizing wavelet transform and Lipschitz exponent estimation, the wavelet vanishing moment plays an important role. The wavelet transform estimates the exponent by ignoring the polynomial p_v . For this purpose, one needs to use a wavelet that has $n > \alpha$ vanishing moments. A wavelet $\psi(t)$ is said to have n vanishing moments if it satisfies the following condition:

$$\int_{-\infty}^{+\infty} x^k \psi(x) dx = 0 \quad \text{for } 0 \leq k < n. \quad (12)$$

The condition (15) demonstrates that the wavelet having n vanishing moments is orthogonal to polynomials of up to degree $n-1$. If the wavelet transform with $n > \alpha$ is applied to (12) and consider the polynomial p_v has degree at most $n-1$, the following equations can be obtained

$$Wp_v(a, b) = \frac{1}{\sqrt{a}} \int_{-\infty}^{+\infty} p_v(t) \psi_{a,b}\left(\frac{t-b}{a}\right) dt = 0 \quad (13)$$

$$Wf(a, b) = W\varepsilon_v(a, b). \quad (14)$$

Therefore, the wavelet transform focuses only on a singular part of a certain function which demonstrates that CWT is suitable for detecting signal singularity due to sudden stiffness reduction. If a square-integrable function $f(t)$ is

Lipschitz $\alpha \leq n$ at $t = v$, then the asymptotic behaviour of the wavelet transform Wf near $t = v$ becomes [18]

$$|Wf(a, b)| \leq Aa^{\alpha+1/2} \left(1 + \left|\frac{b-v}{a}\right|^\alpha\right) \quad (A > 0), \quad (15)$$

where A is a constant. If t is the cone of influence of v then $Wf(a, b) = \langle f, \psi_{a,b} \rangle$ depends on the value of f in the neighbourhood of v . Equation (18) can be reduced to

$$|Wf(a, b)| \leq Aa^{\alpha+1/2}. \quad (16)$$

The high-amplitude wavelet coefficients are in the cone of the influence of the singularity. Normally, it is convenient to use the logarithm form in the estimation of the Lipschitz exponent of acceleration responses at the damage time instant

$$\log_2 |Wf(a, b)| \leq \log_2 A + \left(\alpha + \frac{1}{2}\right) \log_2 a. \quad (17)$$

Equation (18) proves that the local Lipschitz regularity of f at $t = v$ depends on the decay at fine scales of $|Wf(a, b)|$ in the neighbourhood of v . Measuring this decay directly in the time-scale plane (a, b) is not necessary. The decay of $|Wf(a, b)|$ can indeed be controlled from its local modulus maxima values of the wavelet transform coefficients. The modulus maximum is used to describe any point (a_0, b_0) such that $|Wf(a_0, b)|$ is locally maximum at $b = b_0$

$$\frac{\partial Wf(a_0, b_0)}{\partial b} = 0. \quad (18)$$

This local maxima should be a strict local maxima in either the right or left neighbourhood of b_0 , to avoid having any local maxima when $|Wf(a_0, b)|$ is constant.

4.2. Detection on Sudden Damage Event. Normally, the wavelet with at least n vanishing moments is necessary to detect the n th derivative discontinuity of the original signal. The inspection of the acceleration response time histories subjected to various excitations demonstrates that sudden stiffness loss will cause signal discontinuity at the damage instant. Therefore, the Lipschitz exponent of the acceleration response signal should be less than 1. To extract the Lipschitz exponent utilizing the wavelet transform, the minimum number of wavelet vanishing moment is

$$n = 1. \quad (19)$$

Signal singularity due to sudden stiffness reduction is detected by finding the abscissa where the wavelet modulus maxima converge at fine scales. The discrete wavelet transform (DWT) decomposes signal using discrete scales which cannot provide fine division especially for high frequency components of the original signal. The sudden stiffness loss will cause a high frequency damage signal in the original acceleration time history. Therefore, it is rough to utilize the DWT to obtain the Lipschitz exponent estimation and correlate the damage severity. The CWT as an alternative approach can execute continuous transform between the concerned continuous scale section which make it possible to obtain the accurate maxima line and Lipschitz exponent.

In the signal singularity detection on the acceleration responses with sudden stiffness reduction utilizing CWT, the continuity of the modulus maximum of $|Wf(a, b)|$ is another factor to select mother wavelet. If a wavelet $\psi(t)$ is the n th derivative of Gaussian function $\theta(t)$

$$\psi(t) = (-1)^n \frac{d^n \theta(t)}{dt^n}. \quad (20)$$

The modulus maximum of $Wf(a, b)$ belongs to a connected curve that is never interrupted for decreased scales (Mallat, 1998). Furthermore, the corresponding wavelet has n vanishing moments. Following these observations, the n can be taken as 2 in the detection on sudden stiffness reduction and the mother wavelet for CWT is written as

$$\psi(t) = \frac{d^2 \theta(t)}{dt^2}. \quad (21)$$

The wavelet in (20) is usually referred to as the Marr or Mexican hat wavelet and has the following explicit expression:

$$\psi(t) = \frac{2}{\sqrt{3}\sigma} \pi^{-1/4} \left(\frac{t^2}{\sigma^2} - 1 \right) \exp \left(-\frac{t^2}{2\sigma^2} \right). \quad (22)$$

The graph $-\psi(t)$ for $\sigma = 1$ is shown in Figure 3.

5. Case Study

5.1. Damage Time Instant. To examine the validity of the proposed detection approach for identifying sudden damage

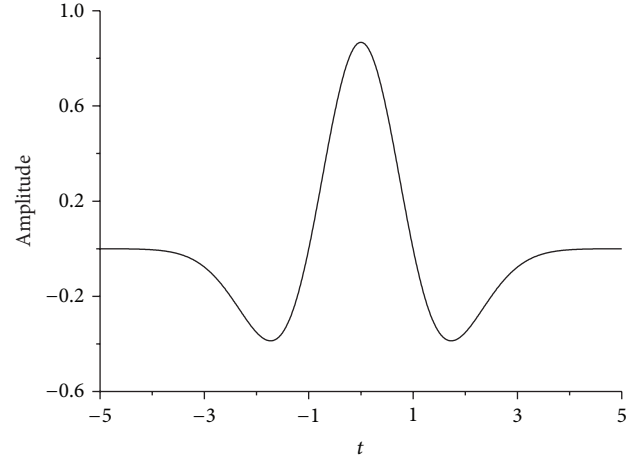


FIGURE 3: The Marr wavelet $(-\psi(t))$ and $\sigma = 1$.

events, the acceleration responses of the example building subjected to the seismic excitation, sinusoidal excitation, and impulse excitation are computed, respectively. The building is subject to a 20% sudden stiffness reduction at times 6.0 s, 6.0 s, and 0.2 s in the first story of the building under seismic excitation, sinusoidal excitation, and impulse excitation, respectively. The time step used in the computation is 0.002 second. Figure 4 displays the time-scale-coefficient plot for 20% sudden stiffness reduction, under sinusoidal, seismic, and impulse excitations, respectively. It can be seen from Figure 4 that the CWT coefficients of the first floor using Marr wavelet are very large only at time $t = 6.0$ second under small decomposition scale 0.5, which is exactly the time instant of the sudden damage event. The CWT coefficients of the first floor at all other time instants are very small, so that the CWT coefficients at time $t = 6.0$ s looks like a spike to indicate the occurrence time of the sudden damage event.

5.2. Selection of Decomposition Scale. Regarding the building excited by El Centro ground motion, CWT coefficients using large decomposition scales, such as 3.0, fail to detect damage instant while the counterparts using fine scales successfully capture the damage event. If the decomposition scales are relatively small, such as 0.5, CWT coefficients can depict the high frequency components of the original signal and the peak of modulus maxima can be observed at damage instant based on a fine scale interval to depict the damage event. With the increase of decomposition scales (>1.0), however, the frequency components reflected by modulus maxima of CWT coefficients gradually decrease. Thus, middle and high frequency components in the original acceleration responses form some modulus peaks, which make it difficult to detect the sudden damage event.

To examine the structural acceleration responses induced by impulse excitation, one can find that only the CWT coefficients with fine decomposition scale can detect the damage instant. In reality, the sudden stiffness reduction will cause a discontinuity in acceleration responses at damage instant and induce high frequency components into

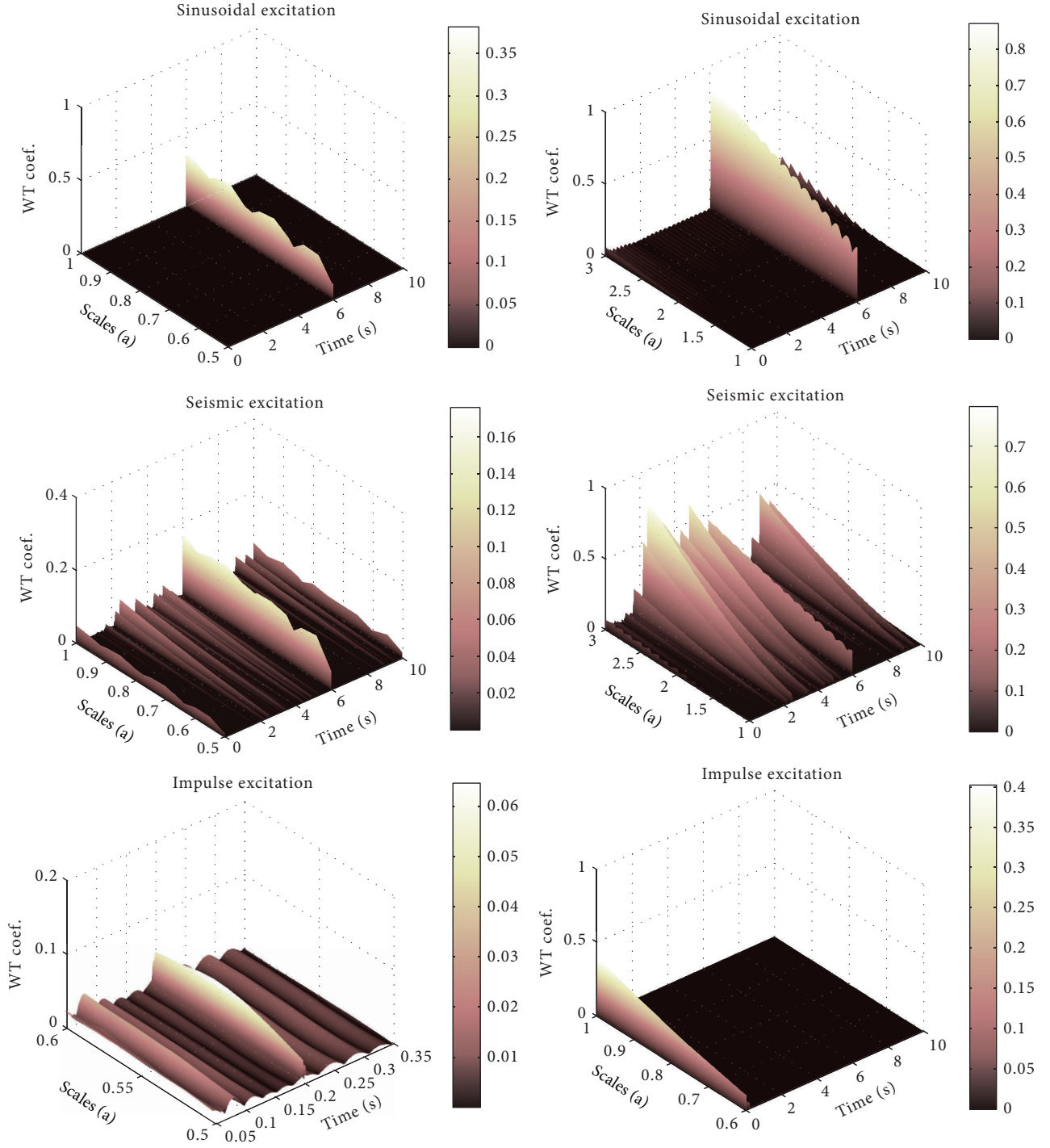


FIGURE 4: Damage detection under different decomposition scales.

the original response signals. Therefore, one can extract the high frequency components from original acceleration responses using the WT and detect the sudden damage event. The frequency components of acceleration responses of the building subjected to sinusoidal excitation are quite simple and the high frequency signal induced by sudden damage is quite different from other signal components. The CWT coefficients can easily detect the signal singularity and

damage event even using coarse decomposition scales. As far as the seismic excited damage building is concerned, the acceleration responses contain more high frequency components than those induced by the sinusoidal excitation. The distinguishing ability in the time-frequency domain under large scale is coarse and it is difficult to capture the sudden damage event under seismic excitations. Under large decomposition scales, it is impossible to distinguish the

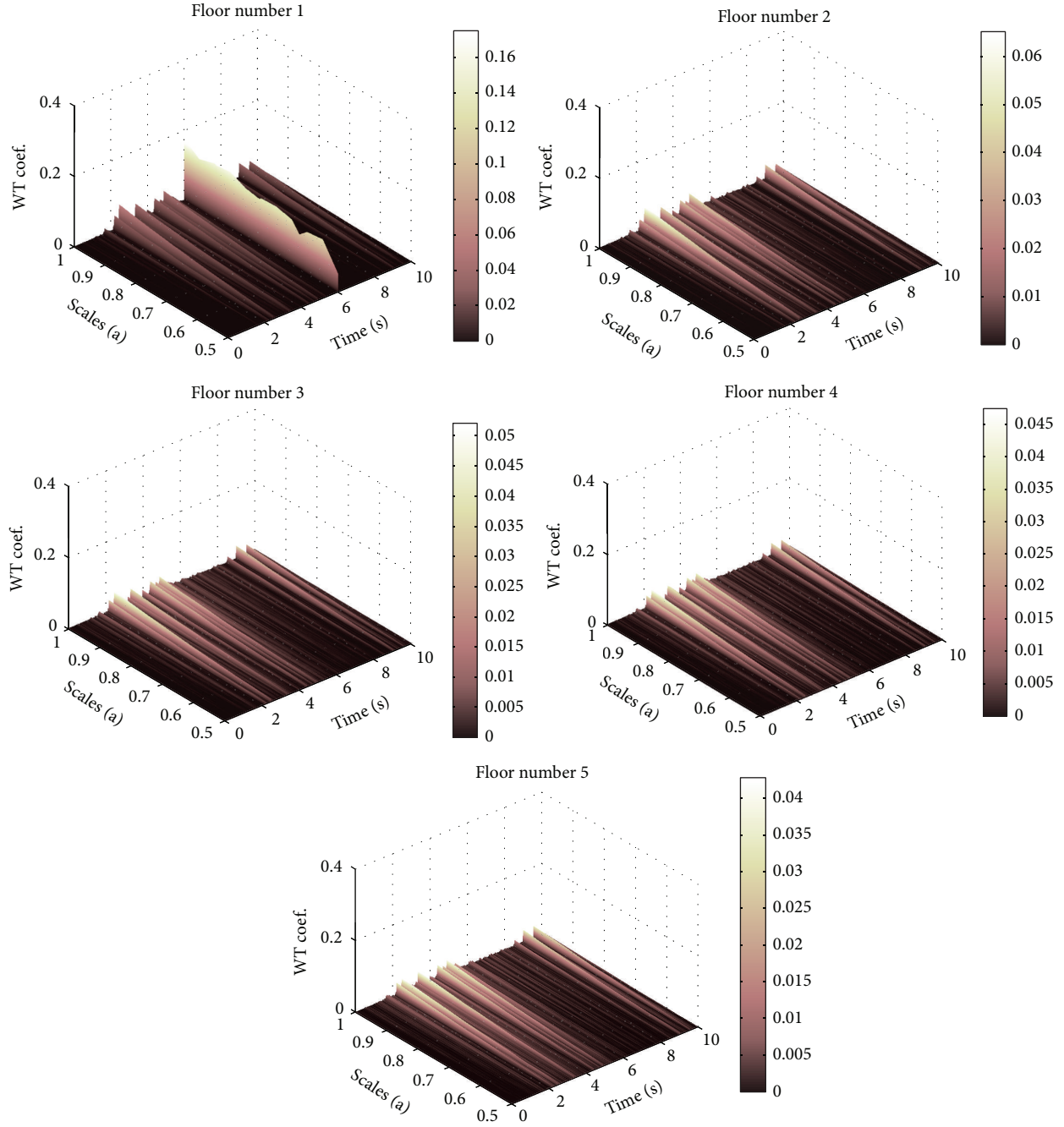


FIGURE 5: Damage detection for each floor under seismic excitation.

modulus maxima due to the sudden damage event and the damage detection is not satisfactory.

5.3. Damage Location. Figure 5 shows the variations of CWT coefficients with time for each floor of the building under the seismic excitation. It is seen that the modulus of CWT coefficients of the first floor is very large only at time $t = 6.0$ second with fine decomposition scales, which is exactly the moment for the 20% sudden stiffness reduction. The variations of CWT coefficients of the first floor are compared

with those of the second, third, fourth, and fifth floors of the building under small decomposition scale 0.5. The sharp spike appears clearly only at the first floor, and no sharp spike emerges in other floors. Therefore, the damage location can be easily identified at the first story of the building by checking the distribution of spikes along the height of the building.

The modulus maxima lines for each floor under sinusoidal and impulse excitations with 20% stiffness loss are also investigated, respectively, and the results are not displayed for space limitation. Again, the modulus maximum lines

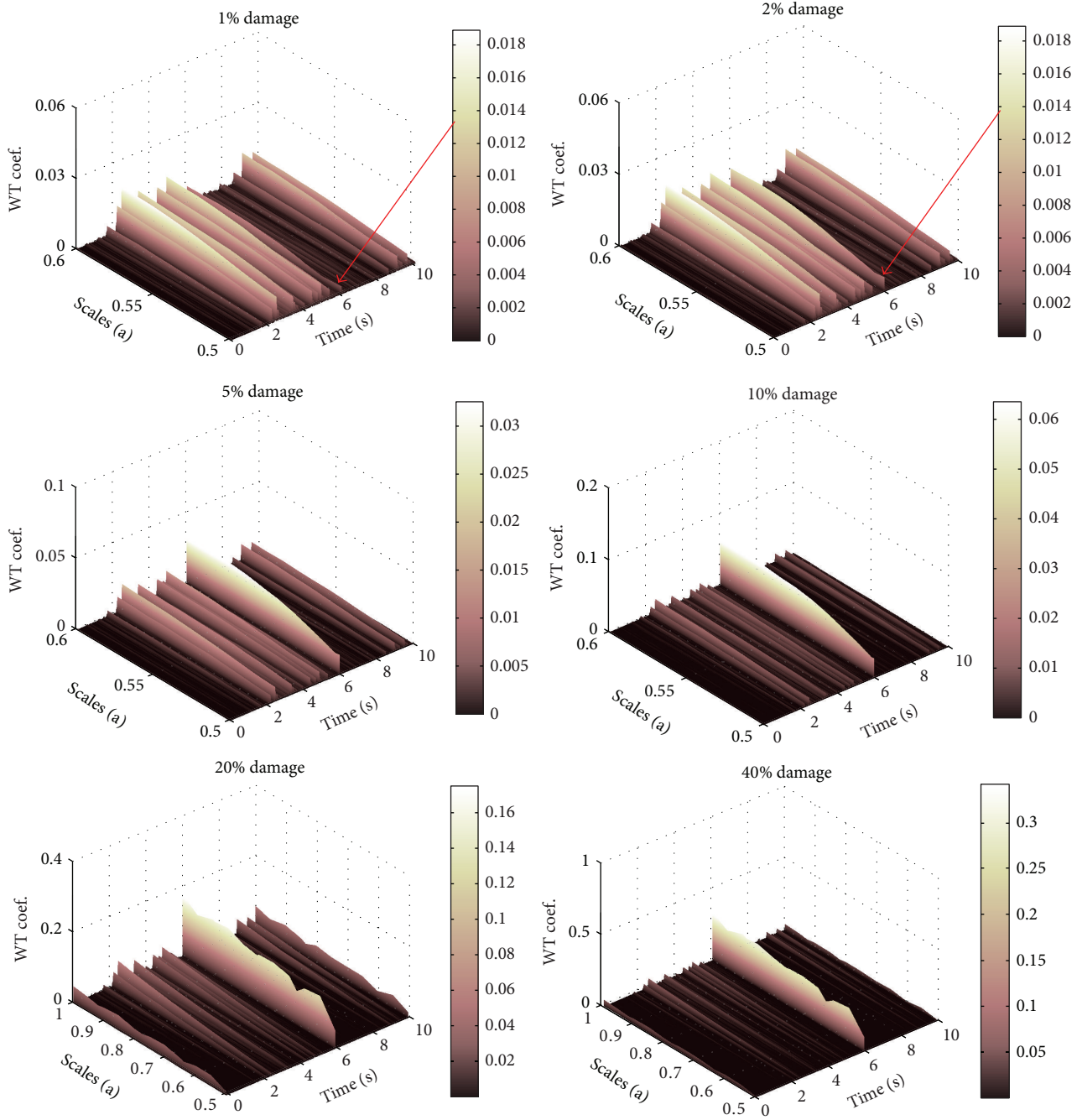


FIGURE 6: Detection results for various severities under seismic excitation.

of CWT coefficients appear only at the moment of sudden stiffness reduction at the first floor. Thus, the damage location can be easily captured from the observed maxima line and its distribution along the height of the building. As far as the impulse excited building is concerned, the CWT based detection approach may not give satisfactory results for the building with small damage event (2% sudden stiffness reduction). This is because the signal fluctuates significantly and the energy of damage signal is quite weak.

5.4. Damage Severity. The parametric study is carried out in this section to investigate the sensitivity of CWT coefficients

to damage severity so as to examine the validity of the proposed damage detection approach. The first floor of the example building is supposed to suffer different levels of sudden stiffness reduction but the damage time instants remain unchanged. The CWT coefficients of the first floor of the building subjected to the seismic excitation are displayed in Figure 6 for the sudden stiffness reduction from 1% to 40%. It can be seen that if the damage severity is no less than 5%, the proposed approach can easily capture the damage features without considering noise contamination with fine decomposition scale. The magnitude of the sharp spike also

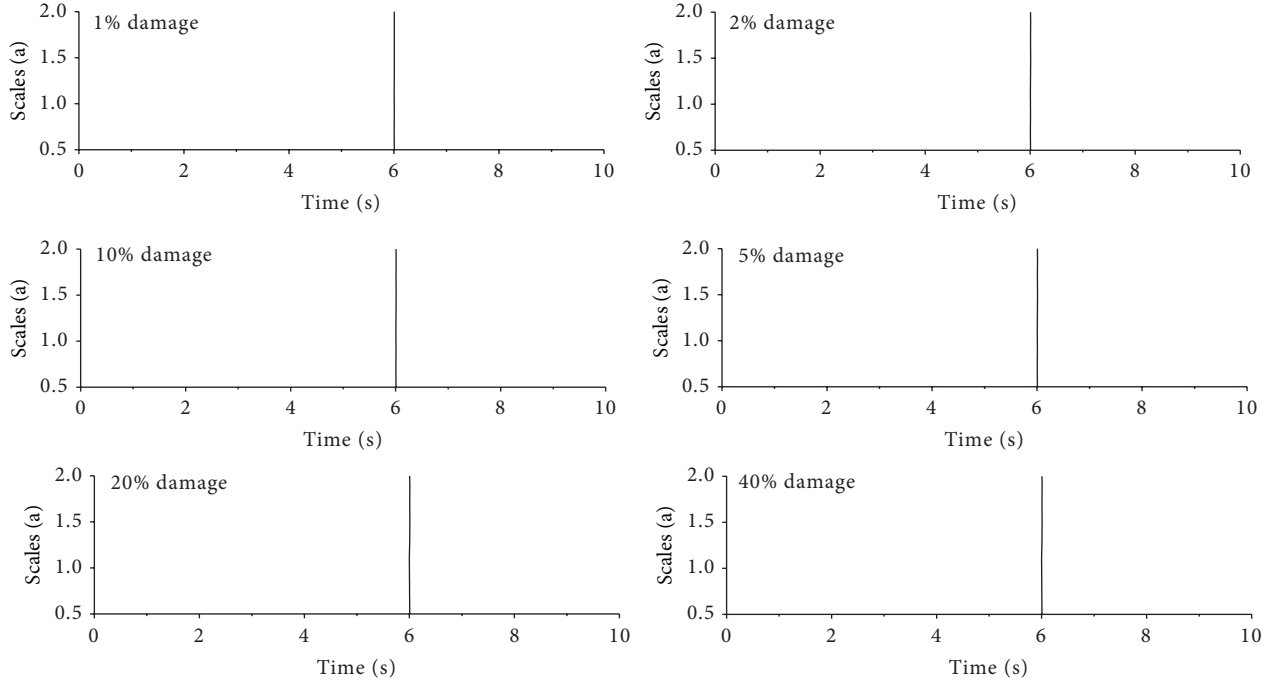


FIGURE 7: Modulus maxima line for various severities under seismic excitation.

TABLE 1: Variations of Lipschitz exponent with damage severity without noise.

Damage severity	1%	2%	5%	10%	20%	40%
Seismic excitation	0.9901	0.8008	0.6092	0.5146	0.4558	0.4086
Sinusoidal excitation	0.9411	0.8202	0.6925	0.5788	0.5144	0.4787
Impulse excitation	0.9991	0.9734	0.9317	0.8863	0.7005	0.5276

increases with the increasing damage severity. Regarding the small damage events, such as 1% and 2% stiffness reduction, small damage signal energy induces the quick reduction of modulus maxima at damage instant. To carefully compare the modulus maxima line of the building with minor damage, a relative larger spike still can be found at damage instant to depict the sudden damage event. Similar observations can be made from the building subject to sinusoidal excitation. For the building under impulse excitation, however, the proposed approach may not provide satisfactory detection quality for the building with very small damage event (damage severity no more than 5%).

Figure 7 displays the modulus maxima line for various damage severities under seismic excitation. It is observed that the damage instant can be indicated without any time excursion even for small damage severities under large decomposition scales. Displayed in Figure 8 is the decay behaviour along the modulus maxima line for the building subjected to 20% sudden stiffness reduction under seismic excitation. It is clear that the modulus maxima become larger with the increasing decomposition scale. The Lipschitz exponent is estimated as 0.4558 by using the well-known linear regression technique.

It is reported by Mallat [18] that the Lipschitz exponents become smaller with the increasing extents of the singularity

in original signals. To investigate the relation between the damage extent and the Lipschitz exponent, the different damage severity under sinusoidal, seismic, and impulse excitations are examined, respectively, by repeating the same estimation procedure and the results are shown in Figure 9. The variations of Lipschitz exponent with damage severity without noise are listed in Table 1. It is found that the magnitude of the Lipschitz exponents gradually decreases with the increasing damage severities. The relationship between Lipschitz exponent and damage severity is different if the building is subjected to different dynamic excitations. The relationship between Lipschitz exponent and damage severity under impulse excitations is closely linear while the counterparts under sinusoidal and seismic excitations seem to be decaying exponent curves.

5.5. Selection of Mother Wavelet. To examine the feasibility of the proposed detection approach based on CWT and Lipschitz exponent, the first floor of the five-story building is supposed to suffer 20% sudden stiffness reduction but the sudden reduction occurs at the same time. The detection quality substantially depends on the characteristics of the mother wavelet such as wavelet vanishing moments and supporting length in the time domain. Thus, six different mother wavelets, Haar, Meyer, Morlet, Symlet-2, Daubechie-2, and

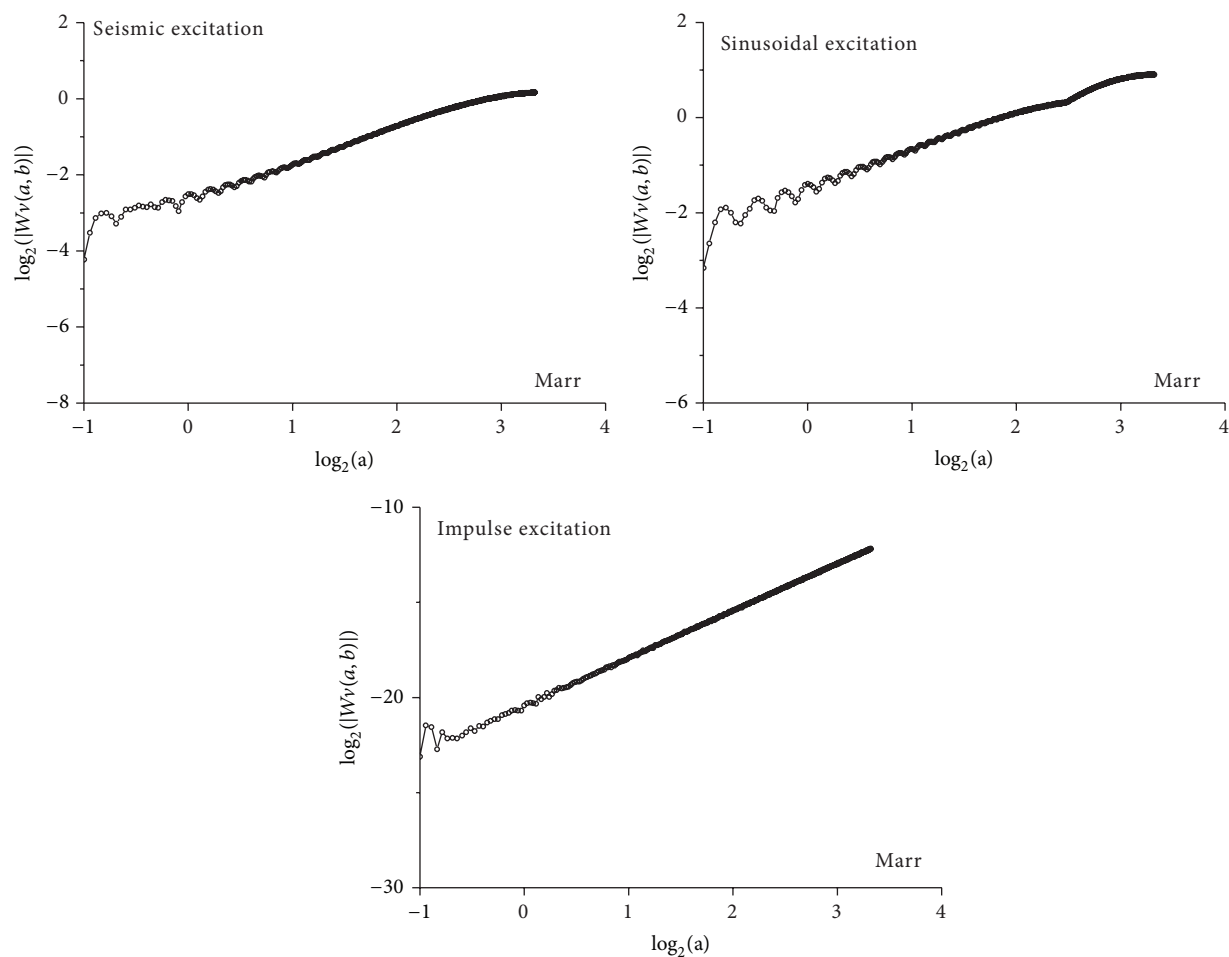


FIGURE 8: Decay behaviour along the modulus maxima line under seismic excitation.

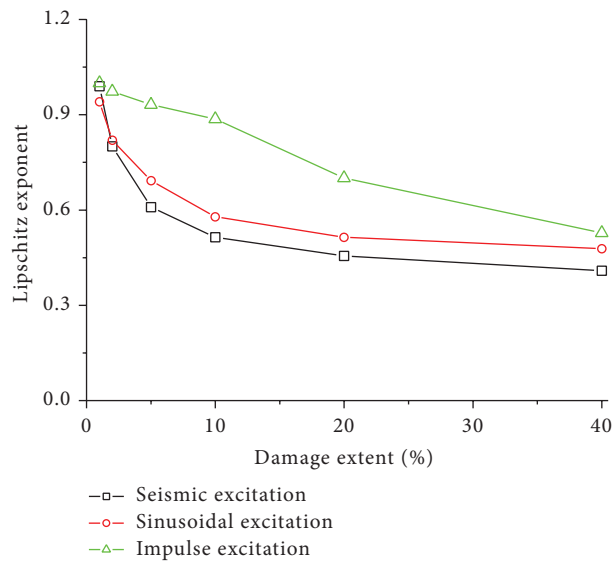


FIGURE 9: Decay behaviour along the modulus maximum line under seismic excitation.

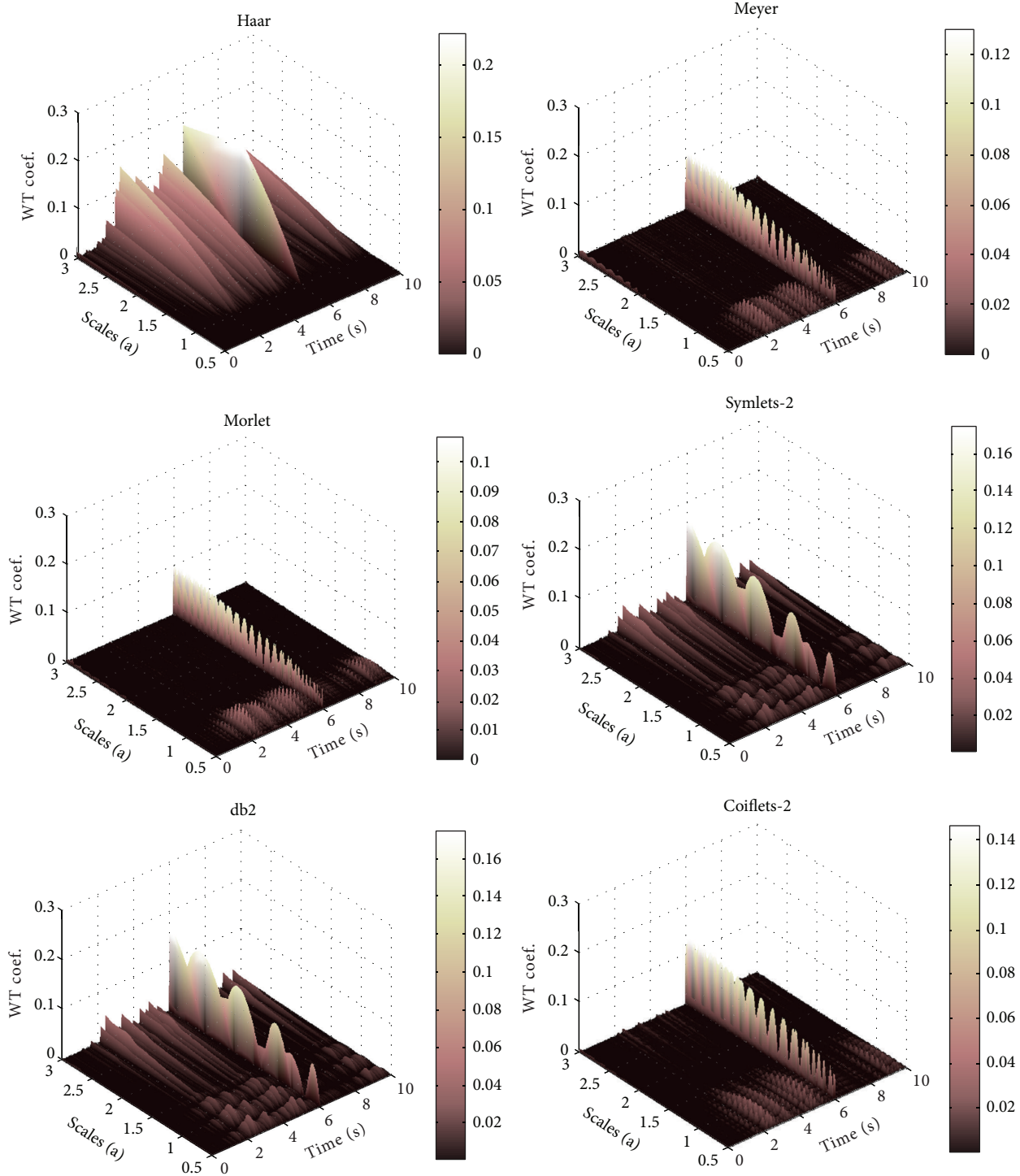


FIGURE 10: Detection results under seismic excitation using different mother wavelets.

Coiflet-2, are utilized to examine the effects of properties of mother wavelets on the detection on the structural sudden damage events. The vanishing moments of the Haar, Meyer, Morlet, Symlet, Daubechie-2, and Coiflet-2 wavelets are 1, indefinite, indefinite, 2, 2, and 2, respectively. The damage detection results under seismic excitation using different mother wavelets are shown in Figure 10. It can be seen that no

matter which mother wavelet is used, the CWT coefficients of the first floor under small decomposition scale (<1.0) are very large only at time $t = 6.0$ second, which is exactly the moment when the stiffness of the first story is suddenly reduced by 20%. The damage indices of the first floor at all other time instants are small so that the CWT coefficients at time $t = 6.0$ second look like a spike to indicate the damage events. This is

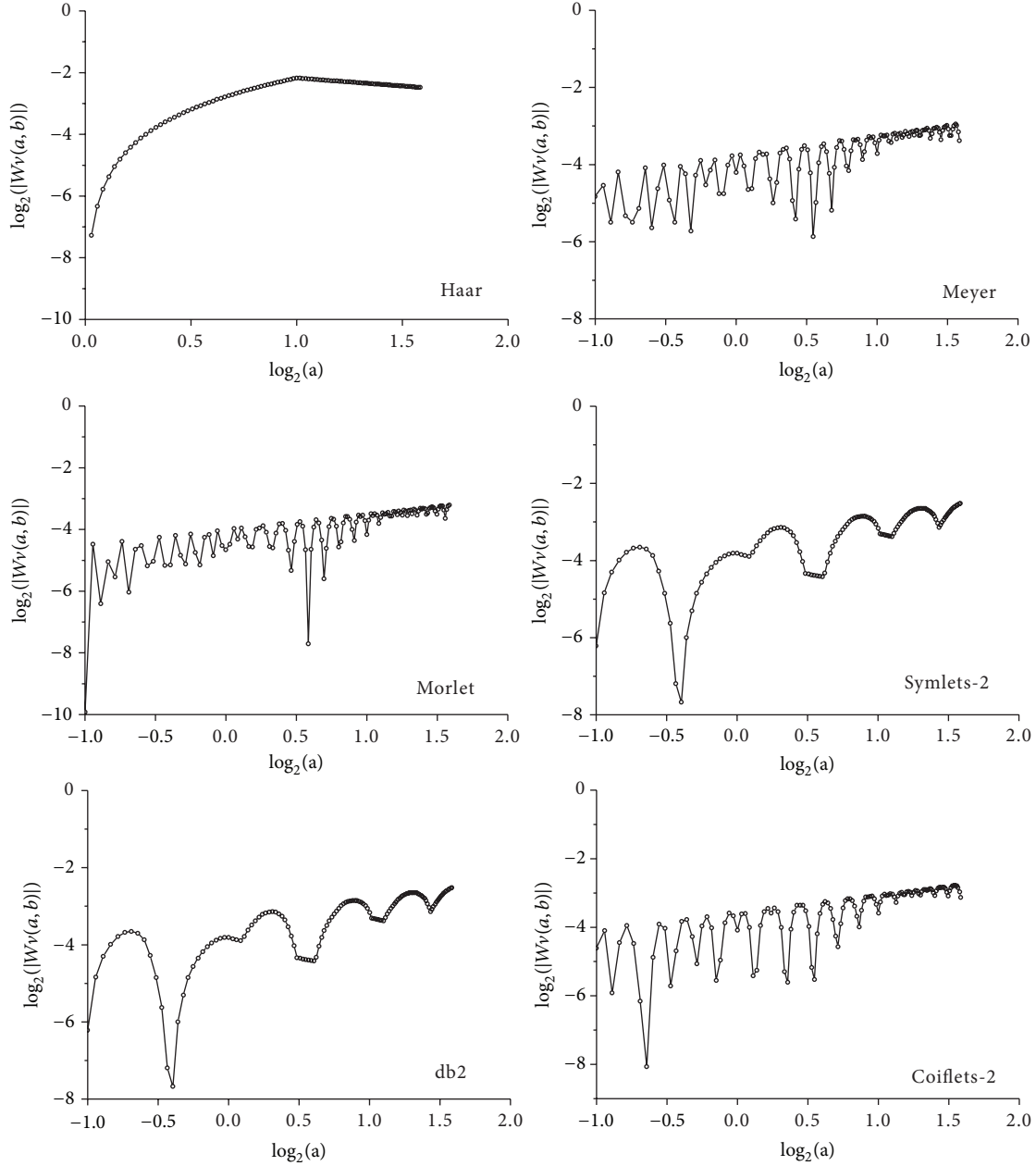


FIGURE 11: Decay behaviour along the modulus maxima line using different mother wavelets.

because all the six mother wavelets have a vanishing moment larger than one to depict the damage events as required by (22).

It is also found that the CWT based approach using all six mother wavelets can accurately detect the damage time instant of the building subjected to sinusoidal excitation and impulse excitation. The decay behaviour along the modulus maxima line for the building subjected to 20% sudden stiffness reduction under seismic excitation is displayed in Figure 11. It is seen that the modulus maxima using other mother wavelets fluctuate to great extents in comparison with that made by using Marr wavelet. Therefore, it is

unreasonable and difficult to obtain the estimation of the Lipschitz exponent through the linear regression technique.

As discussed above, the vanishing moment of a mother wavelet plays an important role in the detection of signal singularity. To this end, the effects of vanishing moments on the detection quality are investigated by using Daubechie and Coiflet wavelets. Figures 12 and 13 display the variations of WT coefficients and the decay behaviour along the modulus maxima line with different vanishing moments. The made observations indicate that the damage time instant and location can be detected with increasing of vanishing moments. However, it is seen from Figure 11 that the fluctuation of

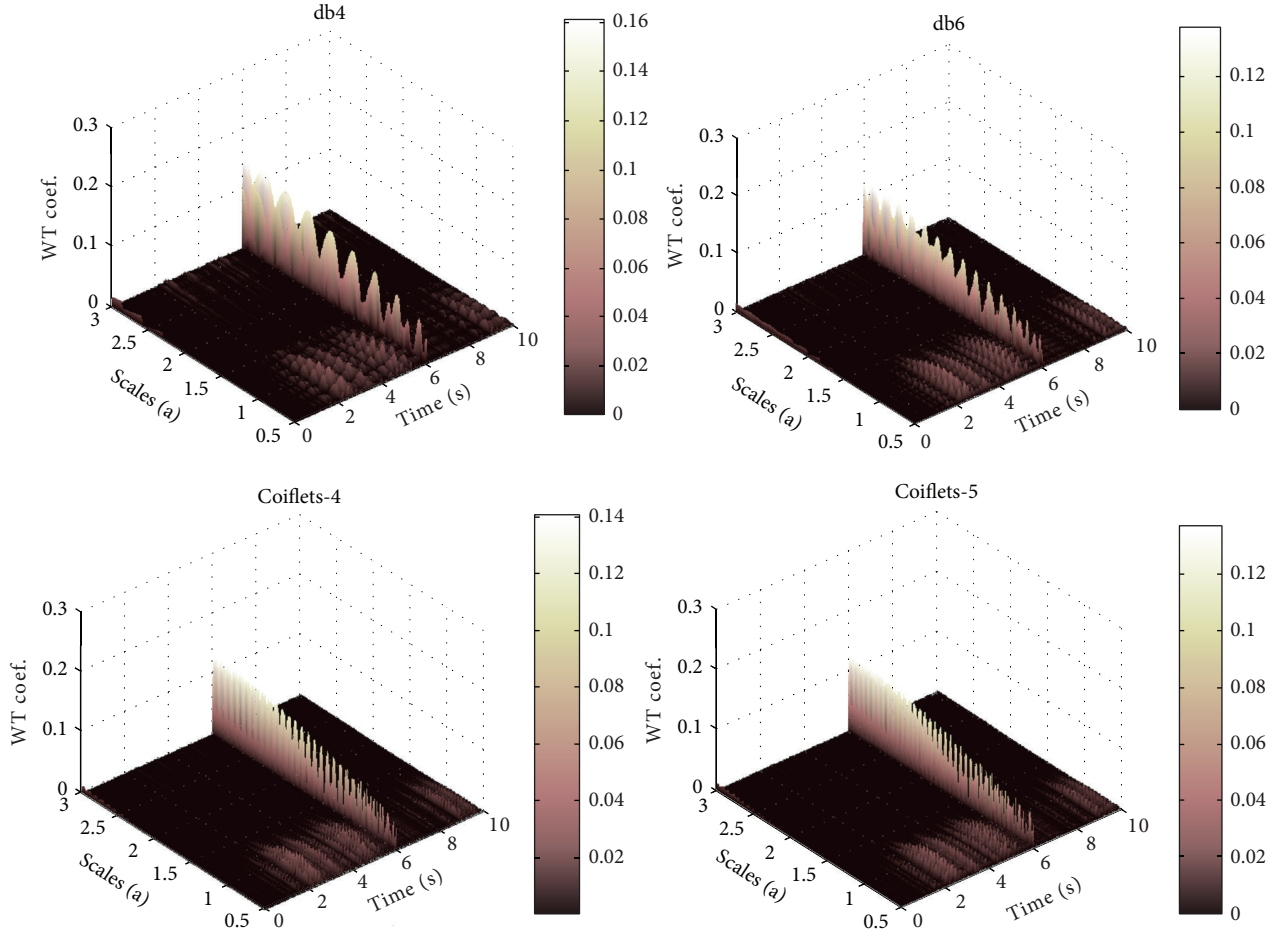


FIGURE 12: Variations of WT coefficients with different vanishing moments.

modulus maxima lines cannot be improved with the increasing vanishing moments of wavelets. Therefore, the detection quality of the CWT based approach depends on the vanishing moment and type of selected mother wavelet.

5.6. Effects of Signal Noise. To effect of the noise contamination is a practical issue need to be addressed before applying the proposed approach to health monitoring and damage detection of real structures. Yang et al. (2004) reported that the damage spike identified could be weakened by measurement noise, and strong measurement noise could lead to the failure of damage detection. Hong et al. [8] found that the damage spike identified from the wavelet transform coefficients could be weakened by the noise contamination. Taking into consideration that the sudden damage event introduces a high frequency component to acceleration responses of a structure, the effects of both measurement noise intensity and frequency range on the damage detection are investigated in this study. The measurement noise in structural responses is assumed to be a random white noise. Three frequency ranges are considered: (1) white noise with frequency range from 0 to 50 Hz; (2) white noise with frequency range from 0 to 100 Hz;

and (3) white noise with frequency range from 0 to 250 Hz. The measurement noise intensity is defined as

$$\text{Noise intensity} = \frac{\text{RMS (noise)}}{\text{RMS (signal)}} \times 100\%. \quad (23)$$

Displayed in Figure 14 are damage detection results using the contaminated acceleration responses at the first floor under the seismic excitation. The noises are introduced with two noise intensities and three noise frequency ranges described above. The sudden stiffness reduction in the first story of the building is 20%. It is seen that the CWT based detection approach can still identify the damage time instant from the contaminated acceleration responses at the first floor for the designated two noise intensities and three noise frequency ranges. Furthermore, the spatial distribution of CWT coefficients along the height of the building can indicate the damage location from the acceleration responses with noise contamination. To check the CWT coefficients shown in Figure 14(a), one can easily find that the noise with low frequency components will not remarkably change the modulus maxima of CWT coefficients under small decomposition scales. With the increase of noise signals with high frequency

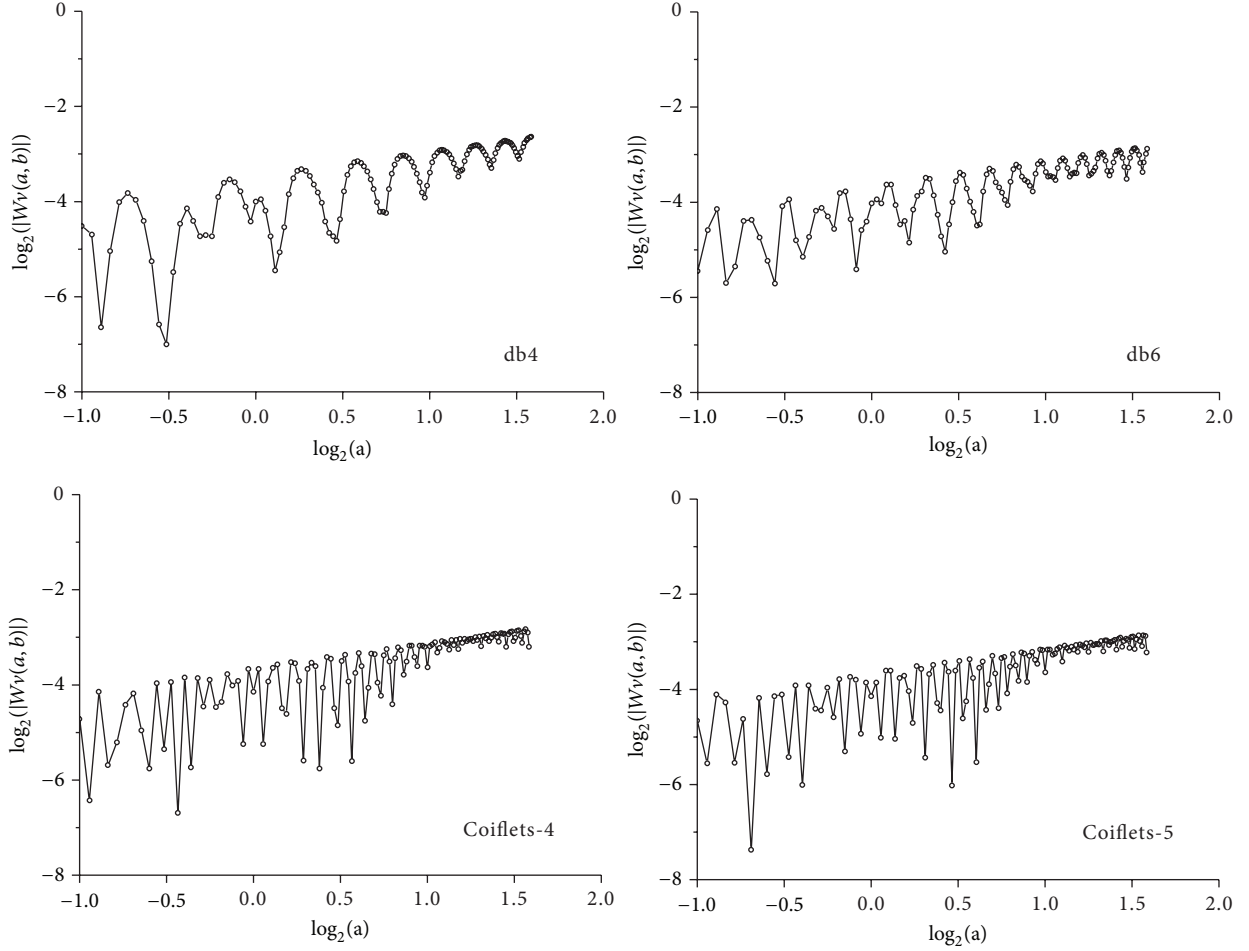


FIGURE 13: Decay behaviour along the modulus maxima line with different vanishing moments.

components, more small spikes of modulus maxima of CWT coefficients can be observed in the small decomposition scale section. In addition, the increase of noise intensity may induce the small spikes to the modulus maxima of CWT coefficients. Similar observations can be made from the detection observations of the example building subjected to the sinusoidal and impulse excitations, respectively, as shown in Figure 15. In the impulse excitation case, however, the proposed approach fails to identify the damage time instant and damage location when the noise frequency range is from 0 to 250 Hz and the noise intensity is 5%.

It is worth examining the effects of noise contamination on the magnitude of Lipschitz exponent. The effects of measurement noise on the magnitude of the Lipschitz exponent under seismic excitation are assessed and the results are listed in Table 2. It can be seen that as long as the damage event can be identified, the magnitude of Lipschitz exponent slightly reduces with increase of noise levels and three noise frequency ranges. This indicates that the effect of measurement noise on the magnitude of Lipschitz exponent is small. The further numerical simulation indicates that the damage can be effectively identified for 20% sudden stiffness reduction even with 40% noise intensity as long

as the noise frequency range is not higher than 50 Hz. However, if the noise frequency range is from 0 to 250 Hz, the reliability of damage detection using the proposed approach deteriorates with the increase of noise intensity. The estimation of Lipschitz exponents for different noise intensity and frequency range under sinusoidal and impulse excitation is carried out. The variations of noise intensities with Lipschitz exponents with noise frequency range 0~250 Hz are displayed in Figure 16. Similar observations to those under seismic excitation can be made, which agrees with the theoretical analysis of signal process (Mallat, 1998). This is because large singularity can be observed at the damage instant with noise contamination, which will further decrease the value of the Lipschitz exponent to some extent.

6. Concluding Remarks

The investigation of detection on sudden damage event of building structures has been carried out in this study. The signal feature of the structural acceleration responses of an example building subjected to sinusoidal, seismic, and impulse excitations due to sudden stiffness reduction is examined. The local signal regularity of the acceleration responses

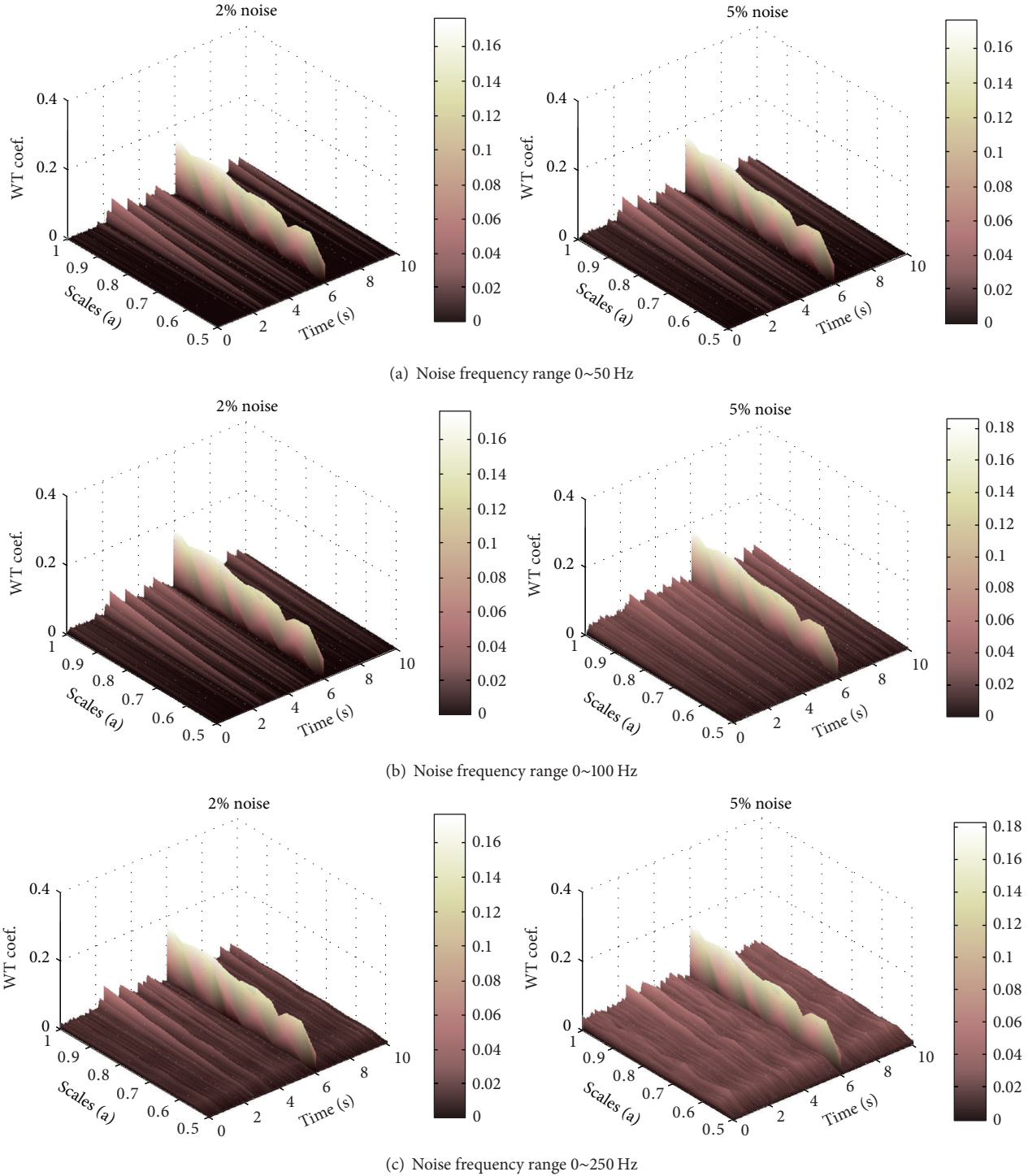


FIGURE 14: Detection results from contaminated acceleration responses (seismic excitation).

is characterized by the decay of the wavelet transform amplitude across scales. Singularities can be detected by the continuous wavelet transform local maxima at fine scales. In this regard, a detection approach based on the CWT is proposed in terms of the decomposed detail coefficients of continuous wavelet transform to detect the damage time instant and location. The Lipschitz exponent is mathematically used to

estimate the local properties of certain function and is applied to reflect the damage severity.

Extensive numerical simulations have been performed on a five-story shear building to assess the performance of the detection approach based on CWT and Lipschitz exponent with and without noise contamination. The made observations indicate that the detection approach proposed

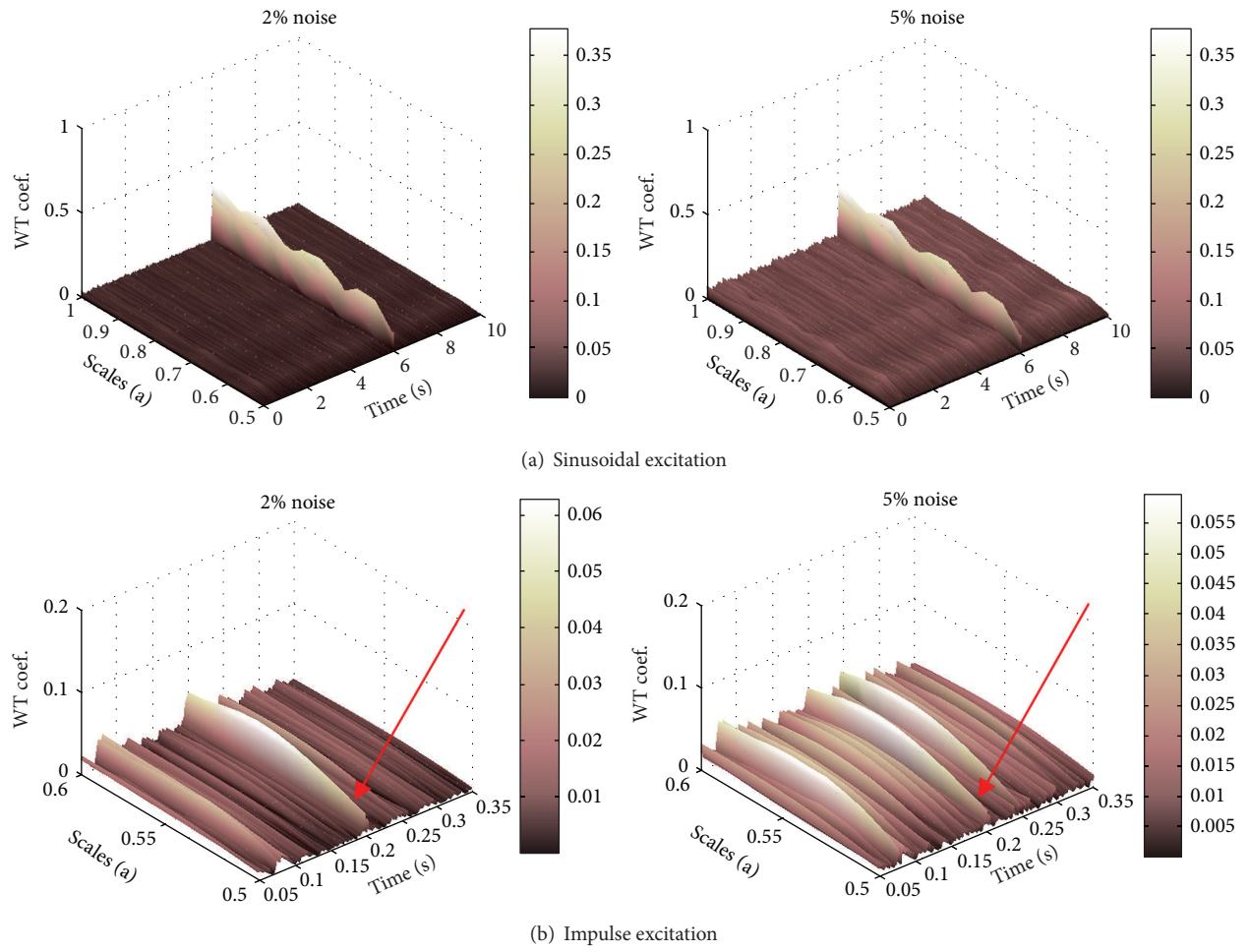


FIGURE 15: Detection results from contaminated acceleration responses (noise frequency range 0~250 Hz).

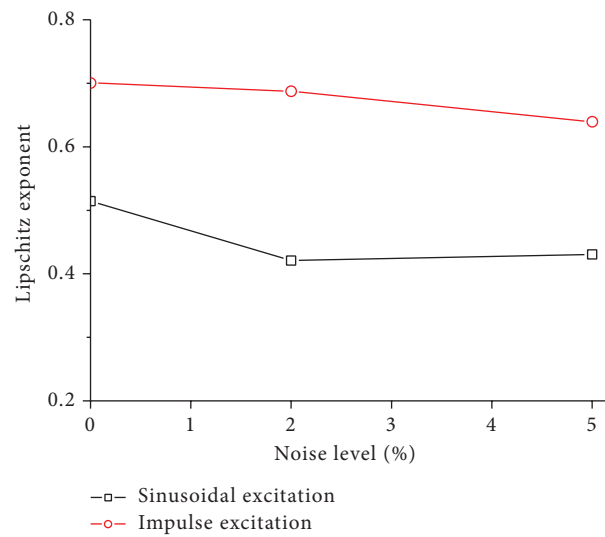


FIGURE 16: Variations of Lipschitz exponent with noise intensity under sinusoidal and impulse excitation.

TABLE 2: Noise effects on Lipschitz exponent (seismic excitation).

Noise level	Noise frequency range		
	0~50 Hz	0~100 Hz	0~250 Hz
No noise	0.3252	0.3252	0.3252
2% noise	0.3249	0.3244	0.319
5% noise	0.3248	0.3204	0.3093

in this study can accurately identify the damage time instant and damage location due to a sudden stiffness reduction in terms of the occurrence time and spatial distribution of coefficient spikes of the CWT. The relationship between Lipschitz exponent and damage severity is different when subjected to different dynamic excitations. The magnitudes of the Lipschitz exponents decrease with the increasing damage severity. The detection quality on the sudden damage even is satisfactory if the noise frequency range is limited. If the noise frequency range is wide enough, the reliability of damage detection quality using the proposed approach gradually decreases with the increase of noise intensity.

Conflict of Interests

The authors declare that there is no conflict of interests regarding the publication of this paper.

Acknowledgments

The authors are grateful for the financial support from the National Natural Science Foundation of China (51178366), the Technological Project of the Chinese Southern Power Grid Co. Ltd. (K-GD2013-0783), the ESI 1% Project of WUT (No.43, chenbo), and the Natural Science Foundation of Hubei Province (2014CFA026).

References

- [1] S. W. Doebling, C. R. Farrar, and M. B. Prime, "A summary review of vibration-based damage identification methods," *The Shock and Vibration Digest*, vol. 30, no. 2, pp. 91–105, 1998.
- [2] K. Gurley and A. Kareem, "Applications of wavelet transforms in earthquake, wind and ocean engineering," *Engineering Structures*, vol. 21, no. 2, pp. 149–167, 1999.
- [3] T. Yi, H. Li, and M. Gu, "Full-scale measurements of dynamic response of suspension bridge subjected to environmental loads using GPS technology," *Science China Technological Sciences*, vol. 53, no. 2, pp. 469–479, 2010.
- [4] T.-H. Yi, H.-N. Li, and M. Gu, "Experimental assessment of high-rate GPS receivers for deformation monitoring of bridge," *Measurement*, vol. 46, no. 1, pp. 420–432, 2013.
- [5] A. Masuda, A. Nakaoka, A. Sone, and S. Yamamoto, "Health monitoring system of structures based on orthonormal wavelet transform," *Seismic Engineering*, vol. 312, no. 1, pp. 161–167, 1995.
- [6] A. Sone, S. Yamamoto, A. Masuda, A. Nakaoka, and R. Ashino, "Estimation of cumulative damage of a building with hysteretic restoring force by using wavelet analysis of strong motion records," *Japan Structural Construction Engineering*, vol. 476, pp. 67–74, 1995.
- [7] W. J. Staszewski and G. R. Tomlinson, "Application of the wavelet transform to fault detection in a spur gear," *Mechanical Systems and Signal Processing*, vol. 8, no. 3, pp. 289–307, 1994.
- [8] J. C. Hong, Y. Y. Kim, H. C. Lee, and Y. W. Lee, "Damage detection using the Lipschitz exponent estimated by the wavelet transform: applications to vibration modes of a beam," *International Journal of Solids and Structures*, vol. 39, no. 7, pp. 1803–1816, 2002.
- [9] J. N. Yang, Y. Lei, and N. E. Huang, "Damage identification of civil engineering structures using Hilbert-Huang transform," in *Proceedings of the 3rd International Workshop on Structural Health Monitoring*, pp. 544–553, Stanford, Calif, USA, 2001.
- [10] Z. Hou and M. Noori, "Application of wavelet analysis for structural health monitoring," in *Proceedings of the 2nd International Workshop on Structural Health Monitoring*, pp. 946–955, Stanford University, Stanford, Calif, USA, 1999.
- [11] Z. Hou, M. Noori, and R. S. Amand, "Wavelet-based approach for structural damage detection," *Journal of Engineering Mechanics*, vol. 126, no. 7, pp. 677–683, 2000.
- [12] H. Sohn, A. N. Robertson, and C. R. Farrar, "Holder exponent analysis for discontinuity detection," *Structural Engineering and Mechanics*, vol. 17, no. 3-4, pp. 409–428, 2004.
- [13] H. T. Vincent, S. L. J. Hu, and Z. Hou, "Damage detection using empirical mode decomposition method and a comparison with wavelet analysis," in *Proceedings of the 2nd International Workshop on Structural Health Monitoring*, Stanford University, Stanford, Calif, USA, 1999.
- [14] J. N. Yang, Y. Lei, S. Lin, and N. Huang, "Hilbert-Huang based approach for structural damage detection," *Journal of Engineering Mechanics*, vol. 130, no. 1, pp. 85–95, 2004.
- [15] Y. L. Xu and J. Chen, "Structural damage detection using empirical mode decomposition: experimental investigation," *Journal of Engineering Mechanics*, vol. 130, no. 11, pp. 1279–1288, 2004.
- [16] B. Chen and Y. L. Xu, "A new damage index for detecting sudden change of structural stiffness," *International Journal of Structural Engineering and Mechanics*, vol. 26, no. 3, pp. 315–341, 2007.
- [17] I. Daubechies, "The wavelet transform, time-frequency localization and signal analysis," *IEEE Transactions on Information Theory*, vol. 36, no. 5, pp. 961–1005, 1990.
- [18] S. Mallat, *A Wavelet Tour of Signal Processing*, Academic Press, San Diego, Calif, USA, 1998.
- [19] B. Chen, Z. W. Chen, G. J. Wang, and W. P. Xie, "Damage detection on sudden stiffness reduction based on discrete wavelet transform," *The Scientific World Journal*, vol. 2014, Article ID 807620, 16 pages, 2014.

Research Article

Probability Model of Hangzhou Bay Bridge Vehicle Loads Using Weigh-in-Motion Data

Dezhang Sun,¹ Xu Wang,² Bin Chen,³ and Baitao Sun¹

¹*Institute of Engineering Mechanics, China Earthquake Administration, Harbin 150080, China*

²*State Key Laboratory Breeding Base of Mountain Bridge and Tunnel Engineering, Chongqing Jiaotong University, Chongqing 400074, China*

³*College of Civil Engineering and Architecture, Zhejiang University, Hangzhou 310058, China*

Correspondence should be addressed to Xu Wang; wx00012224@163.com

Received 7 August 2014; Accepted 6 February 2015

Academic Editor: Gangbing Song

Copyright © 2015 Dezhang Sun et al. This is an open access article distributed under the Creative Commons Attribution License, which permits unrestricted use, distribution, and reproduction in any medium, provided the original work is properly cited.

To study the vehicle load characteristics of bay bridges in China, especially truck loads, we performed a statistical analysis of the vehicle loads on Hangzhou Bay Bridge using more than 3 months of weigh-in-motion data from the site. The results showed that when all the vehicle samples were included in the statistical analysis, the histogram of the vehicles exhibited a multimodal distribution, which could not be fitted successfully by a familiar single probability distribution model. When the truck samples were analyzed, a characteristic multiple-peaked distribution with a main peak was obtained. The probability distribution of all vehicles was fitted using a weighting function with five normal distributions and the truck loads were modeled by a single normal distribution. The results demonstrated the good fits with the histogram. The histograms of different time periods were also analyzed. The results showed that the traffic mainly comprised two-axle small vehicles during the rush hours in the morning and the evening, and the histogram could be fitted approximately using three normal distribution functions. And the maximum value distributions of vehicles during the design life of the bay bridge were predicted by maximum value theory.

1. Introduction

The rapid economic development of China is reflected by the construction of large-span bridges in recent decades. Over 60 bridges with spans of >400 m have been built [1], including several super-large bay bridges, for example, Jiaozhou Bay Bridge [2], Hangzhou Bay Bridge [3], and the cross-sea bridge of Hongkong-Zhuhai-Macao, which is under construction. These bridges play an important role in the development of regional economies, but the dramatic increases in traffic volume will become more severe with growing economic development, especially in some big cities, which may affect the safety of bridges and decrease the normal service life of these structures. In the Yangtze River Delta region, bridges have exhibited problems such as cracking and long-term deflection due to the effects of high traffic. Thus, it is necessary to determine the actual vehicle loads of bridges to provide a reference for the assessment of other bridges in the region.

Many previous studies have addressed vehicle loads. Studies of vehicle loads have been performed outside China for many years, but they have been continued as the traffic loads have increased. These studies only began recently in China, mainly because suitable weighing equipment was rarely available in the past and limited data were acquired. At present, newly built long-span bridges must be equipped with health monitoring systems to monitor the bridge situation [4, 5]. In addition, bridge destruction due to high vehicle loads was rare in the past. However, with the development of the economy, traffic volumes have increased dramatically and the frequencies of heavy vehicles have increased greatly. Based on truck data collected in Ontario, Nowak [6] used the HL-93 truck model to analyze the effects of different truck numbers, bridge lengths and widths on the maximum bending moment, shearing force, and hogging moment of a bridge. Nowak also studied the effects of the dynamic

response of trucks on the bridge and determined the relationship between the truck loads with different lane numbers. Finally, the truck load factor for the load and resistance factor design (LRFD) specification was obtained. Moses [7] found that the truck load adopted in the American Association of State Highway and Transportation Officials (AASHTO) specifications agreed approximately with a normal distribution, where the mean value was 300 kN and the coefficient of variation was 26.5%, which were not inconsistent with those of the LRFD. Based on data collected for vehicles, Fu and You [8, 9] analyzed the vehicle load statistics characteristics and determined the possible maximum value distribution of vehicles during a bridge service life using the extreme value theory, where they obtained the vehicle load factor by reliability index analysis. Based on WIM data for vehicles from two European sites, Obrien et al. [10] studied the effects of various parameters on the fitted results in a truck load model and demonstrated the high sensitivity of the fit. Based on truck data from three sites in Indiana, USA, Chotickai and Bowman [11] developed a truck model based on the fatigue damage analysis of steel. Zhao and Tabatabai [12] also analyzed a standard common vehicle model for the region using six million vehicle samples obtained from Washington, USA.

Using statistical data for the current vehicle loads on National Expressway 110, Mei et al. [13] discussed the characteristic probability distribution of a large number of overloaded vehicles and regular vehicles. They obtained a vehicle load histogram with a multiple-peaked probability distribution, which was weighted based on two normal distributions. After investigating overloaded vehicles transporting coal on Gudianta road in Shanxi Province, China, Zong et al. [14] classified the overloaded vehicles according to nine types based on the loading and axle types of the vehicles, as well as analyzing the overloading and overloading limits for each type of vehicle, thereby determining the relationship between overloading and the overloading limits using linear regression. Based on actual measurements and statistical analysis of the running conditions of vehicles on the Beijing-Shanghai highway, Guo et al. [15] found that the vehicle loads histogram exhibited a characteristic multimodal distribution and they obtained a probabilistic model by curve fitting. Based on the statistical analysis of vehicle load data from several regions, such as uncontrolled overloading, weighing charges, and controlling overloading by constraints, Gong et al. [16] found that the loads of vehicles passing along all roads exhibited multimodal distribution features. Based on data obtained from the traffic axle loads measured using a WIM system, Xu et al. [17] obtained appropriate vehicle load parameters for the actual traffic conditions in Guangdong Province. They found that the measured total weights and axle weights of vehicle loads in Guangdong Province were all higher than the values specified in the regulations. Using basic information for traffic operations acquired by a WIM system, S. W. Sun and L. M. Sun [18] studied the characteristic parameter distributions of many vehicle loads, such as the axle weight and wheelbase, and derived a practical and simple vehicle-based fatigue model.

These previous studies focused mainly on the vehicle loads of road bridges, including urban bridges. However, the vehicle load conditions of bay bridges are different from both of these types. The vehicle loads of busy road bridges mainly comprise multi-axle heavy trucks, whereas those of urban bridges mainly comprise cars, but the vehicle loads of bay bridges include both types. In the present study, the vehicle loads of Hangzhou Bay Bridge were analyzed. Based on WIM data obtained from Hangzhou Bay Bridge for over 3 months, the vehicle load histograms were determined and a probabilistic model of the truck loads was produced. In addition, the maximum value distribution was predicted for vehicles during the reference design period of bay bridges using the maximum value theory, thereby facilitating a better understanding of the vehicle load distributions of bay bridges. These data can provide a basis for the revision of specifications.

2. Data Acquisition

Hangzhou Bay Bridge is a cross-sea bridge that stretches over Hangzhou Bay in China. It officially entered use on May 1, 2008. Its main span is 325 m and its width is 33 m with six lanes of traffic in two directions. It extends for 36 km from Jiaxing City in Zhejiang Province in the north to Ningbo in the south (Figure 1). It is the third longest cross-sea bridge in the world and it is 11 km longer than King Fahd Bridge, which connects Bahrain with Saudi Arabia. In the plan of the Zhejiang expressway, Hangzhou Bay Bridge is named as “Hangzhou Bay-Ningbo channel,” which is one of the “three channels” in the Zhejiang expressway network in the future.

The bridge employs a charging operational mode and the WIM system is embedded near the charging site at both entrances (two directions) to obtain information about vehicles, including the passing time, gross weight, axle weight, wheelbase, axle number, and speed. According to official statistics, there have been up to 19 million passing vehicles since its opening on May 1, 2010, that is, 23,000 per day. In this study, data in the paper were obtained from south entrance WIM system that recording three lane vehicles of the bridge during more than 3 months between September 2012 and January 2013. Before the analysis, the data were preprocessed to remove any obvious errors and meaningless data [19].

3. Statistical Analysis

3.1. Probabilistic Characteristics of the All-Vehicle Analysis. After preprocessing, there were 82 effective days and 931,774 valid data points. Initially, the mean values, standard deviations, and maximum values were calculated for the valid data, which showed that the mean values and coefficients of variation for the vehicle loads were relatively concentrated in specific periods, except the coefficients of variation (COV) which were higher on holidays such as New Year's Day, thereby indicating that the vehicle loads were consistent in the short term; some samples are shown in Table 1.

Figures 2 and 3 show the characteristics of the mean values, maximum values, coefficients of variation, and vehicle

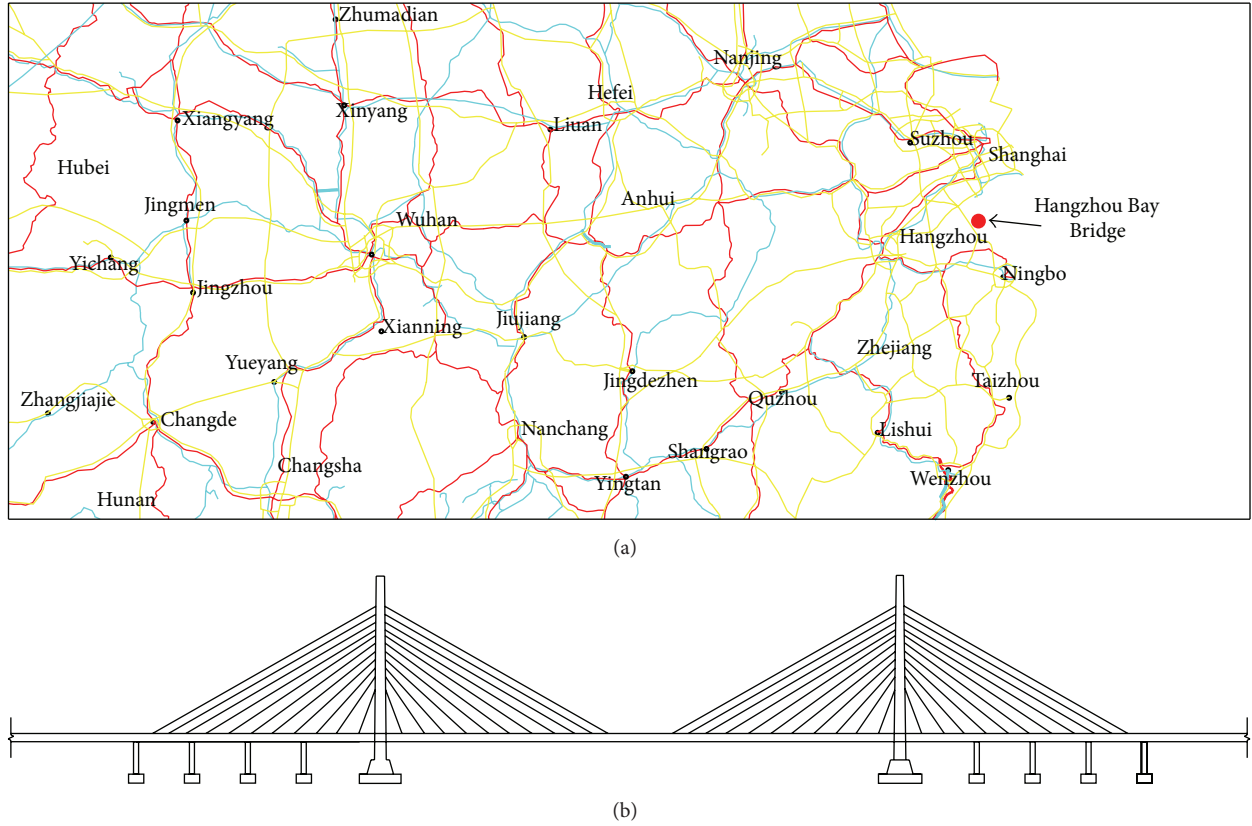


FIGURE 1: (a) Location of Hangzhou Bay Bridge. (b) Facade profile sketch map of the main towers of Hangzhou Bay Bridge.

TABLE 1: Statistical characteristics of the vehicle loads.

Date	Vehicle number	Mean value/ton	Standard deviation/ton	Coefficient of variation	Maximum value/ton
20120916	7408	11.29345	9.787491	0.866652	65.5
20120926	7399	13.15604	10.88008	0.827002	72.4
20121102	14627	7.913687	10.33094	1.305452	72.7
20121103	11351	8.199344	10.54972	1.286654	73.5
20121106	13263	8.948771	11.30286	1.263063	75.1
20121107	13641	8.587805	10.70217	1.246205	80.95
20121110	10426	8.58123	11.2873	1.315347	124.4
20121111	11694	7.499042	9.344368	1.246075	71.3
20121112	11633	8.413505	9.937082	1.181087	71.5
20121114	14232	7.807947	9.695331	1.241726	89.2
20121127	12080	8.341387	10.46041	1.254038	103.5
20121128	11771	8.037461	9.97701	1.241314	102.3
20130101	10459	6.523783	9.956516	1.526187	70.4
20130102	10835	6.878782	10.37906	1.508851	69.9

Note that the vehicle number of Table 1 is just that of one direction of vehicles compared to the average vehicle number of 23000 per day in two directions.

numbers in terms of time and intensity. Figure 2 shows that the different mean values were relatively concentrated and the maximum values generally fluctuated around 70 t, except in a very small number of cases, which demonstrates that some vehicles exceeded the weight limit. Figure 3 shows that the coefficients of variation were almost constant with time and their trends were similar to the vehicle numbers. The higher

vehicle numbers were recorded during holidays, which did not reflect the normal vehicle loads.

The vehicle loads of bridges comprised vehicle loads of various type; thus there was a multimodal distribution, which could not be described by familiar probability distributions. If we suppose that N is the main vehicle type that passes over the bridge and the cumulative probability function of

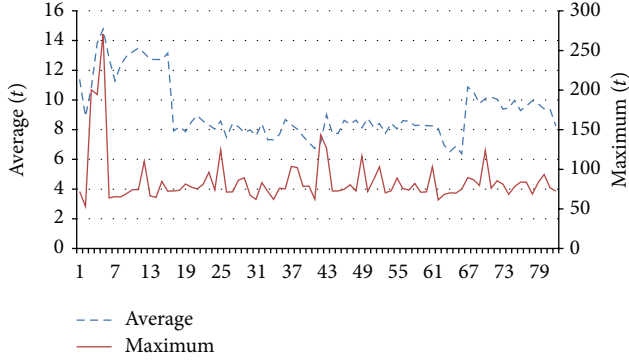


FIGURE 2: Variability in the mean values and maximum values.

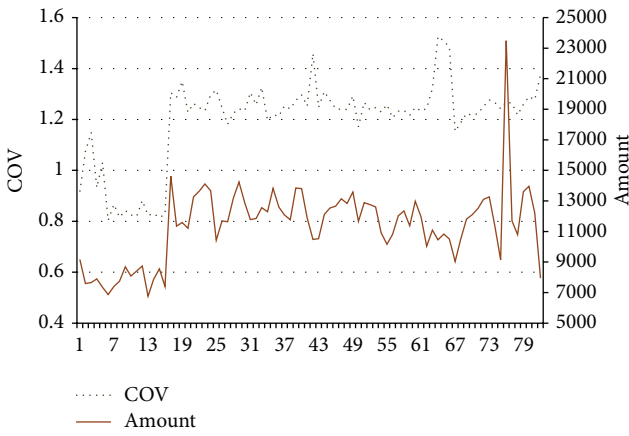


FIGURE 3: Variability in the coefficients of variation and vehicle numbers.

the i th vehicle load is $F_i(x)$, then the probability function of the combined vehicle loads can be represented as follows:

$$F_X(x) = \sum_{i=1}^N p_i \cdot F_i(x), \quad (1)$$

where p_i is a weighting coefficient and $\sum_{i=1}^N p_i = 1$.

Based on (1), the probability density function of the combined vehicle loads can be obtained as follows:

$$f_X(x) = \sum_{i=1}^N p_i \cdot f_i(x). \quad (2)$$

Note that the forms of the cumulative probability distribution and probability density function may differ between (1) and (2), respectively. According to a previous study [7], the probability distribution of vehicle loads can be illustrated using a normal distribution. However, the actual probability histogram exhibited a characteristic multimodal distribution, as shown in Figure 4. The histogram shows the proportions of various vehicles, where the proportion of small vehicles was higher. Therefore, multiple normal distributions were used to fit the histogram. Figures 5–9 show the fitting results obtained using different numbers of normal functions.

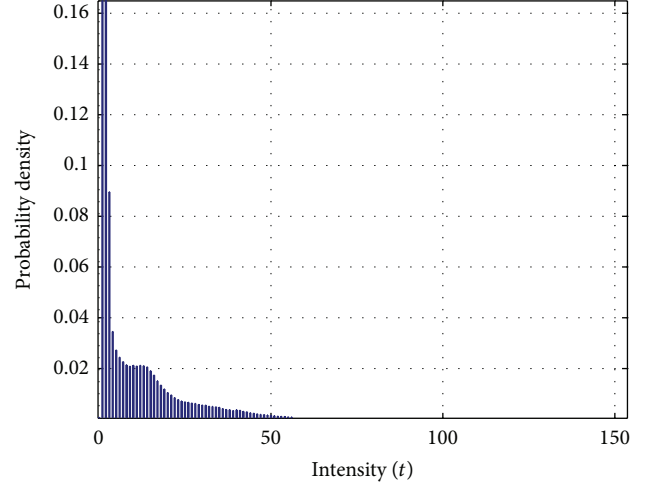


FIGURE 4: Histogram of the vehicle loads.

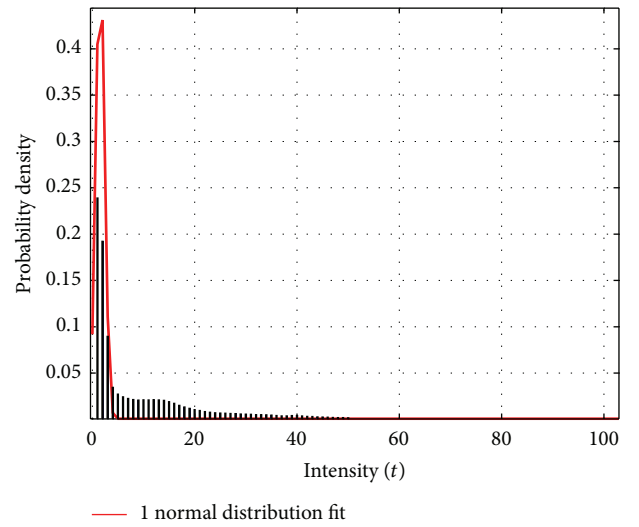


FIGURE 5: One normal distribution fitted.

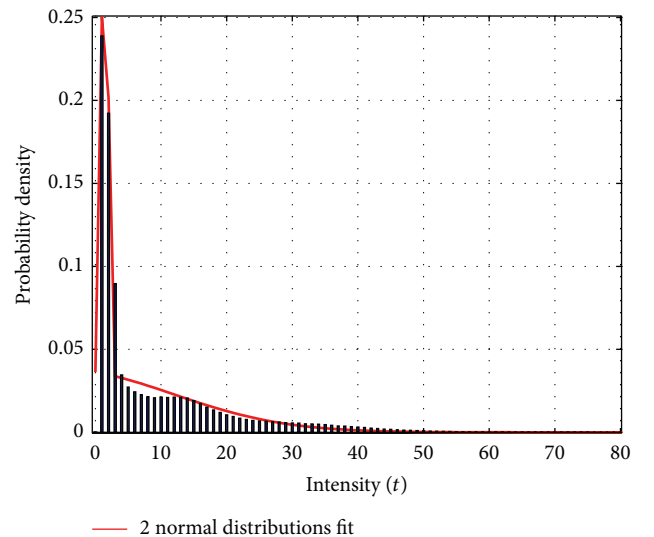


FIGURE 6: Two normal distributions fitted.

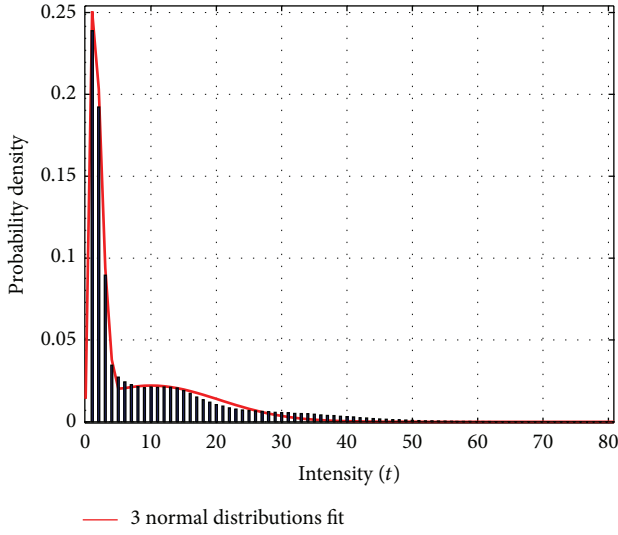


FIGURE 7: Three normal distributions fitted.

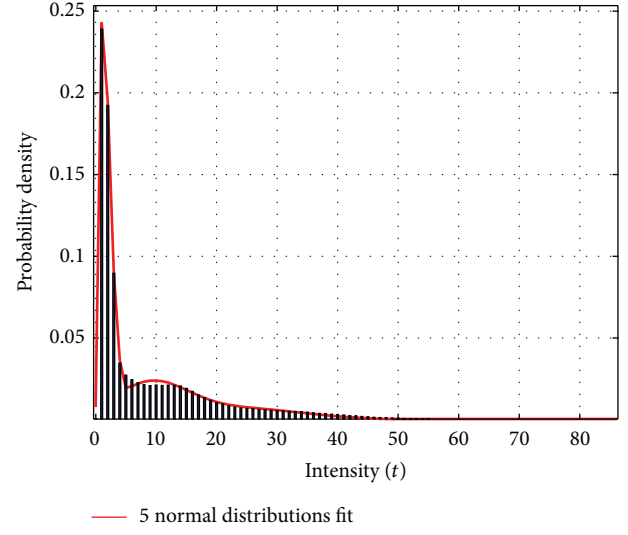


FIGURE 9: Five normal distributions fitted.

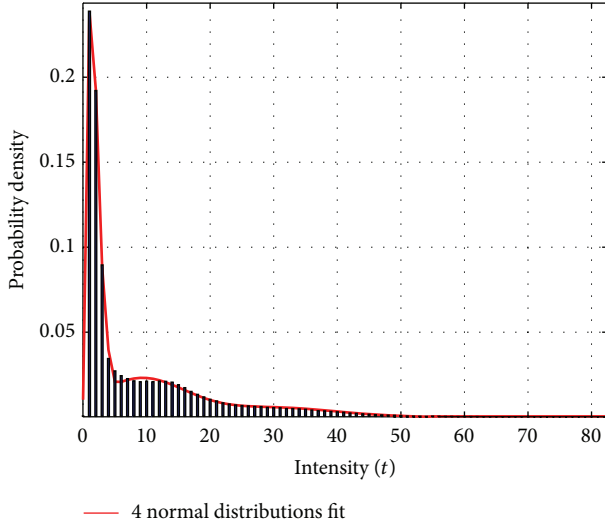


FIGURE 8: Four normal distributions fitted.

The analysis of the index of fit (R -square) showed that the fitting results were the best with five normal functions and was the worst with a single normal function, while those with four, three, and two normal functions were intermediate between these two extremes. The fitting results with a single normal function could only fit the maximum peak value. The difference between the fitting result with five normal functions and four normal functions was very small because the vehicle types passing over Hangzhou Bay Bridge mainly comprised five types of vehicles, that is, two-axle, three-axle, four-axle, five-axle, and six-axle vehicles, and the four-axle, five-axle, and six-axle vehicles sometimes merged with each other in terms of the gross weight. The proportions of the other types of vehicles were very small, the frequencies of appearance were low, and the dispersion degree of the gross weight was very high. Thus, the main problem was to consider the probability distribution of the main vehicle types as

TABLE 2: Probability distribution parameters for the vehicle loads.

	Two-axle	Three-axle	Four-axle	Five-axle	Six- or more axle
Mean value	1.54	14.55	19.5	26.56	31.23
Standard deviation	1.01	5.92	7.89	11.75	11.84

the basis of fitting. In addition, the fitting effect with more than five normal functions was better in the tail. However, the number of normal functions required for fitting should be tested case-by-case. If the reliability of the bridge needs to be studied, the fitting precision of the tail cannot be neglected.

The proportion of two-axle vehicles was 75.4%, which included two-axle small cars, two-axle minivans, and two-axle coaches. The proportion of three-, four-, five-, and six- or more axle vehicles was 7.5%, 5.8%, 4.5%, and 6.8%, respectively. The vehicle types that comprised two-axle vehicles were more frequent than others. The two-axle vehicles were characterized mainly by a multimodal distribution, which was similar to that shown in Figure 4. Table 2 presents the mean values and standard deviations for the different types of vehicles.

3.2. Probability Characteristic of the Truck Loads. Truck load models are always used for the design and performance evaluations of bridges [20, 21]; thus it was necessary to consider the truck load on Hangzhou Bay Bridge. Table 3 shows the proportions of different vehicles in terms of their different load intensities. Two-axle vehicles were the most frequent when the load intensity was <15 t. In general, these comprised two-axle minivans and two-axle large coaches when the gross weight was >5 t. However, the basic models of trucks are all four-axle or more in the specifications [20, 21]; for example, the truck models in the American and Chinese specifications are both based on five-axle trucks. This is

TABLE 3: Proportions of different vehicles in terms of different load intensities.

Number of axles	[5, 10t)	[10–15t)	[15–20t)	[20–25t)	>25t
2	87.1%	57.6%	29.7%	11.6%	2.3%
3	10.8%	22.5%	28.2%	25.7%	6.4%
4	2.1%	11.7%	19.3%	29.6%	17.1%
5	0	5.1%	10.4%	15.6%	25.8%
6	0	3.1%	12.4%	17.6%	48.5%

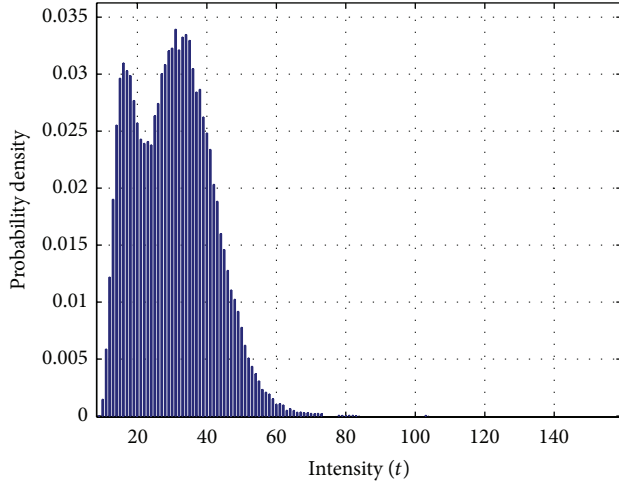


FIGURE 10: Histogram of five-axle (or more) trucks.

because large and heavy trucks have major effects on the safety of bridges. And many bridges were damaged by heavy trucks in recent years [22]. Therefore, a statistical rule based on five-axle (or more) trucks was employed in the present study.

According to the data collected, the numbers of five- and six-axle trucks were 42,116 and 63,424, respectively, and the probability histogram is shown in Figure 10. It can be seen that the five-axle (or more) trucks exhibited multipeak characteristics with a main peak. Figures 11–13 show the results fitted with a normal distribution, log-normal distribution, and Weibull distribution, respectively. Although the fitting results for the curves all satisfied the 95% confidence intervals, the peak or tail sections were not fitted well by some curves and there were obvious offsets according to a visual analysis. It can be seen that the fitting results obtained with the normal distribution and Weibull distribution were all successful, but the fitting of the tail was better using a normal distribution, where the mean value was 29.38 t and the coefficient of variation was 37.2%.

3.3. Characteristic Vehicle Loads in the Morning and the Evening Rush Hour Periods. To determine the vehicle loads during the rush hour periods in the morning and the evening, the probability characteristics in different time intervals were analyzed. The traffic jam conditions on Hangzhou Bay Bridge during the morning and the evening rush hours, and

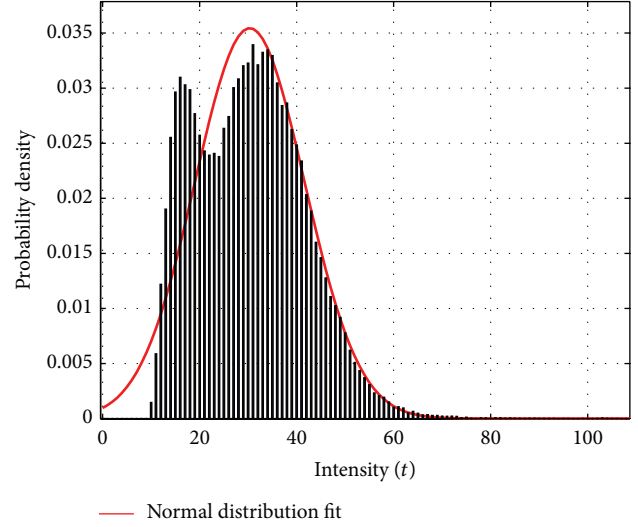


FIGURE 11: Normal distribution fitting.

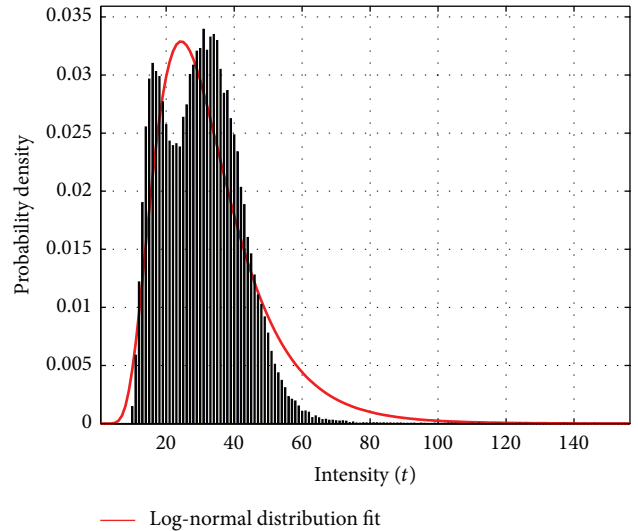


FIGURE 12: Log-normal distribution fitting.

the actual lane loads, were also compared based on the mean speed of vehicles. In general, the rush hour period in the morning occurred from 7:00 am to 9:00 am and the evening period lasted from 5:00 pm to 7:00 pm. Given the length of Hangzhou Bay Bridge, the morning rush hour period extended from 6:00 am to 9:00 am. Figure 14 shows the proportions of vehicles in the morning and the evening rush hour periods based on data mining, which demonstrate that the proportions of vehicles in the morning and the evening rush hour periods were approximately 20%, and the highest level was 27%, which indicates that the traffic was relatively even, but not high, and traffic jams did not form. Figure 15 shows the probability distribution and probability curve fitting for vehicles in the morning and the evening rush hour periods, which demonstrates that the probability distribution had multimodal characteristics, although they are not obvious. The first main peak was sharp and the other

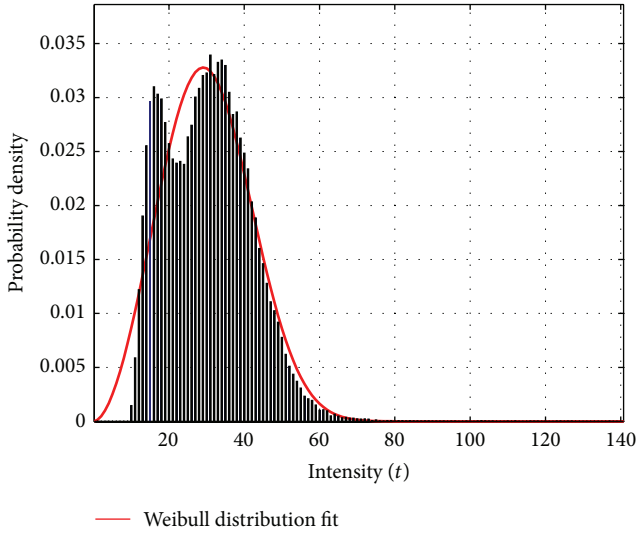


FIGURE 13: Weibull distribution fitting.

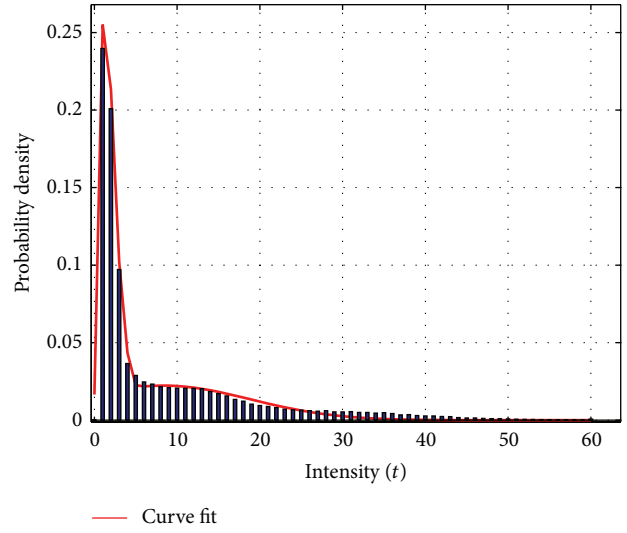


FIGURE 15: Histogram and curve fitting results for vehicle loads in the morning and the evening rush hour periods.

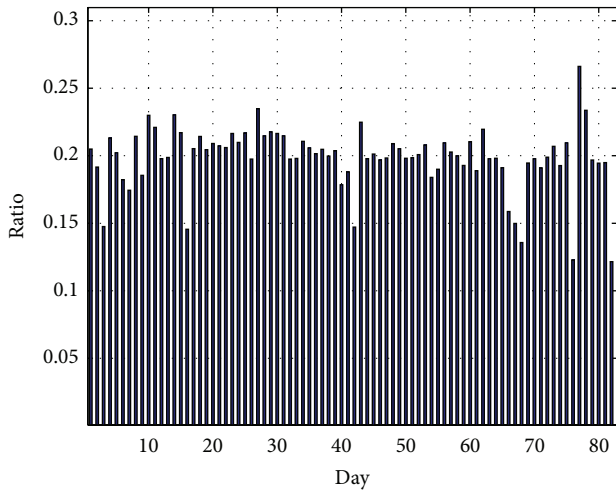


FIGURE 14: Proportions of vehicles in the morning and the evening rush hour periods.

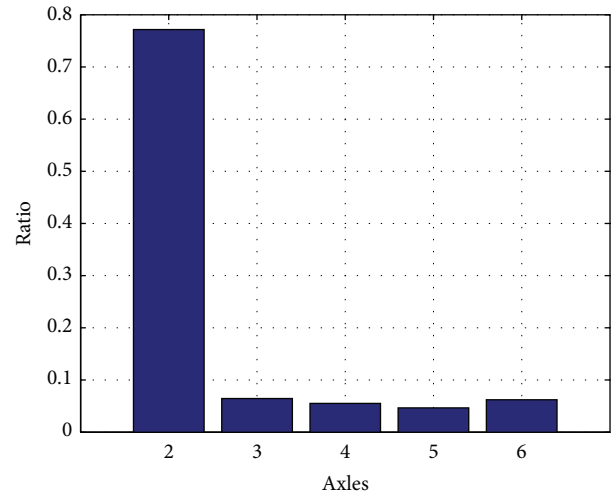


FIGURE 16: Proportions of vehicles with different axle types.

peaks were relatively gradual. Thus, the superposition of three normal distribution functions was used for fitting. Figure 16 shows the proportions of different types of vehicles in the morning and the evening rush hour periods. It can be seen that two-axle vehicles (small cars and two-axle minivans or trucks) comprised most of the vehicles, that is, 77%. To distinguish the proportions of small cars and two-axle minivans or trucks, Figure 17 shows the distribution of two-axle vehicles at different load intensities. It can be seen that two-axle small cars of <5 t accounted for $>70\%$ of the traffic and it is obvious that they formed the majority in the morning and the evening rush hour periods.

The embedded WIM system was located close to a charging station near south entrance; thus the speed of most of the vehicles was relatively low, that is, about 20 km/h in about 90% of the cases. Therefore, we could not analyze

the actual speed and traffic jam condition for vehicles based on the speed measured at the Hangzhou Bay Bridge WIM site.

4. Distribution of the Maximum Value of Trucks during the Reference Design Period

The analysis requires the solution of the maximum problem when the maximum truck load is needed during the reference design period for a bridge. A previous study [23] showed that the truck load is a time-varying random process, which can be modeled as Poisson processes, the intensities of which are also time-dependent variables where the average occurrences can be calculated using a Poisson distribution. Given an average

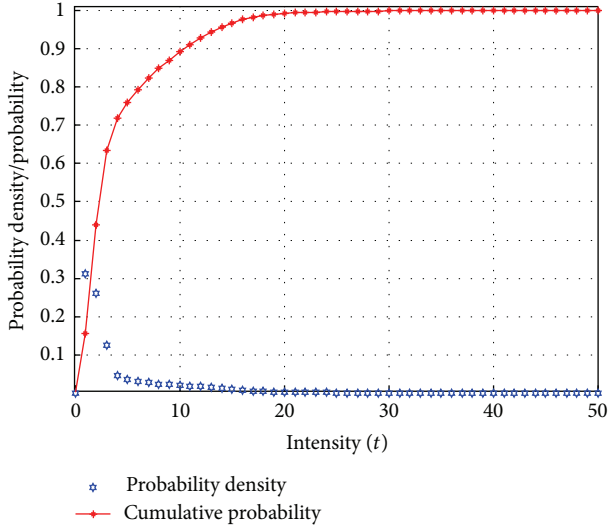


FIGURE 17: Different load distributions of two-axle vehicles.

rate of occurrence λ , the probability of n events occurring within a time interval, $p(n)$ is given by

$$p(n) = e^{-\lambda t} \frac{(\lambda t)^n}{n!}, \quad (3)$$

where t is the time interval and $n = 0, 1, 2, \dots$

Based on the Poisson process and the load characteristics, the following hypothesis can be proposed.

- (1) The truck loads during the bridge service life are completely random and the time interval of an event is very small relative to the overall bridge life.
- (2) The truck loads are also random and statistically time independent during each interval t .
- (3) The probability of each event during a time interval is an incremental process and the possibility of the reoccurrence of the event in a time interval is negligible.

According to the Poisson process, the truck load in each time interval can be considered independent and the intensity distributions are all the same. And in order to simplify the calculation, each time interval is supposed to be equal during the bridge service life and there is no overlap between each interval t . According to reliability theory [24], the maximum truck load during the reference design period of the bridge can agree with the following hypothesis. If supposing that Q_i ($i = 1, 2, \dots, N$) is the load intensity in the i th time interval and Q_T is the load intensity in reference design period T , the problem of determining the maximum value for the trucks becomes the problem of finding the maximum Q_T from N independent Q_i , that is, $\max(Q_1, Q_2, \dots, Q_N)$, which is as follows:

$$\begin{aligned} P(Q_T \leq q) &= P(\text{all } Q_i \leq q) \\ &= P(Q_1 \leq q \cap Q_2 \leq q \cap \dots \cap Q_N \leq q). \end{aligned} \quad (4)$$

According to the above hypothesis of an independent identical distribution, the following equation is obtained:

$$\begin{aligned} P(Q_1 \leq q \cap Q_2 \leq q \cap \dots \cap Q_N \leq q) \\ = P(Q_1 \leq q) \cdot P(Q_2 \leq q) \cdots P(Q_N \leq q). \end{aligned} \quad (5)$$

Suppose that the cumulative probability distribution of the truck load in each time interval is $F_Q(q)$ and the maximum cumulative probability distribution in T is $F_{Q_T}(q)$; then $F_{Q_T}(q)$ can be written as

$$F_{Q_T}(q) = F_{Q_1}(q) \cdot F_{Q_2}(q) \cdots F_{Q_N}(q) = [F_Q(q)]^N. \quad (6)$$

Its probability density is

$$f_{Q_T}(q) = N \cdot f_Q(q) \cdot [F_Q(q)]^{N-1}, \quad (7)$$

where N is an integer.

In the uniform standard of structural reliability design employed in Chinese highway engineering (GB50068-2001) [25], the maximum load distribution in t (one time interval) is considered to be the section distribution of the vehicle load, and the maximum distribution of the load in 100 t is considered to be the maximum value distribution of the vehicle loads during the reference design period (the reference design period is 100 years of Hangzhou bay bridge), which agrees with (6). However, the problem is that a suitable value of t is related to the data quantity and the data quality. Good quality indicates that the stability of the data is relatively good, which means that the variations in the mean value and standard deviation of the data are within the allowable range. Nowak [6] collected data over more than 2 weeks, including 9,250 heavy trucks, and determined the maximum truck load within 75 years by extrapolating the probability distribution over time. Therefore, by combining the reliable statistical data obtained in the present study and the research reported by Nowak, we tested intervals t of 1 week or 2 weeks, which both showed good applicability.

Based on more than 3 months of data and the probability distribution, using (6), the basic distributions for t intervals of 1 week and 2 weeks were obtained as follows:

$$F_{Q_t}(q) = [F_{Q_N}(q)]^{t/N}. \quad (8)$$

Figures 18 and 19 show the distributions with different time intervals, t .

During the extrapolation process, a problem that needed to be considered is the accuracy of the probability distribution in the tail fitted to the data collected. The tail reflects the distribution of heavy trucks; thus the error would be amplified when extrapolating using (6) if handled inappropriately. It should be mentioned that using the load distributions of all vehicle loads (including different axle weights, i.e., two-axle, three-axle, four-axle, or more) is not suitable for solving the maximum value of the vehicle loads. This will cause the fitted results to shift to the peak range, thereby neglecting the tail characteristics, which are important for the maximum value distribution calculation. Therefore, the probability characteristics of the truck load were analyzed

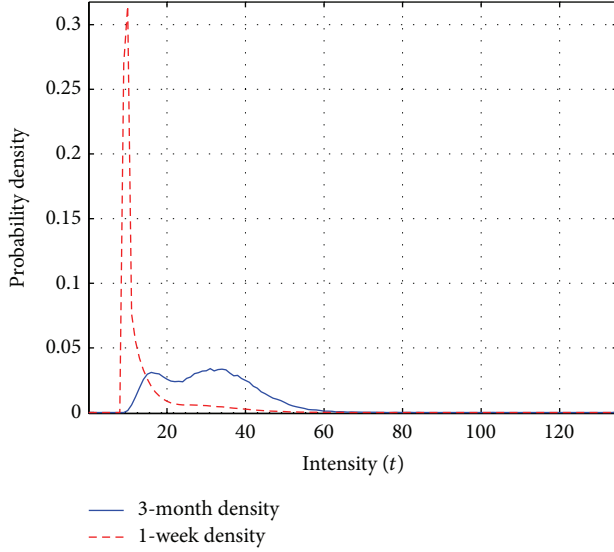


FIGURE 18: Probability density in 1 week.

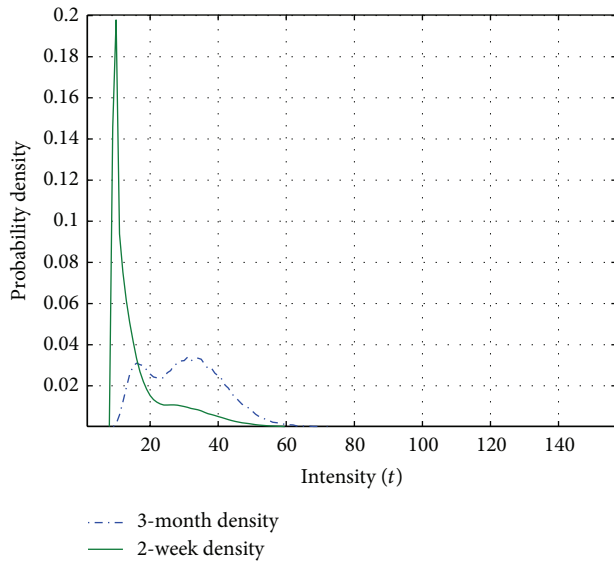


FIGURE 19: Probability density in 2 weeks.

independently in the section above; thus the probability distribution of the truck load reflects the tail features of the statistical distribution and it can be used to analyze the maximum value distribution.

According to (6) and (8), the mean value of the maximum truck load during the reference design period of the bridge is as follows:

$$X_{\text{mean}} = \int_{x_{\min}}^{x_{\max}} x \cdot f_{\max}(x) dx, \quad (9)$$

$$\sigma^2 = \int_{x_{\min}}^{x_{\max}} (x - X_{\text{mean}})^2 \cdot f_{\max}(x) dx.$$

Figure 20 shows the distribution of the maximum truck load during the reference design period. According to (9),

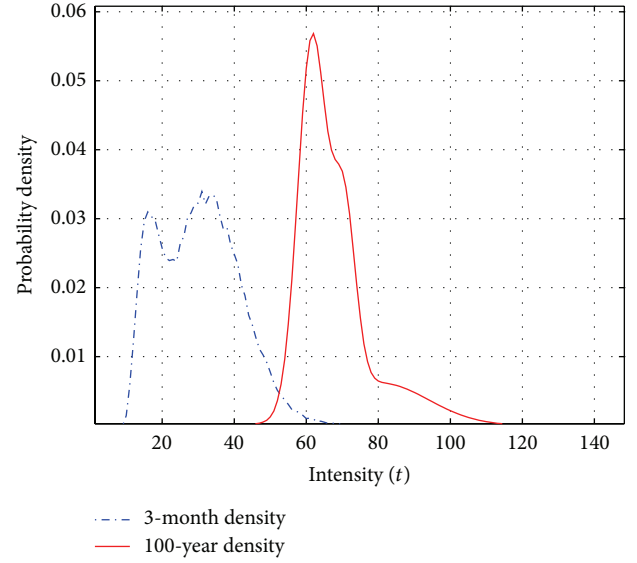


FIGURE 20: Maximum value distribution of the truck loads during the reference design period.

the mean value of trucks can be up to 65.0 t, with a standard deviation of 10.6 t and a coefficient of variation of 16.3%.

5. Conclusions

In this study, a statistical analysis of the vehicle loads on Hangzhou Bay Bridge was performed based on WIM data collected for more than 3 months. The following conclusions can be made.

- (1) The statistical analysis of all the vehicle samples showed that the mean values of the vehicle loads were relatively concentrated and the coefficients of variation were not high. The vehicle load comprised different types of vehicles, thus it was obviously characterized by a multimodal distribution. The fitting results were best using five normal functions, probably because the vehicles that passed over Hangzhou Bay Bridge mainly belonged to five types. And the occurrence frequencies of other types of vehicles were low and the dispersion of the gross weight was high.
- (2) The probabilistic characteristics of trucks with five axles (or more) were analyzed independently and the results showed that a normal distribution fitted well to the peak and tail. The mean value was 29.38 tons and the coefficient of variation was 37.2%. Thus, a normal distribution can be used to describe the probability distribution of the truck load.
- (3) A statistical analysis of the vehicle loads in the morning and the evening rush hour periods was also performed, where the results showed that the vehicles mainly comprised small cars in these periods, which could be fitted approximately using three normal distribution functions.

- (4) Only the truck load samples were used to analyze the maximum value of the truck load, rather than all the vehicle samples. The tail fitting of the histogram agreed well with the probability distribution of the truck load. Because sufficient data were available, the inverse method was used to determine the value of the basic time interval by referring to previous research. The results showed that the mean value of the maximum truck load in 100 years would be up to 65.0 tons with a coefficient of variation of 16.3%.

Disclaimer

The results and conclusions presented in the paper are of authors' and do not necessarily reflect the view of the sponsors.

Conflict of Interests

The authors declare that there is no conflict of interests regarding the publication of this paper.

Acknowledgments

This study is jointly funded by Basic Institute Scientific Research Fund (Grant no. 2012A02), the National Natural Science Fund of China (NSFC) (Grant no. 51308510), and Open Fund of State Key Laboratory Breeding Base of Mountain Bridge and Tunnel Engineering (Grant nos. CQSLBF-Y14-15 and CQSLBF-Y15-5).

References

- [1] Y. J. Ge, "Technical challenges and refinement research on wind resistance of long-span bridges," *Engineering Mechanics*, vol. 28, no. 2, pp. 11–23, 2011 (Chinese).
- [2] <http://baike.so.com/doc/2827423.html>.
- [3] <http://baike.so.com/doc/1780273.html>.
- [4] T.-H. Yi, H.-N. Li, and M. Gu, "Wavelet based multi-step filtering method for bridge health monitoring using GPS and accelerometer," *Smart Structures and Systems*, vol. 11, no. 4, pp. 331–348, 2013.
- [5] H.-N. Li, T.-H. Yi, M. Gu, and L.-S. Huo, "Evaluation of earthquake-induced structural damages by wavelet transform," *Progress in Natural Science*, vol. 19, no. 4, pp. 461–470, 2009.
- [6] A. S. Nowak, "Calibration of LRFD bridge design code," NCHRP Rep. 368, Transportation Research Board of the National Academies, Washington, DC, USA, 1999.
- [7] F. Moses, *Calibration of Load Factors for LRFR Bridge Evaluation*, NCHRP 454, Transportation Research Board, National Research Council, Washington, DC, USA, 2001.
- [8] G. K. Fu and J. You, "Truck loads and bridge capacity evaluation in China," *Journal of Bridge Engineering*, vol. 14, no. 5, pp. 327–335, 2009.
- [9] G. K. Fu and J. You, "Extrapolation for future maximum load statistics," *Journal of Bridge Engineering*, vol. 16, no. 4, pp. 527–535, 2011.
- [10] E. J. O'Brien, B. Enright, and A. Getachew, "Importance of the tail in truck weight modeling for bridge assessment," *Journal of Bridge Engineering*, vol. 15, no. 2, pp. 210–213, 2010.
- [11] P. Chotickai and M. D. Bowman, "Truck models for improved fatigue life predictions of steel bridges," *Journal of Bridge Engineering*, vol. 11, no. 1, pp. 71–80, 2006.
- [12] J. Zhao and H. Tabatabai, "Evaluation of a permit vehicle model using weigh-in-motion truck records," *Journal of Bridge Engineering*, vol. 17, no. 2, pp. 389–392, 2012.
- [13] G. Mei, Q. Qin, and D. J. Lin, "Bi-modal probabilistic model of highway and bridge vehicle loads," *Journal of Tsinghua University*, vol. 43, no. 10, pp. 1394–1404, 2003 (Chinese).
- [14] X. M. Zong, D. L. Hu, and J. Gao, "Vehicle's overload and limiting load standard for bridge safety," *Journal of Chang'an University*, vol. 28, no. 1, pp. 60–65, 2008 (Chinese).
- [15] T. Guo, A. Q. Li, and D. L. Zhao, "Multiple-peaked probabilistic vehicle load model for highway bridge reliability assessment," *Journal of Southeast University (Natural Science Edition)*, vol. 38, no. 5, pp. 763–766, 2008 (Chinese).
- [16] J. X. Gong, W. J. Li, J. L. Zhao et al., "Research on probabilistic model of highway bridge vehicle loads (1)-non-controlling area," *Journal of Highway and Transportation Research and Development*, vol. 27, no. 6, pp. 40–45, 2010 (Chinese).
- [17] Z. F. Xu, Q. Wang, and Y. S. Liu, "Research of vehicle load model for highway bridges in Guangdong Province based on WIM data," *Bridge Construction*, vol. 42, no. 6, pp. 39–44, 2012 (Chinese).
- [18] S. W. Sun and L. M. Sun, "Statistic model of vehicle loads for highway bridges," *Journal of Tongji University (Natural Science)*, vol. 40, no. 2, pp. 198–204, 2012 (Chinese).
- [19] J. Pelphrey, C. Higgins, B. Sivakumar et al., "State-specific LRFR live load factors using weigh-in-motion data," *Journal of Bridge Engineering*, vol. 13, no. 4, pp. 339–350, 2008.
- [20] PR China Ministry of Communications, "General code for design of highway bridges and culverts," Tech. Rep. JTG D60-2004, China Communications Press, Beijing, China, 2004, (Chinese).
- [21] *AASHTO LRFD Bridge Design Specifications*, AASHTO, Washington, DC, USA, 4th edition, 2007.
- [22] D. Z. Sun, *Study on multiple hazards design theory for bridge under earthquakes and heavy truck loads [Ph.D. thesis]*, Department of Lifeline Engineering, Institute of Engineering Mechanics, China Earthquake Administration, Harbin, China, 2012 (Chinese).
- [23] S. E. Hida, "Statistical significance of less common load combinations," *Journal of Bridge Engineering*, vol. 12, no. 3, pp. 389–393, 2007.
- [24] T. T. Soong, *Fundamentals of Probability and Statistics for Engineers*, State University of New York at Buffalo, Buffalo, NY, USA, 2004.
- [25] P.R. China Ministry of Communications, *GB50068-2001, Unified Standard for Reliability Design of Building Structures*, China Communications Press, Beijing, China, 2002, (Chinese).

Research Article

Acoustic Emission Signal Recognition of Different Rocks Using Wavelet Transform and Artificial Neural Network

Xiangxin Liu,^{1,2} Zhengzhao Liang,² Yanbo Zhang,¹ Xianzhen Wu,³ and Zhiyi Liao²

¹ College of Mining Engineering, Hebei United University, Tangshan, Hebei 063009, China

² School of Civil Engineering, Dalian University of Technology, Dalian 116024, China

³ School of Resources and Engineering, Jiangxi University of Science and Technology, Ganzhou 341000, China

Correspondence should be addressed to Zhengzhao Liang; liangzz@dlut.edu.cn

Received 7 August 2014; Revised 26 October 2014; Accepted 28 October 2014

Academic Editor: Ting-Hua Yi

Copyright © 2015 Xiangxin Liu et al. This is an open access article distributed under the Creative Commons Attribution License, which permits unrestricted use, distribution, and reproduction in any medium, provided the original work is properly cited.

Different types of rocks generate acoustic emission (AE) signals with various frequencies and amplitudes. How to determine rock types by their AE characteristics in field monitoring is also useful to understand their mechanical behaviors. Different types of rock specimens (granulite, granite, limestone, and siltstone) were subjected to uniaxial compression until failure, and their AE signals were recorded during their fracturing process. The wavelet transform was used to decompose the AE signals, and the artificial neural network (ANN) was established to recognize the rock types and noise (artificial knock noise and electrical noise). The results show that different rocks had different rupture features and AE characteristics. The wavelet transform provided a powerful method to acquire the basic characteristics of the rock AE and the environmental noises, such as the energy spectrum and the peak frequency, and the ANN was proved to be a good method to recognize AE signals from different types of rocks and the environmental noises.

1. Introduction

Many kinds of rocks are fracturing due to human activity or geological process. It is well known that elastic waves are emitted from rock mass during their fracturing process. Therefore, various symptoms related to the breakdown of rock mass can be detected by the acoustic emission (AE) technique [1, 2].

Rock mass is an environmental geological body; it is formed in a certain environment by mineral composition and structural plane due to movement of geological structures and complex atmospheric environment. Different types of rocks contain different kinds of minerals and different geological structures, such as joints and microcracks. The fracture involves debonding and slipping between the grains, minerals, and geological structures in rocks. Each AE signal is an indication that some part of the released energy due to the rock crack propagation is transformed into an elastic wave. Therefore, different types of rocks will generate different types of elastic waves. Laboratory experiments and field monitoring are often conducted to investigate the characteristics of rock AE signals. These AE signals are often mingled with electric

signals and artificial noises. Therefore, how to distinguish these signals becomes a significant topic in AE investigations [3–5].

Monitoring techniques and artificial intelligence algorithm have been widely used in rock slopes and tunnels [6, 7], concrete dams [8, 9], and high-rise structures [10, 11]. Artificial neural network (ANN) has some capability of learning from examples through iteration, without requiring prior knowledge of the relationships between the process parameters. The major benefits in using ANN are the excellent management of uncertainties, noisy data, and nonlinear relationships. Neural network modeling has become increasingly accepted and is an interesting method for application to the AE technique [4, 5, 12–15].

Many authors have conducted AE investigations using ANN. Kwak and Song constructed a neural network to achieve an intelligent diagnosis for chattering vibration and burning phenomena on grinding operation. The item of static power, dynamic power, peak of RMS, and peak of FFT has been used as an input feature of the neural network to diagnose the grinding faults [12]. Samanta and Al-Balushi presented a procedure for fault diagnosis of rolling element

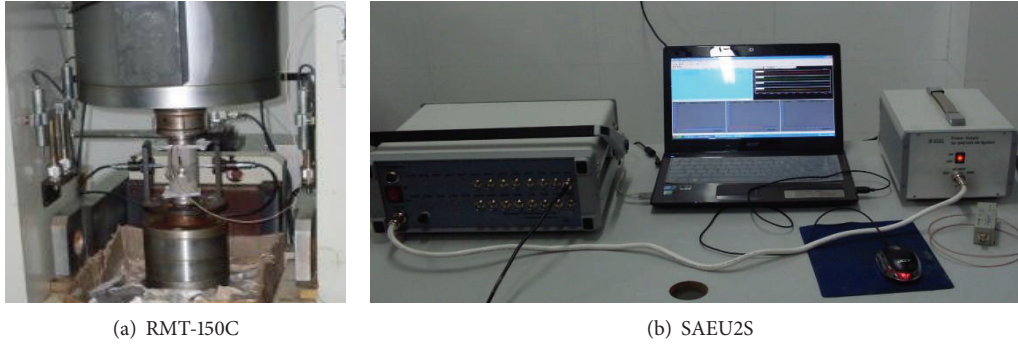


FIGURE 1: The servo controlled rock mechanical test machine RMT-150C and AE monitoring system SAEU2S.

bearings through ANN. The time-domain vibration signal of the rotating machinery with normal and defective bearings has been used as the input feature of the ANN. The results showed that the effectiveness of the ANN can diagnose the physical condition of machine [16]. Samanta et al. compared the performance of bearing fault detection by ANNs and support vector machines (SMVs) [17]. Kim et al. trained an ANN to recognize the stress intensity factor in the time interval of microcrack to fracture by AE measurement [18]. Hill et al. used the AE flaw growth activity to train a back-propagation neural network to predict the ultimate strengths in the remaining six specimens [19]. However, few investigations can be found by using ANN to distinguish rock AE signals and determine their characteristics for different rock types.

The objective of the current research was to develop a neural network for the prediction of rock types or other noises from their AE measurements. The AE signals were recorded in the rock failure process under uniaxial loading. The wavelet analysis helped to obtain the basic parameters of the AE signals of the rocks and the environmental noises. These parameters were used to establish input layers in the ANN. The trained ANN was applied to predict rock types and noise types. The predictions obtained from the ANN are in good agreement with the laboratory experiments. The ANN based on AE measurement can be used to distinguish different rock AE signals and predict different rock specimens in rock engineering.

2. Experiment Preparation and Methods

2.1. Laboratory Experiments. A total of four types of rocks were selected to conduct uniaxial compression. To guarantee the diversity of the rock types, these rock specimens were collected from four mines in China. The granulite specimens were obtained from a gold mine in Fujian province, the limestone specimens were from a tin ore mine in Guangxi province, the granite specimens were from an open pit central in Jiangxi province, and the siltstone specimens were obtained from a mine in the south of Jiangxi province.

All the mechanical tests were conducted on a servo controlled rock mechanical machine RMT-150C (Figure 1(a)). This machine has a visualization operation platform based on

Windows, and it can record the load, stress, and strain during the rock failure process.

An AE monitoring system SAEU2S with 8 parallel detection channels was applied to collect AE events in the compression (Figure 1(b)). Each channel with an AE sensor, a preamplifier, and an acquisition card can collect the parameters of AE events, such as the amplitude, energy, and counts.

2.2. AE Signals. AE signals as well as electronic noises were recorded and processed during the rock fracturing. The AE signals in time domain and frequency domain were analyzed in this section.

2.2.1. The AE Signals in Time Domain. Different rocks generated different AE signals in time domain under the same stress condition. AE counts, cumulative AE counts, energy, rise times amplitudes, event rates, and energy rates are often used to describe the AE features in time domain. Cumulative AE counts can reflect internal damage in the rock specimens.

According to curves of cumulative AE counts, axial stress, and time (Figure 2), the curves can be divided into four periods: pre-linear period, linear period, post-peak and nonlinear period, and residual strength period.

All the AE signals of the specimens show a sudden jump before their final failure, accompanied by a stress drop. The granulite specimens show a sudden increase before failure without precursors. The stress for the granite specimens lasted many times of stress buildup and stress release before final failure. The AE counts for the limestone specimens increased gradually before the peak strength points. The siltstone specimens demonstrated an obvious residual failure process, and the cumulative AE counts reached the peak point after the peak strength points.

The granulite, limestone, and granite specimens showed a hard and brittle failure mode and their curves for the post-peak period were not obtained. The soft siltstone showed slight plastic failure mode.

2.2.2. The AE Signals in Time Domain in Frequency Domain. A continuous wavelet transform (CWT) is used to divide a continuous-time function into wavelets. Unlike Fourier transform, the continuous wavelet transform possesses the

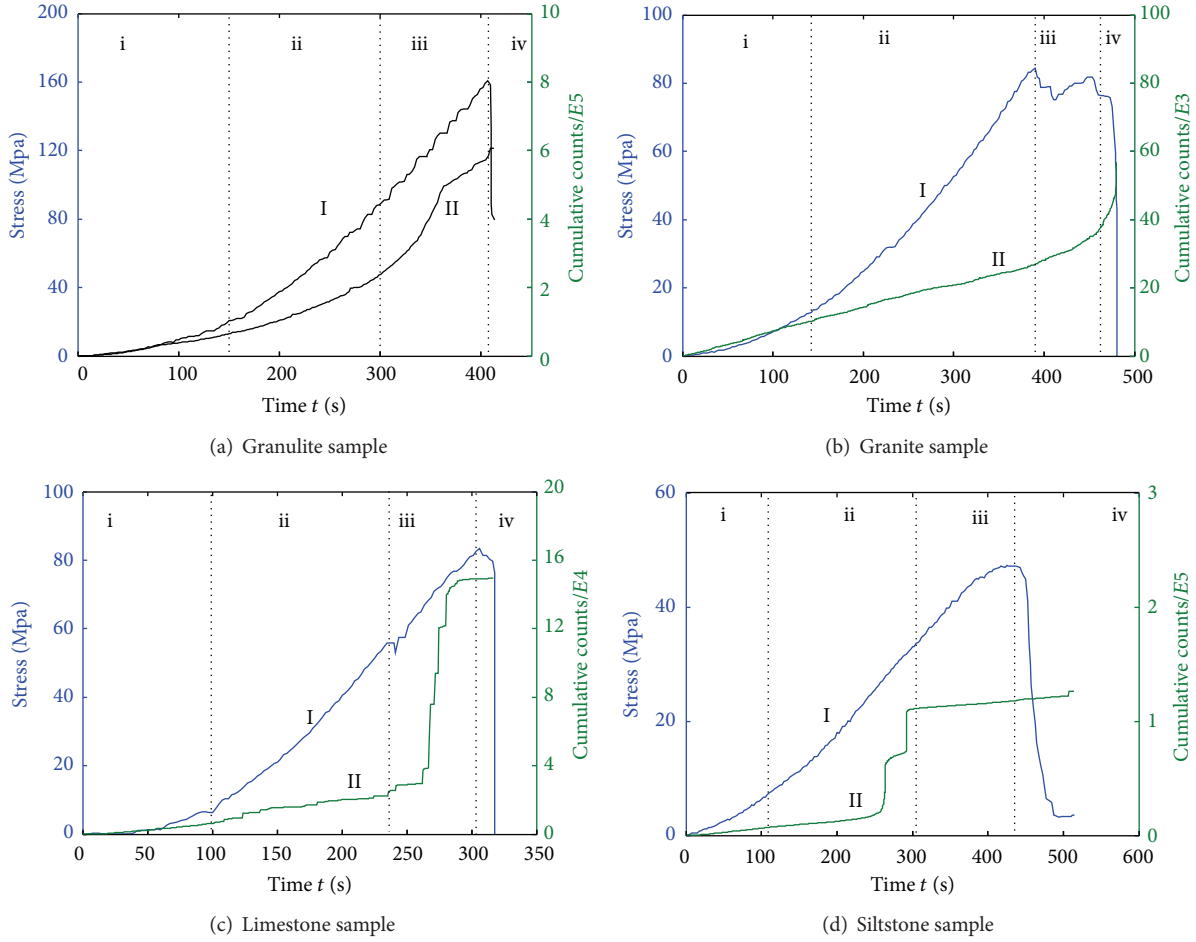


FIGURE 2: Curves of cumulative counts, axial stress, and load time (I: stress-time curve; II: cumulative counts-time curve).

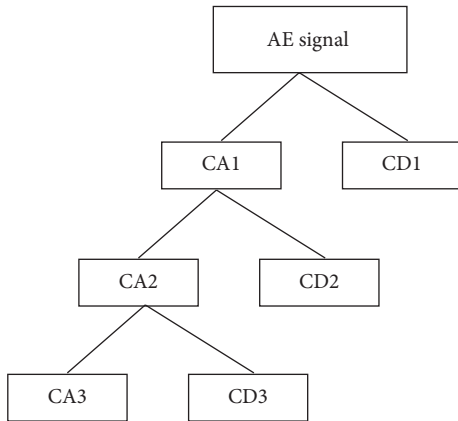


FIGURE 3: Topology structure of wavelet decomposition with 6 layers.

ability to construct a time-frequency representation of a signal that offers very good time and frequency localization. CWT is very efficient in determining the damping ratio of oscillating signals. CWT is also very resistant to the noise in the signal.

According to Mallat theory, the fast wavelet transform algorithm, the signal function can be decomposed into the low frequency component and the high frequency component under the scale j of the wavelet packets transform:

$$\begin{aligned}
 f(n) &= A_0 f(n), \\
 A_0 f(n) &= A_1 f(n) + D_1 f(n), \\
 &\vdots \\
 A_{J-1} f(n) &= A_J f(n) + D_J f(n),
 \end{aligned} \tag{1}$$

where $f(n)$ is the signal function, A_i is the low frequency component coefficient, and D_i is the high frequency component coefficient. So the signal function can be described as follows under the scale J :

$$f(n) = A_J f(n) + \sum_{j=1}^J D_j f(n). \tag{2}$$

A topology structure of a wavelet transform with 3 layers is shown in Figure 2. Figure 3 shows topology structure of wavelet decomposition with 6 layers.

TABLE 1: Energy ratio of the wavelet transformed AE signals in failure.

Decomposition layers	CA6	CD6	CD5	CD4	CD3	CD2	CD1	Band/kHz
Frequency layers/kHz	0~78	78~156	156~312.5	312.5~625	625~1250	1250~2500	2500~5000	
Energy ratio/%								
Granulite	0.61645	4.7345	15.846	74.723	4.0579	0.022976	0.0018851	[156, 625]
Granite	89.339	9.9742	0.47787	0.14506	0.016137	0.16799	0.031258	[0, 78]
Limestone	59.835	35.511	2.4313	1.926	0.26136	0.013166	0.022664	[0, 156]
Siltstone	52.215	44.053	3.5185	0.17952	0.011493	0.0076762	0.015349	[0, 156]

Nowadays wavelet analysis is widely used to analyze nonstationary random signals [20]. The wavelet analysis is a time-frequency localized analysis method, in which the window size is fixed but its shape can be changed, and time- and frequency-window can also be changed, which means the low frequency part with higher frequency resolution and lower time resolution and the high frequency part with a higher time resolution and lower frequency resolution [20]. The wavelet analysis can decompose AE signals both in frequency domain and in time domain. The wavelet analysis provides a kind of adaptive time and frequency domain localization analysis method.

Figure 4 shows relationship between frequency and amplitude of the AE signals in rock final failure stages. The dynamical damage processes and characteristics of different rocks (granite, granulite, siltstone, and limestone) under the stress condition were obtained. It is found that the transformed AE signals for different rock types were different.

The frequency distribution reflected rock fracture and associated AE characteristics. As shown in Figure 4 and Table 1, the frequency domain of the granulite specimens was mainly distributed in CD5 and CD4, taking up more than 90% of all the frequency bands. Most of the frequency of the granulite signals was located in high frequency bands [156, 625 kHz]. The frequency domain of the granite specimens was distributed in low bands from CD1 to CD6, and CA6 took up above 89% of all the signals, which ranged in [0, 78 kHz]. Most of the granite AE signals belonged to low frequency bands, while the AE signals of the limestone specimens mainly concentrated in the frequency of CA6 (59.835%) and CD6 (35.511%).

2.3. The Artificial Neural Network. The artificial neural network can be seen as a set of parallel processing elements, and the suitable mathematical methods can be used to change the weights and thresholds to perform specific functions. The BP neural network can figure out each layer's error derivatives by using the back-propagation algorithm according to the generated weight matrices and threshold matrices. And then, BP adjusts corresponding matrices on the basis of error derivatives and square error sum to approach the mapping relation between the system input variables and output variables step by step. The typical structure of a BP neural network is shown in Figure 5. It has one input layer, one or more hidden layers, and one output layer, with each layer consisting of one or more neurons.

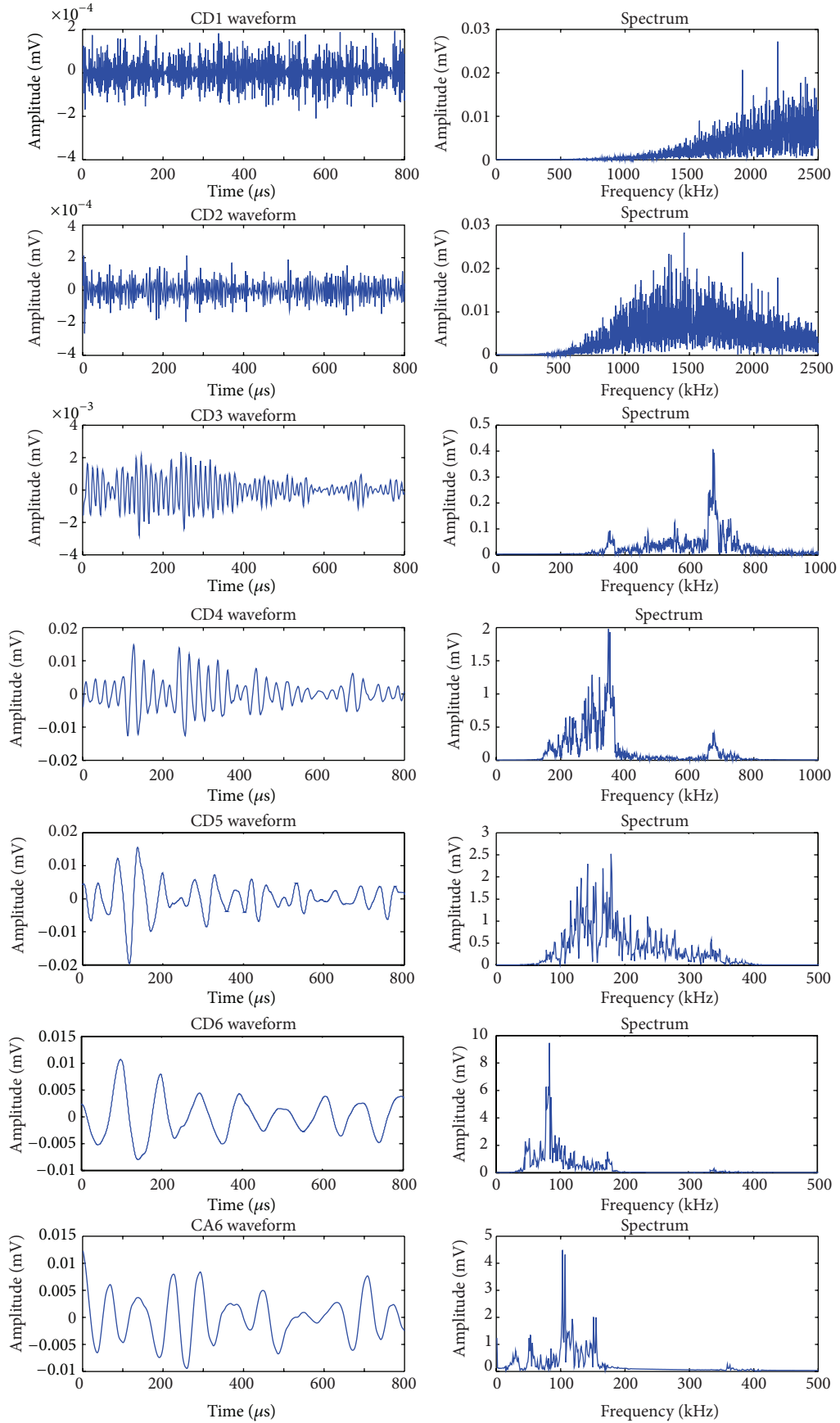
The number of neurons (m) in the input layer is the same as the number of mechanical parameters to be solved, and the number of neurons (n) in the output layer is the number of the measured displacements. Usually, only one hidden layer is needed. The number of neurons (p) in the hidden layer can be specified either manually or by an optimization method. The training specimens are often used to adjust the weight values by making the summed squared error between the displacements from numerical simulation and those from BP network a minimum. For the training specimens, the input parameters can be prepared by the parameter experiment design method, while the corresponding output parameters can be prepared by numerical simulation.

The calculating procedure of a three-layer BP neural network is shown in Figure 6. W_1 and b_1 are weight matrix and threshold matrix between the input layer and the hidden layer, respectively; W_2 and b_2 are weight matrix and threshold matrix between the hidden layer and the output layer, respectively; function f is the transfer function between two adjacent layers. Three transfer functions, including Tan-Sigmoid transfer function (*tansig*), Log-Sigmoid transfer function (*logsig*), and linear transfer function (*purelin*), are the most commonly used transfer functions for multilayer networks.

3. Results and Discussion

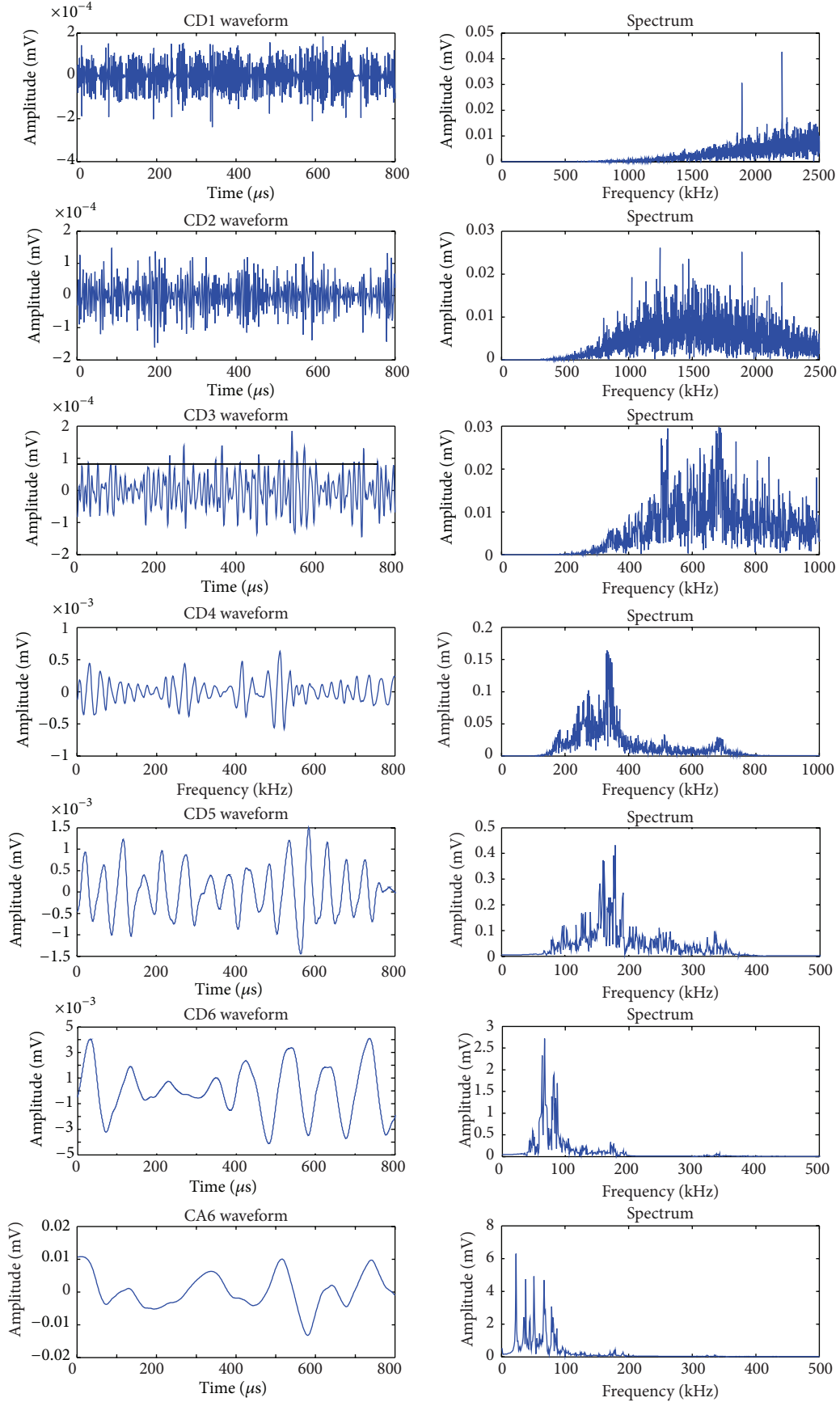
3.1. Mechanical Experiment Results. Figure 7 shows typical fracture patterns for these four types of rock specimens. These rock specimens demonstrated different fracture patterns under uniaxial compression. A shear crack was formed in the granulite specimen, and the rupture is a typical single shear failure mode. Some thin flakes spalled from the granite specimen vertically, and the failure mode is a typical splitter failure. Several parallel cracks occurred in the limestone specimen, which run through the whole specimen from the bottom to the top, accompanied by some small cracks. It had the same tensile failure mode as granite specimen. The siltstone presented a typical slightly plastic rock. The cracks in the siltstone specimen developed relatively slow, and an X fracture pattern was observed on the surface, indicating a typical shear failure mode.

The four types of rock specimens have different failure modes. On the one hand, different types of rocks have different distribution of mineral particle size and hardness of mineral grains and different microgeological structure. On



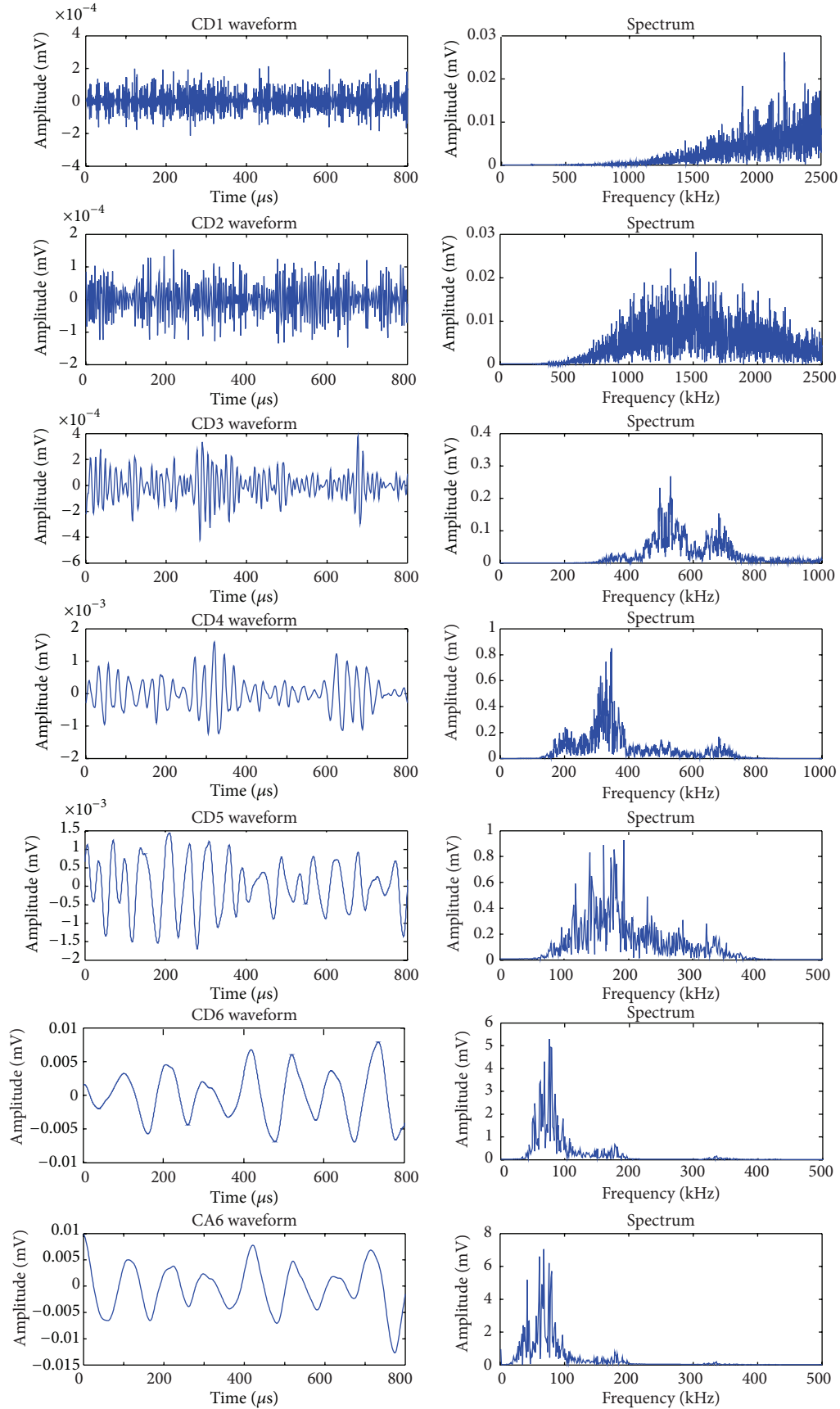
(a) Granulite

FIGURE 4: Continued.



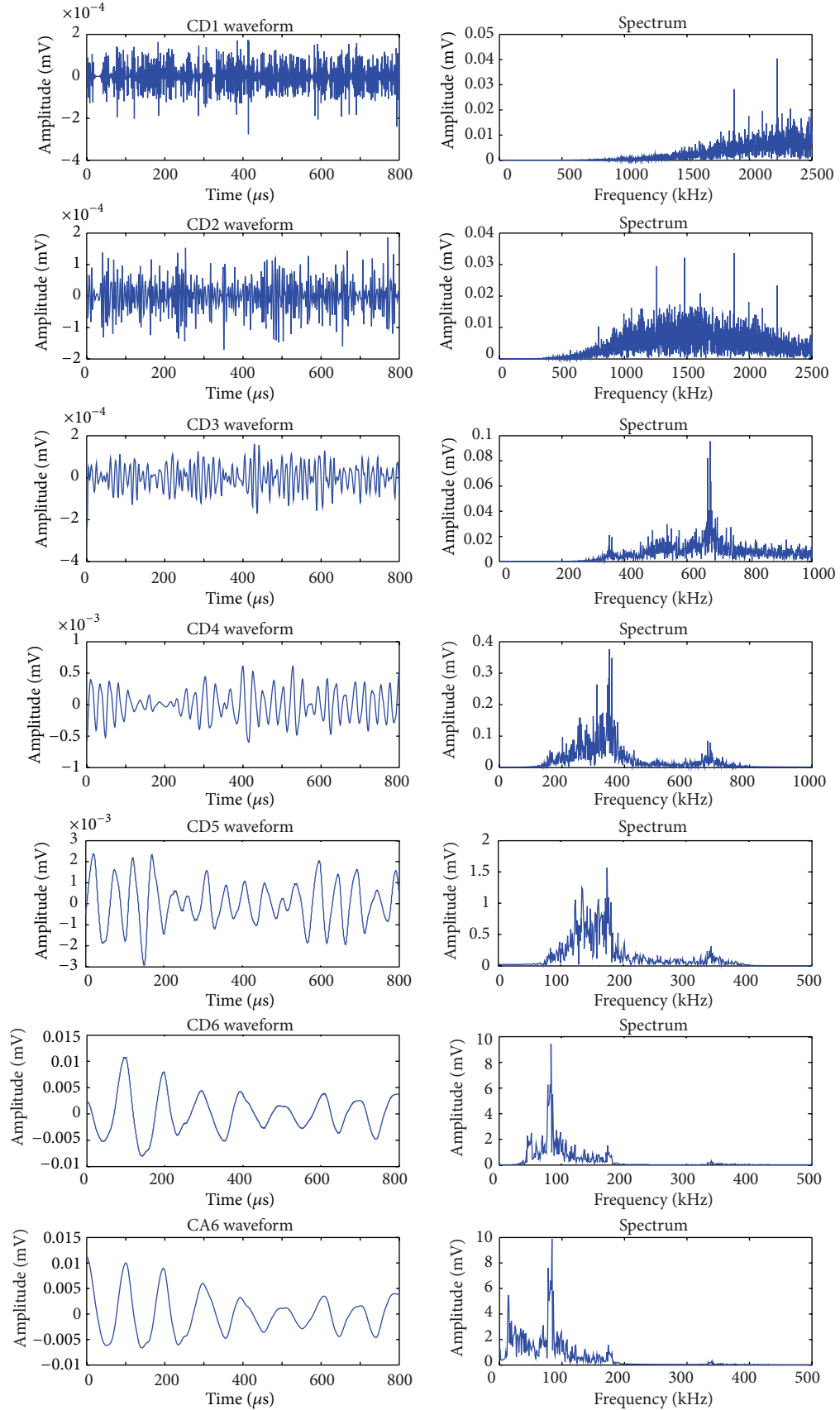
(b) Granite

FIGURE 4: Continued.



(c) Limestone

FIGURE 4: Continued.



(d) Siltstone

FIGURE 4: Six layers of the wavelet decomposition for the rock specimens.

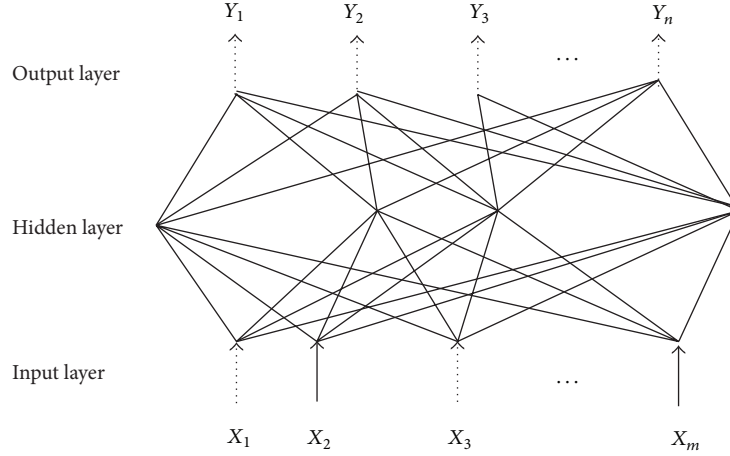


FIGURE 5: Typical structure of a BP neural network [18].

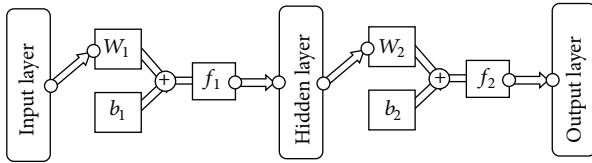


FIGURE 6: Flow chart of BP neural network.

the other hand, different rock contains different properties and scales of weakness structural plane.

3.2. AE Characteristics. Figure 8 shows the curves of the accumulated AE counts as the load increased for the four typical specimens. Figure 9 shows the curves of the AE rate and the load for the specimens. It can be observed that the limestone specimen and the granite specimen produced more AE events than the siltstone specimen and the granulite specimen in beginning loading stage. However, the AE rates of the granite and granulite specimens were higher than the limestone and siltstone specimens. The granite specimen generated the smallest number of the AE events, whereas it had the largest number of the AE rates. The siltstone did not generate a large number of the AE events before the sudden burst failure.

Figure 10 shows the wavelet transformed energy spectrum coefficient of the rock specimens. It can be observed that the spectrum coefficient of the granulite, granite, and limestone specimens was mainly distributed in CA6, CD6, CD5, and CD4 bands. The distribution for the siltstone specimen was distributed in CA6 and CD6 bands.

Table 2 lists the distribution of the frequency band in each layer. The frequency range of the AE signals could be determined by the wavelet transform. The frequency of the hard and brittle rock (the granulite, granite, and limestone specimens) ranged from 0 kHz to 625 kHz. The siltstone belongs to a moderate strength and slightly plastic rock, and the frequency ranged from 0 kHz to 312.5 kHz in a narrower band.

4. The Recognition of the AE Signals Using the ANN

4.1. ANN Structure. The numbers of the neurons in the input layer, output layer, and the hidden layer and a proper transfer function should be determined in a typical ANN structure.

Input layer vector: there were 11 input neurons in the ANN model as shown in Table 3: rise time (X_1), ring count (X_2), energy (X_3), duration time (X_4), amplitude (X_5), peak frequency (X_6), the CA6 value of the wavelet decomposition (X_7), the CD6 value of the wavelet decomposition (X_8), the CD5 value of the wavelet decomposition (X_9), the CD4 value of the wavelet decomposition (X_{10}), and the CD3 value of the wavelet decomposition (X_{11}).

Output layer vector: there were three neurons in the output layer. The output parameters (y_1 , y_2 , and y_3) should be either one or zero. Their combined value indicated the signal types (Table 4). For example, the output value 001 ($y_1 = 0$, $y_2 = 0$, and $y_3 = 1$) predicted the signal generated by a granulite specimen.

According to the number of the input neurons and the output neurons, the number of the neurons in the hidden layer can be obtained as follows [19]:

$$n_1 = \sqrt{n + m} + a, \quad (3)$$

where n_1 , m , and n are the numbers of the neurons in the hidden layer, the input layer, and the output layers, respectively, and a is a constant between 0 and 10. Since the input vector dimension was set to be 11 and the output vector dimension was set to be 3, n_1 could range from 4 to 14. The number of the neurons in the hidden layer was set to be 14 in the ANN model.

Three transfer functions, including Tan-Sigmoid transfer function (*tansig*), Log-Sigmoid transfer function (*logsig*), and linear transfer function (*purelin*), are the most commonly used transfer functions for multilayer networks.

Two transfer functions were required in the ANN structure. The input parameters, such as the rise time, ring count, energy, duration time, and the amplitude, had been

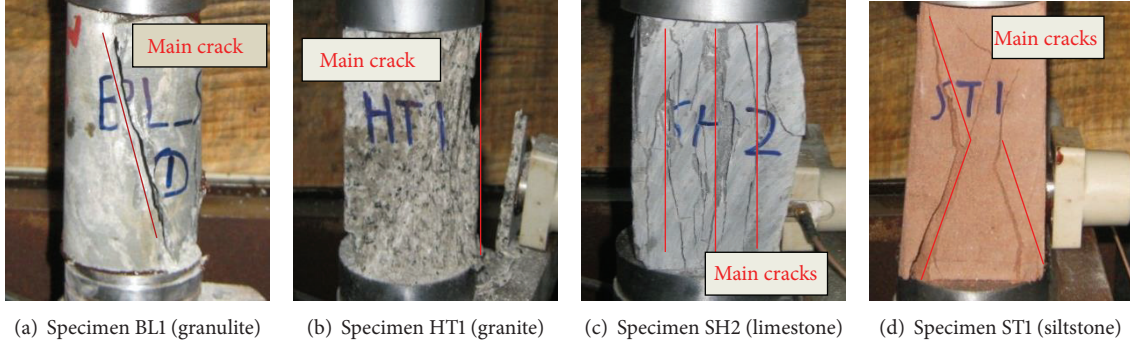


FIGURE 7: Fracture patterns for the four types of rock specimens.

TABLE 2: The distribution of the frequency band in each layer.

	The layer of wavelet decomposition						
	CA6	CD6	CD5	CD4	CD3	CD2	CD1
Frequency range (kHz)	0~78	78~156	156~312.5	312.5~625	625~1250	1250~2500	2500~5000

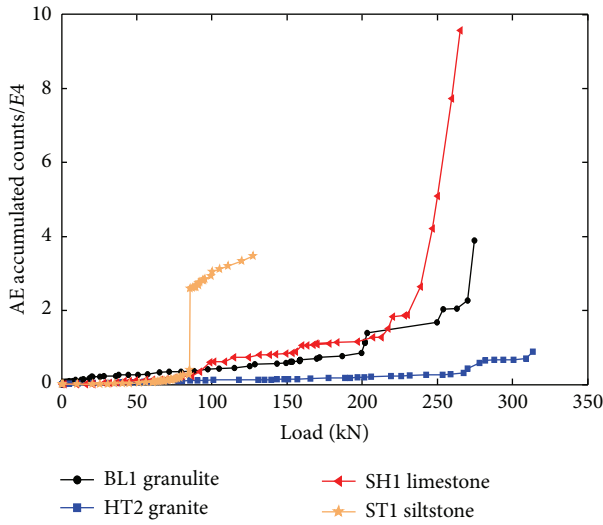


FIGURE 8: The curves of the accumulated AE counts and load for the four specimens.

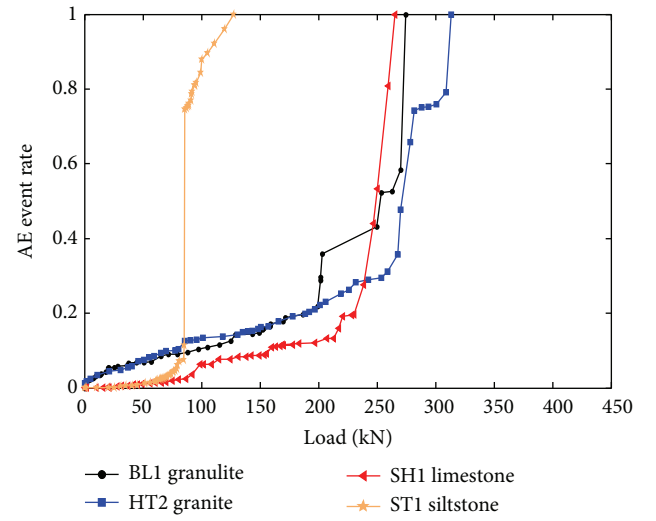


FIGURE 9: The curves of the AE rate and load for the four specimens.

normalized into the range $[-1, 1]$ before input into the transfer function *tansig* as arguments. Compared with the transfer function *purelin*, *logsig* was better to link the hidden layer and the output layer. After one-minute training at the 360th iterative step, the mean squared error was less than 0.005 (Figure 11). For the *purelin* function, the mean squared error did not reach 0.009 until 100,000 steps (Figure 12).

4.2. BP Network Training. Six types of elastic wave signals were considered in the ANN model, including the four types of the rocks, the electrical noise, and artificial knock noise. Totally 120 sets of the rock AE signals (30 sets of the granulite AE signals, 30 sets of the granite AE signals, 30 sets of the limestone signals, and 30 sets of the siltstone AE signals) were used for training. There were 30 sets of the electrical

noise signals and 15 sets of the artificial noise signals for training. The RPROP algorithm was applied in the training, the mean squared error of the objective function was set to be 0.005, the maximum number of iterative steps was 100,000, and the number of independent training times was set to be more than 50. As shown in Figure 13, the mean squared error reached the specified minimum value after 374 training steps.

4.3. ANN Recognition. Some basic parameters, such as the rise time, the ring count, the energy, the duration time, and the amplitude, describing the characteristics of the AE signals, were combined as an input vector in the network. Moreover, the wavelet transform method was applied to decompose the signal waves to obtain the frequency spectrum. The decomposed energy spectra at different layers were also treated as the input parameters. The trained neural

TABLE 3: Input parameters and their signal types.

Rise time/ $a1$	Ring count/ $a2$	Energy/ $a3$	Duration time/ $a4$	Amplitude/ $a5$	Peak frequency/ $a6$	CA6 layer of wavelet decomposition/ $a7$	CD6 layer of wavelet decomposition/ $a8$	CD5 layer of wavelet decomposition/ $a9$	CD4 layer of wavelet decomposition/ $a10$	CD3 layer of wavelet decomposition/ $a11$
-0.9944	-0.9946	-0.9996	-0.9955	-0.2645	0.1404	0.4449	-0.2088	-0.4542	-0.6116	0.0746
-0.9917	-0.8019	-0.9658	-0.8734	0.4908	-0.7638	-0.5627	-0.3218	0.7551	-1.0000	0.0746
-0.9981	-0.9986	-0.9998	-0.9986	-0.3013	-0.7796	-0.6560	-0.7819	-0.8793	0.6216	0.0746
-0.9907	-0.9813	-0.9981	-0.9847	-0.0919	-0.0960	0.2005	-0.1534	-0.0943	-0.8261	0.2388
-0.9986	-0.9989	-0.9997	-0.9826	-0.3833	-0.1998	-0.0113	-0.2583	-0.5884	-0.2963	0.2388
-0.9954	-0.9774	-0.9968	-0.9811	0.0835	-0.8997	-0.9157	-0.8796	-0.8954	0.8161	0.0000
-0.9995	-0.9739	-0.9961	-0.9304	0.0580	-0.7373	-0.6852	-0.7980	-0.8384	0.6148	0.0746
-0.9801	-0.9766	-0.9971	-0.9245	-0.1372	-0.4244	-0.2463	-0.5013	-0.3729	-0.1488	0.0746
-0.9958	-0.9671	-0.9957	-0.9710	0.0580	-0.2490	-0.0722	-0.2650	-0.5771	-0.2764	-0.0896
-0.9991	-0.9644	-0.9954	-0.8638	-0.1796	-0.4675	-0.3698	-0.5240	-0.7964	0.2235	0.6866
									
-0.7740	-0.7066	-0.5099	0.2520	0.9661	-1.0000	-0.9925	-0.9809	-0.2206	0.4489	-0.6567
-0.9092	-0.8845	-0.8938	-0.4225	0.8218	-0.9947	-0.9993	-1.0000	-0.9561	1.0000	-0.8358
-0.8796	-0.8671	-0.7102	-0.1123	0.9123	-0.9911	-0.9945	-0.9418	-0.4143	0.5553	-0.8358
-0.9801	-0.9842	-0.9674	-0.9293	0.7624	-0.9947	-0.9882	-0.8576	0.6103	-0.2624	-0.7015
-0.7032	-0.6484	-0.4425	0.2268	0.9349	-0.9987	-1.0000	-0.9919	-0.9503	0.9891	-0.8507

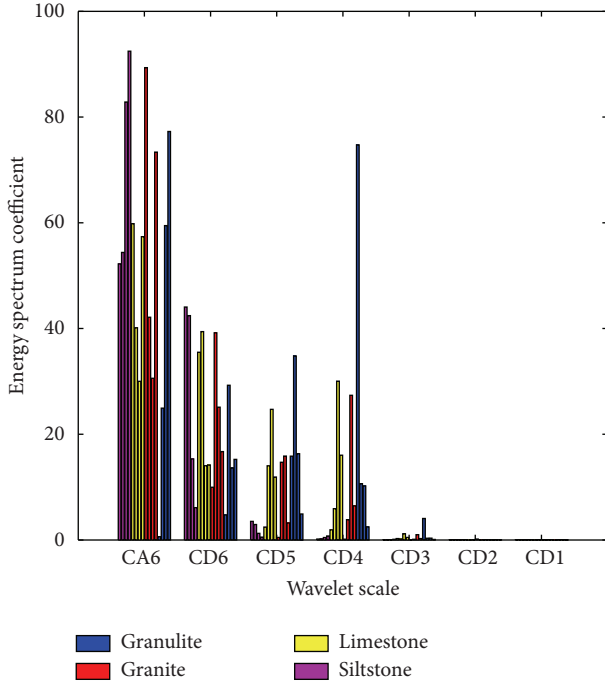


FIGURE 10: The distribution of the energy spectrum after the wavelet transform.

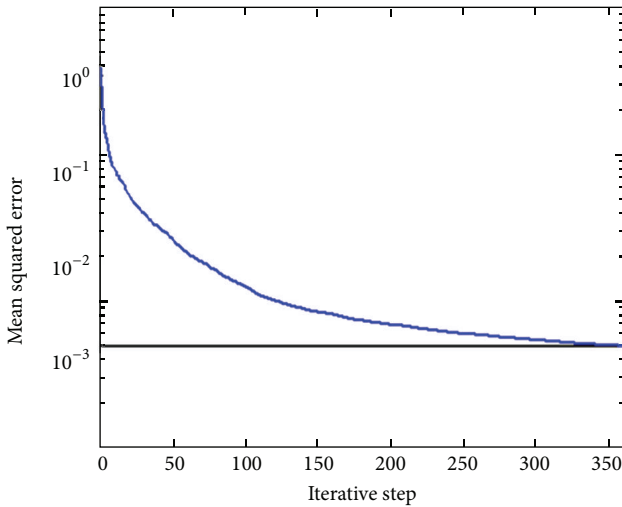


FIGURE 11: Convergence curve using the *logsig* function.

network was used to predict the signal types by establishing the mapping function between the input parameters and the output parameters.

The predicted results proved that the BP neural network based on the wavelet transform analysis can achieve a high accurate ratio to recognize different rock AE signals. Table 5 listed the recognized AE signal types of the 110 sets of signals using the ANN model. There were 20 sets of the granulite

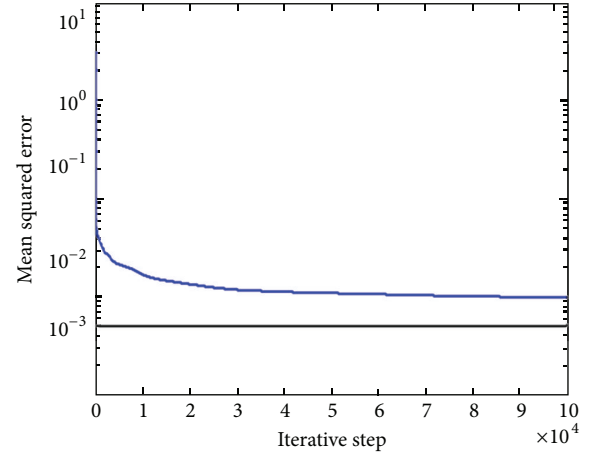


FIGURE 12: Convergence curve using the *purelin* function.

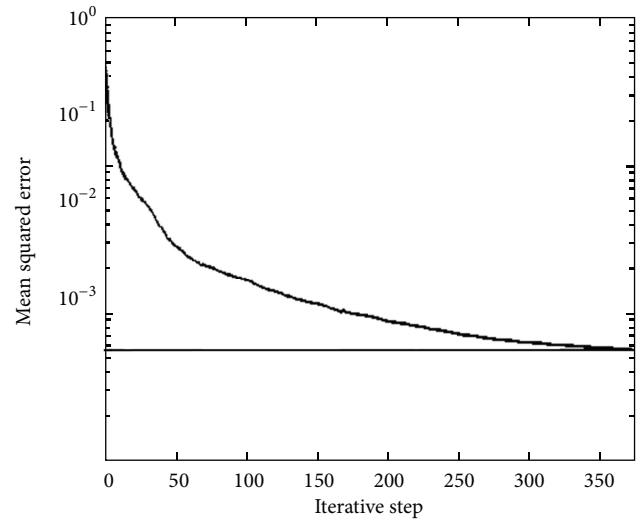


FIGURE 13: The convergence curve in the training.

TABLE 4: Output parameters and their signal types.

Signal type	y_1	y_2	y_3	Output value
Granulite	0	0	1	001
Granite	0	1	0	010
Limestone	0	1	1	011
Siltstone	1	0	0	100
Electrical noise	1	0	1	101
Knock noise	1	1	0	110

signals, 20 sets of the granite signals, 20 sets of the limestone signals, and 20 sets of the siltstone signals. The average accuracy of the signal prediction for the rocks was greater than 90%. It should be noted that all the signals for the granulite, the siltstone, and electrical noises were predicted by the ANN model. Only one set of the limestone AE signals was predicted to be generated by the granulite specimens, and two sets of the granite AE signals were predicted to be generated by the siltstone specimens. Four sets of the knock noise

TABLE 5: Signal type prediction using the ANN.

Signal types	Signal set number	Predicted results						Accuracy
		Granulite	Granite	Limestone	Siltstone	Electrical noise	Knock noise	
Granulite	20	20	0	0	0	0	0	100%
Granite	20	0	17	0	2	0	1	85%
Limestone	20	1	0	19	0	0	0	95%
Siltstone	20	0	0	0	20	0	0	100%
Electrical noise	20	0	0	0	0	20	0	100%
Knock noise	10	0	4	0	0	0	6	60%

signals were recognized as the granite signals, indicating that the signal waves generated by the granite specimens were much similar to the artificial knock signals. Influenced by the random factors and the environmental factors, the accuracy for the artificial knock noise recognition was as low as 60%. To achieve good monitoring results, manmade noises should be reduced or eliminated in laboratory AE tests on rocks.

5. Conclusions

The wavelet transform and artificial neural network were applied to determine rock types from their AE characteristic parameters. The wavelet transform was used to decompose the AE signals, and the artificial neural network (ANN) was established to recognize the rock types and noises (artificial knock noise and electrical noise). The following conclusions can be drawn.

- (1) Different rocks had different rupture features and AE characteristics. The wavelet transform provided a powerful method to acquire the basic characteristics of the rock AE and the environmental noises, such as the energy spectrum and the peak frequency. The signal parameters were input into the network, and the predicted results showed that the wavelet transform method was effective and accurate for AE signal decomposition.
- (2) The ANN was proved to be a good method to recognize AE signals from different types of rocks and the environmental noises. The AE signal parameters decomposed by the wavelet transform composed the input layer, the *tansig* function was selected as the transfer function of the hidden layer, and the *logsig* function was selected as the output layer. The average recognition accuracy of the four kinds of rock AE signals was above 95% in the BP neural network.
- (3) The signals generated by the granite specimens were much similar to the artificial knock signals. The electrical noises were easy to be recognized by the BP neural network, but it had a low accuracy for the artificial knock noise recognition. To avoid adjacent-channel interference, manmade noises should be reduced as much as possible in laboratory AE tests on rocks.

Conflict of Interests

The authors declare that there is no conflict of interests regarding the publication of this paper.

Acknowledgments

This work was supported by the National Program on Key Basic Research Project of China (973 Program) (Grant nos. 2014CB047100 and 2011CB013503), the National Natural Science Foundation of China (Grant nos. 51374088, 51174071, and 51274053), the Natural Science Foundation of Hebei (E2012209047), the Open Research Fund Program of the State Key Laboratory of Coal Mine Disaster Dynamics and Control (Chongqing University) (2011DA105287-FW201403), and the Scientific Research Projects of Colleges and University in Hebei Province (QN2014067).

References

- [1] R. O. Duda, P. E. Hart, and D. G. Stork, *Pattern Classification*, Wiley-Interscience, New York, NY, USA, 2nd edition, 2001.
- [2] A. H. Assi, *Engineering Education and Research Using MATLAB*, InTech, Rijeka, Croatia, 2011.
- [3] Z.-X. Yang, D.-Q. Feng, T.-J. Chen, and H. Wan, "Application of artificial neural networks to nondestructive testing," *Nondestructive Testing*, vol. 24, no. 6, pp. 244–252, 2002.
- [4] R. Yi, S. Liu, and R. Geng, "Application of artificial neural network to acoustic emission testing," *Nondestructive Testing*, vol. 24, no. 11, pp. 488–492, 2002.
- [5] C. Bhat, M. R. Bhat, and C. R. L. Murthy, "Acoustic emission characterization of failure modes in composites with ANN," *Composite Structures*, vol. 61, no. 3, pp. 213–220, 2003.
- [6] Z. Liang, N. Xu, K. Ma, S. Tang, and C. Tang, "Microseismic monitoring and numerical simulation of rock slope failure," *International Journal of Distributed Sensor Networks*, vol. 2013, Article ID 845191, 10 pages, 2013.
- [7] Z. Liang, X. Liu, Y. Zhang, and C. Tang, "Analysis of precursors prior to rock burst in granite tunnel using acoustic emission and far infrared monitoring," *Mathematical Problems in Engineering*, vol. 2013, Article ID 214340, 10 pages, 2013.
- [8] P. Lin, Q. B. Li, and P. Y. Jia, "A real-time temperature data transmission approach for intelligent cooling control of mass concrete," *Mathematical Problems in Engineering*, vol. 2014, Article ID 514606, 10 pages, 2014.

- [9] P. Lin, Q. B. Li, and H. Hu, "A flexible network structure for temperature monitoring of a super high arch dam," *International Journal of Distributed Sensor Networks*, vol. 2012, Article ID 917849, 10 pages, 2012.
- [10] T.-H. Yi, H.-N. Li, and X.-D. Zhang, "Sensor placement on Canton Tower for health monitoring using asynchronous-climb monkey algorithm," *Smart Materials and Structures*, vol. 21, no. 12, Article ID 125023, pp. 1–12, 2012.
- [11] T.-H. Yi, H.-N. Li, and M. Gu, "Optimal sensor placement for structural health monitoring based on multiple optimization strategies," *The Structural Design of Tall and Special Buildings*, vol. 20, no. 7, pp. 881–900, 2011.
- [12] J.-S. Kwak and J.-B. Song, "Trouble diagnosis of the grinding process by using acoustic emission signals," *International Journal of Machine Tools and Manufacture*, vol. 41, no. 6, pp. 899–913, 2001.
- [13] C. Leone, G. Caprino, and I. de Iorio, "Interpreting acoustic emission signals by artificial neural networks to predict the residual strength of pre-fatigued GFRP laminates," *Composites Science and Technology*, vol. 66, no. 2, pp. 233–239, 2006.
- [14] I. Grabec and E. Kuljanić, "Characterization of manufacturing processes based upon acoustic emission analysis by neural networks," *CIRP Annals: Manufacturing Technology*, vol. 43, no. 1, pp. 77–80, 1994.
- [15] J.-S. Kwak and M.-K. Ha, "Neural network approach for diagnosis of grinding operation by acoustic emission and power signals," *Journal of Materials Processing Technology*, vol. 147, no. 1, pp. 65–71, 2004.
- [16] B. Samanta and K. R. Al-Balushi, "Artificial neural network based fault diagnostics of rolling element bearings using time-domain features," *Mechanical Systems and Signal Processing*, vol. 17, no. 2, pp. 317–328, 2003.
- [17] B. Samanta, K. R. Al-Balushi, and S. A. Al-Araimi, "Artificial neural networks and support vector machines with genetic algorithm for bearing fault detection," *Engineering Applications of Artificial Intelligence*, vol. 16, no. 7-8, pp. 657–665, 2003.
- [18] K. B. Kim, D. J. Yoon, J. C. Jeong, and S. S. Lee, "Determining the stress intensity factor of a material with an artificial neural network from acoustic emission measurements," *NDT and E International*, vol. 37, no. 6, pp. 423–429, 2004.
- [19] E. V. K. Hill, P. L. Israel, and G. L. Knotts, "Neural network prediction of aluminum-lithium weld strengths from acoustic emission amplitude data," *Materials Evaluation*, vol. 51, no. 9, pp. 1040–1045, 1993.
- [20] R. Wu, Z. Liao, L. Zhao, and X. Kong, "Wavelets application in acoustic emission signal detection of wire related events in pipeline," *Canadian Acoustics*, vol. 36, no. 2, pp. 96–103, 2008.

Research Article

Life-Cycle Monitoring of Long-Span PSC Box Girder Bridges through Distributed Sensor Network: Strategies, Methods, and Applications

Zheheng Chen,¹ Tong Guo,¹ and Shengyou Yan²

¹Key Laboratory of Concrete and Prestressed Concrete Structure, School of Civil Engineering, Ministry of Education, Southeast University, Nanjing 210096, China

²Jiangsu Province Communications Planning and Design Institute, Nanjing 210005, China

Correspondence should be addressed to Tong Guo; guotong77@gmail.com

Received 1 August 2014; Accepted 20 September 2014

Academic Editor: Ting-Hua Yi

Copyright © 2015 Zheheng Chen et al. This is an open access article distributed under the Creative Commons Attribution License, which permits unrestricted use, distribution, and reproduction in any medium, provided the original work is properly cited.

Structural health monitoring (SHM) has attracted much attention in recent years, which enables early warnings of structural failure, condition assessments, and rational maintenance/repair strategies. In the context of bridges, many long-span steel bridges in China have been installed with the SHM systems; however, the applications of the SHM in prestressed concrete (PSC) bridges are still rather limited. On the other hand, the PSC box girder bridges are extensively used in highway and railway systems and premature damage of these bridges is often reported, resulting in considerable maintenance and/or replacement costs. First, this paper presents a state-of-art review on the SHM of long-span PSC bridges. Monitoring strategies, methods, and previous applications for these bridges are summarized and discussed. In order to well capture the behavior of the bridge during its whole life and to maximize the use of sensors, a life-cycle monitoring strategy is proposed, in which the sensor layout is determined according to requirements for construction monitoring, completion test, and in-service monitoring. A case study is made on a three-span PSC box girder bridge in China. The system configuration, sensor layout, and data communications, and so forth, are presented. The up-to-date monitored structural responses are analyzed and compared with the design values.

1. Introduction

Structural health monitoring (SHM) through distributed sensor network has attracted much attention in recent years [1–5], which enables early warnings of structural failure, condition assessments, and rational maintenance/repair strategies. In the context of bridges, many long-span steel bridges in China as well as in other parts of the world have been installed with the SHM systems; however, applications of the SHM in prestressed concrete (PSC) bridges are still rather limited. On the other hand, the PSC box girder bridges are extensively used in highway and railway systems, and premature damage of these bridges is often reported (i.e., cracks and excessive long-term deflections, etc.), resulting in considerable maintenance and/or replacement costs. Therefore, it is of great importance to develop a specific SHM system for the PSC bridges.

However, as compared with long-span steel bridges, there are several significant differences in the monitoring systems of the PSC bridges. First, the long-span steel bridges usually have longer main spans and are cable-supported; as a result, they are sensitive to vibration. Moreover, higher safety margin is often adopted in the design of supper long-span bridges, considering the catastrophic results or tremendous losses due to collapse. Besides, these bridges usually have high construction budget. For example, the Sutong Bridge [6], with a main span of 1,088 m, costs about 1,450 million USD. Accordingly, it allows a more flexible budget on the SHM system, which is only a very small part of the total cost of the bridge. Therefore, a total number of 1,440 various sensors, that is, anemometers, accelerometers, strain gauges, displacement gauges, GPS, thermistors, humidity meter, clinometers, and corrosion gauges, and so forth, could be installed on the long-span steel bridges.

As to the PSC bridges, they are usually shorter in spans (i.e., ranging from 50 m to 250 m). Larger structural stiffness makes them much less sensitive to vibration. However, some time-dependent behaviors, including shrinkage and creep of concrete and stress relaxation of steel tendons, are important features of the PSC bridges, which result in the loss in prestress of tendons and increase in deflection. Besides, temperature gradient has a significant influence on the behavior of the PSC bridges. However, due to the limit on the construction budget and difficulties in monitoring, only a limited number of items could be monitored.

This paper reports the recent investigation on the SHM systems of long-span (i.e., with the main span of 100 to 300 m) PSC bridges, and discussion is made on the monitoring strategies, methods, and existing applications. A life-cycle monitoring strategy is proposed, which covers the construction stage, completion test, and the service stage, so as to better capture the behavior of the bridge during its whole life and to maximize the use of sensors. A case study in China is provided to further demonstrate the feasibility of the proposed system.

2. Monitoring Strategies, Methods, and Applications

2.1. Monitoring Strategies. A brief summary of the monitoring items of PSC bridges all over the world in recent years [4–21] is provided in Table 1, where it is observed that the monitoring items vary due to different investigation purposes, bridge types, and budgets, and so forth. For example, according to the visual inspection on the Ferriby Road Bridge [12], a three-span skew reinforced concrete slab bridge, several defects were noted which may require maintenance in the future. Therefore, inclinometers were used on elastomeric bearings, and displacement transducers were installed across cracks on the soffit of the slab, which provide basis for the maintenance activities. After the famous collapse accident of the old I35W Bridge, the new I35W Bridge [7] was built, which consists of two prestressed concrete box girders in each traffic direction. To monitor the behavior of the new bridge, a large number of sensors were installed, including vibrating-wire strain gauges, thermistors, linear potentiometers, accelerometers, corrosion sensors, long-gauge fiber, and topography instruments, which monitor the local static strain, temperature, joint and bearings movements, vibrations, corrosion current, average strains, and global deformations, respectively. These sensors provide good data base for the study of long-term performance of the PSC bridges, such as creep, shrinkage, prestress loss, and long-term deflections. In 2008, the Federal Highway Administration (FHWA) launched the Long-Term Bridge Performance (LTBP) program [8], which intended to collect scientific-quality data from the Nation's highway bridges through a minimum 20-year research effort. In the Utah State, several pilot bridges were selected, and sensors including velocity transducers, foil strain gauges, vibrating wire strain gauges, tilt meters, thermocouples, weather station, and traffic camera were installed. According to Table 1, deflection and temperature are the two most frequent monitoring items,

followed by the strain, acceleration, and so forth. Although cracks, corrosion, and prestress loss are also important to PSC bridges, they are difficult to be monitored. Therefore, they are not frequently adopted as monitoring items. In general, the monitoring strategies should be determined according to the monitoring purpose, budget, and the feasibility of monitoring technologies. However, deflection and temperature are two basic monitoring items and should be included.

In addition to the in-service monitoring, monitoring and control on the construction stage and completion tests are also frequently conducted for large bridges, which provide valuable information of the bridges in various stages. However, in real practice, the monitoring in construction stage, completion tests, and service stage are usually separately conducted without sharing of sensors and information, which is waste of construction investment. On the other hand, the sensors used for construction monitoring and control may be well used in the subsequent stages (i.e., completion test and in-service monitoring). Monitored data (i.e., deflection, stress, etc.) in the construction stage and completion tests describe the initial status of the in-service monitoring. The loads in the completion tests are known so that the results of completion tests can be used to determine the major structural parameters and update the baseline finite element (FE) model, providing basis for health monitoring and damage identification in the service stage. Therefore, a life-cycle monitoring strategy is proposed, as shown in Figure 1, in which it is required that the monitoring in construction stage, completion tests, and service stage should be combined to minimize the monitoring costs and maximize the data utilization. In Figure 1, sharing of sensors, data, and condition parameters are illustrated through red, blue, and green lines, respectively.

2.2. Monitoring Methods. As shown in Table 1, deflection is one important monitoring item. Periodical measurement on the bridge through topography is an acceptable choice, but it is not continuous and costly. In the new I35W Bridge, long-gauge fiber optic sensors were used to measure the strain distribution and thus to obtain the average curvature and deformed shape. However, this method requires the fibers to be adhered to the soffit of the girder, which is somewhat difficult in practice. Breakage of fibers and the long-term durability are also concerns of such a method.

On the Jiangjin Yangtze River Highway Bridge with a main span of 240 m, laser video deflection measurement system (LVDMS) was used to monitor the long-term deflection [20]. As deflection at the measuring point occurs, the light spots projected to the projection target move in the opposite direction; see Figure 2(a). The spots shot by the camera can thus be digitalized and be input to the computer to calculate the displacement relative to the fixed point. However, when there are a number of measuring points, multiple laser transmitters must be installed at multiple fixed points of the bridge while it is usually difficult to find so many appropriate installation positions in practice. Similar application was made on the Alwen Bridge [21], where the noncontact Weighted-Stretched-Wire System (NWSWS) was adopted for deflection monitoring. As shown in Figure 2(b),

TABLE 1: Summary of monitoring items on PSC bridges.

Bridge name	Monitoring Items									
	Strain	Deflection or rotation	Support displacement	Acceleration or velocity	Corrosion	Crack	Prestress loss	Traffic camera	Temperature	Weather station
Ferriby Road Bridge (UK)		✓				✓				
PI-57 Bridge (France)				✓					✓	
Lezíria Bridge (Portugal)	✓	✓	✓						✓	
401 Southbound Bridge (USA)	✓	✓	✓				✓		✓	
California Pilot Bridge (USA)	✓	✓		✓				✓	✓	
Utah Pilot Bridge (USA)	✓	✓		✓				✓	✓	✓
Kishwaukee Bridge (USA)	✓			✓		✓			✓	
New I35W Bridge (USA)	✓	✓	✓	✓	✓				✓	
Kamikazue Viaduct (USA)							✓			
A curved bridge (USA)		✓		✓					✓	
West Street On-ramp Bridge (USA)				✓						
North Halawa Valley Viaduct (USA)		✓	✓							
Zhaoqing Xijiang Bridge (China)	✓								✓	
Chongqing Shibampo Bridge (China)	✓	✓							✓	
Xushuigou Bridge (China)	✓	✓							✓	
Jiangjin Yangtze River Highway Bridge (China)	✓	✓				✓			✓	
Anwen Bridge (China)		✓							✓	
Monitored items in total	9	12	4	7	1	2	2	2	12	1

the camera fixed on the bridge moves as deflection occurs, so that the projection of the stretched-wire changes correspondingly. The deflection can thus be obtained by recording and analyzing such movements. Due to that the elevations of the soffits at midspan and piers of long-span PSC bridges vary considerably, installation and maintenance of such systems may be difficult.

On the Jinghang Canal Bridge, as to be presented in detail, a vertical displacement transducer (DT) was adopted to measure the long-term deflection of bridge, based on a hydrostatic leveling system and the application of the communicating vessels principle to an internal hydraulic

system, filled with antifreeze fluid, which is installed along the bridge and reaches the relevant points where the relative vertical displacement is going to be measured. As shown in Figures 2(c) and 2(d), this hydraulic system, in hydrostatic equilibrium, allows the monitoring of the structure's deformed shape through the measuring of the apparent liquid level height at given points and comparing it with reference points where the vertical displacement can be neglected. To avoid the evaporation of the fluid, silicon oil was placed on its surface. The resolution and measurement precision are 0.01 mm and 0.1 mm, respectively. Similar displacement monitoring system has been used on the Lezíria Bridge [9].

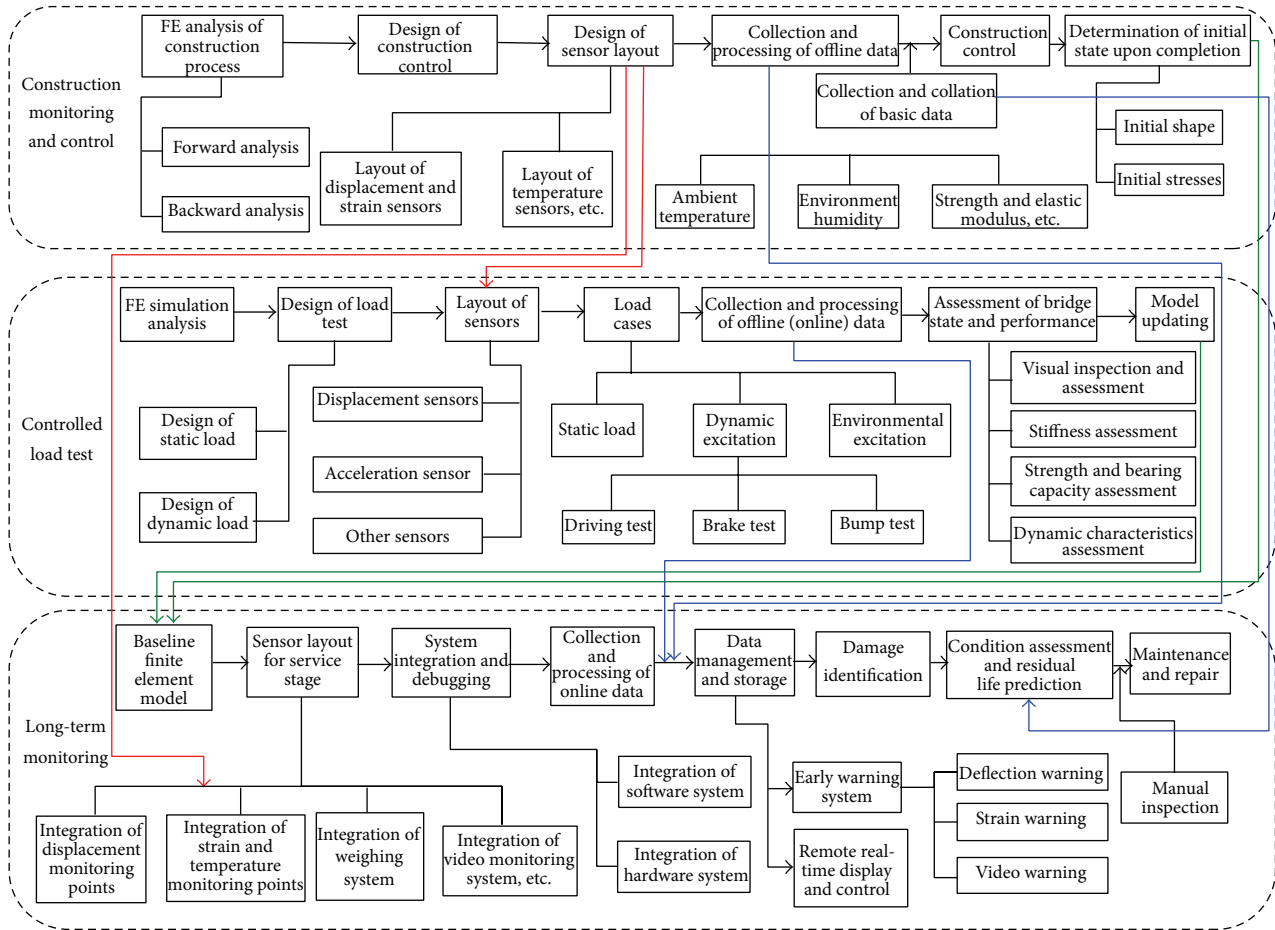


FIGURE 1: Life-cycle monitoring of PSC bridges.

As to the monitoring of prestress loss, most existing applications are for the external tendons. The most commonly used method to measure the posttensioning tendon stress is by attaching strain gages to the strands that form the tendons. However, this method is not applicable when the epoxy-coated strands are used for tendons. For the unbonded tendons, load cell at the ends of anchorage is also an efficient way to monitor the forces. On the US 401 Southbound Bridge [10], which utilized prestressed high performance concrete (HPC) girders, load cells were adopted at the anchorage ends to measure the time-dependent tendon forces; however, the forces at certain points of the tendon cannot be measured using this method. In recent years, the elastomagnetic (EM) sensing has been developed as a nondestructive testing technology, which is based on the elastomagnetic effect of ferromagnetic materials. Subject to external forces, strains or stresses develop in the ferromagnetic material, resulting in the change in magnetic permeability. Thus, the variation in tendon forces can be measured through the measurement on magnetic permeability, as shown in Figure 3. The beneficial features of the EM sensors include (1) noncontact measurement so that the influence on the structure is minimized; (2) rapid response, desirable precision, and reliability; (3) long-term and long-distance monitoring, and (4) monitoring on bonded tendons at multiple cross sections. Pilot study was

made on the Kishwaukee River Bridge [11] (with unbonded tendons) and some bridges in China (with bonded tendons).

Monitoring on cracks is also an important measure to know the evolution of such defects on bridges. Two linear potentiometric displacement transducers (LPDTs) are usually used for such measurements. One of the LPDTs is placed across a crack on the deck soffit and the other is placed across an uncracked region of concrete for temperature compensation [12]. However, this method is only applicable to existing cracks, and only one point could be measured. Recently developed optical fiber based technologies, however, bring possibility to the distributed monitoring by placing the fibers along the concerned area. Existing methods include the BOTDR, the BOTDA (or the PPP-BOTDA), and the long-gauge FBG sensors. Higher resolution and better durability are required for these methods to be applied in real monitoring projects rather than laboratory tests and pilot studies.

Considering that the monitoring of PSC bridges is usually subjected to limited budget, an efficient data collecting and transportation way is required. In this regard, wireless network is more appealing than traditional wire-based methods, as shown in Figure 4. However, the amount of data is also limited. Therefore, data are usually collected and sent in a static or quasistatic way with a relatively low frequency, ranging from 1/60 Hz to 1/600 Hz. In addition, there is not

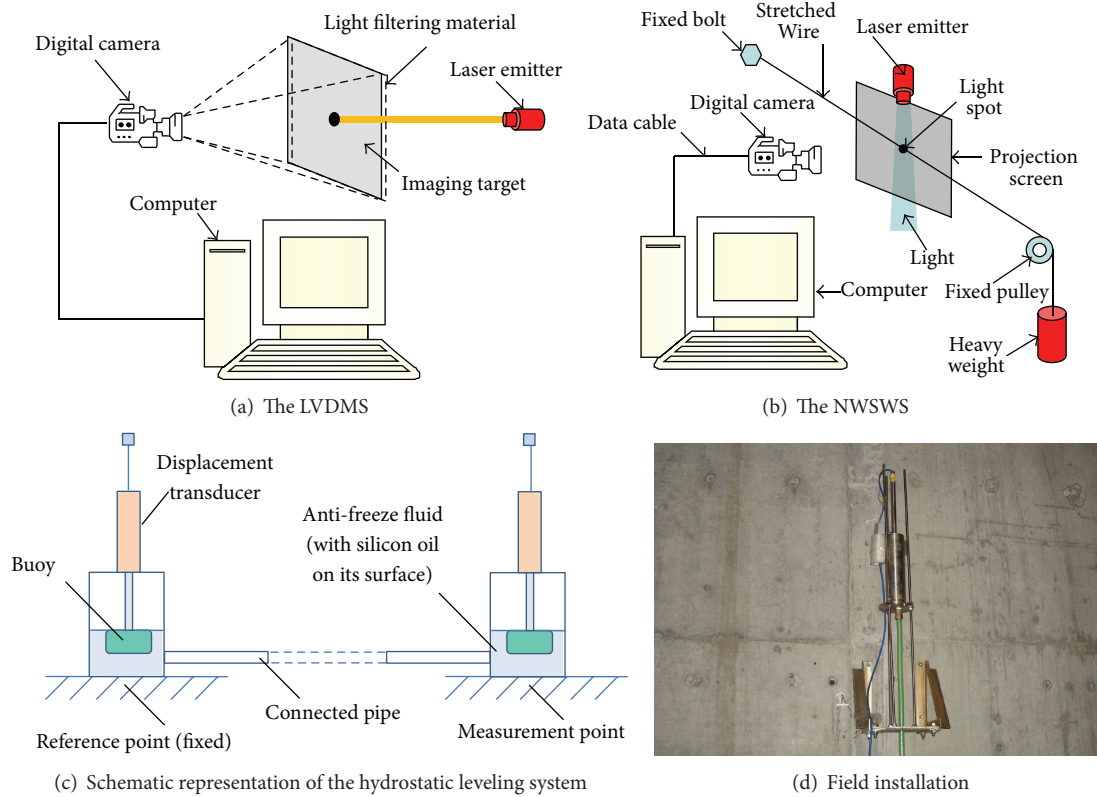


FIGURE 2: Several deflection monitoring systems.

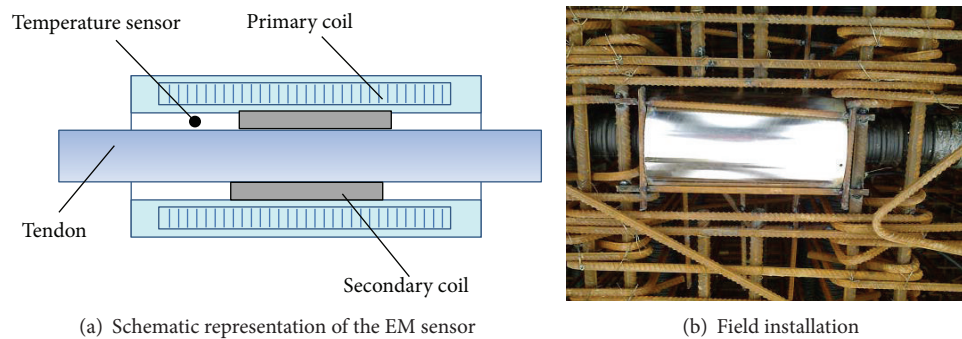


FIGURE 3: Prestress monitoring using EM sensors.

usually a specific monitoring room near these bridges for power supply. Batteries or solar panels are often used instead. However, it is also a good choice to utilize the power from the road lighting system.

Other monitoring items, such as strain, temperature, acceleration, support displacements and corrosion, have been extensively applied and therefore are not repeated here.

3. Case Study

3.1. Bridge under Investigation. The Jinghang Canal Bridge (JCB) is a three-span PSC bridge in Suzhou, China. It has one main span of 150 m and two side spans of 85 m, respectively,

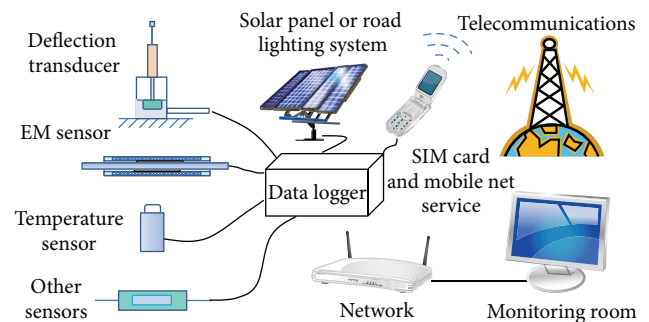


FIGURE 4: Configuration of the monitoring system using wireless network.

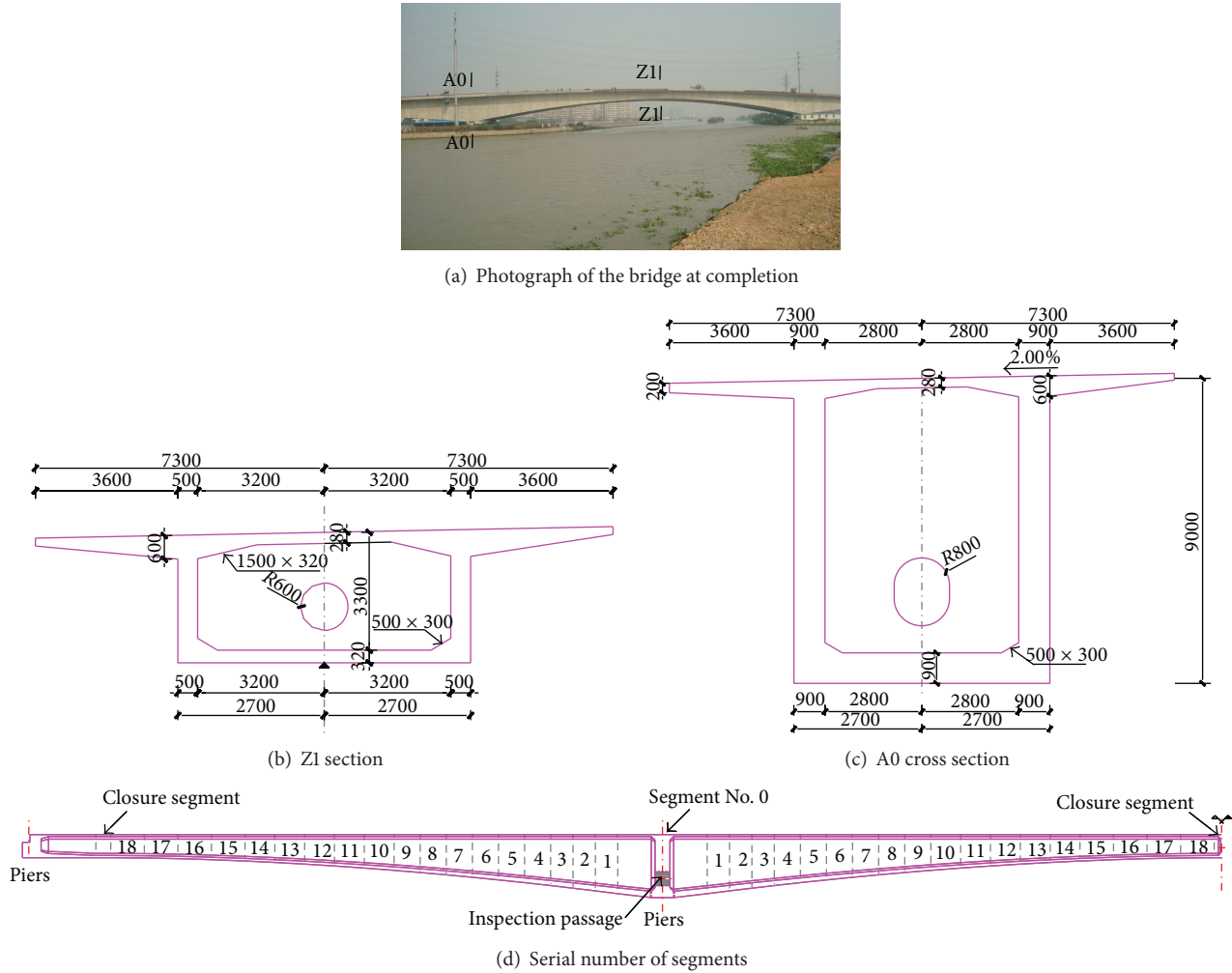


FIGURE 5: Profile and cross sections of the Jinghang Canal Bridge (dimensions in mm).

as shown in Figures 5(a), 5(b), and 5(c). The bridge consists of two separated single-cell box girders in two traffic directions. The top slab of the girder has a total width of 14.6 m and the length of its cantilever is 3.6 m. The width of the bottom flange is 7.4 m and its thickness varies from 90 cm at the supports to 32 cm at the midspan. The height of box girder ranges from 9.0 m at the supports to 3.3 m at the midspan. The web thickness ranges in steps from 90 cm at the supports to 50 cm at the midspan. The main structure was completed on October 29, 2013 and the pavement construction was added by December 15, 2013. The bridge was open to traffic in January, 2014. Figure 5(d) shows the arrangement of the box girder and the Table 2 shows the detailed construction process of the bridge.

According to the monitoring strategy depicted in Section 2, the sensor layout for the monitoring in construction, completion test, and service stages is determined, as shown in Figure 6. In the construction stage, the stresses, and elevations are the emphasis. The construction process of superstructure, as listed in Table 2, lasted for about 237 days. As shown in Figure 6, the across sections with relatively large longitudinal stresses were selected for monitoring, where

sections A1 to A4 are at the end of the segment number 0, sections B1 and B2 are at the middle of the side spans, and sections Z1, Z2, and Z3 are at the midspan and 1/4 span of the main span, respectively. During the completion tests, the stresses sensors for construction monitoring were used, and acceleration sensors were installed to measure the dynamic responses. As to the long-term monitoring, the items include the temperature, strain of reinforcement, and deflections, as shown in Figure 6. In order to minimize the cost of the system, long-term monitoring of temperature and strains utilized some sensors embedded in the bridge for construction monitoring. These sensors are vibrating string gauges with built-in temperature couples, so that strain and temperature can be measured at the same time. The data were collected automatically through the JMBV-8A acquisition module, as shown in Figure 7, and each module has eight channels. The data were collected with a 10 min interval, that is, a sampling rate of 1/600 Hz.

The long-term deflection monitoring used the hydrostatic leveling system, as shown in Figures 2(c), 2(d), and 7(b). Six cross sections were selected for monitoring, including the midspan and 1/4 span of the main span and the side span,

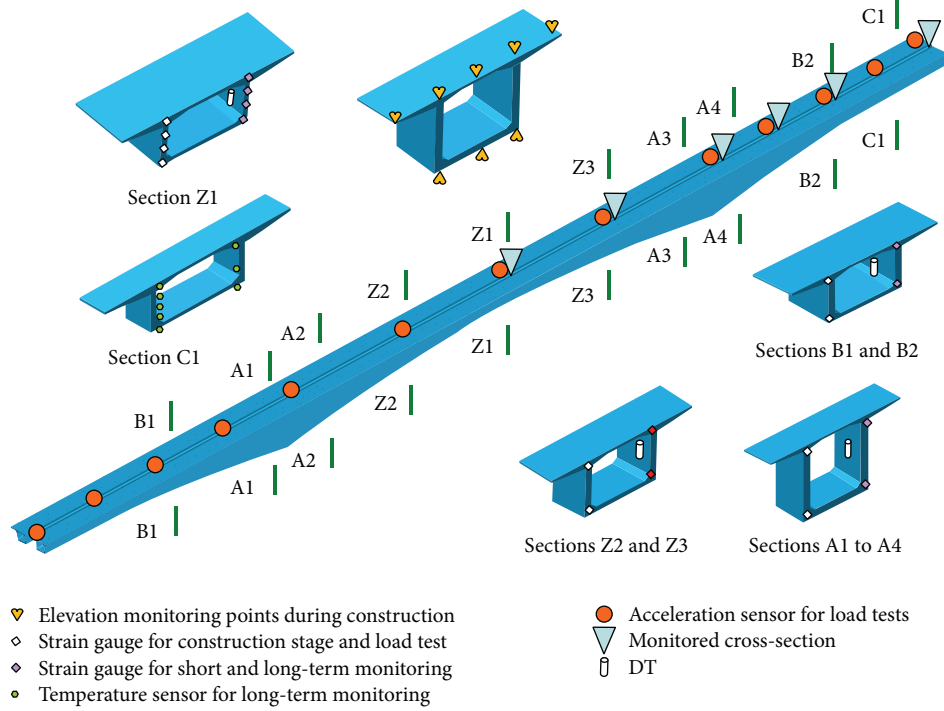


FIGURE 6: Configuration of the monitoring system.

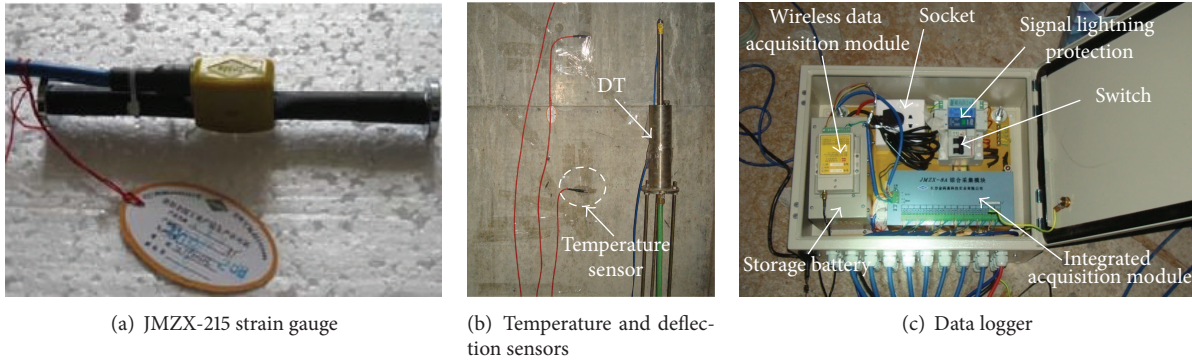


FIGURE 7: Sensors for long-term monitoring.

and two reference cross sections at the piers of main span and side span. Considering the longitudinal slope of this bridge is high (4%), it is not possible to place all the six measuring points at the same elevation. Therefore, two separate systems were adopted. Measuring points at the midspan and 1/4 span of the main span and its support are of the same elevation, while points at the midspan and 1/4 span of the side span and its support are of the same elevation. Each DT was installed on the inner surface of the web of the box girder, as shown in Figure 6. All the measuring points, however, were collected in series through one power cable and one signal cable, and they are finally collected to the bus interface module. All the data were finally sent to the monitoring room at the Southeast University hundreds kilometers away from the bridge site in a wireless way, as shown in Figure 4. The power of the SHM system is supplied by the road lighting system. The total SHM

system is very cheap as compared with those on the long-span steel bridges. Not including the sensors for construction monitoring, the total cost is only about 30 thousand US dollars.

3.2. Monitoring in the Construction Stage. According to Figures 8(a) and 8(b), the monitored stresses agree with the design values. The largest difference between the stresses in the top plates at the upstream side and the design values is 2.23 MPa, which occurred when the segment number 14 was cast, while the largest difference at the downstream side is 2.05 MPa, which occurred as the segment number 7 was cast. The largest differences between the stresses at the bottom plates and the design values are 1.92 MPa and 2.06 MPa, respectively, which occurred during the closure of bridge at midspan. After the completion of main girder,

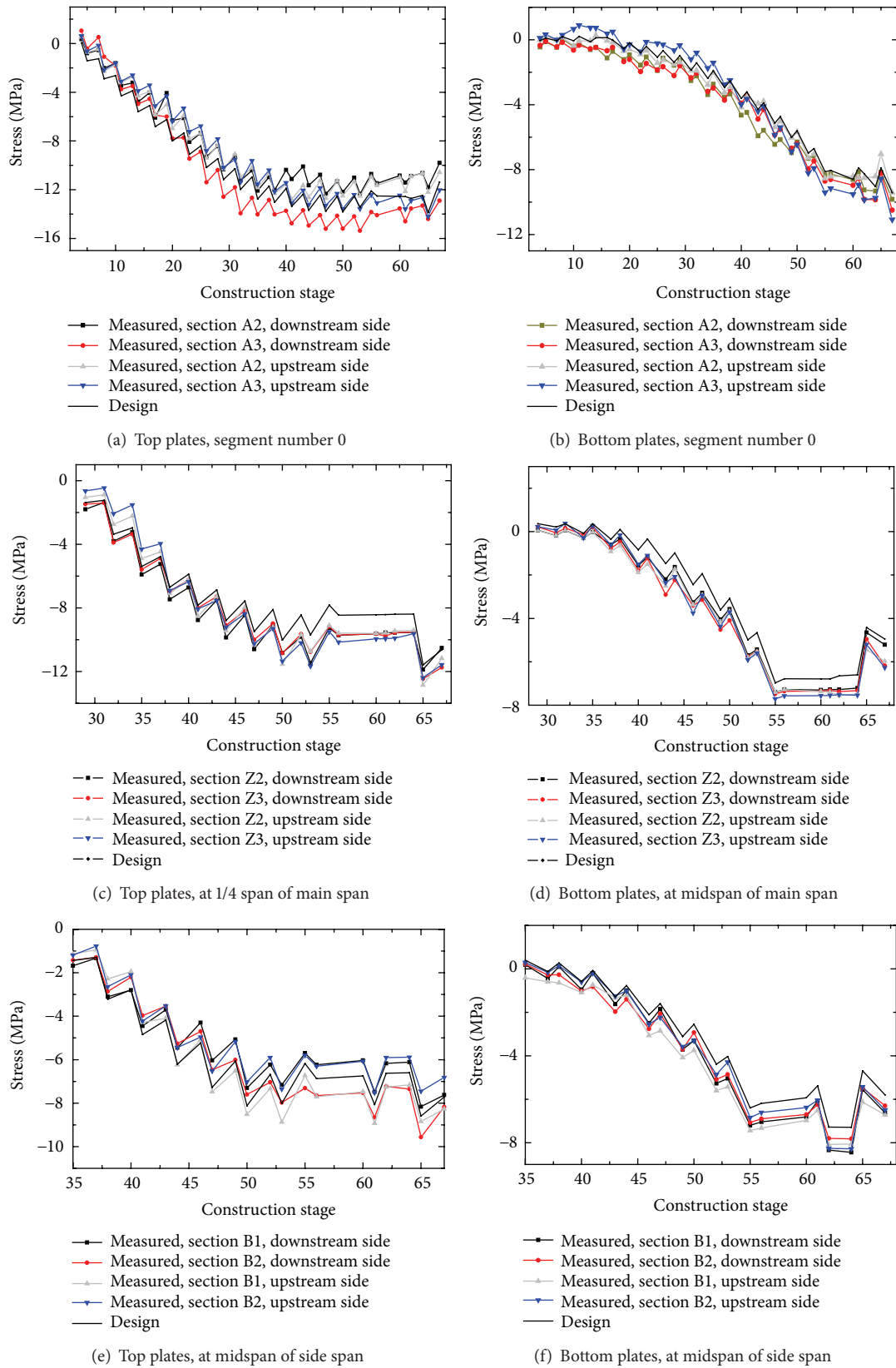


FIGURE 8: Stresses in various construction stages.

TABLE 2: Construction process of superstructure of the Jinghang Canal Bridge.

Construction stage	Construction contents	Duration (day)	Cumulated time (day)
1	Concrete casting of segment number 0	11	11
2	Jacking of tendons in segment number 0	1	12
3	Temporary consolidation and installation of hanging baskets	3	15
4	Concrete casting of segment number 1	7	22
5	Jacking of tendons in segment number 1	1	23
6	Moving forward of hanging baskets	1	24
7	Concrete casting of segment number 2	7	31
8	Jacking of tendons in segment number 2	1	32
9	Moving forward of hanging baskets	1	33
10	Concrete casting of segment number 3	7	40
11	Jacking of tendons in segment number 3	1	41
12 to 54	Concrete casting of segments number 4 to number 17	12 per segment	160
55	Concrete casting of segment number 18	7	167
56	Jacking of tendons in segment number 18	1	168
57	Concrete casting of straight segments in both side spans using brackets	1	170
58	Converting hanging baskets into hoisting baskets in side spans	2	172
59	Counterweight of water tank in both side spans and central span, and installation of stiff steel framework.	1	173
60	Casting of closure segments in side spans and removal of counterweight	7	180
61	Jacking of closure tendons in side spans	3	183
62	Removal of brackets in side spans and temporary consolidation	4	187
63	Converting hanging baskets into hoisting baskets in main spans	2	191
64	Concrete casting of closure segment in main span and removal of counterweight	7	198
65	Jacking of closure tendons in central span	3	201
66	Removal of hoisting baskets in both side and main spans	1	202
67	Construction of bridge deck pavement	35	237

the cross sections have relatively large compressive stresses, which provide desirable conditions for the bridge service.

Figures 8(c) and 8(d) show the monitored stresses at the 1/4 spans of the main span. The largest differences between monitored stress and design values are 1.77 MPa and 1.98 MPa for top plates at upstream and downstream sides, respectively, which both occurred as the tendons in segment number 17 were jacked. The stress differences in bottom plates at the upstream and downstream sides are within 1 MPa. In general, the top plates have larger compressive stresses than the bottom plates.

As to the midspan cross section of the side spans, the comparison between monitored data and calculation is illustrated in Figures 8(e) and 8(f). The largest differences of the stress in the top plates at the upstream and downstream sides are 1.24 MPa and 1.14 MPa, which occurred at the jacking of

tendons in segment number 15 and the closure of the bridge, respectively. For the bottom plates, the largest differences are 1.15 MPa and 1.44 MPa, respectively, which both occurred at the closure of the bridge.

The alignment control of the bridge is an important job which is conducted by controlling the elevations of segments dynamically during the construction process. As shown in Figure 6, there are three monitoring points at the top and bottom plates, respectively, to monitor the deflections, and two monitoring points at two slabs to control the torsion during the construction. For each segment, elevation monitoring is conducted during the installation of form work, before and after concrete casting, before and after jacking of tendons. Through error analysis, the elevation of the next segment is determined. Figure 9 shows the differences in monitored and design elevations upon closure of the bridge, where the largest

TABLE 3: Description of load cases.

Load test	Truck positions	Illustration
Case 1	Nine trucks, symmetrically loaded at the side span in 2 lines and 3 rows	
Case 2	Nine trucks, loaded near the middle of main span in 2 lines and 3 rows; another truck, loaded in the emergency vehicle lane	
Case 3	Nine trucks, loaded near the 1/4 of main span in 2 lines and 3 rows	
Case 4	Nine trucks, loaded at the midspan of main span in 2 lines and 3 rows	

TABLE 4: Stress analysis of test results (upstream).

Load test	Monitored section	Position	Total stress (MPa)	Elastic stress (MPa)	Theoretical stress (MPa)	Residual stress (MPa)	Check coefficient	Relative residual stress (%)
Case 1	B1	Top flange	-1.00	-0.96	-1.90	-0.04	0.51	4.26
		Bottom flange	1.64	1.5	2.60	0.14	0.58	8.53
Case 2	A1	Top flange	0.22	0.2	1.40	0.02	0.14	7.42
		Bottom flange	-1.21	-1.08	-1.50	-0.13	0.72	10.40
Case 3	Z1	Top flange	-0.56	-0.48	-0.90	-0.08	0.53	14.65
		Bottom flange	0.67	0.62	1.10	0.05	0.56	7.51
Case 4	Z2	Top flange	-2.93	-2.76	-2.90	-0.17	0.95	5.79
		Bottom flange	3.20	3.09	4.60	0.11	0.67	3.41

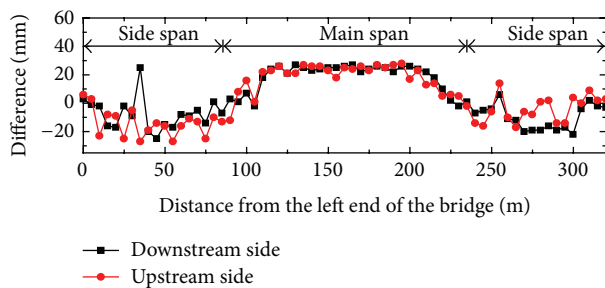


FIGURE 9: Differences between monitored and design elevations.

difference is 28 mm, which is within the maximum permitted error of $L/5000$ (i.e., 30 mm) [22].

3.3. Monitoring in the Completion Tests. The completion tests were conducted on January 14th, 2014, in which both static load tests and dynamic tests were made. In the static tests, there were four load cases, as shown in Table 3, where nine or ten trucks, each with a weight of 350 kN, were adopted. The front axle weight and the two rear axle weights of the trucks

are 70 kN and 140 kN, respectively; and the axle spacing is 350 cm and 135 cm, respectively.

Taking the test results of the upstream girder as examples, the stress and deflection responses are illustrated in Tables 4 and 5, respectively. Both the check coefficients [22] of stress and deflection are all less than 1, indicating that the structure has required bearing capacity and the vertical stiffness. In addition, the relative residual strain and deformation after unloading are less than 20%, indicating that the box girder has desirable restoring ability subjected to the test loads, and the structure basically behaved linear elastically during the tests.

Dynamic load test used the typical pulse method [23]; that is, through collecting microvibration of bridge caused by ambient excitation, the dynamic characteristics of structure, such as vibration frequency, vibration mode, and damping ratio, are obtained. The layout of acceleration sensors is illustrated in Figure 6. Figure 10 shows two typical vibration modes with the corresponding frequencies of 1.11 Hz and 1.58 Hz, respectively, which are, however, slightly larger than the design values (i.e., 1.02 Hz and 1.37 Hz), indicating that the actual stiffness is larger than expected so that the analytical model should be updated accordingly.

TABLE 5: Deflection analysis of test results (upstream side).

Load test	Monitored section	Total deflection (mm)	Elastic deflection (mm)	Theoretical deflection (mm)	Residual deflection (mm)	Check coefficient	Relative residual deformation (%)
Case 1	B1	-16.75	-15.34	-21.7	-1.41	0.71	8.42
Case 3	Z1	-18.41	-15.86	-18.4	-2.55	0.86	13.85
Case 4	Z2	-45.63	-42.13	-58.5	-3.50	0.72	7.67

TABLE 6: Measured DAFs in different tests.

Test	Speed	Amplitude (mm)	Static deflection (mm)	Impact factor	
				Measured value	Design value
Running	10 km/h	0.054	6.7	1.001	1.05
	30 km/h	0.108		1.016	
	50 km/h	0.143		1.021	
Braking	10 km/h	0.117		1.017	
	30 km/h	0.095		1.014	
	50 km/h	0.165		1.025	
Jumping	30 km/h	0.460		—	

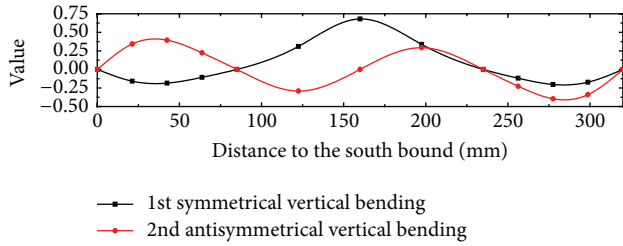


FIGURE 10: Typical tested bending modes.

The dynamic amplification factor (DAF) is another important parameter in bridge design, which was tested under different test circumstances. First, a truck with a weight of 350 kN runs across the bridge at various constant speeds, and the deflection time-history at the midspan was recorded, as shown in Figure 11(a), in which the truck runs at a speed of 30 km/h. In the brake performance test, the same truck ran at the same speed but braked at the midspan. According to Figure 11(a), the deflection time-history is similar to that of the running test. Table 6 further shows that the DAFs in running tests are basically the same with the braking tests, and they changed little with the increase of vehicle speed. The maximum value of impact factor is 1.04, which was in the jumping condition, as shown in Figure 11(b). However, it is still less than the design value of 1.05. In general, the dynamic deflection under vehicle moving deflection is small, showing the desirable dynamic deflection performance.

3.4. Monitoring during the Service Stage. Up to May, 2014, the SHM system of the bridge has been working for more than four and a half months. Figure 12 illustrates the time-dependent deflections at different measuring points after the pavements were constructed. Note that the pavements were added to the decks about 1.5 months after the completion of

the main structure. It is observed that from Figure 12(a) that the deflection fluctuates within a day [24], which is mainly due to the temperature changes in the day and night. Besides, the deflection in general becomes larger as time goes by, which is mainly due to shrinkage and creep of concrete. The deflections of midspan cross section of the main span increase by 15.10 mm and 26.73 mm, 3 month and 6 month after the completion of construction, respectively. On the midspan and 1/4 cross sections of side span, as shown in Figure 12(b), the chambers are observed to increase with time, though they are much less than the deflections in Figure 12(a) because the side spans are significantly shorter than the main span.

Figure 13 illustrates the strain time-histories of the reinforcements at different locations of the bridge. Due to the electromagnetic noise (i.e., the noise inherent in typical data acquisition), there are a number of abnormal signals; however, when these data are filtered, the time-dependent changes could still be observed. According to Figure 13, there are still some daily fluctuations in strain data at all locations, which is probably due to the change in ambient temperature. For the reinforcing bar in the top flange of the main span support, as shown in Figure 13(a), the strain increment is insignificant indicating that concrete shrinkage or creep is not significant in this region, which is possibly due to the large reinforcement ratio and the stress condition at the bridge support. However, there is a mild increase in strain of the reinforcing bar in top flange of midspan section of the main span, as shown in Figure 13(b), showing that the creep effect might be more significant in this region. In general, due to the short monitoring period, the strain increments are not large at all monitoring points [25].

Shown in Figure 14 are the monitored temperature time-histories on June 29th, 2014, where the S-shape curves are observed and the temperatures also vary at different locations. The largest daily temperature fluctuation (from

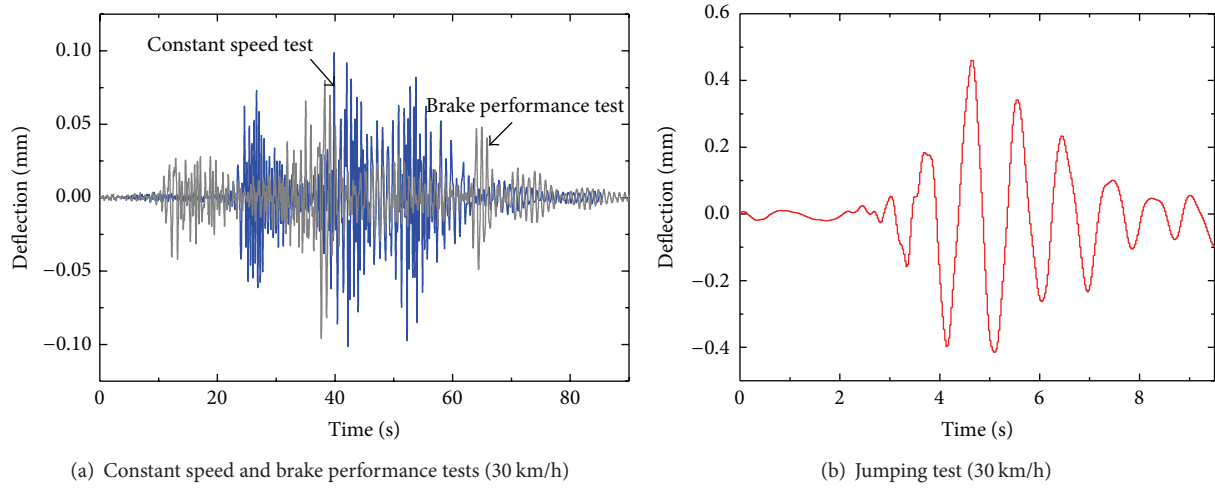


FIGURE 11: Deflection time-histories in dynamic tests.

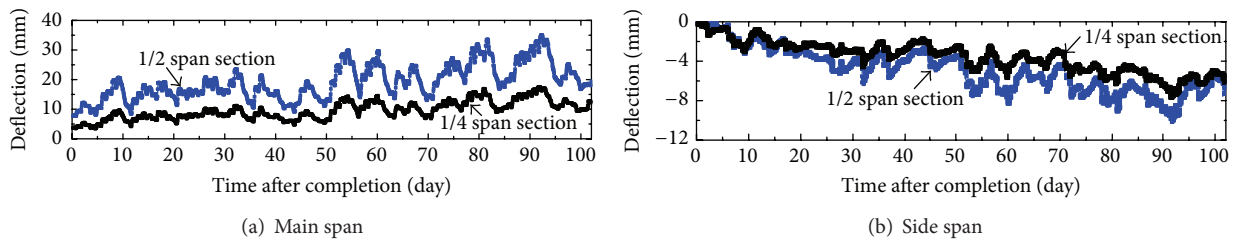


FIGURE 12: Monitored deflection time-histories.

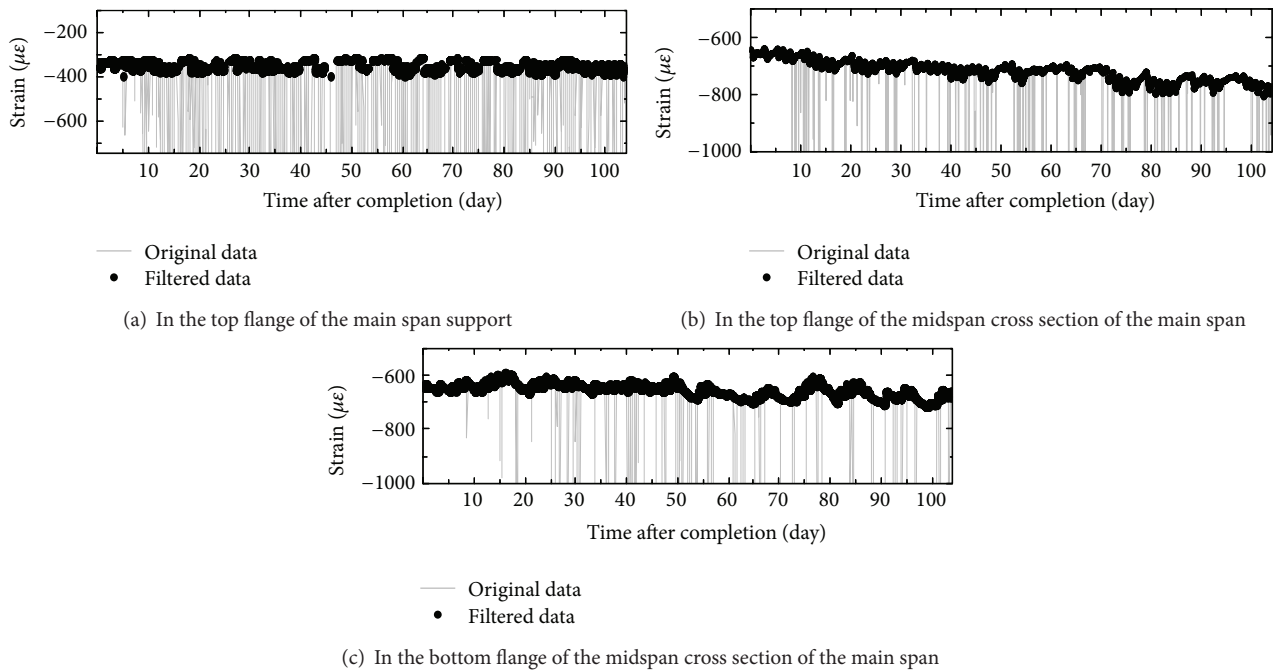


FIGURE 13: Monitored strain time-histories.

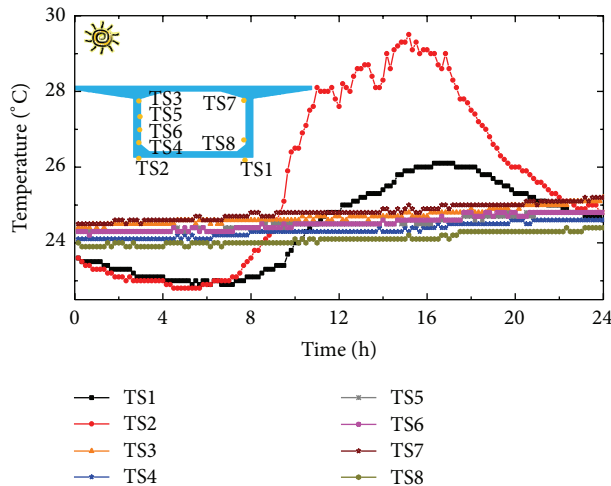


FIGURE 14: Monitored daily temperature time-histories.

22.8°C to 29.5°C) is found at the sensor TS2, which is at the south side of the bottom plates. For the sensor TS1, the largest daily temperature fluctuation is smaller than that of TS2 (i.e., 3.2°C). On the other hand, the temperature fluctuation on the insides surfaces of the box girder is much less significant, and the largest variation is only 0.8°C. Considering that temperature distribution plays a very important role on the short and long-term behavior of PSC box girders, it is necessary to perform such a long-term monitoring on the temperature distribution, based on which more rational analytical model could be obtained and updated.

4. Conclusion

For long-span PSC box girder bridges, their construction is usually a long and complex process, in which there are a number of structural alternations. During the service stage, however, their performance is also influenced by a number of time-variant factors such as concrete shrinkage, creep, and steel relaxation. As a result, the time-dependent behaviors of the PSC box girder bridges are complex. Therefore, it is of great importance to develop a life-cycle monitoring system using distributed sensor network, which is aimed at the most efficient use of sensors during construction, completion test, and long-term service. This paper presents a brief review on the state-of-art investigation on the SHM system of the PSC girder bridges. Strategies, methods, and emphasis of the monitoring on PSC bridges are discussed. A case study is made on a three-span PSC box girder bridge in China to demonstrate the proposed monitoring plan.

According to the monitored stress and deflection data during the construction, the monitored data in general agree well with the design values. Through dynamic adjustment during the construction, the differences are all within the threshold values; however, it is observed that, during the closure of bridge, the construction error might become larger than the other processes, indicating that these processes are the dominating ones in the entire construction.

Under the static load tests, the measured stresses and displacements are all below the design values. The residual stresses and displacements, after the loads were removed, were all very small, showing that the bridge performed elastically during the tests. According to the dynamic tests, the measured natural frequencies are larger than design, showing that the actual structure is stiffer than predicted. Therefore, the analytical model should be updated based upon the field monitored data. In the braking test, the measured DLA is 1.025, so that the design value of 1.05 is reasonable for this bridge. No cracks were found during all the tests.

As to the long-term monitoring, the system effectively combines the sensors for construction monitoring and completion tests, so that the total costs are significantly reduced. The wireless data transmission system successfully sends the quasistatic data to the remote analysis center. However, it is found that the measured time-dependent deflections are larger than design values; considering that the continuous increase in deflection at midspan is one of the main problems of long-span PSC box girder bridges, a more accurate shrinkage and creep model is required in future study. In addition, the extension of the service life of sensors and possible replacement methods of the sensors are of crucial importance for the life-cycle monitoring.

Conflict of Interests

The authors declare that there is no conflict of interests regarding the publication of this paper.

Acknowledgments

The support from the Jiangsu Transportation Department under Grant no. 2011Y03, the Natural Science Foundation of Jiangsu under Grant no. BK2011611, the Education Department of Jiangsu under Grant no. JHB2012-1, and the Fok Ying Tung Education Foundation under Grant no. 131074 is gratefully acknowledged.

References

- [1] C. Boller, F. Chang, and Y. Fujino, *Structural Health Monitoring-An Introduction and Definition*, John Wiley & Sons, London, UK, 2009.
- [2] A. Q. Li, Y. L. Ding, H. Wang, and T. Guo, "Analysis and assessment of bridge health monitoring mass data -progress in research/development of 'structural Health Monitoring,'" *Science in China Series E: Technological Sciences*, vol. 55, no. 8, pp. 2212–2224, 2012.
- [3] T.-H. Yi, H.-N. Li, and M. Gu, "Recent research and applications of GPS-based monitoring technology for high-rise structures," *Structural Control and Health Monitoring*, vol. 20, no. 5, pp. 649–670, 2013.
- [4] T. H. Yi, H. N. Li, and M. Gu, "Optimal sensor placement for structural health monitoring based on multiple optimization strategies," *Structural Design of Tall and Special Buildings*, vol. 20, no. 7, pp. 881–900, 2011.

- [5] T.-H. Yi, H.-N. Li, and M. Gu, "Experimental assessment of high-rate GPS receivers for deformation monitoring of bridge," *Measurement*, vol. 46, no. 1, pp. 420–432, 2013.
- [6] J. F. Liu and Q. W. Zhang, "Dynamic characteristics of a thousands-meter scale cable-stayed bridge," in *Sensors and Smart Structures Technologies for Civil, Mechanical, and Aerospace Systems*, vol. 7647 of *Proceedings of SPIE*, April 2010.
- [7] D. Inaudi, "Long-term static structural health monitoring," in *Proceedings of the Structures Congress*, pp. 566–577, Orlando, Fla, USA, May 2010.
- [8] S. M. Petroff, M. W. Halling, and P. J. Barr, "Monitoring of long term bridge performance (LTBP) program bridges," in *Proceedings of the Structures Congress*, pp. 65–76, 2011.
- [9] C. Rodrigues, C. Felix, A. Lage, and J. Figueiras, "Development of a long-term monitoring system based on FBG sensors applied to concrete bridges," *Engineering Structures*, vol. 32, no. 8, pp. 1993–2002, 2010.
- [10] H. M. Dwairi, M. C. Wagner, M. J. Kowalsky, and P. Zia, "Behavior of instrumented prestressed high performance concrete bridge girders," *Construction and Building Materials*, vol. 24, no. 11, pp. 2294–2311, 2010.
- [11] M. L. Wang, "Long term health monitoring of post-tensioning box girder bridges," *Smart Structures and Systems*, vol. 4, no. 6, pp. 711–726, 2008.
- [12] N. A. Hoult, P. R. A. Fidler, P. G. Hill, and C. R. Middleton, "Long-term wireless structural health monitoring of the ferriby road bridge," *Journal of Bridge Engineering*, vol. 15, no. 2, pp. 153–159, 2010.
- [13] A. Cury, C. Cremona, and J. Dumoulin, "Long-term monitoring of a PSC box girder bridge: operational modal analysis, data normalization and structural modification assessment," *Mechanical Systems and Signal Processing*, vol. 33, pp. 13–37, 2012.
- [14] H. Sousa, J. Bento, and J. Figueiras, "Construction assessment and long-term prediction of prestressed concrete bridges based on monitoring data," *Engineering Structures*, vol. 52, pp. 26–37, 2013.
- [15] H. C. Gomez, P. J. Fanning, M. Q. Feng, and S. Lee, "Testing and long-term monitoring of a curved concrete box girder bridge," *Engineering Structures*, vol. 33, no. 10, pp. 2861–2869, 2011.
- [16] W. Chung, S. Kim, N.-S. Kim, and H.-U. Lee, "Deflection estimation of a full scale prestressed concrete girder using long-gauge fiber optic sensors," *Construction and Building Materials*, vol. 22, no. 3, pp. 394–401, 2008.
- [17] I. N. Robertson, "Prediction of vertical deflections for a long-span prestressed concrete bridge structure," *Engineering Structures*, vol. 27, no. 12, pp. 1820–1827, 2005.
- [18] Y. H. Li, *Performance Analysis and Evolution of Continuous Rigid Frame Bridge Based on Long-Term Health Monitoring*, South China University Technology, Guangzhou, China, 2012 (Chinese).
- [19] G. Liu, *Condition Assessment Research to Large-Span Bridges Based on Long-Term Static Monitoring Data*, College of Civil Engineering of Chongqing University, Chongqing, China, 2010 (Chinese).
- [20] Y. B. Huang, *Study on practical health monitoring system and safety evaluation standard of long-span continuous rigid-frame bridge [M.S. thesis]*, Chongqing Jiaotong University, Chongqing, China, 2012, (Chinese).
- [21] Z. L. Lan, J. T. Zhou, and Z. X. Zhou, "Research of online monitoring system of box girder bridge deflections," *Journal of Chongqing Jiaotong University*, vol. 27, no. 4, pp. 525–528, 2008.
- [22] The Ministry of Communications of the People's Republic of China, *Quality Inspection and Evaluation Standard of Highway Engineering*, China Communications Press, Beijing, China, 2004.
- [23] W.-X. Ren, X.-L. Peng, and Y.-Q. Lin, "Experimental and analytical studies on dynamic characteristics of a large span cable-stayed bridge," *Engineering Structures*, vol. 27, no. 4, pp. 535–548, 2005.
- [24] L. Sun, X. W. Hao, and D. L. Tan, "Health monitoring and assessment system design for large span continuous rigid frame bridges," *Journal of Guangxi University*, vol. 35, no. 4, pp. 621–626, 2010.
- [25] J. Wang and Z. Fang, "Analysis and field measurement of concrete box girder bridges for shrinkage and creep effects," *China Civil Engineering Journal*, vol. 41, no. 1, pp. 70–81, 2008.

Research Article

Running Safety of Trains under Vessel-Bridge Collision

Yongle Li,¹ Jiangtao Deng,^{1,2} Bin Wang,¹ and Chuanjin Yu¹

¹Department of Bridge Engineering, Southwest Jiaotong University, No. 111, North 1st Section of Second Ring Road, Chengdu 610031, China

²The Third Railway Survey and Design Institute Group Co., Ltd., Tianjin 300142, China

Correspondence should be addressed to Yongle Li; lele@swjtu.edu.cn

Received 11 August 2014; Revised 13 December 2014; Accepted 14 December 2014

Academic Editor: Ting-Hua Yi

Copyright © 2015 Yongle Li et al. This is an open access article distributed under the Creative Commons Attribution License, which permits unrestricted use, distribution, and reproduction in any medium, provided the original work is properly cited.

To optimize the sensor placement of the health monitoring system, the dynamic behavior of the train-bridge system subjected to vessel-collision should be studied in detail firstly. This study thus focuses on the characteristics of a train-bridge system under vessel-bridge collision. The process of the vessel-bridge collision is simulated numerically with a reliable finite element model (FEM). The dynamic responses of a single car and a train crossing a cable-stayed bridge are calculated. It is shown that the collision causes significant increase of the train's lateral acceleration, lateral wheelset force, wheel unloading rate, and derailment coefficient. The effect of the collision on the train's vertical acceleration is much smaller. In addition, parametric studies with various train's positions, ship tonnage, and train speed are performed. If the train is closer to the vessel-bridge collision position or the ship tonnage is larger, the train will be more dangerous. There is a relatively high probability of running danger at a low speed, resulting from longer stay of the train on the bridge. The train's position, the ship tonnage, and the train speed must be considered when determining the most adverse conditions for the trains running on bridges under vessel-bridge collision.

1. Introduction

Nowadays, health monitoring plays a very important role in assessing the performances of the civil infrastructures [1–4]. Meanwhile, with the growth of waterway and land transportation, the possibility of vessel-bridge collision increases significantly. To ensure the safety of both bridges and the trains moving on at the occasion of vessel-bridge collision, health monitoring system (HMS) can be installed to monitor the behavior of the trains and bridges in real time [5]. To utilize HMS and distribute the sensors in a rational way, the performances and characteristics of train-bridges system under vessel-bridge collision should be studied firstly as significant references. This study thus focuses on the characteristics of train-bridge interaction under ship collision, which will be beneficial to HMS.

In the study of vessel-bridge collision, available researches have been carried out with emphasis on the force and probability of vessel-bridge collision, structural damage, anti-collision device, and FEM simulation [6–8]. Some empirical formulations were presented by Pedersen and Zhang [9],

which related the energy absorbed by the crushing of ship structures to the maximum impact loads between the ship structure and a bridge pier or girder. A simulation calculation method of vessel-collision was studied by Liang and Cheng [10], which was based on the discussion about the kinetic theory of vessel-collision. The collision force can be known from the deformative force of the springs. Yetal [11] analyzed the vessel-bridge collisions at Japanese coastal strait and concluded that it occurs more likely during daytime rather than evening or the smaller visibility in heavy fog. Employing a statistical method, the vessel-bridge collision possibility was gained in $0.7 \times 10^{-6} \sim 59 \times 10^{-6}$ in six Europe main watercourses (including rivers and straits) [12]. The commonly used probability models for the vessel-bridge collision are AASHTO model [13], European specification model [14], KUNZI model [15], and IABSE model [16]. Numerical simulations carried out by Chen et al. [17] showed that the energy transform, distortion, and stress distribution in the bridge under collision fitted well with the data from field test. The ADINA finite-element code was used by Consolazio and Cowan [18] to compute the force-deformation relationships

for several hopper barge crushing scenarios. Results obtained from the nonlinear finite-element crush analyses were then compared with the empirical crush models found in bridge design specifications.

A scenario of a 12000 DWT bulk cargo collision with a bridge pier was simulated by Wang and Chen [19]. The time history of the ship collision force and the damage of the bridge pier were presented. It was shown that the peak value of ship collision force decreased remarkably due to the failure of concrete. A numerical methodology, performed with an explicit finite-element program, was employed by Lenselink et al. [20] to simulate the dynamic events of collisions where a double hull tanker was struck by another ship. Numerical analysis of vessel-bridge collision was studied by Lehmann and Peschmann [21], of which the angle deviated by about 3° from the perpendicular direction, leaving the mass of the ship and the effect of the moving water out of consideration. An alternative approach was proposed by Pedersen and Zhang [9]. The nonlinear barge and pier responses were coupled together by a shared collision impact force. And numerical procedures were adopted to accelerate the convergence of calculation. Nonlinear finite-element analysis of barge collision with a single bridge pier was performed by Sha and Hao [22].

A lot of analyses on ships or bridges, about the static and dynamic vessel-bridge collision force, were performed as reviewed above. However, it is extremely rare to choose the moving trains as the subject and explore the dynamic response of trains under vessel-bridge collision. For the safety of trains moving on bridges, a dynamic model of coupled train-bridge system is established by Xia et al. [23] to investigate the critical train speeds for running safety subjected to earthquakes. With a model of railway-bridge-system, the dynamic stability of trains moving over bridges shaken by earthquakes is studied by Yang and Wu [24]. Regarding the vessel-bridge collision force as one type of collision loads, Xia et al. [25] discussed the running safety of trains subjected to the collision, in which the influence of the train's position, the tonnage of the ship, and the speed of the train was ignored. Numerical analysis of ship-bridge collision's influences on the running safety of moving rail train was performed by Zhang et al. [26], discussing the effects of train speed and the momentum of impacting ship on the running safety of the rail train. But the influence of the train's position was ignored. Actually, those factors are significant to install the HMS and their effects should be studied in detail.

In this paper, the response history of a single train and a train set crossing a bridge under vessel-bridge collision is investigated. The train's position, the tonnage of the ship, and the speed of the train are involved in parameter studies. The conclusion can provide scientific basis for HMS to monitor the behavior of moving vehicles on bridges under vessel-bridge collision.

2. Force during Vessel-Bridge Collision

2.1. FEM of Vessel-Bridge Collision. A railway cable-stayed bridge (see Figures 1 and 2) and a common bulk carrier are

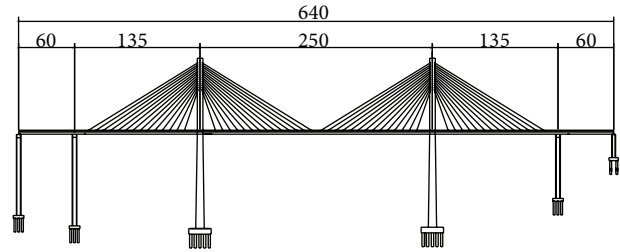


FIGURE 1: General arrangement of the cable-stayed bridge (unit: m).

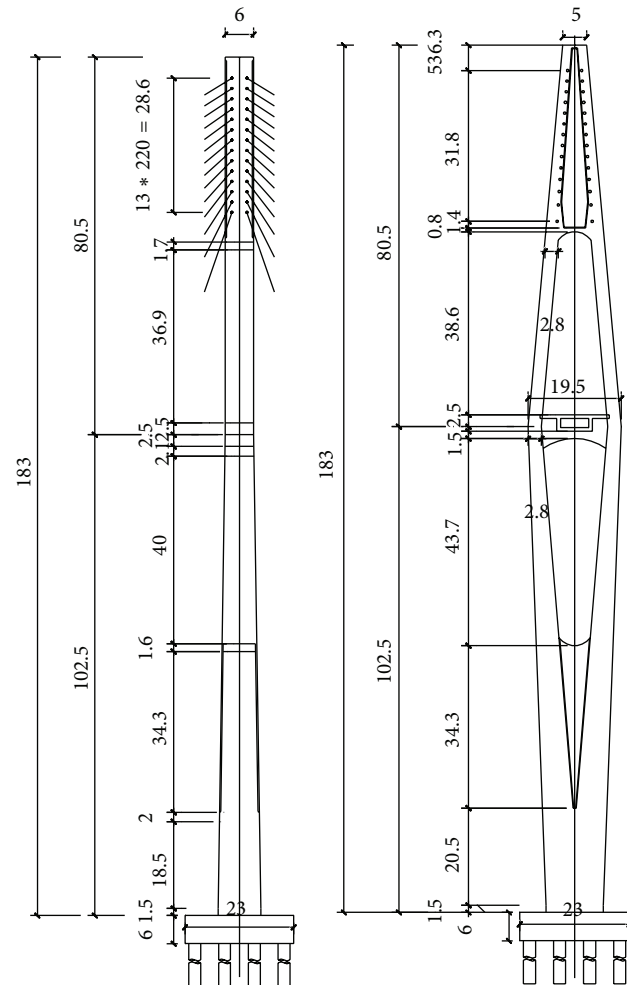


FIGURE 2: Pylon of the bridge (unit: m).

taken as an example. The bridge is a double-pylon cable-stayed bridge with a length of 640 m and a main span of 250 m. The height of its pylons is 183 m and the height of the up part of the pylons above the average water level is 89.5 m. The length, width, depth, summer load line, and weight of the ship are 93.93 m, 15.00 m, 6.70 m, 5.4 m, and 3500 t, respectively. And the thickness of the plate of the bow is 10 mm. A reliable 3D model of the ship and bridge is built using the software LS-DYNA. Plate elements are used to model the bow

while rigid plate elements ignoring deformations are adopted to simulate the stern of the ship. Mesh density becomes higher for the ship model from the stern to the bow. The maximum element size is 1000 mm while the minimum one is 80 mm. Totally, there are 78616 nodes, 79705 quadrilateral plane elements, and 3236 triangular plane elements. Figure 3 shows the FEM of the ship. The bridge pylon is assumed as a rigid-wall model. Figure 4 shows the FEM for both the ship and the bridge, where the girders and piers are all described by using the beam 4 elements, to model the process of vessel-bridge collision.

2.2. Calculated Collision Force. In the simulation, the ship collides with the bridge pylon with a speed of 3 m/s. Figure 5 shows the dynamic process of the vessel-bridge collision. The collision course can be divided into 3 stages. At the first stage, the up deck and the taper surface of the ship collide with the bridge pylon. In the second stage, the bulbous bow collides with the bridge pylon. And the maximum collision force appears in this stage. Then, the collision force reduces with the crushing of the up deck, the taper surface, and the bulbous bow. The third stage is caused by the material hardening of the ship, resulting in the fact that the collision force reaches to a second peak. Then the collision force decays quickly until the collision is over. The time history of the collision force is shown in Figure 6. The maximum collision force is 13.83 MN at 0.63 s, which is between the 0.3 and 0.6 times of the calculated collision force by the railway standard in China. Moreover, the collision process lasts 1.9 s, starting from just a contact of the ship to the bridge pylon. It can also be shown in Figure 6 that there are two peaks in the time history curve of the collision force. Unloading, failure, and damage of the ship appear between the two peaks. Figure 7 shows a sketch of the deformation of the bridge under the collision force. Besides, the maximum impact force in the previous work [26], where a 2000 DWT ship impact onto a pile cap with an initial velocity of 4 m/s was simulated, was 11.2 MN. Compared with this, the result of maximum impact force is reasonable, considering there are differences among the tonnage and the velocity of the ship and the size of the bridge.

3. Responses and Running Safety of Trains under Vessel-Bridge Collision

To consider the coupled dynamics between the trains and the bridge, the responses and running safety of trains are investigated based on the coupled vehicle-bridge vibration with the analysis software BANSYS [27] (bridge analysis system). CRH2 passenger train is set with arrangement of $2 \times (1 \text{ trailer} + 1 \text{ motor} + 1 \text{ motor} + 1 \text{ trailer})$. And the basic parameters of CRH2 are shown in Table 1. German track spectrum with low interference is adopted to simulate the track irregularity, and the space interval of the dynamic time history analysis is 0.2 m. The bridge is made of concrete with a damping ratio of 2.0%. The evaluation indices for the running safety of the train currently used in Ministry of Railways of the PRC [6] are about the derailment factor Q/P_1 (defined

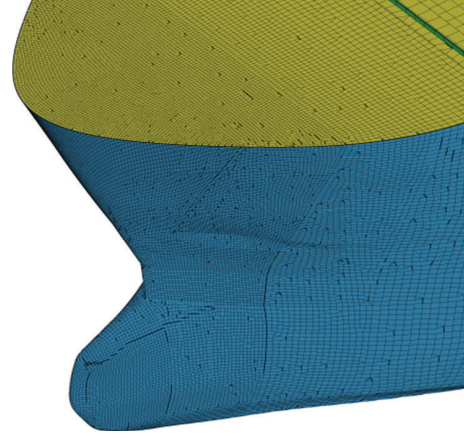


FIGURE 3: FEM for the ship.

TABLE 1: Basic parameters of CRH2.

Vehicle type	Weight/t			Yawing inertia/t·m ²		
	Body	Wheelset	Bogie	Body	Wheelset	Bogie
Motor	39.60	2.00	3.20	1900	0.980	3.20
Trailer	34.10	2.10	2.60	1700	1.029	2.60

as the ratio of the lateral wheel-rail force Q to the vertical wheel-rail force P_1) and the wheel unloading rate $\Delta P/P_2$ (defined as the ratio of the offload vertical wheel-rail force ΔP to the static vertical wheel-rail force P_2). The allowable values of the indices are $Q/P_1 \leq 0.8$ and $\Delta P/P_2 \leq 0.6$.

3.1. Verification. BANSYS can be used to model the coupled behavior between the trains and the bridge. To verify the application of BANSYS to impact analysis, the responses of the bridge under the collision force are solved firstly and compared with the calculated results from the common software LS-DYNA. With the action of the collision force, the lateral bridge displacement curves, calculated after collision in 8 s by BANSYS and LS-DYNA, are compared in Figures 8 and 9. In general, the displacement curves tend to be the same, which indicates that BANSYS used in the collision analysis has realization feasibility. The lateral displacement, generated by the collision force of the ship, reaches maximum value after the collision. In pace with the vessel falling off from the bridge, the movement of the whole bridge is in free vibration and decays gradually.

3.2. Responses of a Single Car under Vessel-Bridge Collision. The motor of CRH2 is employed to investigate the responses of a single car under the vessel-bridge collision. Two positions X_1 and X_2 are defined to illustrate the results conventionally. X_1 is the collision location on the girder in the longitudinal direction of the bridge. X_2 is the location of the head of the train related to the collision location as the vessel-bridge collision. And the positive coordinate direction is the advancing direction of the train, and the collision position is regarded as the origin, which means $X_1 = 0$.

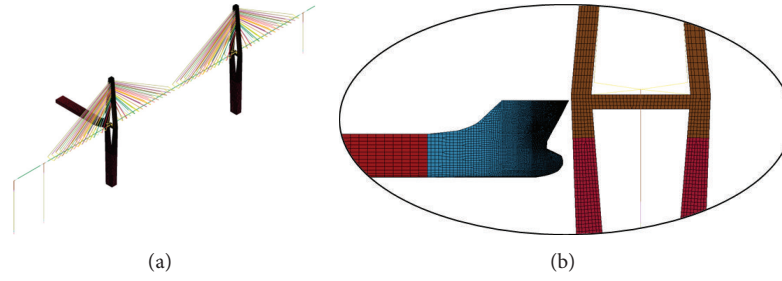


FIGURE 4: FEM for the vessel-bridge collision.

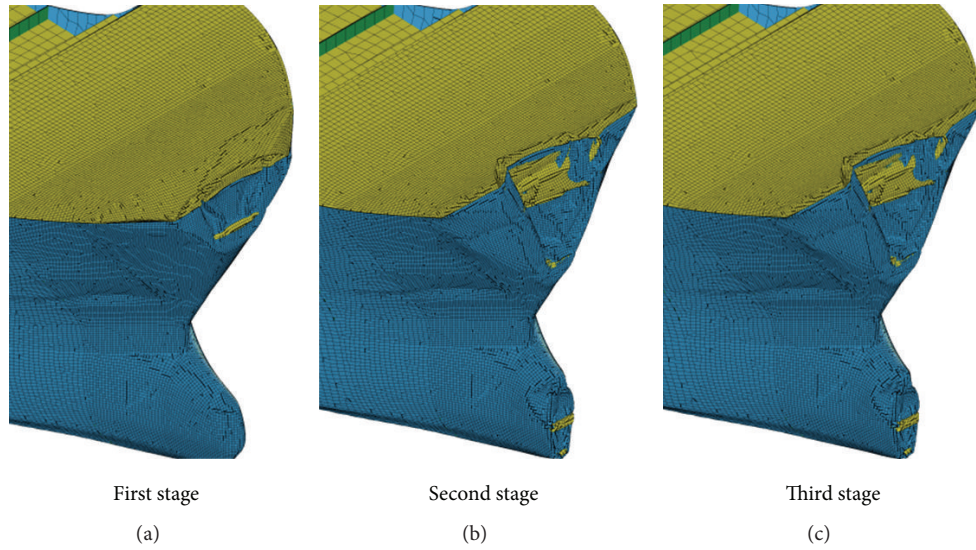


FIGURE 5: Dynamic process of the vessel-bridge collision.

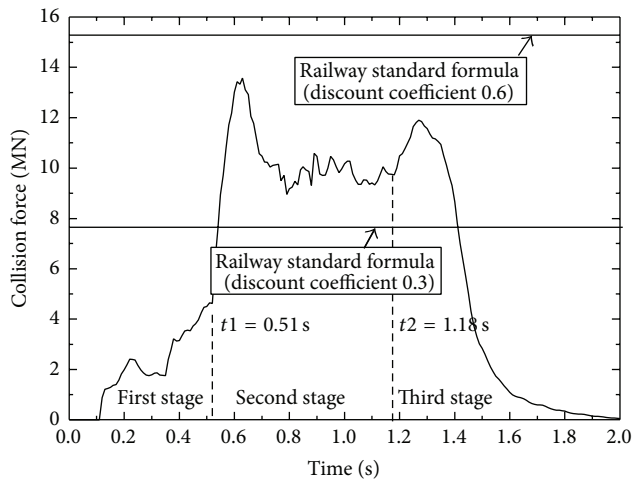


FIGURE 6: Time history curve of the collision force.

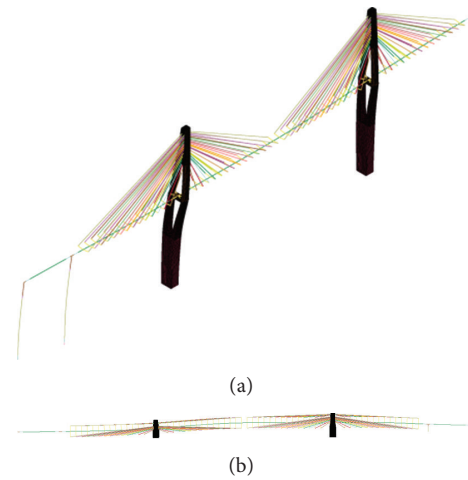


FIGURE 7: Deformation of the whole bridge under collision (amplified 100 times).

The motor moves with a speed of 80 km/h. In the down direction (the train moves from the right to the left), when X_2 is -385 m, the collision happens as the head of the train arrives at point D in Figure 10. The calculation condition is explained in more detail in Table 2. The corresponding lateral

displacement curves of the bridge girder at different locations (points A, B, C, D, and E) are also shown in Figure 10. And the lateral displacement field of the whole bridge in the down direction is described in Figure 11.

TABLE 2: Calculation condition of a single car (motor).

The direction into the bridge	X_2 (m)	The distance between the train and the collision position (m)	Vehicle type	Speed (km/h)
Up (close to the collision position)	-385	385	A single train of CRH2	80

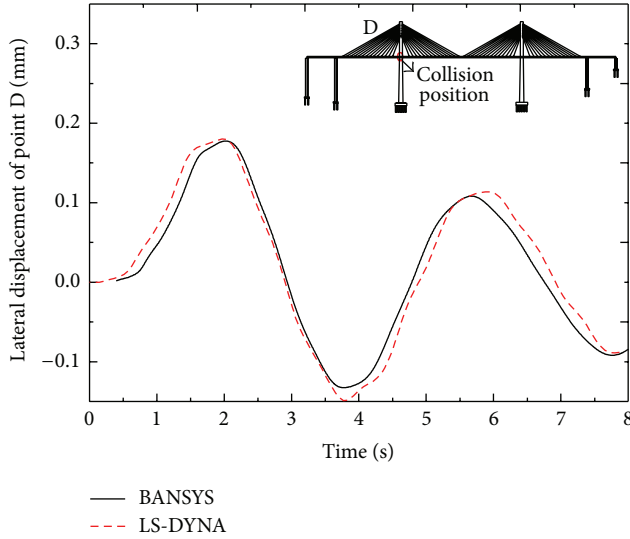


FIGURE 8: Lateral displacement of the girder at the collision position.

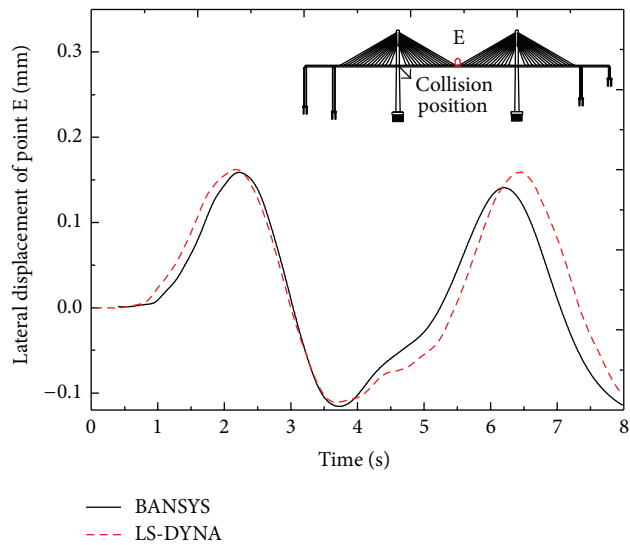


FIGURE 9: Lateral displacement of the girder in the mid-span.

For the motor, the lateral force, wheel unloading rate, and derailment coefficient of the first wheelset are shown in Figure 12. As shown in Figure 12, the collision force causes significant increase of the train's lateral acceleration, lateral wheelset force, wheel unloading rate, and derailment coefficient. However the effect of the collision force on the single car's vertical acceleration is much smaller.

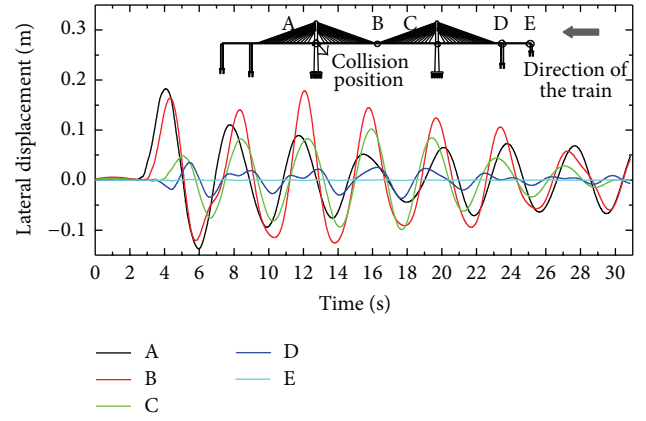


FIGURE 10: Lateral displacement calculated (in the down direction).

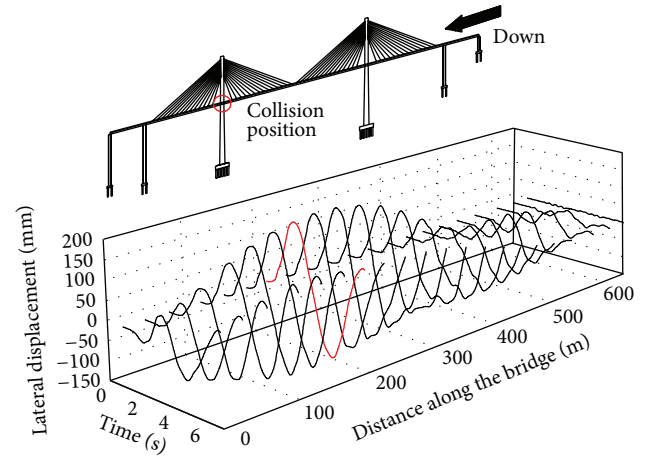
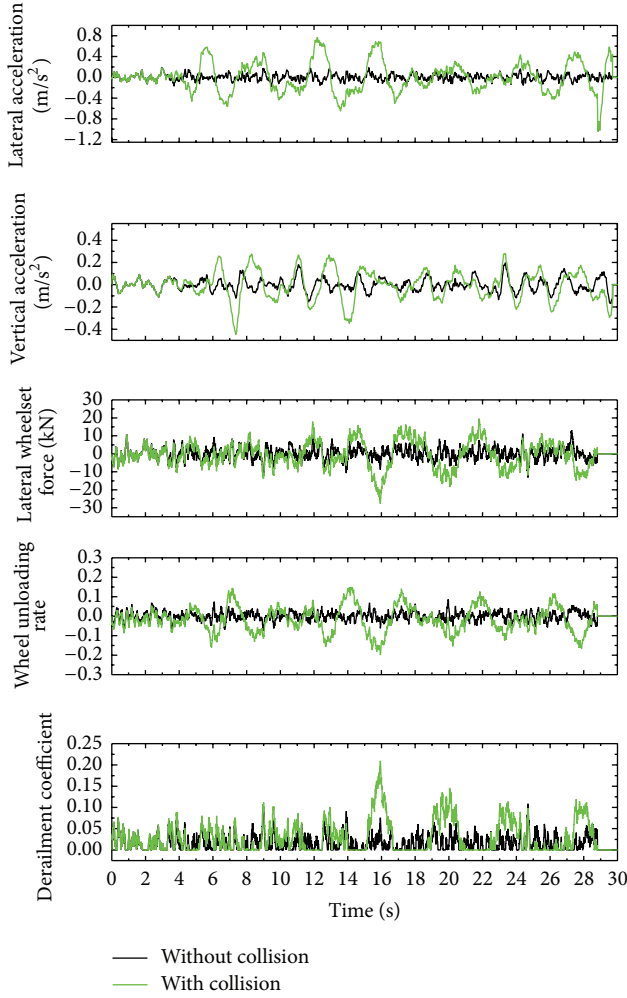


FIGURE 11: Lateral displacement field (in the down direction).

3.3. Responses of a Train under Vessel-Bridge Collision. The train passing by the bridge with $X_2 = -195$ m in the up direction with a speed of 80 km/h is analyzed. The corresponding calculation condition is listed in Table 3. The time history curves of the lateral and vertical acceleration, the first wheelset force, the wheel unloading rate, and derailment coefficient of the first car, the trailer, and the sixth car, the motor, are shown in Figures 13 and 14. Figure 13 illustrates the time history curves of the responses of the first car, the trailer. When the train arrives at the entrance of the bridge and the collision happens at the same time, the maximum value of the trailer's lateral acceleration appears at 2 s and reaches

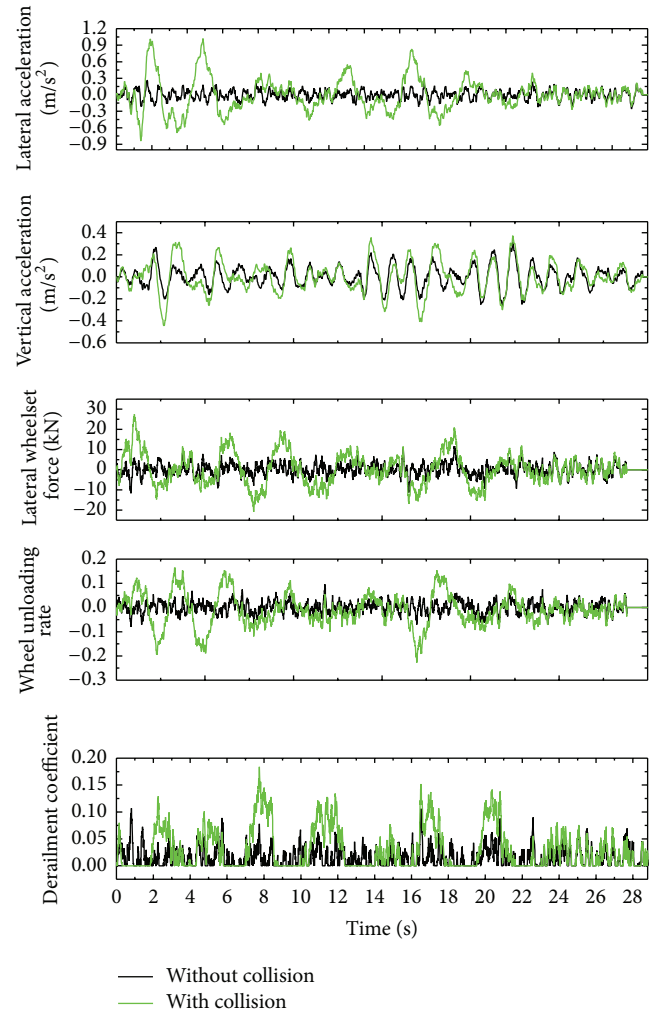
TABLE 3: Calculation condition of a train (in the up direction).

The direction into the bridge	X_2 (m)	The distance between the train and the collision position (m)	Vehicle type	Speed (km/h)
Up (close to the collision position)	-195	195	A train set of CRH2	80

FIGURE 12: Responses of a single car ($X_2 = -385$ m, 80 km/h, in the down direction).

1.016 m/s^2 , which is 3.89 times that without the collision. In addition, the maximum values of the first wheelset force, the wheel unloading rate, and derailment coefficient of the trailer are 2.34, 2.37, and 1.7 times those without the collision, respectively. But the trailer's vertical acceleration has little change with and without the collision.

German track spectrum is adopted to simulate the track irregularity in the paper, which is independent of the collision and the motion of the train. The resultant irregularity input into analysis model is the combination of the simulated irregularity and the bridge deformation. Since the model of the approach bridge is not established, the deformation of

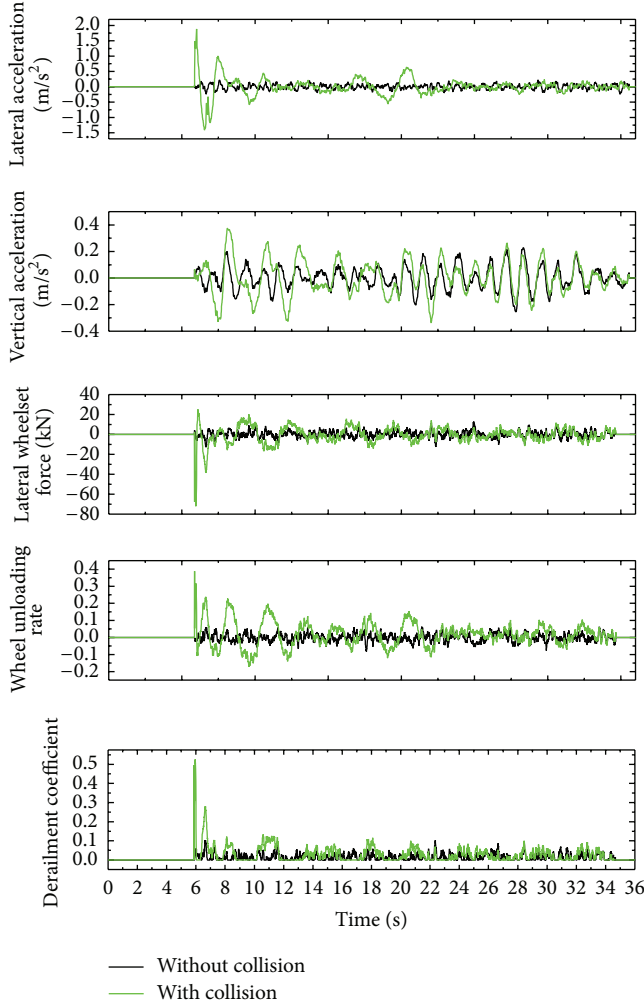
FIGURE 13: Responses of the trailer (the first train, $X_2 = -195$ m, 80 km/h, in the up direction).

approach bridge is regarded as 0. Thus the bridge deformation could increase from 0 to a certain value suddenly at the entrance of the main bridge if a train runs into the main bridge from the approach bridge, which can make the resultant irregularity change suddenly. The sudden change of the resultant irregularity can significantly enlarge the response of the train, which is the reason why there are obvious responses of the train at the entrance or exit of the bridge.

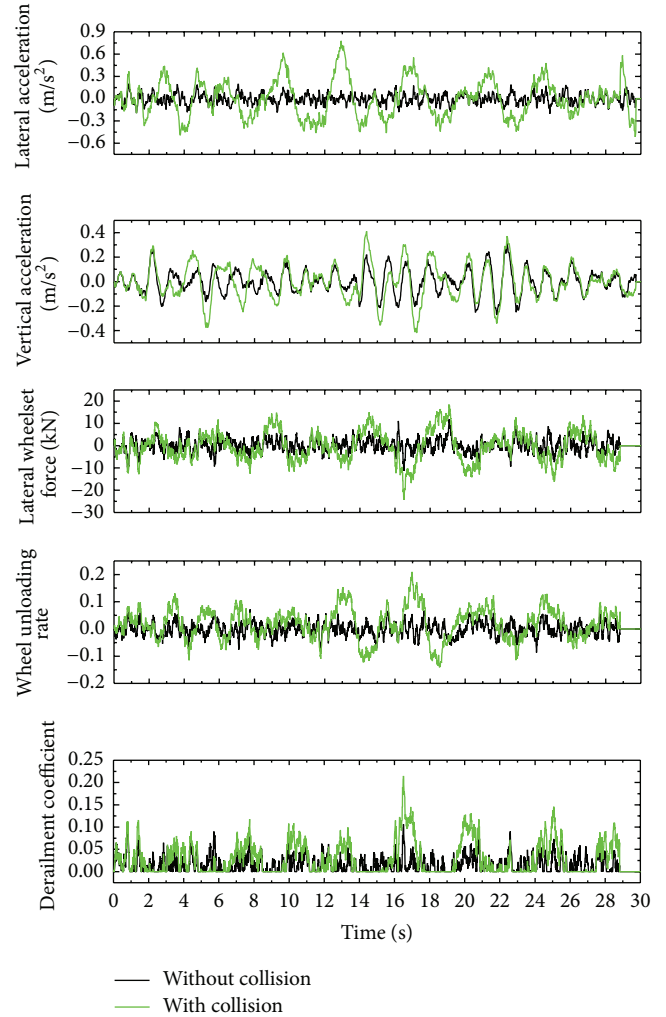
Figure 14 illustrates the time history curves of the responses of the sixth train, the motor car, in the up direction. The motor's lateral acceleration reaches the maximum value in 5.85 s after the collision.

TABLE 4: Calculation condition of a train (in the down direction).

The direction into the bridge	X_2 (m)	The distance between the train and the collision position (m)	Vehicle type	Speed (km/h)
Down (far from the collision position)	-445	445	A train set of CRH2	80

FIGURE 14: Responses of the motor car (the sixth train, $X_2 = -195$ m, 80 km/h, in the up direction).

In the down direction, the train passing by the bridge with $X_2 = -445$ m and a speed of 80 km/h is also studied. The corresponding calculation conditions are listed in Table 4. The time history curves of the lateral and vertical acceleration, the first wheelset force, the wheel unloading rate, and derailment coefficient of the first car of the train, the trailer, and the second car of the train, the motor car, are shown in Figures 15 and 16. As shown in Figure 15, the maximum value of the trailer's lateral acceleration appears at 12.9 s and equals 0.7805 m/s^2 . In addition, the first wheelset force and derailment coefficient of the trailer reach their maximum values at 16.5 s, which are 2.16 and 2.02 times larger than

FIGURE 15: Responses of the trailer (the first train, $X_2 = -445$ m, 80 km/h, in the down direction).

those without collision, respectively. At the same time, the maximum values of the trailer's lateral acceleration and wheel unloading rate are 3.84 and 2.43 times larger than those without collision, respectively. As shown in Figure 16, the motor's lateral acceleration reaches the maximum value at 12.85 s and equals 0.7805 m/s^2 . In addition, the first wheelset force and derailment coefficient of the motor reach the maximum values at 20.31 s. And the maximum values of the lateral acceleration, the first wheelset force, the wheel unloading rate, and derailment coefficient of the motor are 3.37, 1.92, 2.69, and 1.71 times larger than those without the collision, respectively.

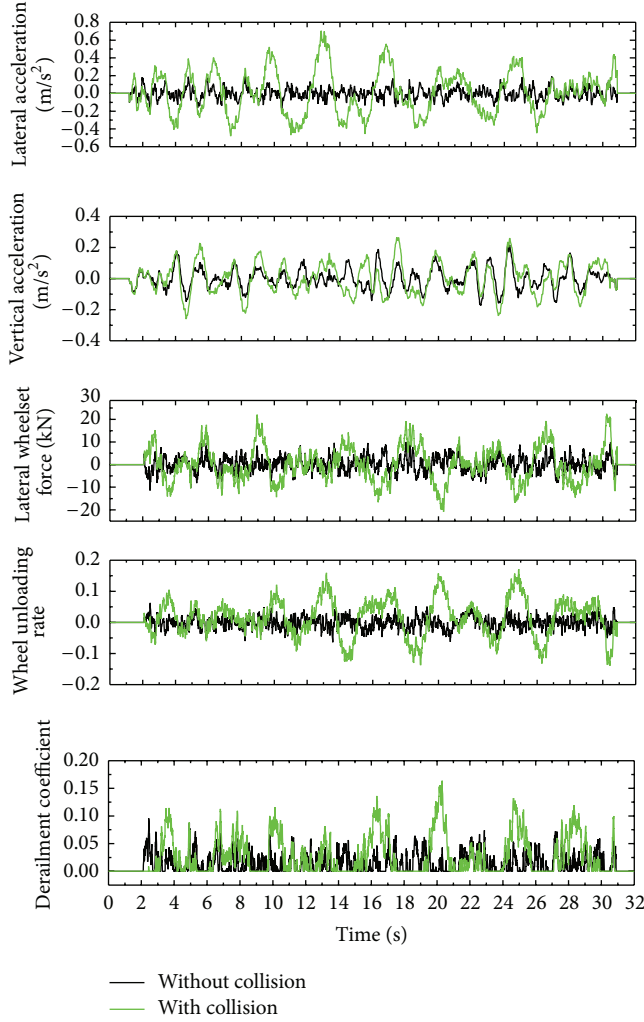


FIGURE 16: Responses of the motor car (the second train, $X_2 = -445$ m, 80 km/h, in the down direction).

4. Parameter Analysis

4.1. Train's Position as Collision. With the difference of X_2 , the train's position on the bridge as collision, the maximum responses of the train are different. Figure 17 shows the maximum values of the lateral and vertical acceleration, lateral wheelset force, wheel unloading rate, and derailment coefficient of the train subjected to collision at various places. It is shown that the maximum responses can be described by oblique upward wavy lines. Meanwhile, the values become very large when the train is located between -70 m and 30 m in coincidence with the collision. The derailment coefficient of the train exceeds 0.8 greatly and reaches its upper limit, at which the computation is no longer convergent. It can be concluded that these positions can be considered as the dangerous zone for the trains. And derailment will occur if the bridge is collided by a 3500 t ship with a speed of 3 m/s.

4.2. The Tonnage of the Vessel. There are two kinds of curves shown in Figure 18 recording the maximum responses of the

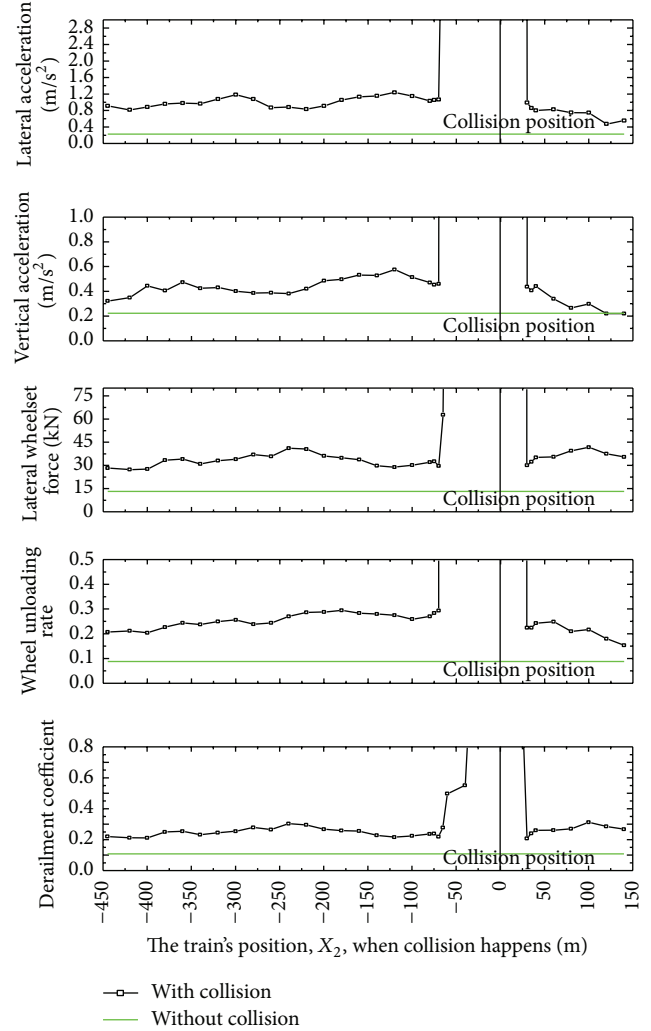


FIGURE 17: Influence of the train's position when collision happens.

train on the different location of the bridge under different collision force from ships, of which the tonnages are 1000 t and 3500 t. From this figure, the influence of the ship tonnage on the responses of the train is obvious. The smaller the tonnage of the collision vessel is, the more the maximum of the train's responses moves towards these without collision. And oblique upward wavy lines can also fit well with the results from the 1000 t ship collision, under which the dangerous region of the train is between -13 m and 30 m. Therefore, it can be concluded that the dangerous region is associated with the ship tonnage.

4.3. Train's Speed. The maximum responses of the train with 5 speeds at two different positions of the bridge under a 3500 t ship collision are shown in Figure 19. From the displacement field of the bridge subjected to the collision, the lateral displacement which is far from the impact location is relatively small. When the collision happens and the train happens to cross the bridge, the maximum responses of the train increase

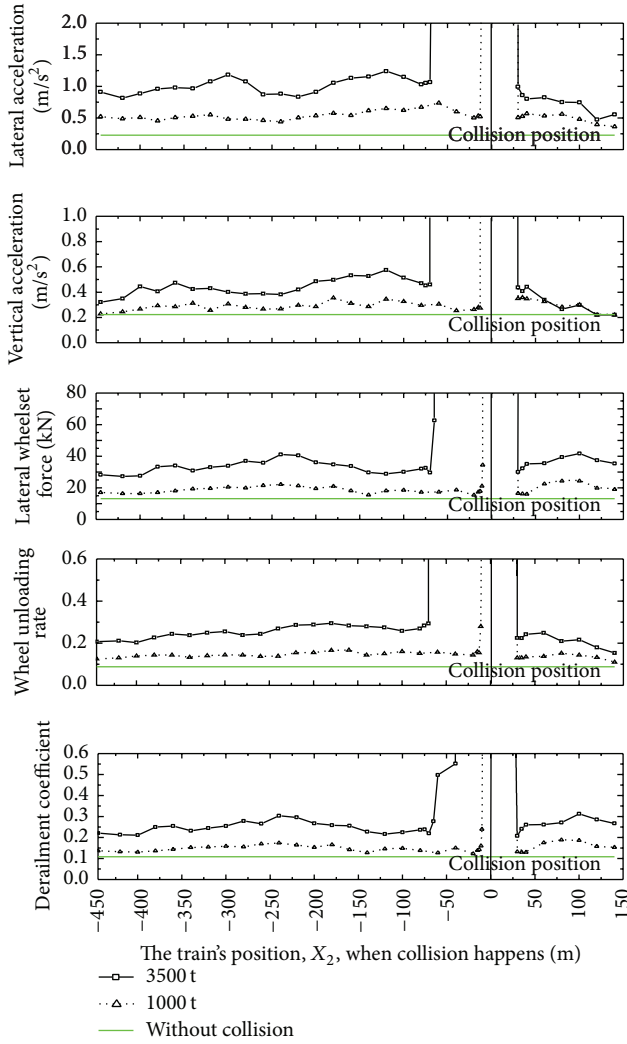


FIGURE 18: Influence of the tonnage of the ship.

with the increase of the train speed. This feature is close to that of the vehicle-bridge coupling without collision [28]. When the collision occurs and the train happens to arrive in the mid-span of the bridge (in the down direction), the effect of the vessel-bridge collision becomes larger, and the change law of the maximum values of train's responses is not in keeping with the increase of the speed well. As the speed increases, the maximum lateral acceleration becomes larger; the maximum vertical acceleration increases under train speed less than 80 km/h and then becomes smaller when the train speed is greater than 80 km/h; the maximum lateral wheelset force and wheel loading rate firstly increase and then decrease when the train speed is less than 80 km/h and become larger under train speed larger than 80 km/h; and the maximum derailment coefficient decreases under train speed less than 80 km/h and firstly increases and then decreases when the train speed is greater than 80 km/h. From the analysis above, the effect of train's speed on the running safety of trains under vessel-collision force is complex resulting from the position and the staying time of the train. When the collision happens

and the train starts to cross the bridge in the sense that the train is far away from the collision, it is more dangerous as the train accelerates. But when the collision occurs and the train happens to arrive in the mid-span of the bridge in the sense that the train is close to the collision, low speed does not imply great safety of the train. When the speed is at a relatively low level, the train may remain on the bridge for a longer time, which could increase the effect of ship collision on train's responses.

5. Conclusions

The following conclusions can be obtained from the study.

- (1) The vessel-bridge collision causes the significant increase of the train's lateral acceleration, lateral wheelset force, wheel unloading rate, and derailment coefficient. These indices are nearly 3.8, 2.1, 2.5, and 1.8 times those without collision, respectively, when a train passes the bridge under vessel-collision force. Yet the effect of the collision on the train's vertical acceleration is much smaller.
- (2) The lateral displacement of the girder close to the collision position (in the down direction) is relatively larger. In addition, the driving condition is associated with the structure form of the approach bridge. Conversely, the lateral displacement far from the impact position (in the down direction) is relatively smaller, and the driving condition here is good as well. Therefore, it has difference in train's response according to the direction into the bridge.
- (3) The maximum responses of the train at different positions of the bridge can be described by oblique upward wavy lines. For the train, the closer it is to the collision position, the more dangerous it will be. At the same time, there is a dangerous zone for the moving train. When the bridge is subjected to the collision, it is possible for the train to derail when it happens to come into this zone.
- (4) The larger the tonnage of the collision ship is, the greater the train's responses are, the bigger the dangerous zone is, and the worse the running safety is.
- (5) The effect of train's speed on the running safety of trains under vessel-collision force is complex resulting from the position and the staying time of the train. There is a relatively high probability of running danger at a lower speed under vessel-bridge collision, resulting from longer stay of the train on the bridge.

Conflict of Interests

The authors declare that there is no conflict of interests regarding the publication of this paper.

Acknowledgments

The authors are grateful to the financial supports from the National Natural Science Foundation of China (U1334201

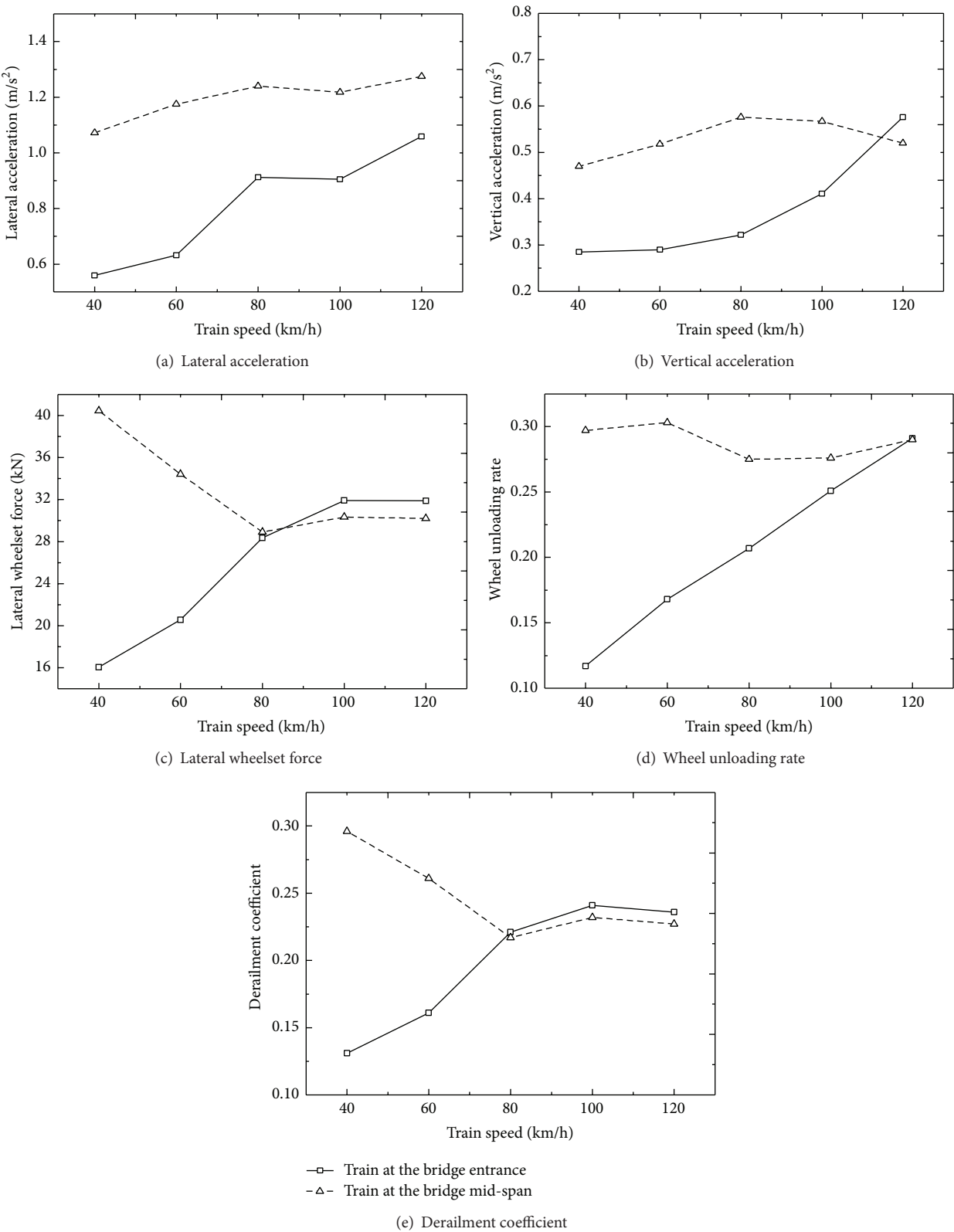


FIGURE 19: Influence of the train's speed.

and 51278434), the National Key Basic Research Development Plan of China (2013CB036206), and the Sichuan Province Youth Science and Technology Innovation Team (15CXTD0005).

References

- [1] B. Chen, Z. W. Chen, Y. Z. Sun, and S. L. Zhao, "Condition assessment on thermal effects of a suspension bridge based on SHM oriented model and data," *Mathematical Problems in Engineering*, vol. 2013, Article ID 256816, 18 pages, 2013.
- [2] H. N. Li, T. H. Yi, L. Ren, D. S. Li, and L. S. Huo, "Reviews on innovations and applications in structural health monitoring for infrastructures," *Structural Monitoring and Maintenance*, vol. 1, no. 1, pp. 1–45, 2014.
- [3] Z. W. Chen, Y. L. Xu, and X. M. Wang, "SHMS-based fatigue reliability analysis of multiloading suspension bridges," *Journal of Structural Engineering*, vol. 138, no. 3, pp. 299–307, 2012.
- [4] T. H. Yi, H. N. Li, and X. D. Zhang, "Sensor placement on Canton Tower for health monitoring using asynchronous-climb monkey algorithm," *Smart Materials and Structures*, vol. 21, no. 12, Article ID 125023, pp. 1–12, 2012.
- [5] T. H. Yi, H. N. Li, and M. Gu, "Experimental assessment of high-rate GPS receivers for deformation monitoring of bridge," *Measurement*, vol. 46, no. 1, pp. 420–432, 2013.
- [6] Ministry of Railways of the People's Republic of China, *Fundamental Code for Design on Railway Bridge and Culvert (TB10002.1-2005)*, 2005, (Chinese).
- [7] T. Y. Dai, *Ship Impact Against Bridge and Its Risk Assessment*, Harbin Engineering University, 2002.
- [8] G. R. Consolazio and D. R. Cowan, "Numerically efficient dynamic analysis of barge collisions with bridge piers," *Journal of Structural Engineering*, vol. 131, no. 8, pp. 1256–1266, 2005.
- [9] P. T. Pedersen and S. Zhang, "The mechanics of ship impacts against bridges," in *Ship Collision Analysis: Proceedings of the International Symposium on Advances in Ship Collision Analysis, Copenhagen, 1st January 1998*, pp. 41–51, Balkema Publishers, A.A./Taylor & Francis, Rotterdam, The Netherlands, 1998.
- [10] W. J. Liang and G. Z. Cheng, "Ship collision force and energy absorbability," *Journal of SSSRI*, no. 2, pp. 23–34, 1992 (Chinese).
- [11] F. Yetal, "Some factors affecting the frequency of accidents in marine traffic," *Journal of Navigation*, vol. 27, pp. 235–252, 1974.
- [12] Ship Collision due to the Presence of Bridges, "Report of Working Group 19 of the Inland Navigation Commission," 2001.
- [13] AASHTO, *LRFD Bridge Design Specification and Commentary*, American Association of State Highway and Transportation Officials, Washington, DC, USA, 1994.
- [14] A. C. W. M. Vrouwenvelder, "Design for Ship Impact according to Eurocode 1 Part 2.7," *Ship Collision Analysis*, 1998.
- [15] C. U. Kunz, "Ship bridge collision in river traffic analysis and design practice," in *Ship Collision Analysis*, 1998.
- [16] O. D. Larsen, "Ship Collision with Bridge," ABSE Structural Engineering Documents, 1993.
- [17] C. L. Chen, R. X. Gao, and H. P. Zhu, "Substructure responses and damage assessment of on building bridge under ship-bridge collision," in *The 20th National Structural Engineering Conference Proceedings*, II book, 2011, (Chinese).
- [18] G. R. Consolazio and D. R. Cowan, "Nonlinear analysis of barge crush behavior and its relationship to impact resistant bridge design," *Computers and Structures*, vol. 81, no. 8–11, pp. 547–557, 2003.
- [19] J. J. Wang and C. Chen, "Simulation of damage for bridge pier subjected to ship impact," *Engineering Mechanics*, vol. 24, no. 7, pp. 156–160, 2007.
- [20] H. Lenselink, K. G. Thung, and H. I. Stipdonk, "Numerical simulations of ship collisions," in *Proceedings of the 2nd International Offshore and Polar Engineering Conference*, pp. 79–88, June 1992.
- [21] E. Lehmann and J. Peschmann, "Energy absorption by the steel structure of ships in the event of collisions," *Marine Structures*, vol. 15, no. 4–5, pp. 429–441, 2002.
- [22] Y. Y. Sha and H. Hao, "Nonlinear finite element analysis of barge collision with a single bridge pier," *Engineering Structures*, vol. 41, pp. 63–76, 2012.
- [23] H. Xia, Y. Han, N. Zhang, and W. Guo, "Dynamic analysis of train-bridge system subjected to non-uniform seismic excitations," *Earthquake Engineering and Structural Dynamics*, vol. 35, no. 12, pp. 1563–1579, 2006.
- [24] Y. B. Yang and Y. S. Wu, "Dynamic stability of trains moving over bridges shaken by earthquakes," *Journal of Sound and Vibration*, vol. 258, no. 1, pp. 65–94, 2002.
- [25] C. Y. Xia, H. Xia, and G. De Roeck, "Dynamic response of a train-bridge system under collision loads and running safety evaluation of high-speed trains," *Computers and Structures*, vol. 140, pp. 23–38, 2014.
- [26] W. W. Zhang, X. L. Jin, and J. W. Wang, "Numerical analysis of ship-bridge collision's influences on the running safety of moving rail train," *Ships & Offshore Structures*, vol. 9, no. 5, pp. 498–513, 2014.
- [27] Y. Li, S. Qiang, H. Liao, and Y. L. Xu, "Dynamics of wind-rail vehicle-bridge systems," *Journal of Wind Engineering and Industrial Aerodynamics*, vol. 93, no. 6, pp. 483–507, 2005.
- [28] Y. Zhou, *Simulation of vehicle-bridge coupling vibration based on ANSYS and SIMPACK [M.S. thesis]*, Southwest Jiaotong University, 2013.

Research Article

Impact Coefficient Analysis of Long-Span Railway Cable-Stayed Bridge Based on Coupled Vehicle-Bridge Vibration

Yongle Li,¹ Shifu Dong,^{1,2} Yulong Bao,¹ Kejian Chen,³ and Shizhong Qiang¹

¹Department of Bridge Engineering, Southwest Jiaotong University, Chengdu 610031, China

²Hubei Provincial Communication Planning and Design Institute, Wuhan 430051, China

³China Railway Eryuan Engineering Group Co., Ltd., Chengdu 610031, China

Correspondence should be addressed to Yongle Li; lele@swjtu.edu.cn

Received 9 August 2014; Accepted 17 October 2014

Academic Editor: Ting-Hua Yi

Copyright © 2015 Yongle Li et al. This is an open access article distributed under the Creative Commons Attribution License, which permits unrestricted use, distribution, and reproduction in any medium, provided the original work is properly cited.

Compared with medium and small span bridges, very limited attention has been paid on the research of the impact coefficient of long-span railway bridges. To estimate the impact effects of long-span railway bridges subjected to moving vehicles, a real long-span railway cable-stayed bridge is regarded as the research object in this study, and a coupled model of vehicle-bridge system is established. The track irregularities are taken as the system excitation and the dynamic responses of the vehicle-bridge system are calculated. The impact effects on main girder, stayed cable, bearings, and bridge tower are discussed at various vehicle speeds. The results show that different components of the long-span railway cable-stayed bridge have different impact coefficients. Even for each part, the impact coefficient is also different at different local positions. It reveals that the impact coefficients in the actual situation may have significant differences with the related code clauses in the present design codes.

1. Introduction

Along with the all-round development of the railways in China, higher train speed, heavier axle load, and greater traffic density have brought out the issue of the dynamic interaction between vehicles and old long-span railway bridges. In addition, long-span railway bridges are also subjected to intensive environmental loadings due to the interaction with the environment conditions [1–3]. The traffic and environmental loading effects in bridges may induce the structural movement and stresses due to the indeterminacy, which may cause the damage events of the structural components even the entire bridge. Therefore, it is essential to understand the static and dynamic responses for the bridge performance assessment with the aids of the various monitoring sensors and techniques [4, 5]. Among the crucial parameters of the bridge, the impact coefficient is commonly utilized for the performance evaluation of the long-span railway bridges. In the bridge design codes, the impact coefficient is defined

as an increase factor of the static loads, which reflects the dynamic effects of the moving vehicles on bridges. The impact coefficient of the bridge, as the comprehensive reflection of the dynamic characteristics and interactions in the vehicle-track-bridge system, plays an important role in the health monitoring, safety assessment, and lifetime prediction for the bridges [2, 6]. To ensure the health and reliability of old long-span railway bridges, it is of great significance to analyze the influence factors and rules of impact coefficient in the theory and engineering application [7–9].

Many researches to quantify the impact coefficient have been conducted by bridge engineers around the world. Matsuura studied the dynamic characteristics of high-speed railway bridges subjected to moving vehicles and indicated that the bridge resonance induced by the regular arrangement of axle load was significant [10]. Bhatti et al. studied the dynamic response of a simply supported truss bridge, which showed that each member bar of the truss had different local impact coefficients [11]. Song et al. investigated the dynamic

amplification factors of a cable-stayed maglev bridges by idealizing the cable-stayed bridge as a simple beam on an elastic foundation [12]. Chen et al. studied the static, dynamic, and fatigue condition of long-span suspension bridges on the basis of structural health monitoring system (SHM) [13, 14].

Existing impact studies primarily focused on simply supported medium or small span bridges, while little attention has been paid on long-span railway cable-stayed bridges [15, 16]. Compared with simply supported bridges, cable-stayed bridge is featured as a flexible structure which can be considered as combined systems of main girder, stayed cable, tower, and pier. Each component of the cable-stayed bridge may have different impact coefficients. However, one bridge only has one specific value of impact coefficient according to the related codes of railway bridges in both China and abroad, which could not reflect the different impact effects on each component.

Coupled vehicle-bridge vibration is applied to analyze the impact effects in this study. To validate the reliability of the algorithm, this paper studies a 32 m simply supported bridge first. Then, a long-span railway cable-stayed bridge is investigated in order to evaluate the impact effects of each component. To some extent, numerical results from this study can serve as valuable reference to the design, construction, and maintenance of long-span railway bridges. Besides, to optimize sensor placement for structural health monitoring [5, 17], impact coefficients can be defined as “health index” to estimate the health and safety of bridges, which are available to identify the vulnerable parts of the bridge in the health monitoring process [18]. Furthermore, the coupled vehicle-bridge vibration analysis could be regarded as a theoretical method to quantify the impact response of bridges in the vibration monitoring based on field testing.

2. Modeling of Coupled Vehicle-Bridge System and Its Verification

2.1. Modeling of Coupled Vehicle-Bridge Vibration System. Self-developed analysis software “Bridge Analysis System” (BANSYS) is employed to analyze the dynamic responses of the coupled vehicle-bridge system [19].

2.1.1. Modeling of Rail Vehicles. A train usually consists of bodies, wheelsets, bogies, and suspension systems, and all the locomotives and coaches can be modeled into mass-spring-damper systems as shown in Figure 1 (e.g., a 4-axle vehicle). Considering the secondary suspension system for a four-axle vehicle, the whole vehicle can be divided into seven rigid bodies: one vehicle body, two bogies, and four wheelsets, and they are connected with each other by springs and dampers. In this study, it is assumed that the degree of freedom (DOF) along the traveling direction can be neglected. Thus, each vehicle body and bogies are specified with five DOFs in the lateral, vertical, floating, rolling, yawing, and nodding directions. The wheelset only has two independent DOFs in the lateral and yawing directions. That is to say, a four-axle vehicle has total 23 DOFs which can indicate the vibration characteristics of a railway vehicle well.

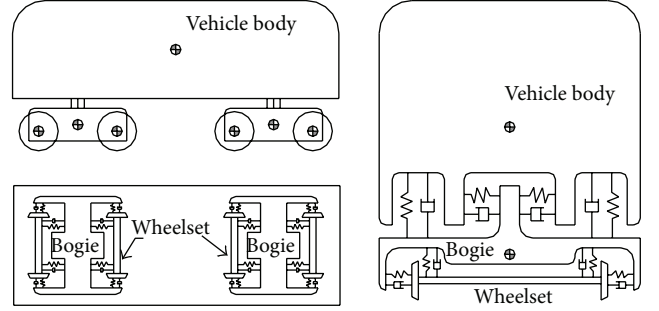


FIGURE 1: Mass-spring-damper model of vehicle.

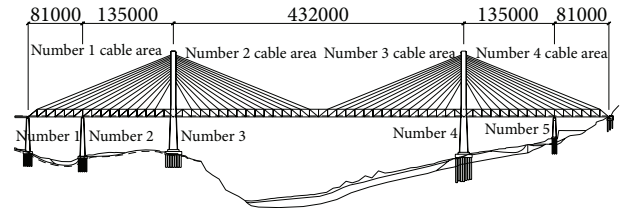


FIGURE 2: Overall arrangement of the cable-stayed bridge (units: millimeters).

2.1.2. Modeling of Hanjiatuo Bridge. Hanjiatuo Bridge shown in Figure 2 has a main span of 432 meters. It is a long-span railway cable-stayed bridge with steel truss deck, two towers, and double cable planes, which belongs to semifloating supported configuration.

A finite element model for the bridge is established using the general FEM software ANSYS. Beam4 is used to model the main girder and tower; Link8 is employed to model the stayed cable; and a three-orthogonal-beam model for the finite element is adopted to simulate the foundation stiffness [20]. The finite element model of the cable-stayed bridge is shown in Figure 3. The results of the dynamic characteristic analysis of the bridge model show that the first, second, and third order mode shapes are the longitudinal, transversal, and vertical bending, respectively. Their fundamental frequencies are 0.159 Hz, 0.287 Hz, and 0.423 Hz, respectively. The first ten natural frequencies and mode shapes are shown in Table 1.

2.2. Verification. Impact coefficient [16, 21] can be defined as amplification in the design traffic load resulting from the interaction of moving vehicles and bridges. The impact coefficient μ is defined as follows:

$$\mu = \frac{(R_{d \max} - R_{s \max})}{R_{s \max}}, \quad (1)$$

where $R_{d \max}$ is the maximum dynamic response in the time history curve while $R_{s \max}$ is the maximum static response value in the time history curve.

In order to validate the reliability of the algorithm, the vertical vibration response of a 32 m simply supported bridge has been investigated [22, 23]. Various vehicle speeds are discussed, and the numerical results are compared with those calculated by the impact formulas presented in the existing

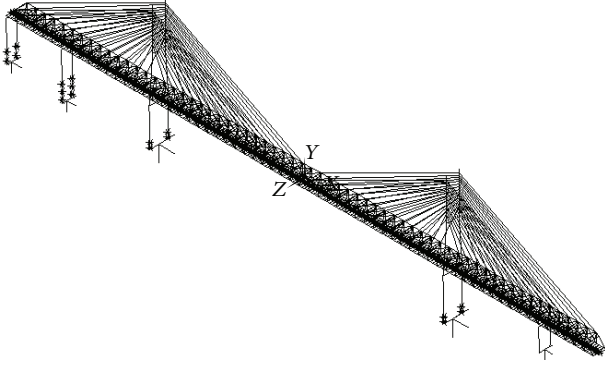


FIGURE 3: Finite element model of the cable-stayed bridge.

TABLE 1: Frequency and vibration shape of the bridge.

Order	Frequency/Hz	Mode shape
1	0.15851	Main girder longitudinal drifting
2	0.28670	Main girder lateral symmetric bending-1
3	0.42343	Main girder vertical symmetric bending-1
4	0.47667	Main girder lateral antisymmetric bending-1
5	0.49741	Main girder lateral antisymmetric bending-2
6	0.70407	Main girder lateral antisymmetric bending-3
7	0.71530	Main girder vertical antisymmetric bending-1
8	0.81917	Tower lateral bending-1
9	0.81918	Tower lateral bending-2
10	0.81973	Pier longitudinal bending

codes. A simply supported bridge with eight spans is shown in Figure 4. It consists of four posttensioned precast simple T-beams.

When a train passes through the simply supported bridge at a constant velocity V , the arrangement of the train axle loads has certain regularity. The train axle load impacted on the bridge equals a cyclic loading with a frequency of f_v ($f_v = V/L_v$). When the loading frequency f_v and the natural frequency of bridge f_b have a relation with integer times i , resonance will be excited on the bridge, and an impact coefficient peak will appear. The resonance speed [24] corresponding to the i th bridge's resonance, (2), is defined as

$$v_i = \frac{f_b \times L_v}{i} \quad (i = 1, 2, 3, \dots), \quad (2)$$

where f_b is the natural frequency of the bridge in Hz; and L_v is the length of the train in meters.

The eight-span simply supported bridge is established based on self-developed analysis software BANSYS. According to the calculation results, the natural frequency of the bridge is 3.864 Hz. A CRH2 passenger train of 26 m length,

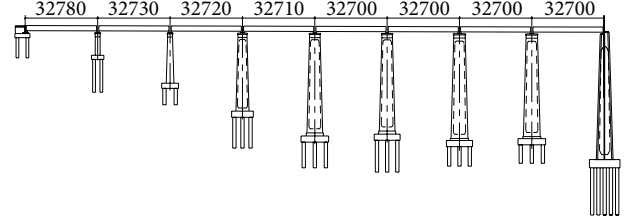


FIGURE 4: General elevation of a simple beam bridge (units: millimeters).

with a train arrangement of $2 \times (1 \text{ trailer} + 1 \text{ motor} + 1 \text{ trailer})$, is employed in this study to investigate the resonance speeds for the bridge, and some parameters of CRH2 are shown in Table 2. The results show that the first three theoretical resonance speeds corresponding to (2) are 361.7 km/h, 180.8 km/h, and 120.3 km/h, respectively.

To study the vertical resonance response of the simply supported bridge at high speeds, the vehicle speed range is set from 100 km/h to 420 km/h with an interval of 10 km/h. The measured track irregularities of Zhengzhou-Wuhan line, as shown in Figure 5, are taken as the system excitation inputs. The dynamic response of the vehicle-bridge system and the static response of the bridge with moving loads passing through the bridge were obtained from BANSYS. Then the maximum dynamic and static responses can be obtained in the time history curves, and according to (1), the curves of the impact coefficients for the vertical displacement and bending moment of the 1st midspan at various vehicle speeds are calculated and shown in Figure 6.

As shown in Figure 6, the impact coefficient for the simply supported bridge does not increase monotonously with the vehicle speed, and some peak values appear in the curves. The peak values of the impact coefficient appear at the speed of 120 km/h and 360 km/h, which is close to the third theoretical resonance speed (120.6 km/h) and the first resonance speed (361.7 km/h) of the bridge. The results show that it is feasible to quantify the impact coefficient with the method of the coupled vehicle-bridge vibration. Meanwhile, the reliability of analysis software BANSYS is validated.

Vibration cancellation phenomenon occurs at the second resonance speed (180 km/h), which leads to the disappearance of resonance. When the train speed simultaneously satisfies conditions of both vibration cancellation and resonance phenomena, cancellation plays a predominant role, and the peak value of impact coefficient disappears [25]. In addition, the impact coefficients for the vertical displacement and bending moment are essentially consistent, and the impact coefficient for the vertical displacement will be studied at the most conditions in the following context.

The comparison of the impact coefficients quantified by the method of the coupled vehicle-bridge vibration with the values calculated by the impact formulas presented in the existing codes [26–29] is shown in Figure 7.

As shown in Figure 7, in the range of the design vehicle speed (200 km/h) except for 120 km/h (the third resonance speed), the impact coefficients obtained from the coupled

TABLE 2: Weight and yawing inertia of CRH2.

Vehicle type	Weight/t			Yawing inertia/t·m ²		
	Body	Wheelset	Bogie	Body	Wheelset	Bogie
Locomotive	39.60	2.00	3.20	1900	0.980	3.20
Trailer	34.10	2.10	2.60	1700	1.029	2.60

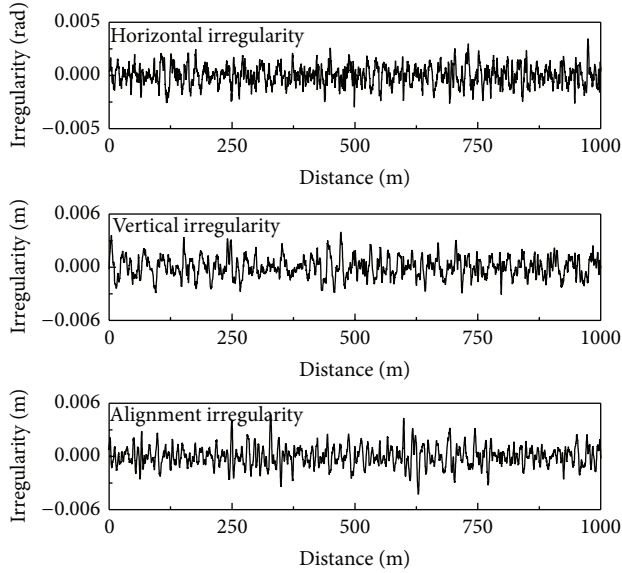


FIGURE 5: Track irregularities of Zhengzhou-Wuhan line.

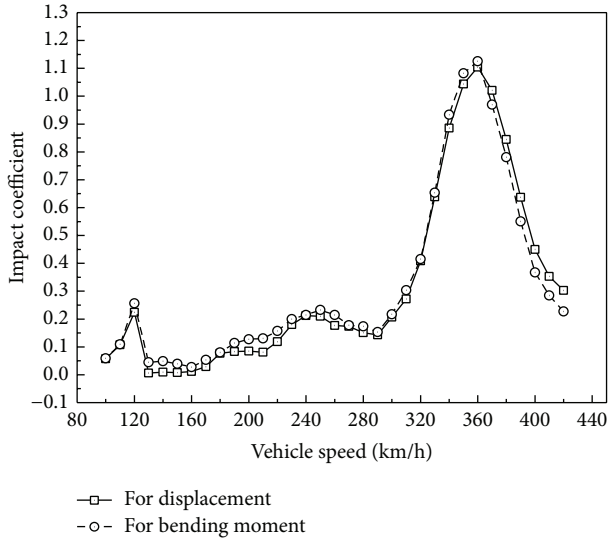


FIGURE 6: Impact coefficients of the 1st midspan.

vehicle-bridge system model satisfy the requirement of *Fundamental Code for Design on Railway Bridge and Culvert* [30]. And the impact coefficients calculated by the code formulas are greater than the numerical results quantified from the coupled vehicle-bridge model at most vehicle speeds.

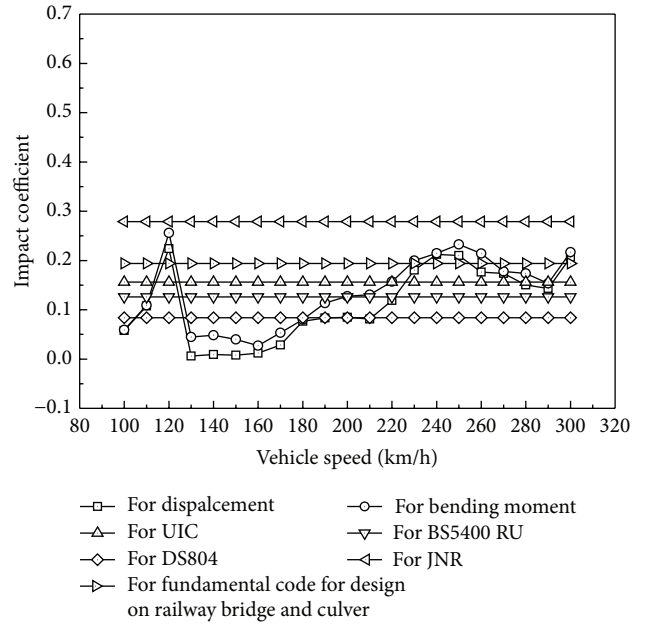


FIGURE 7: Comparison between values from BANSYS and values calculated by code formulas.

3. Analysis of Impact Coefficient for Long-Span Cable-Stayed Bridge

To study impact coefficient of Hanjiatuo Bridge, the analysis software BANSYS is employed to obtain the time history response curves of each component of Hanjiatuo Bridge under static and dynamic traffic loads.

However, in spite of the fact that the impact formulas presented in the existing codes only suit the middle and small span bridges, these formulas are also applied to the design of long-span bridges, which may lead to underestimating the impact coefficients. The impact coefficient of Hanjiatuo Bridge is 0.05 based on *Fundamental Code for Design on Railway Bridge and Culvert* [30].

3.1. Impact Coefficient for Displacement of Main Girder. CRH2 vehicles are passing through the bridge at the speeds of 160 km/h, 200 km/h, and 240 km/h. The impact coefficients for the vertical displacement of the whole main girder are displayed in Figure 8. In order to investigate the relationship between the vehicle speed and the impact coefficient for the main girder, the following vehicle speed range from 100 km/h to 240 km/h with an interval of 20 km/h is studied. The impact coefficients for the vertical displacement of typical positions on each span at various velocities are shown in Figure 9.

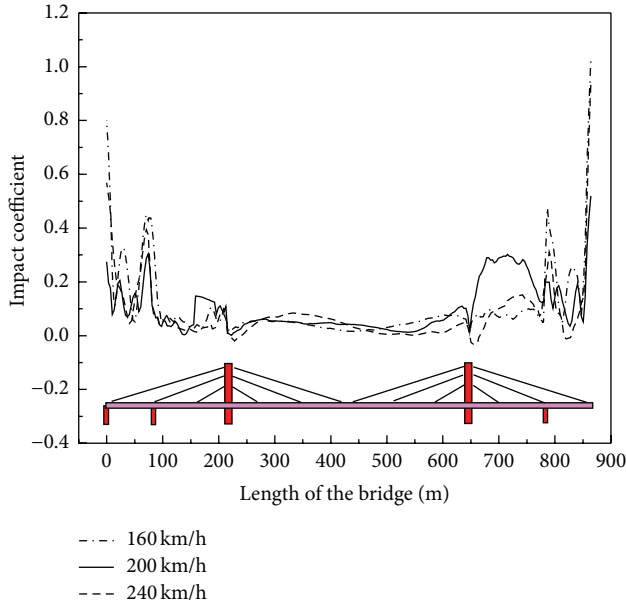


FIGURE 8: Impact coefficients for vertical displacement at different positions of main girder.

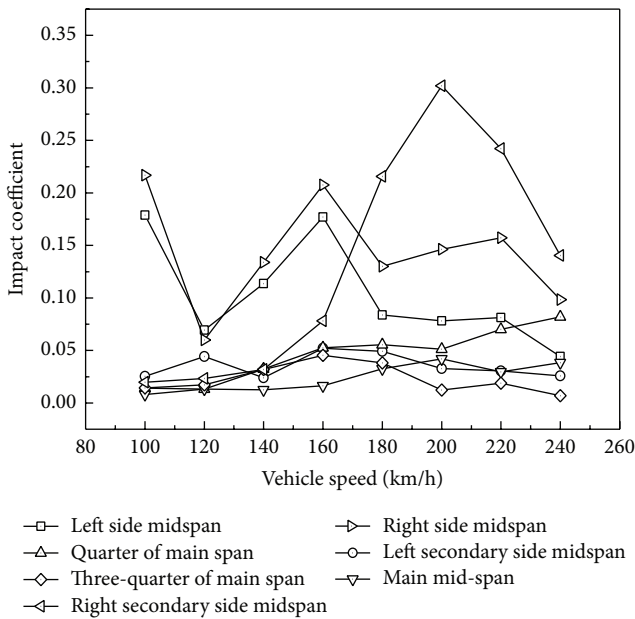


FIGURE 9: Impact coefficients for vertical displacement at typical positions of main girder.

It can be seen from Figures 8 and 9 that the long-span railway cable-stayed bridge has a lower natural frequency due to its flexible nature. Thus, resonance phenomenon occurs hardly in the range of the operational speed. Besides, the coupling effect between spans is strong. The variation of the impact coefficient is not obvious with the increase of the vehicle speed. On the whole, though the vertical displacements of bridge decks near the locations of piers and towers are small, the impact coefficients of the locations are

greater than other locations. The impact coefficient for the vertical displacement of the main span is less than those of the other spans, and the impact coefficient is insensitive to the vehicle speed, which is due to the mitigation of impact effect resulting from the greater span length. The time histories for the vertical displacement of the right secondary side span at the speed of 200 km/h are shown in Figure 10.

3.2. Impact Coefficient for Force of Cable. In order to study the impact coefficient for the force of cables, the stayed cables are divided into four cable areas in the longitudinal direction of the bridge, as shown in Figure 2. The stayed cables in each cable area are numbered from 1 to 14 with the increase of cable length. The vehicle speed range is from 100 km/h to 240 km/h with an interval of 20 km/h. The time histories for the force of cables under both static and dynamic vehicle loads are calculated by BANSYS, and the impact coefficients of each cable area at various vehicle speeds calculated from (1) are shown in Figure 11.

As shown in Figure 11, with the increase of the vehicle speed and the cable length, the variation of the impact coefficient for each cable area differs from each other. It should be specially noticed that the maximum value of the impact coefficient occurs at the first cable of number 4 cable area at the speed of 240 km/h, which approaches 1.11. The impact coefficients of the shorter cables are sensitive to the vehicle speed; the impact coefficients for the force of the cables increase with the increasing vehicle speed.

When the static and dynamic vehicle loads act on the bridge at the speed of 200 km/h, the time histories for the force of three cables numbered 1, 5, and 14 at number 4 cable area are shown in Figures 12, 13, and 14.

3.3. Impact Coefficient for Force of Bearing. In order to study the impact coefficient for the force of bearing, the bridge piers are numbered from 1 to 5 as shown in Figure 2. Beam4 element is employed to simulate bearing, and BANSYS is used to obtain the static and dynamic responses of bearing. When CRH2 vehicles pass through the bridge on the left line at the velocities of 160 km/h, 200 km/h, and 240 km/h, the impact coefficients of the bearings computed are shown in Figure 15. When the vehicles pass through the bridge on the right line at the speed of 200 km/h, the impact coefficients are shown in Figure 15.

It can be seen from Figure 15 that the impact coefficients of the bearings do not augment with the increasing vehicle speed. Generally, the impact coefficients of tower bearings are smaller than those of the pier bearings, and the impact coefficients of the side pier bearings are greater than others. In contrast to the data shown in Figure 16, when vehicles pass through the bridge on the left line, the impact coefficients for the left bearings are less than those for the right bearings; otherwise, the impact coefficients for the right bearings are less than those for left bearing when vehicles pass through the bridge on the right line. The results show that when vehicles pass through the bridge on one side line, even if the forces for the bearings of the other side are less, the impact coefficients are greater.

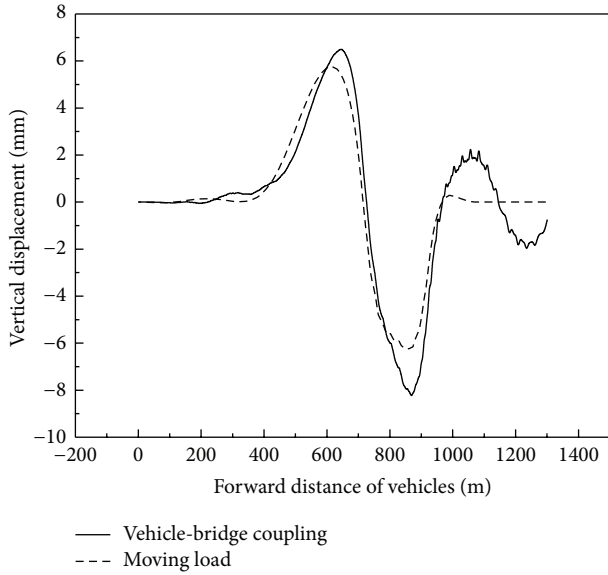


FIGURE 10: Time histories for vertical displacement of right secondary side span (200 km/h).

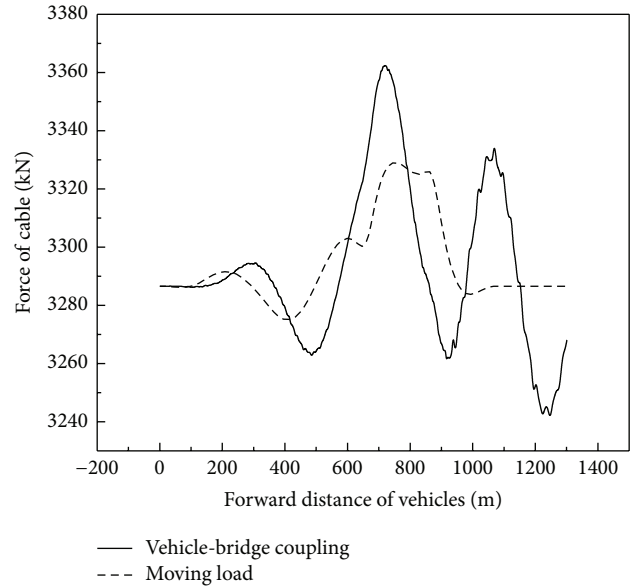


FIGURE 12: Time histories for force of number 1 cable.

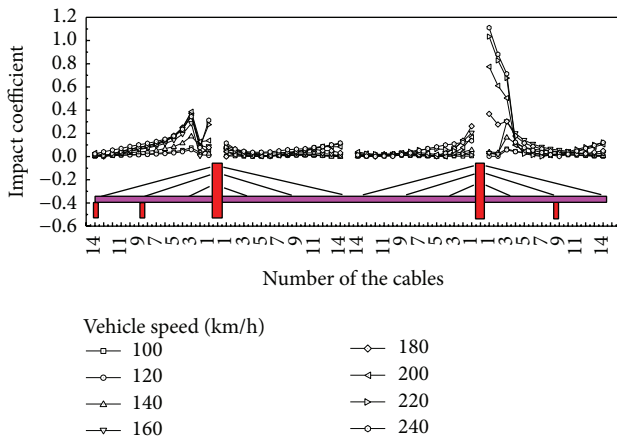


FIGURE 11: Impact coefficients for force of cable.

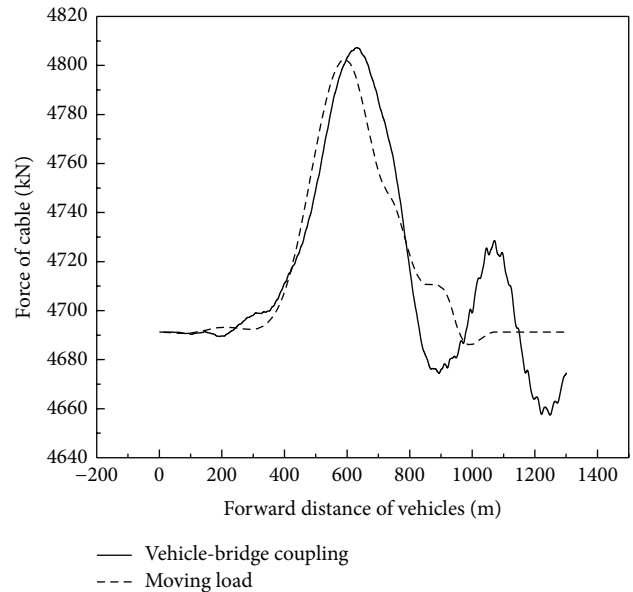


FIGURE 13: Time histories for force of number 5 cable.

3.4. Impact Coefficient for Bending Moment of Bridge Tower. When CRH2 vehicles pass through the bridge with three various velocities, the impact coefficients for the bending moment of the bridge towers are shown in Figure 17. It can be seen that the stress distribution in the anchorage area of the cable-tower is complicated. The impact coefficients can be negative values, and the minimum value is -0.05 . The most obvious impact effect occurs at the element closest to the foundation of the bridge towers. The impact coefficient of number 4 tower at the speed of 240 km/h can approach 1.08. At the vehicle speed of 200 km/h, the time history for the bending moment of the tower element between number 12 and number 13 cables belonging to number 3 tower is shown in Figure 18. It can be seen from Figures 17 and 18 that the impact effect for the upper part of bridge towers is limited.

4. Conclusions

(1) The vertical impact effect of a 32 m simply supported bridge is investigated systematically. The coupled vehicle-bridge vibration system model is employed in the analysis, and the resonance speed computed by BANSYS is in good agreement with that calculated by the theoretical formula. The results show that it is feasible to study the impact coefficient based on the method of the coupled vehicle-bridge vibration.

(2) Different from a simply supported bridge, resonance phenomenon of a long-span railway cable-stayed bridge occurs hardly in the range of the operational speed. And

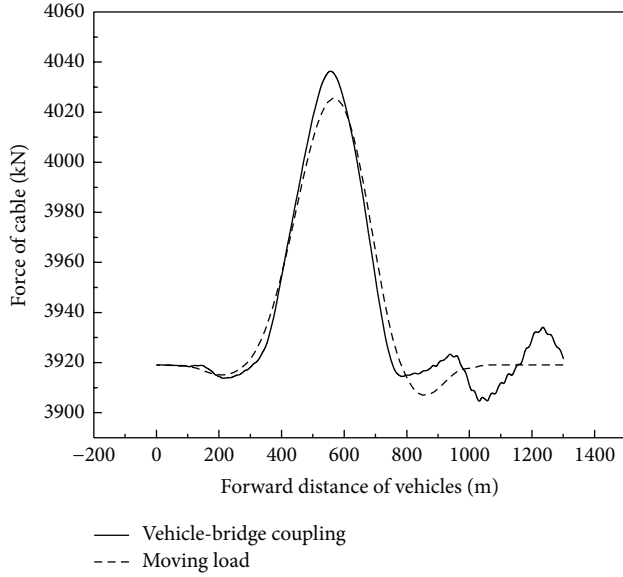


FIGURE 14: Time histories of force of number 14 cable.

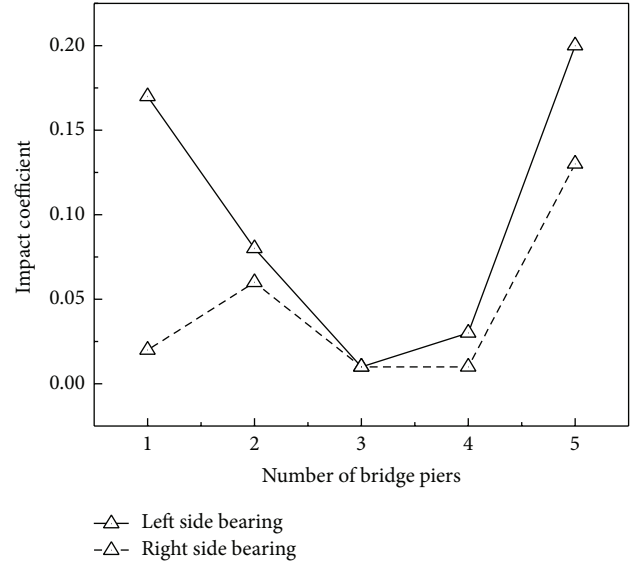


FIGURE 16: Train loading on the right line (200 km/h).

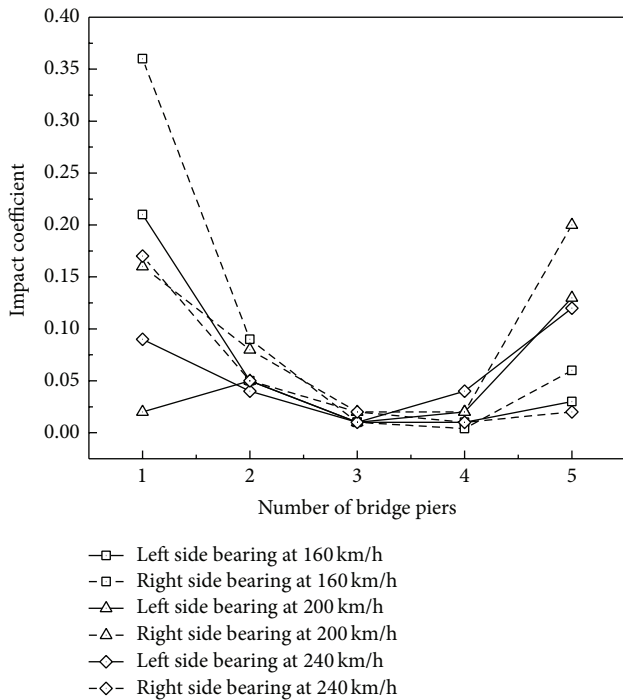


FIGURE 15: Train loading on the left line.

the variation of impact coefficient is not obvious with the increasing vehicle speed due to the strong coupling effects between spans. On the whole, the impact coefficient for the vertical displacement of the main span is less than that for the other spans. The impact coefficient of the right secondary side span is 0.30 while the impact coefficient for the main girder can approach 0.94 at the train leaving side.

(3) The impact coefficient for cable force increases with the increasing vehicle speed generally. The impact coefficients

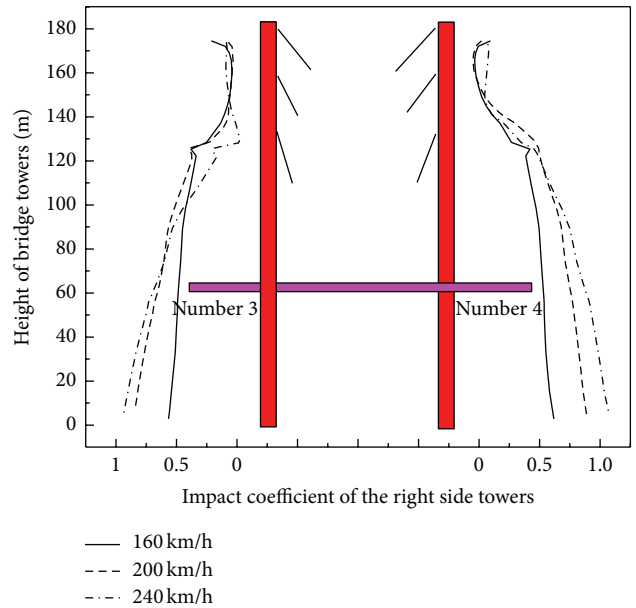


FIGURE 17: Impact coefficients for bending moment of bridge tower.

of shorter cables are sensitive to the vehicle speed, which can approach 1.11.

(4) The impact coefficient for the force on the bearings at the tower is small, while the impact coefficient for the force of the bearings at train entering side is significant, which can be 0.36. Under the condition of unilateral loading on the bridge, the impact effect for the bearings of nonloading side is greater.

(5) On the whole, the closer the foundation of bridge towers, the larger the impact coefficient for the bending moment of the bridge towers, which can approach 1.08. In the anchorage area of the cable-tower, owing to the existence of cables, the stress distribution in this area is complicated and impact coefficients can be negative values.

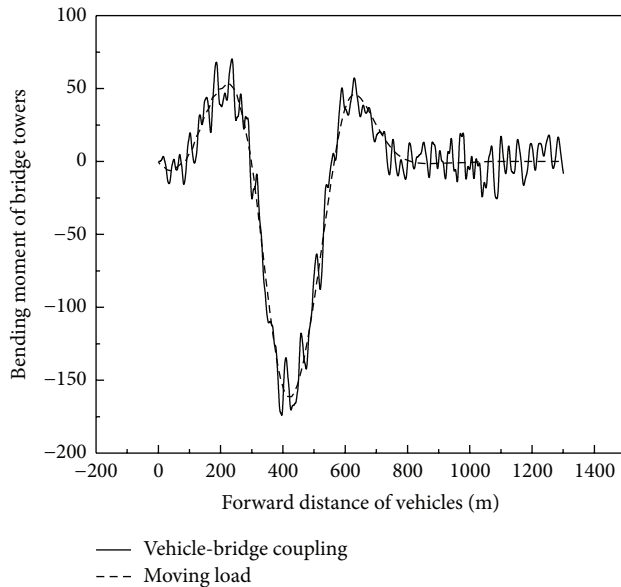


FIGURE 18: Time histories for bending moment of bridge tower.

In a word, different components of the long-span railway cable-stayed bridge have different impact coefficients. Each component also has different impact coefficients at different local positions. And numerical results are significantly different from the design code, except for that of main span, which approaches the design code. Impact coefficients of many positions are much larger than the value calculated by the code (0.05). The design code may focus on the impact coefficient of main span.

Conflict of Interests

The authors declare that there is no conflict of interests regarding the publication of this paper.

Acknowledgments

The authors are grateful to the financial supports from the National Natural Science Foundation of China (no. U1334201 and no. 51278434) and the Special Research Foundation of the National Railway Ministry of China (no. 2009G004-D).

References

- [1] Y. Xia, B. Chen, X.-Q. Zhou, and Y.-L. Xu, "Field monitoring and numerical analysis of Tsing Ma suspension bridge temperature behavior," *Structural Control and Health Monitoring*, vol. 20, no. 4, pp. 560–575, 2013.
- [2] E. S. Hwang and A. S. Nowak, "Simulation of dynamic load for bridges," *Journal of Structural Engineering*, vol. 117, no. 5, pp. 1413–1434, 1991.
- [3] T.-H. Yi, H.-N. Li, and M. Gu, "Experimental assessment of high-rate GPS receivers for deformation monitoring of bridge," *Measurement*, vol. 46, no. 1, pp. 420–432, 2013.
- [4] B. Chen, Z.-W. Chen, Y.-Z. Sun, and S.-L. Zhao, "Condition assessment on thermal effects of a suspension bridge based on SHM oriented model and data," *Mathematical Problems in Engineering*, vol. 2013, Article ID 256816, 18 pages, 2013.
- [5] T.-H. Yi, H.-N. Li, and X.-D. Zhang, "Sensor placement on Canton Tower for health monitoring using asynchronous-climb monkey algorithm," *Smart Materials and Structures*, vol. 21, no. 12, Article ID 125023, 12 pages, 2012.
- [6] M.-K. Song, H.-C. Noh, and C.-K. Choi, "A new three-dimensional finite element analysis model of high-speed train-bridge interactions," *Engineering Structures*, vol. 25, no. 13, pp. 1611–1626, 2003.
- [7] H. Xia, N. Zhang, and R. Gao, "Experimental analysis of railway bridge under high-speed trains," *Journal of Sound and Vibration*, vol. 282, no. 1-2, pp. 517–528, 2005.
- [8] F. T. K. Au, J. J. Wang, and Y. K. Cheung, "Impact study of cable-stayed bridge under railway traffic using various models," *Journal of Sound and Vibration*, vol. 240, no. 3, pp. 447–465, 2001.
- [9] F. T. K. Au, J. J. Wang, and Y. K. Cheung, "Impact study of cable-stayed railway bridges with random rail irregularities," *Engineering Structures*, vol. 24, no. 5, pp. 529–541, 2002.
- [10] A. Matsuura, "Study of dynamic behaviors of bridge girders for high-speed railway," *Journal of JSCE*, vol. 256, no. 12, pp. 35–47, 1976.
- [11] M. H. Bhatti, V. K. Garg, and K. H. Chu, "Dynamic interaction between freight train and steel bridge," *Journal of Dynamic Systems, Measurement and Control, Transactions of the ASME*, vol. 107, no. 1, pp. 60–66, 1985.
- [12] X. D. Song, D. J. Wu, and Q. Li, "Dynamic impact analysis of double-tower cable-stayed maglev bridges using a simple model," *Journal of Bridge Engineering*, vol. 19, no. 1, pp. 34–43, 2014.
- [13] Z. W. Chen, Y. L. Xu, Y. Xia, Q. Li, and K. Y. Wong, "Fatigue analysis of long-span suspension bridges under multiple loading: case study," *Engineering Structures*, vol. 33, no. 12, pp. 3246–3256, 2011.
- [14] Z. W. Chen, Y. L. Xu, and X. M. Wang, "SHMS-based fatigue reliability analysis of multiloading suspension bridges," *Journal of Structural Engineering*, vol. 138, no. 3, pp. 299–307, 2012.
- [15] A. Das, A. Dutta, and S. Talukdar, "Efficient dynamic analysis of cable-stayed bridges under vehicular movement using space and time adaptivity," *Finite Elements in Analysis and Design*, vol. 40, no. 4, pp. 407–424, 2004.
- [16] D. Bruno, F. Greco, and P. Lonetti, "Dynamic impact analysis of long span cable-stayed bridges under moving loads," *Engineering Structures*, vol. 30, no. 4, pp. 1160–1177, 2008.
- [17] T.-H. Yi, H.-N. Li, and M. Gu, "Optimal sensor placement for structural health monitoring based on multiple optimization strategies," *The Structural Design of Tall and Special Buildings*, vol. 20, no. 7, pp. 881–900, 2011.
- [18] Y. Wang, Y. Pei, and Y. Zhao, "Vibration-based damage detection with structural modal characteristics," *The Baltic Journal of Road and Bridge Engineering*, vol. 3, no. 1, pp. 21–28, 2008.
- [19] Y. L. Li, S. Z. Qiang, H. Liao, and Y. L. Xu, "Dynamics of wind-rail vehicle-bridge systems," *Journal of Wind Engineering and Industrial Aerodynamics*, vol. 93, no. 6, pp. 483–507, 2005.
- [20] Y. L. Li, K. Zhao, and X. T. Cai, "Three-Orthogonal-Beam model for finite element simulation of bridge foundation stiffness," *Bridge Construction*, no. 6, pp. 17–20, 2010 (Chinese).
- [21] L. Deng and C. S. Cai, "Development of dynamic impact factor for performance evaluation of existing multi-girder concrete bridges," *Engineering Structures*, vol. 32, no. 1, pp. 21–31, 2010.

- [22] J. D. Yau and Y. B. Yang, "Vertical accelerations of simple beams due to successive loads traveling at resonant speeds," *Journal of Sound and Vibration*, vol. 289, no. 1-2, pp. 210-228, 2006.
- [23] Y. B. Yang, J. D. Yau, and L. C. Hsu, "Vibration of simple beams due to trains moving at high speeds," *Engineering Structures*, vol. 19, no. 11, pp. 936-943, 1997.
- [24] H. Xia, N. Zhang, and W. W. Guo, "Analysis of resonance mechanism and conditions of train-bridge system," *Journal of Sound and Vibration*, vol. 297, no. 3-5, pp. 810-822, 2006.
- [25] H. Xia, H. L. Li, W. W. Guo, and G. de Roeck, "Vibration resonance and cancellation of simply supported bridges under moving train loads," *Journal of Engineering Mechanics*, vol. 140, no. 5, pp. 1-11, 2014.
- [26] UIC, "Loads to be considered in railway bridge design," UIC Code776-IR, France, 1994.
- [27] BSI-BS5400, *Steel, Concrete and Composite Bridge*, 1978.
- [28] DS804: *Vorschrift fur Eisenbahn bracken and sonstige Ingenieur bauwerke*, Deutsche Bundesbahn, 1993.
- [29] Federal Railroad Administration, *Track Safety Standards Compliance Manual*, 2006.
- [30] Ministry of Railways of the People's Republic of China, "Fundamental code for design on railway bridge and culvert," Chinese Standard TB10002.1-2005, 2005, (Chinese).

Research Article

Seismic Fortification Analysis of the Guoduo Gravity Dam in Tibet, China

Peng Lin,¹ Wenwei Zheng,² Bo Huang,³ and Haichao Zhang⁴

¹State Key Laboratory of Hydrosience and Engineering, Tsinghua University, Beijing 100084, China

²China Academy of Building Research, Beijing 100013, China

³MOE Key Laboratory of Soft Soils and Geoenvironmental Engineering, Department of Civil Engineering, Zhejiang University, Hangzhou 310058, China

⁴Guiyang Hydroelectric Investigation and Design Institute, China Hydropower Engineering Consulting Group Co., Guiyang, Guizhou 550081, China

Correspondence should be addressed to Peng Lin; celinpe@tsinghua.edu.cn

Received 26 July 2014; Accepted 12 September 2014

Academic Editor: Bo Chen

Copyright © 2015 Peng Lin et al. This is an open access article distributed under the Creative Commons Attribution License, which permits unrestricted use, distribution, and reproduction in any medium, provided the original work is properly cited.

The primary aim of this research was to analyze the seismic performance of the Guoduo gravity dam. A nonlinear FEM method was implemented to study the deformation, stress, and overall stability of dam under both static and dynamic loading conditions, including both normal and overloading conditions. A dam seismic failure risk control method is proposed based on the cracking mechanism induced by the dynamic load to ensure dam safety and stability. Numerical simulation revealed that (1) under normal static and dynamic loading the symmetry of the displacement distributions is good, showing that the dam abutments and riverbed foundation have good overall stiffness. The stress distribution is a safe one for operation under both normal water loading and seismic loading. (2) Attention should be paid to the reinforcement design of outlets of the diversion dam monoliths, and enhance the capability of sustaining that tensile stress of dam monoliths. (3) The shape of the dam profile has a significant effect on the dynamic response of the dam. (4) By employing the “overload safety factor method,” the overall seismic fortification is as follows: $K_1 = 1.5$, $K_2 = 2\sim 3$, and $K_3 = 3\sim 4$.

1. Introduction

During the last 30 years, over 2000 dams have been constructed for irrigation, energy production, flood control, and recreation purposes in China. Almost 500 large dams have been built on the fringes of the active seismic zone in southwestern provinces in China. Since the failure of dams incurs great losses to society [1–5], all countries pay careful attention to dam safety, especially to those dams exposed to extreme earthquake loading [6–9]. In studying the seismic performance of the different types of dam and other civil structural, field surveys [10, 11], health monitoring [12, 13] and numerical simulation [3, 14, 15] are important research tools. Computational mechanics has made a strong impact on classical continuum mechanics, which includes engineering and structural mechanics [16–18]. Earthquake engineering

has made significant progress with the aid of computational mechanics [19–22]. The overall structural assessment of concrete gravity dams has long been undertaken. The first attempts to apply the theories and methods of fracture mechanics to concrete structures date back to the 1970s [19]. Pioneering analyses were mostly based on linear elastic fracture mechanics (LEFM). Some case studies [20] were based on LEFM theories, including the analysis of cracking in the Fontana dam (USA), the Koyna dam (India), and the Köhlbrein dam (Austria). When nonlinear fracture mechanics (NLFM) models are used [21], a nonlinear dynamic problem has to be solved [22]. The latter nowadays is most challenging due to the large differences in the characteristic time scales of the problem.

During the development of structural seismic theory and analysis methods [6, 7], the three dominant approaches are

based on static theory, pseudostatic theory, and dynamic theory. Static theory assumes the foundation is a continuous homogeneous rigid body. In the 1978 specifications for the seismic design of hydraulic structures seismic load is determined by a simplified, more realistic, pseudostatic method. The method is not really precise; however, dynamic theory is much more realistic because when calculating seismic action, comprehensive consideration of the structure and its natural vibration properties and damping factors is closer to the actual situation. Dynamic theory calculation ultimately comes down to solving the equations of motion of the structure. Two main solution methods are used: (1) the response spectrum method, for the seismic design of damping ratio of the elemental points system in the earthquake under the action of the maximum acceleration response of the curve of the change. The system natural vibration period is generally expressed by the ratio of the maximum peak ground motion acceleration. Standard response spectrum which is shown by the acceleration spectrum is widely used in the calculation of hydraulic structure and has a series of results that can be compared. (2) The time history method is based on the second order differential equations which describe the motions throughout the structure, equations solved by numerical integration, over time in small time increments Δt in an essentially step-by-step integration method. The above two time domain methods fall into the category "time-domain analysis of structural responses."

In the last 30 years, much research aimed at studying the seismic fortification of dams has been carried out. Bouaanani and Renaud [23] presented an original investigation of the sensitivity of floor accelerations in gravity dams to various modelling assumptions relating to impounded reservoirs leading to analytical and coupled dam-reservoir finite element models. Li et al. [24] investigated seismic fortification of the Three Gorges dam based on experimental and numerical methods. Paggi et al. [25] took a multiscale approach for the seismic analysis of concrete gravity dams. Some researchers [26–28] analyzed the nonlinear seismic responses of arch dams caused by nonuniform ground motions and the influence of past loading history [29] and spatial variation inputs [30]. Valamanesh et al. [31] presented an application of the endurance time method for seismic analysis of concrete gravity dams; Omid et al. [32] employed a plastic-damage model using different damping mechanisms to simulate the seismic cracking of concrete gravity dams. Ftima and Léger [33] used rigid block models to analyze the seismic stability of cracked concrete dams. All these studies were effective in analyzing the seismic response of dam structures, and many interesting stability assessment related results were obtained.

The primary aim of the authors' research was to analyze and understand the seismic performance of the Guoduo dam under complex geological conditions. The deformation, stress, cracking risk, and overall seismic stability of the Guoduo were analyzed using a 3D finite element method, under various dynamic and static loadings, and a description is given below. A dam seismic failure risk control method is proposed based on the cracking mechanism induced by the dynamic load to ensure dam safety and stability.

2. Seismic Fortification Analysis Method and Cases

2.1. Introduction to the Guoduo Gravity Dam. The Guoduo hydropower station (Figure 1) includes an under construction dam situated on the Zaqu River in Cangdu County, Tibet. The dam is a roller compacted concrete (RCC) gravity dam with a maximum height of 93 m, a length of 235 m, and a width of 8 m at the crown of the dam, respectively, and a maximum bottom width of 83.2 m. The control river area is 33470 km². The normal water elevation level (EL) is 3418 m and the corresponding capacity is 0.08 billion m³. The primary purpose of the Guoduo hydroelectric power station is to generate 160 MW power for Tibet.

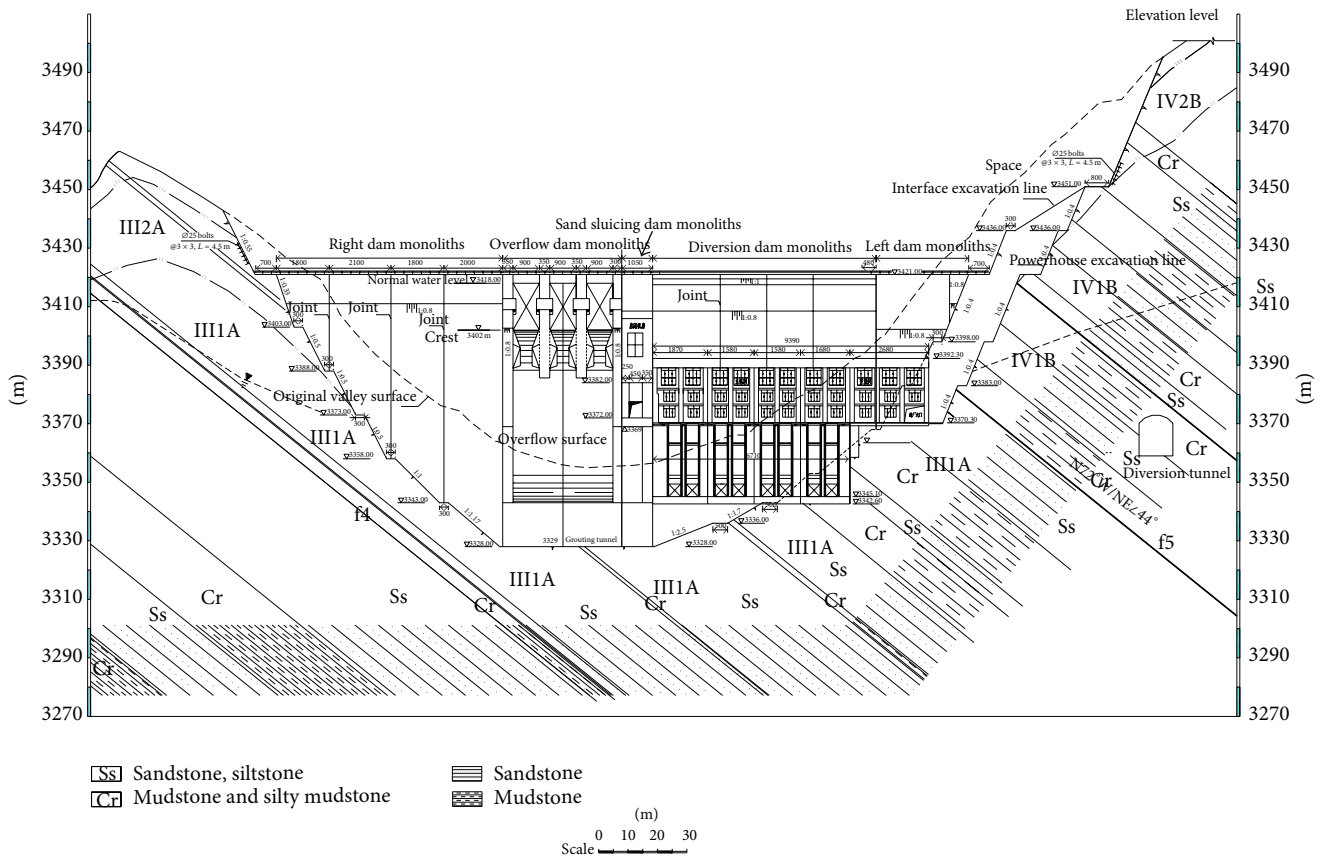
The dam site valley is wide "V" shape, and the slope topographies are relatively good. The left bank terrain slopes at 35° ~40°, and the right abutment is steep, with consideration necessary for a 40° ~45° slope. The main hydraulic structure plane and profile layout are illustrated in Figure 1(b). The lithology of the left abutment is sandstone mudstone, J1ch1, between EL 3400~3435 m. Sandstone, J1ch2, siltstone, mudstone, and silt mudstone layers are distributed above EL 3435 m. Below EL 3400 m, the dam foundation and the right abutment (T3d2) consist of gray thick massive sandstone and siltstone with mudstone. The content of the sandstone and siltstone is high at about 80% of the dam foundation rock mass. The dam site contains six small faults (f2, f3, f4 and f5, f6, and f7). Based on rock mass classification for dam foundations, there is IIIIA type rock mass (Tables 1 and 2) of sandstone and siltstone and IVC type rock mass of mudstone, argillaceous siltstone downstream of the dam site. The gravity dam foundation rock mass is mainly of type T3d2, a hard rock, especially the IIIIA class. The high strength and hard dam foundation rock mass has the bearing capacity to meet the design requirements. However, the concentrated soft rock area presents a problem of uneven deformation threatening the stability of gravity dam foundation. The left abutment was a reverse slope. An approximately 140 m high slope was formed after excavation. The slope is partially unstable due to sliding blocks. The right abutment is an inclined cut slope, 115 m high after excavation. This slope, influenced by lithology and the structure surface, may easily incur a bedding slip.

The dam site has a better than 10% probability in 50 years of a bedrock horizontal peak acceleration of 0.09 g. The horizontal seismic acceleration criterion was of the Guoduo's hydraulic structure 0.09 g. Dynamic loads generated by seismic disturbances must be considered in the design of concrete dams situated in recognized seismic high-risk regions. The possibility of seismic activity should also be considered for dams located outside those regions, particularly when sited in close proximity to potentially active geological fault complexes.

2.2. Numerical Modelling. The 3D nonlinear finite element dynamic analysis code, ABAQUS [34], was employed in this study. The dam-foundation-reservoir system, dam transverse



(a) Snapshot of the Guoduo gravity dam under construction



(b) Vertical profile of the Guoduo dam in the downstream side

FIGURE 1: Geoconditions and vertical profile of the Gouduo gravity dam.

joints, and dam induced joints were simulated under normal and overloading conditions. The 3D finite element analysis adopts the Drucker-Prager (D-P) yield criterion, which can be expressed by (1).

The 3D finite element analysis adopts Drucker-Prager (D-P) yield criterion, which can be expressed in

$$f = \alpha I_1 + J_2^{1/2} - H = 0, \quad (1)$$

TABLE 1: Physical-mechanical parameters of the concrete dam, the rock mass, and faults.

Material	Density (t/m ³)	Permit load (MPa)	Elastic modulus (GPa)	Poisson's ratio	Effective shear strength	
					C' (MPa)	f'
Dam (concrete)	2.40	2.0	22	0.167	0.90	1.2
III2A	2.61	3.4	8.8	0.32	0.70	0.80
III1A	2.70	5.0	17.0	0.30	0.90	1.00
IV2B	2.63	2.0	6.0	0.30	0.50	0.70
IV1B	2.68	3.5	9.0	0.28	0.80	0.90
Weak rock layer of right bank	2.4	1.0	1.5	0.30	0.05	0.40
Fault f2	2.4	1.0	1.5	0.30	0.05	0.35
Fault f3	2.4	1.0	1.5	0.30	0.05	0.35
Fault f4	2.4	1.0	1.5	0.30	0.05	0.35
Fault f5	2.4	1.0	1.5	0.30	0.05	0.35
Fault f7	2.4	1.0	1.5	0.30	0.05	0.35

TABLE 2: Rock mass classification for the Guoduo dam foundation.

Class	Rock mass structure	Rock mass description	Weathering	Uniaxial compression strength (MPa)
III1A	Thick layered structure surface, steep dip structural plane in abutment	Hard rock, intact and massive, high strength, antislip deformation resistance controlled by the structural planes. Weak rock mass is affected by weathering and unloading; local rock mass is poor	Fresh to slightly	Rb > 60 MPa
III2A			Weak	
IV1B	Interbedded or lamellar structure; some structures may cause dam foundation and abutment instability	Rock masses are relatively poor intact, antislip deformation resistance controlled by the structural planes and rock mass of chimeric ability. The rock mass cannot be directly used as dam foundation and must be effectively reinforced before used locally	Fresh to slightly	Rb = 30–60 Mpa
IV2B			Weak	
IVC	Interbedded or lamellar structure; some structures obviously cause dam foundation and abutment instability	Soft rock, rock intact, low strength, antislip, and deformation resistance performance are poor. The rock mass cannot be used as dam foundation and is excavated	Fresh to slightly	Rb < 30 MPa

where I_1 is the first invariant stress, J_2 is the second invariant stress, and α and H are material constants, which can be determined according to

$$\alpha = \frac{3tg\varphi}{\sqrt{9 + 12tg^2\varphi}}, \quad (2)$$

$$H = \frac{3c}{\sqrt{9 + 12tg^2\varphi}},$$

where c is cohesion and φ is friction angle. Equations (1) and (2) also show that the D-P criterion and the M-C (i.e., Mohr-Coulomb) criterion have the same expressions for the plane strain problem. In the π plane, the D-P circle has the intermediate values of the circumscribing circle and the inscribed circle to the M-C hexagon. Nonlinear elastoplastic finite element analysis can determine conditions such as plastic yield, subcritical fracture, and unstable extension and

plot the unbalanced force and point safety factor contours for the upstream and downstream surfaces of the dam.

The stress adjustment process in the nonlinear finite element analysis with the D-P criterion can be listed as follows: stress and strain at the initial point are set to be σ_0 and ϵ_0 and $f(\sigma_0) \leq 0$. For a given load step or iteration, the strain increment $\Delta\epsilon$ at the point can be obtained by the displacement method and the stress can be correspondingly calculated using

$$\sigma_1 = \sigma_{ij}^1 = \mathbf{D} : (\epsilon_0 + \Delta\epsilon), \quad (3)$$

where \mathbf{D} is the elasticity tensor. If $f(\sigma_1) > 0$, then the stress needs adjustment. If the plastic strain increment of the loading step or iteration is $\Delta\epsilon^p$, then the stress after adjusting can be written using

$$\sigma = \sigma_{ij} = \mathbf{D} : (\epsilon_0 + \Delta\epsilon - \Delta\epsilon^p) = \sigma_1 - \mathbf{D} : \Delta\epsilon^p. \quad (4)$$

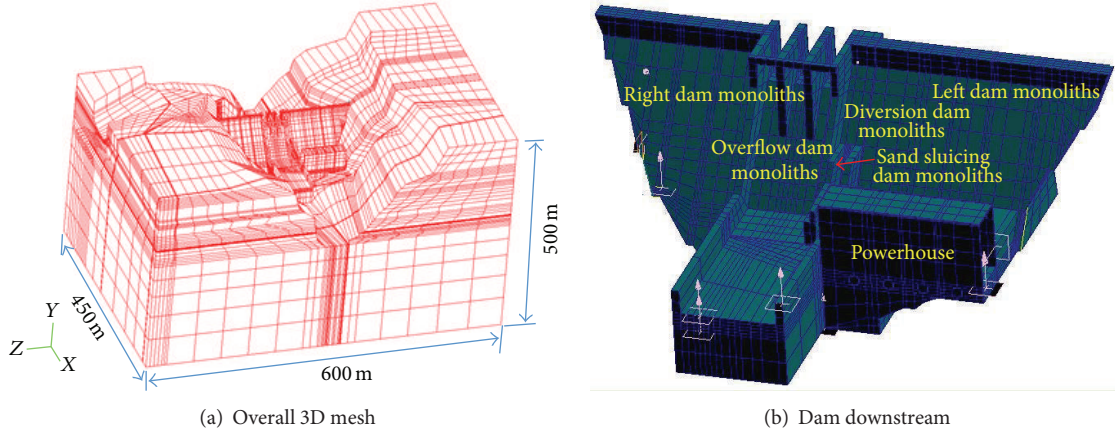


FIGURE 2: Schematic mesh model of Guoduo gravity dam.

Figure 2 depicts the numerical model for the Guoduo gravity dam, which consists of the whole dam structure, and its foundations including faults f2–f7, and the main weak zones of the right slope and rock mass types III2A, III1A, IV2B, and IV1B; see Table 2. In dynamic analysis, the concrete dynamic strength and elastic modulus of the standard value are increased to 30% compared with their static standard value and dynamic tensile strength of concrete is 10% of the dynamic compressive strength. The 3D finite element mesh includes a large proportion representing abutments and is of size 450 m × 600 m × 500 m (length × width × height). The total number of elements is 25805, 10181 of which represent the dam body.

In this study, the main loadings considered were as follows:

- (1) self-weight load;
- (2) upstream, downstream water pressure, the normal upstream water being at EL 3418 m, corresponding to the downstream tail water at EL 3360.91 m;
- (3) sediment pressure, silt elevation of 3378.38 m, density, γ_n , being 8 kN/m³, internal friction angle, ϕ_n , being 10°. The sediment pressure was calculated by

$$p_n = \gamma_n h_n \tan^2 \left(45^\circ - \frac{\phi_n}{2} \right); \quad (5)$$

- (4) the seismic loading horizontal design earthquake acceleration that was 0.09 g. The vertical design earthquake acceleration was 2/3 of the horizontal design earthquake acceleration. Standard spectra were used, respectively, to generate the three directions of the artificial seismic waves (Figure 3);
- (5) the earthquake dynamic water pressure that is calculated using the Westergaard dynamic water pressure formula [35]. Consider

$$p = \frac{7}{8} \rho \sqrt{H(H-Z)} \ddot{v}_g, \quad (6)$$

where p is the dynamic water pressure on some point of the dam surface, ρ represents water density, H is the reservoir

water depth, Z is the height of the point above the dam-foundation interface, and \ddot{v}_g is the acceleration of the dam node.

According to the specifications for seismic design of hydraulic structures (DL5073-2000) [35], in addition to using the dynamic response spectrum that the design institute provides, the time history analysis method should select, for dynamic analysis, a set of observed seismic waves which are similar to the likely site conditions. This study selected the artificial seismic wave inverted by the site spectrum. The response spectrum values derived using formulae (7), spectral curve, are shown in Figure 3, where $\beta_{\max} = 2.25$, features period $T_g = 0.25$ s. The inversed seismic waves and the response spectrum are shown in Figure 3. Consider

$$\beta(T) = \begin{cases} 1 & T = 0 \\ 1 + (\beta_{\max} - 1) \frac{T}{0.1} & 0 \leq T \leq 0.1 \text{ s} \\ \beta_{\max} & 0.1 \text{ s} \leq T \leq T_g \\ \max \left[0.2\beta_{\max}, \beta_{\max} \left(\frac{T_g}{T} \right)^{0.9} \right] & T_g \leq T \leq 3 \text{ s.} \end{cases} \quad (7)$$

2.3. Analysis Cases. The 3D finite element nonlinear dynamic analysis program for the Guoduo gravity dam was executed as follows: (1) for different load cases, checking stresses and deformations of the dam; (2) study of the cracking and failure processes of the dam under normal static and dynamic conditions; (3) evaluation of dam and foundation overall seismic fortification. The numerical results obtained from analysis cases no. 1 to no. 7 are shown in Table 3.

3. Elastic Analysis under Static and Dynamic Loading

In this section, the linear elastic 3D analysis results for the Guoduo gravity dam for Cases 1 and 2 are discussed. Typical dam monolith analyses include the right hand side dam

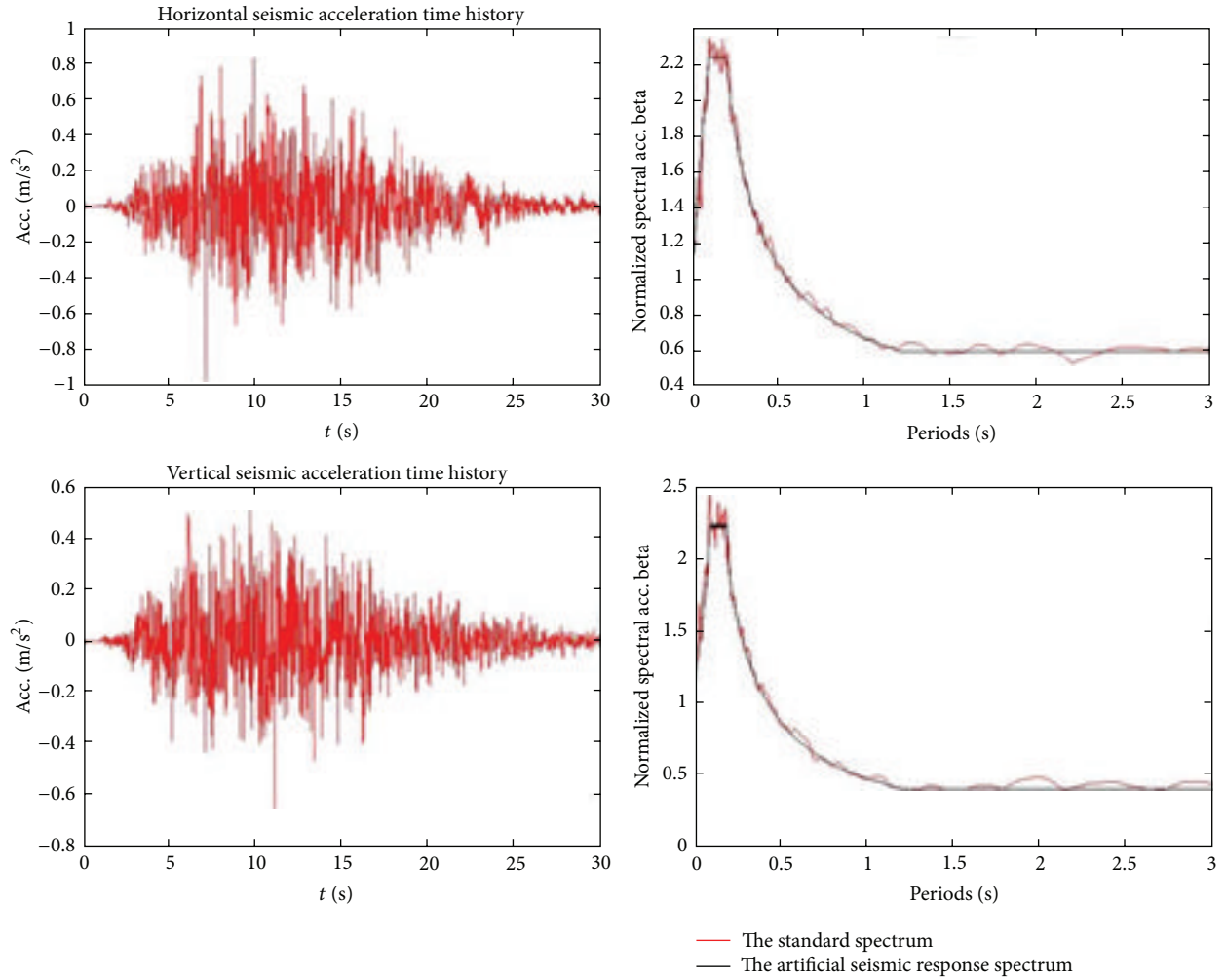


FIGURE 3: Inversed seismic waves and the response spectrum.

TABLE 3: Summary of the analysis cases studied in the 3D finite element modelling.

Analysis case number	Loading combination
1	Static loadings, self-weight + upstream normal water loading + silt load + downstream water load (3D linear elastic)
2	Static and dynamic loadings, Case 1 + design seismic load, horizontal seismic acceleration, 0.09 g (3D linear elastic, response analysis)
3	Static loadings, self-weight + upstream normal water loading + silt load + downstream water load (3D nonlinear)
4	Static and dynamic loadings, Case 3 + design seismic load, horizontal seismic acceleration, 0.09 g (3D linear elastic, time history analysis)
5	Static and dynamic loadings, Case 3 + design seismic load, horizontal seismic acceleration, 0.18 g (3D linear elastic, time history analysis)
6	Static and dynamic loadings, Case 3 + design seismic load, horizontal seismic acceleration, 0.27 g (3D linear elastic, time history analysis)
7	Static and dynamic loadings, Case 3 + design seismic load, horizontal seismic acceleration, 0.36 g (3D linear elastic, time history analysis)

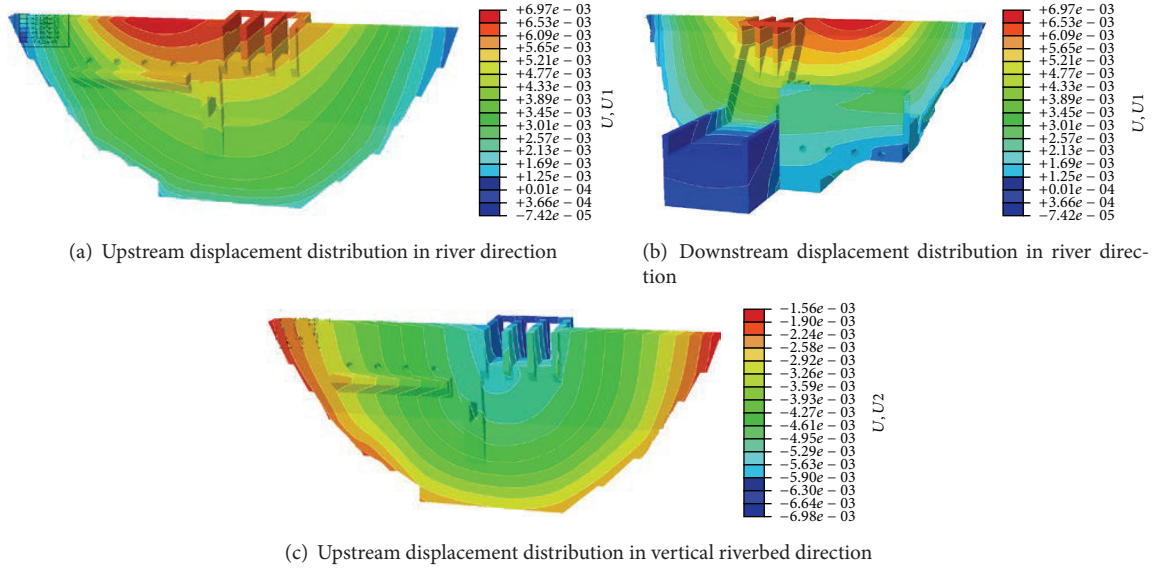


FIGURE 4: Dam displacement contour in various directions under analysis Case 1 (unit: m).

monoliths, the overflow dam monoliths, the diversion dam monoliths, and the left hand side dam monoliths. Four typical profiles are #0+65.4 and #00+97.00 within the diversion dam monoliths, #0 + 127.00 within the overflow dam monoliths, and #0 + 159.00, a right hand side dam monolith.

3.1. Dam Deformation Analysis. Table 4 shows three-dimensional stress and displacement results for the five typical dam monoliths. The displacement distribution of the upstream and downstream surfaces is illustrated in Figure 4. The stress and displacement results for all dam profiles for analysis Cases 1 and 2 are shown in Table 5. For analysis Cases 1 and 2 the symmetry of the displacement distributions is good, which shows that the dam abutments and riverbed foundation possess good overall stiffness. The maximum upstream face and downstream face displacements (along the river direction) of the dam (Figure 4) are 0.697 cm and 1.707 cm, respectively, at the #0+97.00 profile for the diversion dam monolith. The maximum displacements (settlement direction) were 0.679 cm and 0.915 cm, respectively, at the #0 + 127.00 profile of the overflow dam monolith. Three-dimensional analysis results show that the distribution of displacement deformations for typical sections is reasonable, consistent with the characteristics of gravity dam displacement distribution in general, and the settlements are uniform.

3.2. Dam Stress Analysis. For challenging problems in dam design, it is vitally important to investigate clearly the stress distributions in both the dam and its foundation, especially in the tensile zone upstream at the heel of the gravity dam, close to the downstream toe of the dam, and at the dam-foundation contact surface. For analysis Case 1, stress characteristic values for the typical dam monoliths are illustrated in Tables 4 and 5.

For all typical dam monoliths, under analysis Case 1, the maximum principal stress and compression stress level were about 2.308 MPa and 3.232 MPa at the left hand side dam monolith and the toe of diversion dam monoliths, respectively. For all typical dam profiles, under analysis Cases 1 and 2, the maximum principal tensile stresses were about 0.4 MPa (#0 + 159.00) and 2.0 MPa (#0 + 65.40), respectively. The maximum compressive stresses are about 1.4 MPa (#0 + 159.00) and 1.6 MPa (# + 159.00), respectively. Based on the numerical analysis, the tension and compression stress distribution is homogeneous, and the stress levels of the main parts, such as dam heel and dam toe, are within satisfactory limits. The stress distribution, therefore, can be considered safe for dam operation under normal water loading. A local tensile stress occurs at the upper junction of dam and foundation, the outlets of the diversion dam monoliths, and the parts in bending of the sand sluicing, diversion dam monoliths. Attention must, therefore, be paid, to the applied prestressed or other reinforcement designs of these sections so as to provide the capability of sustaining those stresses.

4. Nonlinear Analysis under Static and Dynamic Loading

4.1. Dam Deformation Analysis. For analysis Case 4, Table 5 shows the main stress and the deformation characteristic values for the typical dam profiles. The three-dimensional integral displacement distribution is illustrated in Figure 5. Comparing these results and those for static loading (Tables 4 and 5), the main conclusions are as follows.

- (1) The maximum displacement (along the river direction) (Figure 5) was 2.36 cm, at #0 + 65.40 profile of the diversion dam monolith. The maximum displacement (settlement direction) was 1.10 cm, at

TABLE 4: Three-dimensional stress and displacement results of the five typical dam monoliths (Case 1).

	Left dam monoliths	Overflow dam monoliths	Max.		Diversion dam monoliths	Right dam monoliths	Left dam monoliths	Overflow dam monoliths	Min.		Diversion dam monoliths	Right dam monoliths
			Overflow dam monoliths	Sand sluicing dam monoliths					Sand sluicing dam monoliths	Overflow dam monoliths		
Displacement (cm)												
X	0.392	0.648		0.657	0.697	0.575	0.071	0.112	0.14	0.0879	0.0896	
Y	-0.164	-0.261		-0.282	-0.173	-0.156	-0.343	-0.679	-0.626	-0.596	-0.559	
Horizontal principal stress (MPa)	2.308	0.532		0.308	1.283	2.221	-2.481	-3.16	-2.449	-3.232	-2.709	

Note: X represents river direction and Y represents transverse direction ("-" denotes settlement direction).

TABLE 5: The stress and displacement results of all the typical dam profiles under analysis Cases 1 and 2.

		Max.				Min.			
		Diversion dam monolith (0 + 65.40)		Diversion dam monolith (0 + 97.00)		Diversion dam monolith (0 + 127.00)		Diversion dam monolith (0 + 159.00)	

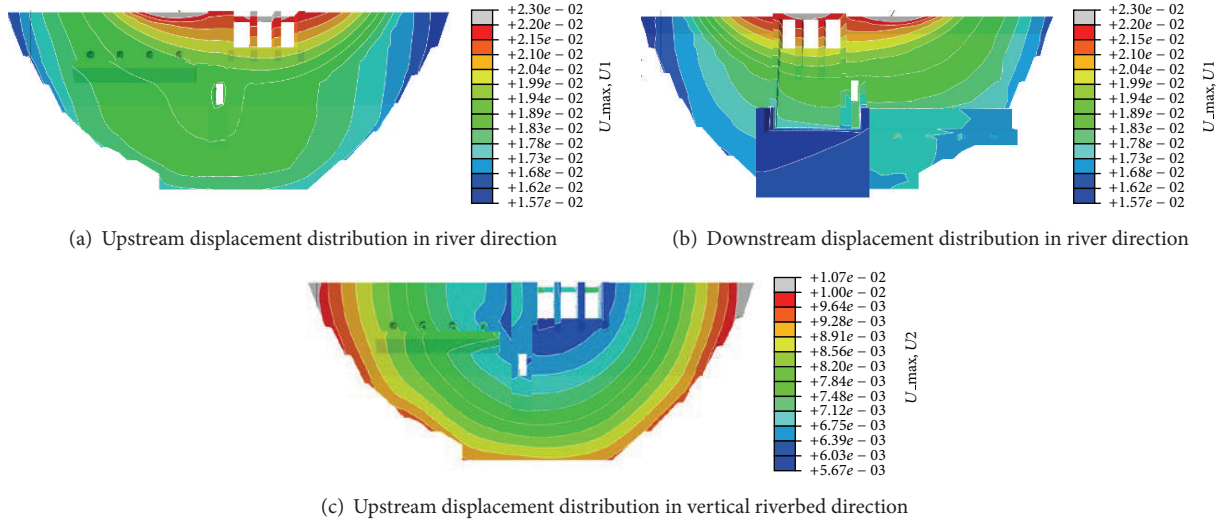


FIGURE 5: Dam displacement contour in various directions under analysis Case 4 (unit: m).

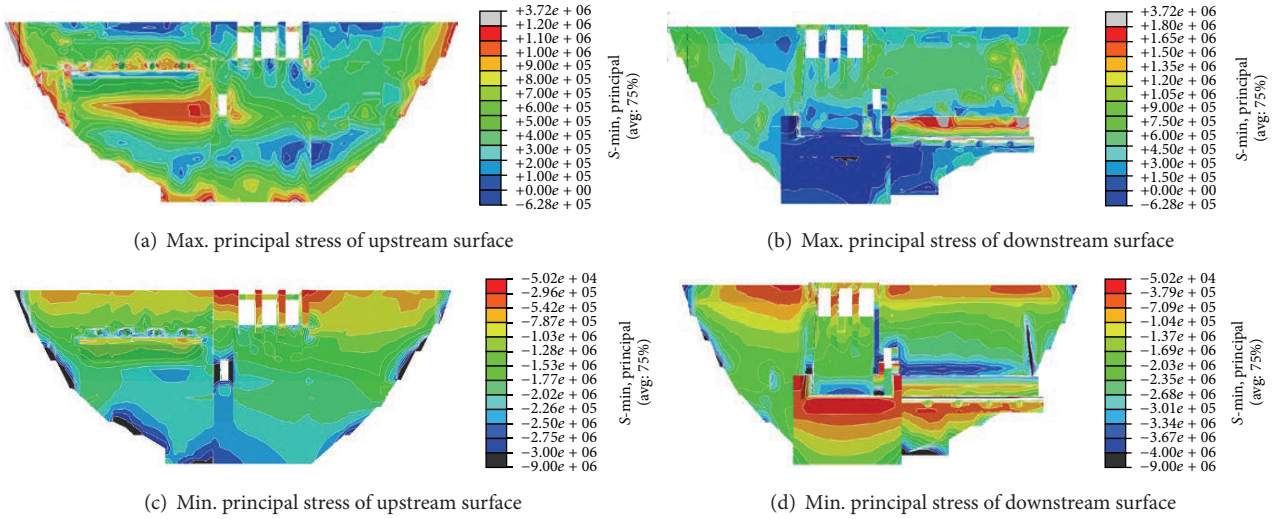


FIGURE 6: Principal stress contour of dam upstream/downstream under analysis Case 4 (unit: Pa).

#0 + 159.00 profile of the overflow monoliths. The three-dimensional analysis results show that the displacement deformation distribution of the typical sections is reasonable, consistent with the characteristics of gravity dam displacements distribution in general, and the settlements are uniform.

- (2) The maximum displacements along the river and in the settlement directions for analysis Case 2 increased by 1.4 and 1.3 times, respectively, when compared with the results of the linear elastic static working condition (analysis Case 1). The maximum displacements along the river and settlement direction under analysis Case 4 increased by about 2 and 1.1 times, respectively, compared with the results for analysis Case 1.

4.2. Dam Stress Analysis. For analysis Case 4, the 3D stress distribution for the Guoduo dam is shown in Figure 6. Figure 7 illustrates the max. and min. principal stresses for typical profiles. The characteristic stress values within the typical monoliths are shown in Table 5.

The overall upstream surface sustained the compression pressure, the maximum tensile principal stress level in the typical dam monoliths being about 1.5 MPa (the left hand side dam monolith downstream side), and the maximum compressive stress is about 3.0 MPa (the wall corner of the sand sluicing dam monolith). For all the typical dam profiles, for analysis Cases 4, the maximum principal stresses are about 2 MPa (#0 + 159.00). The maximum compressive stresses are about 2 MPa (#0 + 65.40).

Based on the numerical analysis Case 4, the tension and compression stress distributions are similar to those

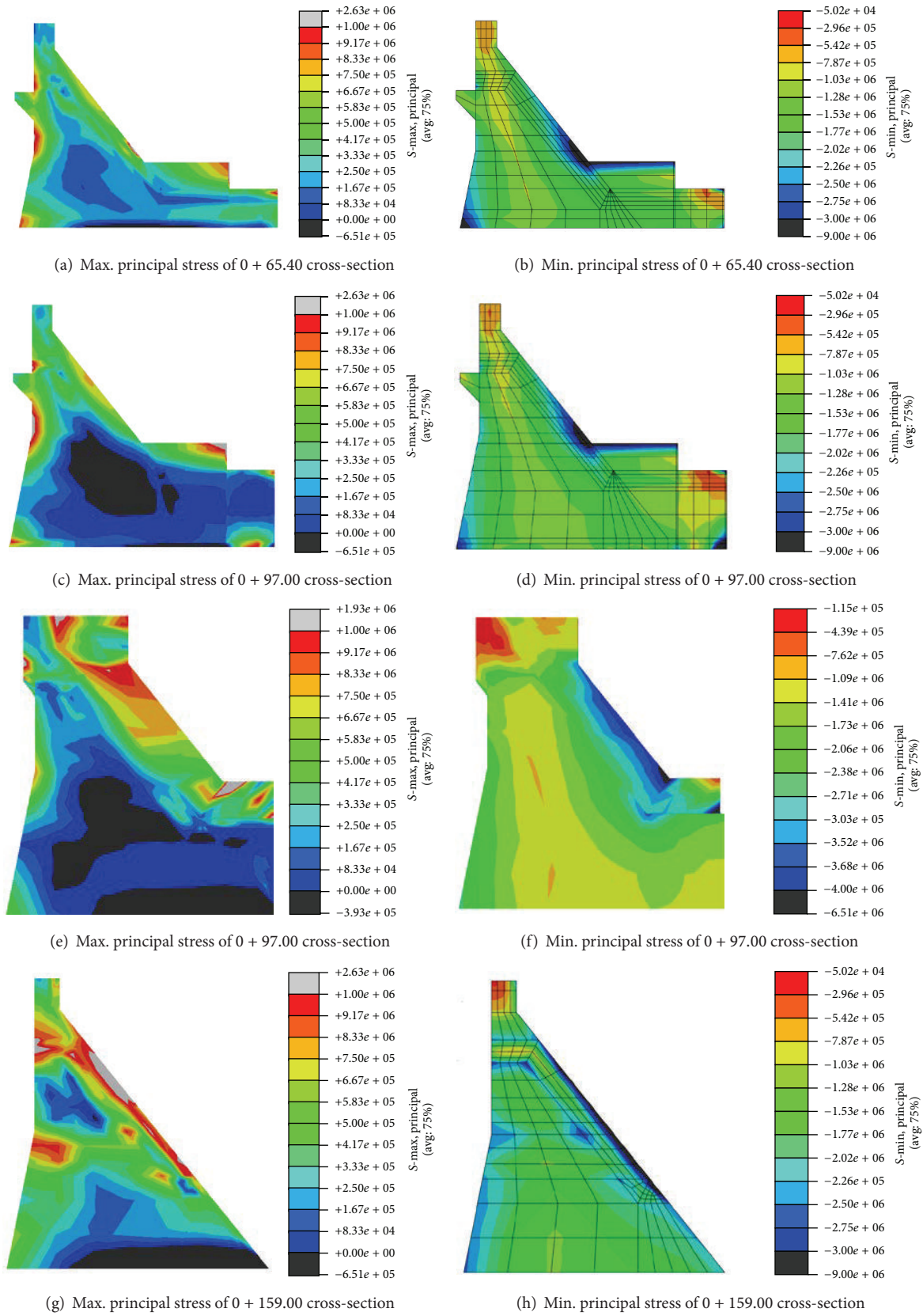


FIGURE 7: Principal stress of typical section under analysis Case 4 (unit: Pa).

TABLE 6: The maximum equivalent plastic strain of the typical dam monoliths. (Analysis Cases 4–7).

		Diversion dam monoliths (0 + 65.40)	Diversion dam monoliths (0 + 97.00)	Overflow dam monoliths (0 + 127.00)	The right dam monoliths (0 + 159.00)
Case 4	Working statuses	Elastic			
Case 5	The maximum equivalent plastic strain	$2.0e - 4$	$2.0e - 4$	$5.833e - 5$	$5.000e - 5$
	Location	Downstream surface			
Case 6	The maximum plastic strain	$5.4e - 4$	$3.625e - 4$	$3.379e - 4$	$2.422e - 4$
	Location	Downstream surface			
Case 7	The maximum plastic strain	$1.001e - 3$	$9.834e - 4$	$1.180e - 3$	$8.169e - 3$
	Location	Downstream surface			

t of Case 2 (Section 3.2). A local tensile stress occurs at the upper junction of dam and foundation, the outlets of the diversion dam monoliths, and the parts in bending of the sand sluicing, diversion dam monoliths. Attention must, therefore, be paid to the applied prestressed or other reinforcement designs of these sections so as to provide the capability of sustaining those stresses. Compared with analysis Case 1, the maximum numerical analysis derived principal stress increased significantly for analysis Cases 2 and 4 (Table 5). The maximum principal stress for Case 4 is four times that for Case 1. Compared with Case 1, the maximum compression stress increased by 13 percent for Case 2 (Table 5) and by 40% for Case 4.

4.3. Seismic Safety Analysis. This section describes an analysis of the ultimate seismic capacity of the dam using the “overload safety factor method,” based on nonlinear finite element analysis. For different analysis cases (Table 3) the instability mechanism and seismic fortification of the dam-foundation system were simulated under overload conditions. Detailed dam failure and the plastic zone locations for the different analysis cases are illustrated in Table 6. The yielding process of the upstream and downstream surfaces is shown in Figure 8.

The numerical results show the following.

- (1) For analysis Case 4, the dam and foundation remained within the elastic range.
- (2) For analysis Case 5, the seismic horizontal acceleration was more than twice as big with yielding appearing in the diversion pipe, flushing hole, pier and beam junctions, pier wall, and the top of the plan. The equivalent plastic strain value was $4.0e - 3$, located in the pier wall near the flushing hole (Figures 8(a) and 8(b)). Yielded zones also occurred in some parts of dam abutments, but the equivalent plastic strain value is small.
- (3) For analysis Cases 5 and 6, the seismic horizontal acceleration was more than twice and three times,

respectively. The maximum plastic strain values were $7.0e - 3$ and $1.0e - 2$, respectively. Dam abutments began to show large yielded zones (Figures 8(c)–8(f)).

- (4) For each overloading step increment above seismic horizontal acceleration (hereafter g_0 means normal seismic horizontal acceleration) those elements yielding were identified and safety factors computed. The safety evaluation methods for high arch dams consist mainly of (1) overloading, (2) strength reduction, and (3) comprehensive tests. In this study, overload safety factor method assumes that the mechanical foundation rock mass parameters remain constant while the seismic horizontal acceleration is increased until the dam and the foundation fail. The overall stability safety factors are defined as follows: $K1$ represents the dam safety factor against initial cracking; a crack initiated at $K1g_0$. $K2$ represents the safety factor against structural nonlinear behaviour. In the nonlinear phase, the downstream dam surface shows a large yield zone during this nonlinear behaviour. The cracks in the dam propagate quickly and multiple cracks coalesce. $K3$ represents the maximum seismic fortification safety factor for the dam-foundation system. At $K3g_0$, the dam foundation fails and dam capacity is lost. Based on numerical analysis, as increase of seismic horizontal acceleration occurs, the equivalent plastic strain increases. When acceleration reached 0.27 g, about 30% of the dam reached the yield stage. Thus, $K1 = 1.5$, $K2 = 2 \sim 3$, and $K3 = 3 \sim 4$.
- (5) Based on numerical analysis, under overloading (dynamic loading), the yielded zones appeared at the stress concentration areas, such as the dam heel, the dam joint face, and bank slope surfaces of the bank upstream and downstream. A large yielded zone appeared in the back tube and planhouse (Figures 8(g) and 8(h)). It is suggested that these yield zones should be reinforced, to improve the overall seismic safety performance of the Guoduo gravity dam.

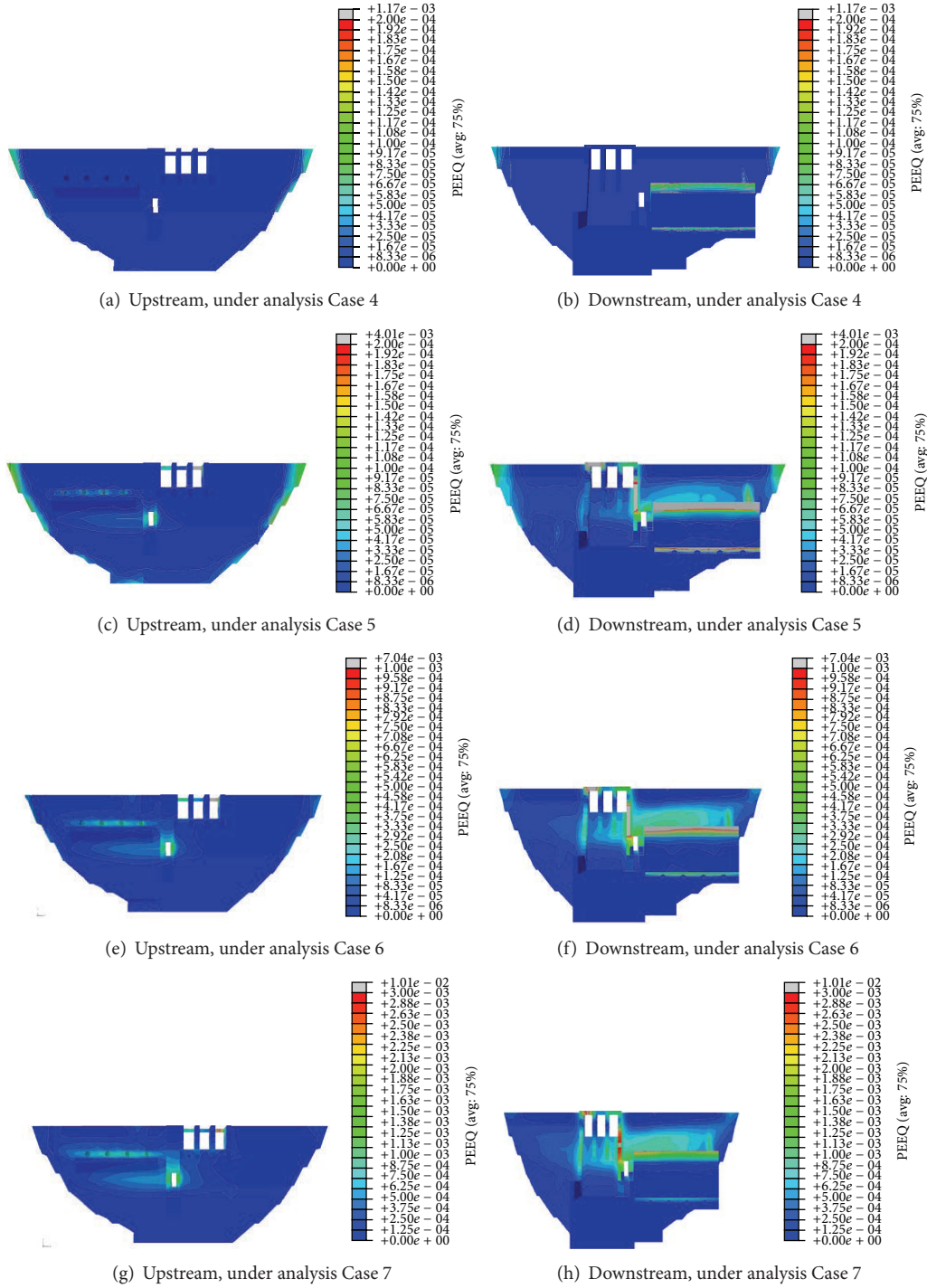


FIGURE 8: Dam upstream/downstream yield zone under various analysis cases.

5. Conclusions

This study analyzed and understood the seismic performance of the Guoduo dam. The geological conditions affecting seismic performance of the Guoduo dam are first discussed below. The deformation, stress, cracking risk, and overall seismic stability of the Guoduo were analyzed using a 3D finite element method, under various dynamic and static

loadings and a description is given below. The following conclusions can be drawn.

For analysis Cases 1, 2, and 4, the symmetry of the displacement distributions is good, which shows that the dam abutments and riverbed foundation have good overall stiffness. The maximum displacements (along the river direction) of the dam were 0.697 cm, 1.707 cm, and 2.36 cm at #0 + 97.00 profile of diversion dam monolith, respectively.

The maximum principal tension stresses at various analyses 1, 2, and 4 were about 0.4 MPa (#0 + 159), 2.0 MPa (#0 + 65.4), and 2.0 MPa (#0 + 159), respectively. The maximum compression stresses at various analyses 1, 2, and 4 were -1.4 MPa (#0 + 159), -1.6 MPa (#0 + 159), and -2.0 MPa (#0 + 159), respectively. Based on the numerical analysis, the stress distribution is safe for dam operation under normal water loading and seismic loading.

Based on the numerical analysis, the tension and compression stresses distribution is homogeneous, and the stress levels of the key components, such as dam heel and dam toe, are within safe limits for dam operation under normal water loading. A local tensile stress occurs at the upper dam foundation junction, the outlets of the diversion dam monoliths, and the parts in bending of the sand sluicing, diversion dam monoliths. Attention, therefore, must be paid to the reinforcement design for these sections to enhance the capability of sustaining tensile stresses. A reinforcement design should control the local cracking risk by selecting the appropriate concrete materials, using small diameter reinforcing bars, and improving temperature control measures for pouring mass concrete during construction.

The shape of the dam profile has a significant effect on the dynamic response of the dam. Numerical results show that highly stressed areas easily occur where there is a sudden change of geometry. In addition, after considering the interaction between the planhouse and diversion dam monoliths, although the planhouse can enhance the overall stiffness and stability of the dam, the high stiffness low down on the dam easily causes stress concentration at the dam downstream surface. This situation is not helpful to the safety of the dam body under strong earthquake action.

Based on numerical simulation, by employing the "overload safety factor method," the overall seismic fortification factors are as follows: $K_1 = 1.5$, $K_2 = 2 \sim 3$, and $K_3 = 3 \sim 4$.

Conflict of Interests

The authors declare that there is no conflict of interests regarding the publication of this paper.

Acknowledgments

This research work was supported by National Natural Science Foundation of China (nos. 11272178 and 51339003), National Basic Research Program of China (973 Program) Grant no. 2011CB013503, and Tsinghua University Initiative Scientific Research Program. The authors are very grateful to Guiyang Hydroelectric Investigation and Design Institute for supporting this study.

References

- [1] L. M. Zhang, "Settlement patterns of soft soil foundations under embankments," *Canadian Geotechnical Journal*, vol. 36, no. 4, pp. 774–781, 1999.
- [2] P. Lin, B. Huang, Q. Li, and R. Wang, "Hazard and seismic reinforcement analysis for typical large dams following the Wenchuan earthquake," *Engineering Geology*, 2014.
- [3] P. Lin, T. H. Ma, Z. Z. Liang, C. A. Tang, and R. K. Wang, "Failure and overall stability analysis on high arch dam based on DFPA code," *Engineering Failure Analysis*, vol. 45, pp. 164–184, 2014.
- [4] H. Tosun, I. Zorluer, A. Orhan, E. Seyrek, H. Savaş, and M. Türköz, "Seismic hazard and total risk analyses for large dams in Euphrates basin, Turkey," *Engineering Geology*, vol. 89, no. 1-2, pp. 155–170, 2007.
- [5] P. Lin, W. Y. Zhou, and H. Y. Liu, "Experimental study on cracking, reinforcement and overall stability of the Xiaowan super-high arch dam," *Rock Mechanics and Rock Engineering*, 2014.
- [6] ICOLD European Club, "Working group on guidelines for the seismic assessment of dams," 2004.
- [7] US Army Corps of Engineers, *Earthquake Design and Evaluation of Concrete Hydraulic Structure Engineer Manual*, 2007.
- [8] J. García-Mayordomo and J. M. Insua-Arévalo, "Seismic hazard assessment for the Itoiz dam site (Western Pyrenees, Spain)," *Soil Dynamics and Earthquake Engineering*, vol. 31, no. 7, pp. 1051–1063, 2011.
- [9] H. Tosun, İ. Zorluer, A. Orhan, E. Seyrek, H. Savaş, and M. Türköz, "Seismic hazard and total risk analyses for large dams in Euphrates basin, Turkey," *Engineering Geology*, vol. 89, no. 1-2, pp. 155–170, 2007.
- [10] T.-H. Yi, H.-N. Li, and M. Gu, "A new method for optimal selection of sensor location on a high-rise building using simplified finite element model," *Structural Engineering and Mechanics*, vol. 37, no. 6, pp. 671–684, 2011.
- [11] B. Chen, Y. Z. Sun, Y. L. Li, and S. L. Zhao, "Control of seismic response of a building frame by using hybrid system with magnetorheological dampers and isolators," *Advances in Structural Engineering*, vol. 17, no. 8, pp. 1199–1215, 2014.
- [12] T.-H. Yi, H.-N. Li, and M. Gu, "Optimal sensor placement for structural health monitoring based on multiple optimization strategies," *The Structural Design of Tall and Special Buildings*, vol. 20, no. 7, pp. 881–900, 2011.
- [13] B. Chen, Y. L. Xu, and X. Zhao, "Integrated vibration control and health monitoring of building structures: a time-domain approach," *Smart Structures and Systems*, vol. 6, no. 7, pp. 811–833, 2010.
- [14] P. Lin, H. Y. Liu, Q. B. Li, and H. Hu, "Effects of outlets on cracking risk and integral stability of super-high arch dams," *The Scientific World Journal*, vol. 2014, Article ID 312827, 19 pages, 2014.
- [15] Z. Z. Liang, C. A. Tang, H. X. Li, T. Xu, and Y. B. Zhang, "Numerical simulation of 3-d failure process in heterogeneous rocks," *International Journal of Rock Mechanics and Mining Sciences*, vol. 41, supplement 1, pp. 323–328, 2004.
- [16] L. C. Li, C. A. Tang, W. C. Zhu, and Z. Z. Liang, "Numerical analysis of slope stability based on the gravity increase method," *Computers and Geotechnics*, vol. 36, no. 7, pp. 1246–1258, 2009.
- [17] Z. Z. Liang, H. Xing, S. Y. Wang, D. J. Williams, and C. A. Tang, "A three-dimensional numerical investigation of the fracture of rock specimens containing a pre-existing surface flaw," *Computers and Geotechnics*, vol. 45, pp. 19–33, 2012.
- [18] L. C. Li, C. A. Tang, G. Li, S. Y. Wang, Z. Z. Liang, and Y. B. Zhang, "Numerical simulation of 3D hydraulic fracturing based on an improved flow-stress-damage model and a parallel FEM technique," *Rock Mechanics and Rock Engineering*, vol. 45, no. 5, pp. 801–818, 2012.
- [19] W. Pal, "Seismic cracking of concrete gravity dam," *Journal of Structural Engineering ASCE*, vol. 102, no. 9, pp. 1827–1844, 1976.

- [20] A. R. Ingraffea, "Case studies of simulation of fracture in concrete dams," *Engineering Fracture Mechanics*, vol. 35, no. 1–3, pp. 553–564, 1990.
- [21] W. Guanglun, O. A. Pekau, Z. Chuhan, and W. Shaomin, "Seismic fracture analysis of concrete gravity dams based on nonlinear fracture mechanics," *Engineering Fracture Mechanics*, vol. 65, no. 1, pp. 67–87, 2000.
- [22] M. L. Ayari and V. E. Saouma, "A fracture mechanics based seismic analysis of concrete gravity dams using discrete cracks," *Engineering Fracture Mechanics*, vol. 35, no. 1–3, pp. 587–598, 1990.
- [23] N. Bouaanani and S. Renaud, "Effects of fluid-structure interaction modeling assumptions on seismic floor acceleration demands within gravity dams," *Engineering Structures*, vol. 67, pp. 1–18, 2014.
- [24] Q. S. Li, Z. N. Li, G. Q. Li, J. F. Meng, and J. Tang, "Experimental and numerical seismic investigations of the Three Gorges dam," *Engineering Structures*, vol. 27, no. 4, pp. 501–513, 2005.
- [25] M. Paggi, G. Ferro, and F. Braga, "A multiscale approach for the seismic analysis of concrete gravity dams," *Computers and Structures*, vol. 122, pp. 230–238, 2013.
- [26] R. Tarinejad, R. Fatehi, and R. S. Harichandran, "Response of an arch dam to non-uniform excitation generated by a seismic wave scattering model," *Soil Dynamics and Earthquake Engineering*, vol. 52, pp. 40–54, 2013.
- [27] M. Ghaemian and M. Sohrabi-Gilani, "Seismic responses of arch dams due to non-uniform ground motions," *Scientia Iranica*, vol. 19, no. 6, pp. 1431–1436, 2012.
- [28] M. Akköse and E. Şimşek, "Non-linear seismic response of concrete gravity dams to near-fault ground motions including dam-water-sediment-foundation interaction," *Applied Mathematical Modelling*, vol. 34, no. 11, pp. 3685–3700, 2010.
- [29] S. Sica, L. Pagano, and A. Modaressi, "Influence of past loading history on the seismic response of earth dams," *Computers and Geotechnics*, vol. 35, no. 1, pp. 61–85, 2008.
- [30] M. Sohrabi-Gilani and M. Ghaemian, "Spatial variation input effects on seismic response of arch dams," *Scientia Iranica*, vol. 19, no. 4, pp. 997–1004, 2012.
- [31] V. Valamanesh, H. E. Estekanchi, A. Vafai, and M. Ghaemian, "Application of the endurance time method in seismic analysis of concrete gravity dams," *Scientia Iranica*, vol. 18, no. 3, pp. 326–337, 2011.
- [32] O. Omid, S. Valliappan, and V. Lotfi, "Seismic cracking of concrete gravity dams by plastic-damage model using different damping mechanisms," *Finite Elements in Analysis and Design*, vol. 63, pp. 80–97, 2013.
- [33] M. B. Ftima and P. Léger, "Seismic stability of cracked concrete dams using rigid block models," *Computers and Structures*, vol. 84, no. 28, pp. 1802–1814, 2006.
- [34] ABAQUS, *ABAQUS User's Manual*, vol. 6.11, 2011.
- [35] The Professional Standards Compilation Group of People's Republic of China (PSCG PRC), "Specification for seismic design of hydraulic structures," Tech. Rep. DL5073-2000, Electric Publish Press, Beijing: China, 2000.

Research Article

Fatigue Performance Assessment of Composite Arch Bridge Suspenders Based on Actual Vehicle Loads

Bin Chen,¹ Xiaozhang Li,¹ Xu Xie,¹ Zheng Zhong,² and Pengzhen Lu³

¹College of Civil Engineering and Architecture, Zhejiang University, Hangzhou 310058, China

²Hangzhou Municipal Facilities Supervision and Administration Center, Hangzhou 310003, China

³College of Civil Engineering and Architecture, Zhejiang University of Technology, Hangzhou 310003, China

Correspondence should be addressed to Xu Xie; xiexu@zju.edu.cn

Received 30 September 2014; Accepted 16 December 2014

Academic Editor: Alicia Gonzalez-Buelga

Copyright © 2015 Bin Chen et al. This is an open access article distributed under the Creative Commons Attribution License, which permits unrestricted use, distribution, and reproduction in any medium, provided the original work is properly cited.

In the through arch bridges, the suspenders are the key components connecting the arch rib and the bridge deck in the middle, and their safety is an increasing focus in the field of bridge engineering. In this study, various vehicle traffic flow parameters are investigated based on the actual vehicle data acquired from the long-term structural health monitoring system of a composite arch bridge. The representative vehicle types and the probability density functions of several parameters are determined, including the gross vehicle weight, axle weight, time headway, and speed. A finite element model of the bridge structure is constructed to determine the influence line of the cable force for various suspenders. A simulated vehicle flow, generated using the Monte Carlo method, is applied on the influence lines of the target suspender to determine the stress process, and then the stress amplitude spectrum is obtained based on the statistical analysis of the stress process using the rainflow counting method. The fatigue performance levels of various suspenders are analyzed according to the Palmgren-Miner linear cumulative damage theory, which helps to manage the safety of the suspenders.

1. Introduction

The development of national economies depends greatly on the effectiveness and reliability of infrastructure systems. In particular, bridges are becoming increasingly important in ensuring the normal operation of transportation networks. Therefore, the smooth running of transportation systems must be facilitated by ensuring the safety of bridge structures. Bridges are affected by cyclic vehicle loads throughout their lifetime, which have uncertain effects on bridge structures. Thus, the fatigue performance of bridge components is very important for resisting vehicle loads [1]. In arch bridges, suspenders are key components that connect the arch rib and the bridge deck in the middle. The dead load and the live load on the bridge deck pass to the arch rib via suspenders. The alternating stress produced by vibration due to vehicles, winds, and earthquakes means that the suspender may suffer fatigue damage in conditions that are far below the static intensity [2, 3]. Large-span arch bridges may have

multiple lanes and the amplitude of the stress variation in the suspender will be greater due to the multilane vehicle loads, which may damage the entire bridge via invalidation of the suspenders. Therefore, the fatigue analysis of suspenders in arch bridges is a major problem, which is being considered increasingly by engineers.

The key aspect of fatigue analysis for suspenders is determining their stress spectrum. Two main methods are used for this purpose: obtaining actual measurements from the bridge and computer-based simulation analysis. Obtaining actual measurement is time consuming and expensive, and the number of points that can be measured is limited. In addition, actual measurements cannot be obtained while a new bridge is being designed. Thus, simulations are used widely. Traffic flow and its load effect are random processes; thus the load effect of vehicle during a time interval is confirmed based on the simulations of this random process. This is the optimal method for confirming the load effect of vehicle based on the simulations of actual traffic data [4–7]. The construction

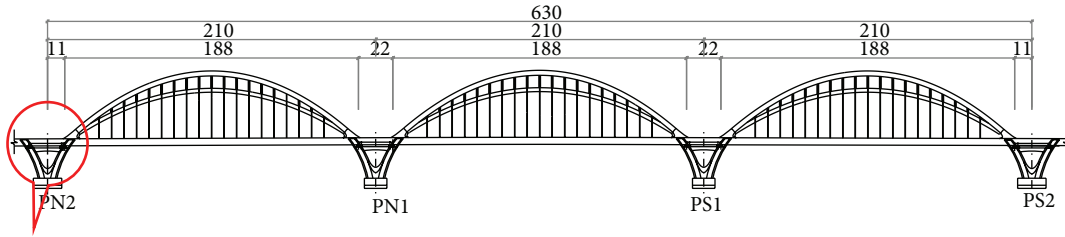


FIGURE 1: Layout of longitudinal section of bridge (m).

of a structure health monitoring system (SHMS) on bridges [8–10] and the widespread application of weigh-in-motion (WIM) systems are very helpful for obtaining more actual traffic data and for developing traffic load models based on the WIM data [11–15]. Using the WIM data, the traffic load effect can be calculated accurately, thereby allowing the prediction of the future load traffic effect and its effect on bridge performance using relevant theory [16–19].

In this study, based on the vehicle load acquisition system in the SHMS of a large-span composite arch bridge, the traffic flow data and a series of traffic flow parameters are obtained, including the vehicle type classification, gross vehicle weight, axle weight, time headway, speed, and transverse distribution of the traffic flow, which are subjected to a statistical analysis. Using the actual statistical parameters measured from a random traffic flow and based on the Monte Carlo method, the bidirectional and multilane random traffic flow is simulated using a FORTRAN program. The influence line of an objective suspender is loaded through the random traffic flow loads to obtain the suspender stress process and the stress spectrum is then obtained using the rainflow counting method. Finally, a suitable $S-N$ curve for the bridge suspender is selected and the fatigue condition of the suspender is analyzed using the Palmgren-Miner linear fatigue cumulative damage criterion.

2. Bridge and SHMS

2.1. Bridge Description. The full length of the objective bridge is 1,855 m. The upper structure of the main bridge comprises a 3×210 m arch bridge (Figure 1). The arch rib system comprises the main arch ribs, vice arch ribs, transverse connecting rods between the main and vice arch ribs, and the lateral braces of the vault. The main beam of the arch bridge is a constant section with a steel-concrete composite beam structure. The composite beam is a double-girder system with a main longitudinal girder, medial horizontal beam, end horizontal beam, and small longitudinal girder. The full height and full width of the composite beam are 4.5 m and 37.7 m, respectively. The space between the main longitudinal steel girders on both sides is 27.6 m, the space between the horizontal steel beams is 4.25 m, and the thickness of the concrete bridge deck is 26 cm. Tie bars are set inside the longitudinal main steel girder. The space between the suspenders along the arch bridge is 8.5 m. The upper and lower ends of the suspenders are anchored in the main arch rib and the main longitudinal steel girder, respectively. Each

suspending point is a single suspender and there are 114 suspenders on the whole bridge.

2.2. Structure Health Monitoring System. The structure health monitoring system (SHMS) installed on the objective bridge comprises a *data acquisition and monitoring subsystem (DAMS)*, *inspection and maintenance subsystem (IMS)*, *data storage and management subsystem (DSMS)*, *warning and safety assessment subsystem (WSAS)*, and *user interface subsystem (UIS)*. The DAMS mainly determines the load source and the structural response. The load sources include the wind load, temperature, vehicle load, and seismic activity. The structural responses include the stress of the steel structure and concrete structure, specific deflection of the bridge, variation in the cable force (including the cable force of sling, the cable force of the tie bar of the main bridge, and the cable force of the external cable on the approach bridge), and the vibration response of the structure (including vibration monitoring of the main arch and main beam). The SHMS comprises 347 sensors. The vehicle load acquisition equipment (Figure 2) can collect many types of information from vehicles that pass over the observed sections, such as the vehicle speed, direction, license plate number, vehicle type, passing time, axle weight, and the gross vehicle weight, which can greatly improve the efficiency and precision of traffic load surveys. Thus, based on the traffic information monitoring and by reconstructing the traffic flow in simulations, the stress variation and the fatigue characteristic of the bridge suspenders under the actual vehicle loads can be analyzed in the present study.

3. Survey of Traffic Conditions

Traffic flow data are acquired for 18 months after the SHMS has been installed and put into operation. These data fully reflected the actual conditions of the traffic loads. During the analysis, some erroneous data are removed to ensure that the data reflected the true conditions of the traffic loads. In addition, by referring to the UK standards, vehicles weighing ≥ 3 tons are classified as trucks and the effect of cars on the bridge fatigue characteristics is omitted.

3.1. Traffic Flow Characteristics. Traffic flow can be divided into daily traffic and hourly traffic. The daily traffic represents the variation in the daily traffic flow during a week and the hourly traffic represents the variation in the traffic flow at each

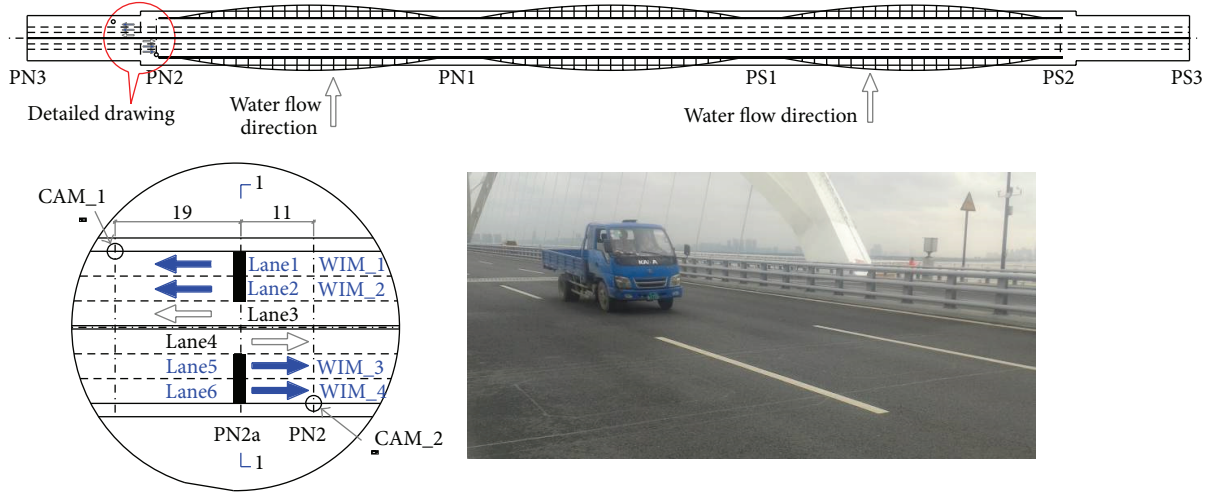


FIGURE 2: Installation positions of vehicle load acquisition system on bridge.

TABLE 1: Traffic flow distributions for vehicles with different axle numbers during two weeks.

Axle number	2	3	4	5	6
First week	183173	2057	1358	396	382
Second week	145413	1602	907	228	259

time of day. Thus, it is reasonable to combine both to analyze the variation in the actual traffic flow. Figure 3 shows that the overall distribution of the daily traffic flow declined from Monday to Sunday over a two-week period. In addition, there are major differences in the daily traffic flow between the first week and the second week, where the maximum daily traffic is ca 32,000 in the first week but only 24,000 in the second week. Furthermore, the total traffic flow had a regular pattern at each time of the day (Figure 4), with a peak at about 09:00, a second peak at about 18:00, and a maximum traffic flow per time interval of ca 2700. Based on the distribution of the traffic flow, two-axle vehicles comprised 97.7% of the total and the vehicle number decreased with the axle number (Table 1).

3.2. Types of Trucks. The effect of small vehicles on bridge performance is very low; thus only trucks are considered in studies of vehicle types and their distributions. Based on the axle space and axle type characteristics determined from the data, the trucks are classified as typical vehicle types. Tables 2 and 3 present the axle weight and axle space data. Some vehicles are removed during the classification and extraction of the vehicle types, such as vehicles with seven axles or more, due to measurement errors and illegal modifications. The results of the vehicle type analysis show that trucks accounted for 19.52% of the total traffic flow, where two-axle heavy trucks and two-axle large buses comprised a high percentage, thereby reflecting the typical characteristics of urban road traffic.

3.3. Gross Vehicle Weight. Different vehicle types have various effects on bridges because of the differences in vehicle

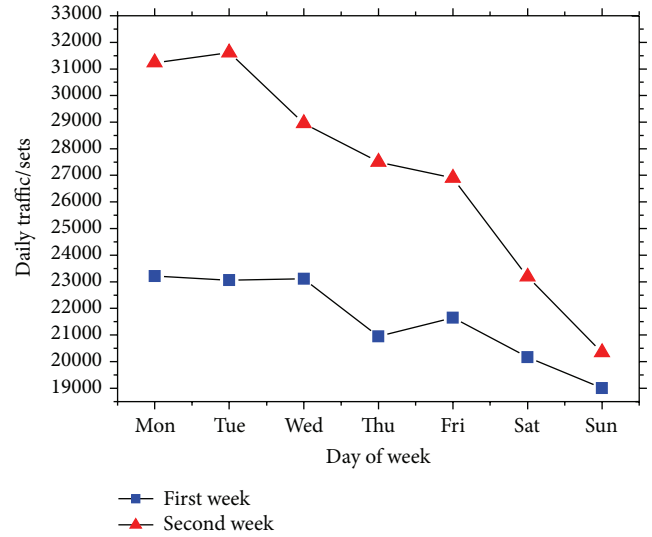


FIGURE 3: Daily traffic flow.

construction and their weight. According to the vehicle type classifications, the probability distribution patterns for the gross vehicle weights of different vehicle types are determined, thereby providing the basis for precise simulations of the measured traffic flow. Other studies have shown that the traffic load may comprise no loads, half loads, and full loads, and the gross vehicle weight probability distribution has a multimodal distribution [20–23], which can be viewed as a linear combination of different probability distributions. Suppose that the probability density function of the i th vehicle load is $f_X(x)$. The probability densities of n traffic loads are combined linearly and the probability density function of the traffic load can then be expressed as

$$f_X(x) = \sum_{i=1}^n p_i f_i(x), \quad (1)$$

TABLE 2: Vehicle classification and axle weight statistics.

Vehicle classification			Average value and deviation of axle weight (t)					
Vehicle type	Axle diagram	Ratio	Axle 1	Axle 2	Axle 3	Axle 4	Axle 5	Axle 6
V21		1.71%	(1.89, 0.54)	(2.30, 1.80)				
V22	○ — ●	8.81%	(3.40, 1.55)	(7.74, 6.57)				
V23		5.91%	(5.05, 1.33)	(9.84, 3.30)				
V31	○ ○ — ●	0.54%	(4.36, 1.42)	(4.48, 2.15)	(1.37, 7.17)			
V32	○ — ● ●	0.60%	(7.68, 3.26)	(13.66, 9.08)	(13.74, 9.50)			
V41	○ ○ — ● ●	0.90%	(6.85, 3.18)	(7.44, 3.50)	(13.97, 9.67)	(15.25, 9.15)		
V42	○ ● — ● ●	0.36%	(4.10, 0.76)	(12.03, 4.29)	(11.96, 4.79)	(11.87, 4.65)		
V51	○ ● — ● ● ●	0.34%	(5.55, 1.24)	(12.53, 4.61)	(11.47, 4.56)	(10.75, 4.16)	(11.23, 4.17)	
V61	○ ○ — ● ● ● ●	0.20%	(4.24, 0.61)	(4.40, 1.35)	(11.29, 4.99)	(9.61, 4.95)	(9.71, 4.75)	(10.49, 5.19)
V62	○ ● ● — ● ● ● ●	0.15%	(5.59, 0.88)	(8.42, 3.80)	(7.98, 3.57)	(9.59, 5.59)	(9.24, 5.18)	(10.30, 5.54)

TABLE 3: Vehicle classification and axle space statistics.

Vehicle classification			Average value and deviation of axle space (m)				
Vehicle type	Axle diagram	Ratio	Axle 1	Axle 2	Axle 3	Axle 4	Axle 5
V21		1.71%	(2.98, 0.35)				
V22	○ — ●	8.81%	(4.72, 0.73)				
V23		5.91%	(6.64, 0.84)				
V31	○ ○ — ●	0.54%	(2.10, 0.74)	(5.75, 1.27)			
V32	○ — ● ●	0.60%	(5.07, 1.40)	(1.54, 0.58)			
V41	○ ○ — ● ●	0.90%	(2.02, 0.52)	(4.76, 0.99)	(1.41, 0.25)		
V42	○ ● — ● ●	0.36%	(3.80, 0.39)	(6.83, 1.01)	(1.37, 0.10)		
V51	○ ● — ● ● ●	0.34%	(3.73, 0.76)	(6.60, 1.40)	(1.43, 0.70)	(1.35, 0.25)	
V61	○ ○ — ● ● ● ●	0.20%	(1.93, 0.34)	(2.74, 0.52)	(6.56, 1.37)	(1.37, 0.21)	(1.37, 0.22)
V62	○ ● ● — ● ● ● ●	0.15%	(3.48, 0.55)	(1.46, 0.22)	(6.97, 1.72)	(1.39, 0.21)	(1.38, 0.21)

where $\sum_{i=1}^n p_i = 1$. In general, the form of the above probability density function $f_i(x)$ can differ, which can be determined according to the fit of the measured vehicle loads. In the present study, $f_i(x)$ has the same form as probability density functions such as the normal distribution and log-normal distribution, but the statistical parameters are different. The parameters are estimated using the most common and the effective expectation maximum (EM) algorithm. Previous studies have shown that satisfactory results can be obtained using the EM algorithm for parameter estimation in mixed distribution models [24]. In our study, we fitted mixed distribution functions with different probability distributions to the gross vehicle weights of different vehicle types using the Kolmogorov-Smirnov ($K-S$) test as a goodness of fit test for the cumulative distribution function. The best results were obtained using a third-order mixed log-normal distribution to fit two-axle vehicles and a third-order mixed normal distribution to fit three-axle, four-axle, five-axle, and six-axle vehicles (Figure 5). In particular, the good fit of the mixed model probability distribution to the tail distribution avoided the poor results obtained when using first-order and second-order mixed model distributions for fitting. Table 4 shows the parameters of the probability distributions for various vehicle types. The gross weight distribution shows that the trucks

mostly had no loads, full loads, and overloads, although very few had half loads in this study.

3.4. Axle Weights of Vehicle. Previous studies have shown that coaches and trucks with two axles and more than four wheels cause the most structural damage to bridges and roads, whereas little damage is caused by other trucks [25]. Trucks with two axles and more than four wheels can be classified as whole vehicles, semitrailers, and full trailers. According to the vehicle type database, the common axle types of vehicle can be classified as one axle, two axles, and three axles, and the common wheel types can be classified as single wheel and double wheel. By combining these vehicle types, the following common combinations of axle and wheel types can be obtained: one axle and single wheel (A1), one axle and double wheel (A2), two axle and double wheel (A3), and three axle and double wheel (A4) (Figure 6).

To further understand the vehicle load patterns, the relationships between the GVW and the axle weights of various vehicle types are analyzed using scatter plots, with the gross weight on the x -axis and the axle load and axle group weight on the y -axis. The scatter plot data are then fitted by a linear regression. The results show that the relationship between the gross vehicle weight and the axle load is linear

TABLE 4: Parameters of the mixed probability distribution for GVW.

Truck type	Distribution type	First distribution			Second distribution			Third distribution		
		t	u	sig	t	u	sig	t	u	sig
V21	Lognormal	0.35	1.14	0.04	0.46	1.32	0.12	0.19	1.87	0.42
V22	Lognormal	0.20	1.26	0.12	0.76	2.37	0.52	0.04	3.43	0.14
V23	Lognormal	0.15	2.18	0.41	0.83	2.73	0.17	0.02	3.36	0.23
V31	Normal	0.54	12.56	3.16	0.43	25.52	7.16	0.03	47.15	8.44
V32	Normal	0.45	16.80	4.86	0.27	35.11	7.23	0.27	65.16	10.11
V41	Normal	0.16	14.29	1.47	0.58	35.97	12.86	0.26	77.78	6.72
V42	Normal	0.12	13.68	1.19	0.63	44.90	7.24	0.26	39.92	13.46
V51	Normal	0.12	17.32	1.96	0.83	54.81	11.11	0.05	74.25	11.02
V61	Normal	0.19	17.71	1.63	0.80	56.85	12.98	0.01	100.61	3.41
V62	Normal	0.26	20.22	2.68	0.72	61.27	14.87	0.01	117.69	5.87

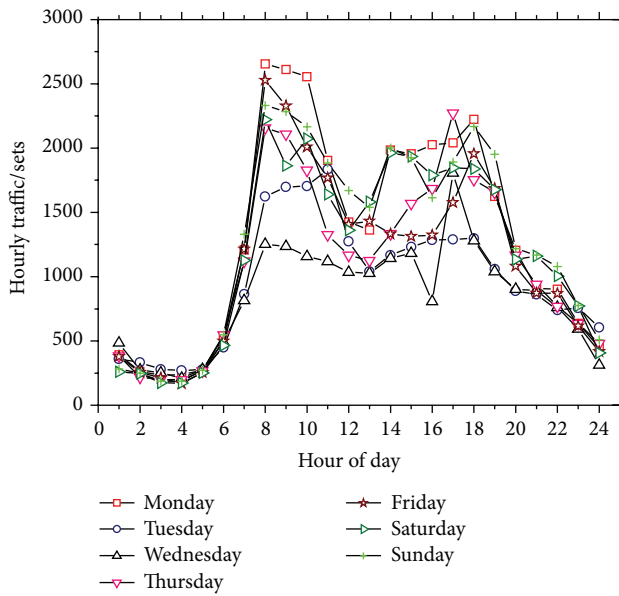


FIGURE 4: Hourly traffic flow.

(Figure 7). In Figure 8, the two front axles (A1 and A2) of V31 and V41 are one axle and single wheel, and their distribution patterns are the same; thus the same straight line is fitted. The results showed that the linear relationship between the axle load and the gross weight is not absolute and it is related to the vehicle type. When the vehicle type is omitted, the linear relationship is changed or disappears.

3.5. Headway and Speed. The movement of vehicles traveling on roads can be classified into free flow and following flow. When the movement of a vehicle is not affected by the vehicles moving in front, it can be referred to as free flow, but otherwise it is known as following flow. According to a study of the traffic load code used in Chinese highway bridge design, the headways for the free flow state and following flow state follow Gamma distributions based on actual measurement data [28]. Other studies have shown

that the traffic loads of medium and small span bridges are controlled by free flows whereas those of large-span bridges are controlled by following flows [29–31]. According to the variation in the traffic flow during a day, the headway that vehicles travel during one day is classified into free flow and following flow according to different time intervals, where the free flow occurs at time intervals with a low density of traffic flow, that is, 00:00–05:00 and 22:00–24:00, and the following flow occurs at time intervals with a high density of traffic flow, that is, 08:00–11:00 and 14:00–18:00, while the headway characteristics of other time intervals vary between the free flow and the following flow. From the headway results obtained in the present study, the maximum is 1,200 s but most of the headways were <3 s; thus the range of the distribution is relatively wide. In practical applications of traffic loads, the superposition of the load effects of two adjacent vehicles is meaningless after the headway exceeds a specific level. Therefore, a time headway distribution pattern of <50 s is considered in the present study. Various probability distributions such as the negative exponential distribution, shifted negative exponential distribution, Erlang distribution, M3 distribution, Weibull distribution, log-normal distribution, and Gamma distribution are used for fitting and the K -S test which is used for the goodness of fit test. The results show that the time headway of the following flows followed a log-normal distribution and the time headway of free flows followed a Gamma distribution, as shown in Table 5.

Vehicle speed is an important parameter that determines the start and end position of a vehicle in the traffic flow and it is also an important factor for determining the load effect of traffic. Different speeds produce variable effects when the same vehicles pass over a bridge. Thus, it is necessary to determine the vehicle speed distribution patterns based on the actual data so the effect of vehicle speed can be considered when simulating the traffic flow and analyzing the load effect of the traffic flow. Figure 8 shows the analysis of the actual vehicle speed data, which demonstrates that the vehicle speed followed a normal distribution, and the specific parameters are shown in Table 6.

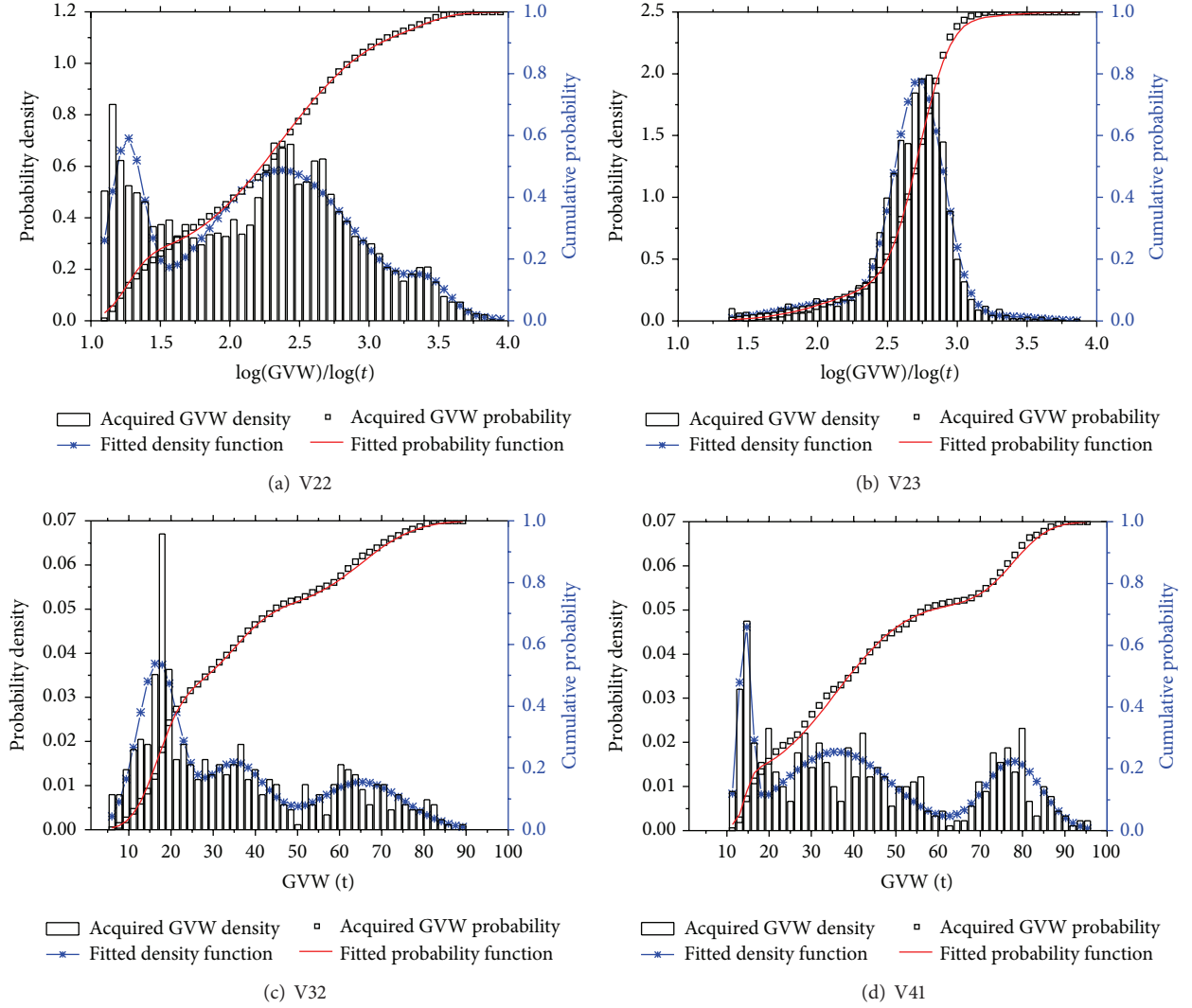


FIGURE 5: Probability distribution of GVW for different truck types.

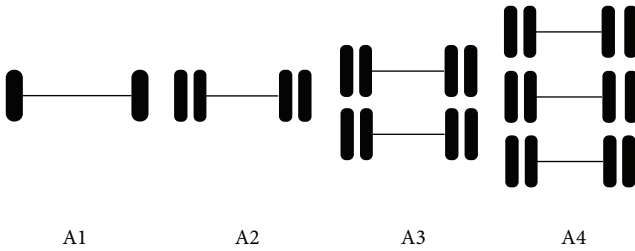


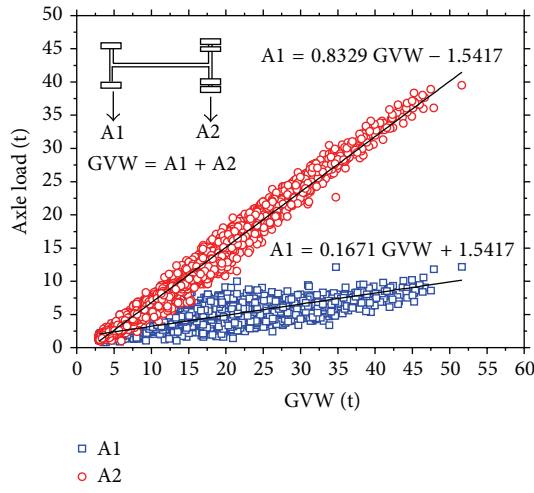
FIGURE 6: Common axle types [26, 27].

TABLE 5: Probability distribution types and parameters for the headways.

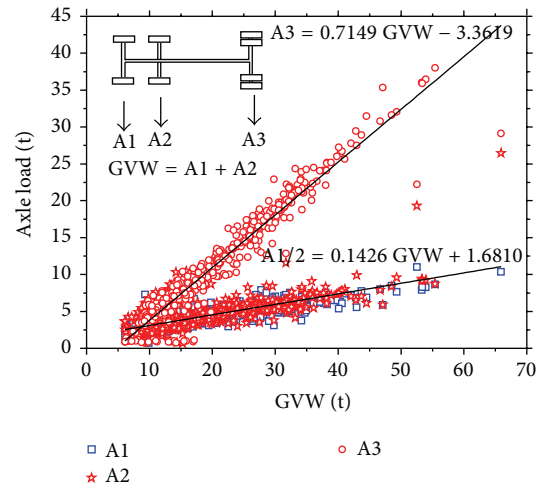
Headway	Distribution type	α	β
Lane 1			
Free flow	Gamma	1.85	10.75
Following flow	log-normal	1.56	0.878
Lane 2			
Free flow	Gamma	1.38	8.74
Following flow	log-normal	0.83	0.58

3.6. Transverse Distribution of the Traffic Flow. The transverse distribution of vehicle loads is an important factor that determines the load effect of vehicles [12]. In the design standards of bridges in China, the transverse distribution of a vehicle is considered in a load layout with respect to the most adverse positions in the transverse direction using the multilane transverse distribution coefficient to

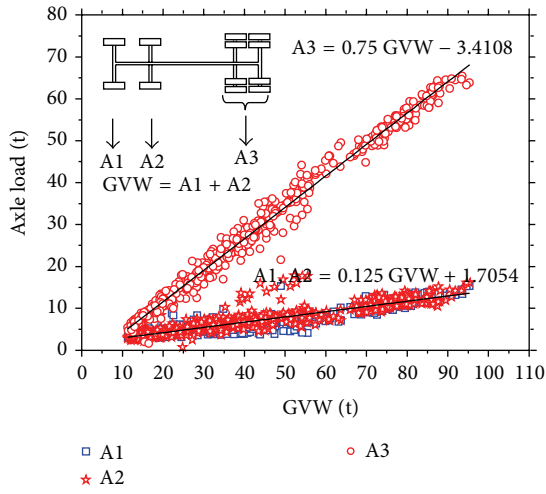
account for the load effect, where this coefficient is studied under the hypothesis that vehicle loads are uncorrelated in various lanes [12]. However, previous studies have shown that different vehicle types all occupied their usual lanes when actual vehicles are considered and the traffic flow compositions generally differed among lanes [12]. Table 7



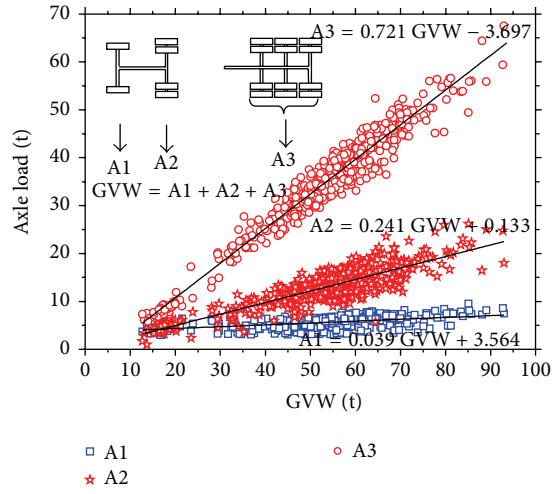
(a) V22



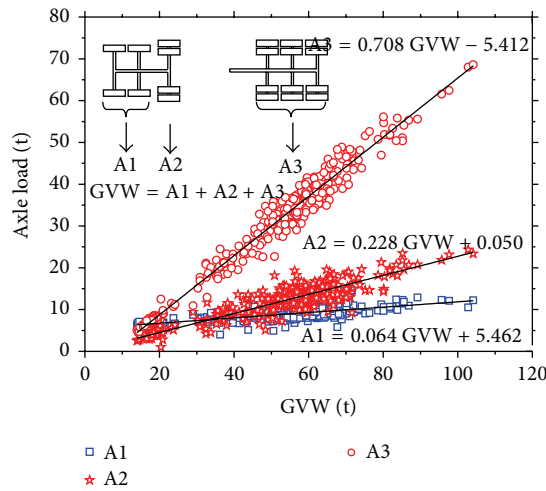
(b) V31



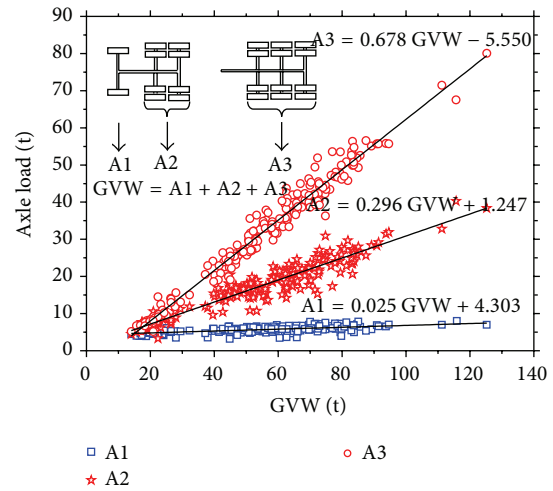
(c) V41



(d) V51



(e) V61



(f) V62

FIGURE 7: Relationships between GVW and axle weights of various vehicle types.

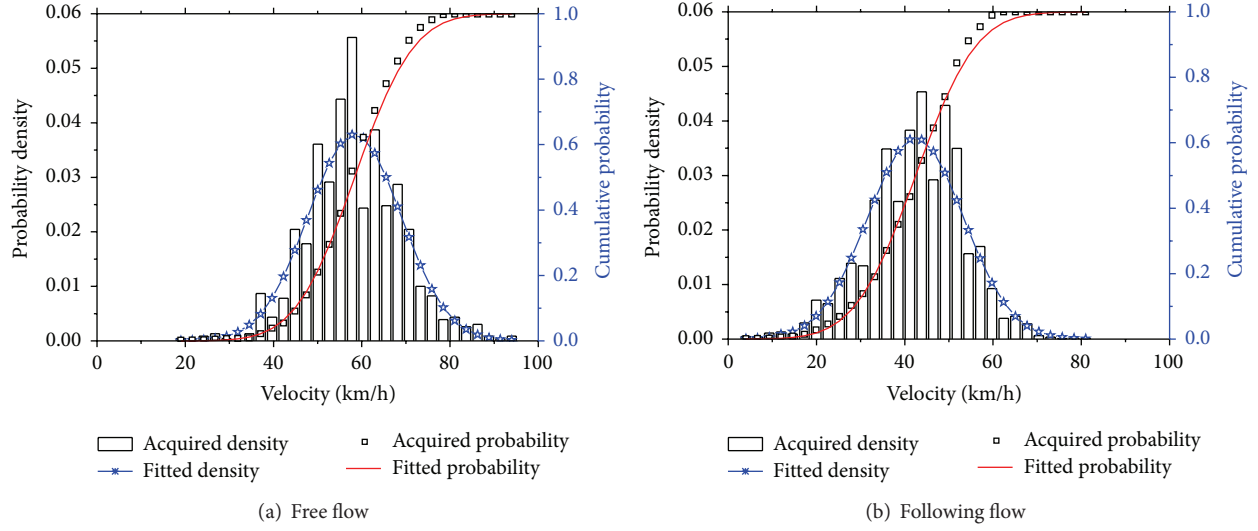


FIGURE 8: Probability distributions for speed with different flow states.

TABLE 6: Parameters of the Gaussian distribution for speed with different flow states.

State	Lane 1		Lane 2	
	μ	σ	μ	σ
Free flow	54.68	16.23	58.12	10.75
Following flow	45.86	19.20	45.02	9.23

TABLE 7: Transverse distribution of the traffic flow.

Axle number	V21	V22	V23	V31	V32	V41	V42	V51	V61	V62
Lane 1	0.60	0.23	0.09	0.02	0.01	0.02	0.01	0.02	0.01	0.01
Lane 2	0.54	0.21	0.08	0.01	0.01	0.01	0.01	0.01	0.01	0.01

shows the transverse distribution for various vehicle types in two lanes.

4. Analysis of Stress Variation

To analyze the fatigue life of suspenders, the stress spectrum of suspenders must first be obtained. Acquiring actual measurements is the most direct method for obtaining the stress spectrum of suspenders, where the measurement points are positioned along the suspender to allow dynamic sampling and long-term monitoring of the stress process. However, the cost of obtaining actual measurements is very high and the process is time consuming, while the stress sampling process is limited. Given these many adverse factors, a computer-based simulation analysis method is developed in this study. First, a spatial finite element model of the bridge is constructed to obtain the influence line of the internal force of a suspender. Second, using the actual statistical parameters of the random traffic flow derived from measurements and based on the Monte Carlo method, random traffic flows traveling in multiple lanes in either direction are simulated

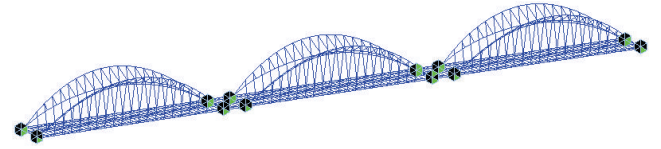


FIGURE 9: FE model of objective bridge.

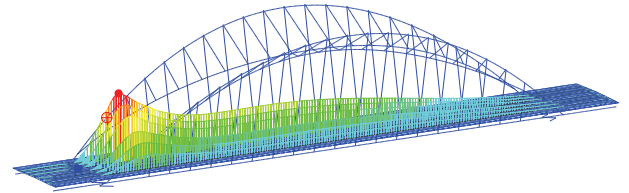


FIGURE 10: Influence line of shortest suspender.

with a FORTRAN program. Third, the influence line of the objective suspender is loaded to obtain the stress process for the suspender and the stress spectrum is then obtained via the cyclic statistics of the stress process. Finally, the fatigue condition of the suspender is analyzed by selecting a suitable S-N curve for the suspenders using the Palmgren-Miner linear fatigue cumulative damage criterion.

4.1. Finite Element (FE) Model. In this study, the Midas software is used to build a spatial model of the objective bridge. Figure 9 shows the FE model. The elements and quantities used for structural modeling are shown in Table 8.

The shortest suspender on the side of the midspan is selected as the subject of the analysis and its influence line is extracted for a lane. Figure 10 shows the influence line.

4.2. Traffic Simulation. The actual traffic situation is very complex, where the difference in vehicle types is great and

TABLE 8: Element types and numbers in FE model.

Substructure	Element type	Element number
Main arch	Beam	132
Vice arch	Beam	120
Suspender	Elements only tensioned	130
Main longitudinal girder	Beam	414
Vice longitudinal girder	Beam	284
Transverse girder	Beam	572
Tie bar cable	Elements only tensioned	16
Transverse bracing	Beam	9
Connecting rod	Beam	102

complex traffic conditions may occur such as traffic jams and overtaking. If a random traffic flow is simulated faithfully according to the actual situation, this requires a considerable amount of programming work and the arithmetic speed is also restricted by the computer's performance. In the present study, the effects of complex traffic conditions, such as traffic jams and overtaking, on the fatigue analysis are not considered. Therefore, when simulating the traffic loads, following travel is assumed and there are no traffic jams or overtaking. The traffic flow in self-lanes is independent. Some parameters, such as the headway, vehicle type, GVW, and axle space, are uncorrelated random variables that followed the measured distributions. The steps employed to produce the random traffic flow are as follows.

- (1) According to the following flow parameters for different lanes, a log-normal distribution is sampled to obtain the time headway, which is then converted into the distance headway according to the vehicle speed.
- (2) According to the actual ratio of vehicle types, a uniform distribution is sampled to obtain the vehicle types.
- (3) According to the actual distributions of different vehicle types, a multimodal normal distribution or a log-normal distribution is sampled to obtain the GVW. The axle load is obtained according to the fitted relationship between the GVW and the axle weight.
- (4) According to the actual axle spaces of different vehicle types, a uniform distribution is sampled to obtain the axle space. And the total vehicle length is calculated.
- (5) If the traffic flow time is less than the assumed value, step (1) is repeated. If the spacing of the next vehicle is less than the total length of the previous vehicle, the total length of the previous vehicle will replace the spacing.

According to these steps, the random traffic flow used for fatigue analysis is produced automatically in the FORTRAN language. Figure 11 shows a flow diagram of the program.

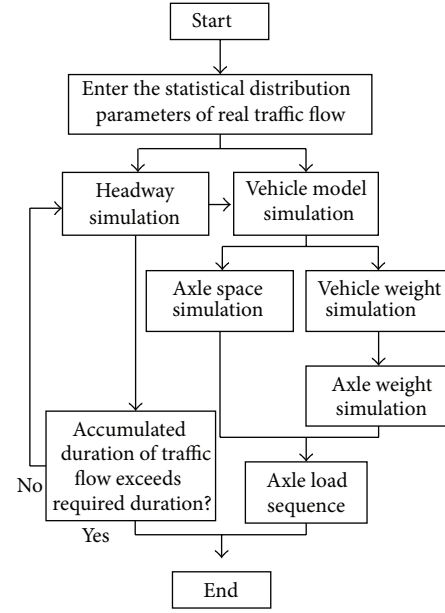


FIGURE 11: Flowchart of random traffic flow simulation program.

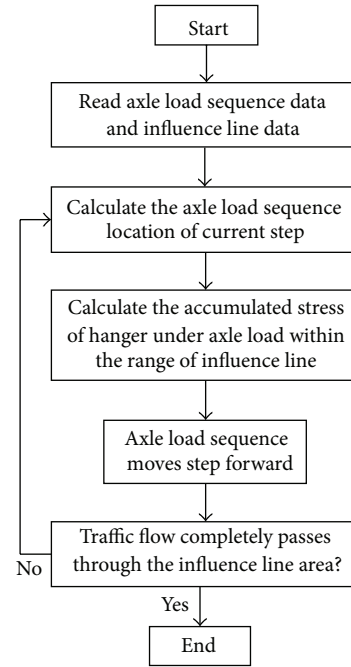


FIGURE 12: Flowchart showing calculation of suspender stress.

4.3. Stress Process and Stress Spectrum of Suspender. The random traffic flow moves across the bridge step by step. At each load step, all of the load responses of the axle load within the range of the influence line are superposed to obtain the total response value of the suspender stress in the current step. The fatigue stress process of the suspender is obtained after the vehicle passed over the bridge. The stress process is also calculated using the FORTRAN language. Figure 12 shows the flowchart of the program.

The stress process refers to the variation in stress during a time interval. The stress spectrum of fatigue is obtained using the statistics from the stress process. Many statistical methods can be used to analyze the stress process. In this study, the rainflow counting method is used.

4.4. Calculation of Fatigue Damage. At present, it is still uncertain which method is the most reasonable for analyzing cyclic loading to determine the cumulative damage to a structure. The linear fatigue cumulative damage theory of Palmgren and Miner is generally used in fatigue analysis of bridge structures [32]. The fatigue damage degree of a component defined by the Miner criterion under variable amplitude loads is

$$D = \sum_{i=1}^k \frac{n_i}{N_i}, \quad (2)$$

where n_i is the time of the stress amplitude $\Delta\sigma_i$, N_i is the time of fatigue failure in a cyclic test, and $\Delta\sigma_i$ is a constant amplitude stress, which is relevant to the fatigue life for a stress amplitude of $\Delta\sigma_i$ in the S - N curve of the fatigue test. When $D \geq 1$, the components are destroyed. The S - N relationships of suspenders are obtained via a previously described fatigue test [33]:

$$\Delta\sigma_i = 12800N_i^{0.27}, \quad (3)$$

where the unit of stress amplitude $\Delta\sigma_i$ is MPa. After formula (3) is substituted into formula (2), formula (4) can be obtained:

$$D = \sum_{i=1}^k \frac{n_i}{(\Delta\sigma_i/12800)^{1/0.27}}. \quad (4)$$

A stress cycle with variable amplitude is generally equivalent to that with constant amplitude. The equivalence principle states that the fatigue accumulation at constant amplitude with equivalent stress D_{eq} is the same as that with variable amplitude under the same load cycles; that is,

$$D_{eq} = \frac{\sum_{i=1}^k n_i}{N_{eq}} = \sum_{i=1}^k \frac{n_i}{(\Delta\sigma_i/12800)^{1/0.27}}, \quad (5)$$

where N_{eq} is the relevant fatigue life for the equivalent stress amplitude $\Delta\sigma_{eq}$. N_{eq} is solved using formula (5) and then substituted into formula (2). The calculated formula for the equivalent stress amplitude $\Delta\sigma_i$ can then be obtained as

$$\Delta\sigma_{eq} = \left(\frac{(\sum_{i=1}^k n_i)^{0.27}}{\sum_{i=1}^k (n_i/(\Delta\sigma_i/12800)^{1/0.27})} \right)^{0.27}. \quad (6)$$

5. Results and Discussions

The random traffic flows are simulated for 24 hours according to the method described above. To verify the characteristics of the random traffic flow produced according to the

distribution of the actual traffic flow, statistical analyses are performed using sampling parameters for the random traffic flow over a period of 24 hours, including the headway, vehicle type ratio, and GVW of various vehicle types. Figure 13 shows the results of the statistical analyses, which demonstrate that the GVWs of various vehicle types in the random traffic flow all agreed with those of the actual traffic flow.

Figure 14 shows the stress process for Number 1 (shortest) and Number 10 (longest) suspenders under the random traffic flow, which demonstrates that the stress on Number 1 suspender varies in the range of 378–400 MPa and that on Number 10 suspender varies in the range of 369–400 MPa. The difference in the minimum value for Number 1 and Number 10 suspenders is about 10 MPa, but the stress ranges have little difference.

The distribution of the stress amplitude is obtained based on a statistical analysis of the stress process, as shown in Figure 15. According to the statistical results, the stress amplitudes under the random traffic flow are very small, where the maximum stress amplitude is less than 24 MPa for Number 1 suspender and the maximum stress amplitude is less than 30 MPa for Number 10 suspender, while the 90% stress amplitude is less than 10 MPa.

According to formula (6), the equivalent stress amplitudes of the suspenders are calculated under variable amplitude loads. The equivalent stress amplitudes of various suspenders are shown in Figure 16. The equivalent stress amplitudes for 10 suspenders ranged from 7.41 to 9.65 MPa. In addition, the dead load stress is also shown in Figure 16; it can be seen that the live load stress amplitude is very small compared with the overall stress value and it only accounted for about 2% of the total stress. These results show that the fatigue damage to suspenders on the objective bridge is very low under the present vehicle loads.

It should be noted that this fatigue analysis is based on the current traffic levels. The traffic flow will increase with the service time of the bridge, while the fatigue performance of the steel wires in the suspenders may degenerate due to the corrosive environment. Thus, although the fatigue damage is low in the current conditions, they should be considered seriously during the later maintenance management of the bridge.

6. Conclusions

(1) In this study, 347 sensors are positioned in the SHMS of the objective bridge and the vehicle load acquisition equipment is embedded in the system to acquire the vehicle loads, as well as obtaining further information about the vehicles that passed over the observed section, such as the vehicle speed, direction, plate number, vehicle type, passing time, axle weight, and gross vehicle weight. This greatly improves the efficiency and accuracy of the traffic load survey.

(2) The traffic flow on the objective bridge mainly comprises ten types of truck (trucks accounted for 19.52% of the total traffic), where the gross vehicle weights of two-axle vehicles follow a third-order mixed log-normal distribution and those of three-axle, four-axle, five-axle, and six-axle

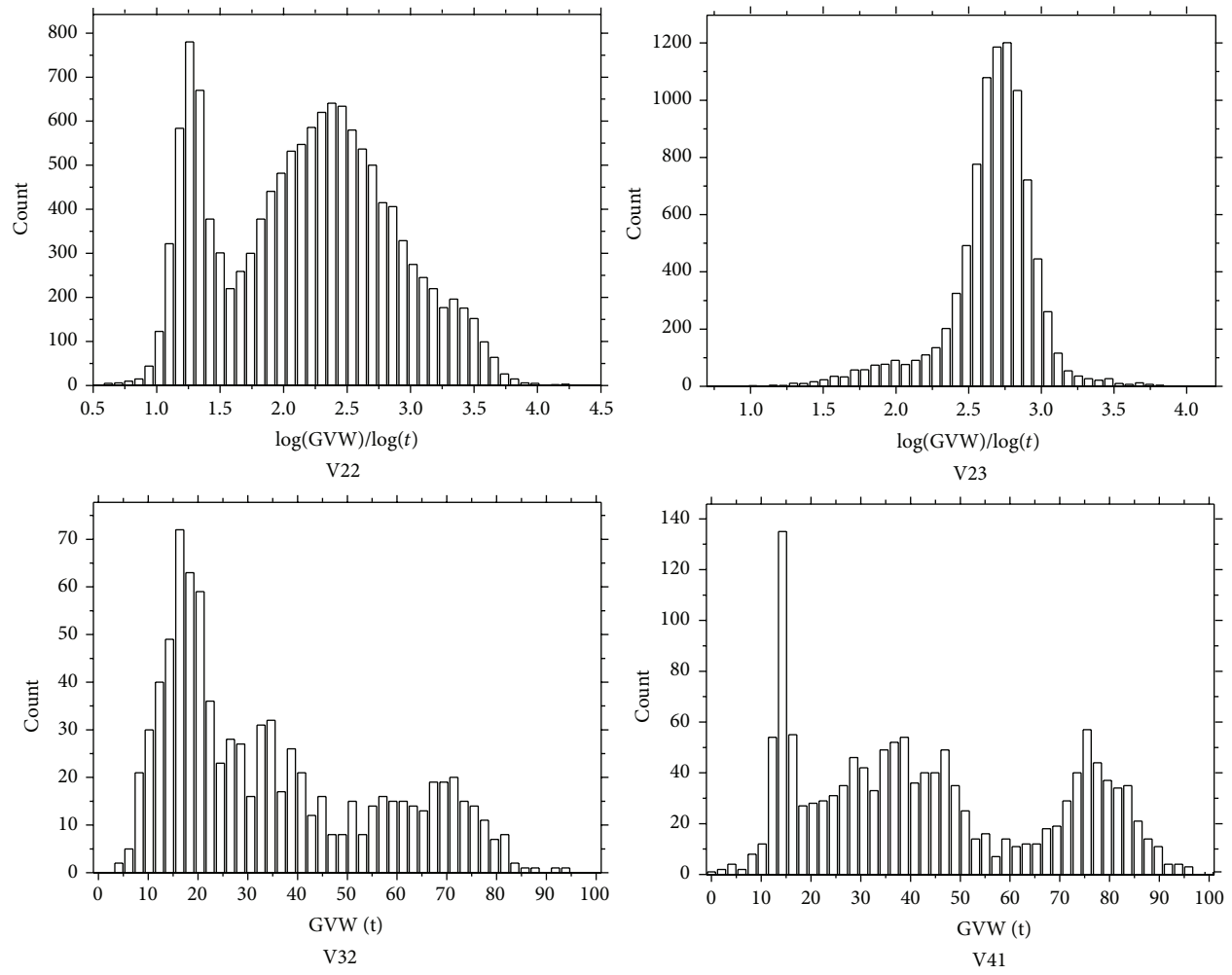


FIGURE 13: GVW probability distributions for simulated traffic flow.

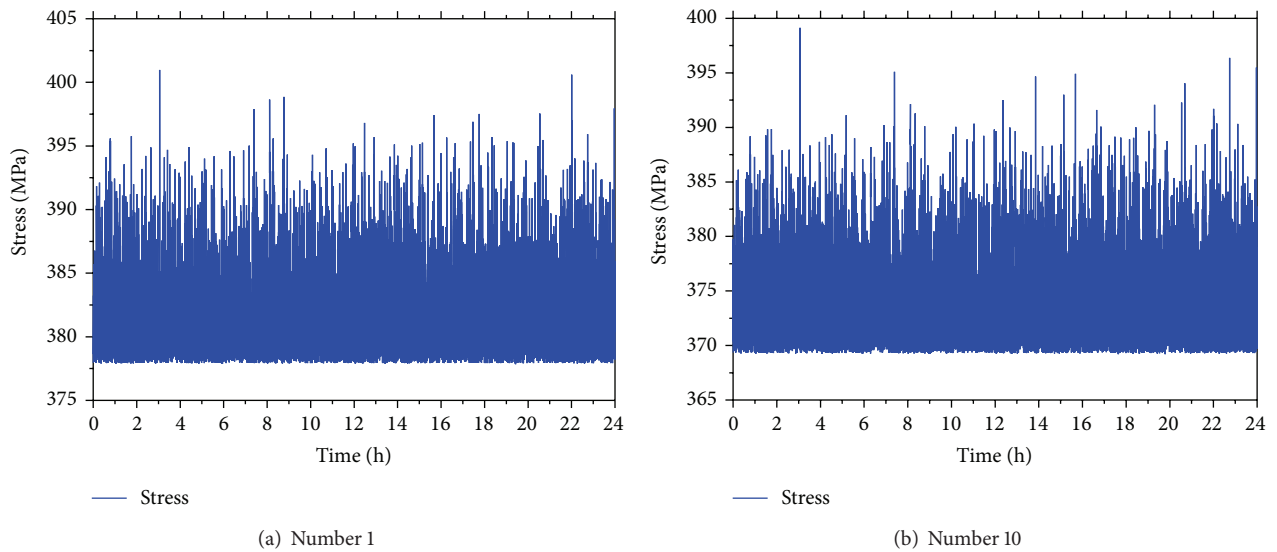


FIGURE 14: Stress processes for the suspenders.

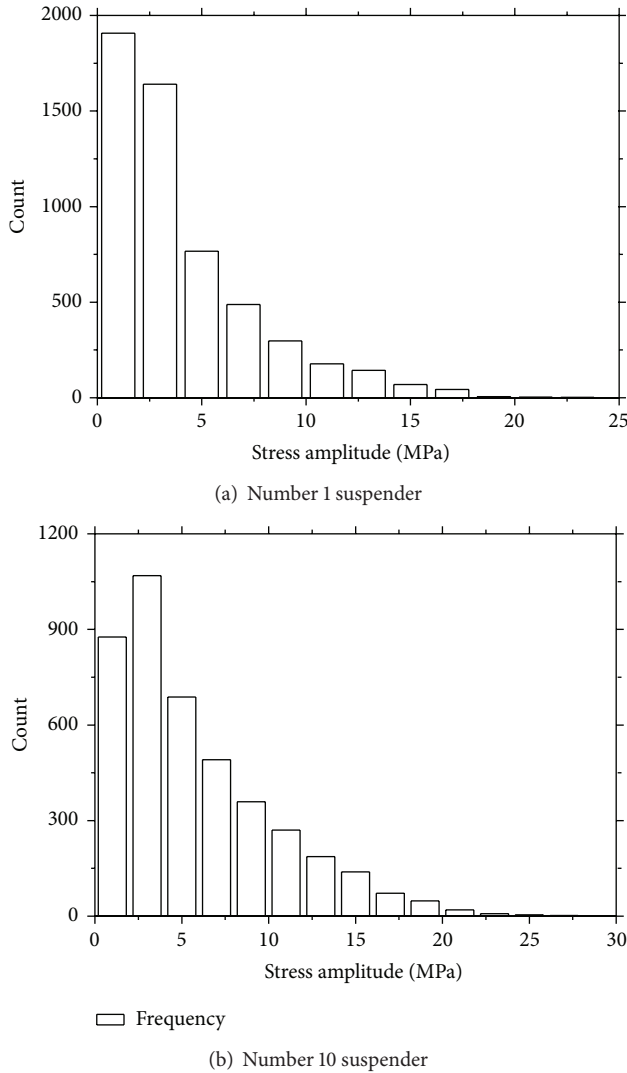


FIGURE 15: Statistical analysis of stress processes.

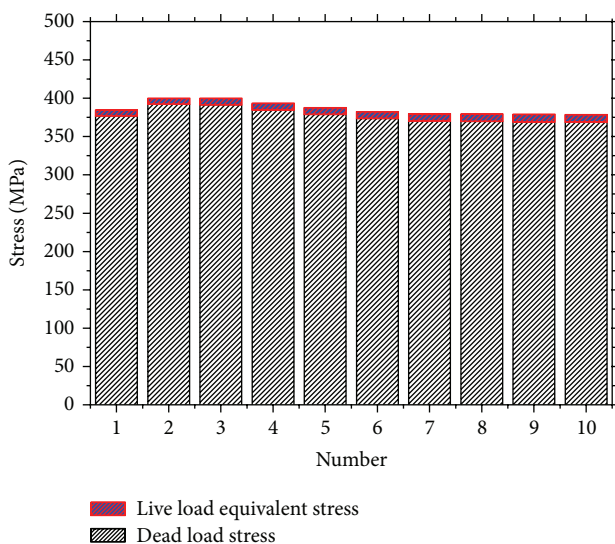


FIGURE 16: Equivalent stress of live load and dead load.

vehicles follow a third-order mixed normal distribution. The gross vehicle weights of various vehicle types with different axle weights have a linear relationship. The headway of the following flow conforms to a log-normal distribution while that of the free flow has a Gamma distribution. The vehicle speed follows a normal distribution.

(3) Using the Monte Carlo method, the random traffic flow is simulated according to a statistical analysis of the data obtained. Based on the loading of the influence line in a random traffic flow, the stress spectrum is obtained according to the cyclic statistics of the stress process. The fatigue conditions of the bridge suspenders are analyzed according to the Palmgren-Miner linear fatigue cumulative damage criterion. The results show that the equivalent stress amplitude of the fatigue load due to vehicles is only 9.65 MPa, which accounts for about 2% of the total force, thereby demonstrating that the suspender fatigue damage is low under the current traffic load.

Disclaimer

The results and conclusions presented in this paper are those of the authors and they do not necessarily reflect the views of the sponsors.

Conflict of Interests

The authors declare that there is no conflict of interests regarding the publication of this paper.

Acknowledgments

This study was funded jointly by the Institute Basic Scientific Research Fund (Grant no. 2012A02) and the National Natural Science Foundation of China (NSFC) (Grant no. 51308510).

References

- [1] W. Zhang, C. S. Cai, and F. Pan, "Nonlinear fatigue damage assessment of existing bridges considering progressively deteriorated road conditions," *Engineering Structures*, vol. 56, pp. 1922–1932, 2013.
- [2] W. Zhang, *Fatigue Performance of Existing Bridges under Dynamic Loads from Winds and Vehicles*, Louisiana State University, Baton Rouge, La, USA, 2012.
- [3] X. W. Ye, Y. H. Su, and J. P. Han, "A state-of-the-art review on fatigue life assessment of steel bridges," *Mathematical Problems in Engineering*, vol. 2014, Article ID 956473, 13 pages, 2014.
- [4] B. Enright and E. J. O'Brien, "Monte Carlo simulation of extreme traffic loading on short and medium span bridges," *Structure and Infrastructure Engineering*, vol. 9, no. 12, pp. 1267–1282, 2013.
- [5] E. J. O'Brien and B. Enright, "Modeling same-direction two-lane traffic for bridge loading," *Structural Safety*, vol. 33, no. 4-5, pp. 296–304, 2011.
- [6] C. C. Caprani, A. Lipari, and E. J. O'Brien, "Load effect of multi-lane traffic simulations on long-span bridges," in *Proceedings of the 6th International Conference on Bridge Maintenance*,

- Safety and Management (IABMAS '12)*, F. Biondini and D. M. Frangopol, Eds., pp. 1460–1467, July 2012.
- [7] M. Gindy and H. H. Nassif, "Comparison of traffic load models based on simulation and measured data," in *Proceedings of the Joint International Conference on Computing and Decision Making in Civil and Building Engineering*, Montréal, Canada, June 2006.
 - [8] T. H. Yi, H. N. Li, and M. Gu, "Recent research and applications of GPS based technology for bridge health monitoring," *Science China Technological Sciences*, vol. 53, no. 10, pp. 2597–2610, 2010.
 - [9] T. H. Yi, H. N. Li, and M. Gu, "Optimal sensor placement for structural health monitoring based on multiple optimization strategies," *The Structural Design of Tall and Special Buildings*, vol. 20, no. 7, pp. 881–900, 2011.
 - [10] T.-H. Yi, H.-N. Li, and M. Gu, "Experimental assessment of high-rate GPS receivers for deformation monitoring of bridge," *Measurement*, vol. 46, no. 1, pp. 420–432, 2013.
 - [11] T. H. T. Chan, T. J. Miao, and D. B. Ashebo, "Statistical models from weigh-in-motion data," *Structural Engineering and Mechanics*, vol. 20, no. 1, pp. 85–110, 2005.
 - [12] X. Y. Zhou, *Statistical Analysis of Traffic Loads and Their Effects on Bridges*, University Paris-EST & IFSTTAR, Paris, France, 2013.
 - [13] C. C. Caprani, *Probabilistic Analysis of Highway Bridge Traffic Loading*, National University of Ireland, University College Dublin, Dublin, Ireland, 2005.
 - [14] J. Zhao and T. Tabatabai, *Analysis of Permit Vehicle Loads in Wisconsin*, Wisconsin Highway Research Program, 2009.
 - [15] B. Chen, Z. Zhong, X. Xie, and P. Lu, "Measurement-based vehicle load model for urban expressway bridges," *Mathematical Problems in Engineering*, vol. 2014, Article ID 340896, 10 pages, 2014.
 - [16] E. J. O'Brien and B. Enright, "Using weigh-in-motion data to determine aggressiveness of traffic for bridge loading," *Journal of Bridge Engineering*, vol. 18, no. 3, pp. 232–239, 2013.
 - [17] D. Hajializadeh, E. O'Brien, B. Enright, E. Sheils, S. Wilson, and C. Caprani, "Probabilistic study of lifetime load effect distribution of bridges," in *Proceedings of the 6th International ASRANet Conference for Integrating Structural Analysis*, Croydon, UK, 2012.
 - [18] G. Fu and J. You, "Extrapolation for future maximum load statistics," *Journal of Bridge Engineering*, vol. 16, no. 4, pp. 527–535, 2011.
 - [19] O.-S. Kwon, E. Kim, and S. Orton, "Calibration of live-load factor in LRFD bridge design specifications based on state-specific traffic environments," *Journal of Bridge Engineering*, vol. 16, no. 6, pp. 812–819, 2011.
 - [20] T. Guo, D. M. Frangopol, and Y. Chen, "Fatigue reliability assessment of steel bridge details integrating weigh-in-motion data and probabilistic finite element analysis," *Computers & Structures*, vol. 112–113, pp. 245–257, 2012.
 - [21] C. Lan, H. Li, and J. Ou, "Traffic load modelling based on structural health monitoring data," *Structure and Infrastructure Engineering*, vol. 7, no. 5, pp. 379–386, 2011.
 - [22] Y. Q. Ni, X. W. Ye, and J. M. Ko, "Monitoring-based fatigue reliability assessment of steel bridges: analytical model and application," *Journal of Structural Engineering*, vol. 136, no. 12, pp. 1563–1573, 2010.
 - [23] E. J. O'Brien, B. Enright, and A. Getachew, "Importance of the tail in truck weight modeling for bridge assessment," *Journal of Bridge Engineering*, vol. 15, no. 2, pp. 210–213, 2010.
 - [24] Y. Q. Ni, X. W. Ye, and J. M. Ko, "Modeling of stress spectrum using long-term monitoring data and finite mixture distributions," *Journal of Engineering Mechanics*, vol. 138, no. 2, pp. 175–183, 2011.
 - [25] J. A. Prozzi and F. Hong, "Optimum statistical characterization of axle load spectra based on load-associated pavement damage," *International Journal of Pavement Engineering*, vol. 8, no. 4, pp. 323–330, 2007.
 - [26] S. Sriramula, D. Menon, and A. M. Prasad, "Axle load variations and vehicle growth projection models for safety assessment of transportation structures," *Transport*, vol. 22, no. 1, pp. 31–37, 2007.
 - [27] D. H. Timm, S. M. Tisdale, and R. E. Turochy, "Axle load spectra characterization by mixed distribution modeling," *Journal of Transportation Engineering*, vol. 131, no. 2, pp. 83–88, 2005.
 - [28] Ministry of Communications and Transportation (MOCAT), "General code for design of highway bridges and culverts," JTG D60-2004, Ministry of Communications and Transportation, Beijing, China, 2004.
 - [29] C. C. Caprani, E. J. O'Brien, and G. J. McLachlan, "Characteristic traffic load effects from a mixture of loading events on short to medium span bridges," *Structural Safety*, vol. 30, no. 5, pp. 394–404, 2008.
 - [30] E. J. O'Brien, A. Hayrapetova, and C. Walsh, "The use of micro-simulation for congested traffic load modeling of medium- and long-span bridges," *Structure and Infrastructure Engineering*, vol. 8, no. 3, pp. 269–276, 2012.
 - [31] C. C. Caprani, "Calibration of a congestion load model for highway bridges using traffic microsimulation," *Structural Engineering International*, vol. 22, no. 3, pp. 342–348, 2012.
 - [32] X. W. Ye, Y. Q. Ni, K. Y. Wong, and J. M. Ko, "Statistical analysis of stress spectra for fatigue life assessment of steel bridges with structural health monitoring data," *Engineering Structures*, vol. 45, pp. 166–176, 2012.
 - [33] K. Takena, C. Miki, H. Shimokawa, and K. Sakamoto, "Fatigue resistance of large-diameter cable for cable-stayed bridges," *Journal of Structural Engineering*, vol. 118, no. 3, pp. 701–715, 1992.

Research Article

Effects of Concrete on Propagation Characteristics of Guided Wave in Steel Bar Embedded in Concrete

Zhupeng Zheng and Ying Lei

Department of Civil Engineering, Xiamen University, Xiamen 361005, China

Correspondence should be addressed to Ying Lei; ylei@xmu.edu.cn

Received 22 June 2014; Revised 22 July 2014; Accepted 28 July 2014; Published 27 August 2014

Academic Editor: Ting-Hua Yi

Copyright © 2014 Z. Zheng and Y. Lei. This is an open access article distributed under the Creative Commons Attribution License, which permits unrestricted use, distribution, and reproduction in any medium, provided the original work is properly cited.

Techniques based on ultrasonic guided waves (UGWs) play important roles in the structural health monitoring (SHM) of large-scale civil infrastructures. In this paper, dispersion equations of longitudinal wave propagation in reinforced concrete member are investigated for the purpose of monitoring steels embedded in concrete. For a steel bar embedded in concrete, not the velocity but the attenuation dispersion curves will be affected by the concrete. The effects of steel-to-concrete shear modulus ratio, density ratio, and Poisson's ratio on propagation characteristics of guided wave in steel bar embedded in concrete were studied by the analysis of the real and imaginary parts of the wave number. The attenuation characteristics of guided waves of steel bar in different conditions including different bar concrete constraint and different diameter of steel bar are also analyzed. Studies of the influence of concrete on propagation characteristics of guided wave in steel bars embedded in concrete will increase the accuracy in judging the structure integrity and promote the level of defect detection for the steel bars embedded in concrete.

1. Introduction

In recent years, techniques based on ultrasonic guided waves (UGWs) have gained popularities and played important roles in the structural health monitoring (SHM) of large-scale civil infrastructures as guided waves have some important advantages, such as the capability of testing over long range with a greater sensitivity, the ability to test multilayered structures, and relatively cheapness due to simplicity and sensor cost [1]. Furthermore, frequency and mode tuning of UGWs can be utilized for evaluation of different types of deterioration or damage because UGWs have many different modes at a single frequency that are sensitive to different defects. Due to the above, various techniques based on guided wave have been proposed for damage detection and condition assessments of aerospace, mechanical, civil engineering structures, and other nondestructive test (NDT) areas. Raghavan and Cesnik [2] presented a review of guided wave for structural health monitoring. Sohn et al. [3] investigated delamination detection in composites through guided wave imaging. Song et al. [4, 5] developed smart piezoceramic transducers with guided wave for concrete structural health monitoring. Giurgiutiu [6] studied lamb wave generation with

piezoelectric wafer active sensors for structural health monitoring (SHM). Wang et al. [7] investigated the effects of a defect's geometric parameters on the two reflection signals in pipe using guided waves and proposed a new strategy for accurate and quantitative pipeline defect characterization. Cobb et al. [8] studied the torsional guided wave attenuation in piping from coating, temperature, and large-area corrosion and obtained experimental results that wave attenuation is a good indicator of general corrosion level. Ahmad and Kundu [9] studied the influence of water flow through pipe networks on damage detection using guided waves. Beard et al. [10] used guided waves to inspect concrete reinforcing tendons and evaluated the effect of factors such as leakage and defect geometry on the inspection. Zhu et al. [11] used ultrasonic guided waves for nondestructive evaluation/structural health monitoring of trusses. The finite element method (FEM) is often carried out to assist structural design [12] and also used to study the guided waves for SHM in the civil infrastructures. Yi et al. [13] used FEM to predict the location of pitting corrosion in reinforced concrete based on guided waves. Simulation results show that it is feasible to predict corrosion monitoring based on ultrasonic guided wave in reinforced concrete. Moser et al. [14] simulated the propagation of elastic

wave in the sheet and tubular structure using FEM. The results are fully consistent with those from experiment, which further proves the validity of the simulation in wave propagation using FEM. Chen [15] used FEM to simulate the defect monitoring by longitudinal guided wave and get the relation curves between reflection coefficient and circumferential length or axial length of the defect in pipe. He et al. [16] studied the propagation of guided waves in bending pipe using FEM. Other recent developments of guided waves for SHM were also discussed in a review prepared by Huang et al. [17].

Among the current available corrosion monitoring techniques in reinforced concrete, the technique based on ultrasonic guided wave has gained more and more popularity in the recent years due to its advantages for monitoring corrosion related damage in reinforcing bars, so it has gained popularities in the recent years [18]. Na et al. [19] used both high (1 MHz) and low frequencies (150 KHz) to study the effect of various bond levels by surrounding the rebar with a polyvinyl chloride polymer (PVC) pipe in RC beams and the effect of debonding location on the received waveforms. They in the same way conducted a comparison of steel concrete interfaces and glass fiber polymer-concrete interfaces using the guided waves [20, 21]. Reis et al. [22] used the fundamental flexural mode below 250 kHz for estimation of corrosion damage in steel reinforced mortar. Wu and Chang [23, 24] used the piezoelectric discs as sensors and actuators to detect debonding in reinforced concrete structures. A set of reinforced concrete square beam specimens with various bond levels were built and tested using guided mechanical waves at lower frequencies. He et al. [25] used frequencies between 1 and 2 MHz to relate the effect of debonding on signals in cylindrical specimens. Dongsheng et al. [26] used five-cycle sinusoidal signals with 120 kHz central frequency to investigate the UGW energy attenuation on the different debonding level between steel bar and concrete in both time-domain and frequency-domain analyses.

All the above test results indicated that the received waveform is less attenuated with the increase in debonding for both low and high frequencies. However, the lower frequencies showed more sensitivity to the change in bond. There was no significant change in the waveform arrival time reported. The location of debonding is not discernible through pulse transmission as reported by Evin et al. [27, 28].

These studies were mostly carried out with simulated debonding. In these cases, it is in fact the free steel bar within the concrete. There is difference in the propagation characteristics of guided waves between the free steel bars and the steel bar surrounded by concrete. However, the research on the effects of concrete on propagation characteristics of guided wave in steel bar embedded in concrete is less reported, because there is a difficulty of limitation of monitoring range of guided wave in reinforced concrete [18, 27]. Unlike guided wave propagation in other multilayered systems, such as a metal pipeline in air, wave energy in steel bars embedded in concrete, will be reduced (i.e., attenuated) at high rates due to leakage into the surrounding concrete. For the defects test of steel bar embedded in concrete, the reflected signals will be very weak, so the general time-frequency methods

are difficult to identify the weak reflection signals of the defects in the detection signals.

In an infinite isotropic solid medium, only two types of independent wave propagation exist, that is, compression and shear waves. Both waves propagate with constant velocities and are nondispersive. When geometry constraints are introduced and the dimensions are close to the wavelength, the wave becomes dispersive and is called a guided wave. Longitudinal, torsional, and flexural waves propagate in isotropic cylinders. The characteristic equation for solid isotropic cylinders was originally independently derived for the special case of longitudinal propagation in the late 19th century [29, 30]. Solutions to this equation contain the phase velocity and frequency (assuming no absorption by the medium). The derivations assume the solid cylinder is traction free and infinite in length and that the wave form has harmonic motion. The characteristic equation for torsional and flexural propagation was later derived [31, 32].

In civil infrastructures, steel bars are usually embedded in concrete, so the existence of concrete is of strong interference with the integrity evaluation of steel bars, which lead to the difficult problem in the detection of steel bars using guided wave based techniques [27]. Steel bar embedded in concrete can be modeled as an isotropic solid cylinder embedded in an infinite isotropic medium. The derivation is similar to the solid cylinder in vacuum; however, displacement and stress boundary conditions must now be met at the interface between the two mediums. In the case of reinforced concrete, a solution includes phase velocity, frequency, and attenuation. So, there is obviously different propagation characteristics of UGWs in steel bars embedded in concrete compared with those in free bars. Therefore, it is important to study the influence of concrete on propagation characteristics of guided wave in steel bars embedded in concrete which will increase the accuracy in judging the structure integrity and promote the level of defect detection for the steel bars embedded in concrete [33, 34].

2. Dispersion Equations of Longitudinal Guided Wave in Reinforced Concrete

For a steel bar embedded in concrete, the guided waves propagate not only along the steel bar but also spread outward, which leads to the wave energy that diffuses from steel bar into the concrete. Furthermore, the change of wave impedance of concrete can also cause the reflection of the waves. Thus, the wave equations of guided waves in steel bar-concrete system can be established based on the 3D elastic wave theory.

The simplified model of a steel bar embedded in concrete is shown in Figure 1, in which the inner layer of medium is the steel bar with the radius a , and peripheral medium is concrete which is infinite in radial direction. Guided waves are assumed to propagate along the Z -direction. In order to facilitate the analysis, the reinforcement was set as round steel bar. In the propagation in the steel bar embedded in concrete, the outward propagation and the attenuation due to

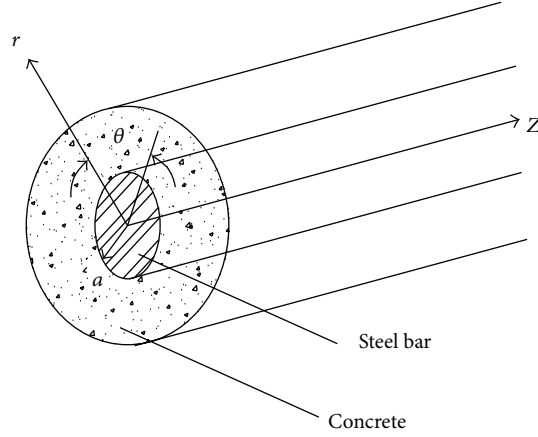


FIGURE 1: Simplified model of steel bar embedded in concrete.

concrete of guided waves can all be expressed by the correlation functions, in which steel bar is regarded as an isotropic elastic rod and the solution of wave equations can be solved by separation variables method.

Displacement of guided waves propagating in steel bar can be expressed by Bessel function [32]. The velocities of longitudinal and shear waves in steel bar-concrete system meet the relations: $C_{LS} > C_{TS} > C_{LC} > C_{TC}$, where C_{LS} and C_{TS} are the velocity of longitudinal and transverse waves in steel bar, respectively, and C_{LC} and C_{TC} are the velocity of longitudinal and transverse waves in concrete, respectively. Only Hankel function can meet the required condition when the wave number k is a complex index [35]. Therefore, Hankel function is chosen to describe the outward propagation of waves which attenuates to zero at infinity. Based on the displacements, the stress components in both steel bar and concrete can be deduced according to the relationships of strain-displacement and stress-strain.

It is assumed that bonding condition at the interface between steel bar and concrete is good and the displacement and stress at the interface are continuous, so

$$\begin{cases} u_r - u'_r \\ u_\theta - u'_\theta \\ u_z - u'_z \\ \sigma_{rr} - \sigma'_{rr} \\ \sigma_{r\theta} - \sigma'_{r\theta} \\ \sigma_{rz} - \sigma'_{rz} \end{cases} = 0, \quad (r = a), \quad (1)$$

where u_r , u_θ , u_z , and u'_r , u'_θ , u'_z are the displacement components of the steel bar and concrete, respectively. σ_{rr} , $\sigma_{r\theta}$, σ_{rz} and σ'_{rr} , $\sigma'_{r\theta}$, and σ'_{rz} are the stress components of the steel bar and concrete, respectively.

Then, substituting displacement and stress into (1), the following matrix can be obtained as follows [23]:

$$\begin{Bmatrix} D_{11} & D_{12} & D_{13} & D_{14} & D_{15} & D_{16} \\ D_{21} & D_{22} & D_{23} & D_{24} & D_{25} & D_{26} \\ D_{31} & D_{32} & D_{33} & D_{34} & D_{35} & D_{36} \\ D_{41} & D_{42} & D_{43} & D_{44} & D_{45} & D_{46} \\ D_{51} & D_{52} & D_{53} & D_{54} & D_{55} & D_{56} \\ D_{61} & D_{62} & D_{63} & D_{64} & D_{65} & D_{66} \end{Bmatrix} \begin{Bmatrix} A_1 \\ A_4 \\ A_6 \\ A'_1 \\ A'_4 \\ A'_6 \end{Bmatrix} = 0, \quad (2)$$

where detailed expressions of D_{ij} ($i, j = 1, \dots, 6$) are related to the displacement and stress components of steel bar and concrete and $A_1, A_4, A_6, A'_1, A'_4$, and A'_6 are unknown coefficients [32].

If there is a nonzero solution to (2), the coefficient matrix of the determinant must be zero, so the following matrix equation is satisfied to obtain the general dispersion equation for the steel bar with infinite length embedded in concrete [36]:

$$|D_{ij}| = 0, \quad (i, j = 1, \dots, 6). \quad (3)$$

There are axisymmetric and nonaxisymmetric modes of waves included in the propagation of guided waves in the steel bar [32]. The axisymmetric mode is the longitudinal mode $L(0, m)$, where the first index refers to the circumferential order of the mode and all of the longitudinal modes are of circumferential order 0; that is, $n = 0$ in (3), and the second index m is a counter variable which means the sequential order of the mode. Then (3) can be further simplified into two subdeterminants, after exchange of rows and columns, and can get the following equations:

$$\underbrace{\begin{Bmatrix} D_{11} & D_{12} & D_{14} & D_{15} \\ D_{31} & D_{32} & D_{34} & D_{35} \\ D_{41} & D_{42} & D_{44} & D_{45} \\ D_{61} & D_{62} & D_{64} & D_{65} \end{Bmatrix}}_{D_a} \underbrace{\begin{Bmatrix} D_{23} & D_{26} \\ D_{53} & D_{56} \end{Bmatrix}}_{D_b} = 0. \quad (4)$$

When subdeterminant $D_a = 0$, it represents the dispersive equation of longitudinal modes, in which only nonzero displacements μ_r and μ_z are included.

When subdeterminant $D_b = 0$, it represents the dispersive equation of torsional modes, in which only nonzero displacement μ_θ is included.

Further, the following definitions are introduced [37]: $Y = ka$, $V = \alpha_s a$, $W = \alpha_c a$, $X = \beta_s a$, and $U = \beta_c a$, where Y

is dimensionless wave number and V , W , X , and U are all dimensionless. On the substitution of these definitions into the equation $D_a = 0$, we will get the disperse equation of longitudinal mode of guided waves in reinforced concrete after simplifying the results into a simple form expressed by dimensionless quantity, as shown in the following [37]:

$$\begin{vmatrix} -VZ_1(V) & YZ_1(X) \\ -YZ_0(V) & -XZ_0(X) \\ \left\{ -\left[\frac{\lambda_s}{\mu_s} (V^2 + Y^2) + 2V^2 \right] \cdot \right. & 2Y [XZ_0(X) - Z_1(X)] \\ \left. Z_0(V) + 2VZ_1(V) \right\} & \\ 2YVZ_1(V) & -[Y^2 - X^2] Z_1(X) \end{vmatrix} \begin{vmatrix} WH_1^{(2)}(W) & -YH_1^{(2)}(U) \\ YH_0^{(2)}(W) & UH_0^{(2)}(U) \\ \left[\frac{\lambda_c}{\mu_c} (W^2 + Y^2) \right. & \left. -2\frac{\mu_c}{\mu_s} Y \cdot \right] \\ + 2\frac{\mu_c}{\mu_s} W^2 & \left\{ [UH_0^{(2)}(U) - H_1^{(2)}(U)] \right\} \\ H_0^{(2)}(W) & \\ -2\frac{\mu_c}{\mu_s} WH_1^{(2)}(W) & \\ -2\frac{\mu_c}{\mu_s} YWH_1^{(2)}(W) & \frac{\mu_c}{\mu_s} [Y^2 - U^2] H_1^{(2)}(U) \end{vmatrix} = 0, \quad (5)$$

where μ_s , ρ_s , and ν_s are the shear modulus, density, and Poisson's ratio of steel bar, respectively, and μ_c , ρ_c , and ν_c are those of concrete, respectively. Z_0 , Z_1 are Bessel functions at orders 0 and 1, respectively. $H_0^{(2)}$, $H_1^{(2)}$ are Hankei functions of the second kind at orders 0 and 1, respectively.

3. Solution of the Dispersion Equation and the Analysis of Dispersion Curve

The following variables are introduced: $(\bar{\alpha}_s a)^2 = (\omega a)^2 / c_{L_s}^2 - (ka)^2$, $(\bar{\alpha}_c a)^2 = (\omega a)^2 / c_{L_c}^2 - (ka)^2$, $(\bar{\beta}_s a)^2 = (\omega a)^2 / c_{T_s}^2 - (ka)^2$, and $(\bar{\beta}_c a)^2 = (\omega a)^2 / c_{T_c}^2 - (ka)^2$. The dimensionless frequency Ω associated with angular frequency ω is defined as $\Omega = \omega a / c_{L_c}$.

Other dimensionless quantities are given by $V^2 = (c_{T_s} / c_{L_s})^2 \cdot \Omega^2 - Y^2$, $X^2 = \Omega^2 - Y^2$, $W^2 = (c_{T_s} / c_{T_c})^2 (c_{T_c} / c_{L_c})^2 \cdot \Omega^2 - Y^2$, and $U^2 = (c_{T_s} / c_{T_c})^2 \cdot \Omega^2 - Y^2$.

Then, the following equations can be derived from the theory of elasticity [22]:

$$\frac{c_{T_j}}{c_{L_j}} = \left[\frac{1 - 2\nu_j}{2(1 - \nu_j)} \right]^{1/2}, \quad \frac{c_{T_s}}{c_{T_c}} = \left(\frac{\mu_s}{\mu_c} \times \frac{\rho_c}{\rho_s} \right)^{1/2}, \quad (6)$$

$$\frac{\lambda_j}{\mu_j} = \frac{2\nu_j}{1 - 2\nu_j}, \quad \frac{\lambda_c}{\mu_s} = \frac{2\nu_c}{1 - 2\nu_c} \times \frac{\mu_c}{\mu_s}.$$

On the substitution of these variables into (5), all variables except frequency and wave number in the dimensionless dispersion equation can be determined by the properties of steel bar and concrete which include shear modulus, Poisson's ratio, and density.

If the parameters of steel bar and concrete are known, only two unknown variables (dimensionless frequency and

dimensionless wave number) are involved in (5). In this paper, the related parameters of steel bar and concrete are selected as those in Table 1.

In order to solve the relationship between dimensionless frequency and dimensionless wave numbers in the dispersion equation (5), the corresponding program is made to solve it. The solving procedures are as follows.

- (1) Find the cutoff frequency of each order mode from a sweep frequency with a specified range, which is the initial root of the equation and also the initial point of the disperse curve of each order mode. Generally, there will be the same number of order modes as that of initial points which have been found within a specified range of frequency, and the corresponding number of disperse curves can be obtained.
- (2) The routine starts from the initial point, in the given step and direction, and converges to the next point which is the second root of the equation.
- (3) Take the second root as the initial point and repeat step 2 and so forth. The routine will end until the specified frequency or upper limit wave number is reached.
- (4) Connect all the found points and a disperse curve will be achieved after.
- (5) Repeat the above process from another initial point and another disperse curve will be achieved in this way. The complete solution to the equation will be gotten until all the disperse curves are finished.

Based on the solutions, the disperse curves between dimensionless frequency and dimensionless wave number of the round steel bar embedded in concrete with different material parameters will be gained by solving (5), as shown in Figures 2–4.

TABLE 1: Related material parameters of steel bar and concrete.

Parameters	Steel bar	Ordinary concrete	High strength concrete
Poisson's ratio	0.2865	0.27	0.20
Density (kg/m^3)	7932	2200	2400
Elastic modulus (MPa)	210000	22000	38000
Shear modulus (MPa)	81600	8600	15800
Velocity of longitudinal wave C_L (m/ms)	5960	3540	4190
Velocity of transverse wave C_T (m/ms)	3260	1980	2570
Density ratio ρ_s/ρ_c		3.6	3.3
Shear modulus ratio μ_s/μ_c		9.5	5.2

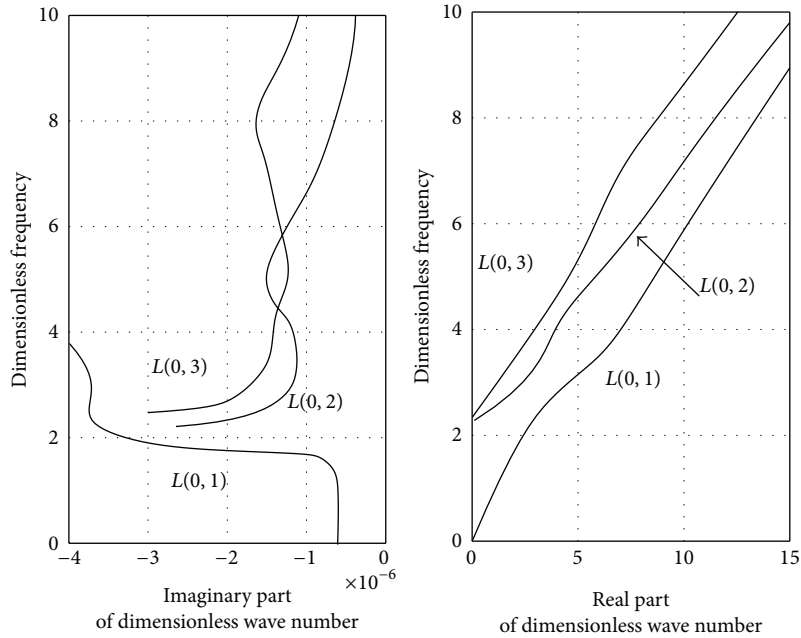


FIGURE 2: Disperse curves of the first three modes of guided waves in steel bar in the air.

From Figures 2–4, it can be observed that, for free steel bar, wave numbers are all real numbers in the solution to the disperse equation, and the corresponding modes of guided waves are free modes or modes without attenuation. For the solid round steel bar embedded in concrete, wave numbers are all complex in the solution to the disperse equation, in which the real part of wave number is corresponding to the propagation of guided waves in the steel bar and the imaginary part is corresponding to the attenuation of guided waves.

It can also be drawn from Figures 2–4 that the disperse curves between dimensionless frequency and dimensionless real wave number are almost the same whether the steel bar is in the air or embedded in concrete which means that the shear and density of surrounded concrete have no effect on the disperse curves; that is, the velocity of guided waves

propagating in the steel bar is only related to the properties of steel bar.

As shown in Figures 3 and 4, the disperse curves between dimensionless frequency and dimensionless imaginary wave number change with the shear and density of concrete. When the concrete has lower shear modulus or density, the imaginary wave number is lower, the spread of the wave attenuation in steel bar is slow, and the transmission distance is further and vice versa.

From the disperse curves in Figure 3 in which steel bar is embedded in ordinary concrete, it can be seen that, for the mode $L(0,1)$, when the dimensionless frequency is less than 1.8, the imaginary wave number is about 1.15, which is reflecting the energy attenuation of guided waves. Analogously, from Figure 4, in which steel bar is embedded in concrete with high strength, it can be seen that, for the same

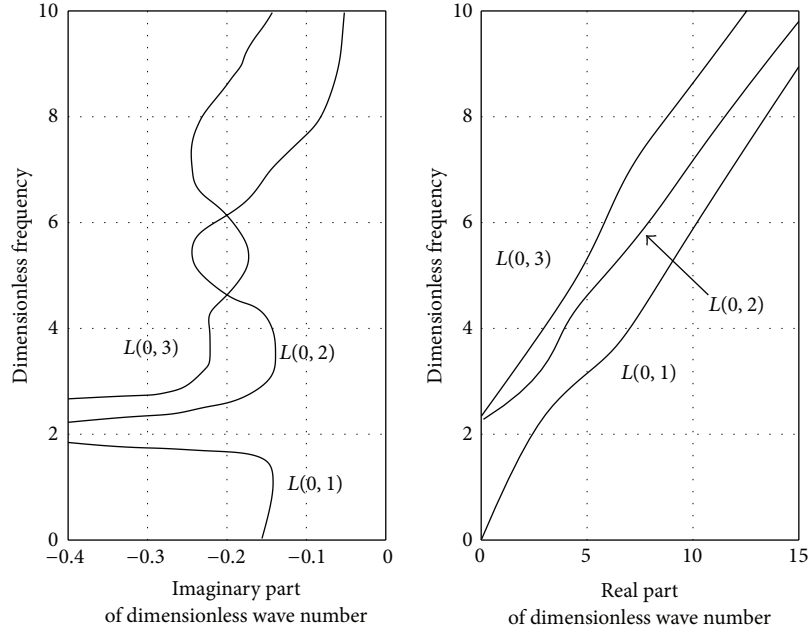


FIGURE 3: Disperse curves of the first three modes of guided waves in steel bar embedded in ordinary concrete.

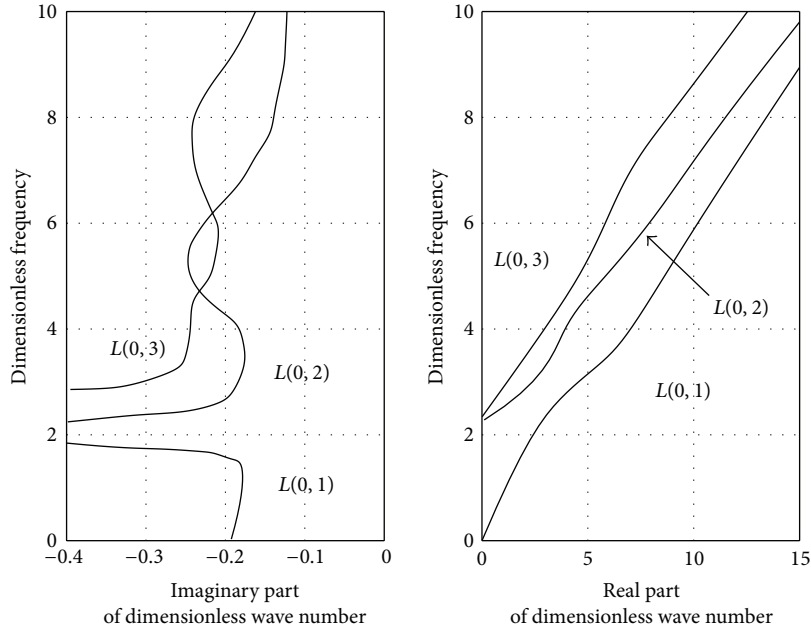


FIGURE 4: Disperse curves of the first three modes of guided waves in steel bar embedded in high strength concrete.

mode $L(0, 1)$, when the dimensionless frequency is less than 1.5, the imaginary wave number is even smaller, that is about 0.19. This means that energy attenuation of guided waves in ordinary strength concrete is slower than that in high strength concrete. And the imaginary wave number of mode $L(0, 1)$ increases quickly with the increase of frequency no matter in ordinary concrete or in high strength concrete.

4. Parametric Analysis

The impact of concrete on the propagation characteristics of guided wave in steel bar can be evaluated by changing the material properties of concrete, which include the factors such as steel-to-concrete shear modulus ratio, density ratio, and ratio of Poisson's ratio. Furthermore, from previous

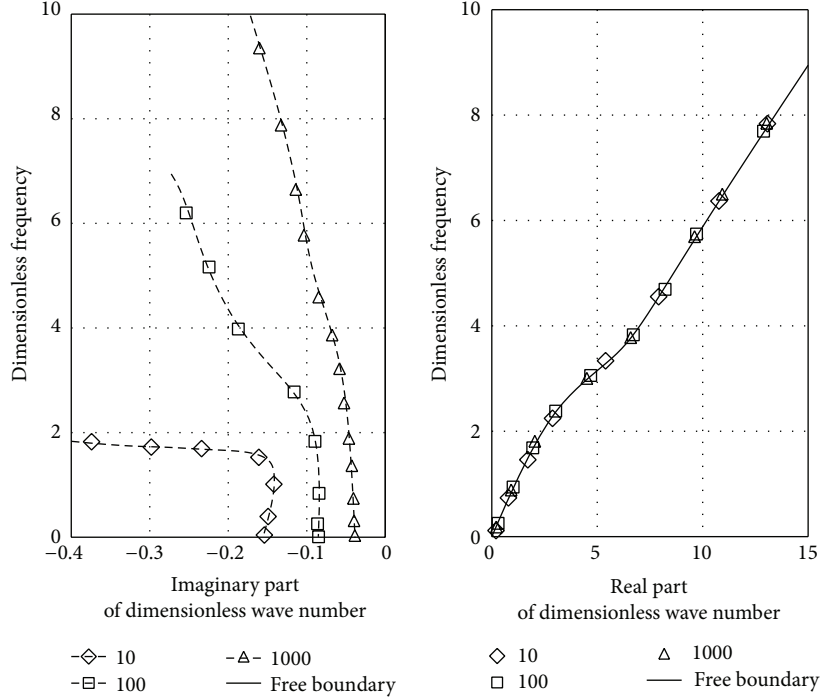


FIGURE 5: Influence on the real and imaginary parts of $L(0, 1)$ by the steel-bar-to-concrete shear modulus ratio.

studies by the authors [38], it is known that the cutoff frequency of the lowest order mode $L(0, 1)$ in steel bar is zero, so those modes propagating along the steel bar will always include it. Thus, the effects of related factors on the lowest order mode $L(0, 1)$ are mainly taken into consideration, which are studied, respectively, in the following part.

4.1. Effect of Shear Modulus Ratio. When the steel bar is embedded in ordinary concrete, the shear modulus ratio is about 10, which will increase when the surrounding concrete becomes softer. Until it is up to a certain extent, the boundary of steel bar can be regarded as a free boundary. By changing the ratio, the relationship between dimensionless wave number and dimensionless frequency can be gained as shown in Figure 5.

From Figure 5, it can be seen that the change of shear modulus ratio has little effect on the real part of dimensionless wave number. However, with the increase of shear modulus ratio (that is, the surrounding concrete becomes more and more soft), the imaginary part of dimensionless wave number, which representing the attenuation of guided waves, becomes smaller and smaller. This shows that the attenuation of energy due to leakage into the surrounding concrete is getting smaller and farther distance of propagation can be achieved. It is considered that no energy leak into concrete in the condition of free boundary, so the dimensionless wave number will be real number.

4.2. Effect of Density Ratio. When the density of concrete is changed and other parameters remain constant, the disperse

relation will surely be affected. While steel bar is embedded in high strength concrete, the steel-to-concrete density ratio is 3.6. Then, decreasing gradually the density of concrete, the steel-to-concrete density ratio will be increased and the change of the disperse curve between dimensionless wave number and dimensionless frequency will be gotten as shown in Figure 6. When the ratio is close to infinity, it indicates that the effect of surrounding concrete can be neglected, or it can be regarded as free boundary.

From Figure 6, it can be seen that the change of density ratio has little effect on the real part of dimensionless wave number. However, with the decrease of density ratio (i.e., the surrounding concrete becomes more and more dense), the imaginary part of dimensionless wave number representing the attenuation of guided waves becomes more and more large which shows that the attenuation of energy due to leakage into the surrounding concrete is getting larger and shorter distance of propagation can be achieved. It is also considered that no energy leak into concrete in the condition of free boundary, so, the dimensionless wave number is real number.

4.3. Effect of Ratio of Poisson's Ratio. As Poisson's ratio of steel bar and concrete can be changed and large changes in the Poisson's ratio of concrete from low grade to high grade take place, the effect on the disperse curve by Poisson's ratio can be gotten by assuming Poisson's ratio of steel bar as a constant of 0.2865 and changing that of concrete, as shown in Figure 7, where ν is Poisson's ratio of concrete.

From Figure 7, it can be found that the variations both in the real and imaginary parts of wave number are small with

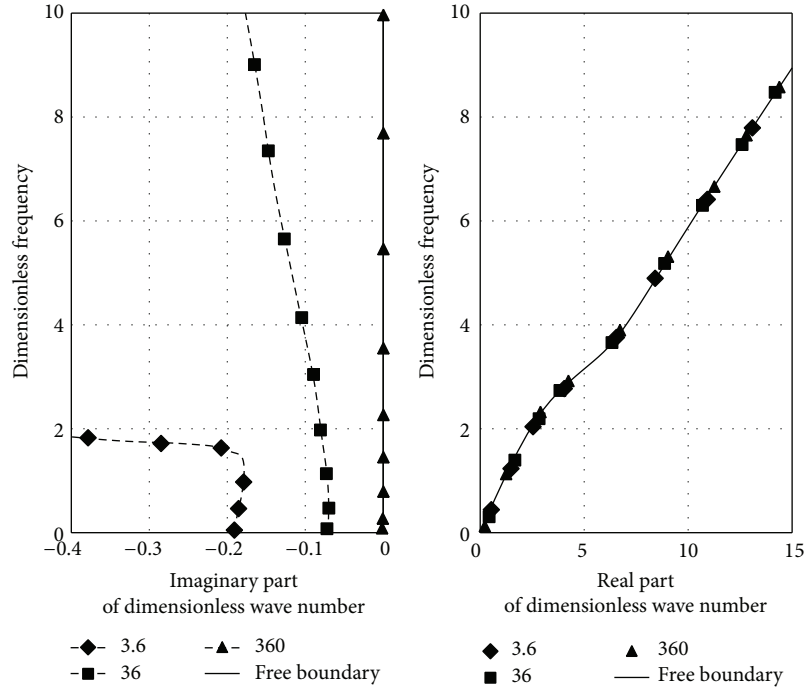


FIGURE 6: Influence on the real and imaginary parts of $L(0, 1)$ by the steel-bar-to-concrete density ratio.

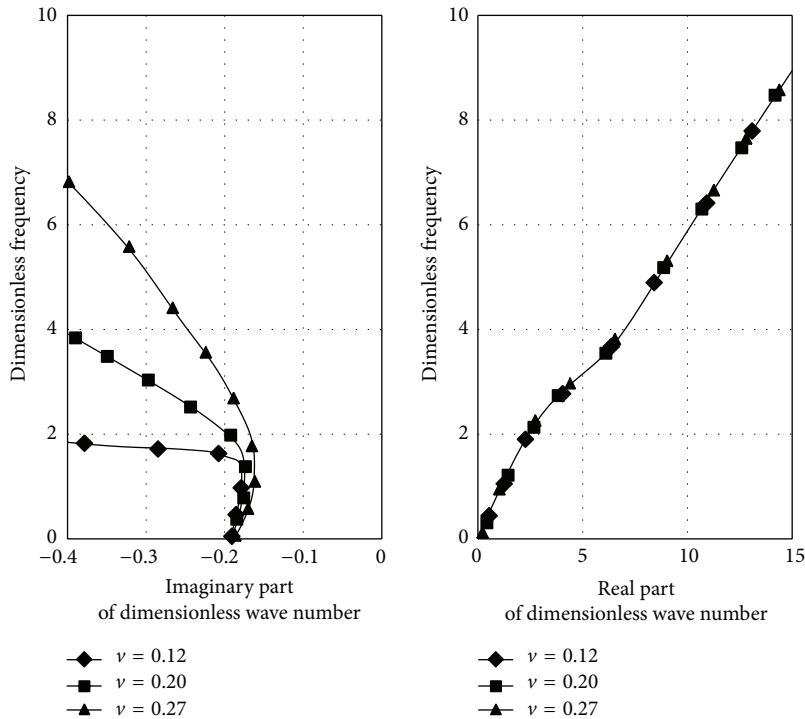


FIGURE 7: Influence on the real and imaginary parts of $L(0, 1)$ by Poisson's ratio of concrete.

the change of Poisson's ratio of concrete in low frequency. When the dimensionless frequency is greater than 1.8, the attenuation will be obviously affected with the increase of frequency and the smaller Poisson's ratio of concrete, the greater the attenuation.

5. Attenuation Characteristics of Guided Wave in Reinforced Concrete

Through the previous definition and analysis, it usually regarding the disperse curve between the imaginary part

of dimensionless wave number and dimensionless frequency as the attenuation curve. In fact, the forward propagation of guided waves in steel bar is a process in which energy attenuates gradually due to the effects of constraints of concrete, impact excitation energy, material damping of steel, and defects on steel bar. If there are much residues or defects in steel bar or its characteristics is close to the surrounding concrete (close density or shear modulus), the waves will vanish due to attenuation after a short distance of propagation and then it will be very difficult to detect the defect of steel bar using the traditional echo method. Based on the research of the attenuation curve, the energy dissipation of guided waves propagating along the steel bar and the effects on the attenuation by material properties, propagation distance, and frequency can be known more clearly, which will be a benefit for the defect detection in the reinforced concrete.

When the steel bar is in the air (free steel bar), the solved imaginary wave number is very small and even close to zero because there is great difference in the physical properties between steel bar and the air. Therefore, its propagation mode is approximated free or no attenuation mode.

For the steel bar embedded in concrete, the imaginary wave number depends on the shear modulus ratio and density ratio between steel bar and concrete. The energy loss of wave can be quantified by the displacement u which is expressed in the steel bar as follows [39]:

$$u = U(a) e^{i(\omega t - k_z z)} = U(a) e^{i(\omega t - k_r z)} e^{k_i z}, \quad (7)$$

in which k_r and k_i are the real and imaginary parts of the wave number, respectively, a is the radius of steel bar, and z is the axial direction of steel bar.

Thus, the attenuation of guided wave along the steel bar can be measured using the amplitude variation of the signal along the z -direction. In (7), the first part $U(a)$ is the function of radius, which is a constant, taking a fixed point along the radius. The second part shows that the wave propagates along the $+Z$ direction. The third part is corresponding to the exponential increase or decrease of wave energy which depends on the symbol of k_i . The solution to the disperse equation in the steel bar surrounded by concrete shows that k_i is negative and its displacement attenuates exponentially along the $+Z$ direction. The attenuating value of displacement along the $+Z$ direction depends on the amplitude of imaginary part of wave number. The attenuation coefficient can be signified by Neper, abbreviated as N_p ,

$$\gamma = \log_e \left(\frac{u_2}{u_1} \right) N_p, \quad (8)$$

where γ is the attenuation coefficient and u_1 and u_2 are the amplitudes of signals at the initial point and last point of measuring. The ratio of amplitudes A is defined as

$$A = \frac{u_2}{u_1} = e^\gamma. \quad (9)$$

In (9), the first two parts have no effect on the amplitude of displacement in z -direction and they can be substituted by a constant E . Thus, the attenuation coefficient is expressed as

$$\begin{aligned} \gamma &= \log_e \left(\frac{E e^{k_i z_2}}{E e^{k_i z_1}} \right) = \log_e e^{k_i (z_2 - z_1)} \\ &= k_i (z_2 - z_1) N_p, \end{aligned} \quad (10)$$

where z_1 and z_2 are the initial and final positions of measurement. The attenuation coefficient can be turned into decibels as shown in the following:

$$\gamma = k_i \text{ nepers/m} = 8.686 k_i \text{ dB/m}. \quad (11)$$

5.1. Steel Bar Embedded in Ordinary Concrete. The disperse curves for steel bar with the diameter of 22 mm embedded in ordinary concrete are shown in Figure 8. In the figure, the green and red dots/circles are the cutoff frequency of each mode and the roots of the dispersive equation, respectively. The involved material parameters are tabulated in Table 1.

By comparing the energy velocity curve to phase velocity curve in Figure 8, it can be seen that when the local minimum value of attenuation is achieved, the corresponding energy velocity at the frequency is the maximum. While the maximum value attenuation is reached, the corresponding energy velocity at the frequency is the minimum.

From the phase velocity disperse curves in Figure 8(a), it can be observed that the fundamental $L(0, 1)$ mode is starting at zero frequency while each higher-order mode is starting from a higher cutoff frequency. Each of the higher modes shows a plateau region around the steel longitudinal bulk velocity line first and then decreases, eventually approaching the transverse wave velocity. The plateau regions correspond to the points of the maximum energy velocity (Figure 8(b)) and minimum attenuation (Figure 8(c)). But $L(0, 8)$ mode shows a different pattern. Instead of each plateau region belonging to a single mode, $L(0, 8)$ breaks from this pattern and links the subsequent plateau regions together to form a single mode that propagates close to the longitudinal bulk velocity of steel. This $L(0, 8)$ mode is chosen for study. At a frequency of 1.72 MHz, the mode exhibits global attenuation minima of 18 dB/m and it is the fastest propagating mode. The phase velocity obtained from dispersion curve at this frequency is 6 Km/s.

By (11), the corresponding amplitude ratio of signals at different propagating distance of guided waves in steel bar embedded in ordinary concrete can be calculated as tabulated in Table 2.

As can be seen from Table 2, for the steel bar embedded in ordinary concrete, after more and more energy leaks into the concrete with the increase of propagation distance, the internal energy becomes less and its particle vibration becomes more and more weak, and then the amplitude ratio of signals is becoming smaller and smaller.

Figure 9 shows the axial displacement U_z and strain energy density (SED) distribution for $L(0, 8)$ mode studied in the present investigation. The energy is concentrated in the central core portion of the bar and has relatively less surface

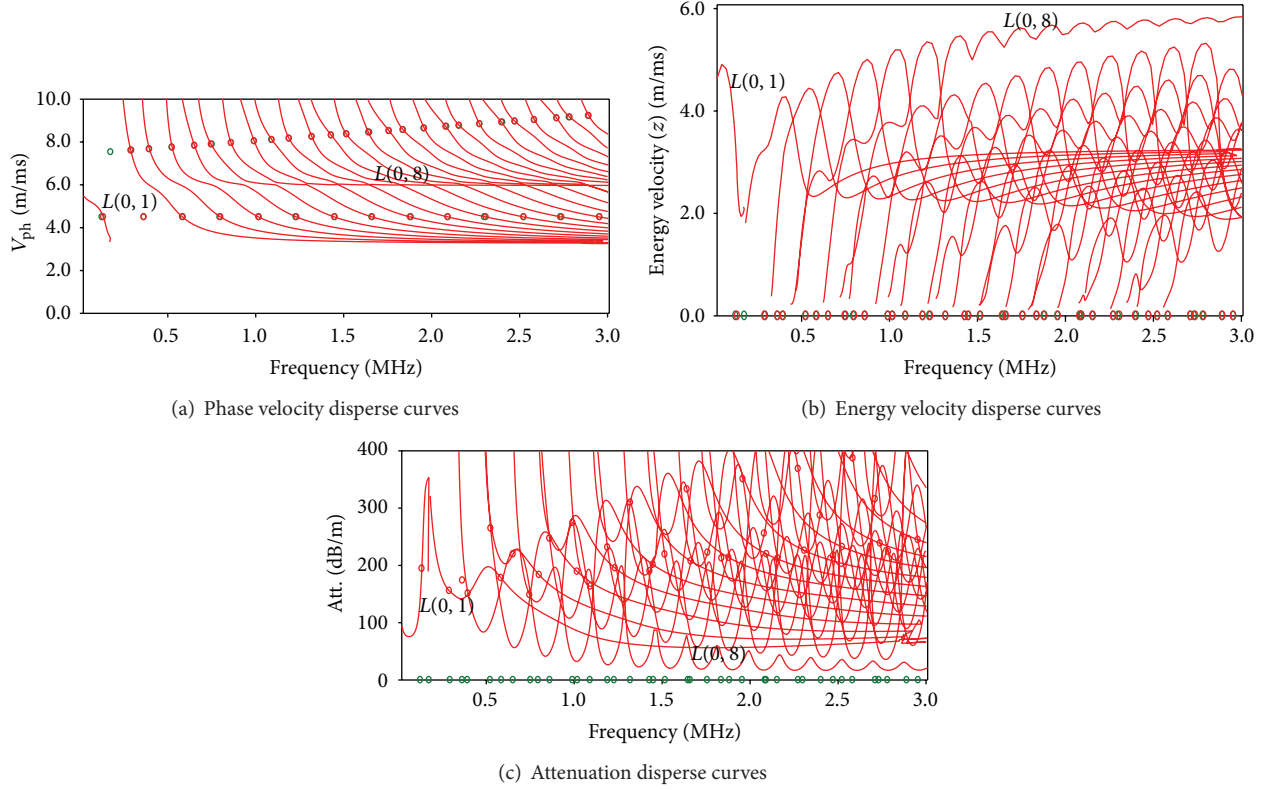
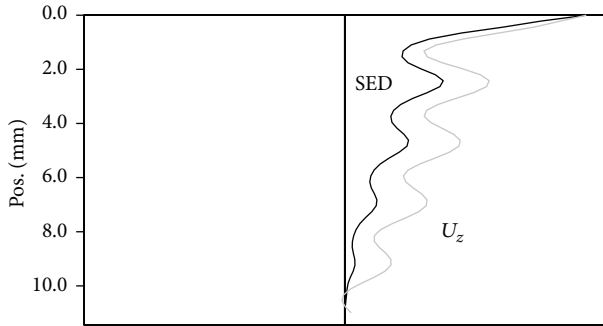


FIGURE 8: Disperse curves of guided waves in steel bar embedded in ordinary concrete.

TABLE 2: Attenuation coefficient and the signal amplitude ratio of mode $L(0, 8)$.

Propagating distance (m)	0	1	1.5	2	2.5	3	5
Attenuation (dB)	0	-18	-27	-36	-45	-54	-90
Amplitude ratio	1.000	0.1259	0.0450	0.0159	0.0056	0.0020	0.00003

FIGURE 9: Mode shape of $L(0, 8)$ at $f = 1.72$ MHz.

component. Hence, it should be more sensitive to local bar topography or loss of material changes and not the surface profile changes.

5.2. Steel Bar Embedded in Concrete with High Strength. The disperse curves for steel bar embedded in high strength concrete with the diameter of 22 mm are shown in Figure 10. In the figure, the green and red dots/circles are the cutoff frequency of each mode and the roots of the dispersive equation, respectively. The involved material parameters are also tabulated in Table 1.

The phase velocity disperse curves in Figure 10(a) show that, similar to those of ordinary concrete, the fundamental $L(0, 1)$ mode is starting at zero frequency while each higher-order mode is starting from a higher cutoff frequency. Each of the higher modes shows a plateau region around the steel longitudinal bulk velocity line first and then decreases, eventually approaching the transverse wave velocity. The plateau regions correspond to the points of the maximum energy velocity (Figure 10(b)) and minimum attenuation (Figure 10(c)). But $L(0, 14)$ mode shows a different pattern. Instead of each plateau region belonging to a single mode, $L(0, 14)$ breaks from this pattern and links the subsequent plateau regions together to form a single mode that propagates close to the longitudinal bulk velocity of steel. At the frequency band corresponding to the plateau regions of modes $L(0, 6)$ and $L(0, 14)$, they are nearly the fastest propagating modes and exhibit global attenuation minima as shown in Figures 10(b) and 10(c). At a frequency of 1.02 MHz, the mode $L(0, 6)$ has the attenuation minima of 36.8 dB/m and at a frequency of 2.95 MHz, the mode $L(0, 14)$ has the attenuation minima of 36.6 dB/m. The phase velocities of the two

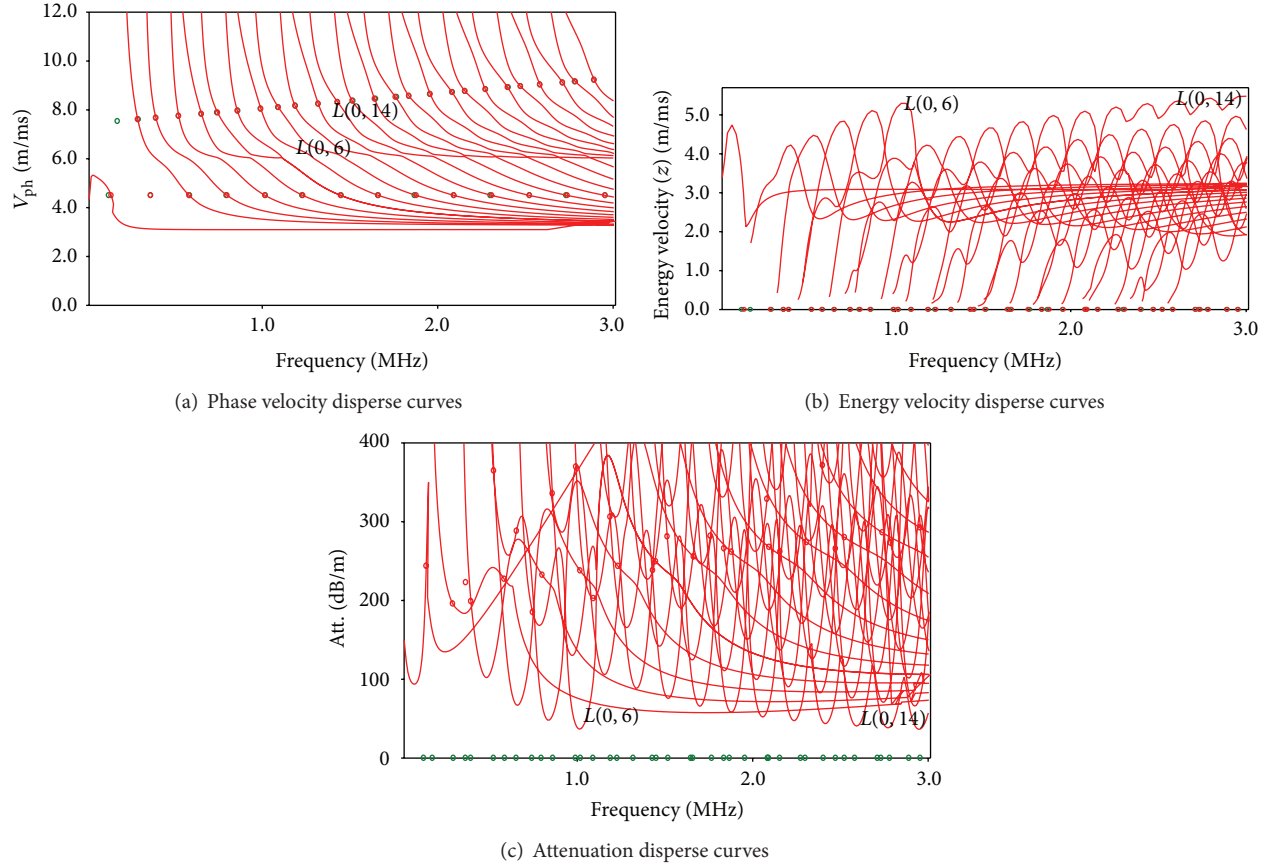


FIGURE 10: Disperse curves of guided waves in steel bar embedded in high strength concrete.

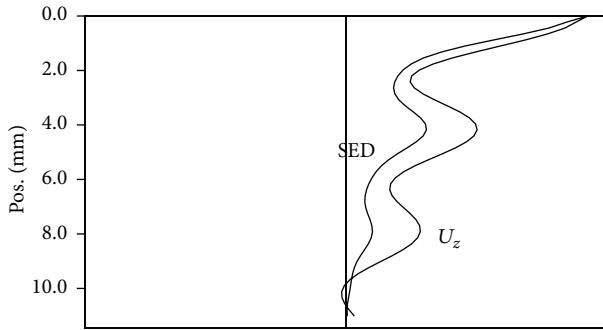


FIGURE 11: Mode shape of $L(0,6)$ at $f = 1.02$ MHz.

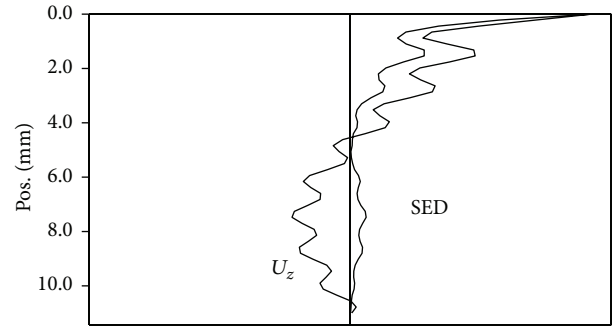


FIGURE 12: Mode shape of $L(0,14)$ at $f = 2.94$ MHz.

modes as obtained from dispersion curves at the frequency corresponding to the minimum attenuation are both about 6 Km/s. The attenuation value of 36.8 dB/m is taken and then the corresponding amplitude ratio of signals at different propagating distance of guided waves in steel bar embedded in high strength concrete is calculated as tabulated in Table 3.

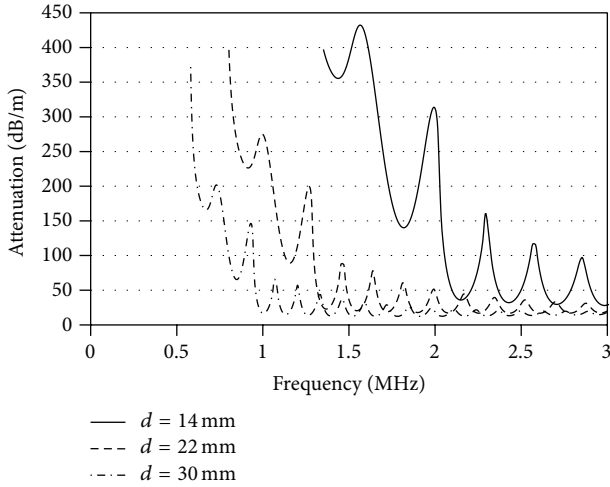
Figures 11 and 12 show the axial displacement U_z and strain energy density (SED) distribution for modes $L(0,6)$ and $L(0,14)$, respectively. It can be seen that the energy of mode $L(0,6)$ is concentrated in the central core portion of the bar and has relatively less surface component. And the energy

of mode $L(0,14)$ is more concentrated in the central core portion of the bar. Hence, it will be less sensitive to the surface profile changes.

From the analysis, it can be drawn that the higher the strength concrete, the more the energy leakage into concrete, the faster the attenuation of guided waves, and the smaller the amplitude ratio of signals at the same position. Guided waves at low frequency mode can propagate very far along the steel bar in the air for the little attenuation, so a few meters of steel bar can be monitored by guided waves based technique [40]. However, while the same steel bar is embedded in ordinary

TABLE 3: Attenuation coefficient and the signal amplitude ratio of mode $L(0, 6)$.

Propagating distance (m)	0	1	1.5	2	2.5	3	5
Attenuation (dB)	0	-36.8	-55.2	-73.6	-92	-110.4	-184
Amplitude ratio	1.000	0.0150	0.0017	0.0002	0.00002	3.0×10^{-6}	6.2×10^{-10}

FIGURE 13: Attenuation disperse curves of mode $L(0, 8)$ in steel bar with different diameter embedded in concrete.

concrete, the monitoring range is just about two meters. Even more, if it is embedded in high strength concrete, the test distance would be very limited because more and more energy leaks into the concrete and, with the increased propagation, the internal energy of steel bar becomes less and its particle vibration becomes more and more weak. Based on the above, it can be concluded that whether it is embedded in ordinary concrete or high strength concrete, the attenuation velocity of guided waves in steel bar is always high and the propagation distance is always short; that is, the detection range is very limited as the signal is very weak after two meters of propagation, which is the difficulty of nondestructive test applying guided waves in reinforced concrete.

5.3. Influence on Attenuation of Guided Wave by Different Bar Diameter. For the given reinforced concrete model, the disperse curves of attenuation of longitudinal mode $L(0, 8)$ for the steel bar embedded in ordinary concrete with the diameter $d = 14$ mm, $d = 22$ mm, and $d = 30$ mm are calculated, respectively, as shown in Figure 13, in which the attenuation curves are denoted by red, blue, and yellow curves, respectively, corresponding to different diameter.

As can be seen from Figure 13, the trends of attenuation disperse curves are undulate and eventually tend to be similar. At the same frequency, the value of attenuation decreases with the increase of diameter. Therefore, for the same steel bar with larger diameter embedded in the same concrete, the energy leaks less into concrete, the spread of wave energy attenuation is slower, and the spread distance is shorter.

6. Conclusions

In reinforced concrete structures, the propagation characteristics of guided waves in steel bar are influenced greatly by its surrounded concrete. In this paper, the impact of concrete on the propagation characteristics of guided wave in steel bar is studied by changing the material properties of concrete. It is found that the higher the excitation frequency, the more obvious the dispersion phenomenon. However, not the velocity but attenuation dispersion curves will be affected by the concrete. The shear modulus and density of concrete have no effect on the real parts of wave number; that is, the propagating velocity of guided waves in steel bar depends only on the material properties of steel bar and has nothing to do with the surrounding concrete. The imaginary part of wave number depends on the steel-bar-to-concrete shear modulus ratio and density ratio. When the concrete has lower shear modulus or density, the spread of the wave attenuation in steel bar is slow and the transmission distance is further.

For a given steel-concrete model, the attenuation extent in signal propagation can be obtained by the attenuation and frequency dispersion curve. It is found that, for the same steel bar with larger diameter embedded in the same concrete, the energy leaks less into concrete, the spread of wave energy attenuation is slower, and the spread distance is shorter. Studying the influence on propagation characteristics of guided wave in steel bars by concrete will increase the accuracy in judging the structure integrity and promote the level of defect/corrosion detection for the steel bars embedded in concrete.

Conflict of Interests

The authors declare that there is no conflict of interests regarding the publication of this paper.

Acknowledgments

This research is supported by Key Science and Technology Project from Fujian Province, China (no. 2013Y0079) and the Research Fund SLDRCE10-MB-01 from the State Key Laboratory for Disaster Reduction in Civil Engineering at Tongji University, China.

References

- [1] T. R. Hay and J. L. Rose, "Interfacing guided wave ultrasound with wireless technology," in *Smart Structures and Materials—Sensors and Smart Structures Technologies for Civil, Mechanical, and Aerospace Systems*, vol. 5391 of *Proceedings of the SPIE*, pp. 314–320, San Diego, Calif, USA, March 2004.

- [2] A. Raghavan and C. E. S. Cesnik, "Review of guided-wave structural health monitoring," *Shock and Vibration Digest*, vol. 39, no. 2, pp. 91–114, 2007.
- [3] H. Sohn, D. Dutta, J. Y. Yang et al., "Delamination detection in composites through guided wave field image processing," *Composites Science and Technology*, vol. 71, no. 9, pp. 1250–1256, 2011.
- [4] G. B. Song, Y. L. Mo, K. Otero, and H. Gu, "Health monitoring and rehabilitation of a concrete structure using intelligent materials," *Journal of Smart Materials and Structures*, vol. 15, no. 2, pp. 309–314, 2006.
- [5] R. L. Wang, H. Gu, Y. L. Mo, and G. Song, "Proof-of-concept experimental study of damage detection of concrete piles using embedded piezoceramic transducers," *Smart Materials and Structures*, vol. 22, no. 4, Article ID 042001, 2013.
- [6] V. Giurgiutiu, "Lamb wave generation with piezoelectric wafer active sensors for structural health monitoring," in *Smart Structures and Materials 2003: Smart Structures and Integrated Systems*, vol. 5056 of *Proceedings of SPIE*, San Diego, Calif, USA, March 2002.
- [7] X. Wang, P. W. Tse, C. K. Mechefske, and M. Hua, "Experimental investigation of reflection in guided wave-based inspection for the characterization of pipeline defects," *NDT & E International*, vol. 43, no. 4, pp. 365–374, 2010.
- [8] A. C. Cobb, H. Kwun, L. Caseres, and G. Janega, "Torsional guided wave attenuation in piping from coating, temperature, and large-area corrosion," *NDT and E International*, vol. 47, pp. 163–170, 2012.
- [9] R. Ahmad and T. Kundu, "Influence of water flow through pipe networks for damage detection using guided waves," in *Nondestructive Testing of Materials and Structures*, vol. 6 of *RILEM Bookseries*, pp. 681–687, 2013.
- [10] M. D. Beard, M. J. S. Lowe, and P. Cawley, "Inspection of steel tendons in concrete using guided waves," *Review of Quantitative Nondestructive Evaluation*, vol. 22, pp. 1139–1147, 2003.
- [11] X. P. Zhu, P. Rizzo, A. Marzani, and J. Bruck, "Ultrasonic guided waves for nondestructive evaluation/structural health monitoring of trusses," *Journal of Measurement Science and Technology*, vol. 21, no. 4, Article ID 045701, 2010.
- [12] Z. P. Zheng, Y. Lei, and X. Xue, "Numerical simulation of monitoring corrosion in reinforced concrete based on ultrasonic guided waves," *The Scientific World Journal*, vol. 2014, Article ID 752494, 9 pages, 2014.
- [13] T. Yi, H. Li, and M. Gu, "Recent research and applications of GPS-based monitoring technology for high-rise structures," *Structural Control and Health Monitoring*, vol. 20, no. 5, pp. 649–670, 2013.
- [14] F. Moser, L. J. Jacobs, and J. Qu, "Modeling elastic wave propagation in waveguides with the finite element method," *Journal of NDT & E International*, vol. 32, no. 4, pp. 225–234, 1999.
- [15] Z. B. Cheng, *Numerical simulation and experimental investigation on crack detection in pipes using ultrasonic guided waves [M. E. thesis]*, Taiyuan University of Technology, 2004.
- [16] C. H. He, Y. X. Sun, Z. Liu, X. Wang, and B. Wu, "Finite element analysis of defect detection in curved pipes using ultrasonic guided waves," *Journal of Beijing University of Technology*, vol. 32, no. 4, pp. 289–294, 2006 (Chinese).
- [17] G. L. Huang, F. Song, and X. Wang, "Quantitative modeling of coupled piezo-elastodynamic behavior of piezoelectric actuators bonded to an elastic medium for structural health monitoring: a review," *Sensors*, vol. 10, no. 4, pp. 3681–3702, 2010.
- [18] Y. Lei and Z. P. Zheng, "Review of physical based monitoring techniques for condition assessment of corrosion in reinforced concrete," *Mathematical Problems in Engineering*, vol. 2013, Article ID 953930, 14 pages, 2013.
- [19] W. Na, T. Kundu, and M. R. Ehsani, "Ultrasonic guided waves for steel bar concrete interface testing," *Journal of Material Evaluation*, vol. 60, no. 3, pp. 437–444, 2002.
- [20] W. Na, T. Kundu, and M. R. Ehsani, "Lamb waves for detecting delamination between steel bars and concrete," *Computer-Aided Civil and Infrastructure Engineering*, vol. 18, no. 1, pp. 58–63, 2003.
- [21] W. Na, T. Kundu, and M. R. Ehsani, "A comparison of steel/concrete and glass fiber reinforced polymers/concrete interface testing by guided waves," *Journal of Material Evaluation*, vol. 61, no. 2, pp. 155–161, 2003.
- [22] H. Reis, B. L. Ervin, D. A. Kuchma, and J. T. Bernhard, "Estimation of corrosion damage in steel reinforced mortar using guided waves," *Journal of Pressure Vessel Technology*, vol. 127, no. 3, pp. 255–261, 2005.
- [23] F. Wu and F. Chang, "Debond detection using embedded piezoelectric elements in reinforced concrete structures, part I: experiment," *Structural Health Monitoring*, vol. 5, no. 1, pp. 5–15, 2006.
- [24] F. Wu and F.-K. Chang, "Debond detection using embedded piezoelectric elements for reinforced concrete structures—part II: analysis and algorithm," *Structural Health Monitoring*, vol. 5, no. 1, pp. 17–28, 2006.
- [25] C. He, J. K. van Velsor, C. M. Lee, and J. L. Rose, "Health monitoring of rock bolts using ultrasonic guided waves, quantitative nondestructive evaluation," in *Proceedings of the AIP Conference*, pp. 195–201, AIP, Reston, Va, USA, 2006.
- [26] L. Dongsheng, R. Tao, and Y. Junhui, "Inspection of reinforced concrete interface delamination using ultrasonic guided wave non-destructive test technique," *Science China Technological Sciences*, vol. 55, no. 10, pp. 2893–2901, 2012.
- [27] B. L. Ervin and H. Reis, "Longitudinal guided waves for monitoring corrosion in reinforced mortar," *Journal of Measurement Science and Technology*, vol. 19, no. 5, Article ID 055702, 2008.
- [28] B. L. Ervin, D. A. Kuchma, J. T. Bernhard, and H. Reis, "Monitoring corrosion of rebar embedded in mortar using high-frequency guided ultrasonic waves," *Journal of Engineering Mechanics*, vol. 135, no. 1, pp. 9–19, 2009.
- [29] L. Pochhammer, "Über die fortpflanzungsgeschwindigkeiten kleiner schwingungen in einem unbegrenzten isotropen kreiszylinder," *Journal für die Reine und Angewandte Mathematik*, vol. 81, pp. 324–336, 1876.
- [30] C. Chree, "The equations of an isotropic elastic solid in polar and cylindrical coordinates, their solutions and applications," *Transactions of the Cambridge Philosophical Society*, vol. 14, pp. 250–369, 1889.
- [31] D. Bancroft, "The velocity of longitudinal waves in cylindrical bars," *Physical Review*, vol. 59, no. 7, pp. 588–593, 1941.
- [32] J. L. Rose, *Ultrasonic Waves in Solid Media*, Cambridge University Press, Cambridge, UK, 1999.
- [33] T. H. Yi, H. N. Li, and H. M. Sun, "Multi-stage structural damage diagnosis method based on "energy-damage" theory," *Smart Structures and Systems*, vol. 12, no. 3-4, pp. 345–361, 2013.
- [34] T. H. Yi and H. N. Li, "Methodology developments in sensor placement for health monitoring of civil infrastructures,"

- International Journal of Distributed Sensor Networks*, vol. 2012, Article ID 612726, 11 pages, 2012.
- [35] A. A. Hanifah, *A theoretical evaluation of guided waves in deep foundations [Dissertation]*, Northwestern University, Evanston, Ill, USA, 1999.
- [36] B. N. Pavlakovic and M. Lowe, *Disperse Users Manual*, Version 2.0.16B, University of London, 2003.
- [37] R. N. Thurston, "Elastic waves in rods and clad rods," *Journal of the Acoustical Society of America*, vol. 64, no. 1, pp. 1–37, 1978.
- [38] Z. P. Zheng, Y. Lei, X. P. Cui, and Y. Song, "Non-destructive test of the steel bar by using piezoceramics sheets," in *Proceeds of 3rd International Conference on Advanced Measurement and Test*, Xiamen, China, 2013.
- [39] D. Liu, A. Zhou, and Y. Liu, "Torsional wave in finite length intact pile," *Chinese Journal of Applied Mechanics*, vol. 2, no. 2, pp. 258–263, 2005.
- [40] J. L. Rose, "A baseline and vision of ultrasonic guided wave inspection potential," *Journal of Pressure Vessel Technology, Transactions of the ASME*, vol. 124, no. 3, pp. 273–282, 2002.

Research Article

Establishment and Application of the Wind and Structural Health Monitoring System for the Runyang Yangtze River Bridge

Hao Wang,^{1,2} Aiqun Li,^{1,2} Tong Guo,^{1,2} and Tianyou Tao^{1,2}

¹ Key Laboratory of C&PC Structures of Ministry of Education, Southeast University, Nanjing 210096, China

² School of Civil Engineering, Southeast University, Nanjing 210096, China

Correspondence should be addressed to Hao Wang; wanghao1980@seu.edu.cn and Aiqun Li; aiquunli@seu.edu.cn

Received 16 June 2014; Accepted 11 August 2014; Published 27 August 2014

Academic Editor: Bo Chen

Copyright © 2014 Hao Wang et al. This is an open access article distributed under the Creative Commons Attribution License, which permits unrestricted use, distribution, and reproduction in any medium, provided the original work is properly cited.

Structural health monitoring can provide a practical platform for detecting the evolution of structural damage or performance deterioration of engineering structures. The final objective is to provide reasonable suggestions for structural maintenance and management and therefore ensure the structural safety according to the real-time recorded data. In this paper, the establishment of the wind and structural health monitoring system (WSHMS) implemented on the Runyang Yangtze River Bridge (RYRB) in China is introduced. The composition and functions of the WSHMS are presented. Thereinto, the sensory subsystem utilized to measure the input actions and structural output responses is introduced. And the core functions of the data management and analysis subsystem (DMAS) including model updating, structural condition identification, and structural condition assessment are illustrated in detail. A three-stage strategy is applied into the FE model updating of RYRB, and a two-phase strategy is proposed to adapt to structural health diagnosis and damage identification. Considering the structural integral security and the fatigue characteristic of steel material, the condition assessment of RYRB is divided into structural reliability assessment and structural fatigue assessment, which are equipped with specific and elaborate module for effective operation. This research can provide references for the establishment of the similar structural health monitoring systems on other cable-supported bridges.

1. Introduction

Bridges represent a key element in terms of the safety and functionality of the entire transportation system. With the worldwide development of transportation, numerous long-span bridges have been constructed to cross wide rivers, seas, or canyons. Due to its prominent spanning capacity and explicit mechanical behaviors, the cable-supported bridge exhibits as one of the most suitable selections among long-span bridges. There are a lot of famous cable-supported bridges implemented all over the world, such as the Akashi Kaikyo Suspension Bridge (1991 m) in Japan, the Great Belt Suspension Bridge (1624 m) in Denmark, and the Russky Island Cable-Stayed Bridge (1104 m) in Russia. In China, a great many long-span cable-supported bridges have also been in operation over the Yangtze River, canyons in the western area, and seas in the eastern region, such as Runyang

Suspension Bridge (1490 m), Sutong Cable-Stayed Bridge (1088 m), Jiangyin Suspension Bridge (1385 m), and Aizhai Suspension Bridge (1176 m).

In their long service periods of several decades or over 100 years, the long-span bridges are inevitable to encounter the long-term loads, fatigue effects, material aging, coupling effects with extreme loads, environmental corrosion, and so forth [1–3]. Subjected to natural actions including serious environmental corrosion, earthquakes, typhoons, thunderstorms, tornados, and so forth, the cable-supported bridge with flexible characteristics may suffer from slow performance deteriorations, severe structural damage, and even collapse in different scales. In addition, the structural performance deterioration will be further aggravated by the continuous increase of traffic loads. All of these factors can lead to the decrease of load bearing capacity and durability of the bridges and therefore influence the safety of structures.

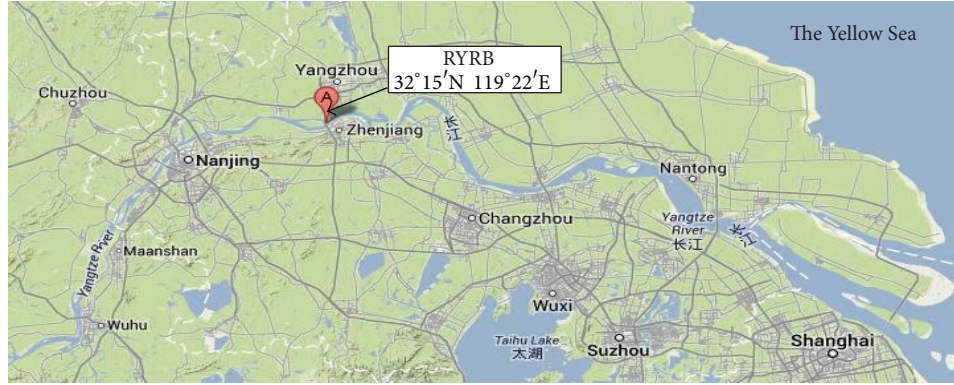


FIGURE 1: Geographical location of RYRB.

As a result, the health status, durability, and safety of the cable-supported bridges in their long-term service periods attract intensive attentions from the government and civil engineers.

In order to ensure the structural serviceability and sustainability, the structural health monitoring system (SHMS) provides an efficient approach to evaluate the safety and durability of a structure during its service life [2–8]. The SHMS usually contains a sensor system, a data acquisition system, a data transmission system, and a data management system. And the SHMS is equipped with two main functions in general. Firstly, a structure installed with a SHMS can be considered as a full-scale experimental platform. The measured environmental loads such as earthquake ground motions, wind speed, wind pressure, vehicles, temperature, and humidity would help understand the environment around the cable-supported bridges and enhance the structural response prediction capabilities. Secondly, the model updating, condition identification, condition assessment, and decision making of long-span cable-supported bridges can be further conducted based on the measured structural responses. Therefore, the SHMS of cable-supported bridges in real time offers the potential to reduce inspection and repair costs, as well as the associated downtime, all while providing increased public safety [9].

Among the various kinds of environmental loads, wind, earthquake, and vehicles play dominant roles on the cable-supported bridges, which may result in severe structural damage or even collapse. For cable-supported bridges constructed in the eastern coastal area of China, wind loads play an important role in their whole-life design due to the distinctive alternate typhoon and strong north wind climate every year. Compared with the comparatively infrequent earthquakes, typhoons in summer and strong north wind in winter will act on these wind-sensitive cable-supported bridges in the eastern coastal region frequently. Therefore, the wind environment around the bridge site needs to be emphatically monitored by the wind and structural health monitoring system (WSHMS), to assure the structural function properly during their long service lives and to prevent them from sudden failure or fatal disaster during strong winds [10, 11].

This paper presents a study on the establishment of the WSHMS for the super-long-span cable-supported bridges existing in hostile environment where typhoon, hurricane, or other strong winds occur frequently. Taking Runyang Yangtze River Bridge (RYRB) as a research object, the contents and functions of WSHMS implemented on RYRB are introduced in detail. The sensory subsystem and the core functions of WSHMS are specifically illustrated. Thereinto, the core functions contain the finite element (FE) model updating, structural condition identification, and structural condition assessment. The research and establishment of WSHMS for RYRB can provide references for the structural health monitoring of other cable-supported bridges located at the similar geographical regions and environment.

2. Engineering Background

2.1. Descriptions of RYRB. Located in the eastern area of China, RYRB is near the entrance of the Yangtze River to the Yellow Sea, as shown in Figure 1. According to the longitude and latitude, the bridge site belongs to the southeastern parts of the Asian continent. Taking account of the adaption of transportation to the development of economy, a super-huge and complicated engineering (RYRB) is put into construction in October, 2000. After nearly five years' harsh construction, RYRB was finally completed and open to traffic in April, 2005.

RYRB is an important lifeline engineering which firstly establishes the highway connection between Yangzhou and Zhenjiang across the Yangtze River in Jiangsu Province of China. It consists of two super-long-span cable-supported bridges, namely, Runyang Suspension Bridge (RSB) and Runyang Cable-stayed Bridge (RCB), as shown in Figure 2. RSB is a single-span hinged and simply supported steel-box-girder suspension bridge with a main span of 1490 m. When it was open to traffic in 2005, RSB was the first longest suspension bridge in China and the third in the world. In addition, the central buckle is applied to increase the overall stiffness of RSB, which is for the first time used in the suspension bridge in China. RCB is a steel-box-girder cable-stayed bridge with three spans (176 m + 406 m + 176 m), double main towers, and double cable planes.



FIGURE 2: View of Runyang Yangtze River Bridge (RYRB).

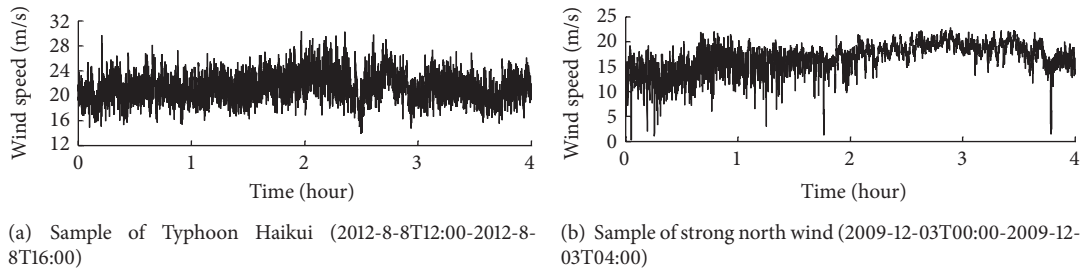


FIGURE 3: Typical wind samples from WSHMS on RYRB.

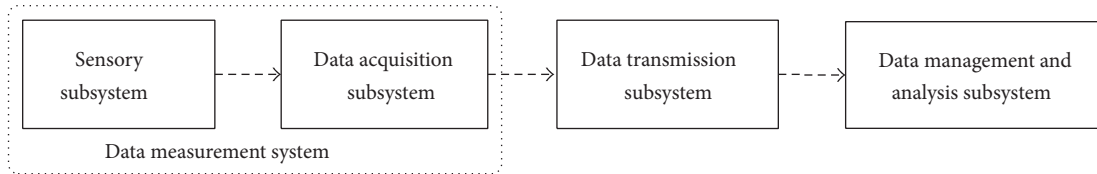


FIGURE 4: The structure of WSHMS of RYRB.

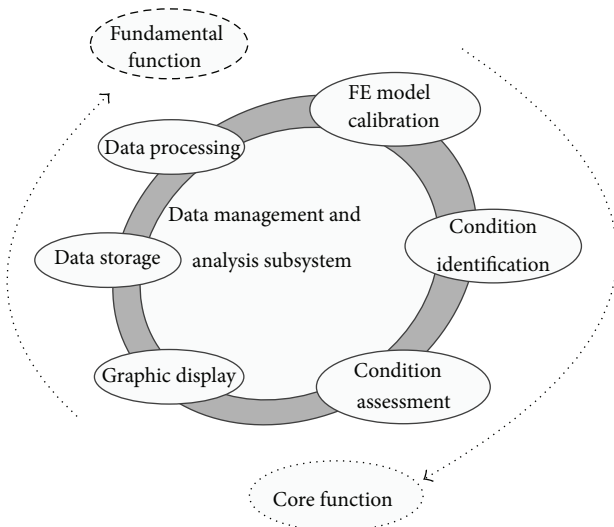


FIGURE 5: Structure of the functions of data management and analysis subsystem.

2.2. Wind Climate at the Bridge Site. The RYRB site belongs to the mid-latitude zone. According to the meteorological survey, the bridge site is dominated by the humid southern

subtropical monsoon climate. Monsoon circulation has a significant influence on the seasonal changes of local weather patterns of RYRB site. The monsoon circulation usually leads to obvious seasonal climate, especially typhoon climate from eastern ocean in summer and the north wind from Siberia in the northwest of China in winter. Considering the performance of flexible structures in a strong wind environment, the wind-resistant stability of RYRB needs to be paid intensive attention to during typhoons and strong winds. As a typical example, Figure 3 shows the recorded wind samples of Typhoon Haikui in 2012 and strong north wind in 2009 from the WSHMS on RYRB.

3. The Structure and Function of WSHMS on RYRB

The WSHMS of RYRB contains four subsystems including sensory subsystem, data acquisition subsystem, data transmission subsystem, and data management and analysis subsystem (DMAS), as can be seen in Figure 4.

The fundamental function of WSHMS on RYRB is realized by sensory subsystem, which contains various transducers to better understand the input loads and measure output structural responses. In order to realize the recording,

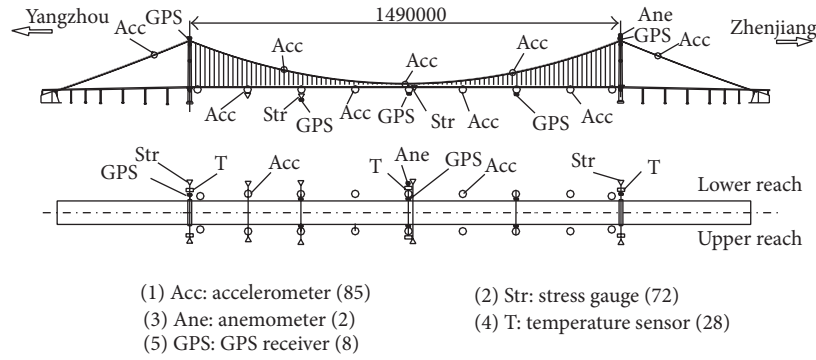


FIGURE 6: Layout of sensor system of RSB (dimension unit: mm).

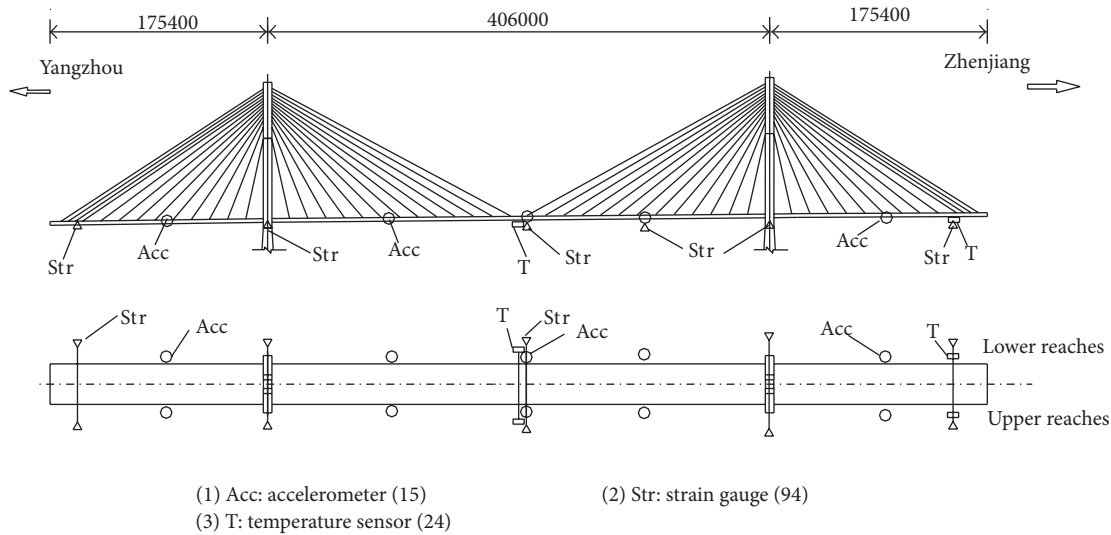


FIGURE 7: Layout of sensor system of RCB (dimension unit: mm).

transformation and quantification of multifarious signal sources, data acquisition subsystem has the functions to collect measured data from sensory subsystem and conduct adjustment and conversion of digital signals. The measured data will be transmitted to DMAS via data transmission subsystem, which is constituted by web server, optical switch, monitoring workstation, and optical fiber network.

As the most important part of the WSHMS on RYRB, the functions of DMAS contain the data processing and storage, graphic display of detected signals, progressive FE model updating, condition identification, and condition assessment based on the acquired data. The first three functions are composed of the fundamental function of DMAS, while the others perform as the core function for structural health assessment and decision making. The detailed function structure of DMAS can be seen in Figure 5.

4. Sensory Subsystem of WSHMS on RYRB

The WSHMS is a technique which can provide structural health conditions for decision making. Based on the WSHMS, the bridge supervisors can reasonably draw up

plans for bridge inspection and maintenance. The main contents and sensors layout of the WSHMS on RYRB are determined mainly by the structural static and dynamic analyses, the importance and durability of structural components, the structural characteristics, the requirements of the system functions, and construction expenditure. Figures 6 and 7 show the sensor layout of RSB and RCB, respectively. The number in the bracket represents the quantity of sensors.

4.1. Sensors Layout of RSB

4.1.1. Main Cable and Suspender Monitoring. The main cable is one of the most important components related to the safety operation of a suspension bridge. Therefore, 32 accelerometers were installed at 4 anchor rooms (8 accelerometers in each anchor room) to monitor the vibrations and frequencies of the typical cables, and likewise the forces of the cables can be achieved based on the relation between the cable tension and the vibration frequency. The vertical and lateral vibration responses of the main cable were monitored by 12 low-frequency single-axis accelerometers, as shown in Figure 8. Considering the large quantity of the suspenders, the suspenders of RSB were periodically tested

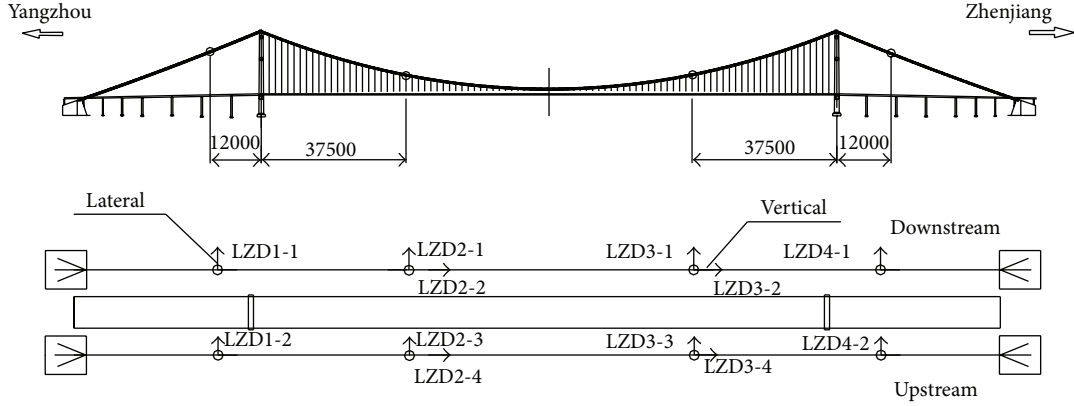


FIGURE 8: Layout of anemometers on the main cable of RSB.

with additional field tests and the measurement results are brought into the whole structural assessment system.

4.1.2. Main Girder Monitoring. Considering both of the structural characteristics of the main girder, the girder monitoring mainly focuses on the overall line type, stress, temperature, and vibration. The Global Positioning System (GPS) is demonstrated with an ability to accurately extract static and quasistatic displacements of the bridge induced by ambient effects [12–15]; thus 6 GPS measuring points are settled at 3 quartered sections to monitor the line type of the main girder, as shown in Figure 6. The monitoring station is set up near the GPS bench marks of China. In order to monitor the longitudinal displacement, 4 linear displacement sensors are installed at two ends of the girder (two in each end). Considering the optimization results of genetic algorithm and the requirements of real-time modal analysis, 29 low-frequency single-axis accelerometers are installed at 9 sections of the girder to monitor the vibration responses.

Considering many factors such as structural deformation and stress layout under static loads, symmetry of the structure, special design of the central buckle, and optimization analysis with the genetic algorithm, 72 strain gauges including fiber sensors, vibrational chord strain gauges, and welding strain gauges are installed at 5 sections of the main girder to monitor the structural stress status. Since the temperature has a significant effect on the fatigue property of welding steel box girder [16], 28 temperature sensors were installed at 3 sections of the main girder to monitor the temperature distribution and changes. Thereinto, 12 temperature sensors are installed on the $L/2$ (L is the span of the RSB) section of RSB and 8 temperature sensors are installed on the side section individually.

4.1.3. Main Tower Monitoring. The main tower is the most important element of a suspension bridge. In order to monitor the vibration response of the two towers, 6 accelerometers are uniformly installed at the upper crossing girder and the mid crossing girder of each tower, which is detailed in Figure 9. In addition, 2 GPS measuring points are settled at

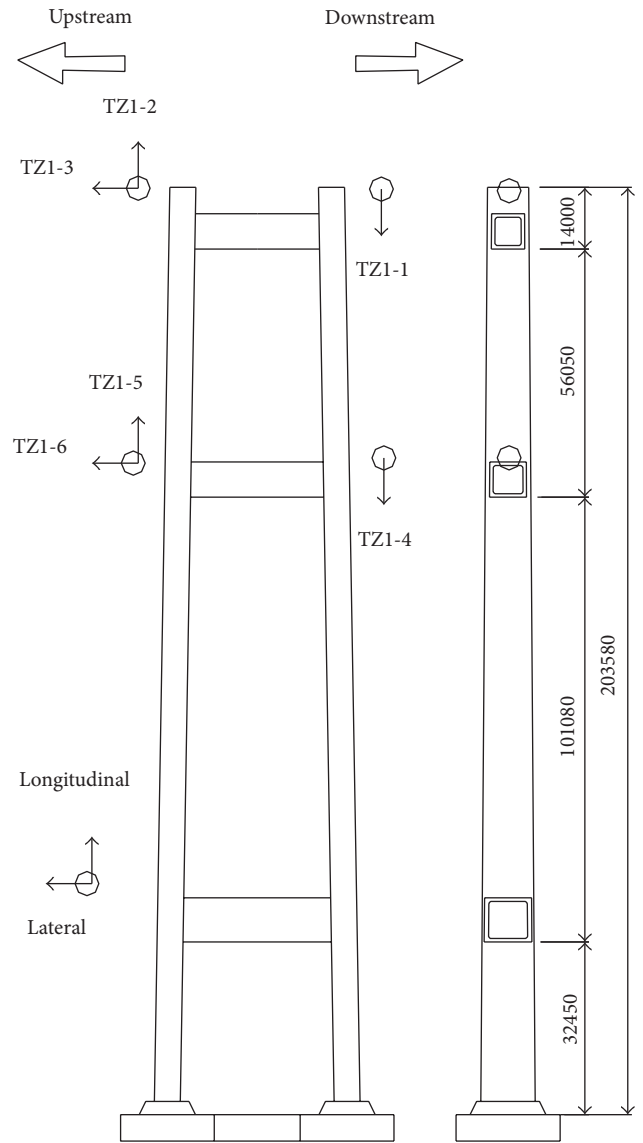


FIGURE 9: Layout of the accelerometers on the main tower of RSB (dimension unit: mm).

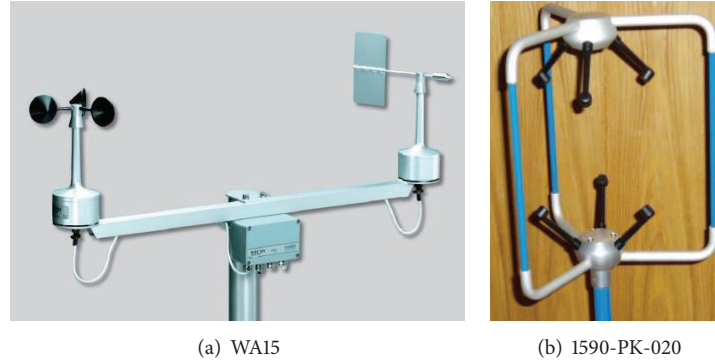


FIGURE 10: Anemometers installed on RSB.

the top of the two towers to monitor the displacements of the towers.

4.1.4. Wind Environment Monitoring. Considering the typical wind environment at the bridge site, two kinds of anemometers are installed on RSB to monitor the wind velocity and wind direction: the WA15 anemometer from the Vaisala Company (Finland) and the 1590-PK-020 3D ultrasonic anemometer from the Gill Instruments Limited (England). Two WA15 anemometers are used in the WSHMS of the RSB (Figure 10(a)), and three 1590-PK-020 3D ultrasonic anemometers are installed only during strong winds (Figure 10(b)). All the anemometers can be utilized to analyze the wind effects acting on RSB [17]. One of the WA15 anemometers is deployed on the top of the south tower (downstream) and the other in the middle of the main span (downstream). North wind is defined as 0° for anemometers data, and clockwise rotation is defined as the positive direction. Long-term successful applications in meteorological studies have shown that the WA15 anemometers can work effectively under all kinds of bad weather and acquire accurate information about wind environment.

The WA15 anemometers in WSHMS collect time history of wind speed and direction with the frequency of 1 Hz, so it can only provide average or maximum data about wind speed and direction. Because of this limitation, three 1590-PK-020 3D ultrasonic anemometers are used in the field test during the strong winds. The 1590-PK-020 anemometer has light weight and small volume. The maximum sampling frequency can reach 32 Hz. Owing to the above features, it is used widely in the wind testing of engineering structures. These three anemometers can be installed in other key positions of the RSB during strong wind periods, so that the wind environment characteristics of strong winds can be measured more accurately and comprehensively.

4.1.5. Traffic Loads Monitoring. Due to the low precision and high price of current vehicle load and vehicle velocity dynamic measurement system, the system was not applied in the WSHMS of RSB. Based on the data provided by the traffic system, the vehicle loads and vehicle velocities on RSB were determined mainly by the traffic loads model, which is built by use of the statistical method.

4.2. Sensors Layout of RCB

4.2.1. Cable Monitoring. The stay cable is one of the most important components in a cable-stayed bridge and its working performance is closely related to the health status of the overall structure. Therefore, the distribution and fluctuation of cable forces must be acquired accurately in order to analyze the working condition of the cables and determine the cable forces in FE model accordingly. Like the suspenders of RSB, the cable monitoring of RCB is complemented with additional periodical field tests, and then the measurements will be integrated into the WSHMS afterwards.

4.2.2. Main Girder Monitoring. The main girder monitoring of RCB mainly contains the monitoring of stress distribution, vibration status, and temperature distribution and fluctuation. As shown in Figure 7, 15 low-frequency accelerometers are installed at 5 sections of the main girder to monitor the vertical and lateral vibration responses. 94 strain gauges including fiber sensors, vibrational chord strain gauges, and welding strain gauges are installed at 5 key sections to monitor the stress distribution on the steel box girder. Considering the symmetry of RCB, 24 temperature sensors are installed at 2 sections ($L/2$ section and side section near Zhenjiang) of the main girder to monitor the temperature distribution and fluctuation all year round.

5. Progressive Finite Element Model Updating of RYRB

An accurate and reliable FE model is essential for the studies on wind resistance, structural health monitoring, and condition assessment [18]. Therefore, establishing a baseline FE model is the research basis for any kind of numerical analysis. Many FE model updating techniques have been proposed based on measured data in order to achieve an FE baseline model suitable for the analysis object. In most of the model updating approaches, the FE baseline model of the structure is obtained by reducing the error between the measured structural response and the calculated response from a numerical model. During the model updating procedure, the corresponding design parameters should be updated simultaneously. Obviously, too many design parameters may

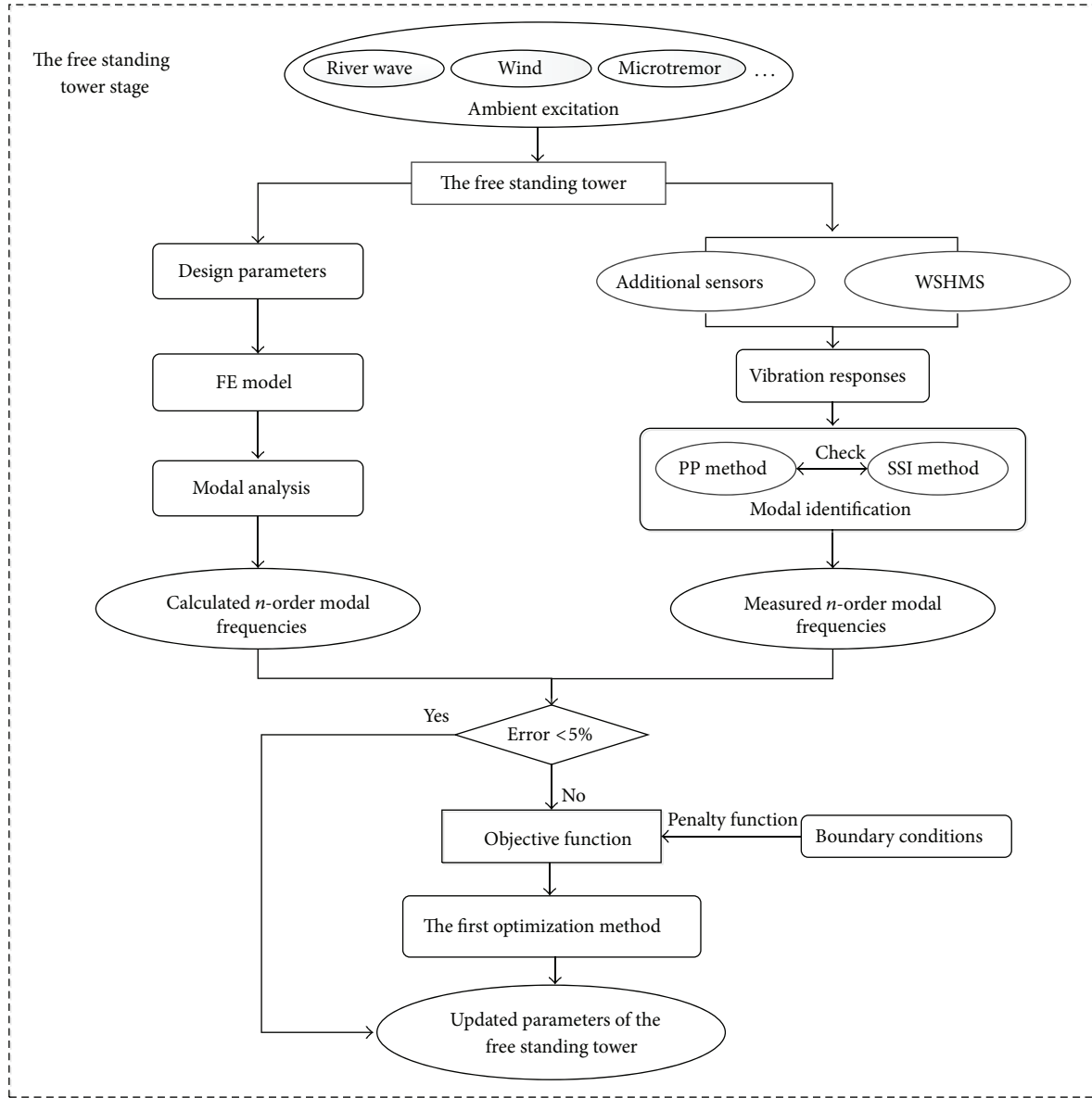


FIGURE 11: FE model updating of the free standing tower stage.

decrease the updating efficiency and increase the complexity of model updating. However, a more accurate FE model will be acquired when taking more input parameters into account. Hence, a tradeoff between the complicity of the optimization and the accuracy of the numerical model has to be made.

Being aware of the aforementioned limitations of model updating technique, a three-stage model updating strategy is proposed for the application in the progressive FE model updating of RYRB. Among the three-stage model updating strategy, the first two stages will provide an initial baseline FE model for the operation stage [18].

5.1. The Free Standing Tower Stage. When the main tower of RYRB is completed, a field test is conducted to examine the structural status. The accelerometers in WSHMS and the additional sensors can record its vibration responses from

ambient excitation, such as river waves, wind, and ground microtremor. Based on the measured structural vibration responses, the structural modal parameters are identified by the peak picking (PP) method. The identification results are then validated and complemented by the stochastic subspace identification (SSI) method. Considering the importance of low order modes, the first n modal frequencies are taken into the model updating process. Other acquired modal frequencies will be used to validate the updated FE model afterwards.

With the initial structural parameters, a FE model of the free standing tower can be established. The cross-section area, moment of inertia, material density, and elastic modulus are taken as the updating parameters based on the parameter sensitivity analysis. The first n modal frequencies of the tower can be calculated by modal analysis, and the error

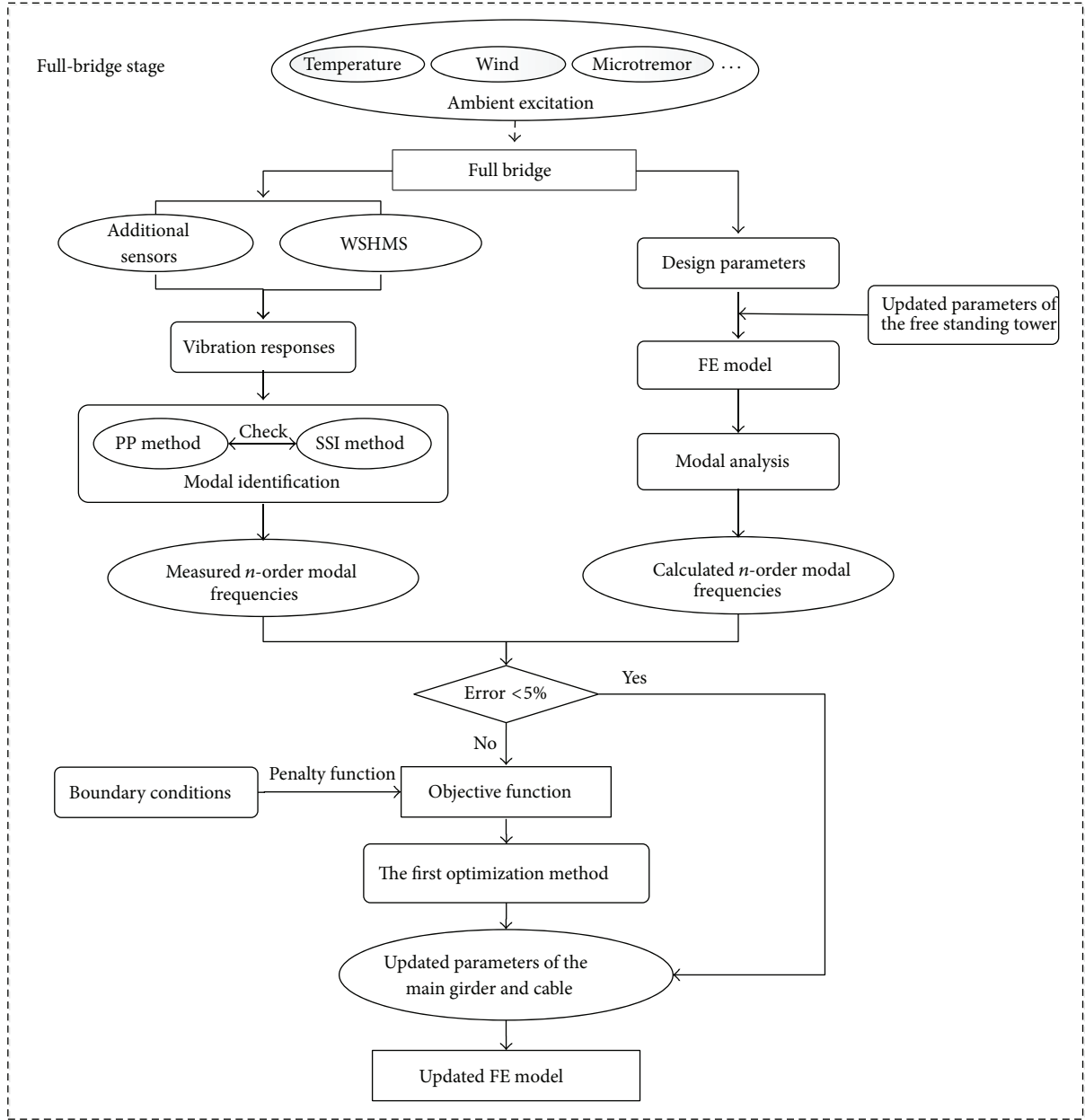


FIGURE 12: FE model updating of full-bridge stage.

between each corresponding calculated and measured modal frequency is defined as a state variable, specified as

$$\text{Error} = \frac{|f_c - f_m|}{f_m}, \quad (1)$$

where f_c is the calculated modal frequency and f_m is the measured modal frequency.

If each error between calculated and measured modal frequency is below the acceptable level 5%, the structural parameters would be permitted for the updated FE model; otherwise a parameter optimization procedure will be carried out. In the procedure, the model updating problem is transformed into a multiobjective nonlinear optimization problem

under constraints of equality and inequality. An objective function is proposed as the sum of the square of errors between the calculated and measured frequencies multiplied by corresponding weighing factors, detailed as

$$J = \sum_{i=1}^n \varphi_i E_i^2 \quad (i = 1, 2, \dots, n), \quad (2)$$

$$\varphi_i = \frac{E_i^2}{\sum_{i=1}^n E_i^2} \quad (i = 1, 2, \dots, n),$$

where J is the objective function; φ_i is the weighing factor; E_i is the error between calculated and measured value of the i th modal frequency. Taking the boundary conditions into

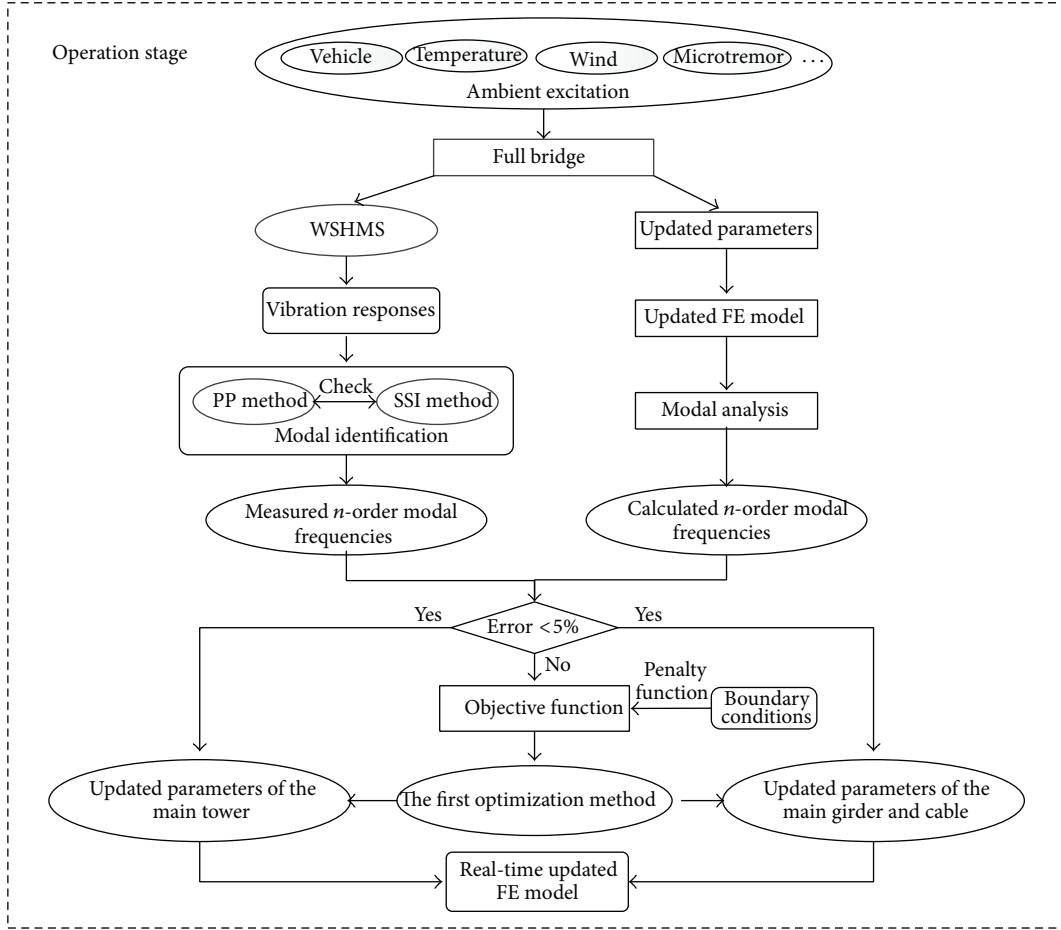


FIGURE 13: FE model updating of the operation stage.

the objective function with penalty function, the updated structural parameters of the free standing tower can be acquired by the first optimization method [18]. The detailed calibration process can be seen in Figure 11.

5.2. Full-Bridge Stage. In the second stage, structural parameters of the steel girder and the main cable will be updated after the construction of RYRB is finished. The model updating procedure is similar to that of the free standing tower. Based on the parameter sensitivity analysis, the selected updating parameters contain the material density, elastic modulus, and moment of inertia of the steel girder as well as the material density and elastic modulus of the main cable. In the establishment of the FE model of full bridge, the updated structural parameters of the free standing tower are employed and they are kept constant during the calibration procedure. In the stage, the first n modes contain vertical bending, lateral bending, and torsional modes of the main girder as well as the longitudinal bending, lateral bending, and torsional modes of the main tower. After the process in Figure 12, the updated parameters of the main girder and cable can be obtained, and an initial FE model with the updated parameters of the full bridge will be finally established.

Before RYRB was open to the traffic, a field load test is conducted and the corresponding static responses can be accurately recorded by WSHMS. Taking the same loading scheme, the structural deformation and stress distribution under the static and dynamic loads can be calculated with the FE model. The measured structural responses during the field load test can be employed to validate the reliability of the acquired FE model, so that an initial baseline FE model can be provided to the operation stage.

5.3. Operation Stage. Compared to construction stage, RYRB suffers from additional vehicle actions and continuous environmental loads in its long service period. Hence, the performance deterioration and partial damage will inevitably occur in some structural components, which may cause the variation of structural dynamic characteristics. A real-time FE model which can reflect the structural material and performance deterioration really needs to be established for structural condition assessment. To make the FE model accurate and reliable during its whole life cycle, the real-time recorded data from WSHMS are employed for validating the real-time updated FE model. Similar to construction stage, the FE model updating of RYRB in operation stage is shown in Figure 13.

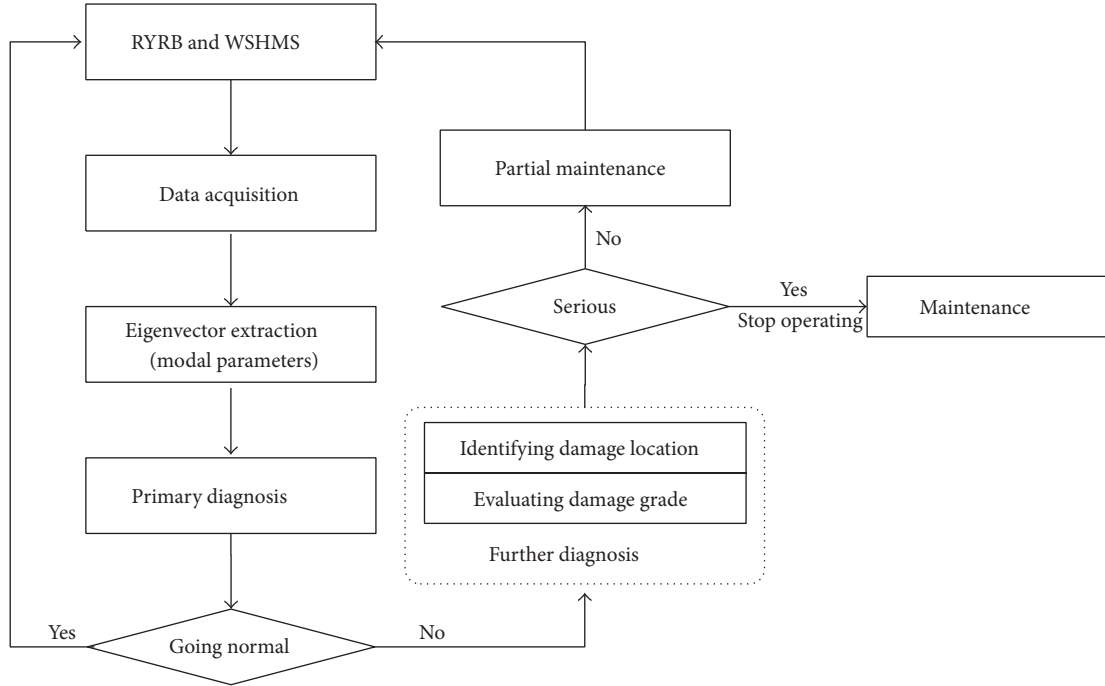


FIGURE 14: Condition identification strategy of RYRB.

6. Condition Identification of RYRB

One of the most important objectives of the WSHMS is to diagnose the damage and health condition of structures during service period. Large quantities of real-time data can be acquired from the WSHMS, which makes the existing problem for structural condition identification is how to convert the structural responses into the structural health information. Condition identification theory or method is just the way to diagnose structural abnormal state or damage. Many researches on structural condition identification using the field tests have been conducted, and the efficiency of structural condition identification based on static and dynamic responses has been validated by experiments [19–23].

The structural condition identification strategy in WSHMS of RYRB is shown in Figure 14. Based on the WSHMS, the structural responses will be recorded and transmitted to DMAS [24]. Some eigenvectors which can describe structural damage status will be extracted from the acquired data. Hereinto, modal parameters including mode frequencies, mode shapes, and damping ratios are selected as the eigenvectors. Furthermore, the modal assurance criteria (MAC) are adopted as the damage indicator to increase the sensitivity of modal parameters to structural damage. The structural condition identification is classified into two ordinal phases; one is primary diagnosis with statistical analysis technique and the other is further diagnosis with neural network. The primary phase only briefly distinguishes whether the modal parameters are abnormal or not, while the further phase will determine the damage location and evaluate the damage grade. Finally, whether a practical

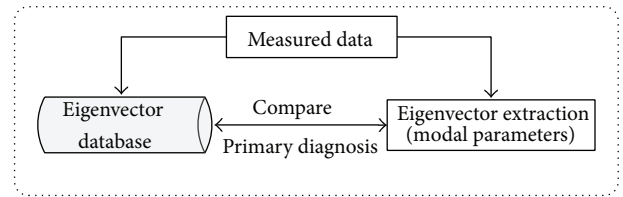


FIGURE 15: Primary damage diagnosis of RYRB.

maintenance is needed would be determined by the structural damage degree.

6.1. Primary Diagnosis Based on Statistical Analysis Technique. The efficiency of primary diagnosis relies on two factors, the extracted eigenvectors and the eigenvector database. Since the completion of RYRB, modal parameters of normally operated structure have been gradually accumulated from WSHMS. And an eigenvector database is set up with the statistical analysis result of accumulated modal parameters. Therefore, the primary diagnosis will depend on the comparison between the real-time extracted modal parameters and the eigenvector database. The primary diagnosis process can be seen in Figure 15.

6.2. Further Diagnosis Based on Neural Network. Due to the large scale of engineering structure and the randomness of influence factor, it is difficult to accurately acquire all the effective data related to local damage. Hence, many condition identification methods lose their own efficacies. But neural network accompanied by genetic algorithm can effectively

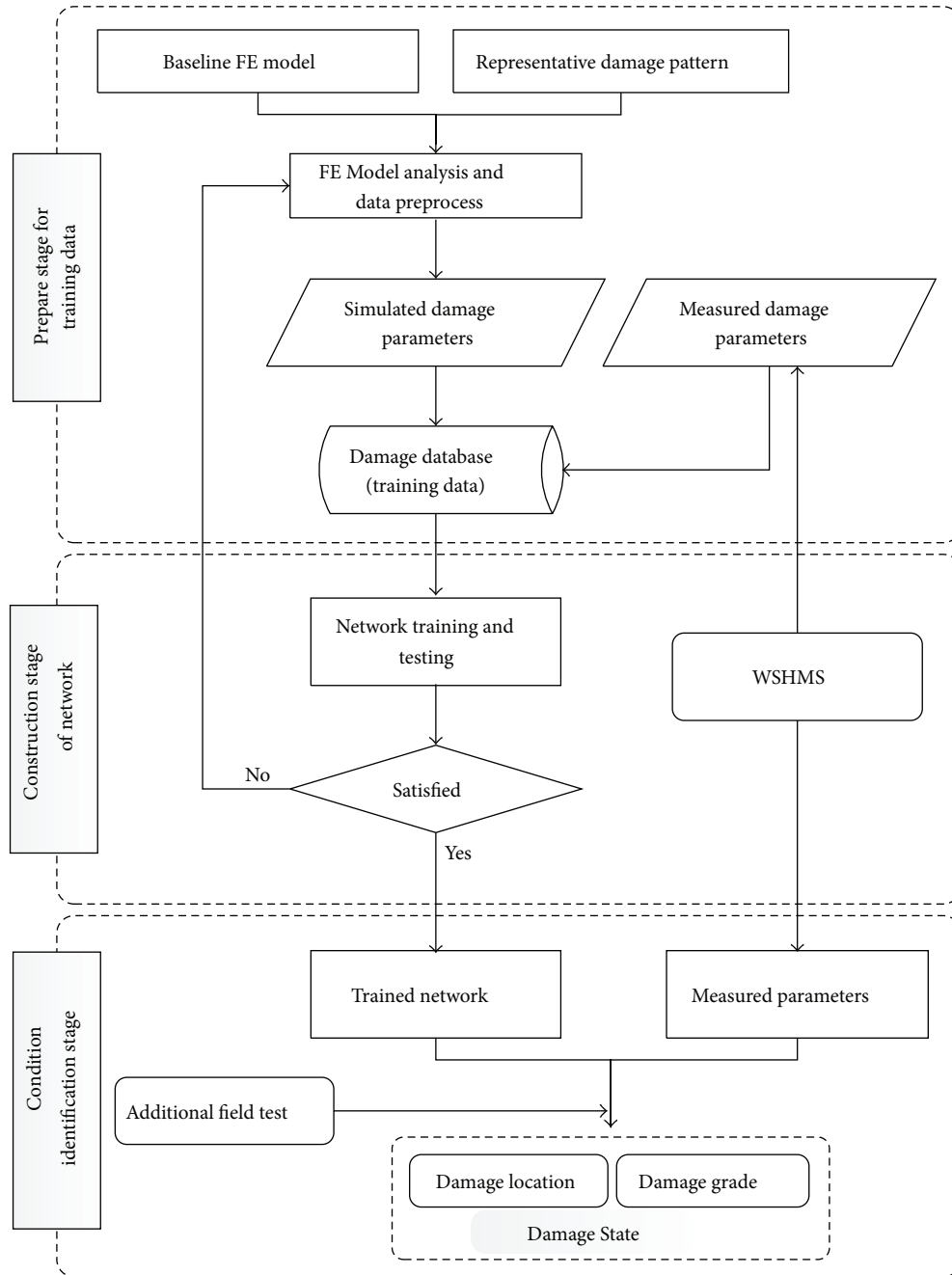


FIGURE 16: Further damage diagnosis based on neural networks.

explain the variation of structural state no matter from intuitive thinking or from uncertain reasoning on account of its strong fault tolerance, robustness, and generalization ability. Meanwhile, the development of computer techniques makes the computational efficiency rapidly increased, which makes it feasible to diagnose the health status of engineering structures.

In the further condition identification of RYRB, BP neural network is utilized to reflect the relationship between structural damage pattern and its characteristics and further identify the damage location combined with the analyses of

structural damage status. The further damage diagnosis of RYRB is divided into three stages, as shown in Figure 16.

The first stage aims to prepare training data for the neural network with the combination of FE analyses and field measurements. With the real-time baseline FE model provided by the model updating and representative damage patterns, the structural parameters embodying partially damage can be well simulated. Based on the measured parameters from the WSHMS, a damage database which stores the training data for neural network would be established. During the second stage, the topological structure of BP neural network

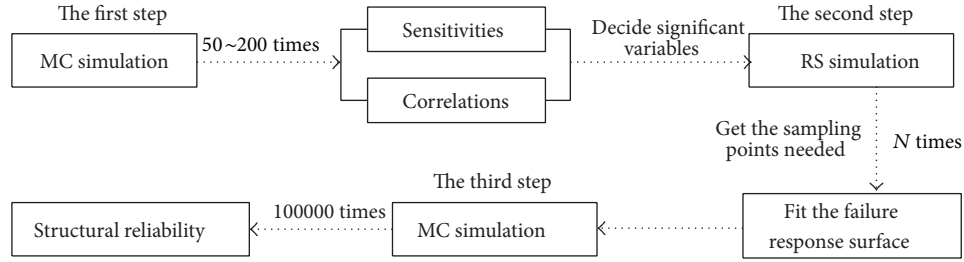


FIGURE 17: The flow chart of the combined simulation method.

is constructed and the network is trained with the sample set from the damage database. If the trained network satisfies with the accuracy requirement, it can be employed to serve for the third stage. The third stage is to assess the damage state of RYRB. Structural damage location and grade can be achieved by inputting the measured modal parameters into the trained BP neural network model. In order to accurately and reliably recognize the real structural damage state including damage location and damage grade, some additional field tests should be conducted near the possible damage locations.

7. Condition Assessment of RYRB

Safe and reliable operation of bridges has become a major concentration of both civil engineers and the government. However, whether current technologies and operational procedures can ensure the necessary serviceability, the cost-effective maintenance and management of bridges still lack an explicit evaluating criterion. These limitations in current practice can be overcome by emerging concepts and tools for accurate condition assessment of civil infrastructures [25]. Conventional bridge condition assessment is generally conducted with measured data from visual inspection, which has been proved to be limited and subjective. The development of structural health monitoring provides a new valuable practice into structural condition assessment. With plentiful data acquired from the SHMS, the condition of in-service bridge structures and insights into actual behavior of bridges under in-service environment can be well recognized based on reliability condition assessment methods [26, 27]. Considering integral security and the fatigue characteristic of steel material, the condition assessment of RYRB is composed of structural reliability assessment and structural fatigue assessment [24].

7.1. Structural Reliability Assessment. In the structural reliability assessment of RYRB, the core part is a combined numerical simulation method which has the advantages of the Monte Carlo (MC) method and the response surface (RS) method. The main procedure can be seen in Figure 17.

The combined method mainly contains the following steps. Firstly, the MC method is used to compute the probabilistic sensitivities and the correlations between random variables (input variables) with 50~200 times of samplings. In this way, the variables that have more significant effect on

the output index can be determined according to probabilistic sensitivity analysis. The comparatively important input variables will be kept for following process while the others will be omitted. Then the failure response surface of different output variables can be fitted through RS simulation. Finally, the MC method (100,000 times of samplings) will be used again to get the structural probability of each main failure mode based on this response surface.

Combined with monitored data from WSHMS, the detailed reliability assessment of RYRB is shown in Figure 18. The whole procedure is mainly divided into three specific parts. In the input module, the environment information and vehicle loads will be processed with statistical method, so that the statistical value of external actions can be input to the evaluating model afterwards. If some structural damage has occurred and been examined by the monitoring system, the damage information can be delivered to the evaluating model as well. In the simulation module, the combined simulation method aforementioned and the updated FE model will be utilized to calculate the reliability of each main failure mode. In the output module, the max stress of girder, cable, and central buckle, the max vertical and horizontal displacements of girder, and the max horizontal displacements of the tower will be displayed. The reliability of the member with extreme responses will be evaluated and the serial number of the perilous member will be recorded with a label. According to the probability index, the structural reliability state and the suggested maintenance action can be given.

7.2. Structural Fatigue Assessment. Fatigue is a prominent problem that exists in steel structures [28, 29]. If the stress fluctuates obviously, stress far less than yield strength can cause the failure of steel members. In the fabrication of steel structures, welding is one of the most frequently used approaches, but welded joints in steel structures are vulnerable to failure by fatigue for the inner flaws or discontinuities [16, 30]. Considering the fatigue accumulation in welded joints of the steel box girder, the structural fatigue assessment of RYRB mainly focuses on the plentiful welded joints between each segment of the deck. The structural fatigue assessment can be seen in Figure 19.

Based on the online original data of strain acquired from WSHMS of RYRB, the recorded data in time domain can be transformed into statistical information at frequency domain with FFT technique. Using multiple linear regression method, a representative sample of strain time-history can be

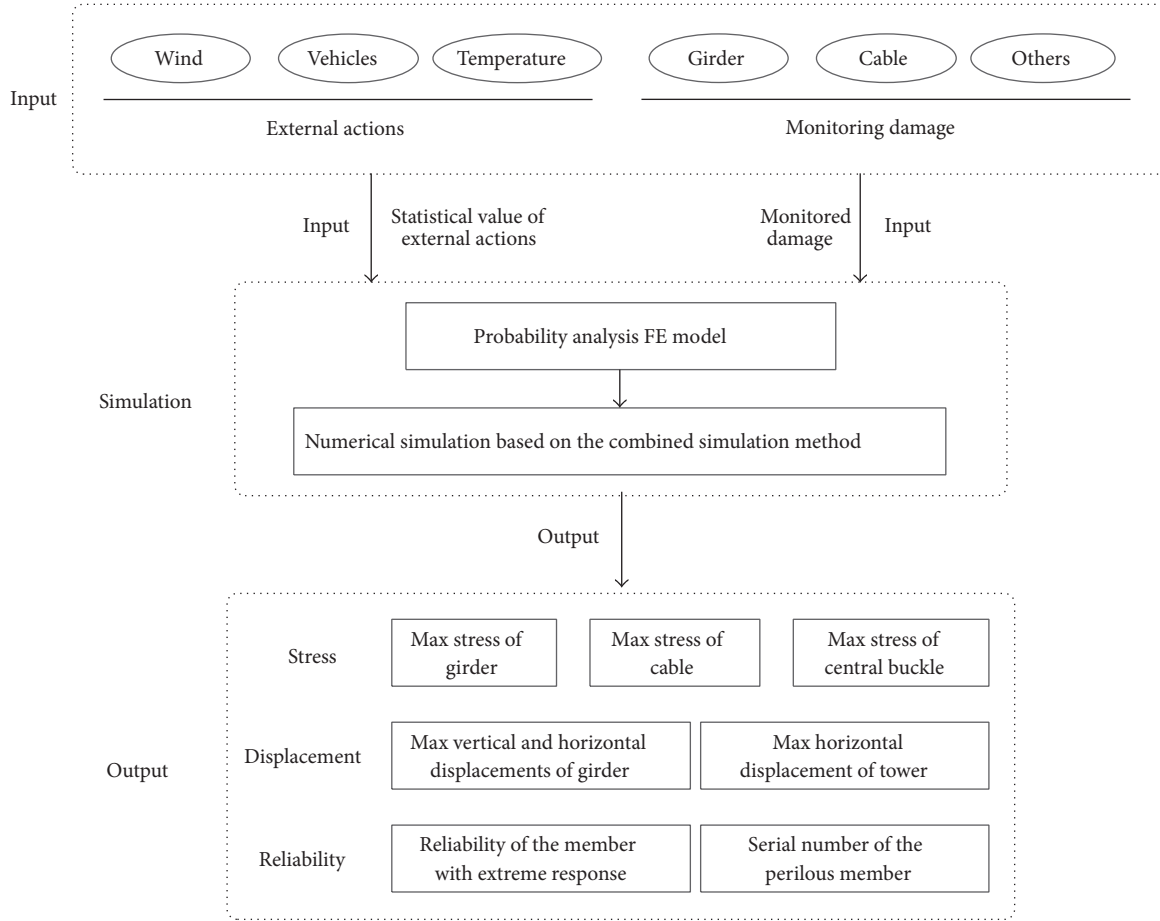


FIGURE 18: Reliability assessment of RYRB.

obtained. Then the rain-flow counting method is utilized to determine the stress spectrum of the representative sample. Since the measured stress is the nominal stress at the location of the gauge, it should be modified with coefficient to obtain the hot-spot stress at the toe of weld. The primary assessment of fatigue life is undertaken based on BS5400 [31] and a modified probability model is proposed as well. Combined with continuum damage mechanics (CDM) model and miner model, the reliability assessment of fatigue life on RYRB will be conducted comprehensively. Hence, the periodic inspection and maintenance scheme for RYRB can be formulated reasonably.

8. Summary and Conclusion

This paper introduces the establishment of a WSHMS for RYRB in China, and the composition and functions of the WSHMS are presented. The WSHMS of RYRB contains four subsystems including sensory subsystem, data acquisition subsystem, data transmission subsystem, and DMAS. Specifically, the sensory subsystem, which is utilized to measure the input actions and structural output responses, and the core functions of the DMAS including model updating, structural condition identification, and structural condition assessment are illustrated in detail.

A three-stage model updating strategy is proposed for the progressive FE model updating of RYRB. Thereinto, the measured structural static and dynamic responses are adopted to acquire the target benchmarks of RYRB and the first-order optimization method is used to enhance the computing rate of convergence. Among the proposed three-stage model updating strategy, the first two stages can provide an initial baseline FE model for the operation stage, and the operation stage offers a real-time FE model for structural condition identification and assessment.

In the WSHMS of RYRB, a two-phase strategy is proposed to carry out the structural damage diagnosis and damage location identification. The primary diagnosis phase briefly distinguishes whether the measured parameters and responses are abnormal or not, while the further diagnosis phase will determine the damage location and evaluate the damage grade. On the basis of structural damage degree, whether a practical maintenance is needed or not can be decided.

Considering the integral security and the fatigue characteristic of steel structures, the condition assessment of RYRB is composed of structural reliability assessment and structural fatigue assessment. Structural reliability assessment serves with a combined numerical simulation method taking the advantages of both the Monte Carlo method and the response

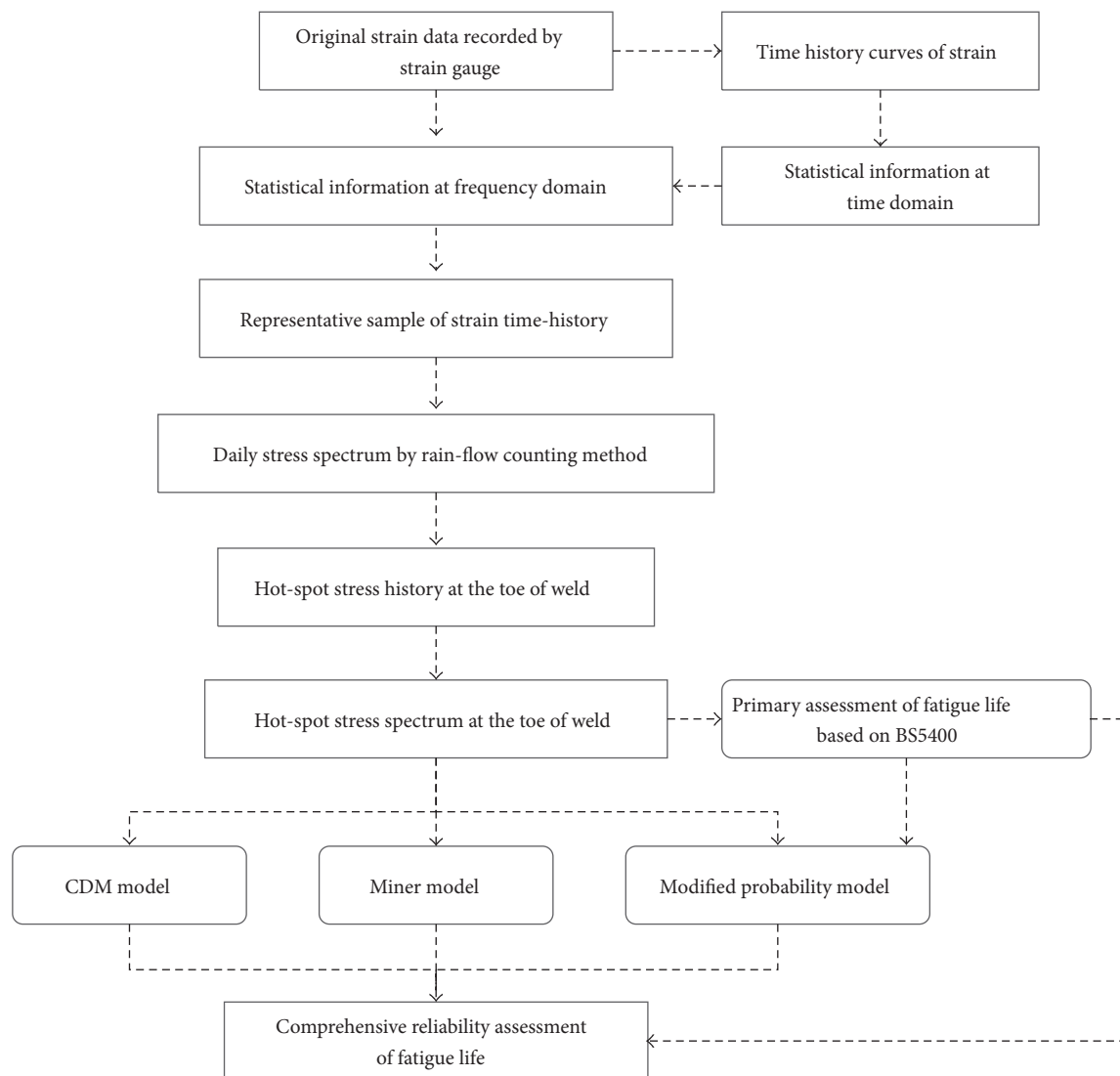


FIGURE 19: Structural fatigue assessment of RYRB.

surface method, while structural fatigue assessment is a comprehensive evaluation with empirical and modified model based on real-time measurements from WSHMS.

Conflict of Interests

The authors declare that there is no conflict of interests regarding the publication of this paper.

Acknowledgment

The supports from the National Science Foundation of China (Grant nos. 51378111 and 51438002), the Major State Basic Research Development Program of China for Young Scientists (973 Program, Grant no. 2015CB060000), the Program for New Century Excellent Talents in University of Ministry of Education of China (Grant no. NCET-13-0128), the Fok Ying-Tong Education Foundation for Young Teachers in the Higher Education Institutions of China (Grant no.

142007), the Jiangsu Transportation Department (Grants nos. 2011Y09-2 and 2011Y03), the Natural Science Foundation of Jiangsu (Grant no. BK2011611), and the Fundamental Research Funds for the Central Universities (Grant no. 2242012R30002) are greatly acknowledged. The authors also would like to acknowledge the Construction Commanding Department of Jiangsu Provincial Yangtze River Highway Bridge and the Structural Health Monitoring Institute of Southeast University.

References

- [1] A. E. Aktan, F. N. Catbas, K. A. Grimmelsman, and C. J. Tsikos, "Issues in infrastructure health monitoring for management," *Journal of Engineering Mechanics*, vol. 126, no. 7, pp. 711–724, 2000.
- [2] J. P. Ou and H. Li, "Recent advances of structural health monitoring in Mainland China," in *Proceedings of the ANCER Annual Meeting*, 2004.

- [3] H. Li, J. Ou, X. Zhao et al., "Structural health monitoring system for the Shandong Binzhou Yellow River Highway Bridge," *Computer-Aided Civil and Infrastructure Engineering*, vol. 21, no. 4, pp. 306–317, 2006.
- [4] A. S. Kiremidjian, E. G. Straser, T. H. Meng et al., "Structural damage monitoring for civil structures," in *Proceedings of the International Workshop on Structural Health Monitoring*, pp. 371–382, 1997.
- [5] J. M. Ko and Y. Q. Ni, "Structural health monitoring and intelligent vibration control of cable-supported bridges: research and application," *KSCE Journal of Civil Engineering*, vol. 7, no. 6, pp. 701–716, 2003.
- [6] J. P. Ou, "Some recent advances of structural health monitoring systems for civil infrastructure in mainland China," in *Proceedings of the Symposium on Network and Center-based Research for Smart Structures Technologies and Earthquake Engineering*, pp. 131–144, Tokyo, Japan, 2003.
- [7] H. N. Li, D. S. Li, and G. B. Song, "Recent applications of fiber optic sensors to health monitoring in civil engineering," *Engineering Structures*, vol. 26, no. 11, pp. 1647–1657, 2004.
- [8] B. Chen, S. L. Zhao, and P. Y. Li, "Application of Hilbert-Huang transform in structural health monitoring: a state-of-the-art review," *Mathematical Problems in Engineering*, vol. 2014, Article ID 317954, 22 pages, 2014.
- [9] B. F. Spencer and S. Cho, "Wireless smart sensor technology for monitoring civil infrastructure: technological developments and full-scale applications," in *Proceedings of the World Congress on Advances in Structural Engineering and Mechanics*, pp. 18–22, Seoul, Republic of Korea, 2011.
- [10] Y. L. Xu and W. S. Chan, "Wind and structural monitoring of long span cable-supported bridges with GPS," in *Proceedings of the 7th Asia-Pacific Conference on Wind Engineering (APCWE '09)*, Taipei, China, November 2009.
- [11] B. Chen, Y. L. Xu, and X. Zhao, "Integrated vibration control and health monitoring of building structures: a time-domain approach," *Smart Structures and Systems*, vol. 6, no. 7, pp. 811–833, 2010.
- [12] Y. Fujino, M. Murata, S. Okano, and M. Takeguchi, "Monitoring system of the Akashi Kaikyo Bridge and displacement measurement using GPS," in *4th Nondestructive Evaluation of Highways, Utilities, and Pipelines*, vol. 3995 of *Proceedings of SPIE*, pp. 229–236, Newport Beach, Calif, USA, March 2000.
- [13] S. Nakamura, "GPS measurement of wind-induced suspension bridge girder displacements," *Journal of Structural Engineering*, vol. 126, no. 12, pp. 1413–1419, 2000.
- [14] T. H. Yi, H. N. Li, and M. Gu, "Wavelet based multi-step filtering method for bridge health monitoring using GPS and accelerometer," *Smart Structures and Systems*, vol. 11, no. 4, pp. 331–348, 2013.
- [15] T. H. Yi, H. N. Li, and M. Gu, "Experimental assessment of high-rate GPS receivers for deformation monitoring of bridge," *Measurement*, vol. 46, no. 1, pp. 420–432, 2013.
- [16] T. Guo, A. Q. Li, and J. H. Li, "Fatigue life prediction of welded joints in orthotropic steel decks considering temperature effect and increasing traffic flow," *Structural Health Monitoring*, vol. 7, no. 3, pp. 189–202, 2008.
- [17] H. Wang, A. Li, J. Niu, Z. Zong, and J. Li, "Long-term monitoring of wind characteristics at Sutong Bridge site," *Journal of Wind Engineering and Industrial Aerodynamics*, vol. 115, pp. 39–47, 2013.
- [18] H. Wang, A. Li, and J. Li, "Progressive finite element model calibration of a long-span suspension bridge based on ambient vibration and static measurements," *Engineering Structures*, vol. 32, no. 9, pp. 2546–2556, 2010.
- [19] K. D. Hjelmstad and S. Shin, "Damage detection and assessment of structures from static response," *Journal of Engineering Mechanics*, vol. 123, no. 6, pp. 568–576, 1997.
- [20] B. H. Oh and B. S. Jung, "Structural damage assessment with combined data of static and modal tests," *Journal of Structural Engineering*, vol. 124, no. 8, pp. 956–965, 1998.
- [21] R. Brincker, L. Zhang, and P. Andersen, "Modal identification of output-only systems using frequency domain decomposition," *Smart Materials and Structures*, vol. 10, no. 3, pp. 441–445, 2001.
- [22] L. M. Khoo, P. R. Mantena, and P. Jadhav, "Structural damage assessment using vibration modal analysis," *Structural Health Monitoring*, vol. 3, no. 2, pp. 177–194, 2004.
- [23] S. H. Sim, B. F. Spencer, and T. Nagayama, "Multimetric sensing for structural damage detection," *Journal of Engineering Mechanics*, vol. 137, no. 1, pp. 22–30, 2011.
- [24] A. Q. Li, Y. L. Ding, H. Wang, and T. Guo, "Analysis and assessment of bridge health monitoring mass data—progress in research/development of "Structural Health Monitoring,"" *Science China Technological Sciences*, vol. 55, no. 8, pp. 2212–2224, 2012.
- [25] A. E. Aktan, D. N. Farhey, D. L. Brown et al., "Condition assessment for bridge management," *Journal of Infrastructure Systems*, vol. 2, no. 3, pp. 108–117, 1996.
- [26] M. Liu, D. M. Frangopol, and S. Kim, "Bridge system performance assessment from structural health monitoring: a case study," *Journal of Structural Engineering*, vol. 135, no. 6, pp. 733–742, 2009.
- [27] H. W. Xia, Y. Q. Ni, K. Y. Wong, and J. M. Ko, "Reliability-based condition assessment of in-service bridges using mixture distribution models," *Computers & Structures*, vol. 106–107, pp. 204–213, 2012.
- [28] Z. W. Chen, Y. L. Xu, Y. Xia, Q. Li, and K. Y. Wong, "Fatigue analysis of long-span suspension bridges under multiple loading: case study," *Engineering Structures*, vol. 33, no. 12, pp. 3246–3256, 2011.
- [29] Z. W. Chen, Y. L. Xu, and X. M. Wang, "SHMS-based fatigue reliability analysis of multiloading suspension bridges," *Journal of Structural Engineering*, vol. 138, no. 3, pp. 299–307, 2012.
- [30] Z. X. Li, T. H. T. Chan, and T. Q. Zhou, "Accumulative damage near crack tip for welded bridge members: fatigue life determination," *Theoretical and Applied Fracture Mechanics*, vol. 43, no. 2, pp. 245–260, 2005.
- [31] BS5400, B. S. I., Part 10, Code of Practice for Fatigue, 1982.

Research Article

Free-Interface Modal Synthesis Based Substructural Damage Detection Method

Shanghong Chen, Wei Lin, Jiexin Yu, and Ai Qi

School of Civil Engineering, Fuzhou University, Fuzhou 350116, China

Correspondence should be addressed to Wei Lin; cewlin@fzu.edu.cn

Received 17 April 2014; Accepted 17 June 2014; Published 15 July 2014

Academic Editor: Bo Chen

Copyright © 2014 Shanghong Chen et al. This is an open access article distributed under the Creative Commons Attribution License, which permits unrestricted use, distribution, and reproduction in any medium, provided the original work is properly cited.

Free-interface modal synthesis method is applied to civil structure, and a substructure method is proposed by introducing the method into global sensitivity method. The substructure expression of the derivatives of eigenvalues and eigenvectors with respect to elemental parameters is obtained. The accuracy of the application of free-interface modal synthesis method is evaluated with different retained modes in substructure, and then the effectiveness of the proposed substructure sensitivity method is illustrated through an 11-storey building under both single- and multidamage cases. Both the damage locations and the extent can be effectively identified. By comparing it with the identical results of global sensitivity method, the proposed method can be faster in detecting the damage location and more stable under multidamage cases. Since this substructure sensitivity method only needs to update sensitivity matrix in the substructure with relative small number of DOFs, it may save much computation effort and become more efficient.

1. Introduction

To ensure the safety of large-scale civil infrastructures, more and more health monitoring systems are adopted to evaluate health condition and also to prevent sudden failure due to accumulation of component damages [1–5]. Nowadays, although more sensors were installed and varieties of data were collected, it encounters a problem on how to derive useful information or identify some early damage through the massive data [6, 7]. An accurate finite element model (FEM) is usually required to provide a baseline of the healthy structure, but, due to uncertainties from geometry, material properties, and boundary conditions, the FEM needs to be first updated through the picked up information [8, 9]. Moreover, by comparing the output change such as natural frequency, mode shape, mode shape curvature, and flexibility changes due to structural aging or adverse environmental effects, it is expected that the system should be able to detect local damages and give maintenance advices [10–12]. As it comes to civil structures, their FEMs usually have large number of DOFs, which will result in equations with huge dimension during the model updating and damage detection

procedure. And it would take on a lot of resources and make the calculation to be very time-consuming [13–15].

Sensitivity-based method is believed to be an effective way in model updating and damage detection. It is based on the fact that a perturbation in parameters will affect the outputs of a structure, such as frequencies and mode shapes [16]. And the derivative of target function with respect to system parameters is defined as sensitivity. Many efforts have been made by researchers [17–21]. In these sensitivity methods, a sensitivity matrix has to be computed at each time step. It will be a tedious work if too many uncertainties are assumed. Substructure method [22] may be an effective approach to the problem. The main idea is to divide a whole structure into many substructures first, and then the calculation can be achieved independently in each substructure. Finally, reconstruction work is done based on the boundary conditions. Chen and Bicanic [20] first proposed a substructure method to calculate eigenvalue and eigenvector. Kron and Li et al. [23–27] proposed a substructure method in time domain to identify local damage under moving vehicular loads without knowledge of the vehicle properties and the time-histories of moving interaction forces. And Weng et al. [28, 29] extent

Kron's method and proposed an inverse substructure method in frequency domain.

This paper attempted to apply free-interface modal synthesis method in civil infrastructure and to introduce the method into the traditional global sensitivity method and to establish a substructure sensitivity method. The derivatives of eigenvalue and eigenvector with respect to system parameters will be calculated with the substructure method. With only those factors within certain substructures having nonzero value, this method is supposed to require few computation efforts and higher efficiency in damage detection. Numerical example is conducted on an 11-storey frame building. In order to maintain the accuracy during damage detection, the accuracy of modal synthesis method will be first discussed and then the damage detection ability of the proposed method will be verified under several damage cases.

2. Free-Interface Modal Synthesis

The idea of modal synthesis method is to first divide a structure into a series of substructures with no bound constraints attached. After acquiring the dynamic characteristics of every substructure, the system equation can be reconstructed by taking the displacement coordinate of each substructure into account, and finally the modal information can be derived from this equation. To facilitate the description, it is assumed that the structure is divided into only two substructures, named substructures a and b . And modal synthesis method with more substructures concerned can also be derived from the following equations.

2.1. Basic Modal Equation of a Substructure. Similar to the whole structure, taking substructure a as an example, the equations of motion with free vibration case can be expressed as

$$[{}^{(a)}M] \{ {}^{(a)}\ddot{x} \} + [{}^{(a)}K] \{ {}^{(a)}x \} = \{ {}^{(a)}f \}, \quad (1)$$

where $[{}^{(a)}M]$ and $[{}^{(a)}K]$ are the mass and stiffness matrices of substructure a , $\{ {}^{(a)}\ddot{x} \}$ and $\{ {}^{(a)}x \}$ represent the substructure's acceleration and displacement vectors in normal coordinate, respectively, and $\{ {}^{(a)}f \}$ is the applied forces on the corresponding DOFs of substructure a .

The eigenvalues and eigenvectors can be solved from the corresponding modal equation in frequency domain. And if only the first q modes are considered and compose a matrix $[{}^{(a)}\Phi]$, then the displacement vector $\{ {}^{(a)}x \}$ can be decomposed as the following equation which is called the first coordinate transformation:

$$\{ {}^{(a)}x \} = [{}^{(a)}\Phi] \{ {}^{(a)}p \}, \quad (2)$$

where $\{ {}^{(a)}p \}$ represents the responses in modal coordinate.

The nodes of the substructure can be divided into two sets: those attached to the interface and those with only internal forces applied on. It is expressed as subscription I

and J , respectively. Then, the displacement vector can be expressed as

$$\{ {}^{(a)}x \} = \begin{Bmatrix} {}^{(a)}x_I \\ {}^{(a)}x_J \end{Bmatrix} = \begin{bmatrix} {}^{(a)}\Phi_I \\ {}^{(a)}\Phi_J \end{bmatrix} \{ {}^{(a)}p \}. \quad (3)$$

By normalizing using mass matrix, the dominate equation of $\{ {}^{(a)}p \}$ in modal coordinate is

$$[{}^{(a)}\widetilde{M}] \{ {}^{(a)}\ddot{p} \} + [{}^{(a)}\widetilde{K}] \{ {}^{(a)}p \} = [{}^{(a)}\Phi] \{ {}^{(a)}f \}, \quad (4)$$

where $[{}^{(a)}\widetilde{M}]$ and $[{}^{(a)}\widetilde{K}]$ are the normalized mass and stiffness matrix of substructure a , and the following modal equation can be further derived:

$$\{ {}^{(a)}\ddot{p} \} + [{}^{(a)}\Omega] \{ {}^{(a)}p \} = [{}^{(a)}\Phi] \{ {}^{(a)}f \} \quad (5)$$

in which $[{}^{(a)}\Omega] = \text{diag}({}^{(a)}\lambda_1, {}^{(a)}\lambda_2, \dots, {}^{(a)}\lambda_q)$ is a matrix containing the eigenvalues of selected substructure and, in accordance with diagonal arrangement, $\{ {}^{(a)}f \}$ is the interface force vector.

2.2. Interface Coordination Conditions. Assuming that only the first n and m modes of substructures a and b are considered during modal synthesis and the number of interface DOFs of the substructure is J , since the two substructures share the same nodes at the interface, there should be displacement coordination equations as

$$\{ {}^{(a)}x_J \} = \{ {}^{(b)}x_J \}. \quad (6)$$

By using (2), this equation can also be written in modal coordinate as

$$[{}^{(a)}\Phi_J] \{ {}^{(a)}p \} = [{}^{(b)}\Phi_J] \{ {}^{(b)}p \}. \quad (7)$$

In order to reconstruct the system equation, it is supposed that the number of the retained modes of each substructure should exceed the number of DOFs of the interface J , that is, to require $n > J$ and $m > J$, and $[{}^{(a)}\Phi_J]$ can be written as

$$[{}^{(a)}\Phi_J] = \begin{bmatrix} {}^{(a)}\Phi_{JS} \\ {}^{(a)}\Phi_{JR} \end{bmatrix}, \quad (8)$$

where $[{}^{(a)}\Phi_{JS}]$ is a nonsingular matrix derived from $[{}^{(a)}\Phi_J]$ and the rest modal vector are formed as $[{}^{(a)}\Phi_{JR}]$. Substituting (8) into (7) yields

$$\begin{bmatrix} {}^{(a)}\Phi_{JS} \\ {}^{(a)}\Phi_{JR} \end{bmatrix} \begin{Bmatrix} {}^{(a)}p_{JS} \\ {}^{(a)}p_{JR} \end{Bmatrix} = [{}^{(b)}\Phi_J] \{ {}^{(b)}p \}. \quad (9)$$

It can be noticed from (9) that those independent modal terms $\{^{(a)}p_{JS}\}$ can be expressed as

$$\begin{aligned} \{^{(a)}p_{JS}\} &= -[^{(a)}\Phi_{JS}]^{-1} [^{(a)}\Phi_{JR}] \{^{(a)}p_{JR}\} \\ &\quad + [^{(a)}\Phi_{JS}]^{-1} [^{(b)}\Phi_J] \{^{(b)}p\} \end{aligned} \quad (10)$$

$$\{p\} = \begin{Bmatrix} ^{(a)}p \\ ^{(b)}p \end{Bmatrix} = \begin{Bmatrix} ^{(a)}p_{JS} \\ ^{(a)}p_{JR} \\ ^{(b)}p \end{Bmatrix} = [T] \{q\}, \quad (11)$$

in which

$$[T] = \begin{pmatrix} -[^{(a)}\Phi_{JS}]^{-1} [^{(a)}\Phi_{JR}] & [^{(a)}\Phi_{JS}]^{-1} [^{(b)}\Phi_J] \\ [I] & 0 \\ 0 & [I] \end{pmatrix} \quad (12)$$

$$\{q\} = \begin{Bmatrix} ^{(a)}p_{JR} \\ ^{(b)}p \end{Bmatrix}.$$

Matrix $[T]$ here can be considered as a transformation matrix for the second coordinate transformation, and $\{q\}$ is the generalized coordinate of the remaining DOFs in this coordinate.

2.3. Reconstructed Modal Equation. Since the boundary condition is assumed to be free for substructures a and b , the following modal equation can be obtained by simply putting their modal equations together:

$$\begin{aligned} \begin{Bmatrix} ^{(a)}\ddot{p} \\ ^{(b)}\ddot{p}_b \end{Bmatrix} + \begin{pmatrix} [^{(a)}\Omega] & 0 \\ 0 & [^{(b)}\Omega] \end{pmatrix} \begin{Bmatrix} ^{(a)}p \\ ^{(b)}p \end{Bmatrix} \\ = \begin{pmatrix} [^{(a)}\Phi_J]^T & 0 \\ 0 & [^{(b)}\Phi_J]^T \end{pmatrix} \begin{Bmatrix} ^{(a)}f_J \\ ^{(b)}f_J \end{Bmatrix}. \end{aligned} \quad (13)$$

By substituting the second coordinate transformation equation (11) and multiplying $[T]^T$ in both ends plus considering that the reaction forces are coupled in the interface nodes, one can reconstruct the system modal equation as

$$\begin{aligned} [M^*] \{\ddot{q}\} + [K^*] \{q\} \\ = [T]^T \begin{pmatrix} [^{(a)}\Phi_J]^T & 0 \\ 0 & [^{(b)}\Phi_J]^T \end{pmatrix} \begin{Bmatrix} ^{(a)}f_J \\ ^{(b)}f_J \end{Bmatrix} = 0 \end{aligned} \quad (14)$$

$$\{^{(a)}f_J\} + \{^{(b)}f_J\} = 0, \quad (15)$$

where

$$[M^*] = [T]^T [T] \quad [K^*] = [T]^T \text{diag} \left(^{(a)}\Omega, ^{(b)}\Omega \right) [T]. \quad (16)$$

By solving (16), the expression of eigenvalue and eigenvector in this coordinate can be obtained, by further using

(2) and (11) for inverse coordinate transformation and then comes the eigenvalue and eigenvector of the whole structure:

$$\{x\} = \begin{bmatrix} [^{(a)}\Phi] \\ [^{(b)}\Phi] \end{bmatrix} [T] \{q\}. \quad (17)$$

3. Modal Synthesis Based Substructure Damage Identification

3.1. Sensitivity Analysis. The dynamic response sensitivity-based model updating method is adopted here with

$$R_e - R_0 = S \{r_u - r_o\} \iff \Delta R = S|_{m \times n} \Delta r, \quad (18)$$

where Δr is the perturbation of the vector of structural elemental stiffness factors and ΔR is the changed structural responses due to damage. And S is the sensitivity matrix of the structural responses with respect to the stiffness factors.

Equation (18) implies that, when performing sensitivity analysis, the sensitivity matrix of the responses with respect to each elemental stiffness factor should be calculated on each time step. For structures with large DOFs, the calculation burden will be huge. Therefore, instead of calculating the sensitivity matrix in the whole structure, it is expected by introducing the substructure method; the calculation can be done in parallel in different substructure. Moreover, for civil structures, usually there are key parts or components which people may concern most. In such situation, one can assume that damage only occurs in certain substructures and there are non-zero values only for those corresponding terms in sensitivity matrix.

3.2. Derivatives of Eigenvalue with Substructure Method. The basic modal equation expressed as equation (14) is written as a truncated Taylor series

$$\frac{\partial (K^* - M^* \lambda_i)}{\partial r} \{q_i\} + (K^* - M^* \lambda_i) \frac{\partial \{q_i\}}{\partial r} = 0, \quad (19)$$

where the parameter r here still represents the changing factor of the whole structure, by multiply $\{q\}^T$ on both ends achieves

$$\{q_i\}^T \frac{\partial (K^* - M^* \lambda_i)}{\partial r} \{q_i\} + \{q_i\}^T (K^* - M^* \lambda_i) \frac{\partial \{q_i\}}{\partial r} = 0. \quad (20)$$

And because of the symmetry of $(K^* - M^* \lambda_i)$ and noticing $(K^* - M^* \lambda_i) \{q_i\} = 0$, the above equation can be simplified as

$$\{q_i\}^T \frac{\partial (K^* - M^* \lambda_i)}{\partial r} \{q_i\} = 0. \quad (21)$$

Then, with substitution of $[M^*]$ and $[K^*]$ into (21), it can be transformed to

$$\{q_i\}^T T^T \frac{\partial (\Omega_m^p - \lambda_i)}{\partial r} T \{q_i\} = 0. \quad (22)$$

Denoting $\{p_i\} = T\{q_i\}$, the above equation can be rewritten as

$$\{p_i\}^T \frac{\partial (\Omega_m^P - \lambda_i)}{\partial r} \{p_i\} = 0. \quad (23)$$

And the first-order derivative of the eigenvalue with respect to elemental parameter can be expressed as

$$\frac{\partial \lambda_i}{\partial r} = \{p_i\}^T \frac{\partial \Omega_m^P}{\partial r} \{p_i\}. \quad (24)$$

Since each substructure is independent, the derivative can be calculated solely in certain substructure which contains the element parameters; otherwise, the irrelevant terms should return a zero value. Consider

$$\begin{aligned} \frac{\partial \Omega_m^P}{\partial r} &= \begin{pmatrix} 0 & 0 & 0 \\ 0 & \frac{\partial \Omega_m^{(r)}}{\partial r} & 0 \\ 0 & 0 & 0 \end{pmatrix}, \\ \frac{\partial \Phi_m^P}{\partial r} &= \begin{pmatrix} 0 & 0 & 0 \\ 0 & \frac{\partial \Phi_m^{(r)}}{\partial r} & 0 \\ 0 & 0 & 0 \end{pmatrix}, \end{aligned} \quad (25)$$

in which Ω_m^P can be calculated by first normalizing the substructures' mass and stiffness matrix and then putting them into one diagonal matrix:

$$\begin{aligned} [\Phi^a]^T M^a [\Phi^a] &= I_{N^a}, & [\Phi^a]^T K^a [\Phi^a] &= \Omega^a \\ [\Phi^b]^T M^b [\Phi^b] &= I_{N^b}, & [\Phi^b]^T K^b [\Phi^b] &= \Omega^b \\ \Omega^P &= \begin{pmatrix} \Omega^a & 0 \\ 0 & \Omega^b \end{pmatrix}, & \Phi^P &= \begin{pmatrix} \Phi^a & 0 \\ 0 & \Phi^b \end{pmatrix}. \end{aligned} \quad (26)$$

By further applying modal truncation and sparse matrix storage in the above procedure, the system resource will be greatly saved during the construction of sensitivity matrix. Subscription m and r refer to the "master" and "residual," respectively. By putting the master or residual eigenvectors of the substructures together, one can get

$$\begin{aligned} \Omega_m^P &= \begin{pmatrix} \Omega_m^a & 0 \\ 0 & \Omega_m^b \end{pmatrix}, & \Omega_s^P &= \begin{pmatrix} \Omega_s^a & 0 \\ 0 & \Omega_s^b \end{pmatrix} \\ \Phi_m^P &= \begin{pmatrix} \Phi_m^a & 0 \\ 0 & \Phi_m^b \end{pmatrix}, & \Phi_s^P &= \begin{pmatrix} \Phi_s^a & 0 \\ 0 & \Phi_s^b \end{pmatrix}. \end{aligned} \quad (27)$$

3.3. Derivatives of Eigenvector with Substructure Method. By using free-interface modal synthesis method mentioned above, the i th eigenvector can be expressed as

$$\bar{\phi}_i = \Phi_m^P \{p_i\} = \Phi_m^P T \{q_i\}. \quad (28)$$

Differentiating this equation with respect to some elemental parameter r results in

$$\frac{\partial \bar{\phi}_i}{\partial r} = \frac{\partial \Phi_m^P}{\partial r} T \{q_i\} + \Phi_m^P T \left\{ \frac{\partial q_i}{\partial r} \right\}, \quad (29)$$

where $\partial \Phi_m^P / \partial r$ represents the derivative of master modes' eigenvector with respect to parameter r . It is noticed that the equation can be solved once $\{\partial q_i / \partial r\}$ was obtained.

Assume that

$$\left\{ \frac{\partial q_i}{\partial r} \right\} = \{v_i\} + c_i \{q_i\}. \quad (30)$$

For $\{v_i\}$, substituting (29) into (19) gives

$$(K^* - M^* \lambda_i) (\{v_i\} + c_i \{q_i\}) = - \frac{\partial (K^* - M^* \lambda_i)}{\partial r} \{q_i\}. \quad (31)$$

Noticing that $(K^* - M^* \lambda_i) \{q_i\} = 0$ and substituting (16) into the equation, (30) can be simplified as

$$X_i \{v_i\} = \{Y_i\}, \quad (32)$$

where

$$\begin{aligned} X_i &= (K^* - M^* \lambda_i) \\ \{Y_i\} &= -T^T \frac{\partial (\Omega_m^P - \lambda_i)}{\partial r} [T] \{q_i\} = -T^T \frac{\partial (\Omega_m^P - \lambda_i)}{\partial r} \{p_i\}. \end{aligned} \quad (33)$$

Considering that there are no duplicated frequencies, then the dimension of X_i is N_m^P and the rank of this matrix should be $N_m^P - 1$. Denoting k th term to be the largest term in $\{q_i\}$, by setting sum of the k th row and column into zero, as well as $Y_k = 0$, (31) becomes

$$\begin{bmatrix} X_{11} & 0 & X_{13} \\ 0 & 1 & 0 \\ X_{31} & 0 & X_{33} \end{bmatrix} \begin{Bmatrix} v_{i1} \\ v_{ik} \\ v_{i3} \end{Bmatrix} = \begin{Bmatrix} Y_{i1} \\ 0 \\ Y_{i3} \end{Bmatrix} \quad (34)$$

from which $\{v_i\}$ can be solved.

In order to solve c_i , the orthogonally of the eigenvector can be expressed as

$$\{p_i\}^T \{p_i\} = 1 \quad \{q_i\}^T T^T T \{q_i\} = 1. \quad (35)$$

Differentiating (34) with respect to r gives

$$\frac{\partial \{q_i\}^T}{\partial r} T^T T \{q_i\} + \{q_i\}^T T^T T \frac{\partial \{q_i\}}{\partial r} = 0. \quad (36)$$

Then, substitute (29) into the above equation,

$$(\{v_i\}^T + c_i \{q_i\}^T) T^T T \{q_i\} + \{q_i\}^T T^T T (\{v_i\} + c_i \{q_i\}) = 0. \quad (37)$$

And the factor c_i can be expressed as

$$c_i = -\frac{1}{2} (\{v_i\}^T T^T \{p_i\} + \{p_i\}^T T \{v_i\}). \quad (38)$$

Thus, the first-order derivative of $\{q_i\}$ with respect to r can be achieved as

$$\left\{ \frac{\partial q_i}{\partial r} \right\} = \{v_i\} - \frac{1}{2} (\{v_i\}^T T^T \{p_i\} + \{p_i\}^T T \{v_i\}) \{q_i\}. \quad (39)$$

Finally, the derivative of eigenvector with respect to elemental parameter r can be obtained through (29).

3.4. Iterative Damage Detection Procedure. Initially, it is assumed that the analytical finite element model is intact, while damage is simulated as a decreasing of elastic modulus in certain element. The damage detection iterative procedure aims to detect the damage location and extent through the convergence of eigenvalue and eigenvector.

Step 1. Acquire the dynamic responses of damaged structure and transform these responses into frequency domain.

Step 2. Set the target function which is to be minimized. Usually, the target function vector will be formed by the first few eigenvalues and eigenvector listed together, and then the root-mean-square (RMS) value of the vector is the target function to be minimized.

Step 3. Construct the sensitivity matrix through substructure modal synthesis approach. The derivative of the target function with respect to every elemental stiffness factor should be calculated. The ones with eigenvalue and eigenvector terms can be solved with (24) and (39), respectively. The feature of the proposed substructural approach is that when calculating the sensitivity matrix, only those substructures which contain the elemental parameter will have non-zero value and need to be calculated; that is, the calculation will be limited to a much reduced dimension.

Step 4. Solve the perturbation vector of elemental stiffness factors Δr from (18) with Least Squares Method or Tikhonov Regularization Technique.

Step 5. The elemental stiffness factors are iteratively updated with $r_{i+1} = r_i + \Delta r$ for the next iteration. Repeat Steps 2–5 until the convergence criterion is met to some level.

Step 6. Calculate the damage index which defines the damage extent of each element.

$$\text{SRF}_i = \frac{\Delta E_i}{E_i} = \frac{E_i^u - E_i^o}{E_i^u}. \quad (40)$$

4. Numerical Studies

4.1. Modal Synthesis on a Frame Structure. Due to the mode truncation, there will be errors while using the modal synthesis method mentioned above. Since it is not expected too much errors caused by the uncertainty of the system parameters, the accuracy of the modal synthesis method is first examined by a simple example. As shown in Figure 1, numerical studies on an 11-storey frame structure are performed to examine the relationship between the number of maintained modes and the accuracy of this method. The finite element model of the structure consists of 24 nodes and 33 planar elements. It is considered that each node has 3 DOFs and there are a total number of 66 DOFs for the whole structure. The first 8 natural frequencies are calculated as 1.0353, 3.3614, 4.3592, 6.3489, 7.0573, 10.147, 11.536, and 14.253 Hz. The frame is disassembled into two substructures with 6 DOFs on the interface.

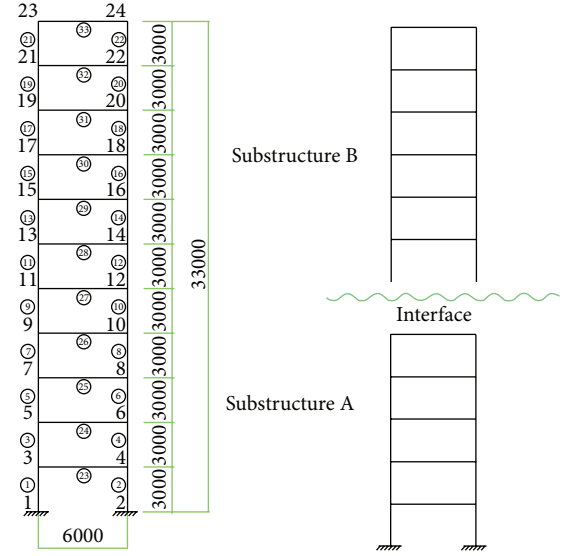


FIGURE 1: Eleven-storey frame structure (unit: mm).

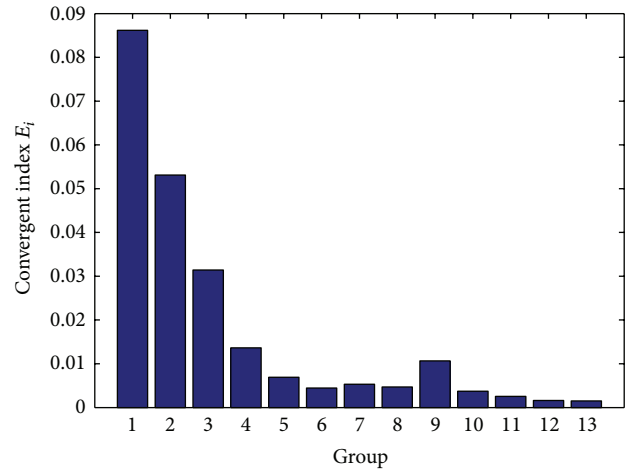


FIGURE 2: Convergent index E_i with increasing retained modes.

The retained modes of the two substructures begin with 6 and 12 in Group 1 and increase by 2 for the next calculation until all the modes are included. Based on the modal analysis, it is expected that there should be a convergent point for the desired accuracy along with the increasing retained modes of the substructures. In this example, the first 8 eigenvalues and eigenvectors are selected to be examined. In order to further discuss how many modes should be retained, the following convergence index E_i is defined. By gradually increasing the retained modes of the substructure, the sum of eigenvalues also increased, and here convergence index E_i is calculated

TABLE 1: Convergent index E_i with different retained modes.

Group	1	2	3	4	5	6	7	8	9	10
Retained modes										
a	6	8	10	12	14	16	18	20	22	24
b	12	14	16	18	20	22	24	26	28	30
C	26859	24728	24514	23767	23447	23285	23182	23060	22952	22711
$E (\times 10^{-3})$	86.2	53.1	31.4	13.6	6.9	4.4	5.3	4.7	10.6	3.7

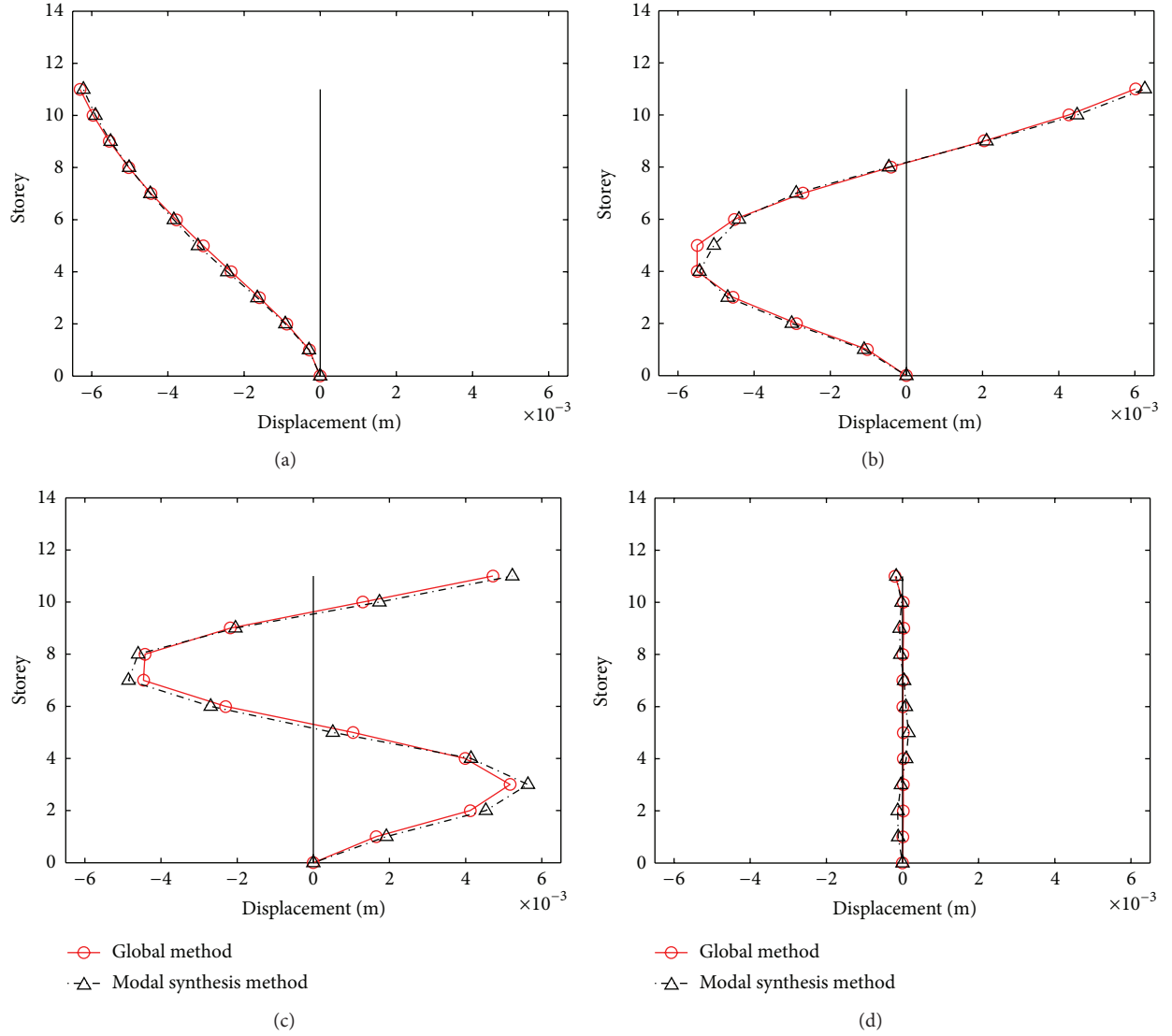


FIGURE 3: The first 4 mode shapes after modal synthesis (Group 4).

by how much percentage the sum of eigenvalues will change with the increasing retained modes:

$$E_i = \left| \frac{C_{i+1} - C_i}{C_{i+1}} \right| \quad (41)$$

$$C_i = \sum_{k=1}^n \omega_k^2.$$

C_i is the sum of eigenvalues after modal synthesis at the i th calculation and n is the first n modes to have certain accuracy.

The convergence index E_i with respect to the retained modes of the substructures is listed in Table 1, the reduction of E_i can be observed from Figure 2 clearly, and there is less convergence after Group 4 where 12 and 18 retained modes were included for substructures a and b . Table 2 further investigates the modal synthesis method

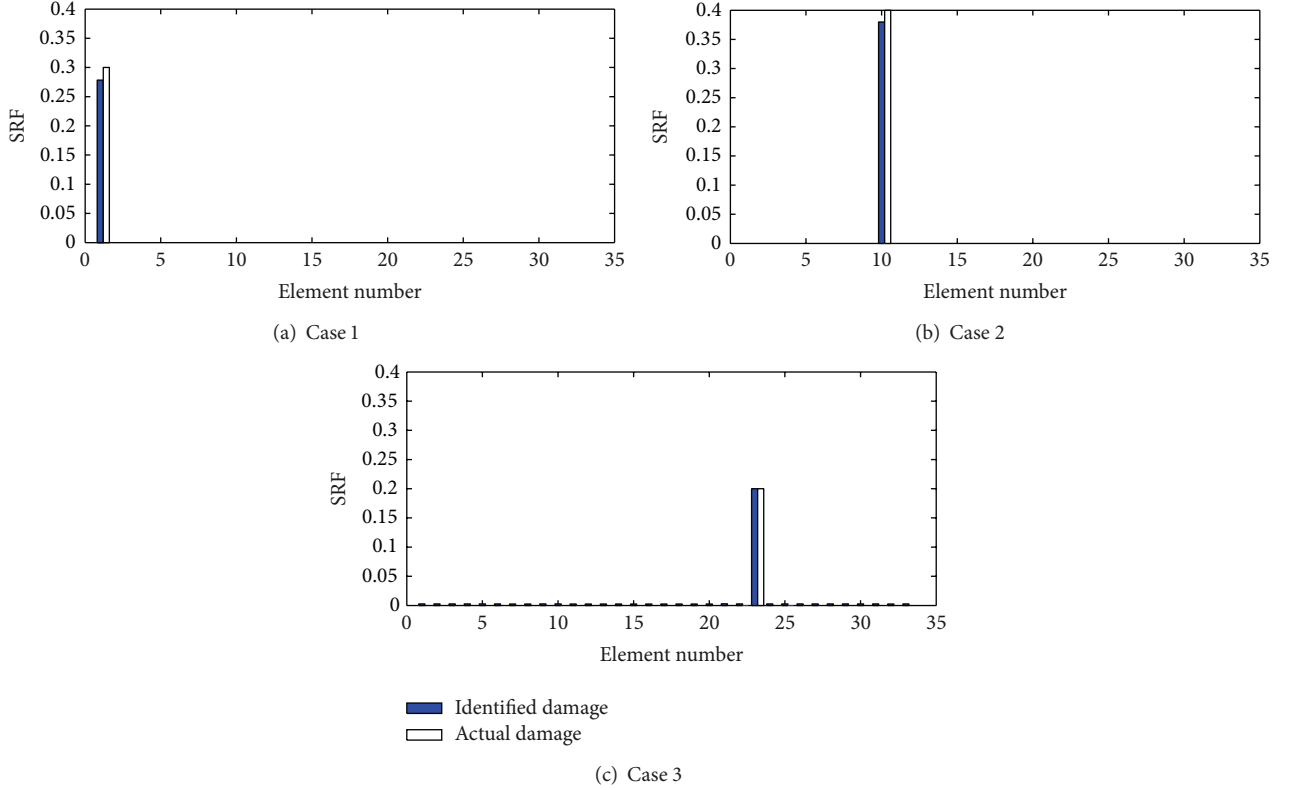


FIGURE 4: Damage detection results using free-interface modal synthesis based substructure sensitivity method.

accuracy of Group 4. It is obvious from the table that the differences of both frequencies and MAC are rather small. The first 8 mode shapes after modal synthesis of Group 4 are plotted in Figure 3.

4.2. Substructure Damage Detection on a Frame Structure. Usually, the experimental data collected by applying damages on some elements and the differences between the analytical and the experimental responses are calculated in target function and are to be minimized during the iteration procedure. For the example discussed in this paper, only the first 8 frequencies and mode shapes are included in the target function expressed as

$$\text{To minimize } \sum_{i=1}^n (w_i |f_i^e - f_i^a| + v_i |\Phi_i^e - \Phi_i^a|), \quad (42)$$

where the superscript “*e*” represents the true value, which means value from the damaged model, and “*a*” represents the analytical value. w_i and v_i are the weight factors applied to the i th frequency and eigenvector terms, respectively.

The whole structure is simply divided as 2 substructures. Meanwhile, the frequencies and mode shapes of the damaged model are first calculated from finite element model and assumed to be known as experimental data. And all the damages are assumed to be loss in the young’s modulus of

TABLE 2: Eigen errors on Group 4.

Modes	Expected frequency (Hz)	Analytical frequency (Hz)	Differences (%)	MAC (%)
1	1.035	1.052	1.6	100
2	3.361	3.44	2.4	99.4
3	4.359	4.512	3.5	99.5
4	6.349	6.477	2	96.4
5	7.057	7.356	4.2	95.9
6	10.147	10.546	3.9	95.5
7	11.536	11.719	1.6	97.6
8	14.253	14.709	3.2	97.1

some elements, and their damage extents are defined by SRF values:

$$\text{SRF}_i = \frac{\Delta E_i}{E_i} = \frac{E_i^u - E_i^o}{E_i^u}. \quad (43)$$

Three single damage cases are first studied, Case 1, Case 2, and Case 3; assumed elemental stiffness reduction happens on elements 1, 10, and 23 referring to Figure 1 by 30%, 40%, and 20%, respectively, while other elements remain unchanged. Figure 4 shows the damage detection results by the proposed free-interface modal synthesis based sensitivity method for the three cases, from which one can see that the proposed

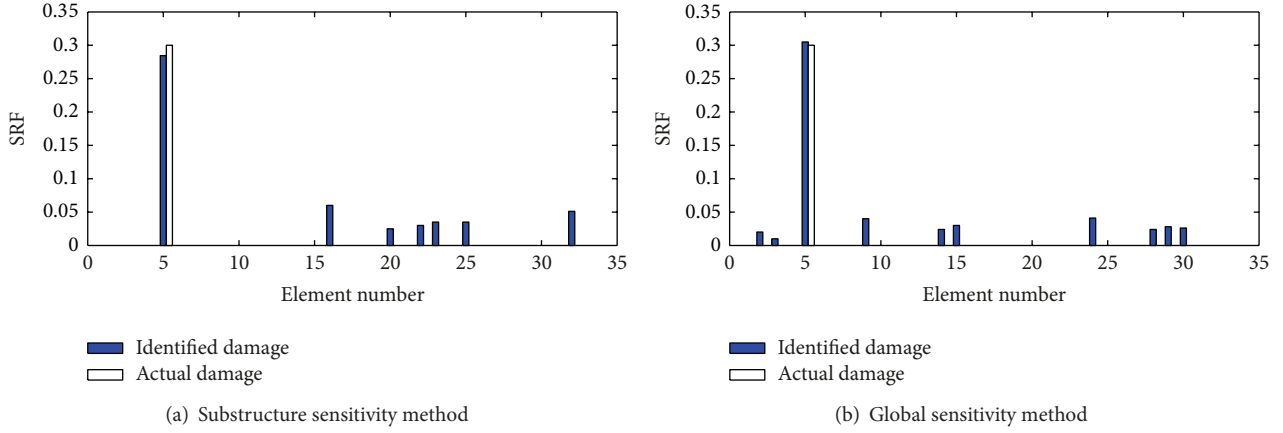


FIGURE 5: Damage detection results (Case 4).

method can detect the damage location perfectly. And the identified damage extents are very close to the true value. Noticing that, although in Case 1 several false detections are found in those undamaged elements, the maximum SRF for these false detection elements is below 0.05, which is ignorable compared to the real damage. It is believed that by optimal choosing the target function for different damage scenario can improve the damage identification results. Therefore, the feasibility of the proposed method can be verified.

4.3. Damage Detection Ability Compared with Traditional Sensitivity Method. In this session, in order to evaluate the detection effectiveness of the proposed method, more damage cases are chosen randomly, including single damage and multidamage cases. The damage detection results of the proposed substructure method are compared with those by traditional global sensitivity method. Three damage cases are listed in Table 3, in which Case 4 is a single damage case, while Cases 5 and 6 are multidamage cases.

For Case 4, both the global and the proposed substructure sensitivity method can detect the damage location and damage extent as well. As compared in Figure 5, for this damage scenario, the traditional sensitivity method will have better detection results. The proposed substructure method has several elements being falsely detected, and some of the SRF values are approximate to 0.1, which is larger than that of the global sensitivity method with maximum false detection value being 0.035. However, the comparison of the updated frequencies and mode shapes with true values listed in Table 4 shows little differences in both first ten frequencies and mode shapes, which proves the feasibility of the proposed method in model updating.

Further examining the convergent procedure, the SRF values of the proposed substructure on iterations 1, 3, 4, and 5 are graphed in Figure 6, from which one can see that the proposed method is able to locate the damage in the very beginning. And along with the convergence, approximate damage extent was found on iteration 4. As compared to the

TABLE 3: Damaged Cases 4, 5, and 6.

	Damage location	SRF
Case 4	Element 5	−30%
Case 5	Element 3 and 8	−30% and −20%
Case 6	Element 1, 2, and 7	−30%, −50%, and −20%

TABLE 4: Frequencies and mode shapes using the proposed substructure method.

Mode	Frequency			MAC (%)
	Experimental data (Hz)	Analytical data (Hz)	Difference (%)	
1	1.032	1.033	0.1	100
2	3.353	3.353	0	100
3	4.29	4.291	0.02	100
4	6.32	6.321	0.02	100
5	6.967	6.969	0.03	100
6	10.129	10.137	0.08	99.9
7	11.46	11.462	0.02	100
8	14.155	14.162	0.05	99.8
9	14.283	14.292	0.06	99.8
10	16.65	16.653	0.02	99.7

global method in Figure 7, where SRF values of iterations 1, 4, 9, and 10 are graphed, the damage location has not been found until iteration 10. As it comes to the damage extent referred to the convergent curves in Figure 8, the global sensitivity method will have a better convergent and a faster convergent rate in this case.

Case 5 is a multidamage case with two elements assumed to have stiffness reduction of 30% and 20%, respectively. Figure 9 compares the detection results of the two methods. Along with some elements being falsely identified with the maximum SRF less than 0.05, the proposed substructure method was able to identify the damage location. And the identified SRF values of the damaged elements are 28.0%

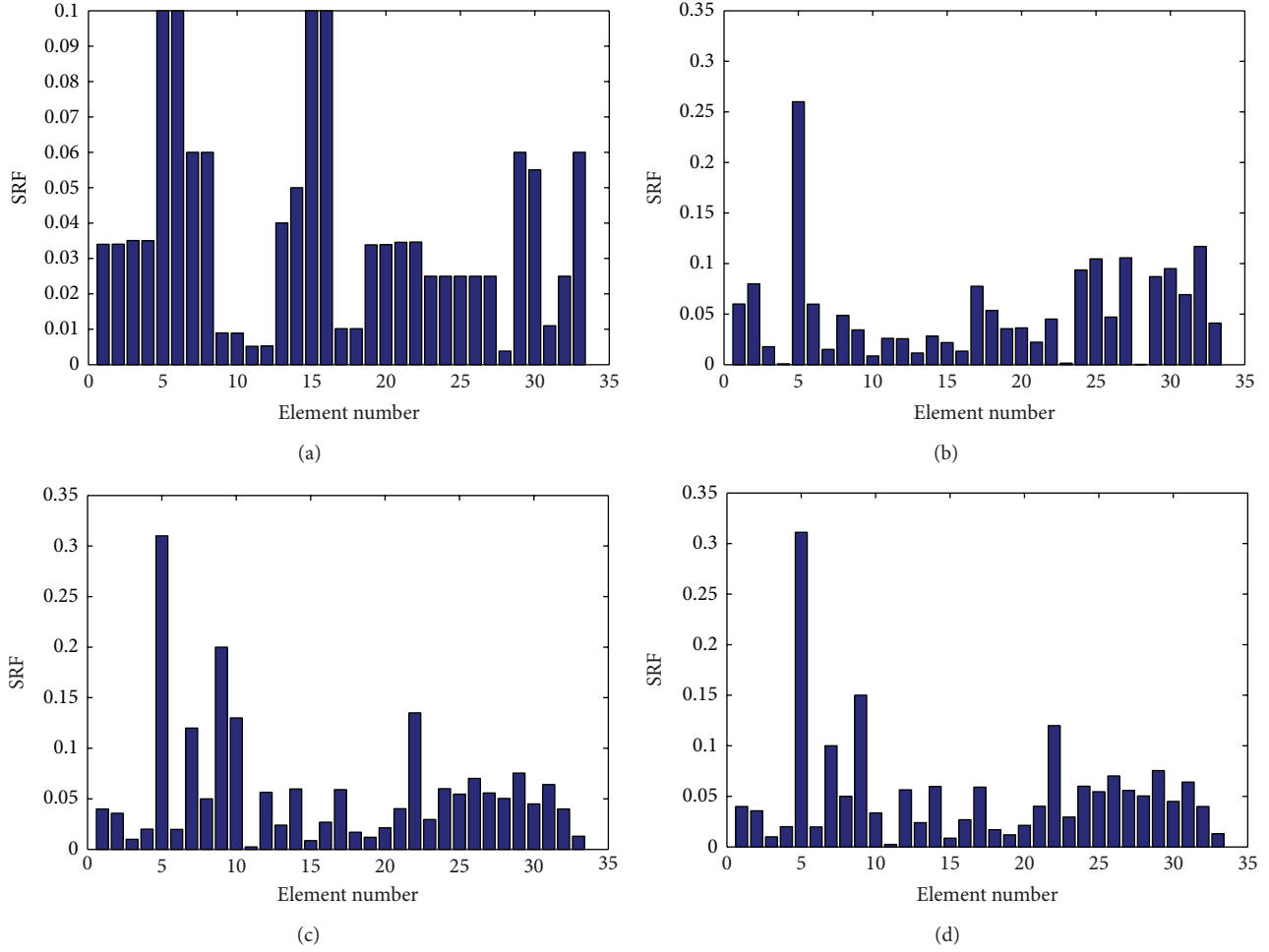


FIGURE 6: SRF values of substructure sensitivity method (iterations 1, 3, 4, and 5).

and 20.3%, which are very close to the true values. As for the global sensitivity method in this case, it fails to identify the damaged elements. Instead of elements 3 and 8, the global method has elements 4 and 7 to be the damaged elements. It is observed from the convergent curves (Figure 10) that the substructure sensitivity method gives a relatively smooth fluctuant and overall steady reduction convergent curve, while the global method gives a convergent curve with severe turbulence in this case. And it refuses to converge only after the value of the target function reaches to 3.3.

Figure 11 shows the identified results of Case 6 where 3 elements are assumed to have stiffness reduction by 30%, 50%, and 20%. The proposed substructure method identifies exact damage locations, and the identical SRF values for elements 1, 2, and 7 are 27.2%, 47.0%, and 18.1%, which are very similar to the preset values 30%, 50%, and 20%. Still there are some falsely identified values in some undamaged elements, but all these values are below 0.05. As for the traditional global method, it also detects the damage location correctly, and the identified SRF values are 33.1%, 49.1%, and 19.8%, which are also approached to the true value. However, compared to

the substructure results, the false identified problem is more serious. For example, the identified SRF value of element 14 is 11.9%.

5. Concluding Remarks

A free-interface modal synthesis method is applied to civil structures, and, by introducing to the sensitivity method, a free-interface modal synthesis based substructure sensitivity method is proposed for damage detection. The derivatives of eigenvalue and eigenvector with respect to elemental parameters are calculated with substructure approach and herein facilitate the calculation burden of sensitivity matrix.

The application of modal synthesis method and the effectiveness of the proposed substructure damage detection method were verified through a frame structure. As the mode truncation may bring errors to the identification procedure, a criterion for retaining mode numbers of substructure was first proposed. Although there is still some slight false identification, overall, the proposed substructure method was

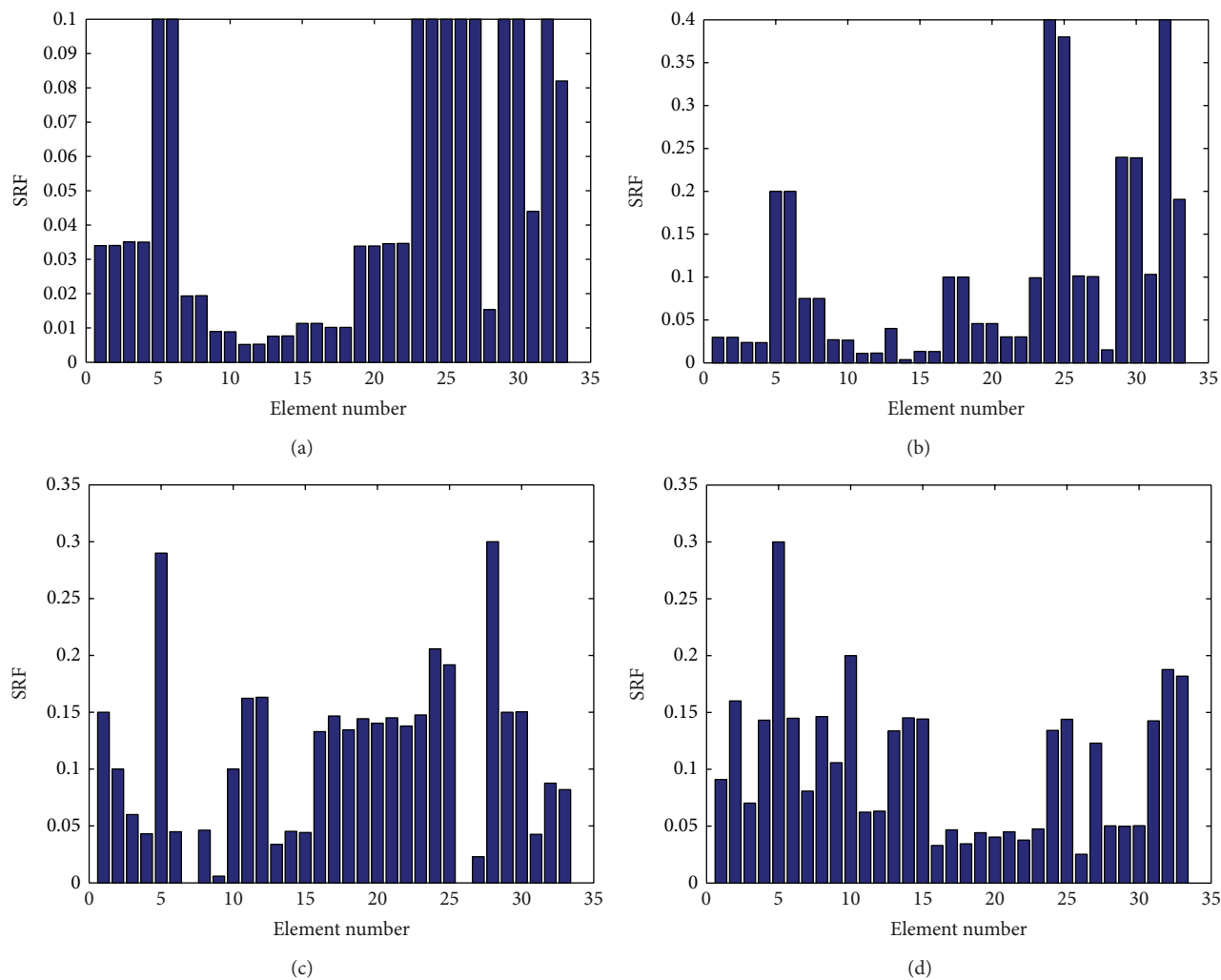


FIGURE 7: SRF values of global sensitivity method (iterations 1, 4, 9, and 10).

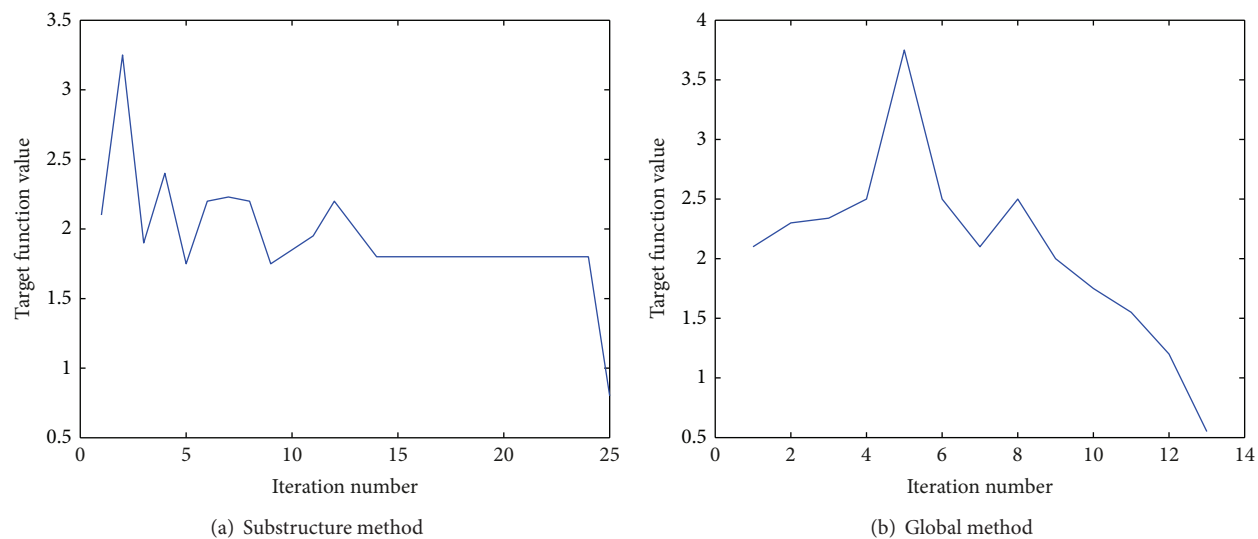


FIGURE 8: Convergent curves of Case 4.

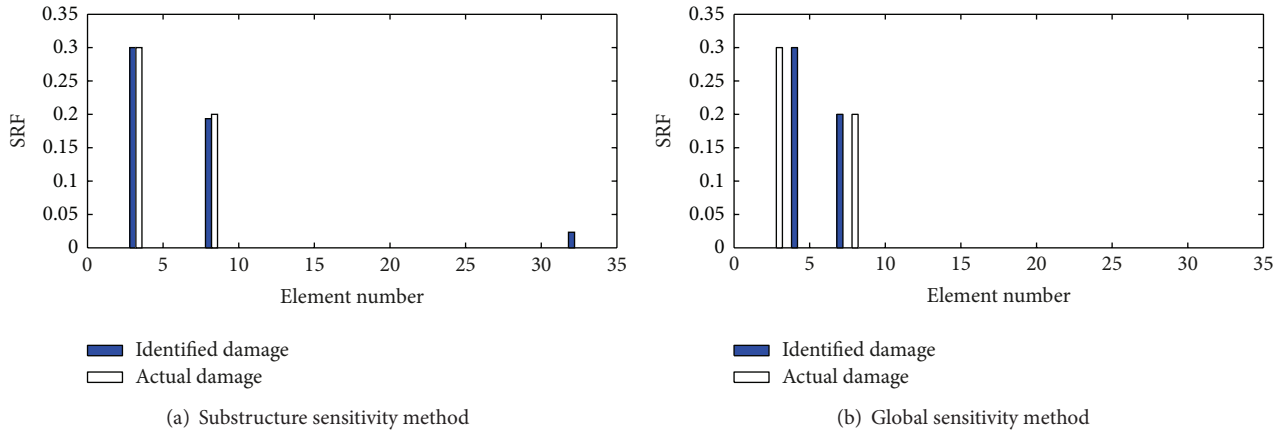


FIGURE 9: Damage detection results (Case 5).

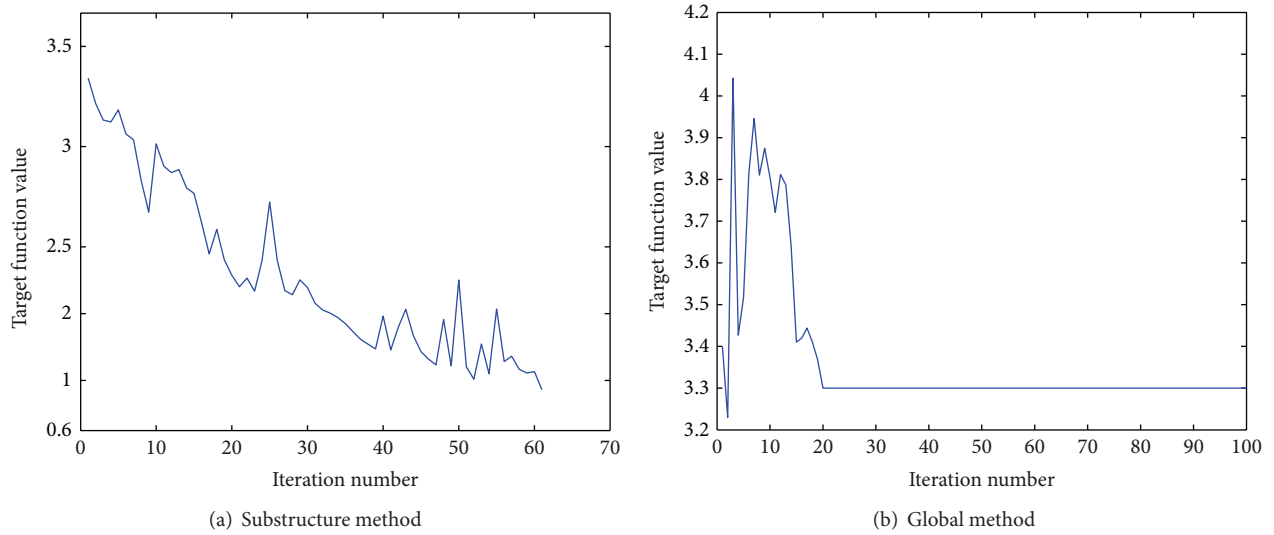


FIGURE 10: Convergent curves of Case 5.

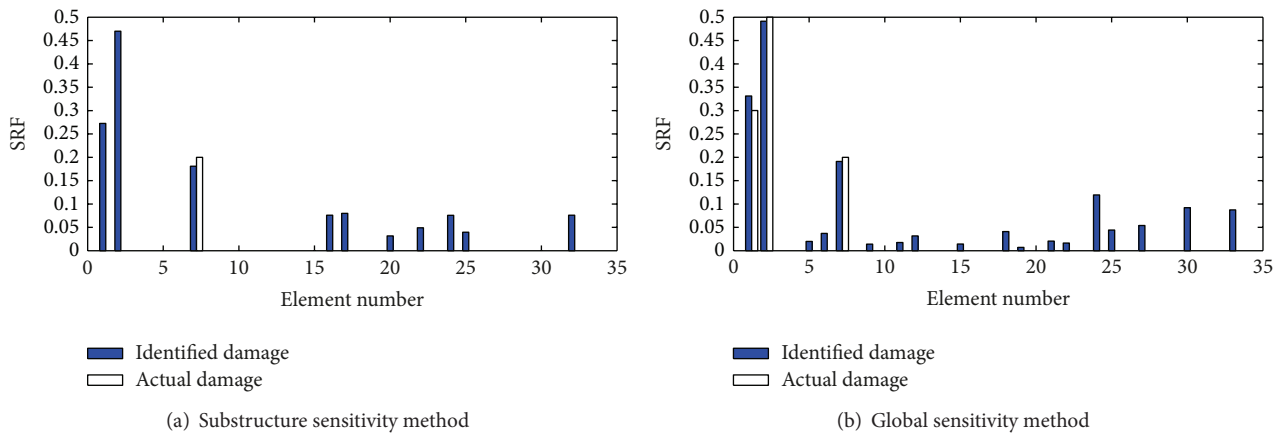


FIGURE 11: Damage detection results (Case 6).

able to identify the damage location as well as the damage extent correctly in both single- and multidamage scenarios. Compared to traditional global sensitivity method, the proposed substructure method has a better speed in detecting the damage location and is even more stable in multidamage cases. More importantly, different from global sensitivity method which takes the whole structure in calculating the sensitivity matrix in every step, the proposed substructure method will only need to calculate and update sensitivity matrix in certain substructure which contains the parameter. And the updating procedure is done within a relative small dimension. By doing so, the proposed substructure method will have fewer calculation and storage burden, and it will be an advantage on model updating efficiency.

Conflict of Interests

The authors declare that there is no conflict of interests regarding the publication of this paper.

Acknowledgments

The authors are grateful for financial support by National Natural Science Foundation of China (no. 51108089), Ph.D. Programs Foundation of Ministry of Education of China (no. 20113514120005), and National Natural Science Foundation of Fujian Province (no. 2011J05128).

References

- [1] Y. Xia, Y. Ni, P. Zhang, W. Liao, and J. Ko, "Stress development of a supertall structure during construction: Field monitoring and numerical analysis," *Computer-Aided Civil and Infrastructure Engineering*, vol. 26, no. 7, pp. 542–559, 2011.
- [2] W. H. Chen, Z. R. Lu, W. Lin et al., "Theoretical and experimental modal analysis of the Guangzhou New TV Tower," *Engineering Structures*, vol. 33, no. 12, pp. 3628–3646, 2011.
- [3] Y. Q. Ni, Y. Xia, W. Lin, W. H. Chen, and J. M. Ko, "SHM benchmark for high-rise structures: a reduced-order finite element model and field measurement data," *Smart Structures and Systems*, vol. 10, no. 4, pp. 411–426, 2012.
- [4] B. Chen, Y. L. Xu, and X. Zhao, "Integrated vibration control and health monitoring of building structures: a time-domain approach," *Smart Structures and Systems*, vol. 6, no. 7, pp. 811–833, 2010.
- [5] B. Chen, S. Zhao, and P. Li, "Application of Hilbert-Huang Transform in Structural Health Monitoring: A State-of-the-Art Review," *Mathematical Problems in Engineering*, Article ID 317954, ART. ID , 22 pages, 2014.
- [6] C. B. Yun, J. J. Lee, and K. Y. Koo, "Smart structure technologies for civil infrastructures in Korea: recent research and applications," *Structure and Infrastructure Engineering*, vol. 7, no. 9, pp. 673–688, 2011.
- [7] Y. Xia, Y. Ni, P. Zhang, W. Liao, and J. Ko, "Stress development of a supertall structure during construction: field monitoring and numerical analysis," *Computer-Aided Civil and Infrastructure Engineering*, vol. 26, no. 7, pp. 542–559, 2011.
- [8] Y. Fujino, D. M. Siringoringo, and M. Abe, "The needs for advanced sensor technologies in risk assessment of civil infrastructures," *Smart Structures and Systems*, vol. 5, no. 2, pp. 173–191, 2009.
- [9] J. M. Ko and Y. Q. Ni, "Technology developments in structural health monitoring of large-scale bridges," *Engineering Structures*, vol. 27, no. 12, pp. 1715–1725, 2005.
- [10] H. Li, T. Yi, M. Gu, and L. Huo, "Evaluation of earthquake-induced structural damages by wavelet transform," *Progress in Natural Science*, vol. 19, no. 4, pp. 461–470, 2009.
- [11] T. H. Yi, H. N. Li, and H. M. Sun, "Multi-stage structural damage diagnosis method based on "energy-damage" theory," *Smart Structures and Systems*, vol. 12, no. 3–4, pp. 345–361, 2013.
- [12] B. Chen, Z. W. Chen, G. J. Wang, and P. X. Wei, "Damage detection on sudden stiffness reduction based on discrete wavelet transform," *The Scientific World Journal*, vol. 2014, Article ID 807620, 16 pages, 2014.
- [13] B. Jaishi and W. X. Ren, "Structural finite element model updating using ambient vibration test results," *Journal of Structural Engineering*, vol. 131, no. 4, pp. 617–628, 2005.
- [14] T. Yi, H. Li, and M. Gu, "Optimal sensor placement for structural health monitoring based on multiple optimization strategies," *Structural Design of Tall and Special Buildings*, vol. 20, no. 7, pp. 881–900, 2011.
- [15] Y. Xia, H. Hao, A. J. Deeks, and X. Zhu, "Condition assessment of shear connectors in slab-girder bridges via vibration measurements," *Journal of Bridge Engineering*, vol. 13, no. 1, pp. 43–54, 2008.
- [16] E. Görl and M. Link, "Damage identification using changes of eigenfrequencies and mode shapes," *Mechanical Systems and Signal Processing*, vol. 17, no. 1, pp. 103–110, 2003.
- [17] Z. R. Lu and S. S. Law, "Features of dynamic response sensitivity and its application in damage detection," *Journal of Sound and Vibration*, vol. 303, no. 1–2, pp. 305–329, 2007.
- [18] S. S. Law, K. Zhang, and Z. D. Duan, "Structural damage detection from coupling forces between substructures under support excitation," *Engineering Structures*, vol. 32, no. 8, pp. 2221–2228, 2010.
- [19] S. S. Law and J. Li, "Updating the reliability of a concrete bridge structure based on condition assessment with uncertainties," *Engineering Structures*, vol. 32, no. 1, pp. 286–296, 2010.
- [20] H. Chen and N. Bicanic, "Assessment of damage in continuum structures based on incomplete modal information," *Computers and Structures*, vol. 74, no. 5, pp. 559–570, 2000.
- [21] S. Živanović, A. Pavic, and P. Reynolds, "Finite element modelling and updating of a lively footbridge: the complete process," *Journal of Sound and Vibration*, vol. 301, no. 1–2, pp. 126–145, 2007.
- [22] S. Weng, Y. Xia, Y. Xu, X. Zhou, and H. Zhu, "Improved substructuring method for eigensolutions of large-scale structures," *Journal of Sound and Vibration*, vol. 323, no. 3–5, pp. 718–736, 2009.
- [23] G. Kron, *Diakoptics: The Piecewise Solution of Large-Scale Systems*, Macdonald and Co., London, UK, 1963.
- [24] J. Li, S. S. Law, and H. Hao, "Improved damage identification in bridge structures subject to moving loads: numerical and experimental studies," *International Journal of Mechanical Sciences*, vol. 74, pp. 99–111, 2013.
- [25] J. Li, S. S. Law, and Y. Ding, "Substructure damage identification based on response reconstruction in frequency domain and model updating," *Engineering Structures*, vol. 41, pp. 270–284, 2012.

- [26] J. Li and S. S. Law, "Substructural damage detection with incomplete information of the structure," *Journal of Applied Mechanics*, vol. 79, no. 4, Article ID 041003, 2012.
- [27] J. Li and S. S. Law, "Substructural response reconstruction in wavelet domain," *Journal of Applied Mechanics*, vol. 78, no. 4, Article ID 041010, 10 pages, 2011.
- [28] S. Weng, Y. Xia, Y. L. Xu, and H. P. Zhu, "Substructure based approach to finite element model updating," *Computers and Structures*, vol. 89, no. 9-10, pp. 772–782, 2011.
- [29] S. Weng, Y. Xia, X. Zhou, Y. Xu, and H. Zhu, "Inverse substructure method for model updating of structures," *Journal of Sound and Vibration*, vol. 331, no. 25, pp. 5449–5468, 2012.